

NASA CONTRACTOR
REPORT

NASA CR-179219

RESEARCH REPORTS - 1987 NASA/ASEE SUMMER FACULTY
FELLOWSHIP PROGRAM

The University of Alabama in Huntsville
Huntsville, Alabama
and
The University of Alabama
Tuscaloosa, Alabama

November 1987

Final Report

Prepared for
NASA, George C. Marshall Space Flight Center
Marshall Space Flight Center, Alabama 35812

{NASA-CR-179219) RESEARCH REPORTS: 1987
NASA/ASEE SUMMER FACULTY FELLOWSHIP PROGRAM
(NASA) 810 p CSCL 20C

N88-15601
--THRU--
N88-15636
Unclass

G3/70 0116702

TECHNICAL REPORT STANDARD TITLE PAGE

1. REPORT NO. NASA CR-179219		2. GOVERNMENT ACCESSION NO.		3. RECIPIENT'S CATALOG NO.	
4. TITLE AND SUBTITLE Research Reports - 1987 NASA/ASEE Summer Faculty Fellowship Program				5. REPORT DATE November 1987	
				6. PERFORMING ORGANIZATION CODE	
7. AUTHOR(S) Editors: G. Karr, E. Cothran, and M. Freeman				8. PERFORMING ORGANIZATION REPORT #	
9. PERFORMING ORGANIZATION NAME AND ADDRESS The University of Alabama in Huntsville and The University of Alabama, Tuscaloosa, AL				10. WORK UNIT NO.	
				11. CONTRACT OR GRANT NO. NGT 01-008-021	
12. SPONSORING AGENCY NAME AND ADDRESS National Aeronautics and Space Administration Washington, D.C. 20526				13. TYPE OF REPORT & PERIOD COVERED Contractor Report	
				14. SPONSORING AGENCY CODE	
15. SUPPLEMENTARY NOTES					
16. ABSTRACT <p>For the twenty-third consecutive year, a NASA/ASEE Summer Faculty Fellowship Program was conducted at the Marshall Space Flight Center (MSFC). The program was conducted by the University of Alabama in Huntsville and MSFC during the period June 1, 1987 and August 7, 1987. Operated under the auspices of the American Society for Engineering Education, the MSFC program, as well as those at other NASA Centers, was sponsored by the Office of University Affairs, NASA Headquarters, Washington, D.C. The basic objectives of the programs, which are in the twenty-fourth year of operation nationally, are (1) to further the professional knowledge of qualified engineering and science faculty members; (2) to stimulate an exchange of ideas between participants and NASA; (3) to enrich and refresh the research and teaching activities of the participants' institutions; and (4) to contribute to the research objectives of the NASA Centers.</p> <p>The Faculty Fellows spent ten weeks at MSFC engaged in a research project compatible with their interests and background and worked in collaboration with a NASA/MSFC colleague. This document is a compilation of Fellows' reports on their research during the summer of 1987. The University of Alabama in Huntsville Report No. 622 presents the Co-Directors' report on the administrative operations of the program. Further information can be obtained by contacting any of the editors.</p>					
17. KEY WORDS Doppler Lidar, Risk Analysis, Spacelink, Fault Diagnosis, Satellite Drag, Holography, Infrared Emission, Power Controllers, Pattern Recognition, AMPS, Propulsion, Atomic Oxygen, TAE, Crystal Growth, Polymer Coatings, MOS Solar Cells, TAE, Crystal Growth, Polymer Coatings,			18. DISTRIBUTION STATEMENT 17 continued - MOS Solar Cells, ADA, SSME, Hypervelocity Impact, Tether, Plasma ARC Welds. Unclassified-Unlimited		
19. SECURITY CLASSIF. (of this report) Unclassified		20. SECURITY CLASSIF. (of this page) Unclassified		21. NO. OF PAGES 850	
				22. PRICE NTIS	

RESEARCH REPORTS

1987 NASA/ASEE SUMMER FACULTY FELLOWSHIP PROGRAM

George C. Marshall Space Flight Center
The University of Alabama in Huntsville

and

The University of Alabama

EDITORS:

Dr. Gerald R. Karr
Chairman of Mechanical Engineering
The University of Alabama in Huntsville

Ms. Ernestine K. Cothran
Assistant for University Relations, Executive Staff
Marshall Space Flight Center

Dr. L. Michael Freeman
Assistant Professor of Aerospace Engineering
The University of Alabama

NASA CR - 179219

PREFACE

This document is a collection of technical reports on research conducted by the participants in the 1987 NASA/ASEE Summer Faculty Fellowship Program at Marshall Space Flight Center (MSFC). This was the twenty-third consecutive year the program has been conducted at MSFC. The 1987 program was administered by the University of Alabama in Huntsville (UAH) in cooperation with MSFC and the University of Alabama (UA). The program was operated under the auspices of the American Society for Engineering Education (ASEE) with sponsorship and funding from the Office of External Relations, NASA Headquarters, Washington, D.C. The MSFC program was one of eight such Aeronautics and Space Research Programs funded by NASA Headquarters in 1987. Similar programs were conducted at seven other NASA centers. The basic common objectives of the NASA/ASEE Summer Faculty Fellowship Program are:

- a. To further the professional knowledge of qualified engineering and science faculty members;
- b. To stimulate an exchange of ideas between participants and NASA;
- c. To enrich and refresh the research and teaching activities of participants' institutions; and,
- d. To contribute to the research objectives of the NASA centers.

The MSFC Faculty Fellows spent 10 weeks (June 1 through August 7, 1987) working with NASA scientists and engineers on research of mutual interest to the University faculty member and the NASA colleague. The editors of this document were responsible for selecting appropriately qualified faculty to address some of the many problems of current interest to NASA/MSFC. A separate document (UAH Report No. 622, September 1987) reports on the administrative aspects of the 1987 program. This document contains the technical reports on research performed by the individual 1987 participants. The NASA/ASEE program is basically a two-year program to allow indepth research by the university faculty member. In some cases, a faculty member has developed a close working relationship with a particular NASA group that has provided funding beyond the two-year limit. The reports are arranged in alphabetical order.

TABLE OF CONTENTS

I.	Anderson, Richard:	"Problems and Possible Solutions Involved in Hard Target Calibration of Coherent Doppler Lidar" 51
II.	Baker, Stephen D.:	"Some Considerations on Measuring the Newtonian Gravitational Constant G in an Orbiting Laboratory"
III.	Batson, Robert G.:	"Risk Analysis Methodology Survey"
IV.	Blake, Jean A.:	"Compilation and Development of K-6 Aerospace Materials for Implementation in NASA Spacelink Electronic Information System"
V.	Bosworth, Edward., Jr.:	"Investigation of Candidate Data Structures and Search Algorithms to Support a Knowledge Based Fault Diagnosis System"
VI.	Bower, Mark:	"Investigation of Low Velocity Impact Damage on Filamentary Composite Materials"
VII.	Bozeman, Robert E.:	"Investigation of the Feasibility of an Analytical Method of Accounting for the Effects of Atmospheric Drag on Satellite Motion"
VIII.	Brooks, Howard L.:	"Resolution of Holograms Produced by the Fluid Experiment System and the Holography Ground System"
IX.	Bykat, Alex:	"Enhancement of Computer System for Applications Software Branch"
X.	Byrd, Gene G.:	"Infrared Emission and Tidal Interactions of Spiral Galaxies"

- | | | |
|--------|-----------------------|--|
| XI. | Callis, Charles P.: | "Evaluation of High-Voltage, High-Power, Solid-State Remote Power Controllers for AMPS" |
| XII. | Carroll, Chester: | "Computer Architectures for the Real-Time Environment" |
| XIII. | Chauhan, Rajinder: | "Verification of Fantastic Integrated Code" |
| XIV. | Choudry, Amar: | "Pattern Recognition Techniques for Failure Trend Detection in SSME Ground Tests" |
| XV. | Floyd, Stephen A.: | "Microprocessor Control and Networking for the AMPS Breadboard" |
| XVI. | Ford, Douglas: | "Equilibrium Retention in the Nozzle of Oxygen Hydrogen Propulsion Systems" |
| XVII. | Fromhold, Albert T.: | "Atomic Oxygen Effects on Metals" |
| XVIII. | Gill, Esther | "The Feasibility of Using TAE as the UIL for the Space Station and for Other Internal NASA Tasks and Projects" |
| XIX. | Han, Samuel Sang-Moo: | "A Numerical Study of Transient Heat and Mass Transfer in Crystal Growth" |
| XX. | Harris, Milton: | "Use of Hydrophilic Polymer Coatings for Control of Electroosmosis and Protein Adsorption" |
| XXI. | Ho, Fat Duen: | "Further Study of Inversion Layer MOS Solar Cells" |
| XXII. | Knoebel, Arthur: | "Can Space Station Software be Specified Through ADA?" |

- XXIII. McDonald, Gary H: "The Determination of Equivalent Bearing Loading for the BSMT that Simulate SSME High Pressure Oxidizer Turbopump Conditions using the Shaberth/Sinda Computer Programs"
- XXIV. McGuire, Stephen C.: "Analysis of Relativistic Nucleus-Nucleus Interactions in Emulsion Chambers"
- XXV. Morrobel-Sosa, Anny: "Raman Spectroscopic Investigations of Hg-Cd-Te Melts"
- XXVI. Parker, Joey K.: "Computer-aided Analysis for the Mechanics of Granular Materials (MGM) Experiment, Part 2"
- XXVII. Patterson, James D.: "Improving the Method of Calculating Electronic Properties of Narrow Bandgap Semiconductors"
- XXVIII. Prince, Mary Ellen: "Expert System Technology"
- XXIX. Schonberg, William P.: "An Investigation of Oblique Hypervelocity Impact"
- XXX. Springer, William T.: "Evaluate the Application of Modal Test and Analysis Processes to Structural Fault Detection in MSFC-STs Project Elements"
- XXXI. Swenson, Frank R.: "Tether Elevator Crawler Systems (TECS)"
- XXXII. Temple, Enoch C.: "Propulsion Estimation Techniques"
- XXXIII. Tucker, Dennis S.: "The Development of Test Methodology for Testing Glassy Materials"

- XXXIV. Walsh, Daniel W.: "Examination of the Physical Processes Associated with the Keyhole Region of Variable Polarity Plasma Arc Welds in Aluminum Alloy 2219"
- XXXV. Yeager, Dorian P.: "Expert System Development for Commonality Analysis in Space Programs"
- XXXVI. Zalik, Robert A.: "The Jeffcott Equations in Nonlinear Rotordynamics"

N88-15602

51-36

116703

27P.

1987

NASA/ASEE SUMMER FACULTY RESEARCH FELLOWSHIP PROGRAM

MARSHALL SPACE FLIGHT CENTER
THE UNIVERSITY OF ALABAMA IN HUNTSVILLE

PROBLEMS AND POSSIBLE SOLUTIONS INVOLVED IN HARD TARGET
CALIBRATION OF COHERENT DOPPLER LIDAR

Prepared By: Richard Anderson
Academic Rank: Professor
University and Department: University of Missouri-
Rolla
Physics

NASA/MSFC:

Laboratory: Information and Electronic
Systems Laboratory
Division: Guidance, Control, and
Optical Systems
Branch: Optical Systems

NASA Colleagues:

James Bilbro
and
William Jones

Date:

August 14, 1987

Contract No:

The University of Alabama
in Huntsville
NGT-01-008-021

PROBLEMS AND POSSIBLE SOLUTIONS INVOLVED IN HARD TARGET CALIBRATION OF COHERENT DOPPLER LIDAR

by

Richard Anderson
Professor of Physics
University of Missouri-Rolla
Rolla, Missouri

ABSTRACT

In this paper the whole field of radiometry is analyzed in light of coherence for our surfaces are irradiated with coherent, polarized light. Definitions of some concepts had to be modified. In light of these modifications the problems in calibration suggested by Kavaya were analyzed and solutions suggested. The most important task is to develop hard targets that exhibit minimal specular reflection (mirror-like and retroreflection) and follows closely a "Lambertian" scattering curve. Bistable reflectometer experiments and integrating sphere measurements should be used to optically characterize the target. Optical and electron microscopy will be used to physically characterize the targets. Since no one is measuring the BRDF matrix, this capability must be developed for preferably both bistatic and monostatic reflectometer measurements. The equipment is expensive and must be developed. If one can prove for a diffuse scatterer that the BRDF matrix is diagonal, the calibration is simplified.

ACKNOWLEDGEMENTS

I am honored to be selected by James Bilbro and William Jones to participate in the Summer Faculty Fellowship Program. I appreciate the opportunity to work on this project for it expands my experience base in optics and this is helpful in both research and teaching. I wish to thank Steve Johnson for answering my question about the laboratory. I also must thank Jack Chambers at II-VI who supplied valuable data on CdS used to construct usual quarter wave plates.

LIST OF FIGURES

<u>Figure Number</u>	<u>Title</u>	<u>Page</u>
1	Fresnal rhomb	3
2	Dual Fresnel rhomb	14
3	Input angle variation	15

LIST OF TABLES

<u>Table Number</u>	<u>Title</u>	<u>Page</u>
1	Index of refraction of ZnSe versus wavelength	4
2	Deviation of the phase with angles above and below the normal to the input face of the rhomb	16
3	Ordinary and extraordinary indices of refraction for CdS	20
4	Deviation of phase angle for a 10.591 μm CO ₂ laser line quarter waveplate at other CO ₂ wavelengths	21

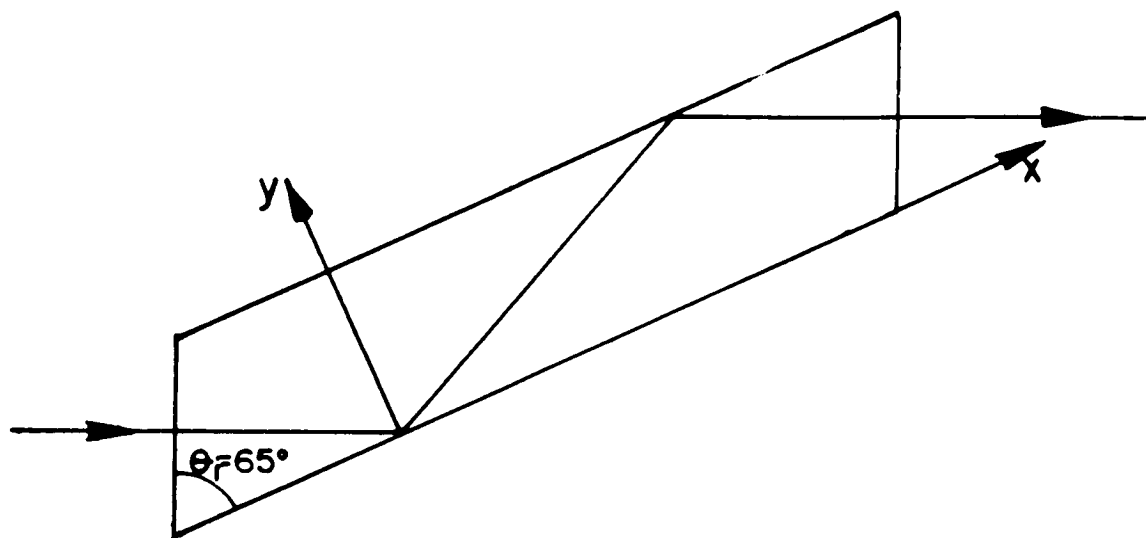
INTRODUCTION

The usual quarter waveplate for the 90-11 μm CO_2 laser emission region is made of CdS and since its ordinary and extraordinary indices of refraction vary over this spectral region, it is necessary to construct a quarter waveplate for each laser line. These devices are custom made and they are very expensive. As a result, in order to produce and analyze circular polarized light it has been suggested that a Fresnel rhomb¹ be used in the place of the usual quarter waveplate. In this paper the phase variation of a 10.6 μm quarter waveplate will be evaluated when it is used at other wavelengths than the designed 10.6 μm . Also the effects of having a beam strike the quarter waveplate at angles between 0-5° at 10.6 μm will be evaluated.

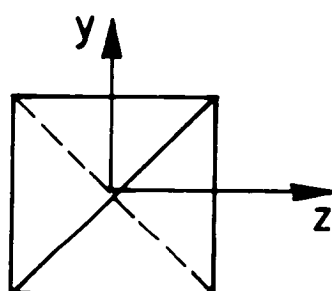
By using a linear polarizer and a ZnSe Fresnel rhomb it is possible to produce right and left hand circular polarized light and analyze this light. The Fresnel rhomb is sketched in Figure 1 with the appropriate angles indicated.

ZnSe has a nearly constant index of refraction over the 9-11 μm region of the CO_2 laser, so the rhomb exhibits no chromatic effects in this spectral region. The index of refraction of ZnSe is given in Table 1. These values are crude but they will indicate accurately enough the phase angle variation of the rhomb. If the rhomb is cut at the proper angle θ_1 and light is polarized along a face diagonal and is incident normally on the entrance face, it is possible to have the light internally reflected twice

with a phase change of $\pm 45^\circ$ between the electric field components parallel to and perpendicular to the plane of incidence. As a result, the rhomb introduces a phase change of $\pm 90^\circ$ between the field components and since the two field components have equal amplitude, circular polarized light results.



Side View
(a)



End View
(b)

FIGURE 1 Fresnel rhomb

Table 1. Index of refraction of ZnSe versus wavelength²

Wavelength μm	Index of refraction n
2.75	2.44
5.00	2.43
7.50	2.42
9.50	2.41
11.0	2.40
12.5	2.39
13.5	2.38
15.0	2.37
16.0	2.36
16.9	2.35
17.8	2.34
18.5	2.33
19.3	2.32
20.0	2.31

OBJECTIVES

The objectives of this research will be to develop and determine the operational characteristics of the Fresnel rhomb.

1. The theory of operation of the rhomb is developed.
2. The phase angle variation with input angle will be examined.
3. The change in phase angle of a 10.6 μm quarter waveplate at various other CO_2 laser lines will be calculated.

THEORY

The incident beam can be divided into two field components as indicated in the above discussion above when the incident beam is incident along the diagonal to the crystal ($\pm 45^\circ$). The light enters the end face of the crystal normal to the surface and it undergoes two internal reflections before it re-emerges parallel to its incident direction, but the beam is laterally displaced. At each internal reflection the reflection and transmission Fresnel coefficients are

$$r_{\parallel} = \frac{\left[n_t \cos \theta_i - n_i \cos \theta_t \right]}{\left[n_i \cos \theta_t + n_t \cos \theta_i \right]}$$
$$t_{\parallel} = \frac{2 n_i \cos \theta_i}{\left[n_i \cos \theta_t + n_t \cos \theta_i \right]} \quad (1)$$

$$r_{\perp} = \frac{\left[n_i \cos \theta_i - n_t \cos \theta_t \right]}{\left[n_i \cos \theta_i + n_t \cos \theta_t \right]}$$

and

$$t_{\perp} = \frac{\left[2 n_i \cos \theta_i \right]}{\left[n_i \cos \theta_i + n_t \cos \theta_t \right]}$$

where in our case $n_t = 1$ and $n_i = n_{\text{ZnSe}} = n = 2.40$.

Now for ZnSe the critical angle becomes $\sin \theta_c = 1/2.40$ and $\theta_c = 24.6^\circ$. This means that internal reflection will occur for a crystal cut with the small corner angle at an angle greater than $\theta_i > 24.6^\circ$. This does not tell us the phase shift that occurs on each internal reflection. It will be assumed that $\theta_i > \theta_c$ and $\sin \theta_i > 1/n$. Now $\cos \theta_t = [1 - (\sin \theta_i)^2]^{1/2}$ and from Snell's law $\cos \theta_t = [1 - (n \sin \theta_i)^2]^{1/2}$. Now since $\sin \theta_i > 1/n$, the $\cos \theta_t$ is imaginary or

$$\cos \theta_t = j n \left[\sin^2 \theta_i - 1/n^2 \right]^{1/2} \quad (2)$$

The Fresnel coefficient becomes

$$r_{||} = \frac{\left[\cos \theta_i - j n^2 \left(\sin^2 \theta_i - 1/n^2 \right)^{1/2} \right]}{\left[\cos \theta_i + j n^2 \left(\sin^2 \theta_i - 1/n^2 \right)^{1/2} \right]}$$

$$= \exp - \left[2j \delta_{||} \right] , \quad (3)$$

where the phase shift on reflection is

$$\tan \delta_{||} = \frac{n^2 \left(\sin^2 \theta_i - 1/n^2 \right)^{1/2}}{\cos \theta_i} \quad (4)$$

and

$$r_{\perp} = \frac{\left[n \cos \theta_i - j n \left(\sin^2 \theta_i - 1/n^2 \right)^{1/2} \right]}{\left[n \cos \theta_i + j n \left(\sin^2 \theta_i - 1/n^2 \right)^{1/2} \right]}$$

$$= \exp - \left[2j \delta_{\perp} \right] , \quad (5)$$

where

$$\tan \delta_{\perp} = \frac{[\sin^2 \theta_1 - 1/n^2]^{2/2}}{\cos \theta_1} \quad (6)$$

The amplitude of the incident waves are equal and each is represented by an equation of the form

$$E_1 = A_1 \exp j [\omega t - k \{y \cos \theta_1 + z \sin \theta_1\}] \quad (7)$$

The two reflected waves have amplitudes

$$E_{r\parallel} = r_{\parallel} E_1 = A_1 \exp j [\omega t - k \{y \cos \theta_1 + z \sin \theta_1\} - 2 \delta_{\parallel}]$$

(8)

and

$$E_{r\perp} = r_{\perp} E_1 = A_1 \exp j [\omega t - k \{y \cos \theta_1 + z \sin \theta_1\} - 2 \delta_{\perp}]$$

The phase difference between the field components is

$$\delta = 2 [\delta_{\parallel} - \delta_{\perp}] \quad (9)$$

so

$$\begin{aligned} \tan(1/2 \delta) &= \tan [\delta_{\parallel} - \delta_{\perp}] \\ &= \frac{[\tan \delta_{\parallel} - \tan \delta_{\perp}]}{[1 + \tan \delta_{\parallel} \tan \delta_{\perp}]} \end{aligned} \quad (10)$$

This last equation can be reduced to a form which allows the calculation of the rhomb angle θ_i if the desired phase shift at each reflection is known. From equation (4) and (6) the relation between the field component phase angles is

$$\tan \delta_{\parallel} = n^2 \tan \delta_{\perp}$$

so

$$\begin{aligned} \tan (1/2 \delta) &= \frac{\tan \delta_{\perp} (n^2 - 1)}{1 + n^2 \tan^2 \delta_{\perp}} \\ &= \frac{\left[\left(\sin^2 \theta_i - 1/n^2 \right)^{1/2} (n^2 - 1) \right] \cos^2 \theta_i}{\cos \theta_i \left[\cos^2 \theta_i + n^2 \left(\sin^2 \theta_i - 1/n^2 \right) \right]} \end{aligned}$$

or

$$\tan (1/2 \delta) = \frac{\cos \theta_i \left(\sin^2 \theta_i - 1/n^2 \right)^{1/2}}{\sin^2 \theta_i}$$

Thus if the phase shift on each reflection is known, the rhomb angle θ_i can be calculated. This theory assumes the crystal is isotropic and this is the case for ZnSe is cubic.

DISCUSSION

A. Fresnel Rhomb

In the design the phase angle is chosen and the two internal reflection give a phase angle of 2δ . Then it is possible to calculate the rhomb angle θ_i to produce this phase change when light is incident normally on the face and is linearly polarized along an end face diagonal. From equation (11), θ_i is

$$\theta_i = \sin^{-1} \left[\frac{\left[(n^2 + 1) \pm \left[(n^2 + 1)^2 - 4n^2 \left(\tan^2(1/2\delta) + 1 \right) \right]^{1/2} \right]}{2n^2 \left(\tan^2(1/2\delta) + 1 \right)} \right]$$

In order to make a quarter waveplate which produces right or left hand circular polarized light, then $2\delta = \pi/2$ or $1/2\delta = \pi/8$. In this case $\theta_i = 25.1^\circ$ which is smaller than the critical angle so no internal reflection occurs or $\theta_i = 65^\circ$ which is the desired rhomb angle.

An interesting device can be produced by placing two rhombs end to end as shown in Figure 2. This device eliminates the lateral displacement of the beam as occurs for a single rhomb but there will be increased beam attenuation. In constructing a quarter waveplate the incident beam is linearly polarized as described previously but on each reflection a phase shift of $\pi/8$ occurs and from equation (12) the rhomb angle is 77.6° .

In Figure 3 is shown a polarized beam which is not

incident normally on the face of the rhomb but has makes a small angle above or below the normal. Then from Snell's law

$$\sin \theta'_i = n \sin \theta'_t \quad (13)$$

and

$$\begin{aligned} \tan(1/2 \delta) &= \frac{\cos \theta''_i \left[\sin^2 \theta''_i - 1/n^2 \right]^{1/2}}{\sin^2 \theta''_i} \\ &= \cos \frac{\left[\theta_i \pm \theta'_t \right] \left[n^2 \sin^2 \left(\theta_i \pm \theta'_t \right) - 1 \right]^{1/2}}{n \sin^2 \left(\theta_i \pm \theta'_t \right)} \end{aligned} \quad (14)$$

The results for light not incident normally on the face of the rhomb are given in Table 1, where the rhomb corresponds to a quarter waveplate for $\theta_i = 65^\circ$. Angles of incidence above the normal are positive and below are negative in the data presented in Table 2. These numbers give an indication of the importance of having a collimated light beam incident normally on the rhomb face.

A topic which needs to be considered is whether a Fresnel rhomb behaves the same as a quarter waveplate. The Jones' matrix³ of a quarter waveplate oriented with the fast axis $+45^\circ$ to the incident polarized beam is

$$T = \begin{bmatrix} \exp - (j \delta_{T\perp}) & 0 \\ 0 & \exp - (j \delta_{T\parallel}) \end{bmatrix}, \quad (15)$$

where the \perp and \parallel field components are E_{\perp} and E_{\parallel} or E_x and E_y and each equals $A(x, y, z, t)$ then

$$E = T E_i = \begin{bmatrix} \exp(-j \delta_{T\perp}) & 0 \\ 0 & \exp(-j \delta_{T\parallel}) \end{bmatrix} \begin{bmatrix} E_{\perp} \\ E_{\parallel} \end{bmatrix} = \begin{bmatrix} E_{\perp} \exp(-j \delta_{T\perp}) \\ E_{\parallel} \exp(-j \delta_{T\parallel}) \end{bmatrix}, \quad (16)$$

where δ_T is the total phase change of each field component. In the case of the Fresnel rhomb the Jones' matrix is

$$T = \begin{bmatrix} \exp(-2j \delta_{\perp}) & 0 \\ 0 & \exp(-2j \delta_{\parallel}) \end{bmatrix} = \begin{bmatrix} \exp(-j \delta_{T\perp}) & 0 \\ 0 & \exp(-j \delta_{T\parallel}) \end{bmatrix}, \quad (17)$$

where $2 \delta_{\perp} = \delta_{T\perp}$ and $2 \delta_{\parallel} = \delta_{T\parallel}$. The matrix is identical to that of the quarter waveplate. The Mueller matrix for the Fresnel rhomb with a general phase shift δ is

$$M(\text{Fresnel rhomb}) = \begin{bmatrix} 1 & 0 & 0 & 0 \\ 0 & 1 & 0 & 0 \\ 0 & 0 & \cos \delta & -\sin \delta \\ 0 & 0 & \sin \delta & \cos \delta \end{bmatrix} \quad (18)$$

and for a phase shift of 90° it is

$$M(\text{Fresnel rhomb}) = \begin{bmatrix} 1 & 0 & 0 & 0 \\ 0 & 1 & 0 & 0 \\ 0 & 0 & 0 & -1 \\ 0 & 0 & 1 & 0 \end{bmatrix} \quad (19)$$

With light incident at $+45^\circ$ to the horizontal the Stoke's vector is

$$S = 1/2 \begin{bmatrix} 1 \\ 0 \\ 1 \\ 0 \end{bmatrix} \quad (20)$$

where the 1/2 factor is the attenuation of the polarizer so the product of the Mueller matrix times the Stoke's vector is

$$S \text{ (R Circular)} = 1/2 \begin{bmatrix} 1 & 0 & 0 & 0 \\ 0 & 1 & 0 & 0 \\ 0 & 0 & 0 & -1 \\ 0 & 0 & 1 & 0 \end{bmatrix} \begin{bmatrix} 1 \\ 0 \\ 1 \\ 0 \end{bmatrix} = 1/2 \begin{bmatrix} 1 \\ 0 \\ 0 \\ 1 \end{bmatrix}, \quad (21)$$

which is right hand circular polarized light.

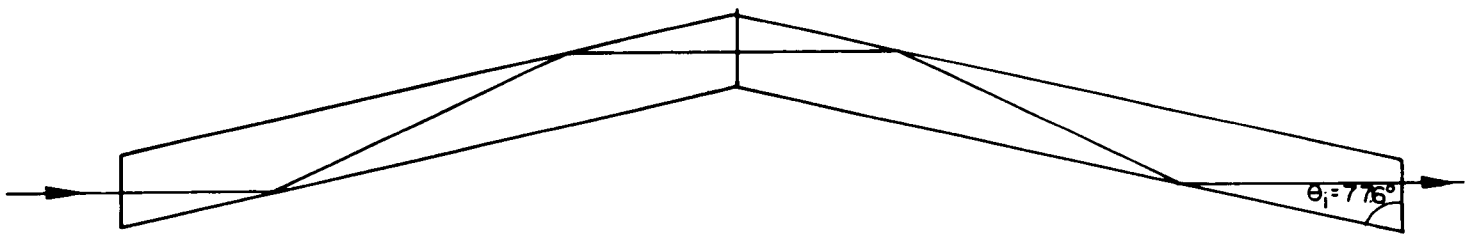
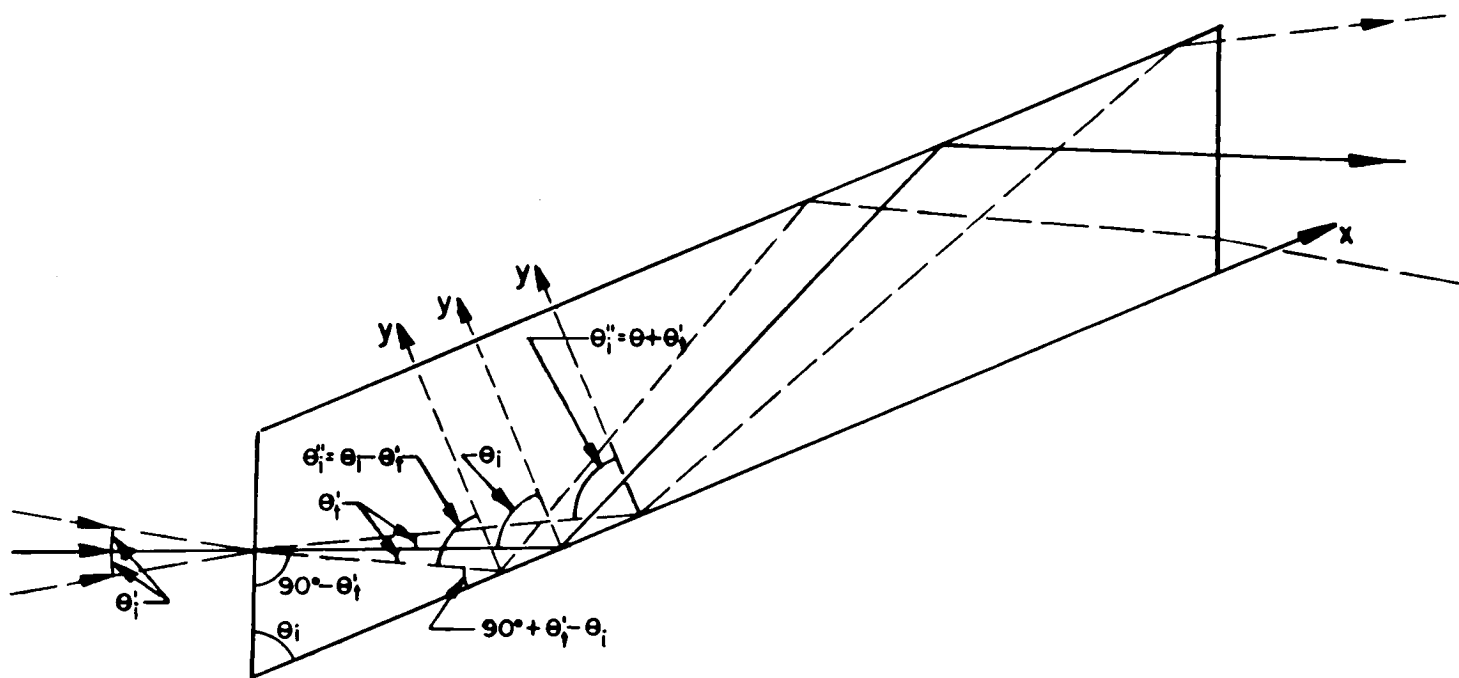


FIGURE 2 Dual Fresnel rhomb



θ_i' Above normal $\theta_i'' = \theta_i - \theta_i'$
 θ_i Below normal $\theta_i'' = \theta_i + \theta_i'$

FIGURE 3 Input angle deviation

Table 2. Deviations of the phase with angles above and below the normal to the Fresnel rhomb.

					Deviation 2δ
Angle θ_i'	θ_t'	$\theta_i' + \theta_t'$	δ	2δ	from 90°
Degrees	Degrees	Degrees	Degrees	Degrees	Degrees
+0.5	-0.21	64.79	45.36	90.72	+0.72
-0.5	+0.21	65.21	44.62	89.24	-0.76
+1.0	-0.42	64.58	45.72	91.44	+1.44
-1.0	+0.42	65.42	44.24	88.48	-1.52
+1.5	-0.63	64.38	46.08	92.16	+2.16
-1.5	+0.63	65.62	43.90	87.80	-2.20
+2.0	-0.83	64.17	46.44	92.88	+2.88
-2.0	+0.83	65.83	43.52	87.04	-2.96
+2.5	-1.04	63.96	46.82	93.64	+3.64
-2.5	+1.04	66.04	43.16	86.32	-3.68
+3.0	-1.25	63.75	47.18	94.36	+4.36
-3.0	+1.25	66.25	42.78	85.56	-4.44
+3.5	-1.46	63.54	47.54	95.08	+5.08
-3.5	+1.46	66.46	42.42	84.84	-5.16
+4.0	-1.67	63.33	47.92	95.84	+5.84
-4.0	+1.67	66.67	42.04	84.08	-5.92
+4.5	-1.87	63.13	48.26	96.52	+6.52
-4.5	+1.87	66.87	41.70	83.40	-6.60
+5.0	-2.08	62.92	48.64	97.28	+7.28
-5.0	+2.08	67.08	41.32	82.64	-7.36

It should be mentioned that the Mueller matrix⁴⁻⁵ for a quarter waveplate with the fast axis at some angle θ to the horizontal is

$$M_{\lambda/4}(\theta) = \begin{bmatrix} 1 & 0 & 0 & 0 \\ 0 & C^2 & CS & -S \\ 0 & CS & S^2 & C \\ 0 & S & -C & 0 \end{bmatrix}, \quad (22)$$

where $C = \cos 2\theta$ and $S = \sin 2\theta$. If the fast axis is assumed vertical, then

$$M_{\lambda/4}(90^\circ) = \begin{bmatrix} 1 & 0 & 0 & 0 \\ 0 & 1 & 0 & 0 \\ 0 & 0 & 0 & -1 \\ 0 & 0 & 1 & 0 \end{bmatrix},$$

which is identical to the Fresnel rhomb. Thus the Fresnel rhomb has all of the polarization characteristics of the quarter waveplate.

B. Quarter Waveplate

The quarter waveplate in the CO_2 wavelength region is constructed of CdS. The index of refraction for the ordinary and extraordinary rays of CdS were supplied by II-VI with the original data coming from Cleveland Crystal. These data are listed in Table 3. A true quarter waveplate is too thin to be constructed so plates with a thickness which are multiples of a quarter wavelength are made. The plates supplied by II-VI are $5 \lambda/4$ plates of thickness 0.1018 cm or 0.0401 in.

With a plate of this thickness the deviation of the

phase angle with the deviation of the beam from normal incidence on the plate is negligible. As an example, for a beam incident at $\pm 3.5^\circ$ from the normal the phase angle deviation is $\pm 0.44^\circ$ and for an incident angle deviation of $\pm 5^\circ$ the phase angle deviation is $\pm 0.88^\circ$.

Table 4 shows the deviation of the phase angle between the field components E and E^\perp of other CO_2 wavelengths for a quarter waveplate designed for the CO_2 10.591 μm line which at this wavelength gives a phase shift of 450° . From these data it is evident that a quarter waveplate designed for a specific wavelength may not be used at another CO_2 wavelength. This means that for each wavelength a new quarter waveplate must be purchased and these are special runs and are expensive. This means that a Fresnel rhomb must be used and the rhomb has input angle limitations and these limitations must be considered for they can lead to large phase shifts that would limit its usefulness.

CONCLUSIONS

The Fresnel rhomb in the 9-10 μm CO_2 laser emission region is a nearly wavelength independent phase retarder as is seen in Table 1. A single quarter waveplate of ZnSe may be made with a small rhomb corner angle of 65° . With light normally incident upon the face and polarized along either diagonal right and left hand polarized light is produced. By using two rhombs with corner angles of 77.6° it is possible to produce a quarter waveplate and this design avoids the lateral displacement of the beam. The greatest problem with the rhomb is that the beam must collimate and incident normally. It is easy to calculate the Mueller matrix for the rhomb and show that it is identical to the quarter waveplate at the same orientation.

It is evident from this study that a quarter waveplate designed for the 10.591 μm CO_2 line cannot be used over the entire emission region of the laser. As a result, it is necessary to use a nearly wavelength insensitive device like the Fresnel rhomb, even though, it is subject to stringent irradiation condition.

Table 3. Extraordinary and ordinary indices of refraction
of CdS⁶

Wavelength μm	Index of refraction		Difference Δn
	n_o	n_e	
9.20	2.2395	2.253	0.0135
9.50	2.237	2.250	0.013
10.0	2.232	2.245	0.013
10.5	2.226	2.239	0.013
10.591	2.226	2.239	0.013
11.0	2.220	2.234	0.014

Table 4. Deviation of phase angle for a 10.591 μm CO₂ laser
laser line quarter waveplate at other CO₂
wavelengths.

CO ₂ wavelength μm		Degrees	Degrees
R(26)	9.239	535.5	85.5
R(24)	9.250	534.9	84.9
P(16)	9.519	500.5	50.5
P(22)	9.569	497.9	47.9
P(28)	9.621	495.2	45.2
R(36)	10.148	469.5	19.5
R(14)	10.289	463.0	13.0
P(14)	10.532	452.4	2.4
P(20)	10.591	450.0	0.0
P(34)	10.741	460.6	10.6

REFERENCES

1. E. Hecht and A. Zajac, "Optics," Addison Wesley, Reading, Mass., 1976.
2. "Precision optics and components," Janos Tech., Inc.
3. R. M. A. Azzam and N. M. Bashara, "Ellipsometry and polarized light," North Holland, Amsterdam, 1977.
4. W. A. Shurcliffe, "Polarized light," Harvard Univ. Press, Cambridge, Mass., 1962.
5. W. S. Bickel and W. M. Bailey, "Stokes vectors and Mueller matrices," Am. J. Phys. 53, 4681 (1985).
6. Jack Chambers, II-VI, private communications.

N88-15603

52-46

11-704

78

1987

NASA/ASEE SUMMER FACULTY RESEARCH FELLOWSHIP PROGRAM

MARSHALL SPACE FLIGHT CENTER
THE UNIVERSITY OF ALABAMA IN HUNTSVILLE

SOME CONSIDERATIONS ON MEASURING THE NEWTONIAN
GRAVITATIONAL CONSTANT G IN AN ORBITING LABORATORY

Prepared by:	Stephen D. Baker
Academic Rank:	Professor
University and Department:	Rice University Department of Physics
NASA/MSFC:	
Laboratory:	Space Science
Division:	Astrophysics
Branch:	High Energy Astrophysics
MSFC Colleague:	C. A. Meegan
Date:	August 11, 1987
Contract No.:	The University of Alabama in Huntsville NGT-01-008-021

ABSTRACT

We have identified no fundamental reason for rejecting the notion of measuring the Newtonian gravitational constant G by observing an artificial binary in a near-earth orbiting laboratory.

ACKNOWLEDGEMENT

I would like to thank the scientists and staff in the Space Science Laboratory for their hospitality and support. My colleague, C. A. Meegan, and Branch Chief Tom Parnell were helpful with practical details and with generally making me feel at home. Susan Burrer and Shelby Morris patiently made many revisions in a manuscript based on the summer's topic. Jena Morris performed some useful calculations for me. Finally, I appreciate the support of the NASA/ASEE Summer Faculty Fellowship Program.

INTRODUCTION

Of the fundamental constants of nature, the Newtonian gravitational constant G is by far the least well known (only about one part in ten thousand, or worse). The use of artificial binaries to determine this constant has been regularly proposed since it became thinkable to have orbiting laboratories. A regular objection to this method has been that, in near earth orbit, the gravitational field of the Earth is changing so rapidly with distance from the earth that "tidal forces" would make the orbits of artificial binaries unstable. This is not the case, however; certain retrograde orbits are indeed stable and could be used to sample the gravitational attraction between two balls for a long time, thus permitting the determination of G .

OBJECTIVES

The objectives of the summer's activity were to become further familiar with the literature relevant to the problem at hand and to draw any further conclusions concerning the feasibility of measuring G in a near earth orbiting laboratory. A secondary objective was to complete a manuscript on this topic, with Adam Falk, begun last summer, for submission to the American Journal of Physics.

REPORT

A common suggestion for measuring the Newtonian gravitational constant in an orbiting laboratory is simply to put two balls in orbit around each other and measure the resulting orbital elements and period of the motion of such an artificial binary, thereby determining G . However, the radial variation with distance of the gravitational field of the earth is so large that "tidal forces" on the balls in near-earth orbit can be several times greater than the gravitational attraction between them. The presence of these relatively strong tidal forces close to the earth has led some writers to assume that two objects will not stably orbit about each other and that this method of measuring G is impossible, or at least impractical. Here is what they say:

Farinella, Milani, and Nobili (1980)

"This means that the physical limits to the density of [the binaries] imply that in a low Earth orbit no stable motion of the test mass around the primary is possible."

Avron and Livio (1986)

"Unfortunately, such an experiment is not possible with the Space Shuttle, the main reason being its low altitude."

Hills (1986)

"If the semimajor axis of the binary is sufficiently large, the tidal field would force its dissociation."

However, Michel Henon in a beautiful series of papers has explored the regions of long-term stability of many classes of orbits of point particles which are moving under their mutual gravitation in a frame which is orbiting about a large third body. He finds that certain retrograde orbits are stable and states (in 1970) that:

"Contrary to the usual [and, evidently, persistent] belief, there is no limiting [orbital] radius for the satellites."

Henon provides a very complete description of what is known as Hill's Problem, where the motion of one of two equal mass balls is described relative to an orbiting frame of reference in terms of dimensionless coordinates:

$$\ddot{z} = -2\dot{x}$$

$$\ddot{x} = 2\dot{z} + 3x$$

$$\ddot{y} = -y$$

where the time unit is chosen to be $T/2\pi$, where T is the orbital period of the spacecraft and the length unit is chosen to be $(m/4M)^{1/3} A$, where M is the mass of the earth and A is the radius of the orbit of the spacecraft.

Since one must use balls of finite density (and therefore finite size) we may investigate the tolerances on the initial conditions of the orbit so that the balls collide neither with each other nor with the walls of the spacecraft. In Figure 1 we show the "launch window" for a 10 kg, 5 cm radius, ball started out on the neutral line at $z = 15$ cm with the velocity components shown on the axes of the figure. The other identical ball is launched symmetrically to maintain the center of mass at the origin.

Trajectories which result in the balls' striking each other or the enclosure of the spacecraft are represented by diamonds or crosses, respectively. For this example, the enclosure is taken to be a cube of edge length 110 cm. Those trajectories which survive for 25 orbital periods about the earth are unmarked. Launching from points other than on the neutral line (the z axis) is, of course, possible, and we find that the allowable ranges on the initial velocities are very similar to those in Figure 1.

While the tidal forces can be significantly reduced by going to a laboratory orbiting the earth at a large radius, it turns out that one does not gain much in terms of allowable ranges of initial velocities. We conclude therefore that tidal forces do not pose any particular problem in using an artificial binary in an experiment to determine G .

Are there other fundamental processes which might make it impossible to carry out such an experiment? We can consider several items:

1. Gradients due to components of the spacecraft. The spacecraft in which the experiment would be performed should be constructed to provide a minimal gradient at the position of the orbiting balls, but it is not difficult to do this. Since the experiment is in free fall, it is the gradient of the gravitational field which affects the relative motion of the balls and not the strength of the field itself. For example, the gradient due to a 100 kg mass a distance 5 m from the center of the experiment gives a gradient only $4.0E-5$ times that of the earth.

2. Fluctuations in the gradient due to orbital eccentricity and non-sphericity of the Earth. The oblateness of the earth would create a variation of about 1% in the earth's gradient if the experiment orbits in a circular polar orbit, and less in an equatorial orbit. Eccentricity of the orbit would also give rise to variations in the gradient (about 1% for variations of 20 km in altitude). These effects are accurately calculable, however, and could be accurately compensated for.

3. Electrical charging of the balls. This should not present insurmountable problems, either. For example, to keep the electrostatic force a million times smaller than the gravitational force between the balls, used in the example shown in Figure 1, the charge on each ball would have to be less than about one picocoulomb, not impossibly small. Larger balls would permit larger charges.

CONCLUSION

We conclude therefore, that there is still no fundamental reason to believe that an experiment to use an artificial binary in a near-earth orbiting laboratory is an unreasonable way to obtain a very good determination of the Newtonian gravitational constant G .

REFERENCES

P. Farinella, A. Milani, and A. M. Nobili, *Astrophysics & Space Science* 73(1980)417

Y. Avron and M. Livio, *Astrophysical Journal* 304(1986)L61

J. G. Hills, *Astronomical Journal* 92(1986)986

M. Henon, *Astronomy & Astrophysics* 30(1974)317, and references therein.

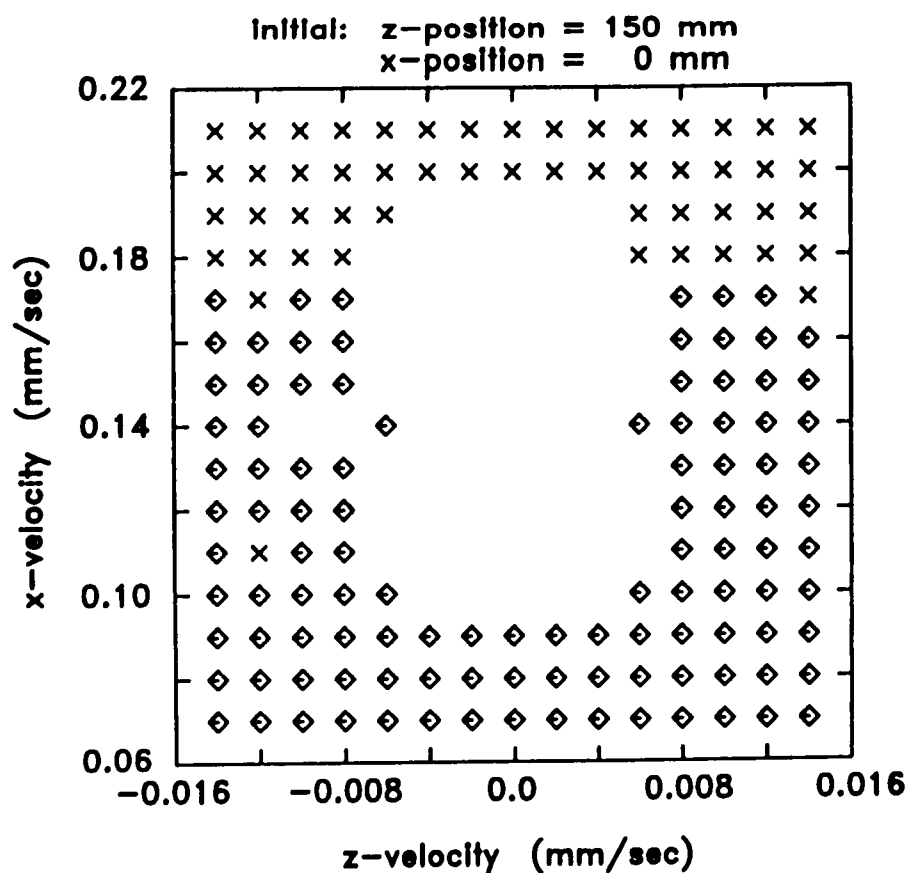


Figure 1

N88-15604

53-65

116705

16P

1987

NASA/ASEE SUMMER FACULTY FELLOWSHIP PROGRAM

MARSHALL SPACE FLIGHT CENTER
THE UNIVERSITY OF ALABAMA IN HUNTSVILLE

RISK ANALYSIS METHODOLOGY SURVEY

Prepared by: Robert G. Batson, Ph.D.
Academic Rank: Associate Professor
University and Department: The University of Alabama
Department of Industrial Engineering

NASA/MSFC:

Directorate: Program Development
Office: Program Planning
Group: Engineering Cost Group
MSFC Colleagues: Joseph W. Hamaker
W. A. Ferguson
Date: July 3, 1987
Contract No: The University of Alabama
in Huntsville
NGT-01-008-021

ABSTRACT

Several NASA regulations specify that formal risk analysis be performed on a program at each of several milestones as it moves toward full-scale development. Program risk analysis is discussed as a systems analysis approach to risk, an iterative process (identification, assessment, management), and a collection of techniques. These techniques, which range from extremely simple to complex, network-based simulation, were surveyed. A Program Risk Analysis Handbook was prepared in order to provide both analyst and manager with a guide for selection of the most appropriate technique.

Various researchers have verified that 85-90% of the risk in complex, technological systems development originates in the technical definition of the system. Risk may be assessed on cost, schedule, or performance individually; the preferred approach is to treat these as dependent random variables and perform an integrated risk assessment. All program risk assessment techniques were shown to be based on elicitation and encoding of subjective probability estimates from the various area experts on a program. Techniques to encode the five most common distribution-types were given. Then, a total of twelve distinct approaches to risk assessment were given. For each approach we identified the steps involved, good and bad points, time involved, and degree of computer support needed.

We discuss why risk analysis should be used by all NASA program managers. How to establish a risk analysis capability and some of the special difficulties in performing a risk analysis were related. Tools available at NASA/MSFC were identified, along with commercially available software. Both an extensive bibliography (150 entries) and a program risk analysis check-list were provided.

Recommendations are to:

1. Perform integrated cost/risk assessment on each program, prior to each RFP release.
2. Require contractors to perform quantitative risk assessments during proposal preparation and after contract award.
3. Select (or hire) a full-time risk analyst in Program Planning, with responsibilities for applications, methods development, interface with other centers, and consulting to program and engineering managers.

TABLE OF CONTENTS

<u>Section</u>	<u>Page</u>
ABSTRACT	III-1
INTRODUCTION	III-1
OBJECTIVES	III-4
TERMINOLOGY	III-6
RISK ANALYSIS METHODOLOGY	III-8
CONCLUSIONS AND RECOMMENDATIONS	III-10
BIBLIOGRAPHY	III-12

INTRODUCTION

The article "GRO Project Beset by Complications" appeared in the 6/14/87 Huntsville Times. The NASA/GSFC Project Manager, Jeremiah Madden, stated "the sheer magnitude and complexity of the GRO program overwhelmed managers and engineers and obscured some of the program's finer details." These complications occur on all space and defense projects, especially those that use unproven technology, attempt a new mission, and/or scale up (or down) the size of the craft used -- for example, the C5A, the Trident Submarine, Space Telescope, and the Stealth Bomber. The specific problems encountered on the GRO project are typical:

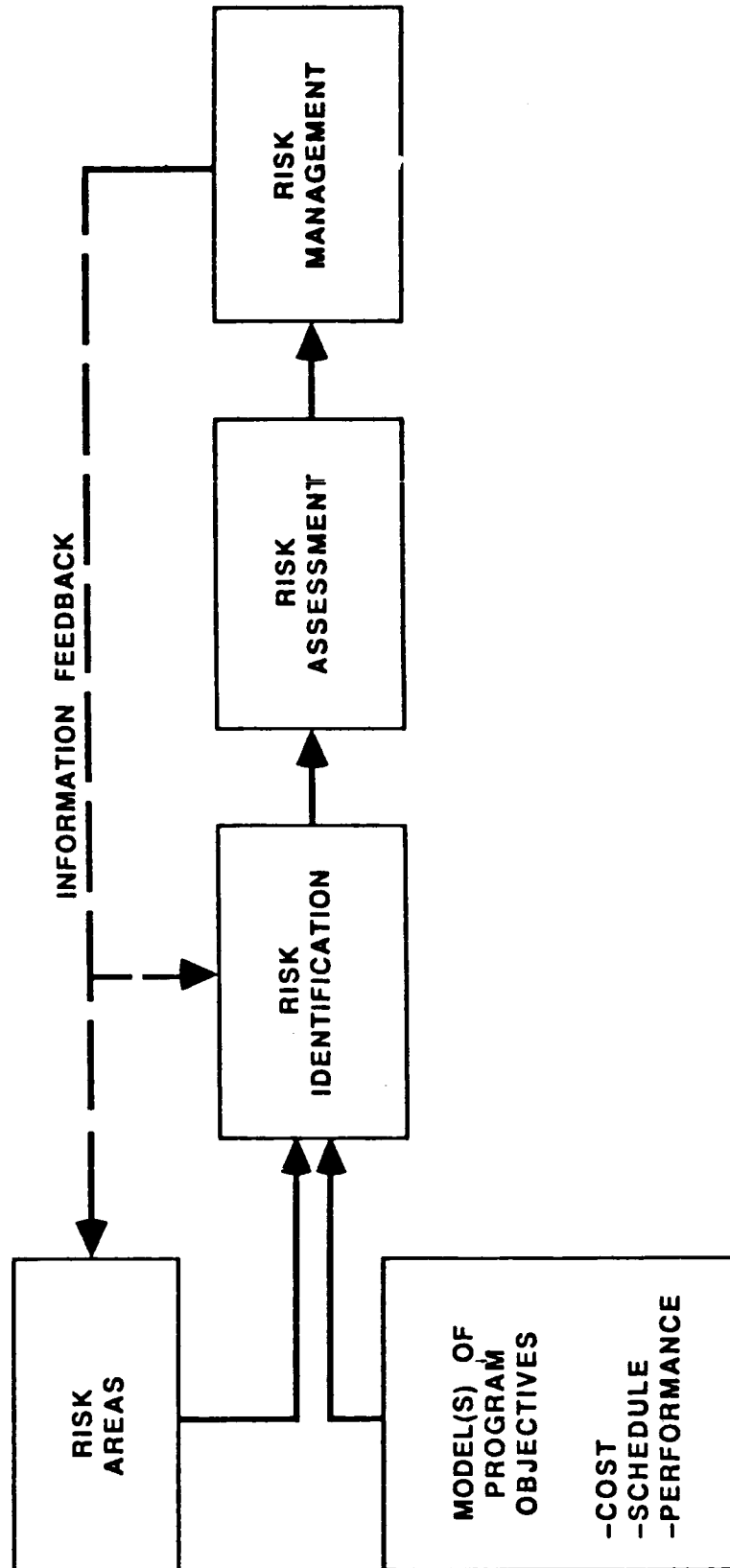
- o manufacturing processes not well-understood
- o manufacturing problems due to materials faults/availability
- o lack of trained manufacturing work force
- o unexpected electromechanical interference between instruments, once integrated
- o redesign of components and tooling

These problems led to a modest cost growth of \$380 million to \$500 million, and a schedule slip from May '88 to early 1990. Space Telescope cost growth is \$500 million to \$1.4 billion. The average cost growth observed in both NASA and DoD projects, from the start of Full-Scale Development (FSD) to the completion of prototype production, has been in the range 30-40%.

This type of track-record for Federal acquisition of large-scale systems has led to Congressional skepticism, public outrage, and occasionally loss of support for the continuation of the project. Since the '60s, DoD and NASA project managers have sought management techniques that will help them control cost growth and schedule slippages. Major General John R. Guthrie, USA, stated at the 1970 DoD Project Managers Conference that:

"the most rudimentary sort of good risk analysis might have enabled us to avoid most of the pitfalls we have encountered. By rudimentary I mean -- did we identify those items which were new and identify the impact on overall system performance if that particular component or subsystem were to experience difficulty?"

Program risk analysis is an iterative process (Figure 1) for identifying, quantifying, and managing the uncertainties associated with complex design and development programs typical to NASA. Others have defined risk analysis as a systems analysis approach to risk, or as a collection of techniques to identify, quantify, and manage risk. In contrast to techniques for quantifying operational risk (e.g., failure modes and effects analysis, fault tree analysis, reliability analysis),



program risk analysis deals with program cost, schedule, and technical performance estimates. The key question to be answered by risk analysis is what are the distributions of probability on the mature (achieved) values of each of these three random variables. In some risk analyses, two of these variables (say, performance and schedule) are thought of as fixed. Then the probability distribution on the mature value of the other (cost) is derived. However, in a comprehensive risk analysis, the dependence among these variables is assessed and uncertainty in one affects the assessment of risk in the other two.

NASA NMI 7100.14A (Major System Acquisition) calls out risk evaluation as a criteria second only to performance for initiating FSD. MMI 7110.1 requires risk analysis and cost risk assessment for both formal project pre-development reviews. Program risk analysis is useful to program managers as both a source of information on the program and as a decision-aiding tool. The reason is that it is a formal, systematic, and documented approach to dealing with uncertainty, versus "seat-of-the-pants" dealing with problems as they arise. It can be used in both Phases A and B, as requirements and design configurations evolve, for the purpose of early identification and resolution of technical uncertainties. Classic risk resolution strategies are parallel development, design/operations trade-offs, and development of back-up solutions. It is probably of most use for assessing the potential for cost and schedule slippages in programs moving into Phase C/D, because this is the point at which significant resource commitments will be made. Risk analysis can be applied to subsystems or instruments, individual technologies, manufacturing processes, and other elements that make up a program; however, its true value is in synthesizing these multiple uncertainties.

OBJECTIVES

Each task team leader and project manager (PM) at NASA/MSFC should become aware of the valuable information available from a program risk analysis. The risk analysis process is iterative and risk analysis should not be viewed as a one-time, check-the-box type activity. This handbook is written with the view of the PM as the consumer for risk analysis, and a range of options is provided so that the appropriate type of analysis, at the right level of detail, may be requested.

This handbook is prepared as a guide and reference source for any NASA employee who is requested to perform a risk analysis in support of the PM. This individual will be referred to as "the risk analyst," although he/she may be a cost analyst, schedule analyst, program analyst, engineer, or scientist. An entire range of risk analysis tools will be provided, along with some guidance for selecting the appropriate technique for a given situation. However, it is always necessary that the risk analyst apply his judgment when initiating a risk analysis at the request of a PM. For example, he must decide what technique is appropriate, given the time available and the software tools he has at his disposal. Another key question is how much access to and cooperation from program personnel the analyst can expect; no meaningful risk analysis can be generating without repeated, probing discussions with practically all program personnel in order to identify technical uncertainties and their potential cost and schedule impacts. Good relations between risk analyst and technical team members is essential if a valid, useful risk analysis is to be conducted. The only alternative, and one that works well, is for the risk analyst to be part of an ad-hoc team of experts, independent of the project, whose job it is to review the project and report to higher authority on its findings.

The selection and support of a risk analyst (or risk analysis group) is an important step for large industry/government design organizations and laboratories. The risk analyst is the alter-ego of top management in his evaluation of a project, much as the quality assurance analyst is for a production facility. He is often feared, avoided, circumvented, and detoured. Other engineers generally view the risk analyst as a nuisance who will take their valuable time, produce nothing new, and perhaps misrepresent their professional judgment. Although it is desirable for the risk analyst to be involved early in programs, and have an established relationship with both PM and project personnel, the fact is that risk analysis is usually a last-minute effort, performed on an ad-hoc basis, prior to some major decision/presentation. The risk analyst is often not at all familiar with the technology or program being analyzed. He must therefore:

1. Educate himself quickly.

2. Acquire the data.
3. Use the data in some pre-developed model.
4. Present recommendations based on model output.

The above discussion clearly reveals that conducting a risk analysis is not an easy job. The risk analyst must be an individual of highest quality in education, technical/program experience, human relations, and recognition of management needs. Many of these positions are filled by individuals with graduate-level training in statistics, operations research, or systems analysis. An undergraduate degree in engineering or hard sciences helps, but is not necessary. Individuals who are enthralled with math models and/or computer techniques generally aren't good risk analysts. The interaction with project personnel, the collection and verification of data, and preparation of finding into a format useful for management are the key activities of the risk analyst.

TERMINOLOGY

Several general references on program risk analysis are given in the Bibliography. The definitions presented below are stated in broad terms and would be accepted by anyone working in the program risk analysis area. Of course, certain organizations and programs within organizations adopt more specific definitions for terms such as "risk area" -- in fact one of the first jobs for a risk analyst newly assigned to a program is to work with the PM on an agreeable set of definitions and working groundrules. Note also that more specialized terminology is used in health and environmental risk analysis, and these terms are not appropriate for program risk analysis.

Definitions

Risk -- the probability of undesirable future consequences of actions (inaction) taken today. Thus risk has a temporal element, and is a function of both probability and consequence.

Program risk -- the probability that the actual cost, time, or performance of a system will fail to match predictions. Also, the degree by which such predictions are missed and the associated consequences.

Potential problem -- an identified, but not yet occurring problem that if actualized, will impose unplanned resource demands, rescheduling, and/or degraded performance, quality, or safety margins.

Risk area -- a collection of related potential problems. Also a common source of several potential problems.

Potential problem analysis (risk identification) -- identification of risk areas and the sequence of interrelated potential problems that stem from them. Also can include identification of immediate cost, schedule, and performance impacts of potential problems, recognizing that potential problems may actualize at one of several levels of severity and that there is a probability associated with each level.

Risk assessment -- using the information from risk identification, and one or more quantitative techniques to synthesize the information, to create an overall assessment of program cost, schedule, or technical risk and also an assessment of the risk contributed by each risk area. May include ranking risk areas by severity or timing in order to identify a course of action.

Risk management -- identifying alternatives, selecting an approach, and taking action in order to reduce risk to levels deemed acceptable by the organization. Action may be directed at risk reduction or in trading one type of risk for another. In some instances, work around plans

and/or contingency budgets are defined as back-up solutions to the selected risk reduction approach.

Probability -- the relative frequency of an outcome of a repeatable, observable experiment. Also, a measure between 0 and 1 assigned to each outcome of an experiment based on its relative frequency.

Subjective probability -- a measure of the lack of information an organization or an individual has about the actual outcome of some future experiment. Essentially, it is a "degree of belief" measure based on human experience and reasoning, as opposed to a "frequency of occurrence" measure.

Probability encoding -- a process whereby the lack of information of an expert is quantified as a subjective probability distribution on a state variable, developed under specific assumptions, in a scientifically correct way, with as much accuracy as is justifiable. Accuracy can be increased by spending more time per encoded variable, or by combining the opinions of several experts.

RISK ANALYSIS METHODOLOGY

A 95-page Program Risk Analysis Handbook was prepared as the primary product of this fellowship. This handbook will be published as a NASA/MSFC Technical Memorandum (TM). The contents will be summarized here.

All risk assessment techniques use subjective probability distributions as input. The process of interviewing a technical expert and determining the nature of the uncertainty in a variable of interest is referred to as "probability encoding." We discuss this process and give algorithms to encode the density function of five distribution types: uniform, triangular, beta, Weibull, and normal.

Twelve distinct techniques for risk assessment were identified and discussed. We grouped these techniques into three classes:

- o Quick Risk Assessment Techniques, which require 1-2 days to implement and use point probability estimates (risk factors) as inputs. These methods require only a hand-held calculator, and include:
 - Equi-risk contours method
 - Risk factor method (RFM)
 - Probabilistic event analysis (PEA)
 - Probabilistic Evaluation and Review Technique (PERT)
 - Analytic Cost Risk Method
 - Method of Moments
- o Standard Risk Assessment Techniques, which require 1-2 weeks to implement and are based on Monte Carlo simulation. These techniques require at least a microcomputer, and include:
 - Simulation of the Critical path
 - Simulation of the Project Network
 - Simulation of the Cost Model
 - Simulation of a Performance Model
- o Integrated Risk Assessment Techniques, which require 1-2 months to implement and are performed using a network-based, simulation package such as GERT, VERT, or RISNET. The techniques are:
 - Integrated Cost/Schedule Risk Assessment, based on direct evaluation of cost and time uncertainty on each activity.

- Integrated Technical/Cost/Schedule Risk Assessment, based on simulation of the occurrence of technical problems and their time/cost penalties.

Note that only in the integrated techniques are time and cost treated dependently. A full discussion of each of these techniques and related reference material may be found in the Program Risk Analysis Handbook. The techniques currently used at NASA/MSFC are indicated by an asterisk in Figure 2 below.

TIME TO IMPLEMENT	BASIS OF TECHNIQUES		
	SUBJECTIVE FACTORS AND/OR POINT PROBABILITIES	SUBJECTIVE PROBABILITY & ANALYTICAL METHODS	SUBJECTIVE PROBABILITY & MONTE CARLO SIMULATION
1 - 2 DAYS	<ul style="list-style-type: none"> ● EQUI-RISK CONTOURS ● RISK FACTOR METHOD ● PROBABILISTIC EVENT ANALYSIS 	<ul style="list-style-type: none"> ● PERT ● ANALYTIC COST RISK ● METHOD OF MOMENTS 	CRITICAL PATH SIMULATION*
1 - 2 WEEKS			SIMULATION OF COST MODEL* SIMULATION OF SCHEDULE NETWORK SIMULATION OF PERFORMANCE MODEL
1 - 2 MONTHS			INTEGRATED COST/SCHEDULE NETWORK SIMULATION INTEGRATED TECHNICAL/COST/SCHED. NETWORK SIMULATION

INDUSTRY/
GOVERNMT.
STANDARD

NETWORK-
BASED
STATE-OF-
THE-ART

* = IN USE AT NASA/MSFC

Figure 2 Summary of Risk Assessment Methodology Alternatives

CONCLUSIONS AND RECOMMENDATIONS

Based on a thorough literature search, the range of quantitative methods for program risk assessment have been presented. As shown in Figure 2 twelve distinct alternatives were identified. These are discussed in detail in the Program Risk Analysis Handbook, prepared as the major product of this fellowship. All methods are based on the Bayesian view of probability; they differ in how subjective probability is collected (level of detail, assumptions, distribution types, etc.) and how these probabilities are combined into an overall assessment of uncertainty. Although "a risk assessment" can be done in a matter of several days, the truly comprehensive risk methods treat technical, cost, and schedule risks in an integrated (network-based) fashion and require at least one month of up-front development. The management benefits of integrated, network-based methods are worth the expense and waiting-time for the initial model output.

The recommendations for NASA/MSFC based on discussions with Program Planning Office personnel and the contents of the handbook are:

1. Commit to performing integrated cost/schedule risk assessment on each program prior to releasing RFPs for the phase in question. Quick risk assessments are, of course, appropriate in certain circumstances.
2. Require contractors to perform quantitative risk assessments as part of their proposal preparation effort. Require that these assessments be submitted as part of the technical volume or as a separate volume, or back-up document. Be explicit that meaningless LOW-MEDIUM-HIGH risk ratings are not acceptable, and that integrated methods are preferred. Require risk analysis be part of the systems analysis/management process after contract award.
3. Select (or hire) a full-time risk analyst to be stationed in Program Planning with the following responsibilities:
 - o Perform risk analyses on all PD studies, with early involvement with PM and study team.
 - o Write risk analysis requirements for all RFPs.
 - o Develop and document databases, questionnaires, and methods.
 - o Plan evolution of tools, either in-house development or outside acquisition.
 - o Train project control personnel to perform risk analyses.

- o Interface with other centers.
 - o Consult with PMs, chief engineers on use of risk analysis on their project.
4. Commit to investing the time and money to build a state-of-the-art capability in program risk analysis at NASA/MSFC.
- o Give selected analyst one year to build background, learn to use tools you have (ARTEMIS, SLAM, and SAM), and to review available methods and computer packages.
 - o Consider purchase of network simulation package designed for risk analysis.
 - RISNET
 - MICRO-VERT
5. Inform technical personnel in PD, and lab personnel supporting PD, about what risk analysis is and how they may be involved. Perhaps include some training in basic statistical concepts (classical and Bayesian) and generally encourage team-work, cooperation in generation of risk information.
6. As experience is gained, consider expanding this handbook to include:
- risk identification methods
 - risk management methods
 - lessons learned
 - case histories
7. Consider expanding from one risk analyst to a risk and decision analysis group.

BIBLIOGRAPHY

Batson, Robert G., Program Risk Analysis Handbook, NASA TM-XXXXX, Marshall Space Flight Center, Huntsville, AL, July 1987.

Whaley, Nona M., "Cost/Schedule/Technical Performance Risk Analysis," Chapter 8 in Cost Estimator's Reference Manual, Stewart and Wyskida (Eds.), Wiley-Interscience, 1987.

Information Spectrum, Inc. Risk Assessment Techniques, Defense Systems Management College Text, Fort Belvoir, Virginia, First Edition, July 1983.

Lockry, R. R., Col., USAF, et al, Final Report of the USAF Academy Risk Analysis Study Team, Deputy for Systems, Aeronautical Systems Division, Wright-Patterson AFB, Ohio, August 1971, (AD 729 223).

Atzinger, E., et al, Compendium of Risk Analysis Techniques, DARCOM Material Systems Analysis Activity, Aberdeen Proving Ground, MD, 1972 (AD 746 245), (LD 28463).

Proceedings of the 1972 U.S. Army Operations Research Symposium -- Risk Analysis, U.S. Army Operations Research Office, Durham, NC, May 1972 (AD 748 407).

Fisher, Gene H., Cost Considerations in Systems Analysis, Chapter 8, Special Topics, Elsevier, New York, 1975.

Martin, Rowe, Sherman, (Eds.), Proceedings: Management of Risk and Uncertainty in the Acquisition of Major Programs, University of Southern California, Held at Colorado Springs, CO, 1981 (AD A100546).

Powell, N., "Risk Analysis Methodology for Engineering Development Contracts," Proceedings of the 14th Annual U.S. Army Operations Research Symposium, Vol. I, U.S. Army Logistics Management Center, Fort Lee, VA (AD B009 955L).

Carlucci, F. C., "Improving the Acquisition Process," Deputy Sec. of Defense Memorandum, Washington, D.C., April 30, 1981.

Lockheed Missiles & Space Company, Systems Engineering Management Guide, Defense Systems Management College Text, Fort Belvoir, VA, 1983.

Williams, R. F., and Abeyta, R. D., (Eds.), Management of Risk and Uncertainty in Systems Acquisition and Proceedings of the 1983 Defense Risk and Uncertainty Workshop, Defense Systems Management College, Fort Belvoir, VA, July 1983.

Farrell, C. E., Martin Marietta Risk Analysis Handbook, Revision 2, Systems Engineering Department, Martin Marietta Denver Aerospace, December 1985.

Rowe, W. D., An Anatomy of Risk, Wiley, 1977.

Kates, R. W., (Ed.), Managing Technological Hazard, University of Colorado, 1977.

Crouch, E., and R. Wilson, Risk Benefit Analysis, Ballinger Publishing, Cambridge, MA, 1982.

McCormick, N. J., Reliability and Risk Analysis, Academic Press, New York, 1981.

Morgan, Granger M., "Probing the Question of Technology-Induced Risk," IEEE Spectrum, pp. 58-64, November 1981.

Morgan, Granger M., "Choosing and Managing Technology-Induced Risk," IEEE Spectrum, pp. 53-60, December 1981.

Morse, Stephen A., A Comparison of Risk Assessment Methodologies, DTIC Defense Logistics Agency, August 1980 (AD A089 346).

Worm, George H., Application of Risk Analysis in the Acquisition of Major Weapons Systems, AFBRMC/RDCB, August 1980, (AD A098 347).

N88-15605

54-82

116706

15P

1987

NASA/ASEE SUMMER FACULTY RESEARCH FELLOWSHIP PROGRAM

MARSHALL SPACE FLIGHT CENTER
THE UNIVERSITY OF ALABAMA IN HUNTSVILLE

COMPILATION AND DEVELOPMENT OF K-6 AEROSPACE MATERIALS
FOR IMPLEMENTATION IN
NASA SPACELINK ELECTRONIC INFORMATION SYSTEM

Prepared By:	Jean A. Blake
Academic Rank:	Professor
University and Department	Alabama A&M University Mathematics
NASA/MSFC	
Division:	Public Affairs Office
Branch:	Public Services & Education
NASA Colleague:	William E. Anderson
Date:	August 7, 1987
Contract No:	The University of Alabama in Huntsville NGT-01-008-021

ABSTRACT

Spacelink is an electronic information service to be operated by the Marshall Space Flight Center. It will provide National Aeronautics and Space Administration (NASA) news and educational resources including software programs that can be accessed by anyone with a computer and modem. Spacelink is currently being installed and will soon begin service.

It will provide:

- Daily Updates on NASA Programs
- Information about NASA Educational Services
- Manned Space Flight
- Unmanned Space Flight
- Aeronautics
- NASA, the Agency
- Lesson Plans and Activities
- Space Program Spinoffs

Lesson plans and activities were extracted from existing NASA publications on aerospace activities for the elementary school. These materials were arranged into 206 documents which have been entered into the Spacelink program for use in grades K-6.

ACKNOWLEDGEMENT

I wish to express my deepest appreciation to the NASA/ASEE Summer Faculty Fellowship Program and its directors for the opportunity afforded me this summer. I extend deep gratitude to Mrs. Ernestine Cothran, Dr. Gerald Karr, and Dr. Willim Snoddy for the roles they played in this endeavor; to the members of the staff in Public Affairs for their tolerance and kindnesses; to Mrs. Vicki Sullivan for her expertise in teaching me word processing, and to the host of others who have lent their help in large and small ways to making my summer's experience a rewarding one. A large measure of my thanks goes to my colleague, Bill Anderson, who assigned me the project and, who did not leave a stone unturned in enabling me to have a fantastic experience.

1. Introduction

The National Aeronautics and Space Administration offers educators a wide range of educational services including speakers, publications, audiovisual materials, software, advanced educational technology, curriculum assistance, electronic communications, in-school satellite programs, student programs and training opportunities. Still in the developmental stage is the educational service Spacelink.

Spacelink is an electronic information service to be operated by the Marshall Space Flight Center. It will provide NASA news and educational resources including software programs that can be accessed by anyone with a computer and modem. Spacelink is currently being installed and will soon begin service.

Spacelink will provide:

- Daily Updates on NASA Programs
- Information about NASA Educational Services
- Manned Space Flight
- Unmanned Space Flight
- Aeronautics
- NASA, the Agency
- Lesson Plans and Activities
- Space Program Spinoffs

The assignment this summer involved compiling lesson plans and activities for implementation in Spacelink. Material for this work was obtained from existing NASA publications on aerospace activities for elementary schools.

2. The Process

The material was first compiled on the word processor resulting in several typewritten pages. These were then organized into 206 documents (See Appendix.) each of which was loaded into the Spacelink program. The documents cover lesson plans and activities for living in space along with other aerospace activities.

The lesson plans for living in space include: food, clothing, communication, health, housing and working.

The lesson on Foods covers the following concepts:

1. The mode of preparation of food for space

2. The variety of food taken into space
3. The characteristics of food taken
4. The reason for the choice of food taken
5. How food is packaged for space
6. The eating utensils used in space
7. How a meal is prepared in space
8. How a meal is eaten in space

The lesson on Clothing covers the following concepts:

1. Appearance
2. Functional quality
3. Convenience
4. Safety features
5. Inventory
6. Body changes and their effect on clothing design

The lesson on Communication aims at teaching that in space:

1. Computers are essential for a successful mission.
2. Communication is handled by computers.
3. Communications satellites effect communication across great distances.

The lesson plan on health covers the following aspects:

1. Personal hygiene
2. The medical supplies and care that are available on the Space Shuttle
3. The necessity for proper waste management within the confines of the orbiter
4. The need to exercise to counteract the effects of living in a weightless environment

5. Personal storage lockers

The lesson plan on housing gives a description of:

1. Space Shuttle deck areas
2. The living areas of the Space Shuttle
3. Sleeping accommodations
4. Hatches and airlocks

The lesson plan on working covers:

1. The importance of each crew member performing specific jobs
2. The interactive roles of the astronauts on Space Shuttle missions
3. The variety of jobs that can be performed in space
4. The effect of weightlessness on the body functions, body measurements and posture of the astronauts
5. The different ways in which astronauts must perform their jobs
6. The role of the manipulator arm
7. The extravehicular gear used for work in space

The other activities cover:

1. The characteristics of the Earth's atmosphere and its magnetosphere which must be considered in planning for flight in the atmosphere or in space
2. The principles of flight in the atmosphere which man had to apply in designing aircraft
3. Rocket engines, which carry with them all the necessary materials for propulsion, and are used to launch flights into the upper atmosphere or into space

4. Some of the technological advances that had to be made in many areas before a vehicle could be launched into space beyond the earth's atmosphere
5. Various types of unmanned satellites
6. The unmanned lunar, solar, and interplanetary satellites and probes that were sent to the moon and into interplanetary space to gather information about the solar system and its members
7. Pilot astronauts and mission specialist astronauts who are carefully selected and well-trained to operate American spacecraft
8. The testing and utilization of man's capabilities in space as he/she paves the way for the acquisition of new knowledge
9. Future projections in the further expansion of space technology and space exploration
10. Suggested research topics on each of the above intended primarily for the intermediate and upper grade levels of the elementary school

CONCLUSIONS and RECOMMENDATIONS

Everyone is aware of the need to develop more scientists in the nation and that mathematics and science at all levels must be strengthened. Since the foundation laid before the college experience is vital for success in a career in science, we must continue to be concerned about the future development of scientists.

One of the historic tasks at NASA has been the stimulation of students in the nation's schools to strive for excellence. Thus far, the material prepared for Spacelink is for use in Grades K-6 which is in keeping with NASA's effort to encourage students to take a greater interest in mathematics and science by attempting to reach them in their formative years. NASA must continue its development of elementary-level materials to be placed alongside the wealth of NASA materials available for secondary teachers and students.

Now that the computer has become the basic underpinning of the space program and society, it is important that this vital resource be maximized in keeping classroom science relevant through the medium called Spacelink.

REFERENCES

Elementary School Aerospace Activities, A Resource for Teachers, NASA, 1977

Living in Space, Books I & II, NASA, 1987

APPENDIX

A Listing of the documents prepared for Spacelink, 1987

Lesson Plans & Activities

Living in Space

Food Lesson Plans

Clothing Lesson Plans

Health Lesson Plans

Housing Lesson Plans

Communication Lesson Plans

Working Lesson Plans

Food Lesson Plans

Background, Grades 1-3

Background, Grades 4-6

Grade 1

Grade 2

Grade 3

Grade 4

Grade 5

Grade 6

Clothing Lesson Plans

Background, Grades 1-3

Background, Grades 4-6

Grade 1

Grade 2

Grade 3

Grade 4

Grade 5

Grade 6

Health Lesson Plans

Background, Grades 1-3

Background, Grades 4-6

Grade 1

Grade 2

Grade 3

Grade 4

Grade 5

Grade 6

Housing Lesson Plans

Background, Grades 1-3

Background, Grades 4-6

- Grade 1
- Grade 2
- Grade 3
- Grade 4
- Grade 5
- Grade 6

Communication Lesson Plans

- Background, Grades 1-3
- Background, Grades 4-6
- Grade 1
- Grade 2
- Grade 3
- Grade 4
- Grade 5
- Grade 6

Working Lesson Plans

- Background, Grades 1-3
- Background, Grades 4-6
- Grade 1
- Grade 2
- Grade 3
- Grade 4
- Grade 5
- Grade 6

Space Science Activities

- Astronauts
- Atmosphere
- Magnetosphere
- Flight in the Atmosphere
- Rockets
- Technological Advances
- Unmanned Earth Satellites
- Unmanned Exploration of the Solar System
- Man in Space
- Projections

Astronauts

- Background
- K-2
- General
- Physical requirements
- 3-4
- General
- Selection
- Physical requirements
- Training

5-6
General
Selection
Physical requirements
Training

Space Science Activities (Atmosphere)

Background
K-2
Weather
Temperature
Density & pressure
3-4
General
Weather
Temperature
Density & pressure
Jet Stream
Ionosphere
Gases & dust
5-6
General
Weather
Temperature
Density & pressure
Jet Stream
Radiation
Ionosphere
Gases & dust

Space Science Activities (Magnetosphere)

Background
General, K-2
3-4
General
Solar Wind
5-6
General
Magnetic lines of force
Radiation belts
Solar wind

Space Science Activities (Flight in the Atmosphere)

Background
K-2
General
Lighter-than-air craft
Heavier-than-air craft
Gravity, thrust drag
Problems of flight

3-4
General
Lighter-than-air craft
Heavier-than-air craft
Lift, gravity, thrust, drag
Problems of flight
International cooperation
5-6
General
Lighter-than-air craft
Heavier-than-air craft
Lift, gravity, thrust, drag
Problems of flight
International cooperation

Space Science Activities (Rockets)

Background
K-2
General
Newton's third law
Fuel
Launch vehicles
Multistaging
3-4
General
Newton's third law
Fuel
Guidance
Launch vehicles
Multistaging
Space Shuttle launch
5-6
General
Newton's third law
Fuel
Guidance
Launch vehicles
Multistaging
Space Shuttle launch

Space Science Activities (Technological Advances)

Background
K-2
General
Power
Navigation and guidance
Data collection
Spacecraft design

5-6
General
Moon
Sun
Planets & interplanetary space
International cooperation

Man in Space
Background
K-2
Man to the Moon
Skylab
Apollo Soyuz Test Project
Space Shuttle
3-4
General
Man to the Moon
Skylab
Apollo Soyuz Test Project
Space Shuttle
International cooperation
5-6
General
Man to the Moon
Skylab
Apollo Soyuz Test Project
Space Shuttle
International cooperation

Projections
Background
K-2
Further exploration of space
Solar system
3-4
General
Further exploration of space
Management of resources
Solar system
Universe
5-6
General
Further exploration of space
Management of resources
Utilization of space environment
Solar system
Universe

3-4
General
Power
Navigation and guidance
Data collection
Spacecraft design
5-6
General
Power
Navigation and guidance
Data collection
Spacecraft design

Unmanned Earth Satellites

Background
K-2
General
Weather & communication
Earth observation
Biosatellites
Physics & astronomy
3-4
General
Weather & communication
Earth observation
Applications technology
Biosatellites
Physics & astronomy
International cooperation
5-6
General
Weather & communication
Earth observation
Applications technology
Biosatellites
Physics & astronomy
International cooperation

Unmanned Exploration of the Solar System

Background
K-2
General
Moon
Sun
Planets & interplanetary space
3-4
General
Moon
Sun
Planets & interplanetary space
International cooperation

55-61
N88-15606 116707
158

1987

NASA/ASEE SUMMER FACULTY RESEARCH FELLOWSHIP PROGRAM

MARSHALL SPACE FLIGHT CENTER
THE UNIVERSITY OF ALABAMA IN HUNTSVILLE

INVESTIGATION OF CANDIDATE
DATA STRUCTURES AND SEARCH ALGORITHMS
TO SUPPORT A KNOWLEDGE BASED
FAULT DIAGNOSIS SYSTEM

Prepared by: Edward L. Bosworth, Jr.
Academic Rank: Assistant Professor
University and Department: The University of Alabama in Huntsville
Computer Science Department
NASA/MSFC:
Laboratory: Systems Analysis and Integration
Division: Space Systems
Branch: Spacelab Payload Integration
NASA Colleague: Michael S. Freeman
Date: September 11, 1987
Contract No: The University of Alabama in Huntsville
NGT-01-008-021

ABSTRACT

The focus of this research was the investigation of data structures and associated search algorithms for automated fault diagnosis of complex systems such as the Hubble Space Telescope (HST). Such data structures and algorithms will form the basis of a more sophisticated Knowledge Based Fault Diagnosis System. As a part of the research, several prototypes were written in VAXLISP and implemented on one of the VAX-11/780's at the Marshall Space Flight Center. This report describes and gives the rationale for both the data structures and algorithms selected. A brief discussion of a user interface is also included.

1. Introduction

This paper will discuss a candidate data structure and associated search algorithm to be used as the basis for a Knowledge Based Fault Diagnosis System. Such a system might also be called an Expert System. The first part of the paper will define the structure and indicate the ways in which it matches the requirements of the fault diagnosis problem. In the second part of the paper, the shortcomings of the algorithm are indicated and indications given of modifications needed in order for the fault diagnosis task to be approached efficiently.

2. Objectives

The objective of this research is to support the development of an Automated Fault Diagnosis System to be used on the Hubble Space Telescope while on orbit. The primary function would be to interpret the downlink health telemetry on the HST and assist the operators in hypothesizing possible system faults and in deciding the proper corrective actions to be taken. Ideally, such a system would monitor performance trends and predict the time at which component operating capability would be so far degraded as to require corrective action.

For the purpose of fault diagnosis, the orbital mission of the Hubble Space Telescope may be divided into two time periods. The first period, lasting about six to nine months, is called the Orbital Verification Mission. This is a time during which all of the systems in the HST will be checked out and during which particular attention will be paid to the possibility of system faults. This period will be characterized by a high volume of system diagnostic information which could well be fed into a Knowledge Based Fault Diagnosis System such as is the subject of this research.

The second and much longer time period in the operation of the HST is the operational phase during which the telescope is expected to be collecting a large amount of scientific data. During this time the normal mode for collection and reporting of system health data will be the low data rate telemetry; i.e., there will be a low volume of data from which to infer the system status. A Knowledge Based Fault Diagnosis System could well be used during this phase, especially if it had the ability to detect potential failures and to devise measurements to be made during a brief period of high data rate health telemetry in order to confirm or deny the hypothesis.

3. Design of the Data Structure and Search Algorithm

The efficiency of a computational solution to any interesting problem depends, in general, on the choice of two items: a data structure appropriate to represent the structure of the problem and an algorithm which can operate efficiently on the selected data structure. One should note that these two are often quite interdependent: it is usually the case that the more appropriate the data structure, the less complex and more efficient the algorithm associated. This section will describe the selection of a data structure which fits the fault diagnosis problem quite well.

3.1 Choice of the Data Structure

As stated above, it is desirable to choose a data structure for at least two reasons: 1) natural description of the problem to be solved, and 2) the expected efficiency of the associated algorithm. For these criteria to be applied, one must first ask the fundamental question of what part of the problem is the more important to be represented efficiently.

In the fault diagnosis problem, the key feature to be represented is the interrelationship of the components in the structure being modeled. The usual method for representing this structure is a design schematic. There are two common data structures which will correspond naturally to a design schematic: a Tree and a Directed Acyclic Graph (DAG). Both of these are specializations of the general graph data structure.

The graph data structure comprises a collection of nodes, usually denoted as V , and a set of edges, usually denoted as E , connecting the nodes. The nodes are also called vertices, hence the symbol V for the set of nodes. One may name the edges by the nodes connected. Thus if

$$V = (V_1, V_2, \dots, V_n) - \text{a set of } n \text{ vertices}$$
$$E = (E_1, E_2, \dots, E_m) - \text{a set of } m \text{ edges}$$

We might name an edge as $E_i = (V_j, V_k)$; thus the edge (V_1, V_2) connects vertex 1 to vertex 2. The degree of a node is the number of edges connected to it.

A graph may be either directed or undirected; i.e., it may have edges which are directed or undirected. The edges in an undirected graph are similar to two way streets connecting intersections; thus if the edge (V_i, V_j) exists, so does the edge (V_j, V_i) . Edges in a directed graph are similar to one way streets in that the existence of an edge (V_i, V_j) does not automatically imply the existence of (V_j, V_i) . If both edges do exist in the graph, they must be called out explicitly in the edge list. Note that an node in a directed graph usually has a number of edges for which it is the first node in the pair and a different number of edges for which it is the second node in the pair describing the edge. The former number is called the "out-degree" of the node; the latter the "in-degree".

The directionality of a graph provides a natural mechanism for the representation of hierarchies normally found in design schematics. Thus the edges in a directed graph might represent the relationship "subcomponent". Note that if V_1 represents a component in the design schematic and V_2, V_3, V_4 represent its subcomponents, this fact may be naturally expressed by the edge list $(V_1, V_2), (V_1, V_3), (V_1, V_4)$. Here the directionality represents the hierarchy; in particular V_1 is not a subcomponent of V_2 . Note that in this representation, the out-degree of a node is the number of immediate subcomponents.

A path in a directed graph, denoted here as $P(i, j)$ is a list of edges in the edge set E which connects V_i to V_j . In a design schematic the existence of a path from V_i to V_j would imply that the component represented by V_j is a subcomponent of V_i . Thus if the edge list for the graph included $(V_1, V_2), (V_2, V_5),$ and (V_5, V_9) , one could construct the paths $P(1, 5), P(1, 9),$ and $P(2, 9)$. Note that edges in the edge list are not usually called paths although they are such in the strict sense.

A cycle in a directed graph is a path of more than one edge which starts and ends on the same node. A graph is said to be acyclic if there are no cycles in it. A directed graph which is acyclic is called, naturally enough, a Directed Acyclic Graph or DAG. Note that the DAG structure is a natural representation of a design schematic because the absence of cycles implements the requirement that no component be a subcomponent of itself.

There are two specializations of a Directed Acyclic Graph which should be considered for representing the design schematic: the tree and a "tree-like DAG". A tree is a DAG with two constraints, one of which is that there be a distinguished node, often called the "root node", which has an in-degree of zero. While it can be shown that a Directed Acyclic Graph must have at least one such distinguished node with in-degree zero, the DAG may have more than one such node. The "tree-like DAG" is a DAG with only one node of in-degree zero. This root node has a natural analogue in the design schematic; it is the entire system not broken into subcomponents.

The main difference between a tree and a tree-like DAG is that the nodes of the tree are constrained to have an in-degree of one whereas there is no such constraint on a tree-like DAG. This would correspond in a design schematic to the requirement that a component be a subcomponent of only one other component. There are components, such as the electric power, which are clearly subcomponents of many other components. Attempts to represent this in a tree structure would cause one node to be constructed for each occurrence of the component and thus lead to inefficiencies in the search process. These inefficiencies are caused by the fact that a fault search algorithm will examine each node in the data structure and thus examine a common subcomponent a number of times, even after its status has been established. The data structure of choice is thus a tree-like Directed Acyclic Graph.

3.2 Choice of an Associated Data Structure

One of the main objectives in the use of a tree-like DAG is the avoidance of multiple representations of the same component in the design schematic. This becomes a concern only when a component is to be added to the DAG. The question: Is it already in the DAG?

In order to develop an answer to the above question, one must look more closely at the structure of a node in a graph. Typically the node has an ID and a label. The ID might be thought of as the "variable name" used in the computer program to reference the node. The label might be thought of as the "schematic name" of the node; i.e., the name of the component in the design schematic which the node represents. Thus, in the above example, node V1 might represent the Pointing Control System. The node ID is "V1". The label is "Pointing Control System".

Suppose one wanted to determine whether or not to create a node with the label "Pointing Control System". It would be necessary to determine whether or not the DAG contained a node with the identical label and to create a new node only in the case that an existing node were not found. The most straightforward approach is extremely inefficient. This approach is to search the DAG every time a node with a new label is considered for insertion.

A more efficient approach to this problem is to create an associated data structure to maintain a list of the labels of nodes in the DAG. This list could be consulted more quickly than the DAG could be searched exhaustively for the label. The only constraint to this approach is that the DAG and associated data structure must be treated as a single abstract data structure with well defined constructor functions. Were either the DAG or the associated data structure manipulated separately, an inconsistency would probably arise and the DAG would become of little use.

3.3 VAXLISP Implementation

The Directed Acyclic Graph was implemented in VAXLISP as a COMMON LISP structure. The following code describes the node structure.

```
(Defstruct (Component
            (:conc-name Node-)
            :predicate)
  "A node for representing a component in the design
schematic"
  (Name Nil)           ;The name in the design schematic
  (Subcomponents Nil)  ; Note the default values.
  (Contained-In Nil)
  (Search-Seq 0))
```

The first slot in the structure contains the schematic name of the component represented by the node. In other words, this is the label of the node. The second slot will contain a structured list, discussed below, of the subcomponents of this component. The third slot contains a list of the components of which this component is itself a subcomponent. The search sequence entry is an integer used by the search algorithm to avoid excessive searching. Its use is also described below.

The associated data structure is a COMMON LISP Hash Table. The hash table is organized by (key, value) pairs. The key of this table will be the label or schematic name of each node. The value will be the ID of the node. Note that the node ID is used internally by the program and is not intended for communication with the user of the system.

The following COMMON LISP construct establishes a hash table of 197 entries as a global variable. The number 197 is chosen as a prime number with a value of about 200. The size of hash tables conventionally is set as a prime number with a value about twice the number of expected entries.

```
(Defvar *Component-List* (Make-Hash-Table: Size 197))
```

In order to understand how the hash table is used, one must understand the operation of the basic retriever function Gethash.

```
(Gethash Schematic-Name *Component-List*)
```

This function caused the hash table *Component-List* to be searched for an entry with a key given by the value of the variable Schematic-Name. If such an entry is found, the value (which here is the ID of the node associated with the schematic name) is returned. If no entry is found, the value Nil (here equivalent to logical FALSE) is returned.

One should also understand the general function Setf.

```
(Setf (Gethash Schematic-Name *Component-List*) Node-ID)
```

This function sets the entry (Schematic-Name, Node-ID) in the hash table. Note that in general, Setf takes as its first argument a retriever function and as its second argument a value to be given to the variable accessed by the retriever function.

As mentioned above, the Directed Acyclic Graph and Hash Table must be accessed as a single abstract data type. A typical function is that which creates a new node. It first checks the hash table to avoid making a duplicate. If it continues, it first updates the hash table and then creates the associated node.

```
(Defun Create-Component (Schematic-Name)
  "Creates a structure node with a component with
  a given name"
```

```
  (Unless (Gethash Schematic-Name *Component-List*)
    (Let
      ((Node-ID (Gensym "NODE-")))
      (Setf (Gethash Schematic-Name *Component-List*)
        Node-ID)
      (Set Node-ID
        (Make-Component: Name Schematic-Name)) )))
```

The basic structure of the above function is the UNLESS clause, which has as its skeletal structure

```
(Unless (Something)(Action))
```

The action form is to be executed if the first form returns Nil, which in this case means that the Schematic-Name is not found in the hash table. The action form works with a temporary binding of the variable Node-ID to a symbol returned by the LISP function Gensym. What we are doing here is creating a new variable name; e.g. NODE-2940, to be used as the ID of the node generated by the function Make-Component, which is the constructor function for the DAG.

3.4 Structure of Slots for Component Lists

Each node in the Directed Acyclic Graph has two slots containing lists of components. These slots are (Contained-In) and (Subcomponents). The structure of the Contained-In slot is a list of the form (Contained-In (V1 V2 V3)) which is merely a list of those components of which the given component is a subcomponent or to which it passes data.

The Subcomponents slot must contain more information than just a list of the subcomponents. This slot should also contain information indicating the dependence of the component on the functioning of its subcomponents. Basically, there are two types of subcomponent lists: AND (the default) and OR. The two lists types may be characterized as follows:

AND - A component modeled by an AND subcomponent list is not more functional than the least functional of its subcomponents. This criterion merely states the fact that most components depend on the proper functioning of all the subcomponents.

OR - A component modeled by an OR subcomponent list is not less functional than the most functional of its subcomponents. This criterion allows for the proper modeling of redundant subcomponents.

While one should note that there might exist real hardware components which have both redundant and non-redundant subcomponents, these can be modeled effectively as a collection of pure AND and OR nodes.

An additional feature thought to be important in the representation of subcomponent lists is an ability to express the dependence of a component on the proper functioning of each subcomponent. Thus each subcomponent is itself represented by a list of the form

(Component-Name Sensitivity-Factor)

Thus, a typical subcomponent slot might resemble one of the following:

(Subcomponents (AND (V1 100) (V2 80) (V3 55)))
(Subcomponents (OR (V5 95) (V6 75)))

3.5 Combination Rules for Subcomponent Functionalities

The functionality of a given component is obviously dependent upon the functionality of its subcomponents. The exact nature of this dependence is different for AND and OR nodes. The combination rules for each class of nodes according to the nature of the subcomponent lists will be discussed in this section.

The basic rule for functionality of an AND node is built around the minimum value function MIN. The formula is given by

$$F = \text{MIN} [A(f_1, s_1), A(f_2, s_2), \dots A(f_n, s_n)]$$

where for each subcomponent we have f_i = the functionality of that subcomponent s_i = the sensitivity factor describing the dependence of the component upon that subcomponent

The A function should follow these two rules

$A(f_i, 0) = 1$ implying that if the component does not depend on the proper functioning of that subcomponent the subcomponent should be combined as functional. This is an extreme case.

$A(f_i, 1) = f_i$ implying that complete dependence should use the functionality factor itself.

There are a number of candidates for the A function, but the following seems to be the best:

$$A(f, s) = 1 + (f - 1) * s$$

The reasons for selection of this function are:

- 1) There is no theoretical reason to prefer a more complex function.
- 2) This function shows the correct behavior.
- 3) The free parameter "s" can be chosen for each subcomponent and component pair so as to show the desired dependency over a reasonable range of functionalities.

The rule for functionality of an OR node is achieved by similar logic:

$$F = \text{MAX} [f_1*s_1, f_2*s_2, \dots, f_n*s_n]$$

3.6 Search Algorithms

Having established the data structure for representing the components to be examined by a fault diagnosis algorithm, it is now time to discuss the design of an algorithm to search through the data structure and isolate the faulty component. This design actually has two such algorithms both built around the concept of a search sequence number.

Search sequence numbers are a generalization of the concept of node marking found in many graph and tree search algorithms. Node marks generally are thought of as Boolean variables having the values TRUE or FALSE. An alternate representation of the node mark would be a search sequence number having only the permissible values 0 or 1.

In a node marking scheme, one also has two search algorithms. The first and simplest visits all nodes in the structure and sets the value of the mark to FALSE or not visited. The second and more focused search visits and marks all unmarked nodes which meet a predefined search criterion. Note that this gives rise to an overhead roughly equal to the search time for a specific item.

In the search sequence approach, there is a global variable which counts sequentially the searches undertaken during the current session. This variable is passed to the search procedure as a parameter in its list of arguments. As the search procedure visits each node it checks that node's search sequence number. If the node's search sequence is equal to the current value of the sequence number used by the search procedure, the node is considered to have been searched previously by this invocation of the search procedure and the node is not further examined. Otherwise the node is marked with the current search sequence number and is evaluated for expansion.

The associated search algorithm, called SWEEP, functions by performing a simple Depth First Search of the data structure and resetting the search sequence number of each node to zero. After having done this, it resets the global search sequence variable to one. Note that this procedure is undertaken to reduce the overhead seen in the simple node marking algorithm. In order to implement this, one must pick a maximum search sequence (say 1000). For a maximum search sequence of 1000, the SWEEP algorithm is called only once per one thousand directed searches. This procedure is similar to using a module counting sequence, but is robust against the ambiguities caused in such schemes when the count exceeds the module base (here 1000) and reverts to a small number (1001 becoming 1). Although it is provable that the search context will allow a high probability of disambiguating such sequence numbers, this more robust approach will guarantee against them with very little additional computational effort.

The search algorithm is a Best First Search with iterative deepening. It is called with two parameters - a node ID and a search sequence number. At each level, the node is examined to see if it is marked with the current sequence number. Should it be so marked, the next node in the search priority list is examined. Should the node not be so marked, it is given the current search sequence number and examined. Part of this examination will be obtaining the subcomponent list and comparing the components in that list to those in the search priority list. Nodes seen in both lists will be marked with a high search priority; i.e. moved to the front of the search priority list. The reason for this is the common observation that if two failed components have a subcomponent in common, then that subcomponent is quite suspect.

3.7 Search Heuristics

There is one fault in the above described search algorithm. That fault is due to the fact that the Directed Acyclic Graph being searched is based on the design schematic of the device under diagnosis.

The advantage of basing a search strategy on the design schematic is obvious. Such an approach allows a very efficient and focused search. This is even true when one allows for faults which commonly occur in the inter-component connections. One can easily write algorithms to assume that certain components are functional but are detached from the main circuit in that their output is becoming lost.

What cannot be handled efficiently by the algorithmic approach are those cases in which the device under diagnosis has components which do not show in the design schematic. A simple example of such a component is a bridging fault or short circuit, both of which represent a connection which is not present in the schematic.

In the algorithmic approach, the design schematic is used as a basis for focusing the search. If this focusing basis be lost, the algorithm will devolve into an exhaustive search of all components and consequently become extremely inefficient. It is for this reason that a heuristic approach to the search must be devised.

The primary use of search heuristics will be to maintain the focus of the search algorithm when it becomes obvious that the fault in the system cannot be explained under the assumptions imposed by the design schematic. These heuristics will make use of device design information and expert engineering judgement in order to postulate the most likely deviation from the design schematic. Although some work has been done in applying these heuristics to simple digital circuits, much work is yet to be done before applying them to devices of the complexity of the Hubble Space Telescope.

4. Conclusions and Recommendations

While it seems obvious that an automated fault diagnosis system would be of considerable benefit in the operation of the Hubble Space Telescope, it is also apparent that an algorithmically based fault diagnosis system will not be sufficiently sophisticated to fulfill the mission.

One of the major modifications which will be necessary to this research is the design of a heuristic to evaluate the list of subcomponents for each node expanded in order to select the node to be next examined. It is this heuristic which will be based on knowledge of the physical design of the component represented by the node being examined and which must make plausible inferences as to additional unrepresented circuit faults.

This research has identified a considerable amount of the algorithmic structure which must underlie a heuristically based fault diagnosis system. It is recommended that future research be undertaken in order to complete the algorithmic approach and extend it to the more satisfactory heuristic approach.

5. References

1. Davis, R.; Diagnostic Reasoning Based on Structure and Behavior, Artificial Intelligence 24 (1984) 347-410
2. Genesereth, M. R.; The Use of Design Descriptions in Automated Diagnosis, Artificial Intelligence 24 (1984) 411-436.
3. Keravnou, E. T. and Johnson L.; Competent Expert Systems, published by McGraw-Hill, 1986.
4. de Kleer, J. and Williams, B.C.; Diagnosing Multiple Faults, Artificial Intelligence 32 (1987) 97-130.
5. Reiter, R.; A Theory of Diagnosis from First Principles, Artificial Intelligence 32 (1987) 57-95.
6. Steele, G. L.; Common Lisp, the Language, published by Digital Press, 1984.

N88-15607

56-24

116708

248

1987

NASA/ASEE SUMMER FACULTY FELLOWSHIP PROGRAM

MARSHALL SPACE FLIGHT CENTER
THE UNIVERSITY OF ALABAMA

Prepared by:	Mark V. Bower, Ph.D., P.E.
Academic Rank:	Assistant Professor
University and Department:	The University of Alabama in Huntsville Department of Mechanical Engineering
NASA/MSFC:	
Laboratory:	Materials and Processes
Division:	Non-Metallic Materials
Branch:	Polymers and Composites
MSFC Colleague:	Frank E. Ledbetter III
Date:	September 22, 1987
Contract No.:	The University of Alabama in Huntsville NGT-01-008-021

INVESTIGATION OF LOW VELOCITY IMPACT DAMAGE ON
FILAMENTARY COMPOSITE MATERIALS

by

Mark V. Bower
Assistant Professor of Mechanical Engineering
The University of Alabama in Huntsville
Huntsville, Alabama

ABSTRACT

This report presents the results of an experimental investigation of the affect of low velocity impact on the residual modulus and residual strength of flat filamentary composite materials. Theoretical analysis of composite materials indicates that the modulus of the material must decrease as impact damage increases. This dectease must also correlate to the decrease in residual strength. This study is an initial investigation to verify these hypotheses.

Graphite/epoxy laminates (AS4/3501-6) of various fiber orientations ($8[0^\circ]$, $2[\pm 45^\circ]$,) were impacted using a falling weight impact tester. Impact energies ranged from 0.42 to 1.55 ft.-lb., with impact velocities from 2.03 to 3.98 ft./sec. The results show that there is a reduction in residual modulus of the plate as the impact energy increases.

ACKNOWLEDGEMENTS

I wish to thank Dr. Gerald Karr, Mr. Frank Ledbetter, and Dr. Jerry Patterson for the opportunity to return to Marshall for this third summer in the NASA/ASEE Summer Faculty Fellowship Program. I have benefitted once again from the opportunity and I look forward to a long and fruitful relationship with each of you.

My special thanks goes to Mr. Frank Ledbetter for his assistance in the conduct of this research. He contributed many ideas which were essential to the success of this project. I greatly appreciate the time he took from his work to assist me throughout the summer.

LIST OF FIGURES

<u>Figure</u>	<u>Title</u>	<u>Page</u>
1	Plot of Impact Load and Impact Energy vs. Time for a Unidirectional Sample. Drop Height of 2.5 inches.	VI-11
2	Plot of Impact Load and Impact Energy vs. Time for a 2[±45°], Laminate. Drop Height of 1.25 inches.	VI-12
3	Plot of Ultimate Tensile Stress vs. Impact Energy for Unidirectional Graphite/Epoxy.	VI-13
4	Plot of Modulus, E_1 , vs. Impact Energy for Unidirectional Graphite/Epoxy.	VI-14
5	Plot of Ultimate Tensile Stress vs. Impact Energy for a 2[±45], Graphite/Epoxy Laminate.	VI-15
6	Plot of Modulus, E_x , vs. Impact Energy for a 2[±45], Graphite/Epoxy Laminate (x is the direction of the axis of the specimen).	VI-16

LIST OF TABLES

<u>Table</u>	<u>Title</u>	<u>Page</u>
1	Results from Tensile Tests on Unidirectional Graphite/Epoxy (AS4/3501-6).	VI-17
2	Results from Tensile Tests on 2[±45], Graphite/Epoxy (AS4/3501-6) Laminates.	VI-18

INTRODUCTION

The concept of a reinforcing materials with filaments dates back to the time of the Egyptian empire. However, the application of this concept has been, until the twentieth century, limited in practice. Developments in chemistry and manufacturing techniques have resulted in the recent growth of the use of filamentary composite materials. As with many of man's developments, the ability to produce a structure from filamentary composite materials has exceeded the understanding and/or the ability to analyze.

The use of filamentary composite materials has grown rapidly since the 1940's. The principal material being glass fibers suspended in an epoxy matrix. The early applications of the material were to non-structural components where the analysis of the additional stiffness provided was not necessary and where damage to the material did not reduce the strength of the structure. The use of fiber glass/epoxy in structural applications has increased as the confidence in the material has grown. Typically, in the early stages of use, analyses performed on these structures involved application of principals derived from the behavior of metals. With the appropriate application of engineering judgement, the structures produced proved to be safe. Today, more advanced fibers are available for use. These new fibers have been developed for application as primary structural members which are lighter than comparable metallic members. As the use of composite materials in critical areas increases it becomes ever more important that the behavior of these materials be thoroughly understood.

One area in which the behavior of filamentary composite materials is only beginning to be understood is in response to damage. Experience with metals has demonstrated that as the level of damage increases in a structure, there is a reduction in the remaining strength of the structure. The damage may be due to either impact loads or fatigue. Composite materials have been shown to have the same basic behavior [1-2]. Composite materials of glass and graphite are more sensitive to impact damage than metals, due to the brittle nature of the fibers. Metals do not demonstrate a reduction in stiffness as the level of damage increases. It is only recently that it has been postulated, and shown, that filamentary composites have a reduction in stiffness

as the level of fatigue increases [3]. It is then proposed that the stiffness of the composite should decrease as the level of impact damage increases. If the modulus of the material is dependent on the damage level, this will adversely affect any analysis of the structure. A positive aspect of this behavior may be that for a specific level of damage, it should be possible to correlate the residual strength with the residual modulus. This then provides a mechanism for easily measuring the residual strength of the structure by non-destructive methods.

The following section presents a statement of the objectives of this research. The third section is a discussion of the rule of mixtures as it applies to the analysis of damaged filamentary composites. The test program is discussed in the section on methodology. The results from the tests performed on the graphite/epoxy panels is presented in the fifth section. Finally, the last section of the report contains the conclusions and recommendations.

OBJECTIVES

The objective of this research is to determine if the modulus of a filamentary composite material is dependent on the level of impact damage.

The initial investigation will attempt to determine the affect of low velocity impact on the residual modulus of graphite/epoxy composite panels. If the residual modulus does depend on the impact damage an attempt will be made to correlate the residual strength with the residual modulus.

THEORY

The rule of mixtures has been proven to be an upper bound on the modulus for a lamina [1]. The rule of mixtures is:

$$E_1 = E_f v_f + E_m v_m$$

where E_1 is the modulus of elasticity of the lamina in the principal material direction, E_f and E_m are the moduli of the fiber and matrix respectively, and v_f and v_m are the volume fractions of the fiber and matrix respectively. In the undamaged state

$$v_m = 1 - v_f .$$

Thus, to determine the modulus of the lamina it is only necessary to know the volume fraction of the fiber or matrix and the moduli of the fiber and matrix. However, if the lamina is damaged the rule of mixtures can only provide an upper bound to the lamina moduli.

The rule of mixtures as adapted to include damage is

$$E_1 = E_f f(v_f, v_d) + E_m v_m$$

where f is a function of the total volume fraction of fibers and the volume fraction of damaged fibers, v_d . The form of f is such that

$$f(v_f, 0) = v_f \quad \text{and} \quad f(v_f, v_f) \geq 0.$$

The first restriction provides that in the undamaged state the original form of the rule of mixtures applies. The second provides that there is a contribution to the stiffness in the principal direction, even if all the fibers are broken (resulting in a directional particulate composite). To fully develop f it will be necessary to analyze the load transfer from one fiber to another around the region of damaged, e.g. broken fibers. It has been shown that there is a characteristic length associated with the load transfer between fibers. This length then will contribute to the volume fraction of the damaged fiber. Development of f from a theoretical analysis is left for future study.

METHODOLOGY

MATERIAL PREPARATION

The material used for this project is Hercules AS4/3501-6 graphite/epoxy. The test panels used were made from prepreg stock according to the cure cycle indicated. Three unidirectional panels, 12 inches by 12 inches, with eight ply were laidup for the tests. Eight ply was selected based on the ASTM guidelines for determining the principal material direction properties. An additional set of four laminate panels were laidup with an orientation of $2[±45°]$. This configuration was selected to investigate the effect of laminate orientation on the level of damage developed.

The unidirectional panels were cut up into ten specimens, ten inches by one inch, after the ASTM method. The four $±45°$ panels were cut into seven specimens, eight inches by one inch.

IMPACT TESTING

An MTS falling weight impact test machine was modified for use in these tests. The falling weight impact test machine used a General Research Corporation data acquisition system. The impact tup of the GRC system had a weight of approximately four pounds. Combined with the carriage the total impactor weight was 8.9 lbs. This was determined to be too large for practical use. After modification the total weight is 6.49 lbs. This is still a large value, however, time did not permit further modifications to reduce the total weight. This introduces a limit to the velocity of impact.

The anvil of the impact tester has a 0.52 inch hole for the tup to pass through. This diameter was selected to provide support to the edges of the one inch wide test specimens. To minimize the cutting of fibers a nylon plate of .15 inches in thickness was used as a support for the specimens. The penetrator hole in the nylon back plate has an outside diameter of 0.53 inches on the specimen side and an interior diameter of 0.52 inches on the anvil side. This also acts to reduce fiber cutting.

For the unidirectional panels nine samples were tested at

drop heights ranging from one inch to three inches. The tenth sample was not impacted to provide an undamaged sample for comparison. The maximum drop height was determined such that there were no fibers cut in an impact. All samples were impacted at their mid points.

The $\pm 45^\circ$ laminates were tested in the same manner as the unidirectional panels. Six of the seven samples were impacted from drop heights from one inch to 2.25 inches.

TENSILE TESTING

The tensile tests were performed using an INSTRON universal test machine. Due to equipment problems it was necessary to measure the specimen elongation by the cross-head deflection. This is a method which is less than desirable and which had a strong adverse impact on the results obtained.

After the samples had been impacted they were prepared for the tensile tests by attaching clamping pads. These pads were attached by adhesives to minimize the fiber breakage due to the jaws of the grips.

The ultimate load for each specimen was obtained directly from the tensile test. The modulus of each sample is a tangent modulus obtained from the cross-head position and load data.

RESULTS

The results obtained from the tests performed are shown in Figures VI-1 through VI-6 and Tables VI-1 and VI-2. Figures VI-1 and VI-2 are plots from the impact tests, while the remaining plots are from the tensile tests.

IMPACT RESULTS

In all of the samples tested the location of the impact site is clearly observable by the naked eye. In the unidirectional samples at higher impact energies the fibers on the side of the sample opposite the impactor were broken along lines perpendicular to the fibers. In addition, some of the samples were clearly fractured lengthwise by the impact.

Figure IV-1 is a plot of the impact load verse time and impact energy verse time for a unidirectional sample at a drop height of 2.5 inches. The load trace is characteristic of the impact of fiber reinforced materials. At a load of approximately 30 lbs the curve has a discontinuity which indicates a fiber or fibers breaking. Again at a load of approximately 190 lbs. there is a sharp drop in load which indicates breaking several fibers. The maximum load is achieved, just prior to more fibers breaking. The oscilations in the load curve at times greater than 10 msec are not related to physical processes occuring in the sample. Rather, they relate to the response of the tup on rebound after impact.

Figure IV-2 is a plot of the impact load verse time and impact energy verse time for a $\pm 45^\circ$ laminate sampled at a drop height of 1.25 inches. Much less fiber breakage is observed in this plot than in that for the unidirectional sample. The changes at approximately 90 lbs. and at approximately 180 lbs. indicate fibers breaking. The loads at which fibers broke do not appear to have any pattern, occuring in a seemingly random pattern.

The energies and velocities of the impacts are listed in Tables VI-1 and VI-2. For the method used to release the carriage the comparatively small standard deviation in the energies is quite surprising.

TENSILE RESULTS

Figures IV-3 and IV-4 show results from the tensile tests of the unidirectional samples. Figure IV-3 is a plot of the average ultimate stress verse the impact energy. The bars indicate one standard deviation above and one standard deviation below the average value. A least squares interpolation of the points yields

$$X(\psi) = -42170 \psi + 171000$$

where ψ is the impact energy, and X is the ultimate stress. The confidence level for the least squares approximation is 0.49 (1.0 indicating a perfect fit). This indicates that a linear least squares approximation does not fit the data well.

The handbook value for ultimate strength is 312.7 kpsi. The ultimate stress obtained in these tests for the undamaged state do not compare to this value. This is probably due to difficulties encountered in clamping the samples without breaking the fibers.

Figure IV-4 is a plot of the modulus of the unidirectional samples verses the impact energy. As in the ultimate stress plot, the bars indicate one standard deviation above and one standard deviation below the plotted average. The plot indicates that there is a reduction in the modulus as impact energy increases. A linear least squares approximation yields

$$E_1(\psi) = -1112000 \psi + 5165000$$

The confidence level for the approximation is 0.53.

The unidirectional modulus obtained in the undamaged state does not compare to the handbook values for this material ($E_1 = 20.7$ Mpsi). One undamaged specimen was tested using a strain indicator. The results of that test produced $E_1 = 20.0$ Mpsi. Since the values are consistent, the conclusion is that the error is systematic, resulting from measuring the elongation by cross-head deflection. This then requires that the data be compared only among these tests or tests performed using the same methods.

The results for the unidirectional samples are listed in Table IV-1.

One important observation of the failure mode for the

unidirectional samples is made. In the samples with discernable breaks in the fibers the flaws did not propagate in the plane of the flaw. Rather, the flaw propagated in the direction of the fibers. The result, a rectangular opening at the site of impact. This observation supports the conclusions reached in [4].

Figure IV-5 is a plot of the average ultimate stress for the $\pm 45^\circ$ laminates verses impact energy. The bars denote the plus one and minus one standard deviation band. There is considerable scatter in the data. Table IV-2 is a list of the results for the $\pm 45^\circ$ laminates. Examining the data it is clear that panel 2 is of higher quality than the other panels. This contributes to the scatter.

A linear least squares approximation of the data in the figure yields

$$X(\psi) = -1450\psi + 18740$$

with a confidence of 0.82.

A plot of the modulus verses the impact energy is shown in Figure IV-6. As with the unidirectional tests the modulus measured does not compare to the expected value ($E = 3.63$ Mpsi). This supports the conclusion that the fault lies in the method of deflection measurement. The plot shows that, again, the modulus decreases as the impact energy increases. Applying a power form of the least squares approximations produces

$$E_1(\psi) = 606400 \psi^{-0.08}.$$

The confidence level is 0.80. The negative exponent demonstrates the inverse relation between modulus and impact energy.

CONCLUSIONS AND RECOMMENDATIONS

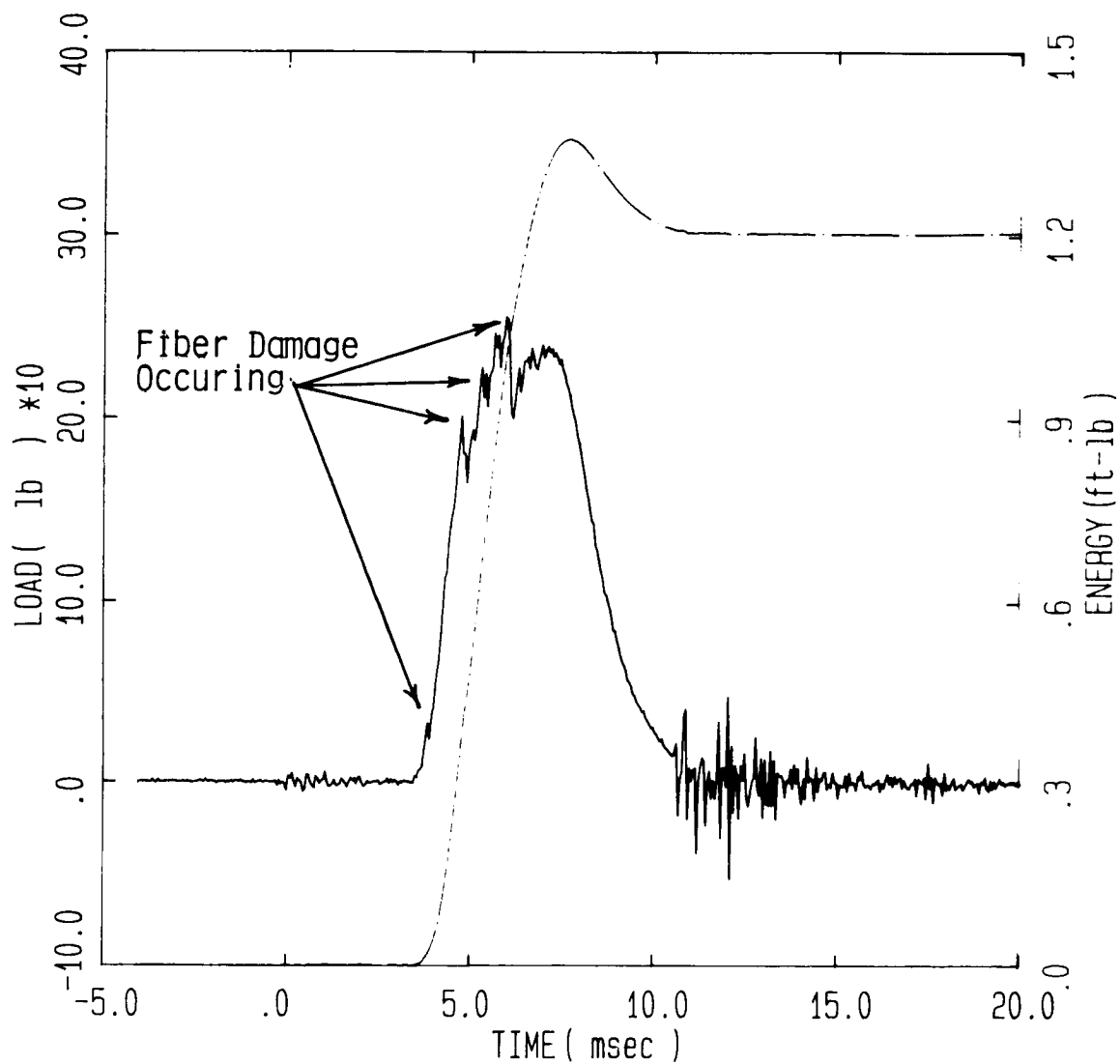
The results from this investigation show that the modulus of a filamentary composite material decreases as the level of impact energy and hence damage increases.

Insufficient data was obtained to determine if a relationship exists between the residual modulus and residual strength.

This is only a preliminary study. Due to equipment problems this data is at best self consistent. Nevertheless, these results call for further investigation. In these investigations larger sample sets should be used and the modulus measurements should be performed using an extenseometer.

ORIGINAL PAGE IS
OF POOR QUALITY

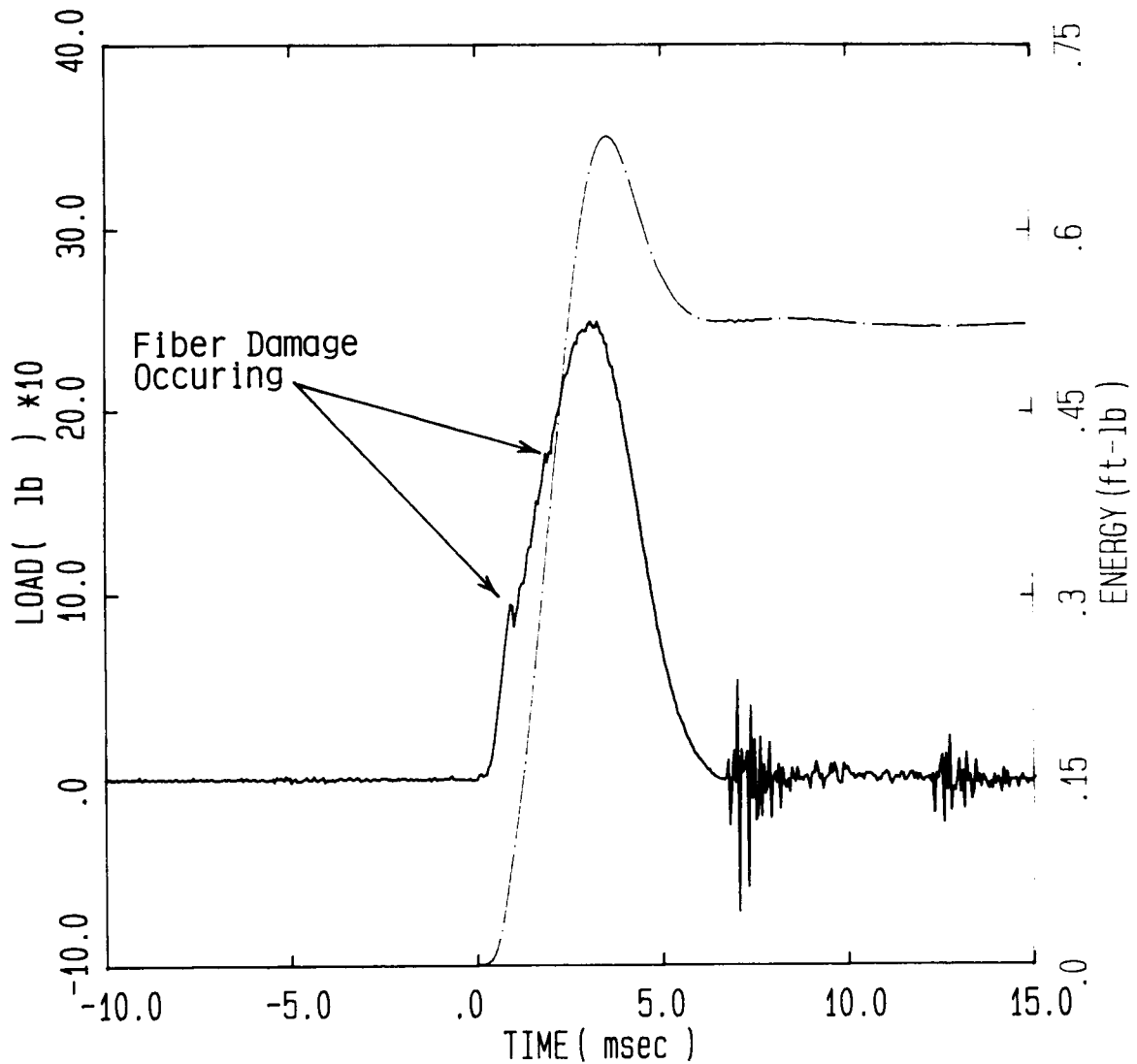
Figure VI-1.
Plot of Impact Load and Impact Energy vs.
Time for a Unidirectional Sample. Drop
Height of 2.5 inches.



Specimen Id	Temp (f)	Veloc. (ft/sec)	Energy (ft-lb)	Time		Load (lb)	Energy	
				(msec)			(ft-lb)	
				Max Ld	Total		Max	Maxld Total
40	70.	3.48	1.22	5.95	10.70	255.3	.982	1.209

ORIGINAL PAGE IS
OF POOR QUALITY

Figure VI-2.
Plot of Impact Load and Impact Energy vs.
Time for a 2[±45°], Laminate. Drop Height
of 1.25 inches.



Specimen Id	Temp (f)	Veloc. (ft/sec)	Energy (ft-lb)	Time (msec)		Load (lb)		Energy (ft-lb)	
				Max	Total	Max	MaxId	Total	
08	70.	2.52	.64	3.05	6.55	248.8	.640	.524	

Figure VI-3.
Plot of Ultimate Tensile Stress vs. Impact
Energy for Unidirectional Graphite/Epoxy.

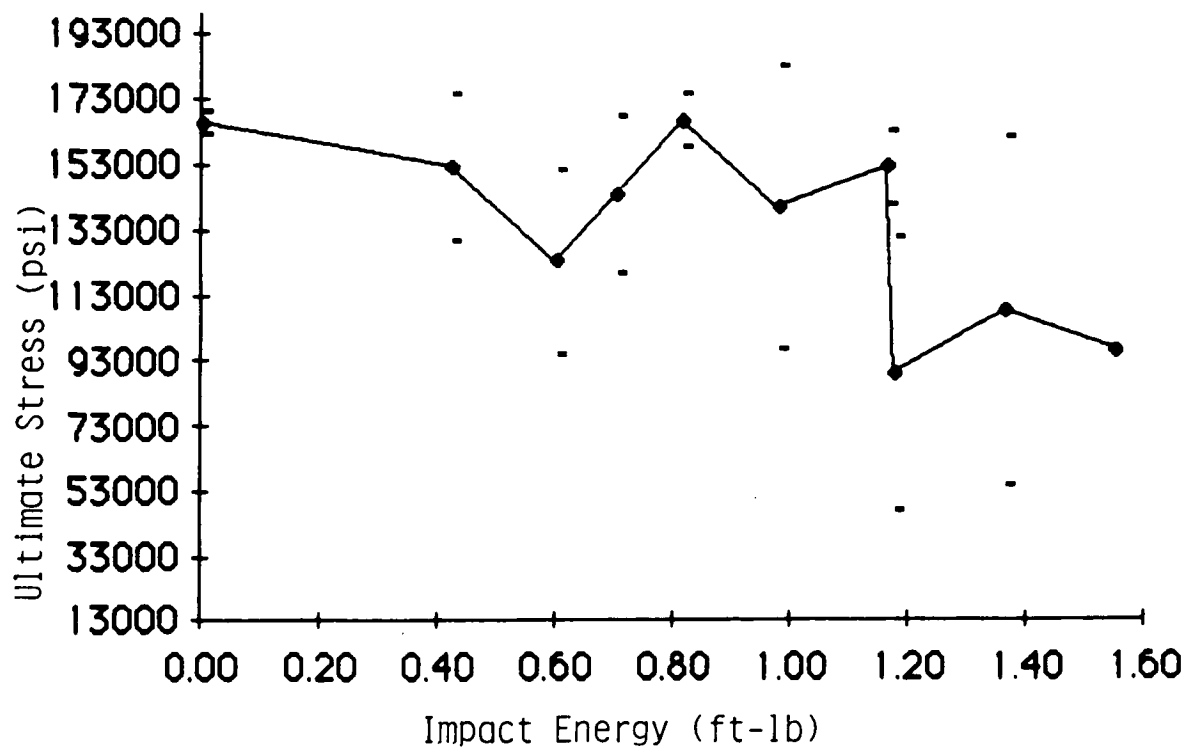


Figure VI-4.
Plot of Modulus, E_1 , vs. Impact Energy
for Unidirectional Graphite/Epoxy.

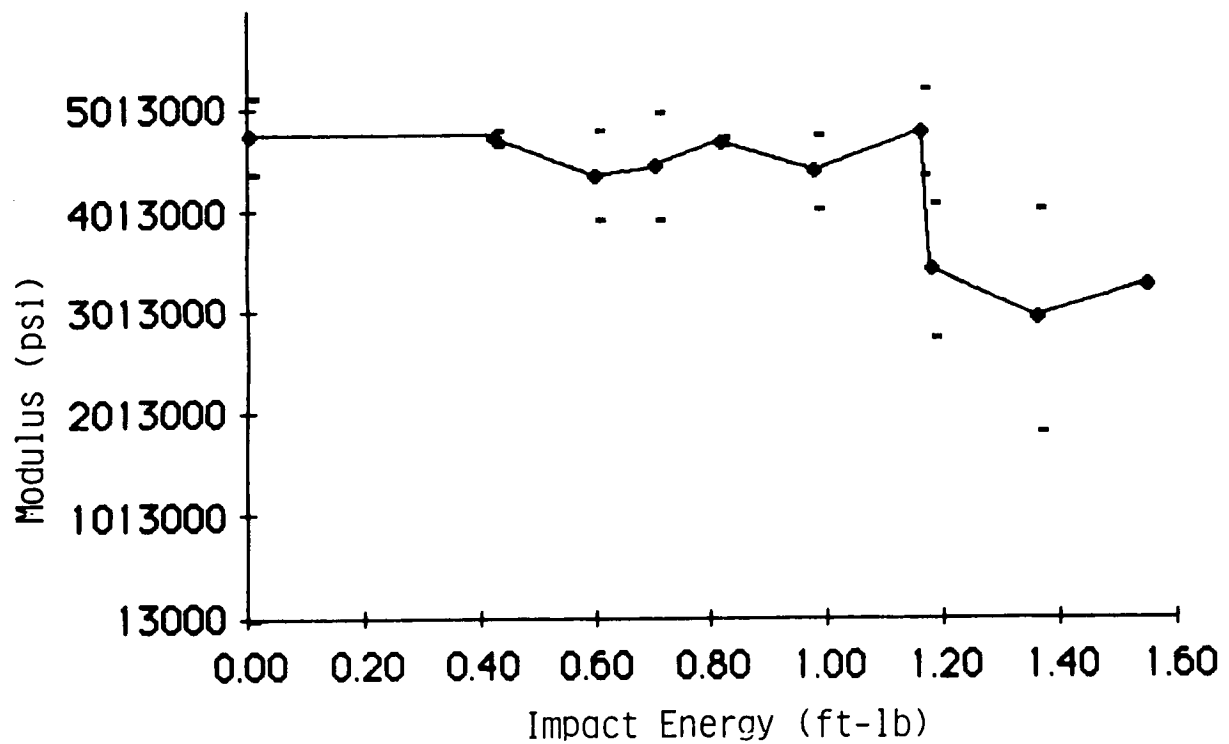


Figure VI-5.
Plot of Ultimate Tensile Stress vs. Impact VI-14
Energy for a 2[±45], Graphite/Epoxy Laminate.

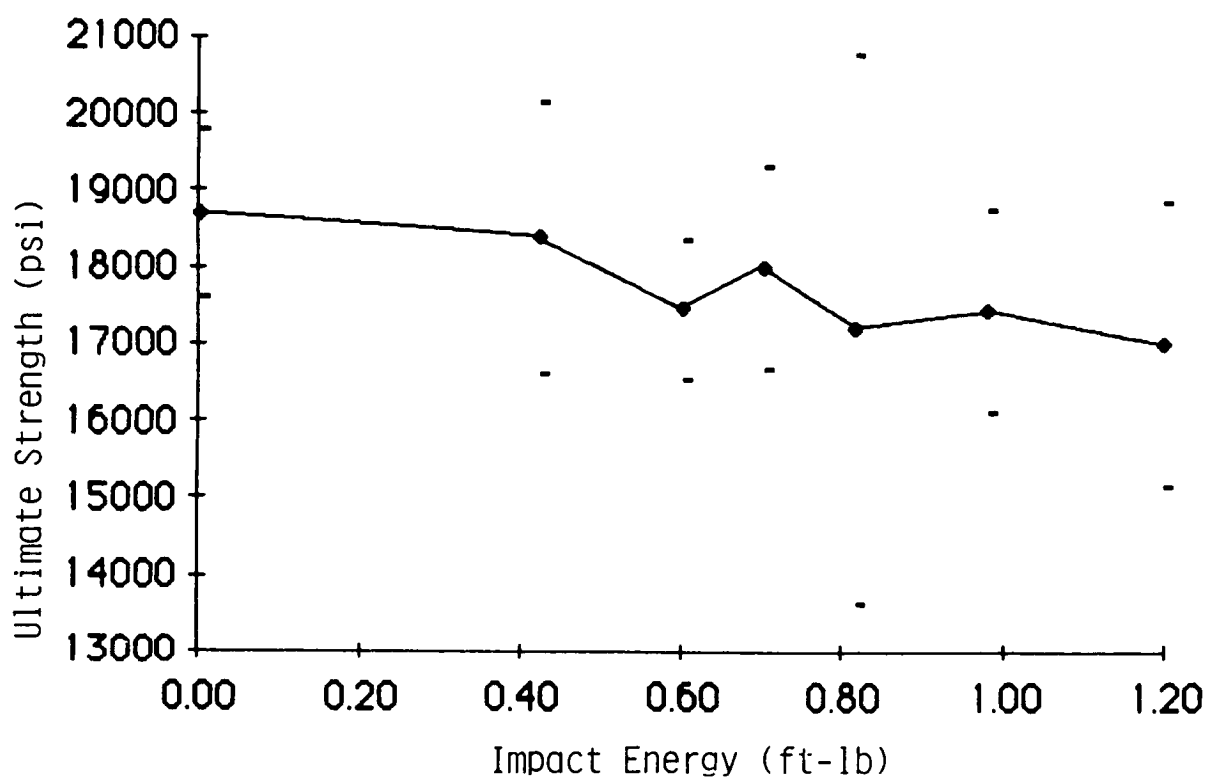


Figure VI-6.
Plot of Modulus, E_x , vs. Impact Energy for VI-15
a 2[±45], Graphite/Epoxy Laminate (x is the
direction of the axis of the specimen).

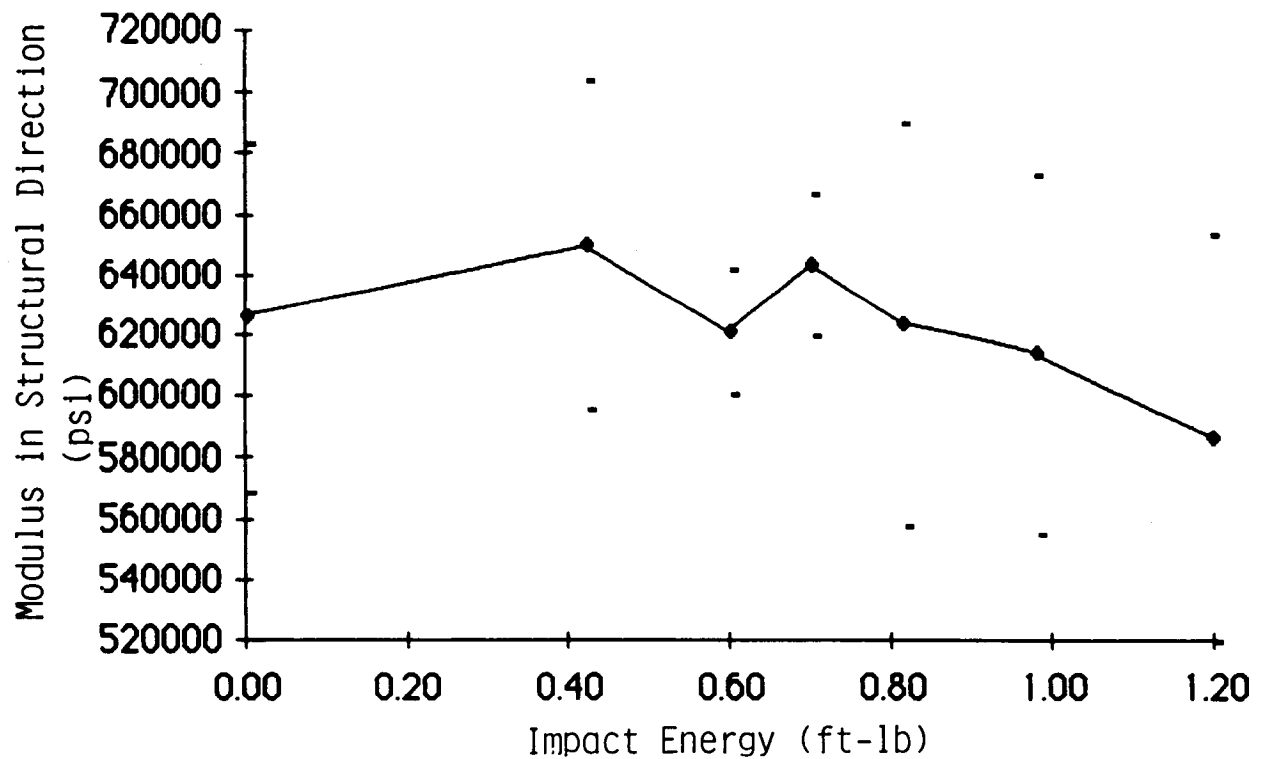


TABLE VI-1.
Results from Tensile Tests on Unidirectional
Graphite/Epoxy (AS4/3501-6).

Drop Height in	Panel Number	Impact Energy ft-lb	Ultimate Stress kpsi	Modulus Mpsi
0.00	2	0.00	167.1	4.49
	3	0.00	169.3	5.02
	Average	0.00	166.2	4.75
1.00	1	0.52	170.3	4.78
	2	0.45	127.3	4.79
	3	0.44	160.5	4.66
1.25	Average	0.46	152.7	4.74
	1	0.61	155.7	4.87
	2	0.60	102.5	4.06
1.50	3	0.55	113.1	4.19
	Average	0.59	123.8	4.37
	1	0.72	153.8	4.84
1.75	2	0.74	161.5	4.66
	3	0.76	116.5	3.86
	Average	0.74	143.9	4.46
2.00	1	0.87	175.0	4.70
	2	0.84	167.2	4.72
	3	0.95	158.8	4.64
2.25	Average	0.87	167.0	4.69
	1	0.95	138.9	4.39
	2	1.01	98.0	4.05
2.50	3	0.99	184.0	4.78
	Average	0.98	140.3	4.41
	1	1.14	158.9	5.14
2.75	2	1.12	159.2	4.32
	3	1.09	139.2	4.90
	Average	1.12	152.4	4.79
3.00	1	1.18	136.6	4.19
	2	1.22	75.0	3.09
	3	1.13	57.1	3.00
	Average	1.18	152.7	3.43
	1	1.37	59.9	1.84
	2	1.36	165.9	4.03
	3	1.36	100.3	2.96
	Average	1.36	108.7	2.94
	3	1.55	96.7	3.27

TABLE VI-2.
Results from Tensile Tests on 2[±45],
Graphite/Epoxy (AS4/3501-6) Laminates.

Drop Height in	Panel Number	Impact Energy ft-lb	Ultimate Stress kpsi	Modulus kpsi
0.00	1	0.00	18.8	
	2	0.00	19.9	640.
	3	0.00	18.9	675.
	4	0.00	17.3	563.
	Average	0.00	18.7	626.
1.00	1	0.42	17.6	578.
	2	0.45	21.0	706.
	3	0.41	17.8	672.
	4	0.41	17.1	645.
	Average	0.42	18.4	650.
1.25	1	0.56	17.9	631.
	2	0.64	18.5	614.
	3	0.61	17.3	596.
	4	0.59	16.3	645.
	Average	0.60	17.5	621.
1.50	1	0.70	16.8	620.
	2	0.75	19.7	671.
	3	0.64	18.5	628.
	4	0.72	17.1	655.
	Average	0.72	18.0	643.
1.75	1	0.83	18.0	651.
	2	0.72	20.5	642.
	3	0.80	18.2	675.
	4	0.91	12.1	527.
	Average	0.87	17.2	624.
2.00	1	1.00	17.3	624.
	2	0.99	19.0	658.
	3	0.97	17.8	648.
	4	0.96	15.8	528.
	Average	0.98	17.5	615.
2.25	1	1.10	17.4	648.
	2	1.09	19.5	610.
	3	1.48	15.5	597.
	4	1.12	15.7	492.
	Average	1.36	17.0	587.

REFERENCES

1. Jones, R.M., Mechanics of Composite Materials, McGraw-Hill, New York (1975).
2. Carlsson, L.A. and Pipes, R.B., Experimental Characterization of Advanced Composite Materials, Prentice-Hall, Englewood Cliffs, New Jersey (1987).
3. Almorgrabhy, M., "An Investigation of the Effect of Fatigue Damage on Residual Modulus and Internal Damping" a Master's Thesis, The University of Alabama in Huntsville, in progress.
4. Bower, M.V., "Fracture Toughness Testing of Epoxy Matrix Composite Materials," NASA CR-178709 (1985).

N88-15608⁵⁷⁻¹⁸

116709

17P.

1987

NASA/ASEE SUMMER FACULTY RESEARCH FELLOWSHIP PROGRAM

MARSHALL SPACE FLIGHT CENTER
THE UNIVERSITY OF ALABAMA IN HUNTSVILLE

INVESTIGATION OF THE FEASIBILITY OF AN ANALYTICAL
METHOD OF ACCOUNTING FOR THE EFFECTS OF ATMOSPHERIC
DRAG ON SATELLITE MOTION

Prepared By:	Robert E. Bozeman
Academic Rank:	Professor
University and Department	Morehouse College Mathematics Department
NASA/MSFC Laboratory:	Systems Analysis and Integration
Division:	Mission Analysis
Branch:	Orbital Mechanics
NASA Colleague:	Larry D. Mullins
Date:	August 7, 1987
Contract No:	The University Of Alabama in Huntsville NGT-01-008-021

ABSTRACT

An analytic technique for accounting for the joint effects of earth oblateness and atmospheric drag on close-earth satellites is investigated. The technique is analytic in the sense that explicit solutions to the Lagrange planetary equations are given; consequently, no numerical integrations are required in the solution process. The atmospheric density in the technique described in this report is represented by a rotating spherical exponential model with superposed effects of the oblate atmosphere and the diurnal variations. A computer program implementing the process is discussed and sample output is compared with output from program NSEP (Numerical Satellite Ephemeris Program). NSEP uses a numerical integration technique to account for atmospheric drag effects.

ACKNOWLEDGEMENTS

The author wishes to express his gratitude to all persons of the Orbital Mechanics Branch at MSFC for making his tenure a delightful and rewarding experience. Special thanks are extended to his NASA colleague - Larry D. Mullins for devoting many hours of his time in consultation on this project and to Lewis Wooten for his many helpful suggestions and assistance in computer programming concerns.

INTRODUCTION

In order to accurately predict orbital lifetimes and obtain trajectory data on close-earth satellites, it is generally accepted that joint effects due to perturbations such as atmospheric drag and the oblateness of the earth must be included in the mathematical model. However, inclusion of these joint perturbative effects usually leads to coupled systems of nonlinear differential equations that are difficult to solve in closed form - i.e., obtain an exact solution. Consequently, most computational procedures that attempt to account for joint effects make use of numerical integration techniques to generate solutions to the coupled equations. Although these procedures can produce accurate results, they are often found to be time-consuming in their execution because of the numerical integrations involved. Because of this, persons working in real-time satellite tracking activities are continually seeking better ways of accelerating the solution process.

This report is an attempt to evaluate and test an analytic model that includes the joint effects of oblateness and drag and requires no numerical integration in its execution. The theory for this model was developed by Sean C. H. Chen ([4],[5]). Chen's development commences with the Lagrange Planetary equations for the classical orbital elements. From the outset the development considers jointly the coupled effects of oblateness and drag and is not the superposition of two separate developments. Consequently, it is considered to be a mathematically rigorous theory.

The solutions to the variational equations of motion are derived using a two-variable asymptotic expansion. Perturbations due to the second harmonic are considered as first order effects and perturbations due to the third and fourth harmonics and the drag force are considered as second order effects for the series expansion. The atmospheric density model used in the development of the solutions is a rotating spherical exponential model with superposed effects of the oblate atmosphere and the diurnal variation.

A computer program based on the drag theory of Chen is described and sample output is discussed.

GENERAL FORM OF SOLUTIONS

The general form of the solutions to the equations of motion for the drag problem will be briefly described. The solutions themselves are quite lengthy and will not be included in this document. The interested reader can consult references [4] and [5] for complete details.

The equations of motion of a particle of mass m , under the attraction of a mass M , but acted on by perturbing forces $F = (R, S, W)$, can be derived in terms of the classical orbital elements - $a, e, i, \Omega, \omega, M$. Here, a is the semi-major axis; e is the eccentricity; i is the inclination of the orbit; Ω is the right ascension of the ascending node; ω is the argument of perigee; and M is the mean anomaly. The Lagrange planetary equations for the orbital elements can be expressed in the general form:

$$\begin{aligned}
 da/dt &= ((2a^2)/\sqrt{\mu p}) [e(\sin v)R + (p/r)S] \\
 de/dt &= \sqrt{p/\mu} [(\sin v)R + \{((r+p)\cos v + er)/p\}S] \\
 di/dt &= [(r \cos u)/\sqrt{\mu p}] W \\
 d\Omega/dt &= [(r \sin u)/(\sqrt{\mu p} \sin i)] W \\
 d\omega/dt &= (1/e)(\sqrt{p/\mu}) [-(\cos v)R + (r/p + 1)(\sin v)S - \\
 &\quad \{ (re(\sin u)(\cot i))/p \} W] \\
 dM/dt &= n - (1/\sqrt{\mu a}) [(2r - (p/e)\cos v)R + \{((r+p)\sin v)/p\}S]
 \end{aligned} \tag{1}$$

In the above expressions, r is the magnitude of the position vector between the two bodies, n is the mean motion, v is the true anomaly, u is the argument of latitude, $p = a(1-e^2)$, and $\mu = k(m+M)$, (k = gravitational constant).

In deriving solutions to the planetary equations, Chen assumes that the perturbing forces F are of the form $F = F(C) + F(D)$ where $F(C)$ are the conservative forces which includes the earth's oblateness and $F(D)$ is the drag force. The drag force per unit mass is represented by

$$F(D) = -0.5CD(A/m)\rho \bar{v} \tag{2}$$

where CD is a nondimensional drag coefficient, m is the mass of the satellite, \bar{v} is the velocity of the satellite relative to the atmosphere, A is the effective cross

sectional area of the satellite and ρ represents the local atmospheric density. The analytic model for the density is taken to be:

$$\begin{aligned}\rho &= \rho_0 \exp(-(h-h_0)/H)[1 + F(A\cos v + B\sin v)] \\ F &= (\text{RHO1}-\text{RHO2})/(\text{RHO1}+\text{RHO2}) \\ \rho_0 &= \text{RHO1}/(1+F) \\ H &= -2ae/\ln(\text{RHO3}/\text{RHO1})\end{aligned}\tag{3}$$

where RHO1 is a value of the density computed at the center of the diurnal bulge, RHO2 is a density value computed at perigee height at a point opposite the bulge and RHO3 is a density value computed at apogee height at a point under the bulge. A, B, h, and h_0 are parameters that depend on the position of the point under consideration.

The Lagrange planetary equations (system (1)) with $F(C)$ replaced by the earth gravitational potential up to and including the fourth harmonic and with $F(D)$ replaced by (2) and (3) are solved analytically for the orbital elements. A two variable asymptotic expansion technique is used to generate the solutions. The solution for each orbital element is obtained and expressed in the form:

$$X = X(\text{OBLATE}) + X(\text{DRAG})$$

where X represents any of the orbital elements, $X(\text{OBLATE})$ is the part of the solution generated by the conservative forces and $X(\text{DRAG})$ is the portion generated by the drag effects. The solutions are quite lengthy and will not be reproduced here. The $X(\text{OBLATE})$ components are contained in reference [5] (pages 6-3 -6-7) and the $X(\text{DRAG})$ components are contained in reference [4] (pages 6-1 - 6-7) .

PROGRAM DESIGN AND SAMPLE OUTPUT

The Analytic Satellite Ephemeris Program (ASEP) now in use in the Orbital Mechanics branch of the Mission Analysis Division at Marshall Space Flight Center is designed to accurately simulate the motion of a satellite in earth orbit (see [10]). The solution to the satellite motion is completely analytic and requires no numerical integrations for its execution. The program is based on the theoretical work of Sean C.H. Chen as described in [5] and only includes perturbations due to the oblate earth. Atmospheric drag effects are not included. In designing a test program that included both oblateness and drag perturbations, a subroutine (ORBIT) from the ASEP program was selected for modification. Subroutine ORBIT accepts initial values for the orbital elements as input and generates a detailed trajectory. In designing the program, several tasks were executed:

- (1) The mathematical development of the analytic solution derived by Chen and contained in [4] and [5] was reviewed;
- (2) All subroutines in ORBIT that were impacted by the drag terms were identified and appropriately modified;
- (3) A driver (main calling program) for ORBIT was written.

As a result of the above tasks, a test program resulted. The components of the program and a brief description of each are listed below:

- BDRAG - the main driver program.
- BORBIT - BORBIT is the ORBIT subroutine from ASEP containing minor changes to reflect the inclusion of the drag terms.
- BRATES - BRATES contains modifications to subroutine RATES of ASEP that are used to generate the secular terms in the solution of the orbital element.
- BSECTM - BSECTM is used together with BRATES to generate the secular terms.
- BLPTRM - BLPTRM contains modifications to sub-

routine LPTERM of ASEP that are used to generate the long period components of the solution.

- FIT - Program FIT evaluates the constants H , F and ρ_0 , given in (3). These values are needed for the local density.

The drag terms are primarily accounted for in the subroutines BRATES, BSECTM, and BLPTRM. The modifications are quite extensive and are included in the Appendix. The interested reader can compare the expressions in the three subroutines with the solutions for the orbital elements contained in [4] and [5].

The test program described above has been coded and implemented and the results compared with output from NSEP (Numerical Satellite Ephemeris Program). NSEP handles the drag effects by a numerical integration process. The NSEP program has been used extensively and found to be accurate. However, the implementation is slow because of the numerical integrations involved.

Results from the analytic model (no numerical integrations required) described in this document are compared with NSEP output. A comparison of agreement between the two procedures is made simply by subtracting the corresponding values given by the two techniques for the orbital elements. A difference of zero would indicate that both procedures gave the same value for that element at the given time. Charts #1 and #2 give the deviations in five orbital elements over a ten day period. It can be noted from the charts that there is reasonably good agreement for the eccentricity, argument of perigee, and right ascension of the ascending node. However, both samples indicate less than favorable comparisons in the semi-major axis and the mean anomaly. It is believed that better comparisons will result once a good fit of the parameters H , F , and ρ_0 needed for the atmospheric density, is obtained.

COMPARISON WITH NSEP OUTPUT
[X(NSEP)-X(ANALYTIC),X= ORBITAL ELEMENT]

INPUT DATA

$\rho = 5.80595D-11$
-0

F = -.01599

H = 49797.8(M)

INITIAL CONDITIONS: a = 6755.734(km) e = .019193
 Ω = 3.77821(deg) ω = 180.0(deg)
 i = 57.0(deg) M = 0.00(deg)

ORBITAL ELEMENT _____ MISSION ELAPSED TIME (DAYS)

	4	6	8	10
SEMI-MAJOR AXIS(KM)	-.575	-.868	-1.168	-1.467
ECCENTRICITY	-.00032	-.00046	-.00063	-.00076
RIGHT ASCENSION OF ASCENDING NODE(DEG)	.03	.04	.06	.07
ARGUMENT OF PERIGEE (DEG)	.03	.03	.17	.28
MEAN ANOMALY(DEG)	4.50	10.13	17.89	27.93

CHART #1

COMPARISON WITH NSEP OUTPUT
[X(NSEP)-X(ANALYTIC),X= ORBITAL ELEMENT]

INPUT DATA

$\rho = 4.45D-11$ $F = 0.99$ $H = 1039000(M)$

INITIAL CONDITIONS: $a = 6755.734(km)$ $e = .019193$
 $\Omega = 3.77821(deg)$ $\omega = 180.0(deg)$
 $i = 57.0(deg)$ $M = 0.00(deg)$

ORBITAL ELEMENT _____ MISSION ELAPSED TIME (DAYS)

	4	6	8	10
SEMI-MAJOR AXIS(KM)	1.635	2.480	3.326	4.182
ECCENTRICITY	-.00024	-.00034	-.00046	-.00053
RIGHT ASCENSION OF ASCENDING NODE(DEG)	.04	.06	.09	.12
ARGUMENT OF PERIGEE (DEG)	-.27	-.39	-.41	-.43
MEAN ANOMALY(DEG)	4.75	10.47	18.33	28.45

CHART #2

CONCLUSIONS

An analytic model for accounting for joint effects of earth oblateness and atmospheric drag on close-earth satellites has been described. Preliminary tests indicate reasonable results when compared with output generated by the NSEP program (Numerical integration routine). However, more test cases will be required before a final determination can be made on the accuracy of the analytic process. Also, it will be useful to compare output from the analytic method with actual data collected from observations of close-earth satellite motion. Such data was not available during the period of this report.

A number of authors have pointed out the difficulty in describing a realistic model of the atmospheric density because it depends on position and time in a very complex manner. In the model tested in this report, it was necessary to fit three constants F , ρ_0 , and H in order to describe the atmospheric density. This fitting was done by first using the Jacchia model to calculate values of the density at specific points in the diurnal bulge. These values are used to compute the numerical values of the three parameters. More research is required on this process so that a determination can be made on when a "good" fit has been obtained. Additionally, in the tests conducted in this study, only one fitting of the constants was done for the entire ten-day mission. It is anticipated that better results will be obtained if the constants were updated at least every twenty-four hours. This updating process needs to be tested.

REFERENCES

1. Barry, B.F., Pimm, R.S. & Rowe, C.K., "Techniques of Orbital Decay and Long-Term Ephemeris Prediction For Satellites in Earth Orbit", Computer Sciences Corp., Huntsville, Alabama, November 1971.
2. Brouwer, D. and Hori, G.I., "Theoretical Evaluation of Atmospheric Drag Effect in the Motion of an Artificial Satellite", The Astron. J., Vol. 66, pp. 193-225, 1961.
3. Chen, C.H., "A Note on the Motion of an Artificial Satellite Around an Oblate Planet With A Small Eccentricity", Northrop Services, Inc., Technical Note TN-242-1144, Huntsville, Alabama, October 1972.
4. Chen, C. H., "Ephemeris Generation For Earth Satellites Considering Earth Oblateness and Atmospheric Drag", Northrop Services, Inc., M-240-1239, Huntsville, Alabama, May 1974.
5. Chen, C.H., "The Motion of an Artificial Satellite Around an Oblate Planet", Northrop Services, Inc., Technical Note TN-242-1114, Huntsville, Alabama, July 1972.
6. Danby, J.M.A., "Fundamentals of Celestial Mechanics", The Macmillan Company, New York, 1962.
7. Fitzpatrick, P.M., "Principles of Celestial Mechanics", Academic Press, New York and London, 1970.
8. Kozai, Y., "The Motion of a Close Earth Satellite", The Astronomical Journal, Vol. 64, 367-377, November 1959.
9. Liu, J.F., "A Second-Order Theory of an Artificial Satellite Under the Influence of the Oblateness of Earth", Northrop Services, Inc., Technical Memorandum M-240-1203, Huntsville, Alabama, January 1973.
10. McCarter, James W., "Analytic Satellite Ephemeris Program - ASEP", Marshall Space Flight Center, Alabama, June 1982.
11. Smart, W.M., "Celestial Mechanics", John Wiley and Sons, New York, 1953.
12. Zee, C.H., "Trajectories of Satellites Under the Combined Influence of Earth Oblateness and Air Drag", Celestial Mechanics, 3, pp. 148-168, 1971.

```

c
c-----+
c
c          B R A T E S
c-----+
c
c          This routine computes the following quantities :
c
c          1. Mean Motion
c          2. Perturbed Mean Motion
c          3. Nodal regression rate
c          4. Rate of rotation of the Line of Apsides.
c          5. Lambda dot   (one of the regularized elements)
c          6. Nodal Period
c          7. Kepplerian Period
c
c-----+
c

```

```

c
SUBROUTINE BRATES
DOUBLE PRECISION PI,TPI,PO2,OME,AMU,RE,POLR,AMI,POL,OE,ME,
*IME,CAR,EMI,APMI,RANMI,MAMI,UMI,TAMI,LAMMI,IMI,PM,AK2,AAK2,
*AK4,PERK,PERN,MMOT,LAMDOT,PMMOT,APDOT,RANDOT,
*CD,A,DM,RP,B,H,FE,Q0,DRG,RHONUL,G,DB,DBSQR,DBCUBE,ESQR,
*DD,EL,Q,B0,B1,YA,ZA,YE,ZE,YI,ZI,PA,PE,DPI,P1A,P1E,YISTAR,
*ZISTAR,PISTAR,YIISTR,ZIISTR,Y3I,Z3I,QIISTR,Q3I,P1I,TDG,
*TPIOT,ELM,BB2,DADOT,DEDOT,DIDOT,DRADOT,DAPDOT,DMADOT,
*MBF0,MBF1,F,ALI
REAL NODPER,KEPPER
COMMON/BLOK1/PI,TPI,AMU,RE,POLR,AJ2,AJ3,OME,PO2,AJ4
COMMON/BLOK8/AMI,EMI,IMI,APMI,RANMI,MAMI,UMI,TAMI,LAMMI
COMMON/BLOK11/MMOT,PMMOT,APDOT,RANDOT,LAMDOT
COMMON/BLOK12/JCIRC
COMMON/BLOK17/POL(6),OE(6),ME(6),IME(6),CAR(6)
COMMON/BLOK57/NODPER,KEPPER
COMMON/BLOK110/DADOT,DEDOT,DIDOT,DRADOT,DAPDOT,DMADOT
COMMON/BLOK111/PA,PE,DPI,PISTAR,Q3I
COMMON/BLOK113/DRG,F,RHONUL,H,ALI
DATA DPR/57.29577951D+0/RPD/.0174532925D+0/EL/.0000729D+0/
DATA B/6.356780D+6/
CALL UNSIME
OME2=1.-EMI**2
BB=.5*SIN(IMI)**2
AA=1./3.-BB

```

```

PM=AMI*OME2
MMOT=DSQRT(AMU/AMI**3)          ! mean motion
AK2=1.5*AJ2*(RE/PM)**2
AAK2=AK2*(PM/AMI)**2
AK4=AJ4/(AJ2**2)
RANDOT=-AK2*MMOT*COS(IMI)*(1.-AK2*(-1.5+10./3.*BB+EMI**2
*(-1./6.-5./12.*BB)-3.*AA*SQRT(OME2)+35./18.*AK4*(-6./7.+3.*BB)
*(1.+1.5*EMI**2)))          ! Nodal Regression rate
APDOT=AK2*MMOT*((2.-5.*BB)+AK2*(4.-103./6.*BB+215./12.*BB**2+
*EMI**2*(7./12.-.75*BB-15./8.*BB**2)+(AA+15.*AA**2)*SQRT(OME2)
*+35./18.*AK4*(12./7.-93./7.*BB+21.*BB**2+EMI**2*(27./14.-189./
*14.*BB+81./4.*BB**2))))    ! Rot. rate of line of apsides
PMMOT=MMOT*(1.+AK2*SQRT(OME2)*((1.-3.*BB)+AK2*(11./6.-26./3.*BB
*+125./12.*BB**2+EMI**2*(2./3.-4./3.*BB-5./3.*BB**2)+21./2.*AA**2
**SQRT(OME2)+35./18.*AK4*EMI**2*(9./14.-45./7.*BB+45./4.*BB**2)))
*)          ! perturbed mean motion
LAMDOT=MMOT*(1.+AAK2*((3.-8.*BB)-AAK2*(35./6.-155./6.*BB+85./3.*
*BB**2+AA+51./2.*AA**2+35./18.*AK4*(12./7.-93./7.*BB+21.*BB**2)))
*)          ! Lamda dot (regularized element)
PERN=(TPI/(PMMOT+APDOT))/3600.    ! Nodal Period

```

```

NODPER=PERN
PERK=TPI/MMOT/3600.          ! Kepplerian (2-body) Period
KEPPER=PERK

```

```

C
D  TYPE *, 'RHONUL = ', RHONUL
D  TYPE *, 'F      = ', F
D  TYPE *, 'H      = ', H
  RP = AMI*(1.-EMI)
  FE = (RE -B)/RE
  Q0 = RE*FE*SIN(IMI)**2*SIN(APMI)**2/H
  G  = DRG*RHONUL*EXP(-(AMI-RP)/H + Q0)
  DB = AMI*EMI/H
D  TYPE *, 'DB = ', DB
  DBSQR = DB**2
  DBCUBE = DBSQR*DB
  ESQR  = EMI**2
  DD    = EL/MMOT*SQRT(OME2)*COS(IMI)
  Q      = (RE-B)/H*SIN(IMI)**2
  B0     = MBF0(DB)
  B1     = MBF1(DB)

```

C
C
C

DEFINITION OF PK (K = A,E,I)

$$\begin{aligned} \text{YA} &= (1.-\text{DD})^{**2} + \text{EMI}^{**2}*(1.5+\text{DD}) \\ \text{ZA} &= 2.*\text{EMI}*(1.-\text{DD}^{**2})-\text{ESQR}/\text{DB}*(1.5+\text{DD}) \\ \text{YE} &= \text{EMI}*(1.-\text{DD})*(1.+3.*\text{DD})-\text{EMI}^{**2}/(2.*\text{DB}) \\ \text{ZE} &= (1.-\text{DD})^{**2} + \text{EMI}^{**2}*(0.5-\text{DD})-\text{EMI}/(2*\text{DB})* \\ 1 \quad &(1.-\text{DD})*(2.+5.*\text{DD}) + \text{EMI}^{**2}/\text{DB}^{**2} \\ \text{YI} &= (1.-\text{DD})+\text{EMI}^{**2}/2.*(1.-13.*\text{DD}) \\ \text{ZI} &= -2.*\text{EMI}*(1.-2.*\text{DD})-\text{EMI}^{**2}/(2.*\text{DB})*(1.-13.*\text{DD}) \\ \text{PA} &= \text{YA}*\text{B0} + \text{ZA}*\text{B1} \\ \text{PE} &= \text{YE}*\text{B0} + \text{ZE}*\text{B1} \\ \text{DPI} &= \text{YI}*\text{B0} + \text{ZI}*\text{B1} \end{aligned}$$

C
C
C

DEFINITION OF P1A,P1E,AND P1I

$$\begin{aligned} \text{P1A} &= -0.5*(1.-3./8.*\text{Q})*\text{PA} \\ \text{P1E} &= -0.5*(1.-3./8.*\text{Q})*\text{PE} \\ \text{Y1STAR} &= (1.-\text{DD})+\text{ESQR}/2.*(1.-13.*\text{DD})-4.*\text{EMI}*\text{DD}/\text{DB}- \\ 1 \quad &3.*\text{ESQR}*(1.+3.*\text{DD})/\text{DBSQR} \\ \text{Z1STAR} &= -2.*\text{EMI}*(1.-2.*\text{DD})-1./\text{DB}*(2.*(1.-\text{DD})-2.5*\text{ESQR}* \\ 1 \quad &(1.+3.*\text{DD}))+8.*\text{EMI}*\text{DD}/\text{DBSQR}+6.*\text{ESQR}*(1.+3.*\text{DD}) \\ 2 \quad &/\text{DBCUBE} \\ \text{P1STAR} &= \text{Y1STAR}*\text{B0} + \text{Z1STAR}*\text{B1} \\ \text{Y1ISTR} &= 1./\text{DB}*(2.*\text{EMI}*\text{DD}-6./\text{DB}*((1.-\text{DD})-.75*\text{ESQR}*(5.-\text{DD}))+ \\ 1 \quad &48.*\text{EMI}/\text{DBSQR}) \\ \text{Z1ISTR} &= 1./\text{DB}*(1.-\text{DD})-\text{ESQR}/2.*(11.+ \text{DD})-4.*\text{EMI}*(3.+ \text{DD})/\text{DB}+ \\ 1 \quad &12./\text{DBSQR}*((1.-\text{DD})-.75*\text{ESQR}*(5.-\text{DD}))-96.*\text{EMI}/\text{DBCUBE} \\ \text{Y3I} &= 1./\text{DB}*(2.*\text{EMI}*\text{DD}-3./\text{DB}*(1.-\text{DD})*(1.+ \text{ESQR})+ \\ 1 \quad &24.*\text{EMI}/\text{DBSQR}-60.*\text{ESQR}/\text{DBCUBE}*(2.5-.5*\text{DD})) \\ \text{Z3I} &= 1./\text{DB}*((1.-\text{DD})-\text{ESQR}/2.*(1.+3.*\text{DD}))-2.*\text{EMI}/\text{DB}* \\ 1 \quad &(3.+2.*\text{DD})+3./\text{DBSQR}*(2.*(1.-\text{DD})+\text{ESQR}/2.*(29.-9.*\text{DD})) \\ 2 \quad &-48.*\text{EMI}/\text{DBCUBE}+60.*\text{ESQR}*(5.-\text{DD})/\text{DB}^{**4}) \\ \text{Q1ISTR} &= (1.-\text{ESQR})*(\text{Y1ISTR}*\text{B0}+\text{Z1ISTR}*\text{B1}) \\ \text{Q3I} &= (1.-\text{ESQR})*(\text{Y3I}*\text{B0}+\text{Z3I}*\text{B1}) \\ \text{P1I} &= -0.5*(1.-.5*\text{Q})*(\text{DPI}-.5*\text{P1STAR}+\text{Q1ISTR}+2.*\text{Q3I}) \end{aligned}$$

C
C
C

COMPUTATION OF ORBITAL ELEMENTS WITH DRAG

$$\begin{aligned} \text{TDG} &= \text{TPI}/\text{MMOT}*(1.-\text{AK2}*\text{SQRT}(\text{OME2})*(1.-3.*\text{BB})) \\ \text{TPIOT} &= \text{TPI}/\text{TDG} \\ \text{ELM} &= \text{EL}/\text{MMOT} \end{aligned}$$

```

BB2    = SIN(IMI)**2
DADOT  = -TPIOT*(2.*G*AMI**2*(PA + Q*P1A))
DEDOT  = -TPIOT*(2.*G*AMI*OME2*(PE + Q*P1E))
DIDOT  = -TPIOT*(.5*G*AMI*ELM*SIN(IMI)/SQRT(OME2)*(DPI + Q*P1I))
DRADOT = -TPIOT*(G*AK2*MMOT*AMI*(COS(IMI)*((7./2.*PA-4.*EMI*
1      PE) + Q*(7./2.*P1A-4.*EMI*P1E)) + .25*ELM*BB2/
2      SQRT(OME2)*(DPI + Q*P1I)))
DAPDOT = TPIOT*(G*AK2*MMOT*AMI*((2.-5./2.*BB2)*((7./2.*PA-4.*
1      EMI*PE) + Q*(7./2.*P1A-4.*EMI*P1E)) + 5./4.*ELM*
2      BB2*COS(IMI)*(DPI + Q*P1I)))
DMADOT = TPIOT*(G*AK2*MMOT*AMI*(SQRT(OME2)*(1.-3.*BB)*
1      ((7./2.*PA-3.*EMI*PE) + Q*(7./2.*P1A-3.*EMI*P1E))
2      + .75*ELM*BB2*COS(IMI)*(DPI + Q*P1I)))
RETURN
END

```

```

c
c-----+
c               B S E C T M
c-----+
c
c       This routine computes the Secular terms of the solution
c       to the satellite motion.
c
c-----+
c
SUBROUTINE BSECTM
  DOUBLE PRECISION T,TO,TF,TAPO,TPER,GET,AMI,EMI,IMI,APMI,
  *MAMI,UMI,TAMI,LAMMI,GSTC,JULDAY,APSEC,RANSEC,MASEC,
  *MMOT,PMMOT,APDOT,RANDOT,LAMDOT,PRIN,DADOT,DEDOT,
  *DAPDOT,DMADOT,DRASEC,DAPSEC,DMASEC,DASEC,DESEC,DISEC,
  *RANMI,LAMSEC,DIDOT,DRADO
  COMMON/BLOK2/T,TO,TF,TAPO,TPER,GET,DAYNO,JULDAY,GSTC
  COMMON/BLOK8/AMI,EMI,IMI,APMI,RANMI,MAMI,UMI,TAMI,LAMMI
  COMMON/BLOK11/MMOT,PMMOT,APDOT,RANDOT,LAMDOT
  COMMON/BLOK12/JCIRC
  COMMON/BLOK20/APSEC,RANSEC,MASEC,LAMSEC
  COMMON/BLOK110/DADOT,DEDOT,DIDOT,DRADOT,DAPDOT,DMADOT
  COMMON/BLOK112/DASEC,DESEC,DISEC
  CALL UNSIME
  RANSEC=RANMI+RANDOT*(T-TO)
  DRASEC=DRADOT*(T-TO)**2
  RANSEC=PRIN(RANSEC+DRASEC)
  IF(JCIRC.EQ.2) GO TO 1
  LAMSEC=PRIN(LAMMI+LAMDOT*(T-TO))
  RETURN
1 APSEC =APMI+APDOT*(T-TO)
  DAPSEC = DAPDOT*(T-TO)**2
  MASEC =MAMI+PMMOT*(T-TO)
  DMASEC = DMADOT*(T-TO)**2
  DASEC = DADOT*(T-TO)
  DESEC = DEDOT*(T-TO)
  DISEC = PRIN(DIDOT*(T-TO))
  APSEC = PRIN(APSEC+DAPSEC)
  MASEC = PRIN(MASEC+DMASEC)
  RETURN
END

```

```

c
c-----+
c               B L P T R M
c-----+
c
c      This routine computes the Long Period Terms that are a
c      part of the satellite ephemeris solution equations.
c
c-----+
c
SUBROUTINE BLPTRM
DOUBLE PRECISION OME,PO2,PI,TPI,AMU,RE,POLR,T,TO,TF,TAPO,
*GET,POL,OE,ME,IME,AMI,PM,REOA,REOP,EMI,IMI,APMI,RANMI,
*UMI,TAMI,LAMMI,BB,ALP,BO,ABET,QOB,EOB,APSTAR,MMSTAR,
*ELP,RANLP,MALP,LAMLP,ETAB,ZMB,AK42,AK2,AK32,MMOT,
*APDOT,RANDOT,LAMDOT,ETAI,TPER,MAMI,ILP,APLP,PMMOT,
*CD,A,DM,RP,B,H,FE,Q0,DRG,RHONUL,G,DB,DBSQR,DBCUBE,
*Q,B0,B1,MBF0,MBF1,PA,PE,DPI,PISTAR,Q3I,TDG,TPIOT,ELM,EP,
*EB,DB1,EBSQR,Y1A,Z1A,Y1E,Z1E,Y1I,Z1I,Y1ISTR,Z1ISTR,Q1A,Q1E,
*Q1I,Q1ISTR,P2A,P2E,P2I,P3I,Y3W,Z3W,Y3M,Z3M,Q3W,Q3M,P2W,
*Y5A,Z5A,Y5E,Z5E,Y5I,Z5I,Y5ISTR,Z5ISTR,P5A,P5E,P5I,P5ISTR,Y6I,
*V6I,Y6W,U6W,Z6W,V6W,U6M,Z6M,V6M,P6I,P6W,P6M,EPS1,ALDOT,
*SEPS1,COISQ,SISQ,APDT,RADT,EL1,EL2,EL3,EL4,EL5,EL6,EL7,EL8,
*SLW,SLW0,DLW,DLW0,SLOW,SLOW0,DLOW,DLOW0,SL3W,SL3W0,
*SLO3W,SLO3W0,DLO3W,DLO3W0,SNA,SNA0,SNB,SNB0,SNC,
*SNC0,SND,SND0,SNE,SNE0,SNF,SNF0,SNG,SNG0,SNH,SNH0,CSA,
*CSB,CSB0,CSC,CSC0,CSD,CSD0,AWBAR,APRIM,BPRIM,ACPRM,
*ADLPM,AOPRIM,B0PRIM,AC0PRM,BS0PRM,A0DLPM,DAPM,DS2W,
*DS4WI,DC2W,DC2WI,DSI,DSISQR,GOEP,REOPSQ,ALPD,ELPD,DILP,
*APLPD,DMALP,U6I,Z6I,F,ALI,ESQR,DD,EL,P2M,DLMDA,DL3W,
*DL3W0,CSA0,BSPRM,DS2WI,DS4W,RANLPD
COMMON/BLOK12/JCIRC
COMMON/BLOK1/PI,TPI,AMU,RE,POLR,AJ2,AJ3,OME,PO2,AJ4
COMMON/BLOK2/T,TO,TF,TAPO,TPER,GET,DAYNO,JULDAY,GSTC
COMMON/BLOK17/POL(6),OE(6),ME(6),IME(6)
COMMON/BLOK14/BB,ALP,BO,ABET,QOB,EOB
COMMON/BLOK11/MMOT,PMMOT,APDOT,RANDOT,LAMDOT
COMMON/BLOK21/ELP,ILP,APLP,RANLP,MALP,LAMLP,ALPD
COMMON/BLOK8/AMI,EMI,IMI,APMI,RANMI,MAMI,UMI,TAMI,LAMMI
COMMON/BLOK111/PA,PE,DPI,PISTAR,Q3I
COMMON/BLOK113/DRG,F,RHONUL,H,ALI
DATA PI/3.141592654D+0/TPI/6.283185307D+0/

```



```

DATA AJ2/1.0827E-3/AJ3/-2.56E-6/AJ4/-1.58E-6/
DATA RE/6378160.D+0/AMU/3.986012D+14/EL/.0000729D+0/
DATA DPR/57.29577951D+0/B/6.356780D+6/RPD/.0174532925D+0/
CALL UNSIME
AA=1./3.-.5*SIN(IMI)**2
BB=1./3.-AA
OME2=1.-EMI*EMI
PM=AMI*OME2
C  TYPE 2002,APMI,AJ2,RE,EMI,BB,MMOT,T,TO
C2002 FORMAT(D20.12,E20.7,/,3D20.12,3D20.12)
APSTAR=APMI+1.5*AJ2*(RE/PM)**2*(2.-5.*BB)*MMOT*(T-TO)
MMSTAR=MAMI+MMOT*(T-TO)*(1.+1.5*AJ2*(RE/PM)**2*
*SQRT(OME2)*(1.-3.*BB))
AK2=1.5*AJ2*(RE/PM)**2
AK32=.5*AJ3/AJ2
REOA=RE/AMI
REOP=RE/PM
AK42=AJ4/(AJ2*AJ2)
S2I=SIN(2.*IMI)
C2WS=COS(2.*APSTAR)

C2AP=COS(2.*APMI)
SI=SIN(IMI)
CI=COS(IMI)
C2I=COS(2.*IMI)
CTI=CI/SI
S2WS=SIN(2.*APSTAR)
S2AP=SIN(2.*APMI)
SWS=SIN(APSTAR)
SAP=SIN(APMI)
CWS=COS(APSTAR)
CAP=COS(APMI)
IF(JCIRC.EQ.1) GO TO 1
ILP=AK2*S2I/(2.-5.*BB)*EMI*EMI*(-7./48.+5./16.*BB+35./18.*AK42*
*(9./56.-3./8.*BB))*(C2WS-C2AP)-AK32*REOP*EMI*CI*(SWS-SAP)
ELP=-AK2*2.*OME2*SI*SI/(2.-5.*BB)*EMI*(-7./48.+5./16.*BB+35./18.*
*AK42*(9./56.-3./8.*BB))*(C2WS-C2AP)+AK32*REOP*(SWS-SAP)*SI
RANLP=AK2*.5*CI/(2.-5.*BB)*(EMI*EMI*(-7./12.+5./2.*BB)+EMI*EMI*
*BB/(2.-5.*BB)*(-35./12.+25./4.*BB)+35./18.*AK42*(EMI*EMI*(9./14.-
*3.*BB)+EMI*EMI*BB/(2.-5.*BB)*(45./14.-15./2.*BB)))*(S2WS-S2AP)+
*AK32*REOP*EMI*CI/SI*(CWS-CAP)

```

$$\begin{aligned} \text{APLP} = & .5 * \text{AK2} / (2. - 5. * \text{BB}) * (\text{BB} * (-7./6. + 5./2. * \text{BB}) + \text{EMI} * \text{EMI} * (7./12. - 79./ \\ & * 12. * \text{BB} + 45./4. * \text{BB} * \text{BB}) + 4. * \text{BB} * (13. - 30. * \text{BB}) / (2. - 5. * \text{BB}) * \text{EMI} * \text{EMI} * (7./48. \\ & * -5./16. * \text{BB}) + 35./18. * \text{AK42} * (\text{BB} * (9./7. - 3. * \text{BB}) + \text{EMI} * \text{EMI} * (-9./14. + 105./ \\ & * 14. * \text{BB} - 27./2. * \text{BB} * \text{BB}) + 4. * \text{BB} * (13. - 30. * \text{BB}) / (2. - 5. * \text{BB}) * \text{EMI} * \text{EMI} * (-9./56 \\ & * . + 3./8. * \text{BB})) * (\text{S2WS} - \text{S2AP}) + \text{AK32} * \text{REOP} * (\text{SI} / \text{EMI} - \text{EMI} * \text{CI} * \text{CI} / \text{SI}) * \\ & * (\text{CWS} - \text{CAP}) \\ \text{MALP} = & .5 * \text{AK2} * \text{SQRT}(\text{OME2}) / (2. - 5. * \text{BB}) * (\text{BB} * (7./6. - 5./2. * \text{BB}) * (1. - 5./2. * \text{E} \\ & * \text{MI} * \text{EMI}) - 35./18. * \text{AK42} * (\text{BB} * (9./7. - 3. * \text{BB}) * \text{OME2})) * (\text{S2WS} - \text{S2AP}) - \text{AK32} * \text{REO} \\ & * \text{P} * \text{SQRT}(\text{OME2}) * \text{SI} * (1./\text{EMI} - \text{EMI}) * (\text{CWS} - \text{CAP}) \\ \text{RP} = & \text{AMI} * (1. - \text{EMI}) \\ \text{FE} = & (\text{RE} - \text{B}) / \text{RE} \\ \text{Q0} = & \text{RE} * \text{FE} * \text{SIN}(\text{IMI}) ** 2 * \text{SIN}(\text{APMI}) ** 2 / \text{H} \\ \text{G} = & \text{DRG} * \text{RHONUL} * \text{EXP}(-(\text{AMI} - \text{RP}) / \text{H} + \text{Q0}) \\ \text{DB} = & \text{AMI} * \text{EMI} / \text{H} \\ \text{DBSQR} = & \text{DB} ** 2 \\ \text{DBCUBE} = & \text{DBSQR} * \text{DB} \\ \text{ESQR} = & \text{EMI} ** 2 \\ \text{DD} = & \text{EL} / \text{MMOT} * \text{SQRT}(\text{OME2}) * \text{COS}(\text{IMI}) \\ \text{Q} = & (\text{RE} - \text{B}) / \text{H} * \text{SIN}(\text{IMI}) ** 2 \\ \text{B0} = & \text{MBF0}(\text{DB}) \\ \text{B1} = & \text{MBF1}(\text{DB}) \\ \text{BB} = & .5 * \text{SIN}(\text{IMI}) ** 2 \end{aligned}$$

C
C
C

COMPUTATION OF LONG PERIOD ORBITAL ELEMENTS WITH DRAG

$$\begin{aligned} \text{TDG} &= \text{TPI} / \text{MMOT} * (1. - \text{AK2} * \text{SQRT}(\text{OME2}) * (1. - 3. * \text{BB})) \\ \text{TPIOT} &= \text{TPI} / (\text{TDG}) \\ \text{ELM} &= \text{EL} / \text{MMOT} \\ \text{EP} &= 1.5 * \text{AJ2} \\ \text{EB} &= \text{EMI} / \text{DB} \\ \text{DB1} &= 1. / \text{DB} \\ \text{EBSQR} &= \text{EB} ** 2 \end{aligned}$$

C
C
C

DEFINITION OF P2K(K = A,E,I,W,M) AND P3I

$$\begin{aligned} \text{Y1A} &= \text{EB} * (4. * (1. - \text{DD}) - 3. * \text{EB} * (17./2. - 5. * \text{DD})) \\ \text{Z1A} &= \text{DB1} * ((1. - \text{DD}) ** 2 + \text{ESQR} * (17./2. - 5. * \text{DD}) - 8. * \text{EB} * (1. - \text{DD}) \\ &+ 6. * \text{EBSQR} * (17./2. - 5. * \text{DD})) \\ \text{Y1E} &= \text{DB1} * ((1. - \text{DD}) ** 2 + \text{ESQR} * (11./2. - 3. * \text{DD}) - 3. * \text{EB} * (1. - \text{DD}) \\ &* (3. + .5 * \text{DD}) + 12. * \text{EBSQR} * (11./2. - 3. * \text{DD})) \\ \text{Z1E} &= \text{DB1} * (\text{EMI} * (1. - \text{DD}) * (3. + \text{DD}) - \text{DB1} * (2. * (1. - \text{DD}) ** 2 + 5. * \text{ESQR} * \\ &(11./2. - 3. * \text{DD})) + 3. * (\text{EMI} / \text{DBSQR}) * (1. - \text{DD}) * (6. + \text{DD}) - \end{aligned}$$

1
1
1
1

```

2      24.*ESQR/DBCUBE*(11./2.-3.*DD))
Y1I   = EB*(2.*DD+3.*EB*(.5+1.5*DD))
Z1I   = DB1*((1.-DD)-ESQR*(.5+1.5*DD)-4.*DD*EB-3.*EBSQR*
1      (1.+3.*DD))
Y1ISTR = DB1*(2.*EMI*DD-6./DB*((1.-DD)-.75*ESQR*(5.-DD)))+
1      48.*EMI/DBSQR)

Z1ISTR = DB1*((1.-DD)-.5*ESQR*(11.+DD)-4.*EB*(3.+DD)+
1      12./DBSQR*((1.-DD)-.75*ESQR*(5.-DD))-96.*EMI/DBCUBE)
Q1A   = OME2*(Y1A*B0+Z1A*B1)
Q1E   = OME2*(Y1E*B0+Z1E*B1)
Q1I   = OME2*(Y1I*B0+Z1I*B1)
Q1ISTR = OME2*(Y1ISTR*B0+Z1ISTR*B1)
P2A   = .5*PA-Q1A
P2E   = .5*PE-Q1E
P2I   = .5*(DPI-PISTAR-2.*Q1I)
P3I   = .5*(.5*PISTAR-Q1ISTR+2.*Q3I)
Y3W   = DB1*((1.-DD)**2/EMI+EMI*(5./2.-DD+1.5*DD**2)-3./DB*
1      (1.-DD)*(3.+5*DD)+12.*EMI/DBSQR*(11./2.-3.*DD+
2      .5*DD**2))
Z3W   = DB1*((1.-DD)*(2.+1.5*DD)-DB1*(2.*(1.-DD)**2/EMI+EMI*
1      (43./2.-11.*DD+9./2.*DD**2))+6./DBSQR*(1.-DD)*
2      (3.+5*DD)-24.*EMI/DBCUBE*(11./2.-3.*DD+.5*DD**2))
Y3M   = DB1*((1.-DD)**2/EMI+EMI*(5./2.+5*DD**2)-3./DB*(1.-DD)
1      *(3.+5*DD)+12.*EMI/DBSQR*(11./2.-3.*DD+.5*DD**2))
Z3M   = DB1*((1.-DD)*(2.+1.5*DD)-DB1*(2.*(1.-DD)**2/EMI+EMI*
1      (43./2.-9.*DD+5./2.*DD**2))+6./DBSQR*(1.-DD)*
2      (3.+5*DD)-24.*EMI/DBCUBE*(11./2.-3.*DD+.5*DD**2))
Q3W   = SQRT(OME2)*(Y3W*B0+Z3W*B1)
Q3M   = SQRT(OME2)*(Y3M*B0+Z3M*B1)
P2W   = -Q3W
P2M   = -Q3M

```

C
C
C

DEFINITION OF P5K (K = A,E,I,I*)

```

Y5A   = 2.0*EMI*(1.-DD**2)-ESQR/DB*(9./2.-DD)
Z5A   = (1.-DD)**2 + ESQR*(1.5+DD)-EB*(1.-DD)*(3.+DD)+
1      2.*ESQR/DBSQR*(9./2.-DD)
Y5E   = (1.-DD)**2+ESQR*(.5-DD)-EB*(1.-DD)*(2.+1.5*DD)+
1      3.*ESQR/(2.*DBSQR)*(5.-DD-3.*DD**2)

```

Z5E = EMI*(1.-DD)*(1.+3.*DD)-DB1*(1.-DD)*(1.-DD+ESQR*
 1 (3.+2.*DD))+EMI/DBSQR*(1.-DD)*(4.+3.*DD)-
 2 3.*ESQR/DBCUBE*(5.-DD-3.*DD**2)
 Y5I = -2.*EMI*(1.-2.*DD)+ESQR/(2.*DB)*(1.+7.*DD)
 Z5I = (1.-DD)+ESQR/2.*(1.-13.*DD)+EB*(1.-3.*DD)-
 1 ESQR/DBSQR*(1.+7.*DD)
 Y5ISTR = -2.*EMI*(1.-2.*DD)-DB1*(2.*(1.-DD)-ESQR/2.*(7.+DD))
 1 +6.*EMI/DBSQR*(1.+DD)
 Z5ISTR = (1.-DD)+ESQR/2.*(3.-7.*DD)+EB*(1.-7.*DD)+2./DBSQR
 1 *(2.*(1.-DD)-ESQR/2.*(7.+DD))-12.*EMI/DBCUBE
 2 *(1.+DD)
 P5A = Y5A*B0+Z5A*B1
 P5E = Y5E*B0+Z5E*B1
 P5I = Y5I*B0+Z5I*B1
 P5ISTR = Y5ISTR*B0+Z5ISTR*B1

C
C
C

DEFINITION OF P6K (K = I,W,M)
 Y6I = DB1*((1.-DD)-ESQR/2.*(1.+3.*DD)-3.*EB*(1.+DD)+
 1 6.*ESQR/DBSQR*(1.-DD))
 U6I = OME2*Y6I
 Z6I = DB1*(2.*EMI*DD-DB1*(2.*(1.-DD)+ESQR/2.*(1.-9.*DD))+
 1 6.*EMI/DBSQR*(1.+DD)-12.*ESQR/DBCUBE*(1.-DD))

V6I = OME2*Z6I
 Y6W = DB1*((1.-DD)*(2.+1.5*DD)-3.*EB*(5./2.-.5*DD))
 U6W = SQRT(OME2)*Y6W
 Z6W = DB1*((1.-DD)**2/EMI+EMI*(5./2.-DD+ 0.5*DD**2)-
 1 2./DB*(1.-DD)*(2.+1.5*DD)+6.*EMI/DBSQR*(5./2.-.5*DD))
 V6W = SQRT(OME2)*Z6W
 U6M = U6W
 Z6M = DB1*((1.-DD)**2/EMI+EMI*(5./2.-.5*DD**2)-2./DB*(1.-DD)
 1 *(2.+1.5*DD)+6.*E/DBSQR*(5./2.-.5*DD))
 V6M = SQRT(OME2)*Z6M
 P6I = U6I*B0+V6I*B1
 P6W = U6W*B0+V6W*B1
 P6M = U6M*B0+V6M*B1

C
C
C
C

DEFINITION OF AWBAR,A',A0',B',B0',A'',A0'',AC',AC0',BS',BS0'

ALDOT = MEAN RATE OF THE SUN RELATIVE TO THE EARTH

C ALI = INITIAL MEAN LONGITUDE OF THE SUN AT TIME TO
 C EPS1 = THE OBLIQUITY OF THE ECLIPTIC
 C DLMDA = ANGLE IN RIGHT ASCENSION THAT CENTER
 C OF BULGE LAGS THE SUN
 EPS1 = 23.44D0*RPD
 ALDOT = (0.9856D0*RPD)/86400.D0
 DLMDA = 30.D0*RPD
 SEPS1 = SIN(EPS1)
 COISQ = COS(IMI/2.):**2
 SISQ = SIN(IMI/2.):**2
 APDT = AK2*MMOT*(2.-5./2.*SIN(IMI):**2)
 RADT = -AK2*MMOT*COS(IMI)
 EL1 = ALDOT + APDT
 EL2 = ALDOT - APDT
 EL3 = ALDOT-RADT+APDT
 EL4 = ALDOT-RADT-APDT
 EL5 = ALDOT + 3.*APDT
 EL6 = ALDOT - 3.*APDT
 EL7 = ALDOT-RADT+3.*APDT
 EL8 = ALDOT-RADT-3.*APDT
 SLW = ALI+APMI+EL1*(T-TO)
 SLW0 = ALI+APMI
 DLW = ALI-APMI+EL2*(T-TO)
 DLW0 = ALI-APMI
 SLOW = ALI-RANMI+DLMDA+APMI+EL3*(T-TO)
 SLOW0 = ALI-RANMI+DLMDA+APMI
 DLOW = ALI-RANMI+DLMDA-APMI+EL4*(T-TO)
 DLOW0 = ALI-RANMI+DLMDA-APMI
 SL3W = ALI+3.*APMI+EL5*(T-TO)
 SL3W0 = ALI+3.*APMI
 DL3W = ALI-3.*APMI+EL6*(T-TO)
 DL3W0 = ALI-3.*APMI
 SLO3W = ALI-RANMI+DLMDA+3.*APMI+EL7*(T-TO)
 SLO3W0 = ALI-RANMI+DLMDA+3.*APMI
 DLO3W = ALI-RANMI+DLMDA-3.*APMI+EL8*(T-TO)
 DLO3W0 = ALI-RANMI+DLMDA-3.*APMI
 SNA = SIN(SLW)
 SNA0 = SIN(SLW0)
 SNB = SIN(DLW)
 SNB0 = SIN(DLW0)
 SNC = SIN(SLOW)
 SNC0 = SIN(SLOW0)
 SND = SIN(DLOW)

SND0 = SIN(DLOW0)
 SNE = SIN(DL3W)
 SNE0 = SIN(DL3W0)

SNF = SIN(SL3W)
 SNF0 = SIN(SL3W0)
 SNG = SIN(DLO3W)
 SNG0 = SIN(DLO3W0)
 SNH = SIN(SLO3W)
 SNH0 = SIN(SLO3W0)
 CSA = COS(SLW)
 CSA0 = COS(SLW0)
 CSB = COS(DLW)
 CSB0 = COS(DLW0)
 CSC = COS(SLOW)
 CSC0 = COS(SLOW0)
 CSD = COS(DLOW)
 CSD0 = COS(DLOW0)

C

AWBAR = (RE/PM)**2*MMOT*(2.-5./2.*SIN(IMI)**2)
 APRIM = .5*SEPSI*SIN(IMI)*(EP/EL2*SNB-EP/EL1*SNA)
 1 + SISQ*EP/EL3*SNC + COISQ*EP/EL4*SND
 BPRIM = -.5*SEPSI*SIN(IMI)*(EP/EL2*CSB-EP/EL1*CSA)
 1 + SISQ*EP/EL3*CSC-COISQ*EP/EL4*CSD
 ACPRM = EP/4.*SEPSI*SIN(IMI)*(1./EL6*SNE-1./EL5
 1 *SNF-1./EL2*SNB+1./EL1*SNA)+
 2 EP/2.*COISQ*(1./EL8*SNG+1./EL3*SNC)
 3 + EP/2.*SISQ*(1./EL7*SNH+1./EL4*SND)
 BSPRM = EP/4.*SEPSI*SIN(IMI)*(1./EL6*SNE-1./EL5
 1 *SNF+1./EL2*SNB-1./EL1*SNA)+
 2 EP/2.*COISQ*(1./EL8*SNG-1./EL3*SNC)
 3 + EP/2.*SISQ*(1./EL7*SNH-1./EL4*SND)
 ADLPM = -EP**2/2.*SEPSI*SIN(IMI)*(1./EL2**2*CSB-1./EL1
 1 **2*CSA)-SISQ*EP**2/EL3**2*CSC-
 2 COISQ*EP**2/EL4**2*CSD
 A0PRIM = .5*SEPSI*SIN(IMI)*(EP/EL2*SNB0-EP/EL1*SNA0)
 1 + SISQ*EP/EL3*SNC0 + COISQ*EP/EL4*SND0
 B0PRIM = -.5*SEPSI*SIN(IMI)*(EP/EL2*CSB0-EP/EL1*CSA0)
 1 + SISQ*EP/EL3*CSC0-COISQ*EP/EL4*CSD0
 AC0PRM = EP/4.*SEPSI*SIN(IMI)*(1./EL6*SNE0-1./EL5
 1 *SNF0-1./EL2*SNB0+1./EL1*SNA0)+

```

2      EP/2.*COISQ*(1./EL8*SNG0+1./EL3*SNC0)
3      +EP/2.*SISQ*(1./EL7*SNH0+1./EL4*SND0)
BS0PRM = EP/4.*SEPSI*SIN(IMI)*(1./EL6*SNE0-1./EL5
1      *SNF0+1./EL2*SNB0-1./EL1*SNA0)+
2      EP/2.*COISQ*(1./EL8*SNG0-1./EL3*SNC0)
3      +EP/2.*SISQ*(1./EL7*SNH0-1./EL4*SND0)
A0DLPM = -EP**2/2.*SEPSI*SIN(IMI)*(1./EL2**2*CSB0-1./EL1
1      **2*CSA0)-SISQ*EP**2/EL3**2*CSC0-
2      COISQ*EP**2/EL4**2*CSD0

```

C

```

DAPM  = APMI+APDT*(T-TO)
DS2W  = SIN(2.*DAPM)
DS2WI = SIN(2.*APMI)
DS4W  = SIN(4.*DAPM)
DS4WI = SIN(4.*APMI)
DC2W  = COS(2.*DAPM)
DC2WI = COS(2.*APMI)
DSI    = SIN(IMI)
DSISQ  = DSI*DSI
GOEP   = G/EP
REOPSQ = (RE/PM)**2

```

C

```

ALPD  = -TPIOT*(2.*GOEP*AMI**2*(Q*P2A/(2.*AWBAR)*
1      (DS2W-DS2WI)+ F*P5A*(APRIM-A0PRIM)))
ELPD  = -TPIOT*(2.*GOEP*AMI*OME2*(Q*P2E/(2.*AWBAR)*
1      (DS2W-DS2WI)+ F*P5E*(APRIM-A0PRIM)))

DILP  = -TPIOT*(.5*GOEP*AMI*ELM*DSI/SQRT(OME2)*((PISTAR+Q*
1      P2I)/(2.*AWBAR)*(DS2W-DS2WI)+ Q*P3I/(4.*AWBAR)*
2      (DS4W-DS4WI)+ F*(P5I*(APRIM-A0PRIM)+ P5ISTR*
3      (ACPRM-AC0PRM)-2.*P6I*(BSPRM-BS0PRM))))
RANLPD = TPIOT*(GOEP*REOPSQ*MMOT*AMI*COS(IMI)*(Q/(4.
1      *AWBAR**2)*(7.*P2A-8.*EMI*P2E)*(DC2W-DC2WI)-
2      F*(ADLPM-A0DLPM)*(7.*P5A-8.*EMI*P5E)))
APLPD  = TPIOT*(GOEP*AMI*SQRT(OME2)*(Q*P2W/AWBAR*
1      (DC2W-DC2WI)-2.*F*P6W*(BPRIM-B0PRIM)))-TPIOT*
2      (GOEP*REOPSQ*MMOT*AMI*(2.-5./2.*DSISQ)*(Q/(4.*
3      AWBAR**2)*(7.*P2A-8.*EMI*P2E)*(DC2W-DC2WI)-
4      F*(ADLPM-A0DLPM)*(7.*P5A-8.*EMI*P5E)))
DMALP  = -TPIOT*(GOEP*AMI*(Q*P2M/AWBAR*(DC2W-DC2WI)-
1      2.*F*P6M*(BPRIM-B0PRIM)))-TPIOT*(GOEP*REOPSQ*

```

```

2      MMOT*AMI*SQRT(OME2)*(1.-1.5*DSISQ)*(Q/(4.*
3          AWMAR**2)*(7.*P2A-6.*EMI*P2E)*(DC2W-DC2WI)-F*
4      (ADLPM-A0DLPM)*(7.*P5A-6.*EMI*P5E)))
      ILP  = ILP + DILP
      ELP  = ELP + ELPD
      APLP = APLP + APLPD
      RANLP = RANLP + RANLPD
      MALP = MALP + DMALP
      RETURN
1 ETAB=QOB*ALP*SIN(BO*(T-TO)+ABET)+EOB
      ETAI=QOB*ALP*SIN(ABET)+EOB
      ZMB=ALP*COS(BO*(T-TO)+ABET)
      RANLP=.5*(AJ3/AJ2)*REOA*CTI*(ZMB-ALP*COS(ABET))
      LAMLP=-.5*(AJ3/AJ2)*REOA*C2I/SI*(ZMB-ALP*COS(ABET))
      ILP=-.5*(AJ3/AJ2)*REOA*CI*(ETAB-ETAI)
      RETURN
      END

```


58-35
N88-15609 116710
218

1987

NASA/ASEE SUMMER FACULTY FELLOWSHIP PROGRAM

MARSHALL SPACE FLIGHT CENTER
THE UNIVERSITY OF ALABAMA IN HUNTSVILLE

RESOLUTION OF HOLOGRAMS
PRODUCED BY THE FLUID EXPERIMENT SYSTEM
AND THE HOLOGRAPHY GROUND SYSTEM

Prepared by: Howard L. Brooks
Academic Rank: Assistant Professor
University and Department: DePauw University
Department of
Physics & Astronomy

NASA/MSFC:
Laboratory: Test
Division: Systems & Components
Branch: Experiments and
Components

MSFC Colleague: Thomas L. Denton

Date: August 7, 1987

Contract No.: The University of
Alabama in Huntsville
NGT-01-008-021

RESOLUTION OF HOLOGRAMS
PRODUCED BY THE FLUID EXPERIMENT SYSTEM
AND THE HOLOGRAPHY GROUND SYSTEM

Howard L. Brooks
Assistant Professor of Physics and Astronomy
DePauw University
Greencastle, Indiana

ABSTRACT

The Fluid Experiment System (FES) was developed for the purpose of studying low temperature crystal growth of triglycine sulfate from solution in a low gravity environment onboard Spacelab. The first flight of FES was in 1985 on SL 3. FES uses an optical system to take holograms of the growing crystal that can be analyzed after the mission in the Holography Ground System (HGS) located in the Test Laboratory at Marshall Space Flight Center (MSFC). Microscopic observation of the images formed by the reconstructed holograms is critical to determining crystal growth rate and particle velocity. FES and HGS were designed for a resolution of better than 20 micrometers, but initial observation of the flight holograms show a limit of 80 micrometers. This paper investigates the resolution of the FES holograms, and the role of beam intensity ratio and exposure time on the resolution of HGS produced holograms.

ACKNOWLEDGEMENTS

I am grateful for the opportunity that I have had to participate again in the Summer Faculty Fellowship Program. The work that I completed this summer would not have been possible without the advice and assistance of Thomas L. Denton, David L. Johnston, and Todd C. MacLeod.

I also appreciate the support of Bobby J. Johnson, Jim J. Lindsay, and Richard N. Stone that allowed me to finish the project. Discussions with Bill Witherow, Rudy Ruff, Ravi Lal, and Helen Johnson were very helpful during the course of this investigation.

I would like to thank Dr. Gerald Karr and Ernestine Cothran for their support and encouragement throughout the program. This second summer at Marshall Space Flight Center has been enjoyable and I am glad that the National Aeronautics and Space Administration and the American Society for Engineering Education provided me with another chance to work in Huntsville.

INTRODUCTION

The Fluid Experiment System (FES) was developed for the purpose of studying the growth of crystals in the low gravity environment aboard Spacelab. An optical system surrounding the test cell produces holograms during the entire growth period of the crystal. After the flight, the holograms are developed and allow the investigator to reconstruct an accurate three dimensional image of the cell. It is possible to complete a detailed study of this image with a microscope.

According to the design specifications of FES, the limiting resolution of the holograms should be less than 20 micrometers. However, the initial observations of the flight holograms placed the limit at 80 micrometers. This paper continues to investigate the resolution of the flight holograms in two ways. First, the flight holograms have been reconstructed and examined under the microscope. Second, a series of holograms of the test cell were produced in the Holography Ground System (HGS) under a variety of conditions. The goal of this two fold approach is to determine the ultimate resolution of the holograms and the optimal conditions for producing holograms on future flights.

OBJECTIVES

The objectives of this work were to:

1. Microscopically analyze reconstructed images of holograms of the crystal growth test cell from the Fluid Experiment System, flown on Spacelab 3, to determine the resolution of the holograms.
2. Construct holograms of the test cell in the Holography Ground System to determine variables that impact resolution.
3. Provide recommendations on changes to improve the ultimate resolution of the holograms of the cell.

THEORY

Resolution refers to the ability to separate two small objects (Department of Defense, 1962). This is somewhat different than the ability to detect isolated objects. It is possible to see single objects that are smaller than the resolution limit of an optical system, but it would be impossible to be certain that it is a single object. For the purpose of this paper, the ability to see an object will be referred to as detectability.

When considering the ultimate resolution of an image that is reconstructed from a hologram many different factors affect resolution including illumination, contrast, film, and aperture. A fundamental limitation is the use of coherent light from the laser to construct and reconstruct the hologram, which reduces the resolution because of the reinforcing nature of the diffraction patterns (Caulfield, 1970).

For holography, the illumination problems centers on the nature of the beams that are used to construct the holograms. First it is important to start with point source of laser light that had a small bandwidth (Smith, 1975) which is easily accomplished in HGS with the Spectra Physics Model 125 laser and the spatial filter. The ratio of the reference beam intensity to the object beam intensity should be between 3 and 10 (Meyer-Arendt, 1972, Stroke, 1969, Abramson, 1981). The insertion of a diffuser plate into the object beam may improve the overall illumination of the object, but will introduce a speckle pattern into the hologram that will mar small details (Caulfield, 1970).

The contrast between the object and the background also affects resolution. It is much more difficult to see a small bright red object against a red background, as is the case in the FES holograms, than it is to see a white object on a black background. Resolution under low contrast

conditions may be only one-third of the resolution under optimum high contrast conditions (Department of Defense, 1962).

It is important to use the proper type of film to record the hologram. The film must have a uniform, fine grain emulsion which is very sensitive to the 632.8 nm light from the laser. Care must be exercised in processing the film to avoid distorting the emulsion. Despite these cautions, the resolution limit of the film used in FES and HGS is on the order of 1 micrometer (Klein, 1970 and Stroke, 1969).

Resolution is also limited for holograms by the distance that the film is placed from the object and the aperture of the opening between the object and the film, in a manner that is similar to the resolution limit of conventional lens system (Caulfield, 1970). This restriction for the FES system would limit resolution of primary holograms to 2 micrometers and the transverse holograms to 4 micrometers.

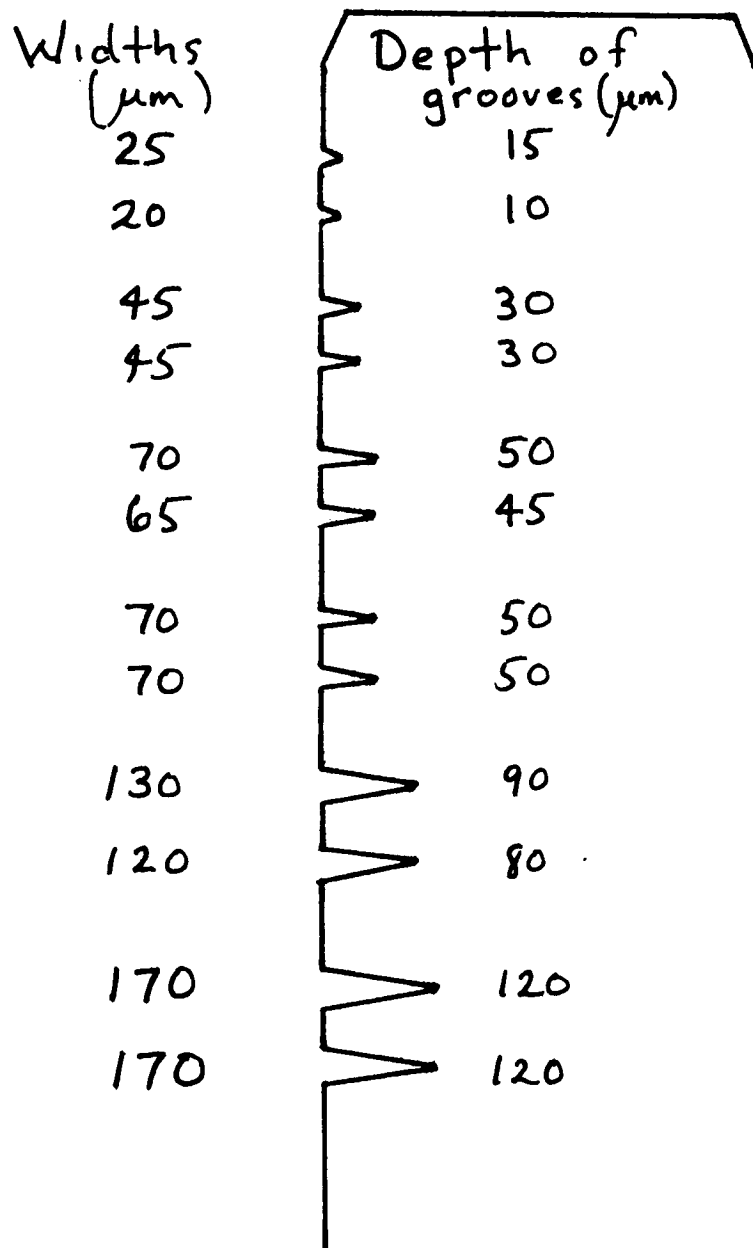
Even if the holograms are recorded under optimal conditions, it may be difficult to achieve good resolution in the reconstructed images for many different reasons. The reconstruction beam needs to be as identical as possible to the original reference beam. It should be of a similar bandwidth and wavelength, unless additional magnification is desired by reconstructing with a longer wavelength (Francon, 1974). The beam must strike the film at the same angle as the reference beam in order to avoid astigmatic images and spherical aberrations (Caulfield, 1970). Of course the conventional optics in the microscope must have better resolving power than the holographic image.

PROCEDURE

Analysis of reconstructed holograms was completed on HGS using the modified microscope and hologram holder locations with the auxiliary turning mirror. The hologram holder is mounted on HGS between BS3 and the test cell. The turning mirror is inserted between M1 and BS1, and directs the reconstruction beam toward the hologram holder. The hologram is mounted in the holder in order to project a real image of the cell toward the outer edge of the table. The microscope is mounted near the edge of the table and directly observes this real image.

Since there are no small particles of known size in the test cell, a dummy sting was machined from aluminum to provide a reference target for determining resolution in the HGS produced holograms. Six pairs of grooves were cut near the tip of the sting (see Figure 1). These grooves ranged in depth from 10 to 120 micrometers and were from 20 to 170 micrometers wide. The exact dimensions of the grooves were determined by direct microscopic observation. Holograms were produced on HGS of the sting alone and the sting in Cell 101 which was filled with water. Primary holograms were produced in the manner described by TAI in the operators manual (TAI, 1984) with the diffuser plate inserted in the object beam. Transverse holograms were produced by removing M3, rotating BS4 out of the beam reflected from M6 and using the auxiliary turning mirror to send the reference beam to the hologram holder located in the standard position (see Figure 2.) Neutral density filters were introduced into the beams to produce various intensity ratios. These ratios were determined from the power readings obtained at the film plane by the Newport 815 power meter.

Most of the holograms were developed in the standard manner (TAI, 1984), although a few sets were processed in the automatic developing tank that had been previously used for the flight holograms.



Partial View (not to scale)

Figure 1- Optical Sting, FES TI 007

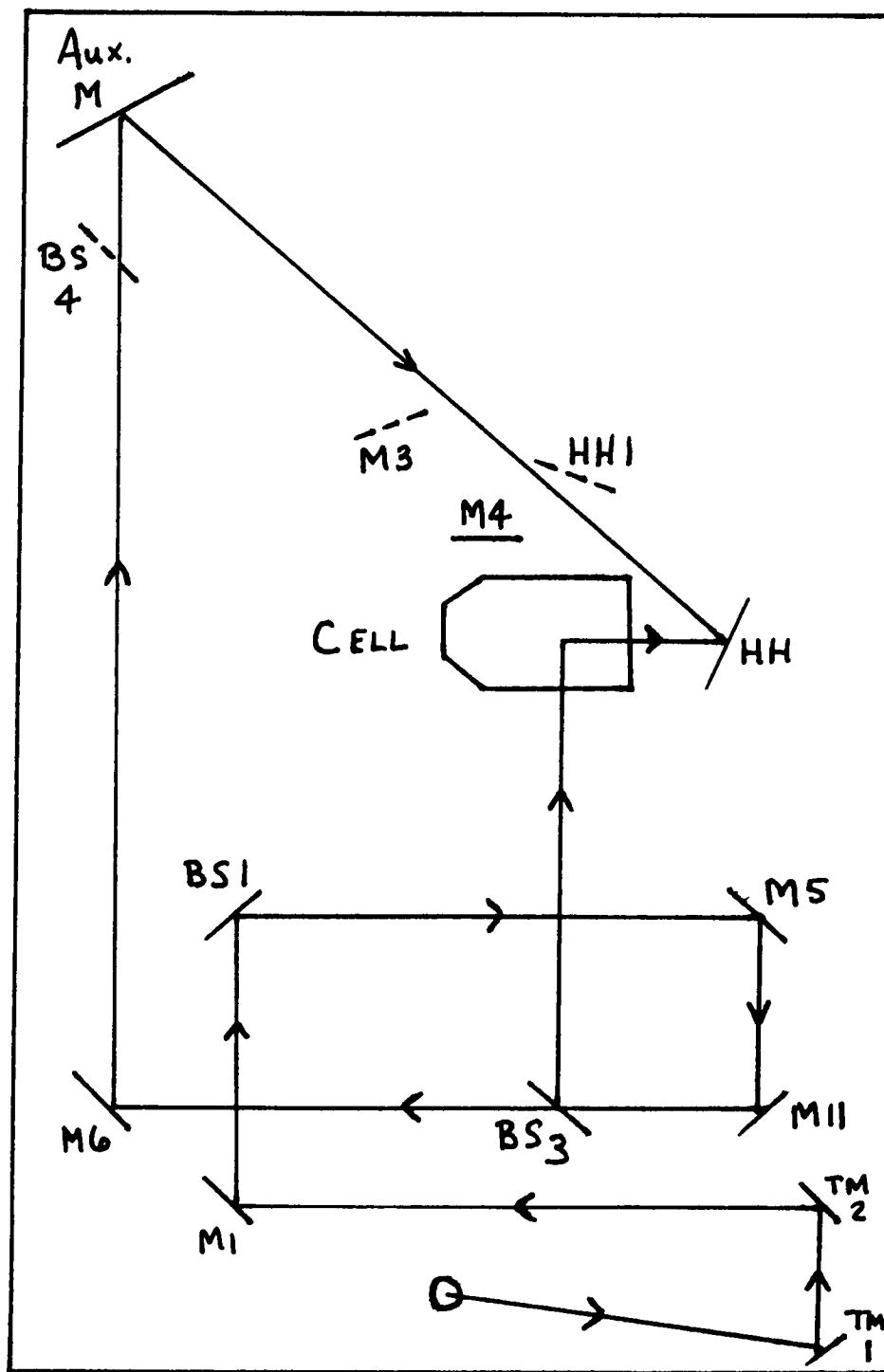


Figure 2- Modified HGS Configuration for Transverse Holograms

RESULTS

Resolution of the flight holograms was investigated for the calibration cell, Cell 203, and Cell 204. It was possible to observe the USAF 1951 resolution target in the calibration cell in both the primary and transverse holograms. Small particles, less than 100 micrometers, were only observed in the transverse holograms of Cells 203 and 204. Resolution of the optical sting, FES TI 007, was investigated in the transverse direction for the sting alone and the sting installed in Cell 101 with water, both at room temperature and at 45 degrees Celsius.

Holograms of the calibration cell were recorded during the Spacelab 3 mission both before and after the three test cells were installed on the optical bench. The resolution limits were determined as the width of a line pair of the smallest resolvable element in the USAF 1951 target. Prior to cell installation, the resolution of primary holograms (using Hologram Sequence # 1) was better than 35 micrometers and the transverse limit (using Hologram Sequence #T017) was better than 62 micrometers. After the test cell runs observations of primary sequence #348 and transverse sequence #T371, showed no change in the resolution limit.

It was very difficult to detect small particles in the holograms of the test cells. Since no small particles of known size were in the cells, the only way to determine the limit of detectability was with a systematic search of the cell volume. The microscope has a limited field of view, about 1 mm deep and 25 mm in cross section, even at low magnification. The scanning of the test cell with the microscope was a tedious process.

No particles or bubbles were found in the primary holograms of Cells 203 and 204 that were smaller than 100 micrometers. Probably the back lighting

of the object beam on the small particles coupled with the speckle pattern caused by the diffuser plate made it impossible to observe tiny objects.

The first transverse hologram of Cell 203 showed 17 spherical objects between 25 and 100 micrometers in diameter. These objects were scattered throughout the cell with 4 located in the region near the crystal. In the next hologram, taken about seven minutes later, the particles near the crystal are not seen while the far field particles are still in their same positions. The disappearance of these particles near the crystal can be explained if the small pieces were triglycine sulfate crystal which would have dissolved into the hot solution. Efforts to detect the floater crystals, which became very large during the growth period, while still very small were unsuccessful. Unfortunately there was a gap of almost eight hours in the holograms that were recorded of the flight cell. The last hologram before the gap shows no small particles in the observable portion of the solution near the crystal and the next hologram displays the floater crystals that are about a millimeter in diameter.

Small particles were also found in the transverse holograms of Cell 204. Typically 6 to 12 particles were found in each image. These particles were located in the back portion of the cell, as seen through the transverse window, and appeared to drift slowly through the solution. The smallest spherical particle was 20 micrometers in diameter, and some of the particles definitely appeared as cylinders, 20 to 30 micrometers in diameter and 100 or more micrometers long. It did not appear that these objects changed size throughout the growth period, suggesting that they were not crystalline material.

All primary configuration holograms of the optical sting produced on HGS failed to show any evidence of the grooves near the tip. As was the case with

the flight primary holograms, this failure is explained by the fact that the cylindrical sting is back illuminated by the object beam and fails to reflect light from the sting onto the film. The only possible way to detect the grooves would be to see the profile of the sting which is not possible because of the speckle pattern introduced by the diffuser plate.

Table 1 summarizes the transverse holograms of the optical sting that were produced on HGS. These holograms show a face on view of the grooves. The quality of the image depended on the beam ratio and the exposure time. For the optical sting only the best image, with a detectability of less than 20 micrometers, was recorded with a 10:1 beam ratio and a 100 ms exposure. The 2:1 beam ratio exposure at 500 ms also showed all the grooves as did the 30:1 100 ms hologram. It is significant to note that all exposures at the 10:1 beam ratio showed all the grooves on the optical sting. The less favorable beam ratios only had good resolution for one exposure times.

The transverse holograms of the optical sting installed in Cell 101 exhibit the same dependency on beam ratio and exposure time. Again the best holograms were at the 20:1 ratio. There appeared to be no effect on the detection with the heated cell. The use of the automatic development tank permitted over exposed holograms to be underdeveloped and usable. In fact, the 20:1 1 and 2 second exposures and 100:1 200 ms, all overexposed, were the best of the auto-developed sequences.

Considering the role of beam intensity ratio on the resolution of the holograms, it was decided to measure power of the beams on the FES optical bench and the influence of the test cell on the beam intensities in HGS. The locations of the power measurements are shown in Figure 3 and Figure 4 shows the power readings for light entering Cell 101 on HGS. Table 2 summarizes the power

measurements from the FES table and estimated power readings with a cell in place. The cell has four windows in the primary direction, each of which absorbs some of the light. The inner, thick windows transmit 88% of the incident light. The outer, thin windows transmit 94% of the incident light. The diffuser plate in HGS transmits 24% of the light. Calculations using the best available value for the extinction coefficient for water at the 632.8 nm wavelength (Hale and Query, 1973) indicate that 97% of the light will be transmitted through 10 cm of water. The result of having all the windows and the water in the beam will be an overall transmission of 66% under ideal conditions (ignoring the effect on the transmission coefficient of a saturated triglycine sulfate solution) for the primary beam without diffuser and 16% for the primary beam with diffuser. Independent measurements of the transmission coefficients for both the primary and transverse object beams were made by taking the appropriate power ratio of light entering the test cell to that reaching the film plane (see Figure 4). For the primary object beam without diffuser, the measured transmission coefficient to the film plane is 50% and for the diffused primary beam the coefficient is 9%. It appears that the beam ratios for the flight holograms which can be analyzed with the microscope are on the order of 40:1 or larger (see Table 3).

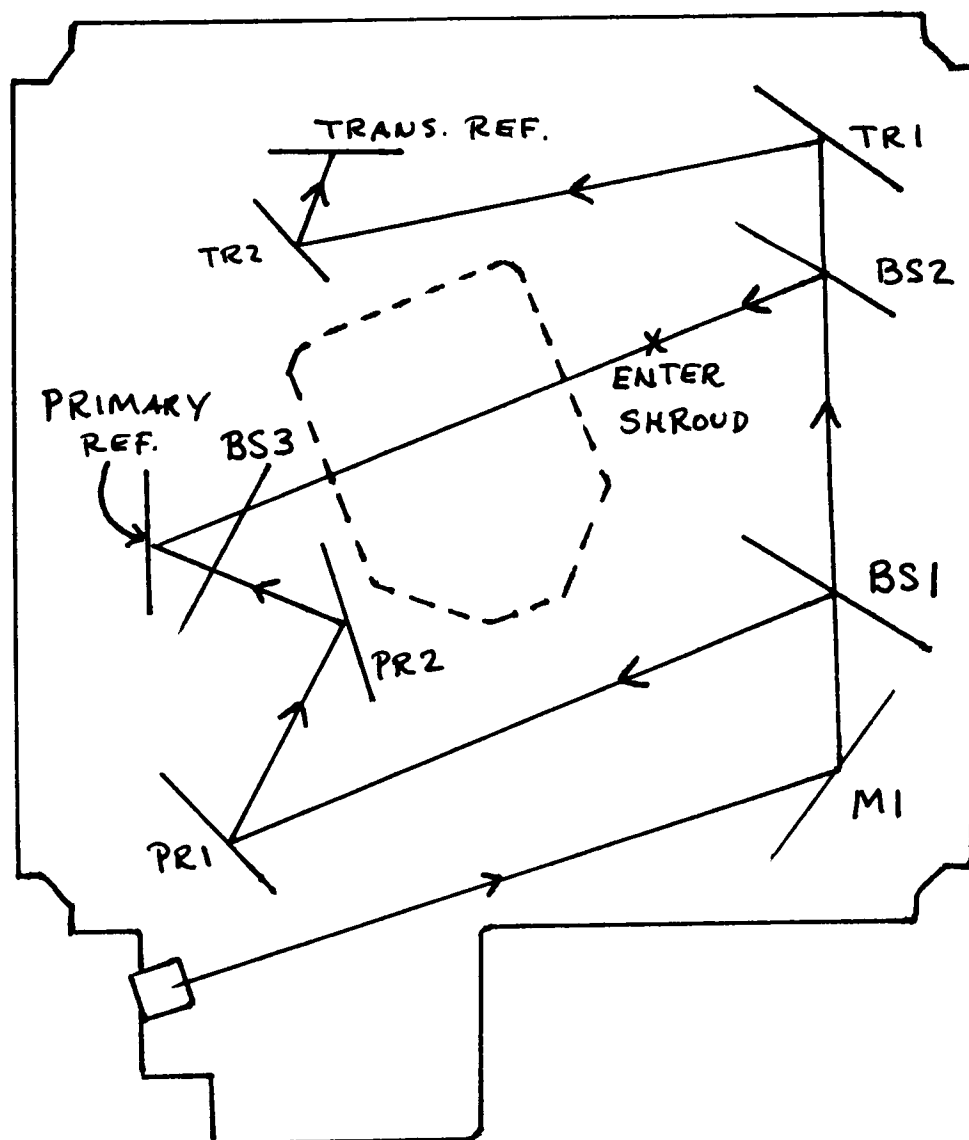


Figure 3- FES optical bench with measurement locations marked.

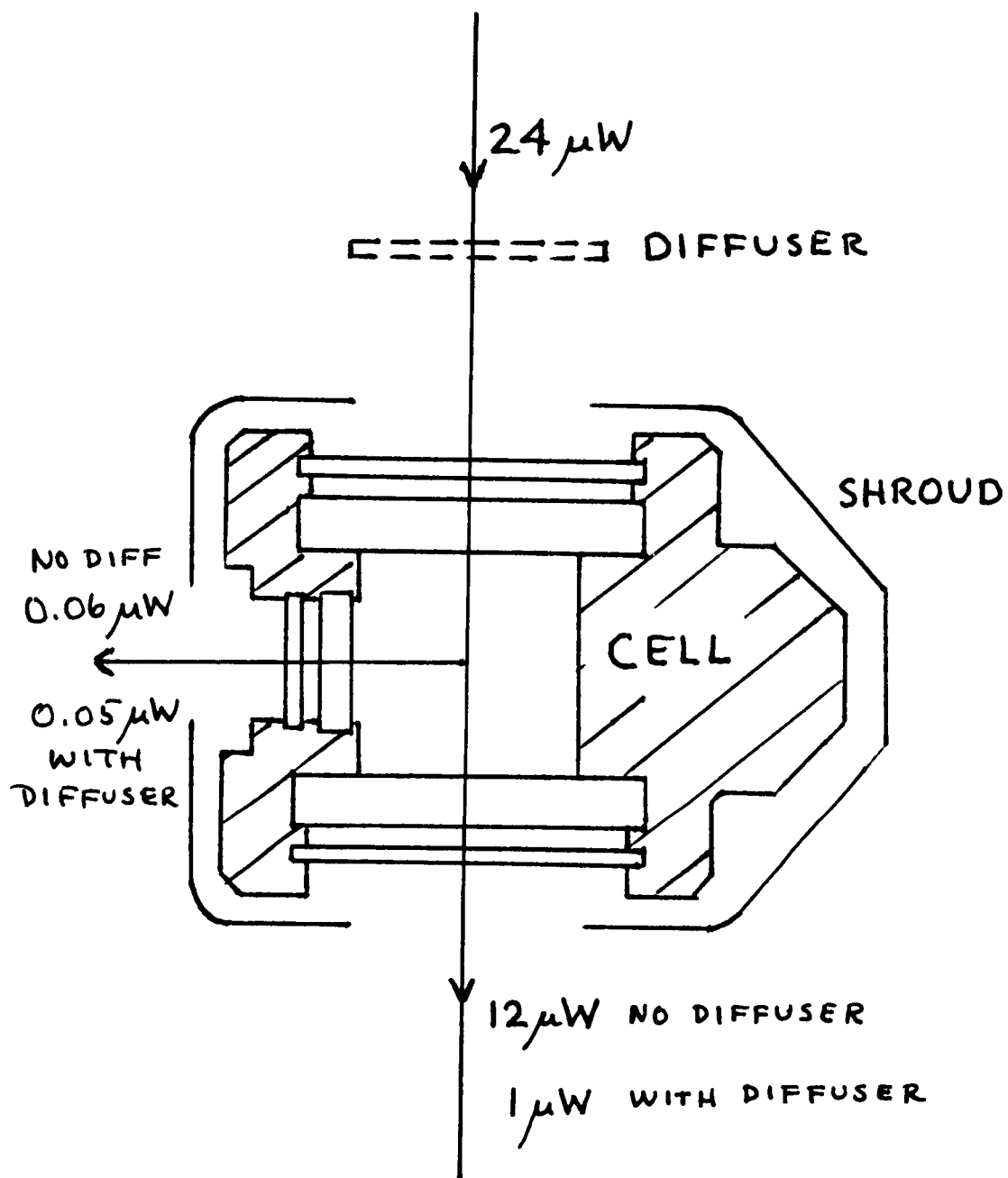


Figure 4- Cell 101 with power readings for appropriate beams indicated.

TABLE 1
Transverse Optical Sting Holograms Produced in HGS

No.	Beam Ratio	Exposure	Cell Temp		Comments
1	30:1	20 ms	No	Cold	poor
2	30:1	50 ms	No	Cold	poor
3	30:1	100 ms	No	Cold	Best of set
4	30:1	200 ms	No	Cold	Too Dark
5	2:1	500 ms	No	Cold	Best of set
6	2:1	1 s	No	Cold	partial
7	2:1	2 s	No	Cold	incomplete
8	10:1	100 ms	No	Cold	Best of set
9	10:1	200 ms	No	Cold	OK
10	10:1	500 ms	No	Cold	OK
11	100:1	20 ms	Yes	Cold	poor
12	100:1	50 ms	Yes	Cold	Best
13	100:1	100 ms	Yes	Cold	partial
14	100:1	200 ms	Yes	Cold	Too dark
15	100:1	200 ms UD	Yes	Cold	poor
16	100:1	500 ms UD	Yes	Cold	Very dark
17	20:1	100 ms	Yes	Cold	Nothing
18	20:1	200 ms	Yes	Cold	poor
19	20:1	500 ms	Yes	Cold	Good
20	20:1	1 s	Yes	Cold	Best
21	20:1	2 s	Yes	Cold	Too Dark
22	20:1	2 s UD	Yes	Cold	Good
AUTO DEVELOPED HOLOGRAMS FOLLOW (23-36)					
23	20:1	100 ms	Yes	Cold	poor
24	20:1	200 ms	Yes	Cold	Nothing
25	20:1	500 ms	Yes	Cold	fair
26	20:1	1 s	Yes	Cold	Best
27	20:1	2 s	Yes	Cold	OK
28	20:1	200 ms	Yes	Hot	partial
29	20:1	500 ms	Yes	Hot	partial
30	20:1	1 s	Yes	Hot	Best
31	20:1	2 s	Yes	Hot	OK
32	20:1	9.2 s	Yes	Hot	partial
33	100:1	20 ms	Yes	Hot	poor
34	100:1	50 ms	Yes	Hot	poor
35	100:1	100 ms	Yes	Hot	poor
36	100:1	200 ms	Yes	Hot	Best

NOTE : UD = underdeveloped

TABLE 2
POWER MEASUREMENTS ON FLIGHT BENCH
(IN MICROWATTS)

PRIMARY REFERENCE	65
TRANSVERSE REFERENCE	13
ENTERING CELL SHROUD	127
PRIMARY OBJECT NOT DIFFUSED (WITHOUT CELL)	14
PRIMARY OBJECT NOT DIFFUSED (EST. WITH CELL)	7-9
PRIMARY OBJECT DIFFUSED (EST. WITH CELL)	0.6-2
TRANSVERSE OBJECT NOT DIFF. (EST. WITH CELL)	0.3
TRANSVERSE OBJECT DIFF. (EST. WITH CELL)	0.26

TABLE 3
ESTIMATED FLIGHT BEAM INTENSITY RATIOS

PRIMARY

WITHOUT DIFFUSER	7 - 9:1
WITH DIFFUSER	32 - 100:1

TRANSVERSE

WITHOUT DIFFUSER	43:1
WITH DIFFUSER	50:1

NOTE: Range of values in primary ratios show the difference between the calculated and measured transmission coefficients for the test cell.

CONCLUSIONS AND RECOMMENDATIONS

After completing this study, it appears that it is possible to detect particles about 20 micrometers in diameter in the FES holograms that were recorded on the SL-3 mission. However, only a small number of particles were found; many more particles were removed from the cell in the post flight draining of the cells. The inability to see most of the small particles may be a result of the large reference to object beam intensity ratios that are apparently built in to the FES optical bench. The lack of detectable small particles in the primary holograms is explained by a combination of the bad beam ratio, poor lighting angle for the particles, and the speckle pattern introduced into the holograms by the diffuser plate.

The HGS produced holograms confirm that proper beam ratio and exposure time are critical to achieving good resolution in the reconstructed images. If the beam ratio is much larger than 20:1 then the image clarity suffers. Underexposure of the hologram makes it impossible to see small details, but slightly overexposed holograms exhibit good detectability.

If small particles are going to be intentionally introduced into the test cell, for the purpose of determining fluid velocity, then another series of holograms should be made of the test cell with particles. This series should determine the optimum exposure time and beam ratio to easily detect the particles.

Regardless of the addition of small particles to the cell, it is recommended that the caps in the test cells be grooved in a fashion similar to the optical sting. A hologram of the grooved cap, before it is retracted, would insure that the actual flight cell is not adversely affecting the

resolution of the holograms. The modified cap would give the investigator a known small feature at a known place in the cell.

Depending on the final results of the series of holograms of the test cell with small particles, action should be taken to reduce the beam intensity ratios on the FES optical bench. Changing the value of the first beam splitter could improve the primary ratio as would a change in the value of the beam splitter just in front of the primary film plane. Changing the beam splitter that separates the object beam and the transverse reference beam could help both ratios. The insertion of a neutral density filter in the transverse reference beam would help the transverse ratio.

Exact changes could be more easily determined if the HGS optical bench was equipped with optical components that match those of the FES flight bench. The optical elements also should be obtained that would permit HGS to record both primary and transverse holograms during the same test.

The Fluid Experiment System and Holography Ground System have the capacity to provide detailed information on the growth of crystals in the low gravity environment of Spacelab. With a few minor adjustments even more data can be retrieved from future flights.

REFERENCES

- Abramson, N., The Making and Evaluation of Holograms, Academic Press, New York, NY, (1981).
- Caulfield, H. J. and S. Lu, The Applications of Holography, Wiley and Sons, New York, NY, (1970).
- Department of Defense, Optical Design Military Standardization Handbook, MIL-HDBK-141, Defense Supply Agency, Washington, DC, (1962).
- Francon, M., Holography, trans. by G. M. Spruch, Academic Press, New York, NY, (1974).
- Hale, G. M. and M. R. Querry, "Optical Constants of Water in the 200 nm to 200 micrometer Wavelength Region", APPLIED OPTICS, vol. 12, no.3, pp. 555-62, (1973).
- Klein, H. A., Holography, J. B. Lippincott, Philadelphia, PA, (1970).
- Meyer-Arendt, J. R., Introduction to Classical and Modern Optics, Prentice Hall, Englewood Cliffs, NJ, (1972).
- Smith, H. M., Principles of Holography, Second Edition, Wiley and Sons, New York, NY, (1975).
- Stroke, G. W., An Introduction to Coherent Optics and Holography, Second Edition, Academic Press, New York, NY, (1969).
- TAI Corporation, HGS Users Manual vol. 1 and HGS Technical Operations Manual vol. 2, Contract # NAS8-35426, Huntsville, AL, (1984).

N88-15610

59-61

116711

438

1987

NASA/ASEE SUMMER FACULTY RESEARCH FELLOWSHIP PROGRAM

Marshall Flight Space Center
The University of Alabama in Huntsville

ENHANCEMENT OF COMPUTER SYSTEM
FOR APPLICATIONS SOFTWARE BRANCH

Prepared by:	Alex Bykat
Academic Rank:	Professor
Affiliation:	University of Tennessee at Chattanooga Center of Excellence - Computer Applications
NASA/MSFC:	
Laboratory:	Information and Electronic Systems
Division:	Software and Data Management
Branch:	Applications Software
NASA Colleague:	Delano R. Hyter
Date:	August 5, 1987
Contract No:	The University of Alabama in Huntsville NGT-01-008-021

ENHANCEMENT OF COMPUTER SYSTEM
FOR APPLICATIONS SOFTWARE BRANCH

Alex Bykat
Professor of Computer Science
Center of Excellence - Computer Applications
University of Tennessee
Chattanooga, TN

ABSTRACT

This report presents a compilation of the history of a two month project concerned with a survey, evaluation and specification of a new computer system for the Applications Software Branch of the Software and Data Management Division of Information and Electronic Systems Laboratory of Marshall Space Flight Center, NASA.

Information gathering consisted of discussions and survey of branch activities, evaluation computer manufacturers literature, and presentations by vendors. Information gathering was followed by evaluation of their systems. The criteria for the latter were: the (tentative) architecture selected for the new system, type of network architecture supported, software tools, and to some extent the price.

The information received from the vendors, as well as additional research, lead to detailed design of a suitable system. This design included considerations of hardware and software environments as well as personnel issues such as training. Design of the system culminated in recommendation for a new computing system for the Branch.

ACKNOWLEDGEMENTS

I would like to express my appreciation of the hospitality extended during my tenure at Marshall Flight Space Center. I am quite impressed with the efforts of both, Ernestine Cothran, NASA/University Relations and Gerald Karr - NASA-ASEE Program Coordinator, to provide a meaningful and all-round experience during the program.

My thanks and appreciation go also to Mr. Ray H. Craft and Mr. Delano R. Hyter for, not only providing a cordial and productive atmosphere, but also for their efforts in providing the opportunity to participate in their program.

Finally, my thanks go to Dr. G.R. Wallace, Mr. J.H. Lucas, and Mr. D.J. Aichele, for supporting and helping to identify sources for further cooperation with MFSC.

CONTENTS

1. Introduction.	6
2. Planning.	8
2.1. Project activities.	8
2.2. Resource allocation.	9
2.3. Resources available and needed.	9
3. Project specification.	10
3.1. General discussion.	10
3.2. Project specification.	14
4. System survey and analysis.	14
4.1. Current system.	14
4.2. Survey.	15
4.3. Analysis.	16
5. Baseline design.	17
5.1. Local Area Network (LAN).	17
5.2. Towards the future.	19
5.3. Application development software.	21
5.4. Software for embedded systems.	21
6. Information gathering.	22
6.1. Operating system.	22
6.1.1. VMS.	22
6.1.2. UNIX.	23
6.2. Systems reviewed.	25
7. Detailed design.	27
7.1. Personnel.	27
7.2. Hardware.	27
7.3. Software.	30
7.3.1. General management.	30
7.3.2. Project management.	30
7.3.3. Software development.	30
7.3.4. Document preparation.	32
7.3.5. Training tools.	32
8. Conclusion.	33
9. Appendix 1: Software development life cycle.	35
10. References.	37
11. Glossary.	38
12. Index.	41

FIGURES

Fig. 2.1.1. Project stages: Define, Design.	8
Fig. 2.1.2. Project stages: Accept, Install.	8
Fig. 3.1.2.1. Software Engineering functions.	12
Fig. 5.1.1. Applications Software Branch computing system architecture.	19
Fig. 6.1.2.1. Unix structure.	24
Fig. 7.2.1. Applications Software Branch computing system architecture.	29

1. Introduction.

This report presents a compilation of the history of a two month project concerned with a survey, evaluation and specification of a new computer system for the Applications Software Branch of the Software and Data Management Division of Information and Electronic Systems Laboratory of Marshall Space Flight Center, NASA. The project was allocated to me within the framework of the Summer Research Faculty Program conducted between NASA and various universities.

The general philosophy that I adopted for execution of this project follows a typical project management pattern; the main difference is in human resources involved. In this project both aspects, the project management and project development are executed by one and the same person, namely me.

Thus, one constraint in this project is the size of personnel: one person. Another definite constraint was related to the framework of the Summer Program and to the first constraint: time available was somewhat less than two man-months.

As it should be with any project, I started the project by planning the general path that the project would follow. This planning phase included identification of project activities, resources available, and resource allocation.

The planning phase was followed by project analysis and culminated with detailed specification of the requirements of the project.

The first two phases were then followed with a survey and analysis of the existing computer system. This phase consisted mainly of interviews of the branch personnel, discussions of their past and present projects, design of survey forms and collection and evaluation of the survey information. (The survey form is included in [Bykat, 1987].)

The next stage, system analysis - analysis of information gathered in the two prior stages - resulted in some interesting data concerning the resources used in past projects. For example, the survey revealed that whereas 92% write and compile their code, only 62% use debugging tools and only 23% use software monitors to evaluate the efficiency of the code. (The survey results are presented in section 4.2.)

The problem definition stage yielded sufficient information to formulate the base design of the system. Essentially, it became clear that a distributed system based on networked workstations, and supported with centralized file system would suit and benefit development of projects dealt with by the branch.

Thus the design stage of the project was initiated. I started by collection and selection of information of some leading commercial system vendors which support computing functions prevalent in the branch. This stage consisted mainly of collection and review of

the vendors data describing their offerings. A number of system were reviewed - they are listed in section 6.2.

Information gathering was followed by information consolidation. Here, the vendors offerings were re-evaluated and only a few were "short listed". The criteria were: the (tentative) architecture selected for the new system, type of LAN supported, software tools, and to some extent the price. From this short list, five vendors were contacted. The requirements of the system were presented to the vendors (see section 3.2) and detailed discussion followed. The vendors were requested to prepare a presentation of their proposed systems.

The information received from the vendors, as well as additional research, lead to detailed design stage of the system. This design included considerations of hardware and software environments as well as personnel issues such as training. A draft of this paper was prepared and distributed to branch management and selected technical personnel for comments.

The input from reactions to the draft paper was then reviewed, evaluated and incorporated. The final recommendation was then prepared and the project was concluded. The recommendation calls for a distributed heterogeneous system of multivendor hardware, interconnected with a local area network, and providing an integrated software development environment.

The following sections provide detailed account of the various stages of the project, and specify some of the considerations that have lead to the final recommendation.

2. Planning.

2.1. Project activities.

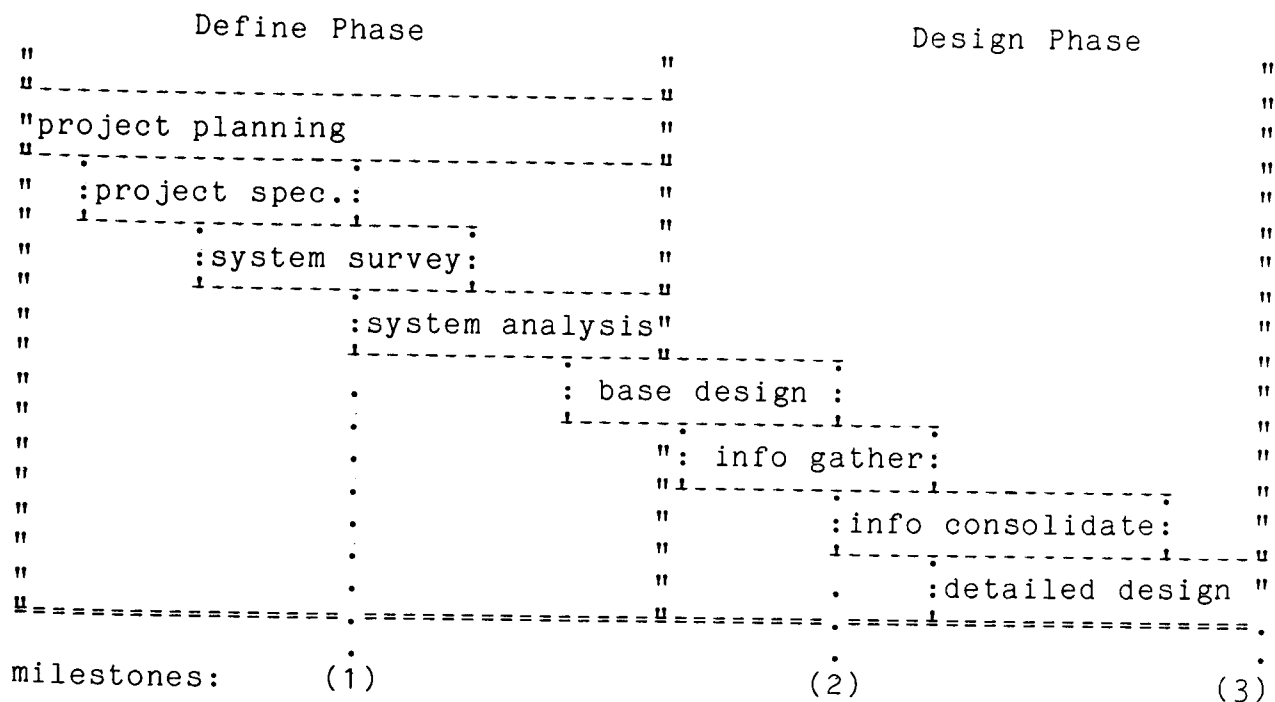


Fig. 2.1.1. Project stages: Define, Design.

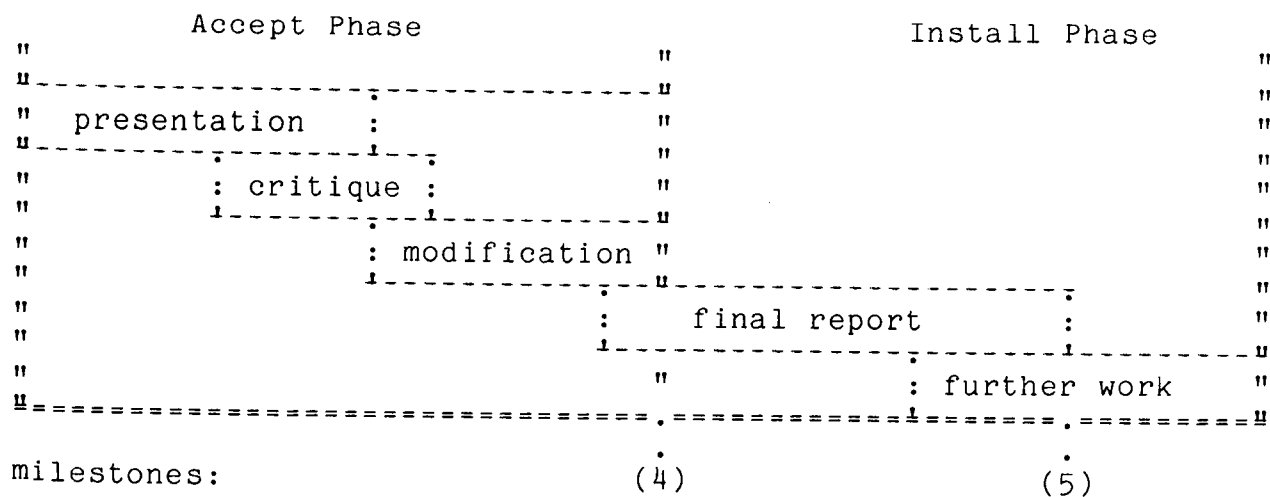


Fig. 2.1.2. Project stages: Accept, Install.

Milestones.

- (1) specification written and accepted.
document: "Specification statement".
- (2) baseline design completed.
document: "System design specification".
- (3) detailed design completed.
document: "Proposed system".
- (4) detailed system design accepted.
document: modified "Specification statement".
- (5) summer project concluded.
document: final report.
- (6) further work considerations.

2.2. Resource allocation.

Definition	weight	days
Problem specification	1	1.5
Survey of current system	4	6
Analysis	2	3
Planning	1	1.5
Design		
Baseline design	1	1.5
Information gathering	4	6
Information consolidation	6	9
Detailed design	2	3
Acceptance		
Presentation	3	4.5
Critique	1	1.5
Modification	2	3
Installation		
Report	3	4.5
Follow-Up		
Further work	1	1.5
Continuation	?	?

2.3. Resources available and needed.

Time (9 wks)	45
seminars and other activities	-5

Total time available: 40

3.1. General discussion.

Survey, evaluate and recommend systems and tools to support software engineering functions of the Applications Software Branch which includes requirements through sustaining engineering. [Hyter, 1987]

To evaluate the existing system and to propose a new system the above specification needs to be refined. In particular, the following questions need further explanation:

- (1) What type of applications does the branch engage in?
- (2) What software engineering functions does the branch engage in?
- (3) What type of capabilities have to be supported?
- (4) What type of tools are needed to support these capabilities?
- (5) What type of system is suitable for this branch?

3.1.1. Type of applications:

Information processing

Examples are engineering calculations, information retrieval etc.

System software

Real-time software

Business software

payroll, inventory...

Scientific software

large amount of numerical computation:
engineering calculations, CAE,
system simulation...

Symbolic manipulation software

artificial intelligence,
pattern recognition...

Process control

The salient features of this type of application are the formatting of input data by machine (and possibly people) and formatting of output for machine consumption.

Examples are instrumentation control, real time data gathering, automated manufacturing, etc.

Real-time software

The salient feature of this type of application is interaction with 'real world' events. Frequently these applications reside on processors packaged within a product.

Examples are data gathering, device monitoring, on-board flight control; weapon systems, etc.

After discussions with management and members of the Applications Software Branch, the following supplementary information was received.

3.1.2. Software engineering functions:

Typical software engineering functions consist of the following stages [see also Miller, 1979]:

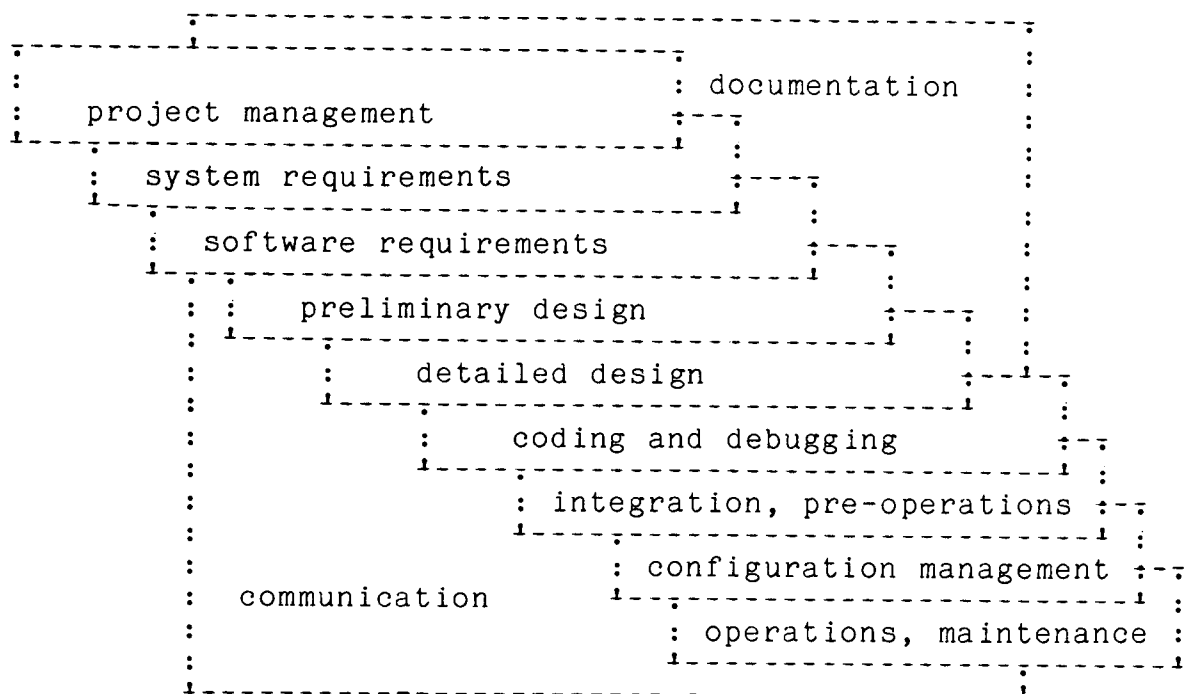


Fig. 3.1.2.1. Software Engineering functions.

The Applications Software Branch projects fall within these functions. Generally, the functions of this branch can be described as [Lucas, 1986]:

Application software development and sustaining engineering;
Support software management and development.

3.1.3. System capabilities required:

Efficiency in numerical computation;
Interactive graphics display: both input and output;
Fair amount of real time processing;
Data acquisition from sensors;
General purpose computation.

Languages used:

predominant: Fortran
occasional: assembly, Pascal, PL/M

In addition to above, it is perceived that in coming applications ADA will be used as the major language of this branch.

Operating systems used:

VMS, INTEL360, RT-11, RSX-11

3.1.4. Tools needed:

System capabilities/tools considered should include:

Simulators, emulators, logic analyzers, debug and diagnostic aids;
Computer aided requirements analysis, design, code generation, test generation and documentation;
Project management and configuration control;
Cost, training, productivity, quality, and flexibility to support a variety of projects;
Networks. [Hyter, 1987].

System architecture:

Two major types of computer system architecture that have to be considered are:

- a) centralized, and
- b) distributed.

Further, a decision is to be reached on the processor architecture:

- a) uniprocessor,
- b) multiprocessor, or
- c) parallel processor.

Scope of the system:

budget: \$600,000
personnel size: 25

Typical hardware engineering questions need to be answered:
class of hardware that best addresses functions to be supported,
commercial availability of such hardware and its cost,
type of interfacing required,
what constraints are present (size, environment...).

Information collected in answering the above questions lead to a refinement of the project specification presented in the next section.

3.2. Project specification.

Narrative.

Survey, evaluate and recommend a computing system consisting of appropriate hardware and software tools to support software engineering functions of the Applications Software Branch.

The software tools will form

- (a) integrated project management environment
- (b) integrated program development environment.

The system is to be capable of sustaining development of applications which exhibit:

- high numeric computation component,
- interactive color graphics manipulations,
- real time data acquisition from sensors,
- real time control, and
- general purpose computation.

The goal of the system is to provide a software environment for activities which span software design and implementation life cycle, and in particular:

- project planning, specification design,
- design implementation, verification, and
- installation

of software products.

Languages supported by the system will include FORTRAN and ADA, and possibly C and a good Prolog environment for use in rapid prototyping of projects.

An immediate expected benefit of the selected system is to support and promote high productivity both in software project development activities and implementation of these projects.

Computer characteristics.

A general commercial system is required. The system must be able to support at least 25 users running a mix of document preparation, telecommunications, project management, and code development software.

Hardware interfaces.

The system must support standard serial and parallel ports, and a LAN interface (Ethernet).

Software functions.

Software should include a project management environment, code development environment, document preparation tools and telecommunication tools.

4. System survey and analysis.

4.1. Current system.

Currently the computer system serving the Applications Software Branch is organized into a number of stand alone and time sharing centralized computing systems. These systems include:

- INTEL 8080 - A stand alone computer operating under ISIS II operating system. Languages supported are Assembler, FORTRAN-80, PL/M. Also supported is ICE-80 product development tool for 8080 CPU. This computer is utilized mainly for the MEA project.
- PDP-11/23,
PDP-11/73 - A stand alone computer operating under RT-11 and RSX-11 operating system. Languages supported are FORTRAN. The PDP-11/23 is utilized mainly for the BATSE project.
- VAX 11/7xx,
mVAX II - A number of timeshared dedicated computers operating under VMS operating system. Languages supported are FORTRAN, Pascal, PL/1. These computers are used for the HOSC project, the POCC project and the Space Telescope project.

The mode of operation of these computers is predominantly development of the software in a high level language, compilation and subsequent transfer (if necessary) of the object code to the target computer. Some projects were written in an assembly language and subsequently assembled and ported to a target computer.

Project groups within the branch are, typically, small and consist of 3-8 programmers. Although groups work on independent projects, some groups are divided into a number of teams. Further, project groups frequently work on programs which are targeted for different types of hardware. Majority of software is developed in FORTRAN.

4.2. Survey.

To get a better understanding of the capabilities used in the past projects developed by the branch, I have conducted a survey of the personnel. Out of 20 technical personnel, 13 have responded to the survey. The information is presented below.

Capabilities used:

graphics:	6 (46%)	port interfacing:	4 (31%)	
device drivers:	5 (38%)	communications:	7 (54%)	sound: 0

Languages used:

FORTRAN: 12 (92%) PL/M: 1 (8%) C: 1 (8%) ADA: 5 (38%)
PASCAL: 2 (15%)

OS used:

VMS: 11 (85%) UNIX: 1 (8%) INTEL360: 4 (31%) RSX: 1 (8%)

Software development tools used:

compiler: 12 (92%) interpreter: 1 (8%) editor: 12 (92%)
emulator: 1 (8%) file manager: 3 (23%) code manager: 0
debugger: 8 (62%)

Evaluation tools:

software monitor: 3 (23%) hardware monitor: 0

Project management tools used:

GANTT: 0 HIPO: 0 Milestone: 3 (23%) PERT: 0
Flow charts: 5 (38%) Costing: 0 Data Flow: 3 (23%)
Storage maps: 0 Coverage matrix: 0

Document preparation tools used:

screen editor: 10 (77%) wp: 3 (23%)

Networking tools used:

Ethernet: 4 (31%)

Hardware used:

VAX: 11 (85%) PDP: 2 (15%) IBM: 3 (23%) INTEL: 7 (56%)

Programming background:

Average Programming experience: 8 yrs
BS Degree: 11 (85%) MS: 2 (15%)
Math: 8 (62%) CS: 4 (31%) Phys: 1 (8%)

4.3. Analysis.

Current system consists of a number of stand alone computing systems with no communication lines between them. Some of these systems are outdated and should be replaced. In particular the INTEL 8080 is an old 8 bit architecture. The PDP 11/23 is similarly in its advanced years.

The majority of projects are small to medium size, and should be supported by a system suited for this mode of operation. The particular advantage of software development in small sized

projects is little inertia that needs to be considered when making source modifications and design changes. This makes it suitable for an approach to software development in terms of reusable, interchangeable, and configurable tools.

I have noted above, that the hardware currently in use shows signs of aging. However, the age of the hardware is not the major disadvantage; in fact it is the general architecture of the departmental system, or rather a lack of it.

Given that the majority of the Applications Software Branch' projects are developed in high languages, it would be conducive both to the improvement in productivity and to improvement in job satisfaction to provide an integrated programming environment.

An integrated software project requires frequent use of common information and data, eg. global files, cross-compilation tools etc. When the project is developed on a number of stand-alone systems, this requirement creates a problem of information integrity, decreases productivity, and magnifies the probability of problems during system integration.

Thus, the programming environment should be based on a locally distributed system architecture, linked together via a local network.

The need for porting the developed software to target systems can be resolved by provision of appropriate cross-compilers or cross-assemblers.

The "interchangeable, reusable and reconfigurable tools" paradigm of software development is well supported by Unix environments. In fact, Unix thrives on creation of tools with clean interfaces, and subsequent creation of larger programs by building interfaces which use those tools as communicating cooperating processes.

Unix environment also possesses facilities for "compile source to object and download object to (non-Unix) target" operations which are important in the projects developed in the Applications Software Branch (eg. MEA project).

5. Baseline design.

Analysis of typical branch activities indicates that the programming environment should be based on a locally distributed system architecture, linked together via a local network. Such a system may consist of a number of networked general-purpose workstations supported by compute and file servers.

Each of these workstations would be capable of functioning in a stand-alone mode thus off-loading the system servers; for compute intensive tasks the compute server would be used.

The file server will provide a central file system (with file security) to ensure the integrity of official versions of the project files, while the individual node storage capacity would be used for single user development, back up and other administrative chores.

5.1. Local Area Network (LAN).

LAN allows configuration of a locally distributed computing system. Among the major advantages of such a system one can count:

- architecture - can be used as a number of stand-alone systems or as a distributed system.
- fault tolerance - failure of one part of the network has only a limited effect on the operation of the network.
- incremental - new nodes can be added when needed, allowing the system to grow together with the organization
- common database - supports development and maintenance and access to common departmental databases of programs, files and other information.
- data integrity - file server can regulate access to the official version of the information.
- data security - file server can permit or deny access to information.
- communication - allows communication and interchange of expertise; allows electronic mail communication.
- reusability - promotes software reusability and sharing thus increasing productivity by reducing development effort.
- productivity - see above.
- quick response - single user nodes can be dedicated to individual tasks.
- cost - allows sharing of hardware devices and software products.
- fun - brings the computing system to programmers office and consequently increases job satisfaction (and productivity).

Given the preceding discussion, we no longer can ask whether the computer systems for the Applications Software Branch should be linked via a LAN, but merely what LAN.

Besides the usual considerations of speed, bandwidth, reliability, simplicity of use and cost, a major concern when choosing a LAN is compatibility with other network existing in the organization. Since MFSC/NASA has a number of branches and divisions with computer systems connected via Ethernet, it seems that a natural choice for this branch is therefore Ethernet LAN.

the latter case, the local storage may be configured to be a part of the main file system (yielding a distributed file system), or it may be used for local storage individual to each node. In either case, the network software must provide transparent file system operations.

Similar considerations apply to distributed/central compute power of the system.

5.2. Towards the future.

Networked workstation concept advocated in this paper is an adaptation of a distributed system architecture. Such a system has a growth potential due to the ease of exchange, addition and removal of member nodes (see also section 5.1). A set of nodes in the system may consist of multi-vendor devices and computers, with the particular mix to be tuned to prevailing project requirements. Thus, a distributed system allows creation of a heterogeneous system.

Supported with a good network management software, this distributed system will offer total transparency of architecture to individual clients. At the same time, it will allow maximal utilization of systems resources.

The transparency of the system will manifest itself in promotion of perception of the resources of the system as belonging totally to the individual user. These resources can be as diverse as uniprocessors, specialized graphics devices, supercomputers, array processors, dedicated AI machines, general scientific computers, specialized finite-element machines, special storage devices, various supporting peripheral devices, etc.

To achieve such transparency, the system must be supported by appropriate network management software. This software must provide data independence as well computation independence of existing or future computer architectures.

Data independence (eg. based on the eXtended Data Representation (XDR)) provided in a multi-vendor system allows for ease of integration of new computer architectures without unwarranted commotion due to physical incompatibility with existing components of the system. Computation independence (eg. based on Remote Procedure Call (RPC)) supports integration of the computational power of the new computer, much as data independence supports data exchange.

Some such software tools are commercially available today, some will become available in the near future, yet others are still "flights of fancy".

In particular, the Network File System (NFS) by Sun Microsystems Inc. provides data sharing transparency, remote login facilities etc. NFS is a component of Sun's Open Network Computing (ONC)

which provides an environment consolidating resources of multi-vendor computers operating under a variety of operating systems. NFS translates client file system into appropriate destination system commands, eliminating the need to learn new command languages. File sharing as well as file locking, and record locking is supported. The NFS system is based on Unix environment.

A particular strength of NFS is its ability to handle heterogeneous computing systems, its portability, as well as its independence of transport protocols (the latter is achieved through the RPC layer). For example, NFS is reported to have been implemented on machines such as Apollo, Cray, DG, HP, IBM PCs, mVax-II, Vax 11, Wang, etc, and has been ported to run under operating systems such as DEC Ultrix, VMS (Wollongong), Berkeley 4.2, System V.2, MS-DOS, DG MV 4000 and, ofcourse, SUN-OS.

The recently announced Network Computing System (NCS) by Apollo Computers Inc. promotes distributed computing via remote procedure calls to network resources and originating from a client process. NCS provides software (written in C) which runs on Unix systems in a heterogeneous networked environment. When ported on these machines, this software allows "packets of computation" belonging to the same process to be distributed and executed on various machines in accordance with availability of currently unused computational power.

Both of the above network systems coexist with the standard transfer protocol TCP/IP.

5.3. Application development software.

Software development tools required are:

- operating system, command languages, programming languages, symbolic debuggers, linkers, library managers, source control systems, full screen multiple window editors, other editors.

Databases and file systems:

- Databases are developed and serve groups of people. In a program development environment, the group is a project team. The personnel accesses and modifies the database, and therefore data compatibility, distributed processing, integrity and security are of major importance.

Project management:

- Project management software should support methods for requirement formulation, performance evaluation, quality and reliability testing, planning, costing. This software should include:

- planning tools:

- milestone charts, PERT chart generator, GANTT chart generator, costing chart generator.

tracking tools:

software version control, modification control, object module librarian, bug report generators.

design tools:

flowcharts, HIPO charts, storage maps, coverage matrix (system functions v. program names).

documentation aids:

PDL, structured charts, data flow diagrams.

performance and evaluation:

software monitor, hardware monitors.

5.4. Software for embedded systems.

To improve productivity, software for embedded systems may be developed in high level language on modern workstations. Object code can then be generated by a cross-compiler and ported run on the target system. Testing and evaluation of the run efficiency of this software (on the target system) should also be performed in a high productivity environment. To afford this approach, emulators and logic analyzers are needed.

An emulator allows the developer to see the "role" that the software would be playing on the target system. The emulator frequently allows a good measure of control over the execution of the software, so that the software can be tuned and various tests conducted to compare the run properties of the new version versus the old one.

In addition to cross-compilers, disassemblers may be used to convert object code to assembly code. The latter may then be used to run "regression tests" to compare the object codes of an old version against that of a new version.

6. Information gathering.

6.1. Operating system.

The operating system used predominantly in the Applications Software Branch projects is the VAX/VMS running on various DEC machines. It is evident, therefore, that there is some existing expertise of this system among current personnel. However, it should be realized that a good application development environment would insulate the user from the operating system. Consequently, the existing expertise with VMS is not taken as a constraint in the choice of a new system.

A major alternative to VMS is the operating system Unix. A particular advantage of Unix is its pervasiveness on a majority of hardware. Concomitant with this is, of course, transportability of

programs developed under Unix, as well as a very large software base.

Further, Unix is fast becoming a standard in federal government (Unix is specified in 70% of government procurement [GCN, 1987a]) and industry - it has been the OS of choice in Universities for a number of years. The armed forces have also recognized the importance of Unix. For example, both Army and Air Force are procuring Unix based systems; each has requested 20,000 32 bit systems. (The Army contract is estimated at \$600 Million, while the Air Force contract -- Project 251 -- is estimated at \$3 Billion [GCN, 1987b].)

6.1.1. VMS.

VAX/VMS is a multiuser, timesharing operating system for DEC VAX line of hardware. The system supports demand paging and swapping to satisfy memory requirements of its processes. A VMS process has a limit of 4 GB of memory, with a 1 GB limit per program.

VMS provides good program development tools, and supports various languages such as Fortran, C, Pascal, Ada, Cobol etc. It sustains electronic mail, and supports networking (Ethernet, DECnet).

VMS can be supplemented with various specific application packages and environments. Of particular interest are the VAX ADA and VAXset.

VAX ADA can be integrated with VMS to provide the standard VMS tools such as: debugger, record management services, run-time library, Digital Command Language and, of course, VMS file system.

VAXset is an optional toolset which together with the standard VMS tools mentioned above represent the VAX/VMS software engineering environment. This tool set consists of:

- Language-Sensitive Editor (LSE) -

- A multi-window screen editor with language syntax sensitivity provided by language-specific templates.

- Code Management System (CMS) -

- A program library system used for source-code and documentation control of software projects.

- Module Management System (MMS) -

- A set of procedures for identifying dependencies of a system, and automatic rebuilding of the system in accordance with changes in referred modules.

- Test Manager (DTM) -

- Facilitates user-designed regression testing of the project software, generation of benchmarks and result review.

- Performance and Coverage Analyzer (PCA).

- Automates collection and analysis of data for program performance evaluation and generation of appropriate reports.

Good tools notwithstanding, a main disadvantage of VAX/VMS is its proprietary nature. Though the installed base of DEC computers is large, the VMS base is restricted to the VAX series. Selection of a proprietary system implies smaller software base (compared to a that of an industry standard system), and limits future expansion and hardware changes.

6.1.2. UNIX.

Unix is fast becoming a standard in federal government and industry - it has been the OS of choice in Universities for a number of years.

For our purposes, the following general features of Unix are its particular strengths:

- multiuser,
- multitasking,
- portable to multivendor computing systems,
- good development environment:
 - numerous tools,
 - utilities,
 - powerful user interface,
 - easy linking of programs into large applications
- good software project tools:
 - source-code control system,
 - make utility,
 - documentation tools.

A major criticism of early versions of Unix pertained to its rather cryptic command names and its, rather obtuse, user interface. These 'blots on the Unix character' have been erased by the software interfaces provided on most workstation vendors. In fact, it is my opinion that the original criticism was mainly related to 'fear of the unknown' by the critics for it is unusually easy to shape and bend Unix interface to conform with user's personal wishes.

Unix can be perceived as having the following layered structure:

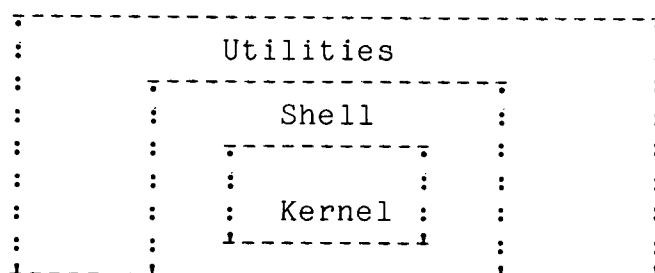


Fig. 6.1.2.1. Unix structure.

with the layers comprised of:

Utilities:

networking, software development tools, file manipulation, languages

Shell:

command language interpreter, C language

Kernel:

operating system functions

Of the three layers, the programmer interacts normally with the utilities and possibly the shell; the primitive functions of the kernel are accessed only for special hardware manipulation.

UNIX provides a "Programming WorkBench" environment which supports large project development. This environment is suitable for development of programs which are to be compiled and run on non-Unix target systems, including target real-time systems which differ markedly from timesharing environment. The Programming WorkBench includes facilities such as [Mitze, 1981] :

- flexible remote job entry
- source-code control system
- control over interface specification
- control over changes in documentation, source and data
- modification-request control system
- easy recreation of older versions
- control over official and test versions
- make files for compile and link mixes
- variety of documentation tools
- text processing tools
- electronic mail

Over 90% of Unix is written in the programming language C . Since the function of a programming language is to make system resources available to the program, C is particularly useful in a Unix environment. In fact, C is the "official" language in Unix systems. C is an "intermediate level" language, providing the syntax and control constructs of a high level language, as well as power and flexibility of a low level language. It affords access to Unix source, libraries and utilities modules (promoting code reusability) as well as access to machine resources at primitive level. It is suitable for complex small, medium and large program development.

In short, coming from IBM personnel:

"Unix provides considerable functional power to the individual user, provides multi-user capabilities where needed, is open-ended, and has a large user and application base." [Henry, 1986]

6.2. Systems reviewed.

The following is a brief summary of the offerings reviewed for the new computer system.

Apollo. (Domain 3000)

A 32 bit workstation based on 68020. 2/4/8 MB RAM with 86/170/380 MB disk. Fair resolution (1024x800) with 15" color display. Runs at 16 MHz. Supports 3 terminals. Ethernet. Good user interface.

Unix. Good software development environment provided by Teledyne (TAGS) and Apollo's DSEE. The latter caters for development, management and maintenance of software, and provides the following capabilities: inter-module dependency tracking, automatic change notification, source code history control, task management and system configuration management.

Languages supported are Fortran 77, Pascal, C, Lisp and ADA (the latter is expected within a month).

Sun Microsystems. (3/52M)

A 32 bit workstation based on 68020. 4/32 MB RAM with 72/140/575 MB disk. Good resolution (1152x900) with 19" monochrome display. Runs at 15 MHz, rated at 1.5 MIPS. Unix. Ethernet. Good software development environment. Good user interface.

HP. (318M)

A 32 bit workstation based on 68020. 4 MB RAM with 80/571 MB disk. Fair resolution (1024x768) with monochrome 17" display. Runs at 16.6 MHz. Unix (HP-UX). Insufficient information on software environment.

DEC. (Vaxstation 2000)

A 32 bit workstation. 4/6 MB RAM with 42 MB disk. Fair resolution (1024x864) with 19" color display. Rated at 1 MIPS. Ethernet. Ultrix. Good software management environment (CMS; MMS: similar to Unix sccs). Good user interface - VAX Workstation Software (VWS).

Apple. (MAC II)

A 32 bit workstation based on 68020. 1/8 MB RAM with 20/40/80 MB disk. Low resolution (640x480) with 13" color display. Runs at 16 MHz and is rated at 2 MIPS. Unix A/UX. New machine, inexpensive but software environment is in question. EtherTalk.

Compaq. (Deskpro 386/40)

A 32 bit workstation based on 80386. 1/4 MB RAM with 40/70/130 MB disk. Poor resolution (EGA). Runs at 16 MHz and is rated at 3 MIPS. Unix V.3. New machine, inexpensive but software environment is in question.

Rational. (R1000/200-20)

A uniprocessor ADA machine. 32 MB RAM with 2 GB disk.

Supports from 16 to 32 users. Ethernet. Good ADA environment but what about the rest? Young company (2yrs).

Convex. (C-1)

A supermini. 8/128 MB Ram with 414 MB disk. 64 bit words with speed rated at 60 MOPS. Can support 160 users. Unix. Insufficient information.

Integrated solutions. (Optimum V8S)

A 32 bit workstation based on 68020 with 2/10 MB RAM and 140/280 MB hard disk. High resolution (1280x1024) with a 19" color display. Runs at 16MHz. Supports 16 users. Has a proprietary Transparent Remote File System. Good user interface in the form of Desktop Manager. Unix 4.2. Ethernet.

Encore. (Multimax-320)

A 32 bit parallel processor supermini based on NS32032 with 4/128 MB RAM and 515/4120 MB hard disk. Speed rated at 1.5 MIPS per CPU. Basic configuration has 2 processors, cost \$139,000. Can be configured to have 20 processors. Works out at \$11,000 for each two additional processors. Can support from 20 to 250 users. Unix (UMAX). Insufficient information on software supported for this machine. Ethernet.

Harris. (HS-20)

A 32 bit workstation based on 68000 with 1MB RAM and 50MB hard disk. Relatively low resolution (832x600) with a 19" color display. Speed rated at .575 MIPS. Expensive for what it offers. Insufficient information on software supported for this machine. Unix. Ethernet.

Motorola. (M6600)

A 32 bit workstation based on 68020. Unix. Apparently supports 128 users. Insufficient information.

Prime.

Runs under operating system PRIMOS. Proprietary system. No Ada, no C, no Ethernet (?). Insufficient information.

7. Detailed design.

7.1. Personnel.

The personnel of the branch numbers 24 and consist of the following general categories:

a) branch management	1
b) project management	2
c) technical (programming)	19
d) clerical (secretaries)	2

Each of the above categories requires different software environments, though any category may very well use any of the

software available. These requirements can be categorized into the following environments:

1. general management (category a)
2. project management (category a, b, c)
3. software development (category b, c)
4. document preparation (category a, b, c, d)

Though it would be very desirable to have all four of the above unified under one environment, it is, at present, rather difficult to find a commercial system providing this amount of integration. However, in a general workstation environment (such as Sun Microsystems, Apollo Computers, and similar) integration of at minimum of environments 3 and 4 is the norm.

Finally, another component should be available to the branch, namely:

5. training tools (category a, b, c, d)

On line help facilities are nowadays provided with (just about) all software. Whereas helpful - and at times indispensable - to an experienced user, on line help should be complemented with tutorials, computer assisted instruction (CAI) tools, as well as hot line facilities and on site courses. Of course, good hardcopy manuals are a must.

7.2. Hardware.

The programming environment should be based on a locally distributed system architecture, linked together via a local area network. This system should consist of a number of networked general-purpose high-performance workstations supported by compute and file servers. Interfaces must be provided to attach and/or to access existing computer systems. The latter may function as additional servers.

Each workstation should be configured with sufficient RAM memory (at least 6 MB) and with local storage facilities (hard disk and streamer tape). In such configuration each workstation will be capable of functioning in a stand-alone mode thus off-loading the system servers; for compute intensive tasks access to (existing or new) compute server should be available.

Servers will provide interfaces between compatible devices on the LAN, and allow sharing of these devices among the network's nodes.

File server can be an existing minicomputer or a powerful workstation with sufficient mass storage to serve the database requirements of the branch. The file server will provide a central file system (with file security) to ensure the integrity of official versions of the project files, while the individual node storage capacity would be used for single user development, back

up and other administrative chores. In addition, as need arises, local storage should be configurable into a part or whole of the file system for the branch (yielding a distributed file system). This will provide facilities for close communication on smaller projects, while preserving access to the general information depositories for the branch (such as documentation aids, reusable libraries, etc.).

Similar considerations apply to distributed/central compute power of the system.

The computer system for the Applications Software Branch should be linked via a LAN. Besides the usual considerations of speed, bandwidth, reliability, simplicity of use and cost, a major concern when choosing a LAN is compatibility with other networks existing in the organization. Since IAN of MFSC is based on Ethernet, the latter should form the network backbone for this branch.

(Ethernet is a baseband channel, optimized for LAN communications, which offers high-bandwidth and high transmission speeds for interconnection of intelligent nodes. Further, Ethernet interfaces are commercially available for many workstations and computers.)

Network architectures based on Ethernet offer (via application layer of OSI) resource sharing, transparent file system operations, remote file and system access, distributed database management, network management, and so on.

A basic configuration for the new computer system is presented in the following diagram. Other nodes and servers may be needed; in particular addition of a print server and a terminal server may be desired.

Supported with a good network management software, the proposed heterogeneous distributed system will offer total transparency of architecture to individual clients. At the same time, it will allow maximal utilization of systems resources.

These resources can be as diverse as uniprocessors, specialized graphics devices, supercomputers, array processors, dedicated AI machines, general scientific computers, specialized finite-element machines, special storage devices, various supporting peripheral devices, etc.

To achieve such transparency, the system must be supported by appropriate network management software. This software must provide data independence as well computation independence of existing or future computer architectures.

Suitable network management system is exemplified by Network File System (NFS) by Sun Microsystems Inc., and the recently announced Network Computing System (NCS) by Apollo Computers Inc. (see section 5.2). Both NFS and NCS are open system. These systems

seem to evolve towards parallel execution of computational activities of a client over the available network resources. (As a guide, this is a rather coarse grain parallelity at the moment.)

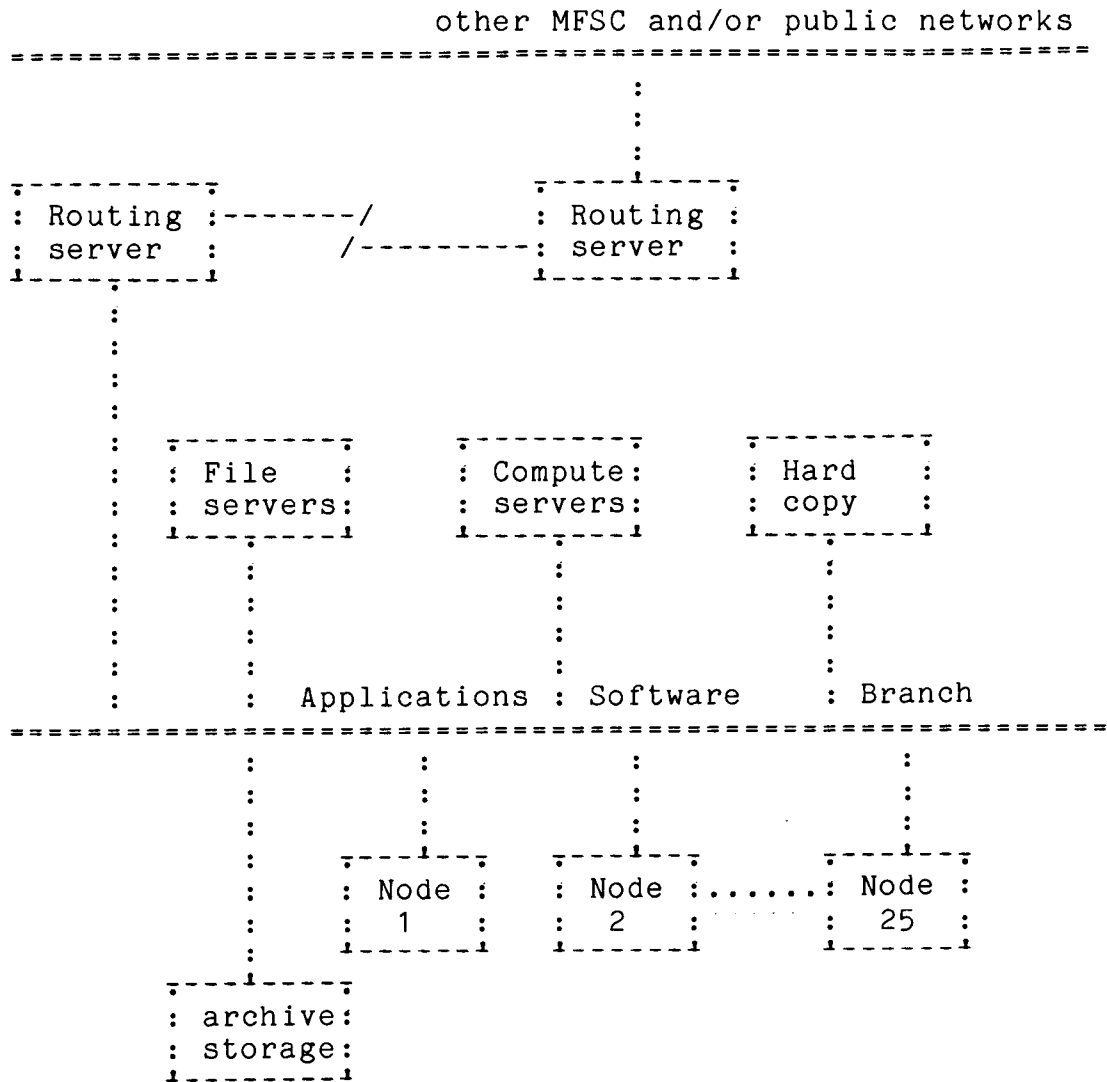


Fig. 7.2.1. Applications Software Branch computing system architecture.

7.3. Software.

7.3.1. General management.

The following are software tools used in general management: scheduler, spreadsheet, access control, electronic mail, resource measurement, cost estimation, work breakdown structure (WBS).

For additional discussion see section 5.3.

7.3.2. Project management.

The following are software tools used in project management:
scheduler, project tracking, spreadsheet, access control,
electronic mail, resource measurement, WBS.

For additional discussion see section 5.3.

7.3.3. Software development.

Software development tools should support all of the software engineering functions (see section 3.1.2). Thus, I shall classify the software under the following software engineering activities.

- R - Requirements specification and analysis.
- D - Design and analysis.
- P - Program generation and testing.
- S - System integration and testing.
- C - Configuration management.

The following is a glossary of a minimal set of tools that I perceive as indispensable in a software engineering toolkit:

Consistency checker.

verifies mutual consistency of requirements and design for specific functions.

Cross-referencer.

provides cross-reference information of use and misuse of program components.

Design language processor.

Creates automatically documentation of the program design, as it progresses through its various stages. Particularly useful for validation and evaluation of the system design.

Diagnostic and debugging tools.

Tools for identification, isolation and eradications of program errors.

Emulator.

A software tool allowing execution on a host computer of a program written for a target computer.

Program Logic analyzer.

analyses and provides information about the logic structure of a specified program.

Program flow analyzer.

A program that provides source code statement frequency and timing data in test executions of a system.

Program sequencer.

A program verification tool for forcing test executions of every branch and every accessible statement in a systems code.

Simulator.

A program that provides on the host computer the (precise) effect of execution of instructions native to a target computer.

Requirements language processor.

A language and its processor for unambiguous formal specification of requirements for a software project.

Software monitor.

A memory resident tool that captures and exhibits performance statistics of a software system.

Syntax directed editor.

An editor using knowledge of a language to prevent, diagnose and correct syntax errors.

Trace program.

A program that captures and exhibits chronological history of events in an execution of a software system.

The following table show the coverage of the software engineering functions by the above mentioned tools:

	: R	: D	: P	: S	: C	:
Consistency checker.	: X	: X	:	:	:	:
Cross-referencer.	:	:	: X	:	:	:
Design language processor.	:	: X	:	:	:	:
Diagnostic and debugging tools.	:	:	: X	:	:	:
Emulator.	:	:	:	: X	:	:
Logic analyser.	:	: X	: X	:	:	:
Program flow analyser.	: X	:	: X	: X	:	:
Program sequencer.	:	:	: X	:	:	:
Simulator.	:	: X	:	: X	:	:
Requirements language processor.	: X	:	:	:	:	:
Software monitor.	:	:	: X	: X	:	:
Source code control system	:	:	: X	: X	: X	:
Syntax directed editor.	:	:	: X	: X	:	:
Trace program.	: X	: X	: X	: X	:	:

In addition to the above, the branch will require 'specialized' tools for real time applications and target computer evaluations. These tools will include:

Hardware logic analyzer.

An electronic device that monitors the logic states of digital systems and stores the results for subsequent display and analysis.

In-circuit emulator.

An emulator allowing alteration of control paths, monitoring and changes of memory registers and memory locations, etc.

7.3.4. Document preparation.

The following are software tools used in document preparation:

Graphics editor, word processor with spelling checker, grammar checker, dictionary generator.

7.3.5. Training tools.

The following are software tools used for training:

Training manuals, reference manuals, tutorials, CAI tutorials, on-site training.

8. Conclusion.

This project is concerned with a survey, evaluation and specification of a new computer system for the Applications Software Branch of the Software and Data Management Division of Information and Electronic Systems Laboratory of Marshall Space Flight Center, NASA.

The computer system serving currently the Applications Software Branch is organized into a number of stand alone and time sharing centralized computing systems. These systems include INTEL 8080, PDP-11/23, PDP-11/73, and a number of VAX 11/7xx and mVAX II. The mode of operation of these computers is predominantly development of software in Fortran, compilation and subsequent transfer (if necessary) of the object code to the target computer.

The obsolescence of some of the above system hardware, lack of support of current software engineering technology, and the projected technological and software needs of future Space Station projects entail a need for a new system able to support current and future software engineering environments of the branch.

My recommendation to the Branch is to acquire a distributed, heterogeneous system consisting of current, multivendor hardware interconnected with a local area network, and supported by appropriate software to provide an integrated software design and development environment.

The hardware should consist of high-performance workstations running a Unix operating system. The workstations should be configured with sufficient memory (6-8 MB) to support software development activities and a hard disk storage of sufficient capacity (140 MB) to offload the LAN traffic by restricting the swapping, paging and other system related operations to the local disk. Suitable candidates are SUN, Apollo or mVax.

The network architecture is to be based on system which provides a presentation layer over and above a transport protocol such as TCP/IP. This presentation layer has to support a kaleidoscope of computer hardware and must provide transparency of file and compute operations to be performed in this heterogeneous environment. A suitable candidate would be NFS (SUN Microsystems) and possibly NCS (Apollo Computers).

No special interfaces are currently required beyond the serial and parallel provided as standard ports on most workstations. However, in addition to the general purpose workstations, the branch will require special purpose workstations such as, for example, mAnalyst 2000 by NWIS for hardware logic analysis and in-circuit emulation.

The software development environment is to consist of components such as general and project management, code design and development, configuration management, document preparation, and personnel training.

Such system, in my judgement, will offer immediate productivity gains, increase in job satisfaction, virtual "plug in" expandability, and a suitable platform for insertion of future technology, thus assuring not only continued currency but also longevity of the system without undue proclivity to obsolescence.

9. Appendix 1: Software development life cycle.

The following are various phases of a software development life cycle adopted by MFSC/NASA, [Aichele, 1983]. For a comparison, I follow this with the more generalized specification as understood in industrial organizations.

Conceptual

Initial definition of system requirements. Preliminary functional specification and software configuration.

Results in:

Request For Proposal (RFP),
Data Requirements Document (DRD),
Work Breakdown Structure (WBS),
Statement Of Work (SOW).

Requirements

Elaboration of requirements of DRD. Construction of software management and development plan.

Results in:

Interface Control Documents (ICD), and
final Software Requirements Document (SRD).

Design

Preliminary design leading to Preliminary Software Design Specification. Detailed design follows and

results in:

Software Design Specification (CODE-TO),
Programmer's Handbook, and
Software Test Specification.

Code and Debug

Module coding debugging.

Results in:

Initial internal software delivery.

Verification

Verification of logic of the debugged software. Formal change control and problem report procedures start from this phase.

Results in:

delivery of the software, and
Functional Configuration Inspection (FCI) document which
ascertains conformance with requirements.

Validation

Evaluation of system/software compatibility and software performance.

Results in:

final software delivery and configuration inspection,
software user manual, and
validation report.

System Integration

Final test of software at the highest possible system level.

Results in:

Systems Acceptance Review (AR).

Operations and Maintenance

as indicated by the title.

Results in:

final and permanent MFSC record of the project.

For a comparison, the following is a specification of software life cycle practiced in industrial environments, [Shooman, 1983].

Conceptual

definition of system needs, and of system requirements

System specification

Hardware-software operational specification and System operational specification

Preliminary design

RFP, preparation of proposal followed by proposal modification and selection

Detailed design

module coding, software design and functional specification

Verification

module test, system integration, test simulation and acceptance testing

Field deployment and maintenance

minor design modifications, discovery and fixing of field bugs. Final check and data gathering, field release

10. References.

- (1) Aichele, D.G. "MSFC Software management and development requirements", EB41, MA-001-006-ZE, Jan 1983
- (2) Bykat, A. "Evaluation of Applications Software Branch' Computing System", EB43, June 1987
- (3) Craft, R.H. "S&E Director's review: Applications Software Branch", EB43, March 1987
- (4) Illingworth, V. "Dictionary of computing", Oxford U.P., 1983
- (5) Government Computer News, June 19, 1987, p.53
- (6) Government Computer News, July 17, 1987, p.1
- (7) Henry, G.G. "IBM RT PC architecture and design decisions" IBM SA23-1057, 1986
- (8) Hyter, D. "Task for Summer Faculty", letter to DX01/Ernestine Cothran, EB43 (87-14), 4/21/1987
- (9) Lucas, J.H. "Software and data management division", EB41, October 1986
- (10) Miller, E. "Automated tools for software engineering", IEEE 1979
- (11) Mitze, R.W. "The Unix system as a software engineering environment", in Hunke (ed), "Software Engineering Environments", North-Holland, 1981
- (12) NASA-MFSC, "Information and Electronic Systems Laboratory", U.S. Gov. 730-067/40100, 1987
- (13) Rauch-Hindin, W. "Software tools: new ways to chip software into shape", Data Communications, Apr.1982, pp.83-113
- (14) Shooman, M.L. "Software engineering", McGraw-Hill, 1983
- (15) Weston, C.D., Stewart, G.A., Byte, Feb. 1987

11. Glossary.

- (1) BATSE:
Burst And Transient Source Experiment.
- (2) Client:
machine capable of accessing server's resources.
- (3) DRD:
Data Requirements Document.
- (4) Emulator:
A software tool allowing execution on a host computer of a program written for a target computer.
- (5) Ethernet:
a baseband channel suitable for high speed transmission of data in LAN communications.
- (6) File server:
provides a file system and services for a network of machines.
- (7) GANTT chart:
a bar chart such as tasks v. time.
- (8) Heterogeneous system:
A networked system consisting of a set of multi-vendor computers of possibly different architecture, integrated into a single system.
- (9) HOSC:
Huntsville Operations System Center.
- (10) ICD:
Interface Control Document.
- (11) IMC:
Image Motion Compensation.
- (12) Integrated Program Development Environment:
An integrated set of programs and tools designed to facilitate development of software. Typical components are: full screen (windowing) editor, help facilities, programming language processors, symbolic debuggers, monitoring tools, source control and management tools, document generation tools.
- (13) Integrated Project Management Environment:
An integrated set of programs and tools designed to facilitate design and management of software projects. Typical components are: planning tools, charting tools, facilities, programming design language, monitoring tools, reporting management tools, document generation tools.

- (14) LAN:
Local Area Network - a network linking devices scattered over a limited geographic area and providing for high speed high bandwidth communication between these devices.
- (15) Milestone:
a measurable significant achievement in course of project development.
- (16) MEA:
Materials Experiment Assembly.
- (17) Modification-request control system:
manages request of modifications, error reports, and debugging progress.
- (18) Monitor:
a device which inspects and collects data during execution to determine efficiency and utilization of a unit (software or hardware).
- (19) Network:
a number of workstations (or computer systems) interconnected and capable of exchanging information using a common communication protocol.
- (20) Node:
a single addressable unit on a network. A number of devices can be connected to a node.
- (21) PERT:
Program Evaluation and Review Technique. An activity network which represents the project's progress. The nodes of the network represent milestones, while the branches represent activities which culminate in that milestone.
- (22) POCC:
Payload Operations Control Center.
- (23) RFP:
Request For Proposals.
- (24) RPC:
Remote Procedure Call: a set of functions providing for machine and operating system independent access of components of a heterogeneous computing system.
- (25) Server:
machine that provides a resource to a network.
Eg. file server - provides a file system and services for a network of machines.

- (26) Simulator:
A program that provides on the host computer the (precise) effect of execution of instructions native to a target computer.
- (27) Software Engineering:
an approach to engineering software, paying particular attention to software life cycle consisting of planning, design, implementation, verification and maintenance.
- (28) Software Tool:
A computer program used to develop, test, analyze, or maintain another computer program or its documentation.
- (29) Source-code control system:
preserves different versions of the source and provides a list of changes between the versions.
- (30) SOW:
Statement Of Work.
- (31) SRD:
System Requirements Document.
- (32) System:
An assembly of interacting components, all functioning towards achieving a specified goal. Components of a computer system typically include personnel, hardware, and software.
- (33) TCP/IP:
Transmission control protocol/internet protocol.
- (34) User:
person logged in on a client.
- (35) WBS:
Work Breakdown Structure.
- (36) Workstation:
a single user machine; either a stand-alone or a client. The major characteristics of a workstation are defined [Weston, Stewart, 1987] as:
32 bit microprocessor, 1-2 MIPS, 20+ MB hard disk, high-resolution monitor with 1 MPIXELS, floating point coprocessor, graphics operations, array processing, multi-user operating system (eg.UNIX).

12. Index.

- AI 20, 28
- Application 10
- AR 36
- BATSE 15, 38
- Benefit 14
- Client 38
- Consistency checker 30
- Cross-compiler 21
- Cross-referencer 30
- Disassembler 22
- DRD 35, 38
- Emulator 22, 30, 38
 - in-circuit 32, 33
- Ethernet 18, 28, 38
- File server 17, 27, 38
- GANTT 21, 38
- Hardware logic analyzer 32
- Heterogeneous system 20, 38
- HOSC 15, 38
- ICD 35, 38
- IMC 38
- Integrated program development environment 14, 38
- Integrated project management environment 14, 38
- LAN 17, 38
 - Ethernet 18, 28
- Languages 14
- logic analyzer 33
- Management 14
- MEA 15, 39
- Milestone 9, 39
- Modification-request control system 24, 39
- Monitor 21, 39
- NCS 20, 29
- network 39
 - Client 38
 - File server 38
 - LAN 38
 - NCS 20, 29
 - NFS 20, 29
 - node 19, 28, 39
 - ONC 20
 - Server 39
 - User 40
 - Workstation 40
- Network Computing System 20, 29
- Network File System 20, 29
- NFS 20, 29
- ONC 20
- PERT 21, 39
- POCC 15, 39
- print 19, 28
- Program flow analyzer 30
- Program Logic analyzer 30

- Program sequencer 31
- project
 - benefit 14
 - definition 10
 - development 14
 - management 14
 - specification 14
- Resource 9
- RFP 35, 39
- RPC 39
- server 19, 28, 38, 39
 - print server 19, 28
 - terminal server 19, 28
- Simulator 31, 39
- Software 14
 - tool 23, 40
- Software Engineering 39, 40
- Software monitor 31
- Source-code control system 23, 24, 40
- SOW 35, 40
- SRD 35, 40
- Syntax directed editor 31
- system 12, 13, 40
 - capabilities 12, 13
 - functions 11
 - Scope 13
- TCP/IP 21, 40
- Tool 40
- Tools 12, 14
- Trace program 31
- Unix 17
- User 40
- WBS 35, 40
- Workstation 40

N88-1561E₁₀-90

116712
198

1987

NASA/ASEE SUMMER FACULTY FELLOWSHIP PROGRAM

MARSHALL SPACE FLIGHT CENTER

INFRARED EMISSION AND TIDAL INTERACTIONS
OF SPIRAL GALAXIES

Prepared by:	Gene G. Byrd, Ph.D.
Academic Rank:	Professor of Astronomy
University and Department:	University of Alabama Physics and Astronomy
NASA/MSFC:	
Laboratory:	Space Sciences
Division:	Astrophysics
Branch:	X-Ray Astronomy
MSFC Colleague:	Martin Weisskopf
Date:	August 15, 1987
Contract No.:	The University of Alabama in Huntsville NGT-01-008-021

INFRARED EMISSION AND TIDAL INTERACTIONS OF SPIRAL GALAXIES

by

Gene G. Byrd
Professor of Astronomy
University of Alabama
Tuscaloosa, Alabama

ABSTRACT

We use computer simulations of tidal interactions of spiral galaxies to attempt to understand recent discoveries about infrared(IR) emitting galaxies by Telesco (MSFC), Wolstencroft and Done(Royal Observatory, Edinburgh). We find that the stronger the tidal perturbation by a companion the more disk gas clouds are thrown into nucleus crossing orbits and the greater the velocity jumps crossing spiral arms. Both these tidally created characteristics would create more IR emission by high speed cloud collisions and more IR via effects of recently formed stars. This expectation at greater tidal perturbation matches the observation by Telesco et al. of greater IR emission for spiral galaxies with closer and/or more massive companions. The greater collision velocities found at stronger perturbations in our models will also result in higher dust temperature in the colliding clouds as Telesco et al. also observe. In the IR pairs that Telesco et al. examine, most have only one member, the larger, detected and when both are detected, the larger is always the more luminous. In our simulations and in a simple analytic description of the strong distance dependence of the tidal force, we find that the big galaxy of a pair is more strongly affected than the small in conformity with the results of Telesco et al.

ACKNOWLEDGEMENTS

I would like to express my appreciation to Martin Weisskopf for being my NASA host during this summer. I also appreciate Charles Telesco's conversations on infrared galaxies and sharing his results in advance of publication. Finally, I would like to thank Shigeki Miyaji and Roger Bussard for helpful conversations and computer assistance.

LIST OF FIGURES

<u>Fig.No.</u>	<u>Title</u>	<u>Page</u>
1	Grid used in computer program	10
2	Example of Spiral arm generation during simulation	11
3	Number of particles in grid bins of disturbed disk in step 901, Figure 2	12
4	Average radial velocities of particles in grid bins, step 901, Fig. 2	13
5	Disturbed disk in a closer encounter than Figure 2	14
6	Average velocity of particles in grid bins of closer encounter run (Figure 5)	15

1. INTRODUCTION

In order to understand the problem, method, and conclusions of this project it is necessary to recall some background information about spiral galaxies. Spiral galaxies consist of three main parts: the nuclear bulge, the galactic disk and the halo.

The galactic disk consists of stars, hydrogen gas, and dust with the first most important in terms of mass etc. The galactic disk is about 100,000 light years or 30,000 parsecs (30 kpc) across. The material in the galactic disk travels in near circular orbits around its center at 200-250 km/s. The surface density of stars and to a greater degree gas and dust are enhanced in the spiral arms. These arms (usually two) spiral outward from the nucleus in the disk.

The nuclear bulge consists of a concentrated swarm of stars in much more random orbits than the disk material. In the very center of the nuclear bulge is a 1/2 to 1 kpc nuclear disk composed of denser gas in circular orbits around what may be a massive black hole.

The halo is a mysterious component which is as large or larger than the galactic disk. The halo is roughly spherical and contains globular clusters of stars, solitary stars and mysterious undetected dark matter in random tilted orbits. The halo is thought to be roughly equal in mass to the galactic disk although there is considerable disagreement about this.

Most of the mass of the gas in the galactic disk interior to the sun's orbital radius is in molecular

⁹
hydrogen clouds (~5 x 10⁵ solar masses). Beyond the sun's orbital radius the hydrogen is primarily atomic but still in clouds. The molecular cloud surface density peaks at 6 kpc from the center with a minimum near the nucleus then another maximum at the center in the nuclear disk (see review by Mihalas and Binney 1981). The gaseous disk is very thin, about 120 pc. Most of the clouds are scattered evenly over
⁵
the disk in angle. These typical clouds are around 10

solar masses and about 20 pc in size. They are very cold, about 2 degrees Kelvin, probably because massive blue stars are not forming in them (Elmegreen 1986). The velocity dispersion among the clouds is a few km/s, much smaller than the disk stellar velocity dispersion.

In contrast, another population of clouds, those with warm cores (about 11 degrees Kelvin) are concentrated in the spiral arms. These clouds are greatly outnumbered by the cold clouds. Formation of groups of O/B stars evidently warms these clouds. These clouds are mostly aggregated in complexes of about a million solar masses (Soloman and Sanders 1986). The formation of these complexes is apparently the result of inelastic encounters among the clouds when they are crowded together in the stellar spiral arms of the disk (Kwan and Valdes 1983, Tomiska 1984). It may be that star formation and gravitational tides upon leaving the spiral arms break up these complexes. They are not found outside the arms and the stellar associations in them are only 10 to 20 million years old, the time to cross an arm.

2. OBJECTIVES

This project will involve infrared(IR) emission by spiral galaxies. This is primarily from heated dust within the gas clouds. the dust can be heated by visual radiation from luminous newly formed stars. The thick dust clouds around such stars do not let the visible out well in contrast to the IR which passes out easily. Another mechanism to generate IR which is more direct is the collision of clouds. If their relative velocity is great enough (greater than 50 km/s), dissociation and ionization of the hydrogen will occur at the collision interface. The resulting visual radiation from the hydrogen will be absorbed and then re-emitted by the dust as IR radiation (Harwit et al. 1987).

My project this summer is related to recent work by C. Telesco (MSFC), R.D. Wolstencroft and C. Done (Royal Observatory, Edinburgh). Telesco et al. (1987) used IRAS data and a sample of interacting pairs of galaxies compiled by Arp and Madore (1987). Telesco et al. studied the emission at 60 and 100 micrometers, defining the parameter R to be the ratio of the 60 to the 100 micrometer fluxes. If

R is larger than 0.5 the galaxy is defined to be "hot", smaller "cool". An R of 0.5 is roughly 60 degrees Kelvin which is hot compared to the 5 degrees typical of molecular clouds in our galaxy.

Telesco et al. measured the angular sizes of pair members and their separations of European Southern Observatory Sky Survey photographs. They could estimate masses of the pair members from the empirical relationship

1.5

that mass is proportional to size . They then could estimate a tidal perturbation parameter equal to the perturber mass (in terms of the galaxy mass) divided by the distance of of the perturber cubed (in terms of the galaxy radius).

Telesco et al. found: (a) a correlation between temperature R and the degree of tidal perturbation in IR emitting pairs. Also stronger tidal perturbation goes with greater IR energy output, (b) a rule that when only one member of a pair was detectable it was the larger member. If both were detectable, the larger was more luminous.

During this summer, I used computer simulations to try to better understand the reasons for (a) and (b) above. I was also interested in the mechanism and location of the IR emission i.e. is it via collisions of clouds and/or via star formation?

3. THE COMPUTER PROGRAM

Our principal tool is a two-dimensional polar coordinate FFT n-body program by Miller (1976, 1978). the coordinate grid of this program is well suited for study of disk galaxies providing high spatial resolution where it is most needed, near the center (see Figure 1). We use about 60,000 particles to simulate the disk of the spiral galaxy. Each part of the disk acts gravitationally on all other parts of the disk, i.e. the disk is self-gravitating.

Major parameters of our study were the ratio of the halo mass to the disk mass and the velocity dispersion in the galaxy's disk. We expect the halo to have a high velocity dispersion and, therefore, to be much more stable than the "cooler" disk. Accordingly, we followed Miller (1978)

and considered the halo to be inert. Increasing the halo to disk mass helps stabilize the disk, as does increasing the disk velocity dispersion (Toomre 1964). The spatial softening due the program grid and a constant in the gravitational potential formula assumed have the same stabilizing effect as the velocity dispersion (Miller 1971,1974,1978). Using Miller (1978), the spatial softening of our model disk is equivalent to a velocity dispersion of about 1.5 times that sufficient to stabilize it against small axisymmetric perturbations. This assumed dispersion is about that seen in stellar disks of spiral galaxies. We thus used only this softening to simulate the stellar disk velocity dispersion. The-halo-to-disk mass ratio is taken to be one.

4. PREVIOUS USE OF THE PROGRAM

This program has been used to study the onset of global instability and subsequent changes in a disk composed primarily of stars (Miller 1978). The unmodified program has also been used to study the onset of global instabilities in a gaseous disk (Cassen, Smith, Miller 1981). We have modified the program to simulate a finite rather than the infinite disk studied by Miller and co-workers. We also modified the program to simulate the tidal effect of a companion on the disk of a spiral galaxy. We also used this version to study the capture and orbital decay of satellites of disk galaxies (Byrd, Saarinen, Valtonen 1986) and the creation of spiral arm spurs by large gas complexes in galaxy disks (Byrd, Smith, Miller 1984).

The most recent use of this program and most relevant use to the present project is simulate the tidal triggering of Seyfert galaxy activity by companions (Byrd, Sundelius and Valtonen 1986; Byrd, Valtonen, Sundelius, and Valtaoja 1987). In this investigation, the companions may trigger inflows of disk material into the nucleus to fuel activity there. We have used the program to simulate the tidal action of the companion on the disk of a spiral galaxy and show that the tidal strengths at which large inflows appear match those of the observed companions of Seyferts.

Our fundamental method for estimating gas cloud flow into the nuclear regions was very crude. We simply counted how many of the 60,000 particles/step were thrown into orbits crossing the 1 kpc nuclear region. This fraction times the assumed fraction of the disk in gas (0.10) times

11

the assumed disk mass (1×10^{11} solar masses, 20 kpc) equals the rate gas entered the nuclear regions. From observations, the rate was required to be greater than or equal to 0.5 solar masses/yr. This gas, once thrown into such orbits, will collide with other gas clouds or the nuclear disk to flow into the "engine". Small scale accretion processes near the central black hole were beyond the scope of our investigation.

According to our simple previous calculations, smaller tidal perturbations result in weaker inflows in our model. Tidal perturbation levels (as previously defined) of 0.01 to 0.1 (depending on the mass of the halo) are necessary to produce the required inflows. Dahari (1984) finds observationally that most spiral galaxies perturbed at these levels or greater are Seyferts.

5. AN EXAMPLE OF A PROGRAM RUN AND OUTPUT

In the example shown in Figure 2, we see the shapes generated during an encounter of a galaxy with a perturber 0.22 of the galaxy's mass which approaches in a zero energy orbit to within two disk radii of the galaxy. The halo to disk mass ratio is assumed to be one. The disk has 60,000 particles.

The time covered is about three revolutions of the disk edge. Circular orbit velocity in the disk is 208 km/s. The darkness in the figure indicates particle surface density. The unit of length in the program is equal to about one

11

kpc. The total mass of the galaxy is 2×10^{11} solar masses. The disk of the galaxy is 20 units in radius, about 1/3 of the grid radius. The perturber enters the grid on the right at 0 degrees and swings by in a counter clockwise sense, the same as the disk rotation and the measurement of the angular position of the perturber.

Figure 3 shows a display of the number of particles in each of the bins in our example run. The underlines show the density peaks along a spiral arm created by the tidal

action. The horizontal bin rows are by azimuth every 10 degrees starting zero at the top. The 24 columns are radial with the edge of the grid at the right.

Figure 4 shows the average radial velocities of the particles in the bins (zero for bins with no particles or with zero rv). For an undisturbed disk, all values should be zero since the particles are initially in circular orbits. However, there are inward (-) and outward (+) velocities as a result of the tidal perturbation. Divide the values by three to get velocities in km/s. We see the velocity differences in Figure 4 are not large compared to the original circular orbital velocity of 208 km/s.

6. EXPLAINING RESULTS FOUND BY TELESKO ET AL.

We will use these displays of the results of the above and other computer runs to explain the reasons found by Telesko et al. in their observations. First, let us consider the first two correlations for IR emitting pairs of interacting galaxies. As we noted in our earlier work on Seyfert galaxies, stronger tidal perturbation results in greater inflow into the nuclear regions. Considering our previous "example" run, we find that it causes no inflow to the 1 kpc nuclear regions. Note how the radial velocities in the bins near the center are zero in Figure 4.

Now consider a stronger run with the mass increased to 0.44 the galaxy's mass and the close approach distance 0.75 of its value in the other run. This reduction results in an increase in tidal perturbation to 5x the previous value. Figure 5 shows the shape of the disturbed galaxy 900 time steps (900 million years) after the perturber entered the grid. Counts within the program show that at least 1/3 of the disk particles are thrown into orbits crossing the inner 1 kpc, much more than in the weaker perturber run.

Figure 6 shows the radial velocities in the different bins for this stronger run. Surprisingly, the radial velocities inward near the nucleus are only around 20 km/s. The high surface densities near the center help result in the large total inflow. However, the IR emission from the nucleus (due to the inflow) would probably be created later in the nuclear disk (via star formation etc.), rather than from the velocity of collision with the disk.

However, the stronger run shows interesting events in the disk. The radial velocity deviations are about five times those in the weaker run. Inward and outward flows of about 100 km/s are seen. In particular, large inward and outward velocities are found in outer and inner bins respectively at the same azimuth. It seems that in the outer disk collisions at speeds sufficient to excite IR directly will occur. Of course, after these collisions one would expect massive stars to quickly form and produce indirect IR emission. So IR emission should be seen from the disk of the galaxy as well as the nuclear regions.

The correlation between temperature and tidal perturbation is explained also. Greater velocity differences resulting from stronger perturbation encounters result in more energy release in collisions, greater grain temperatures and hotter IR temperature emission.

The final pattern that Telesco et al. found was that most interacting pairs detectable in IR had only one detectable member. When both were detected, the larger was always more IR luminous.

The strong variation of tidal force with distance (inverse cubed) is probably the major factor in the large versus small pattern. Consider the following example of a massive primary and a companion galaxy one-half the mass of the primary. They are two disk radii of the primary apart. The nearer edge of the primary to the secondary has a tidal perturbation on it eight times that on the primary's center. The far edge has a tidal perturbation only one-third that at the center.

1.5

The secondary galaxy is smaller by a factor of 0.5. The perturbation at the center of the secondary is the same as at the center of the primary. The nearer edge of the secondary is perturbed by a factor of only 1.8 times that at the secondary's center while the far edge factor is 0.6. The difference between the two edges is not so great as for the primary and the near edge is not perturbed nearly so strongly as the near edge of the primary. We thus see that the size of the galaxy relative to the distance of its perturber is very important.

The two computer runs discussed earlier show this effect of size relative to separation. Recall that the encounter distance was decreased by 25% in the second run. The closer encounter result is much more asymmetric with the nearer arm much stronger. The surface density asymmetry between the two main arms in the close encounter is 2/1 in the close encounter but it is only 1.1/1 for the far encounter. The strength of the stronger arm and the arm-interarm contrast is greater for the closer encounter.

We have also done a run of a disk perturbed by a symmetric tidal field to the same level at the center as our close encounter above. Interestingly, the nuclear inflow is much smaller for the symmetric, distant perturber run. Possibly the strong asymmetric arm structure helps promote nuclear inflow after it forms.

The above explains results found by Telesco et al. for small versus large members of a pair. The fact that the more massive galaxy is larger relative to the pair separation than the less massive could be the cause of the emission difference.

7. SUMMARY AND LIMITS OF CONCLUSIONS

We see that the IR emission could come from the disk as well as the nucleus according to our simulations. Increasing the strength of the perturbation should increase the emission and make it occur at a higher temperature. The larger size of the more massive pair member relative to the pair separation causes its emission to be stronger. Also the disk emission should be more asymmetric in the more massive member for the same reason. These patterns match those observed by Telesco et al.

The above conclusions apply to tidally interacting but not colliding spirals or merging galaxies. The conclusions also do not apply to the case where one galaxy tears significant amounts of material from the other. This could be one way for the small galaxy to be more luminous in some cases. Unfortunately, the IRAS data is not good enough to show the morphology of IR emission within the pair members. While some nearby systems show the expected asymmetries, a large enough sample observed sufficiently well will be an important project for the future.

REFERENCES

- Arp, H.C. and Madore, B.F. 1987. A Catalogue of Southern Peculiar Galaxies and Associations (David Dunlap Observatory: Ontario, Canada) in press.
- Byrd, G. G., Smith, B. F., and Miller, R. H. 1984, Astrophys. J. 286, 62.
- Byrd, G.G., Saarinen, S., Valtonen, M.J. 1986 Monthly Notices Roy. Astron. Soc. 220, 619.
- Byrd, G. G., Valtonen, M.J., Sundelius, B. and Valtaoja, L. 1986 Astron. Astrophys. 166, 75.
- Byrd, G.G., Sundelius, B., and Valtonen, M. 1987 Astron. Astrophys. 171, 16.
- Cassen, P.M., Smith, B.F., Miller, R.H., and Reynolds, R.T. 1981, Icarus 48, 377.
- Dahari, O. 1984, Astron. J. 89, 966.
- Elmegreen, B.G. 1986, "Molecular Clouds and Star Formation: An Overview" in Protostars and Planets II, eds. D.C. Black and M.S. Matthews, Univ. of Arizona Press, Tucson, Arizona, p. 33.
- Harwit, M., Houck, J.P., Soifer, B.T. and Palumbo, G.G.C. 1987 Astrophys. J. 315, 28.
- Kwan, T. and Valdes, F. 1983 Astrophys. J., 271, 604.
- Mihalas, D. and Binney, J. 1981, Galactic Astronomy-Structure and Kinematics (W.H. Freeman, San Francisco) p. 545-565.
- Miller, R.H. 1971, Astrophys. and Space Science 14, 73.
- Miller, R.H. 1974, Astrophys. J. 190, 539.
- Miller, R.H. 1978, Astrophys. J. 224, 32.
- Sanders, D.B., Solomon, P.M. and Scoville, N.Z. 1984, Astrophys. J. 276, 182.
- Solomon, P.M. and Sanders, D.B. 1986, "Star Formation in a Galactic Context: The Location and Properties of Molecular Clouds," in Protostars and Planets II, ed. D.C. Black and M. S. Matthews, Univ. of Arizona Press, Tucson, Arizona, p. 59.
- Telesco, C.M., Wolstencroft, R.D. and Done, C. 1987 (private communication).
- Tomiska, K. 1984, P.A.S.J. 36, 457.
- Toomre, A. 1964, Astrophys. J. 139, 1217.

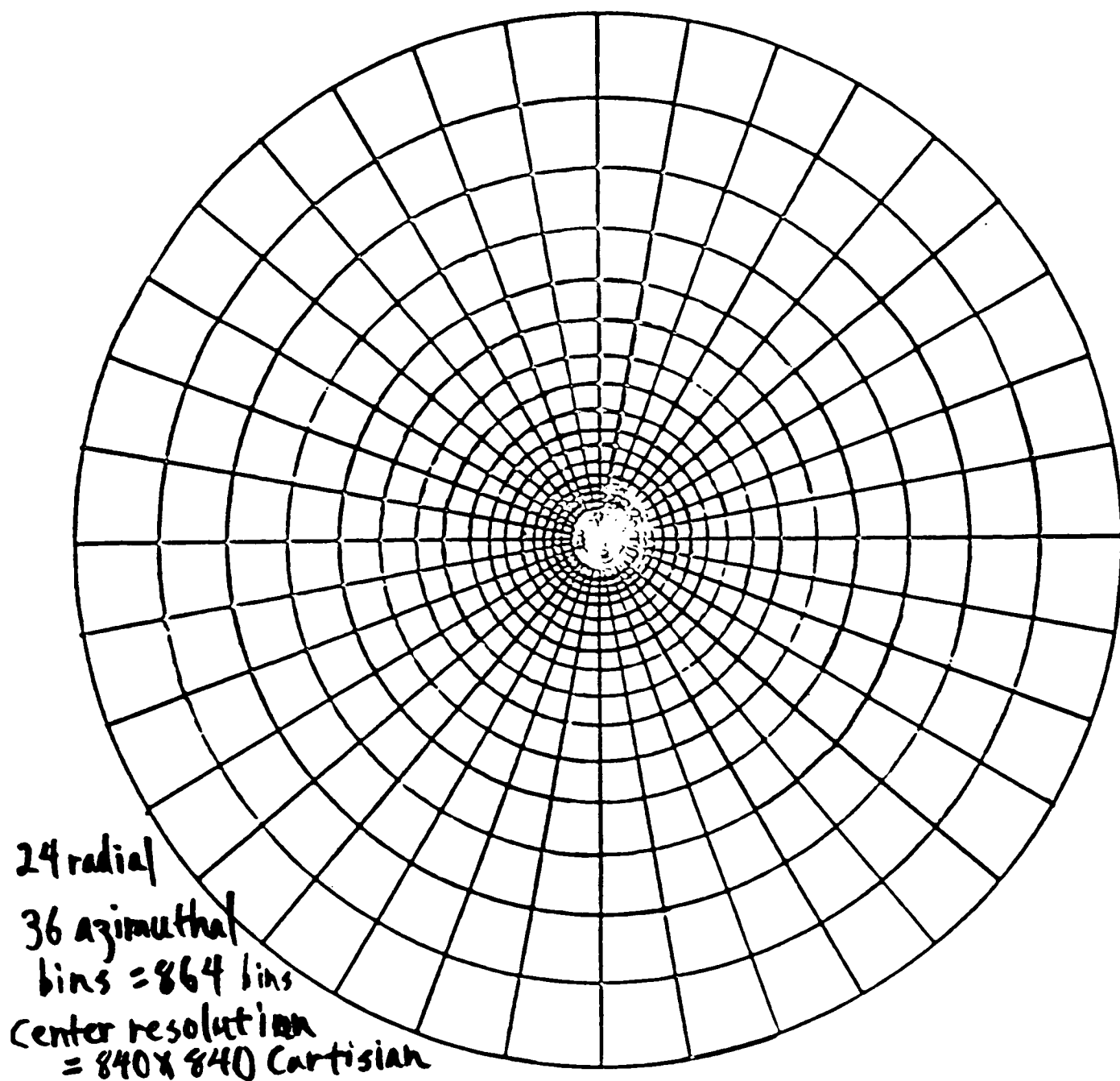


Figure 1-Grid used in computer program.

ORIGINAL PAGE IS
OF POOR QUALITY

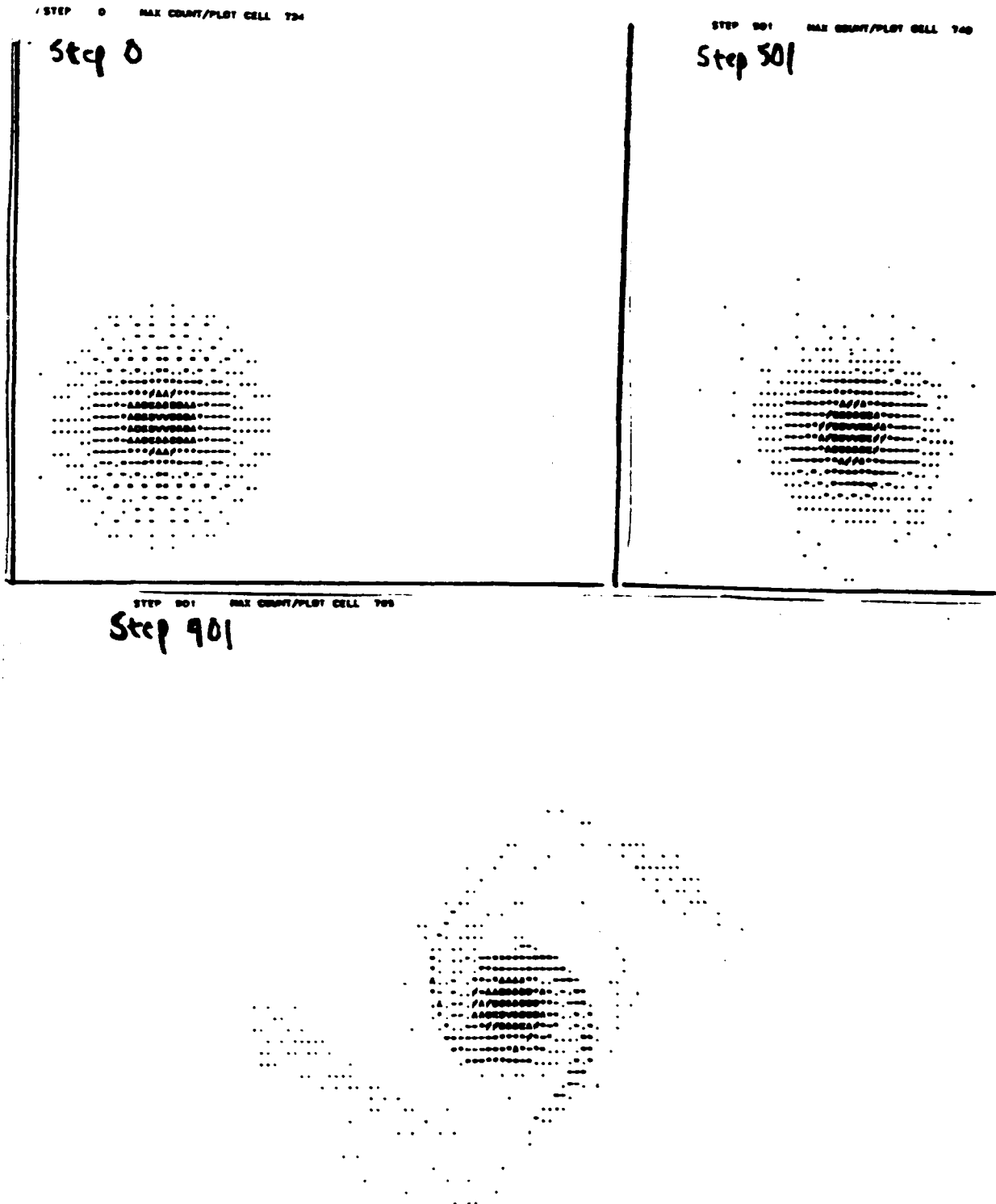


Figure 2-Example of spiral arm generation during simulation

center radial bins edge

1	2	3	4	5	6	7	8	9	10	11	12	13	14	15	16	17	18	19	20	21	22	23	24
11.0	27.0	32.0	38.0	44.0	57.0	44.0	86.0	87.0	0107.0	99.0	0138.0	91.0	0184.0	0289.0	76.0	3.0	3.0	0.0	0.0	0.0	0.0	0.0	0.0
11.0	27.0	32.0	38.0	45.0	51.0	50.0	90.0	76.0	0104.0	88.0	0151.0	0211.0	0228.0	92.0	3.0	4.0	0.0	0.0	0.0	0.0	0.0	0.0	0.0
11.0	27.0	32.0	38.0	46.0	49.0	53.0	82.0	75.0	81.0	0158.0	46.0	0126.0	0266.0	0154.0	0106.0	6.0	2.0	0.0	0.0	1.0	0.0	0.0	0.0
11.0	27.0	32.0	38.0	46.0	45.0	53.0	83.0	75.0	89.0	0155.0	54.0	0147.0	0250.0	76.0	85.0	15.0	5.0	0.0	4.0	7.0	0.0	0.0	0.0
11.0	27.0	32.0	38.0	47.0	46.0	56.0	89.0	79.0	94.0	0115.0	58.0	0135.0	0220.0	83.0	0118.0	33.0	5.0	0.0	3.0	15.0	0.0	0.0	0.0
11.0	27.0	32.0	38.0	45.0	49.0	61.0	88.0	89.0	0124.0	87.0	79.0	0147.0	0242.0	87.0	0100.0	71.0	9.0	0.0	12.0	12.0	0.0	0.0	0.0
11.0	27.0	32.0	38.0	42.0	54.0	61.0	91.0	83.0	0102.0	76.0	0100.0	0135.0	0220.0	48.0	74.0	0108.0	60.0	0.0	10.0	9.0	0.0	0.0	0.0
11.0	27.0	32.0	38.0	43.0	54.0	80.0	72.0	74.0	0104.0	74.0	0134.0	0135.0	0241.0	73.0	48.0	79.0	74.0	2.0	46.0	7.0	0.0	0.0	0.0
11.0	27.0	32.0	38.0	44.0	48.0	88.0	61.0	73.0	0109.0	53.0	0137.0	0203.0	0146.0	0124.0	90.0	0188.0	0105.0	45.0	0255.0	2.0	0.0	0.0	0.0
11.0	27.0	32.0	38.0	47.0	52.0	81.0	61.0	67.0	0133.0	55.0	0135.0	0206.0	80.0	0120.0	0118.0	0197.0	28.0	0328.0	85.0	0.0	0.0	0.0	0.0
11.0	27.0	32.0	38.0	47.0	54.0	64.0	64.0	66.0	0115.0	63.0	0126.0	0223.0	52.0	68.0	0122.0	0184.0	0123.0	0181.0	0.0	0.0	0.0	0.0	0.0
11.0	27.0	32.0	37.0	45.0	70.0	54.0	57.0	61.0	0120.0	56.0	0146.0	0207.0	72.0	0102.0	0233.0	89.0	0262.0	6.0	0.0	0.0	0.0	0.0	0.0
11.0	27.0	32.0	37.0	42.0	65.0	48.0	50.0	74.0	0105.0	58.0	0146.0	0184.0	0127.0	0159.0	0194.0	0252.0	37.0	0.0	0.0	0.0	0.0	0.0	0.0
11.0	27.0	32.0	37.0	46.0	63.0	42.0	52.0	75.0	0105.0	55.0	0217.0	0105.0	0139.0	0159.0	0128.0	0280.0	3.0	0.0	0.0	0.0	0.0	0.0	0.0
11.0	27.0	32.0	38.0	48.0	68.0	37.0	57.0	75.0	0101.0	75.0	0211.0	0160.0	0119.0	0176.0	0210.0	0110.0	4.0	0.0	0.0	0.0	0.0	0.0	0.0
11.0	27.0	32.0	38.0	53.0	56.0	39.0	68.0	80.0	0116.0	0100.0	0185.0	74.0	0120.0	0131.0	0451.0	38.0	9.0	0.0	0.0	0.0	0.0	0.0	0.0
11.0	27.0	32.0	39.0	53.0	47.0	50.0	70.0	72.0	0108.0	0128.0	0143.0	97.0	0123.0	0338.0	0229.0	15.0	0.0	0.0	0.0	0.0	0.0	0.0	0.0
11.0	27.0	32.0	40.0	53.0	39.0	49.0	81.0	87.0	0101.0	0187.0	62.0	0103.0	0130.0	0428.0	64.0	11.0	0.0	0.0	0.0	0.0	0.0	0.0	0.0
11.0	27.0	31.0	40.0	51.0	35.0	57.0	72.0	72.0	0103.0	0171.0	77.0	0126.0	0170.0	0360.0	49.0	5.0	0.0	0.0	0.0	4.0	0.0	0.0	0.0
11.0	27.0	32.0	40.0	44.0	41.0	66.0	68.0	95.0	86.0	0153.0	63.0	0134.0	0233.0	0210.0	41.0	5.0	0.0	0.0	3.0	14.0	9.0	0.0	0.0
11.0	27.0	32.0	40.0	43.0	48.0	58.0	71.0	0111.0	86.0	0126.0	0121.0	0110.0	0296.0	0121.0	65.0	13.0	0.0	0.0	8.0	32.0	3.0	0.0	0.0
11.0	27.0	32.0	40.0	47.0	57.0	58.0	62.0	0104.0	0128.0	52.0	0123.0	0135.0	0299.0	80.0	70.0	8.0	0.0	4.0	11.0	0.0	0.0	0.0	0.0
10.0	27.0	32.0	40.0	45.0	60.0	64.0	67.0	96.0	0111.0	43.0	0107.0	0152.0	0295.0	74.0	84.0	12.0	0.0	7.0	0.0	0.0	0.0	0.0	0.0
11.0	27.0	32.0	38.0	44.0	59.0	61.0	76.0	90.0	0101.0	42.0	0122.0	0145.0	0278.0	58.0	0125.0	25.0	1.0	2.0	10.0	25.0	0.0	0.0	0.0
11.0	27.0	33.0	38.0	46.0	58.0	59.0	82.0	67.0	80.0	40.0	0150.0	0137.0	0244.0	78.0	0137.0	22.0	18.0	9.0	45.0	9.0	0.0	0.0	0.0
12.0	27.0	32.0	38.0	45.0	55.0	64.0	98.0	50.0	0105.0	49.0	0177.0	0228.0	0167.0	95.0	0139.0	53.0	77.0	61.0	56.0	0.0	0.0	0.0	0.0
11.0	27.0	32.0	38.0	47.0	52.0	70.0	74.0	49.0	73.0	67.0	0173.0	0301.0	80.0	93.0	0106.0	99.0	0156.0	0196.0	84.0	0.0	0.0	0.0	0.0
11.0	27.0	32.0	38.0	44.0	53.0	68.0	82.0	45.0	96.0	0147.0	0144.0	0199.0	68.0	82.0	0105.0	0130.0	0219.0	0275.0	0.0	0.0	0.0	0.0	0.0
11.0	27.0	32.0	38.0	45.0	53.0	68.0	78.0	40.0	99.0	0149.0	0109.0	0175.0	77.0	58.0	0115.0	0246.0	0207.0	5.0	0.0	0.0	0.0	0.0	0.0
11.0	27.0	32.0	38.0	44.0	56.0	71.0	63.0	49.0	0127.0	0138.0	0115.0	0193.0	79.0	64.0	0100.0	0315.0	0137.0	0.0	0.0	0.0	0.0	0.0	0.0
11.0	27.0	32.0	38.0	44.0	53.0	71.0	63.0	62.0	0102.0	0139.0	0140.0	0146.0	94.0	61.0	0226.0	0260.0	28.0	0.0	0.0	0.0	0.0	0.0	0.0
11.0	27.0	32.0	38.0	46.0	54.0	69.0	57.0	76.0	0115.0	0126.0	0130.0	0153.0	97.0	80.0	0345.0	0137.0	0.0	0.0	0.0	0.0	0.0	0.0	0.0
11.0	27.0	32.0	38.0	46.0	54.0	69.0	57.0	76.0	0115.0	0126.0	0130.0	0153.0	97.0	80.0	0345.0	0137.0	0.0	0.0	0.0	0.0	0.0	0.0	0.0
11.0	27.0	32.0	38.0	45.0	55.0	59.0	64.0	89.0	90.0	0104.0	0141.0	93.0	77.0	0164.0	0409.0	38.0	0.0	0.0	0.0	0.0	0.0	0.0	0.0
11.0	27.0	32.0	38.0	46.0	56.0	56.0	61.0	0112.0	0106.0	90.0	0185.0	77.0	98.0	0273.0	0349.0	8.0	0.0	0.0	0.0	0.0	0.0	0.0	0.0
11.0	27.0	32.0	38.0	45.0	60.0	49.0	60.0	0106.0	0107.0	84.0	0182.0	51.0	0119.0	0279.0	0262.0	17.0	0.0	0.0	0.0	0.0	0.0	0.0	0.0
11.0	27.0	32.0	38.0	44.0	60.0	53.0	62.0	0112.0	0117.0	94.0	0134.0	84.0	0182.0	0317.0	0118.0	3.0	0.0	0.0	0.0	0.0	0.0	0.0	0.0

Figure 3-Number of particles in grid bins at step 901, Fig. 2.

STEP 201 MAX COMMIT/PLANT CELL 1202

X-14

STEP 900 RAD VEL AV

X-15

Figure 6-Av. velocity of particles in grid bins, closer encounter run of Figure 5.

511-53
N88-15612 4/6713
248

1987

NASA/ASEE SUMMER FACULTY FELLOWSHIP PROGRAM

MARSHALL SPACE FLIGHT CENTER
THE UNIVERSITY OF ALABAMA IN HUNTSVILLE

EVALUATION OF HIGH-VOLTAGE, HIGH-POWER, SOLID-STATE
REMOTE POWER CONTROLLERS FOR AMPS

Prepared by:	Charles P. Callis
Academic Rank:	Associate Professor
University and Department:	The University of Tennessee At Martin, School of Engineering Technology and Engineering
NASA/MSFC:	
Laboratory:	Information and Electronic Systems
Division:	Electrical
Branch:	Electrical Power
NASA Colleague:	David J. Weeks
Date:	August 25, 1987
Contract No:	NASA-NGT-01-008-021

ABSTRACT

The Electrical Power Branch at Marshall Space Flight Center is developing a Power System Development Facility where various power circuit breadboards are under development and evaluation. This project relates to the evaluation of a particular remote power controller(RPC) energizing high power loads. The Power System Development Facility equipment permits the thorough testing and evaluation of high-voltage, high-power, solid-state remote power controllers. The purpose of this work is to evaluate a Type E, 30 Ampere, 200 V DC remote power controller.

Three phases of the RPC evaluation are presented. The RPC is evaluated within a low-voltage, low-power circuit to check its operational capability. The RPC is then evaluated while performing switch/circuit breaker functions within a 200 V DC, 30 Ampere power circuit. The final effort of the project relates to the recommended procedures for installing these RPC's into the existing Autonomously Managed Power System(AMPS) breadboard/test facility at MSFC.

ACKNOWLEDGMENT

I am grateful for the opportunity to have participated for the past two years in the NASA/ASEE Summer Faculty Program. I acknowledge with thanks the smooth and professional administration of the entire program by Dr. Gerald Karr and Ms Ernestine Cothran.

I am particularly grateful to Mr. Dave Weeks for sponsoring me in his laboratory for the past two summers and assisting me with my projects and presentations. His encouragement and interest have reboosted my research interests. Through the laboratory assistance of Mr. Weeks I have been able to produce two NASA/ASEE Summer Faculty Documents and two acceptable papers for the Inter-society Energy Conversion Engineering Conference during the past two years.

Thanks to Mr. Bob Kapustka and Ms Yvette Johnson for assisting me with my laboratory measurements. I am especially grateful to Ms Rita Brazier for taking the time to assist with a summer faculty report while keeping up with her regular duties. I am thoroughly impressed and extremely grateful for the helpful, friendly, and cooperative spirit shown to me by all the employees of the Electrical Branch.

LIST OF FIGURES

	PAGE
Fig. 1. MSFC Power Systems Development Facility	XI-4
Fig. 2. Autonomously Managed Power System	XI-5
Fig. 3. RPC Test Set-Up	XI-9
Fig. 4. RPC Test Circuit Arrangement	XI-10
Fig. 5. Normal Turn-On	XI-11
Fig. 6. Normal Turn-Off	XI-11
Fig. 7. Turn-On Into Heavy Load	XI-12
Fig. 8. Slow Overcurrent Trip	XI-12
Fig. 9. Turn-On Into Short	XI-13
Fig.10. Short Circuit From Full Load	XI-13
Fig.11. Slow Overcurrent Trip Characteristics	XI-14

List of Tables

	Page
Table 1. RPC General Characteristics	XI-7
Table 2. RPC Type E Characteristics	XI-7
Table 3. RPC Control Cable Configuration	XI-15
Table 4. Slow Overcurrent Trip Times	XI-15

TABLE OF CONTENTS

	PAGE
Introduction	XI-1
Objectives	XI-2
The Power Systems Development Facility	XI-3
The Autonomously Managed Power System	XI-3
Remote Power Controllers	XI-6
Background	XI-6
RPC Design Features and Requirements	XI-6
Evaluation of a Type E, 200V DC, 30 A RPC	XI-8
Installation of RPC's in AMPS	XI-16
Conclusions and Recommendations	XI-18
References	XI-19

INTRODUCTION

'Space Power Automation' is becoming a more aggressively pursued research area. A considerable number of publications have already been published, and the conference proceedings are including more publications on the subject each year. Along with the topic of 'Space Power Automation', the phrase, 'Autonomously Managed Power System' is also being used quite frequently to describe the area of space power research and development.

The Electrical Power Branch at Marshall Space Flight Center is developing a Power System Development Facility where various electrical power systems breadboards are under development and evaluation. These include a modular 5KW, 440 V, 20 KHZ Breadboard, a 24 KW, 200 V DC Autonomously Managed Power System (AMPS) breadboard/test facility, a 25 KW space station Core Module Power Management and Distribution (CM/PMAD) system breadboard, and computer/AI workstations.

A specific item to be evaluated in the Power System Development Facility is the Remote Power Controller (RPC). The high-voltage, high power, solid-state remote power controller for aerospace applications will be incorporated into the power circuit breadboards for testing and evaluation. The purpose of this paper is to provide background information on the power breadboard facility, provide general information regarding remote power controllers, and to present the results of an evaluation of a Type E, 200 V DC, 30 AMP, remote power controller. A recommended procedure for incorporating these RPC's into the AMPS Breadboard in the existing Power System Development Facility is also included.

OBJECTIVES

The objectives of this work included the following:

- I. Prepare the RPC for non-destructive evaluation by:
 - A. Securing the base of the RPC to an appropriate heat sink.
 - B. Installing protective zener diodes at the power FET's position within the RPC.
- II. Design and construction of the RPC operational test board to permit:
 - A. Sending "ON" commands to the RPC.
 - B. Sending "OFF" commands to the RPC.
 - C. Providing annunciation lamps to indicate "ON" and "TRIPPED" conditions of the RPC.
 - D. Provide terminals for receiving telemetered information from the RPC.
- III. Plan and conduct RPC high voltage and low voltage tests to measure:
 - A. Effect of reducing RPC control voltage.
 - B. Characteristics of telemetered signals from the RPC.
 - C. Response of RPC to control commands.
 - D. Voltage across and current through the RPC during:
 1. Normal "TURN ON".
 2. Normal "TURN OFF".
 3. Turn on into overcurrent type loads and short circuits
 - E. Times associated with fast and slow overcurrent trips.
 - F. Ability of RPC to produce "SOFT TURN ONS".
 - G. Voltage drop across the switch during normal operation.
- IV. To present a recommended procedure for installing RPC's into the existing power development facility.

THE POWER SYSTEMS DEVELOPMENT FACILITY

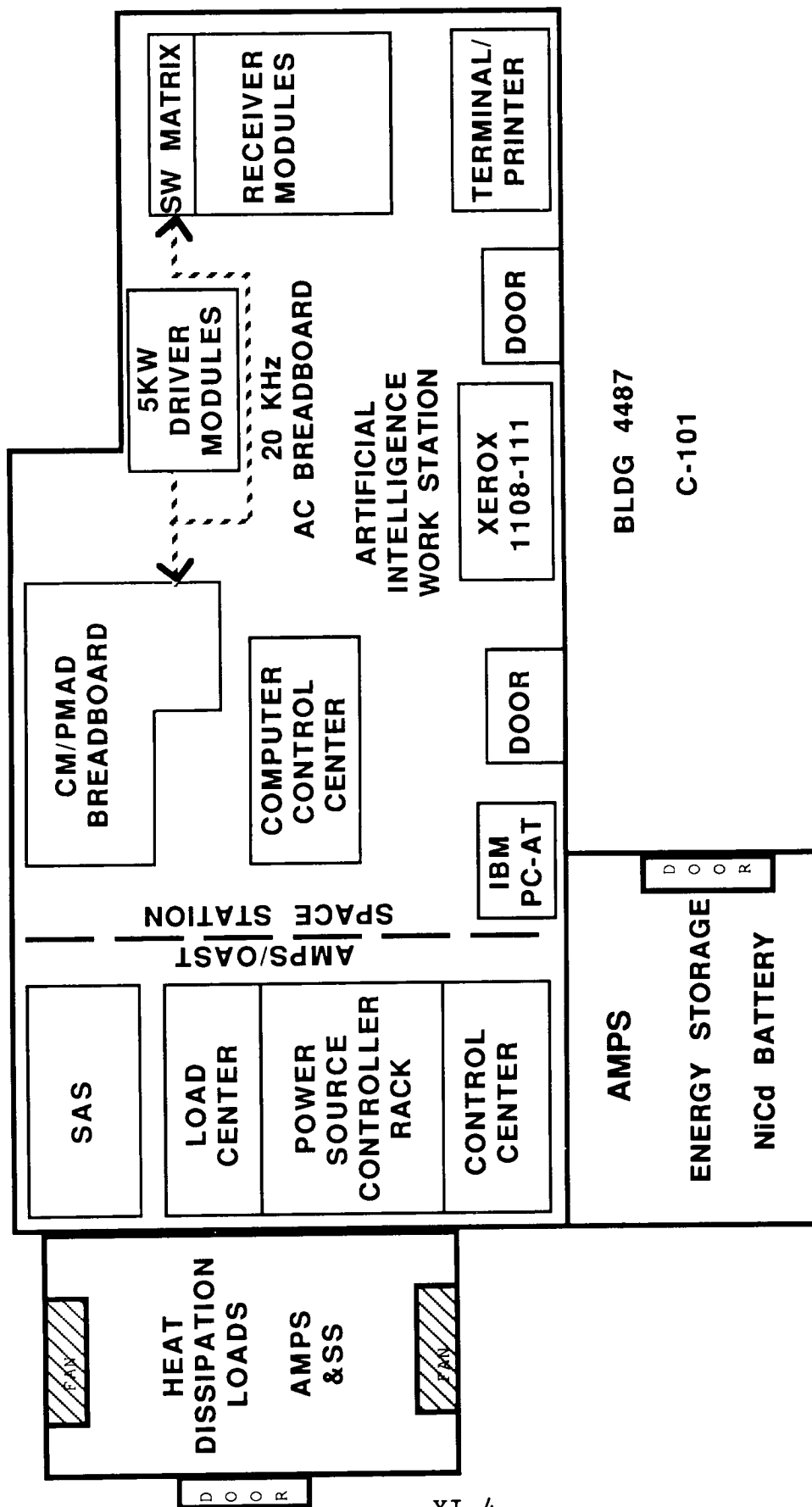
Under the direction of the Electrical Power Branch of the Electrical Division of the Information and Electronic Systems Laboratory the Power System Development Facility has been established and continues to be developed.(Fig.1) The author's NASA/ASEE 1986 report provides a general description of the facility and describes the rationale associated with the gradual development of the facility(Ref.1). The most important and valuable quality of the facility is its flexibility and adaptability wherein a wide variety of future power circuit concepts and breadboards can be tested and evaluated(Ref.2 through 5).

The facility is equipped with a wide variety of computers, printers, and software development workstations for producing the necessary test software associated with all the power system breadboards(Ref.1). The host computers, equipment-embedded computers, and artificial intelligence computers, associated with AMPS, are connected via an ethernet(Ref.1 through 5).

The Autonomously Managed Power System:

The Autonomously Managed Power System (AMPS) is a proof-of-concept breadboard of an end-to-end high voltage, high power electrical power system. It is essentially comprised of photovoltaic electrical energy collection simulators, battery energy storage facilities, and a large load center.(Fig.2) The breadboard has a 75 KW solar array simulator for the power generation source. The energy storage sub-system consists of a 168 cell nickel-cadmium battery with 189 ampere hour capacity. The load facility within AMPS consists of 21 KW resistive loads which can be configured in almost any arrangement in units as small as 0.33 KW, and fed from any of the available busses. A 3 KW load is also available as a pulsed load to produce power circuit noise simulation at frequencies between 30 HZ and 20 KHZ.(Ref.1 through 5).

MSFC POWER SYSTEMS DEVELOPMENT FACILITY



XI-4

Figure 1

AUTONOMOUSLY MANAGED POWER SYSTEM

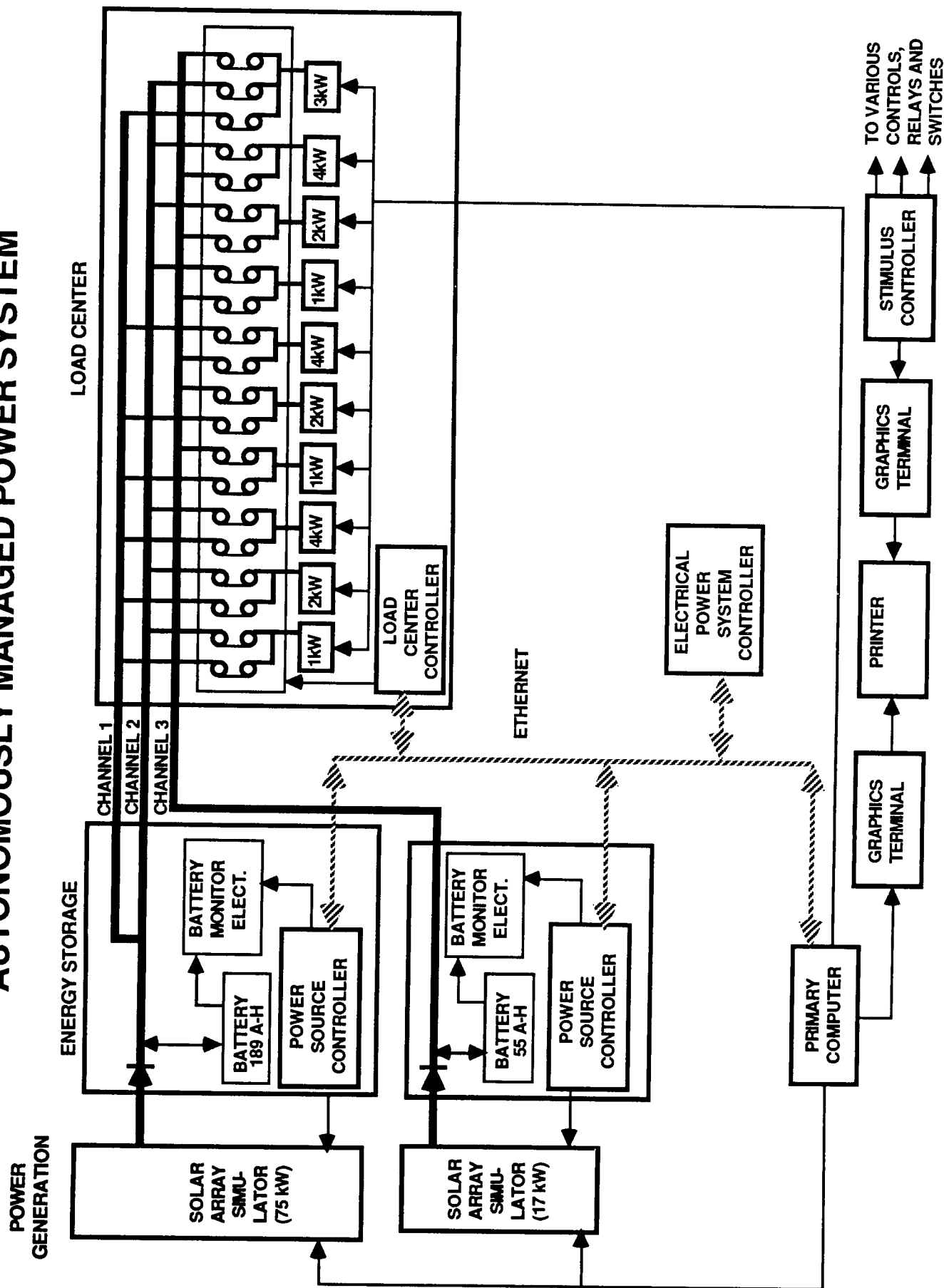


Figure 2

REMOTE POWER CONTROLLERS

In space power automation, remote power controller(RPC) generally refers to a solid-state, remote controlled device used to energize a high power load by using a low power, low voltage signal to produce switching which connects/disconnects the load with its supply voltage. For spacecraft electrical power systems, the solid-state RPC is greatly preferred over the ordinary electromechanical relay for accomplishing power switching and circuit breaking operations.

Background:

RPC's have been in development for many years, and the desirable characteristics are well established. The general RPC specifications which are accepted today are given in Table 1.(Ref.14). Although the particular performance specifications vary greatly for the various types of RPC's, the general features of the RPC appear to be the most interesting. For example, a "good" RPC should provide "soft" turn on and turn off characteristics as applied to the energizing and current change within a particular load. This is often referred to as causing the current to "ramp" to and from its maximum value for the load. Also, the "good" RPC should have overcurrent protection to protect itself and its load. Generally the overcurrent protection features provide for inverse-time type of overcurrent tripping associated with currents approaching 100-200% load currents. An instantaneous tripping feature is also included, which provides for microsecond types of trips associated with pre-set extremely high currents such as 300% overload currents.

RPC Design Features and Requirements:

A rugged RPC is expected to protect itself and its load when the supply voltage for the load is instantly shorted or is turned on into a short.

The need for the continued development of RPC's capable of providing power switching/circuit breaker action becomes obvious when one reviews the recent literature concerning the speculative values for the power requirements for future spacecraft.(Ref 6-8). During the past few years considerable effort has been made in developing RPC's capable of providing switch/circuit breaker action in higher voltage DC systems(Ref. 9-13). The development goal of providing RPC's capable of switching high power at high voltage in times of a few microseconds, while providing "current-ramping", "soft turn-on", thermal type overcurrent protection is not easily attained.

TABLE I.—GENERAL RPC SPECIFICATIONS

Rated operating voltage, V dc	150 to 1200
Rated output current, A dc	≤ 100
Control power source, V dc	28 ± 7
Low control power protection	Shutdown for < 21 V
Control voltage	TTL compatible
On-and-off control signals	Logic "O" (low)
Overload trip indication	TTL signal—high after trip
Overload reset	Resets on "off" command
Turnon delay, ms	100 max.
Rise and fall times, μs	100 desired
Voltage drop at rated load, V dc	2.0 max.
Power dissipation off, W	0.5 max.
Efficiency at 20 to 100 percent of rated load current, percent	≥ 99 (including control power)
Overload tripout	Proportional to I^2t
Fault response time, μs	3
Fault trip level	2 to 3 per unit
Operating temperature, °C	– 50 to 75
RPC protection	RPC must be self-protecting under all conditions including maximum fault current

Table 1 (Reference 14)

RPC CHARACTERISTICS

	RPC model			
	A	E	F	G
Operating voltage, V	– 750	300	150	800
Full load current, A	0.04	35	100	10
Switching time (on/off), μs	5	50	250	100
Fault turnoff time, μs	120	2	3	3
Switch-on drop at full load, V	0.25	1.7	2.0	3.8
Efficiency, percent	99.9	99.4	98.7	99.5
Device	MTP1N100	IRF350 or VNM005A	IRF250	BUZ54A

Table 2 (Reference 14)

Evaluation of a Type E, 200 V DC, 30 A RPC:

The particular RPC being evaluated is referred to as a Type E RPC. The general characteristics of the Type E are given in Table 2. The RPC was equipped with a 9-pin connector for attaching a control cable. The control cable configuration is given in Table 3. A control circuit for the RPC test was designed to provide commands to the RPC and to receive telemetered information and status signals during operation of the test. The essential features of the test board circuit are given in Table 3. The test set-up is shown in figure 3, with the test circuit arrangement in the left foreground, and the test RPC shown on the right.

The test circuit is shown in figure 4. The general nature of the feedback from the RPC via the control cable is given in Table 3. The telemetered information provided through the control cable provides an analog voltage indicative of load current through the switch and the voltage appearing across the switch. The oscilloscope photos reflect the fact that the switch recovers the load supply voltage when the RPC has opened the switch. The voltage measured across the switch becomes the voltage drop associated with the RPC switch when the load is energized and the supply voltage nearly all appears across the load. The general performance of the test RPC is shown with typical oscilloscope photos in figures 1-10.

The photos in figures 5 and 6 show the soft current rise through the switch and the passing of the supply voltage from the switch to the load during normal turn-on and turn off. Figure 7 is an oscilloscope photo showing the switch current and voltage transients during turn on into an 80 amp load (267% overload). This overload would produce a thermal, or timed, trip not shown on this trace. Figure 8 simply shows the recorded time required for a thermal trip to occur as associated with a particular overload. Figures 9 and 10 are included to show switch response to sudden overloads or shorts. In the event of a sudden overload or short which produces a steady state current of over 90 amps, the RPC ramps the current to 90 amps and performs its fastest turn-off, which is accomplished within one or two micro-seconds. Table 4 is included to show the inverse-time characteristics of the slow overcurrent trip feature of the RPC.

The only problem encountered during the evaluation procedures, was associated with the failure of an opto-isolation circuit related to the "on" feedback signal of the RPC control circuitry. During the low voltage test phase, a short was placed across the load position, causing the RPC to trip, and produce a trip indication on the control board. The failure of the opto-isolation circuit caused the RPC to also produce an "on" indication when



RPC Test Set-Up

Figure 3

POWER CIRCUIT FOR RPC EVALUATION

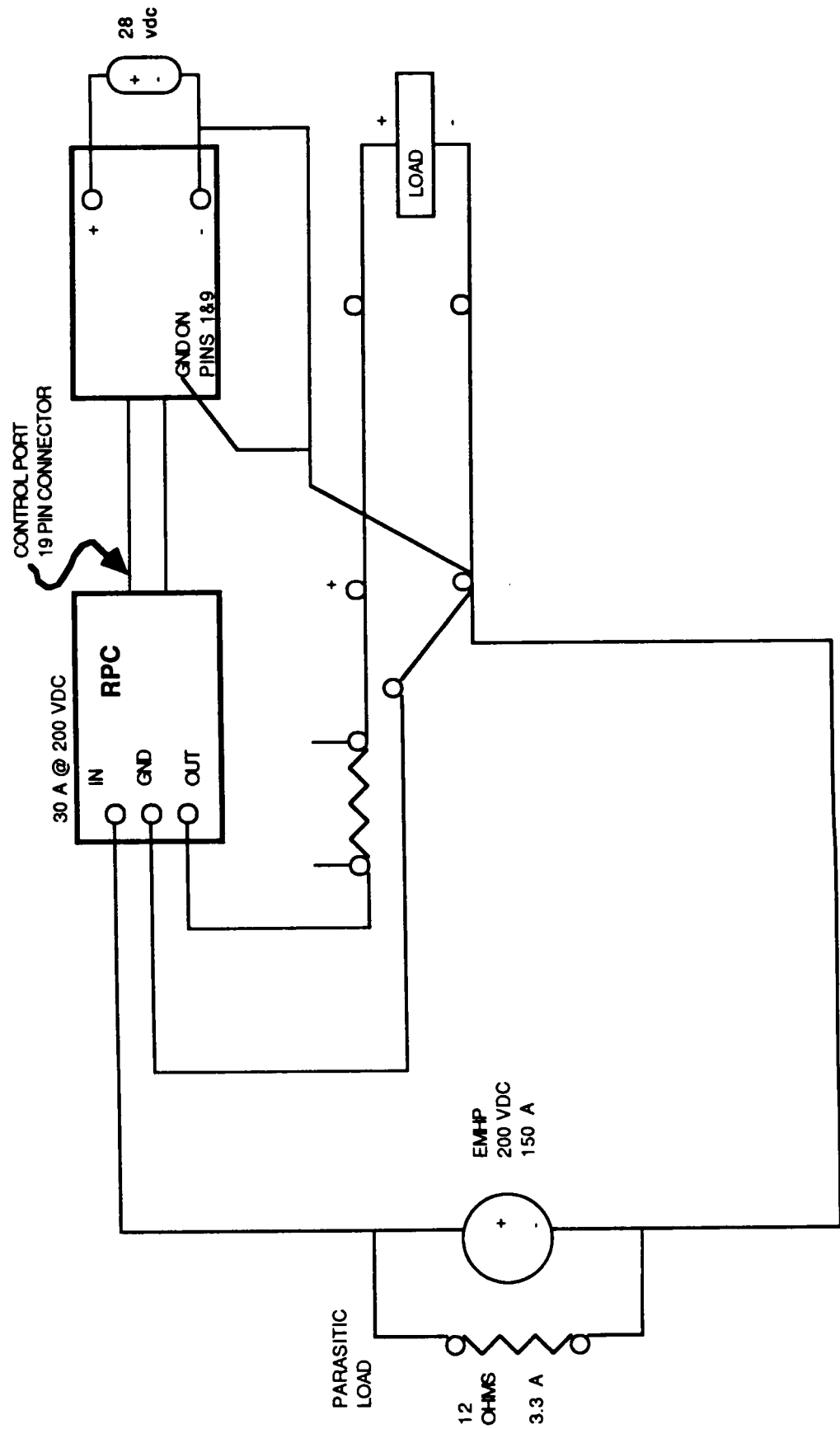


Figure 4

ORIGINAL PAGE IS
OF POOR QUALITY

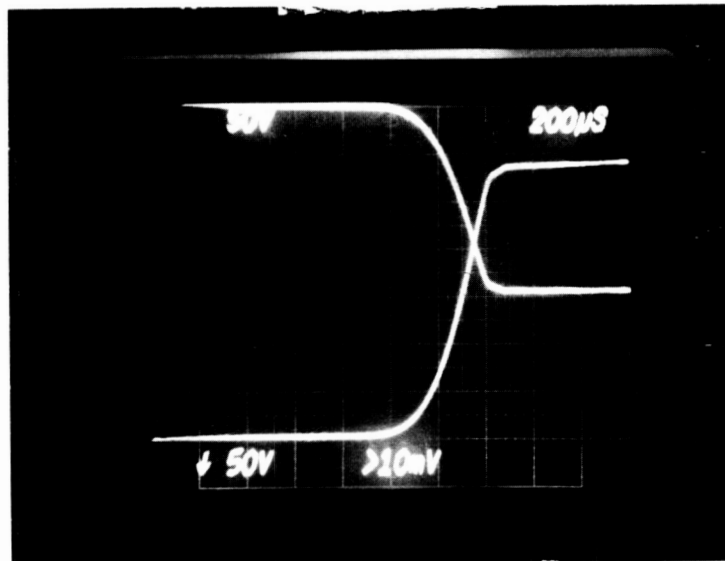


Figure 5 - Normal Turn On
(5 AMP/DIV, 50 V/DIV)

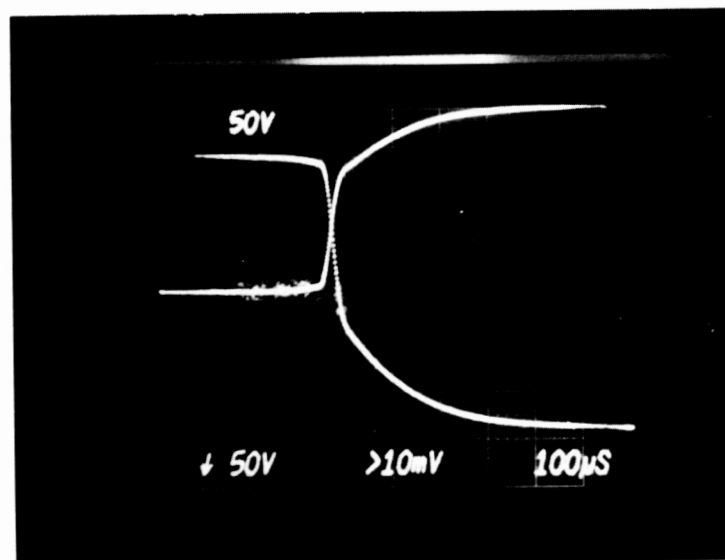


Figure 6 - Normal Turn Off
(5 AMP/DIV, 50 V/DIV)

ORIGINAL PAGE IS
OF POOR QUALITY

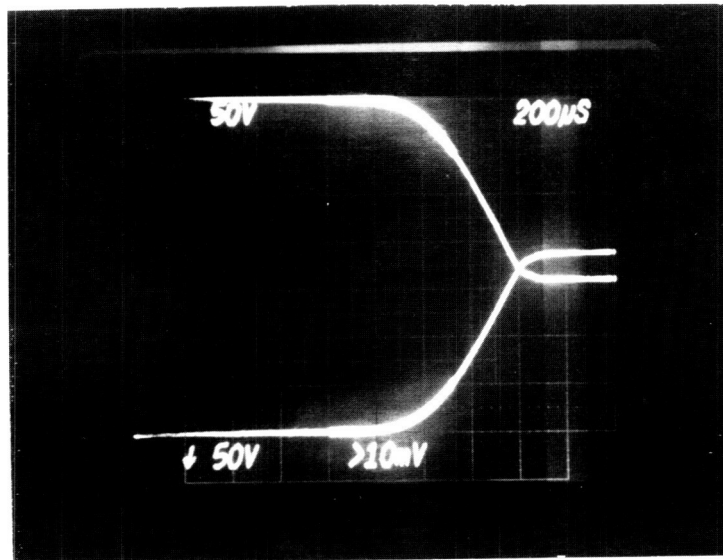


Figure 7 - Normal Turn On into 80 AMP
Load. (20 AMP/DIV, 50 V/DIV)

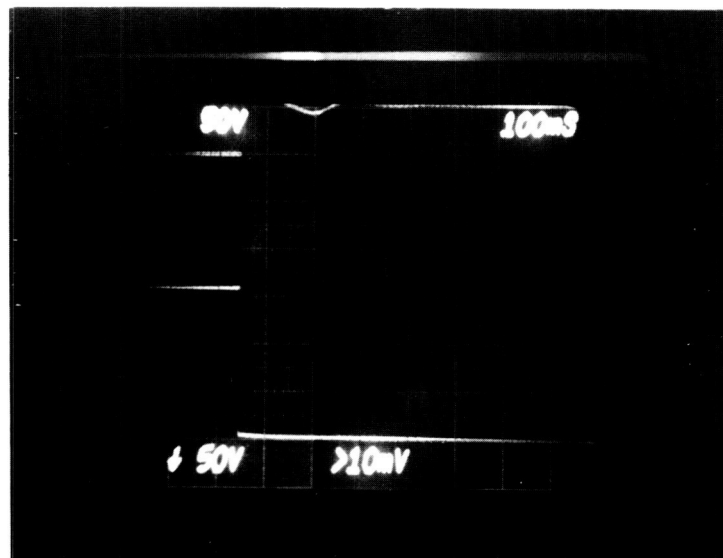


Figure 8 - Slow Overcurrent Trip
(10 AMP/DIV, 50 V/DIV), 2.5 seconds
to trip at 60 AMPS

ORIGINAL PAGE IS
OF POOR QUALITY

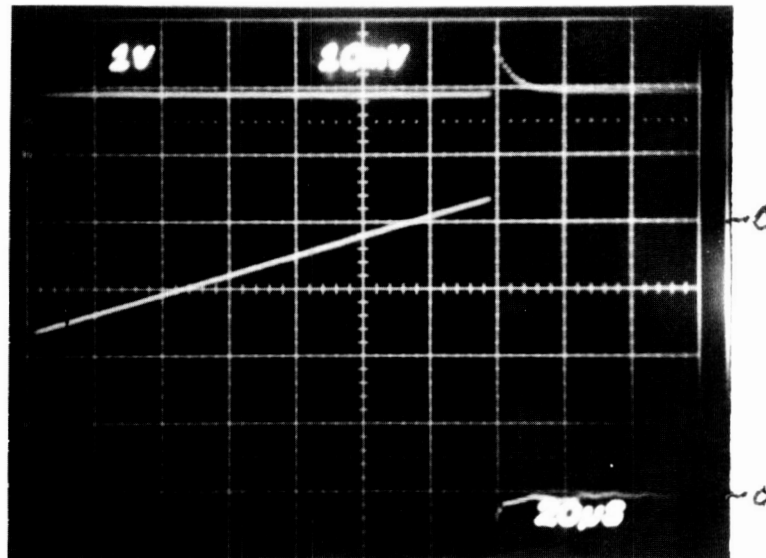


Figure 9 - Turn On into Short
(20 AMP/DIV, 100 V/DIV)
(Reference 14)

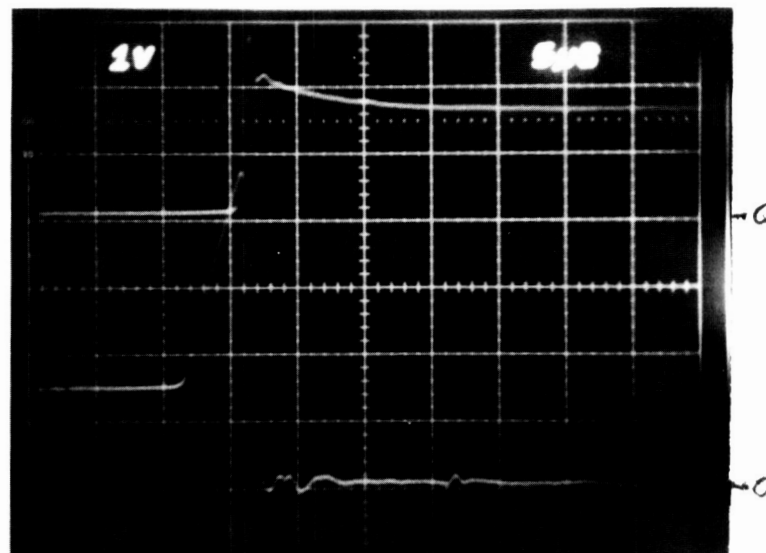


Figure 10 - Short from Full Load
(20 AMP/DIV, 100 V/DIV)
(Reference 14)

SLOW OVERCURRENT TRIP CHARACTERISTICS

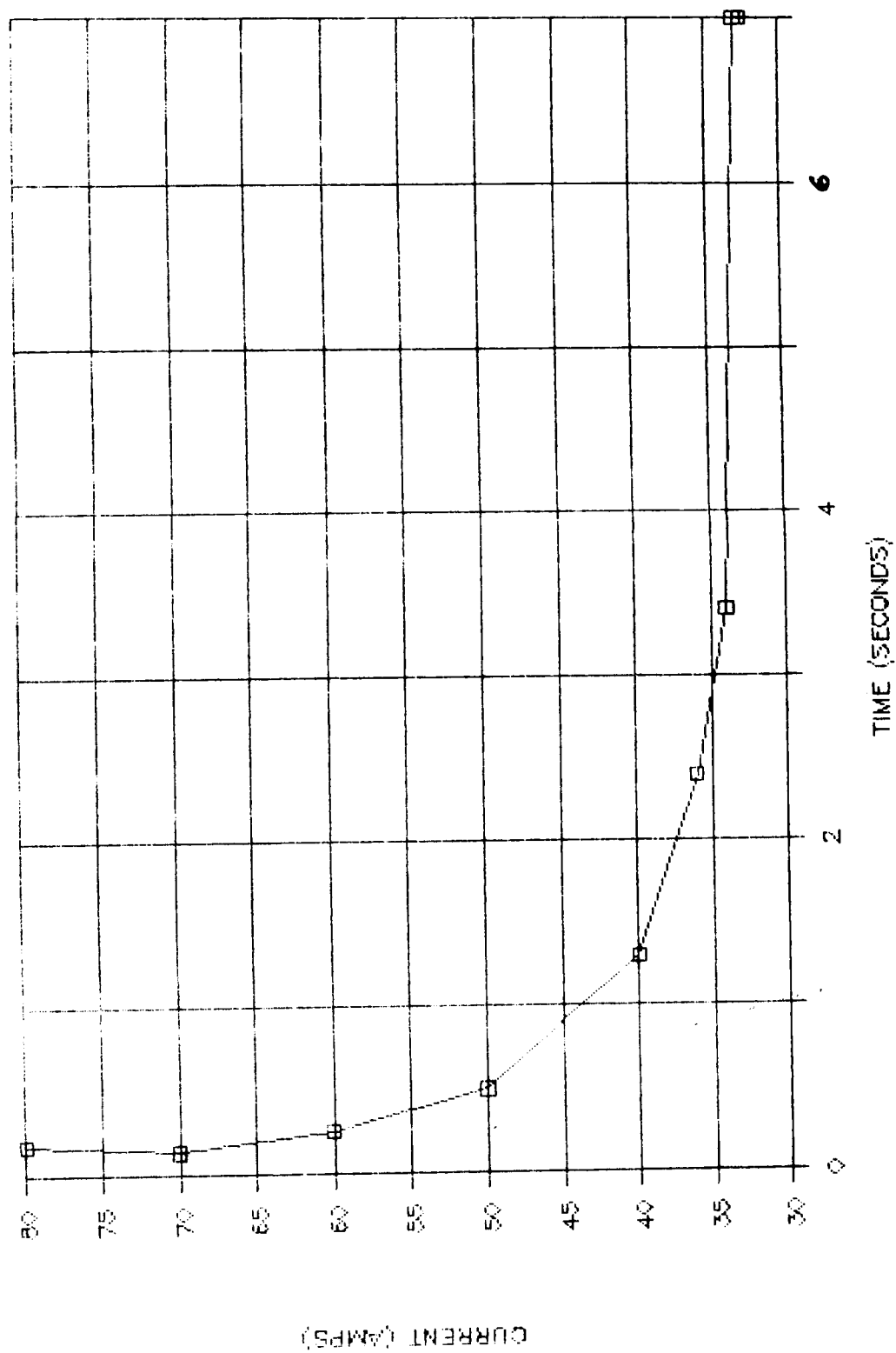


Figure 11

CONTROL CABLE CONFIGURATION

CONDUCTOR #	FUNCTION
1.	PROVIDE GROUND. THIS GROUND IS BOTH THE LOW POTENTIAL OF THE CONTROL VOLTAGE AND THE MAIN SUPPLY VOLTAGE FOR ENERGIZING THE LOAD.
2.	+28 VDC. EXTERNALLY PROVIDED DC VOLTAGE FOR OPERATION OF CONTROL CIRCUITS IN RPC.
3.	"COMMAND ON". MOMENTARY GROUND COMMANDS THE RPC TO TURN THE SWITCH ON AND APPLY MAIN SUPPLY VOLTAGE TO LOAD.
4.	"TRIPPED OFF". LOW VOLTAGE FEEDBACK FROM THE RPC INDICATES THAT THE RPC INTERRUPTED POWER TO THE MAIN LOAD DUE TO OVERCURRENT OR FAULT IDENTIFICATION.
5.	"COMMAND OFF". MOMENTARY GROUND COMMANDS THE RPC TO TURN THE SWITCH OFF AND DE-ENERGIZE THE LOAD.
6.	FEEDBACK FROM RPC TO INDICATE LOAD CURRENT OR CURRENT THROUGH THE SWITCH. (ANALOG VOLTAGE).
7.	"ON". LOW VOLTAGE FEEDBACK FROM THE RPC INDICATES THAT THE RPC IS ON AND CURRENT IS BEING CONDUCTED THROUGH THE LOAD.
8.	FEEDBACK FROM RPC TO INDICATE VOLTAGE APPLIED TO LOAD. (MEANING VOLTAGE IS EXTENDED THROUGH THE SWITCH TOWARD LOAD). ANALOG VOLTAGE PROPORTIONAL TO ACTUAL VOLTAGE.
9.	COMMON GROUND. (REDUNDANT CONNECTION)

Table 3

SLOW OVERCURRENT TRIP TIMES

CURRENT (AMPS)	TIME (SECONDS)
32.6	7
33	7
34	3.4
36	2.4
40	1.3
50	0.5
60	0.25
70	0.13
80	0.17

Table 4

the unit was actually "off". After the opto-isolation circuit was repaired, the problem was repeated three times. At that point, voltage surge protection was installed at the installation site of the opto-coupler. Suppression capacitors and zener diodes were installed as the protection devices. No further failures were produced.

INSTALLATION OF RPC'S IN AMPS

The existing AMPS breadboard utilizes approximately 20 electromechanical relays to configure a desired load and perform load balancing operations. Considerable engineering design changes would be required to remove these RPC simulators and replace them with solid state RPC's. It seems appropriate to incorporate a few RPC's into AMPS as soon as possible, so that the existing facility breadboard may begin a more realistic test of spacecraft components.

It appears that two 200 V DC, 30 A RPC's could appropriately be installed in AMPS with a minimum number of hardware and computer software changes. The positive cable at the battery and the positive cable at the Solar Array Simulator output could be interrupted and routed through a Type E RPC. The 28 V DC supply for the RPC control circuits is not available in AMPS. Some signal-conditioning interfacing would also be needed to provide computer control of the installed RPC's.

The two RPC's would provide redundant switches associated with the battery and the Solar Array Simulator output. However, the "soft turn-on" and intelligent overcurrent protection provided by the RPC's would permit greater latitude with added fault-interruption capability during regular AMPS experiments.

A second phase related to the incorporation of RPC's into AMPS would be a project to replace the electromechanical relays(RPC simulators) with RPC's. The original design of AMPS should accommodate this project. It is expected that most of the effort required on this project would be related to software changes to accommodate the additional control and feedback associated with the RPC's. For those who may be involved in the relay/RPC exchange, a few observations are offered. The existing 120 V AC relay coil supply voltage will need to be replaced by a 28 V DC supply to energize the RPC control circuitry. The contacts presently used to turn on the relay coils, will need to be replaced by momentary ground switches to turn the RPC on and off.

Reasonably good detail of the existing circuitry is available on print no. D771232, sheet 2 of 3. and the SOTCHER(sub-contractor) print no. 1237B. A good example for review is the RPC Simulator

no. 1, related to the low, medium, and high switching of one of the 4 KW loads. Present logic uses 12 V DC signals to energize 12 V relay coils, and the contacts of these to energize 120 V AC relays to accomplish the necessary switching. One should not forget that the RPC's also provide analog voltage feedback related to current through the switch and voltage across the switch, in addition to "on" and "tripped" annunciation signals. During the relay/RPC exchange these "extras" should produce no problem, even if they are not used by AMPS after the exchange. The existing relays are three-pole, single throw, and are energized with 120 V AC, 60 HZ; and of course are noisy when operated. Each of the existing relays occupies only about 3 inches by 5 inches of horizontal space in the AMPS cabinets, with six per horizontal rack. The "quiet" RPC's will need much more space; but there is ample space in unoccupied racks below the existing relays.

Eighteen RPC's will be needed to replace the relays that are presently used in configuring loads. The highest current that will be switched by any of these RPC's will be that of two thirds of the current related to one of the 4 KW loads (13.33 Amps). If eighteen or more RPC's can be obtained for the project, it would seem appropriate to replace the relays used in load configuring. However, if only a few RPC's will be available, I recommend the installation of them in more obvious, more critical sites; such as in-line breakers in the Solar Array Simulator output or the battery output.

CONCLUSIONS AND RECOMMENDATIONS

The power System Development Facility of the Electrical Power Branch is rapidly becoming a very complete and sophisticated power system breadboard development laboratory. The AMPS breadboard offered an excellent environment and test site for the Type E RPC's evaluated.

The Type E RPC performed well within its acceptable specifications. Its performance during the more stressful tests demonstrated the ruggedness required of a high-power switch/breaker for spacecraft applications.

The Type E RPC should offer considerable enhancement to the AMPS breadboard. The installation will necessarily require some software changes; but the flexibility of the breadboard will allow a relatively simple adaption. The installation of the RPC's in the AMPS breadboard will permit logging of additional evaluation and characterization time on the RPC's themselves, add additional "smart" overcurrent protection to the breadboard, and demonstrate the flexibility of the MSFC Power Systems Development Facility.

REFERENCES

1. Callis, C. P.: Autonomously Managed Electrical Power Systems. NASA Contractor Report (Research Reports-1986 NASA/ASEE Summer Faculty Fellowship Program). NASA CR-178966, Paper XIII.
2. Bechtel, R.T. and D.J. Weeks: Autonomously Managed High Power Systems. Proceedings of the 20th IECEC, 164-170(1985).
3. Lepisto, J.W.: Autonomously Managed Electrical Power System. Proceedings of the 21st IECEC(1986).
4. Weeks, D.J.: Application of Expert Systems in the Common Module Electrical Power System. Proceedings of SPIE, Vol. 580, Space Station Automation(1985).
5. Final Report: Space Power Distribution System Technology, TRW Report No. 34579-6001-OT-00, Volumes 1-3, Contract NAS8-33198, March 1983.
6. Renz, D.: Design Considerations for Large Space Electric Power Systems. NASA TM-83064, 1983.
7. Synchronous Energy Technology. NASA CP-2154, 1980.
8. Cassinelli, J.E.: Solar Array Switching Power Management Technology for Space Power Systems. (TRW-37243, TRW Space Technology Labs: NASA Contract NAS3-22656.) NASA CR-167890, 1982.
9. Corbett, R.E.: Development of High Voltage High Power Satellite Power Systems. Proceedings of the 13th IECEC. Vol. 1. Society of Automotive Engineers, 1978, pp.37-43.
10. Sollo, C.: Distribution Voltages for High Power Satellites. IECEC (1982)
11. Waddington, D.: Logic-Controlled Solid-State Switchgear for 270 V DC. IEEE, 1973, pp. 170-179.
12. Baker, D.E.: Aerospace Technology Development of Three Types of Solid State Remote Power Controllers for 120 V DC . (WAED-75-01E, Westinghouse Electric Corp.; NASA Contract NAS3-17771.)NASA CR-134772, 1975.
13. Billings, W.W.: Solid State Remote Power Controllers for High Voltage DC Distribution Systems. NAECON '77: Proceedings of the National Aerospace and Electronics Conference. IEEE, 1977, pp. 186-192.
14. Sturnman, J.C.: High-Voltage, High-Power, Solid-State Remote Power Controllers for Aerospace Applications. NASA Technical Paper 2437, Mar. 1985.

omit

1987

NASA/ASEE SUMMER FACULTY FELLOWSHIP PROGRAM

MARSHALL SPACE FLIGHT CENTER
UNIVERSITY OF ALABAMA IN HUNTSVILLE

COMPUTER ARCHITECTURES FOR THE REAL-TIME ENVIRONMENT

Prepared by:	Chester Carroll
Academic Rank:	Professor
University and Department:	University of Alabama, Tuscaloosa Electrical Engineering

NO REPORT RECEIVED

N88-15613^{5/2-37}

116714
138

1987 NASA/ASEE SUMMER FACULTY FELLOWSHIP PROGRAM

MARSHALL SPACE FLIGHT CENTER

THE UNIVERSITY OF ALABAMA IN HUNTSVILLE

VERIFICATION OF FANTASTIC INTEGRATED CODE

PREPARED BY: Rajinder Singh Chauhan
ACADEMIC RANK: Assistant Professor
UNIVERSITY AND DEPARTMENT: North Carolina A&T State
University/Mechanical Engineering
NASA/MSFC:
LABORATORY: Systems Analysis and Integration
DIVISION: Systems Engineering
BRANCH: Thermal Systems Branch
MSFC COLLEAGUE: Kenneth McCoy

ABSTRACT

FANTASTIC is an acronym for Failure Analysis Nonlinear Thermal and Structural Integrated Code. This program has been developed by Failure Analysis Associates, Palo Alto, California for MSFC in order to improve the accuracy of solid rocket motor nozzle analysis. Its first version has been released and received by the Thermal Systems Branch of MSFC. FANTASTIC has three modules:

- a. FACT: It is the thermochemical analysis module
- b. FAHT: It is the heat transfer analysis module
- c. FAST: It is the structural analysis module

All modules have keywords for input of data. Work is in progress for the verification of FAHT module. This is being done by using data for various problems with known solutions as inputs to the FAHT module. The information obtained by running these programs is used to pinpoint problem areas of this code and passed on to the developer for removing bugs from this code. As a result of this procedure, Failure Analysis Associates have revised the first version of the FANTASTIC code and a new improved version has been released and received by the Thermal Systems Branch. Further work to verify the new version is continued:

ACKNOWLEDGEMENT

I wish to acknowledge the NASA/ASEE Summer Faculty Fellowship Program, along with Gerald Karr, the UAH Program Director and Ernestine Cothran, MSFC Program Coordinator.

I owe my gratitude to NASA/MSFC colleagues Kenneth McCoy and Dallas Clark of Thermal Systems Branch, Systems Analysis and Integration Laboratory.

I am grateful to Betty K. Golden of Thermal Systems Branch for typing this manuscript.

ORIGINAL PAGE IS
OF POOR QUALITY

ORIGINAL PAGE IS
OF POOR QUALITY

1. Introduction

Failure Analysis Associates, Palo Alto, California has developed an advanced computer code for MSFC to improve the accuracy of the solid rocket motor analysis. The computer code is called "FANTASTIC", an acronym for Failure Analysis Nonlinear Thermal and Structural Integrated Code. The code incorporates a higher order integration scheme for modeling steep temperature and strain gradients. It has a modular design and is intended as a multi-purpose thermostructural analysis code.

FANTASTIC has not been verified before. In order to use this code for the intended purpose outlined above, it is necessary to verify it. The purpose of this report is to give an overview of the procedure followed to verify this code.

2. Procedure

FANTASTIC consists of three modules:

1. FACT: It is the thermochemical analysis module
2. FAHT: It is the heat transfer analysis module
3. FAST: It is the structural analysis module

Because FANTASTIC can be used for a stand-alone thermal or structural analysis, FAHT module was chosen for verification purpose. FAHT module accepts data under numerous keywords. All keywords of FAHT are divided into three blocks:

1. PARAMETER Block: This block is used to provide a title and analysis procedure (i.e., steady or transient etc.) options.
2. MODEL Block: This block is used to provide the details of the model geometry, material, and boundary conditions.
3. INCREMENT Block: This block is used to provide the loading history in the form of various types of incremental loads.

A list of the keywords under each block is given in Table 1. The data must be input as required by the program format.

ORIGINAL PAGE IS
OF POOR QUALITY

2-1 MODEL Geometry

The first requirement in setting up the numerical problem for execution by FAHT is to define the domain of solution. Then this domain is divided into appropriate number of "finite elements". There are various types of elements and an element can have nodes ranging from 2 (link element) to 20 (isoparametric hexahedron element). A list of the names for various types of elements covered by FAHT is given in Table 2. As a general rule more accuracy is obtained by selecting eight noded planar element than four noded planar element for the same curved geometry. In three dimensional problems up to 20 noded elements may be chosen depending upon the geometry. Each node is fixed by a set of coordinates which are input under an appropriate keyword in the MODEL block.

2.2 Material Description

There are a total of 12 FAHT material types. Each material type is defined by a set of properties. For example Type 1 - Thermal: Linear Isotropic material requires three properties namely mass density, specific heat, and thermal conductivity whereas Type 41 - Isothropic three-component charring and decomposing material requires 32 properties to be specified. A list of FAHT material types is given in Table 3.

2.3 Loading Conditions

Loading conditions treated by FAHT include convection, enclosure radiation, lumped heat capacity, and heat sink/source. The convection option is implemented through the keyword *HEATCONVECTIONBC group. The radiant heat exchange option is implemented through the *ENCLOSURERADIATION and *VIEWFACTOR groups. Lumped heat capacity option is implemented via the *LUMPEDHEATCAPACITY group. A volumetric heat sink or source can be defined as a function of time or temperature via the *HEATGENERATION GROUP.

2.4 Boundary Conditions

Boundary conditions for the heat transfer analysis may be specified in terms of prescribed temperature or heat flux along external boundaries or internal surfaces (e.g., contact resistance or heat flux across gaps between surfaces). This option is implemented via the *TEMPERATUREBC and *HEATFLUXBC groups.

ORIGINAL PAGE IS
OF POOR QUALITY

2.5 Initial Conditions

Initial temperatures may be specified in FAHT at each node. Internal heat generation rates can also be specified as functions of time or temperature.

3. Illustrative Example

Consider a two-dimensional steady state heat transfer in a material with constant thermal conductivity. A schematic showing the boundary conditions is given in Figure 1. The geometry has 32 elements. Each element has four nodes. Thus the total number of nodes is 45. The element type from Table 2 is type number 21, planar quadrilateral. The material type is assumed to be type number 1, thermal: linear isotropic. Therefore, three properties namely mass density, specific heat, and thermal conductivity are required to be specified. This information is given in the material library section of the FAHT user's manual. The input for the implementation of FAHT for this problem under suitable keywords of the PARAMETER block, MODEL block, and the INCREMENT block respectively is given below. Explanations for the input data are also given:

PARAMETER BLOCK

*TITLE

Two Dimensional Steady State Heat Transfer

*TEMPERATURE

This keyword is used because the heat transfer analysis is to be performed in the next time period.

*ENDPARAMETER

This keyword is used to define the end of the PARAMETER block.

MODEL Block

*NODE

This group is used to define nodal coordinates. A node setname must also be defined for a group of nodes.

ORIGINAL PAGE IS
OF POOR QUALITY

NODESET 2

Here NODESET is the name of the node set consisting of all 45 nodes.

1 0.0 0.0

The first number 1, denotes a node which is assigned number 1 with coordinates $x = 0.0$, $y = 0.0$. The next two numbers 0.0 and 0.0 denote the x and y coordinates of node 1.

9 2.0 0.0 1

The first number 9, denotes a node which is assigned number 9 with coordinates $x = 2.0$, $y = 0.0$. The next two numbers 2.0 and 0.0 denote the x and y coordinates of node 9. The last number 1, denotes the increment for nodes between nodes 1 and 9. The coordinates of nodes 2 through 8 are generated automatically by the build in generator in the code. We can similarly input the coordinates of the remaining nodes as given below.

10	0.0	0.25	
18	2.0	0.25	1
19	0.0	0.50	
27	2.0	0.50	1
28	0.0	0.75	
36	2.0	0.75	1
37	0.0	1.00	
45	2.0	1.00	1

*ELEMENT

This group is used to define element connectivity. Each element must be assigned a unique element number. An element set name must also be defined for each group of elements.

ELSET 21 1

The name of the element set consisting of all 32 elements is ELSET. The number 21 denotes the element type number and the next number 1 denotes the material number for the elements in this set.

1 1 2 11 10 7 1

ORIGINAL PAGE IS
OF POOR QUALITY

The first number 1 denotes an element of the set. The next four numbers 1, 2, 11, and 10 denote that the element is connected by these four nodes. The next two numbers 7 and 1 denote that there are 7 similar elements with increment 1. This data line, therefore, covers input for eight elements 1 through 8. The data for remaining elements is input similarly as below:

9	10	11	20	19	7	1
17	19	20	29	28	7	1
25	28	29	38	37	7	1

*SET

This group is used to define additional node and element sets. Each set must be assigned a unique set name. A node set or an element set may be defined as a list of (node or element) numbers or as a list of (node or element) number ranges.

NODESET 1 1 2

Here NODESET 1 is the name of a node set consisting of nodes 1 through 9. Number 1 denotes that the set-type is node set. (If this number is 2, it would have denoted that the set type is element set). The next number 2 denotes the list type. Here it means that we are going to input a range of set nodes.

1 9

The number 1 denotes the first node number and number 9 denotes the last node number (range from node 1 through 9).

NODESET 2 1 1

Here NODESET 2 is the name of the node set consisting of nodes 18, 27, 36, and 45. Number 1 denotes the settype (here node set) and the next number 1 denotes that the list type is for a list of node(s) given below.

18 27 36 45

*TEMPERATUREBC

10	383.0
19	707.0
28	924.0
37	1000.0

ORIGINAL PAGE IS
OF POOR QUALITY

Above we have input for specified temperatures at nodes 10, 19, 28, and 37. Another method to input specified temperature boundary condition for a node set is shown below:

NODESET 1 0.0

NODESET 2 0.0

All nodes in NODESET 1 and NODESET 2 have a specified temperature of 0.0.

*PROPERTY

This group is used to define material properties.

1 1

The first number 1 denotes the material number and the second number 1 denotes the material type (in this example - thermal: linear isotropic). So, three properties namely mass density, specific heat, and thermal conductivity are input in that order as below:

1 1 1

*END MODEL

This keyword is used to define the end of the MODEL block.

*PRINT

This group is used to select the desired printed output printcode 10 is used for printing of temperatures.

NODESET 10

With this input temperatures for all nodes in the set NODESET are printed.

*ENDINCREMENT

This keyword is used to define the end of the INCREMENT block.

ORIGINAL PAGE IS
OF POOR QUALITY

4. CONCLUSIONS

Ten problems with known solutions were used for input of data to FAHT. Based on the runs made and their results, it was found that FAHT needed revision because of bugs in the program. For example, the program was not able to recognize a few keywords for input of data.

The solutions of many problems did not match the known solutions. This indicated that the program needed an overhaul. This information was passed on to the developer, Failure Analysis Associates. Based on these results, the developer has been able to remove bugs and has supplied MSC with a new version of FANTASTIC with workable FAHT module.

TABLE 1 VARIOUS DATA BLOCKS AND KEYWORDS FOR FAHT

PARAMETER Block

*TITLE
 *FACT
 *TEMPERATURE
 *POREPRESSURE
 *FAST
 *TRANSIENT
 *NONLINEAR
 *ENDPARAMETER

MODEL Block

*NODE
 *ELEMENT
 *SET
 *CROSSECTION
 *PROPERTY
 *MATERIAlDIRECTION
 *TEMPERATUREBC
 *PRESSUREBC
 *HEATFLUXBC
 *MASSFLUXBC
 *INITIALTEMPERATURE
 *INITIALPRESSURE
 *HEATCONVECTIONBC
 *THERMALGAPCONTACT
 *LUMPEDHEATCAPACITY
 *HEATGENERATION
 *NONLINEARHEATBC
 *TIMETEMPFUNCTION
 *ENCLOSURERADIATION
 *VIEWFACTOR
 *ENDMODEL

INCREMENT Data Block

*TRANSIENT
 *NONLINEAR
 *RESTART
 *PRINT
 *REPORT
 *POST
 *ENDINCREMENT

Table 2: FAHT Element Types

Type Number	Element Description	Number of Nodes
11	Link	2
21	Planar quadrilateral	4
22	Planar quadrilateral	8
25	Axisymmetric quadrilateral	4
26	Axisymmetric quadrilateral	8
31	Solid hexahedron	8
32	Solid hexahedron	20
41	2-D planar interface	4
42	2-D planar interface	6
45	Axisymmetric interface	4
46	Axisymmetric interface	6
51	3-D interface	8
52	3-D interface	16

Table 3: FAHT Material Types

Type Number	Material Description	Number of Properties
1	Thermal: linear isotropic	3
2	Thermal: time or temperature dependent isotropic	6
11	Diffusion: linear isotropic	4
12	Diffusion: time or temperature dependent isotropic	8
21	Thermal: linear orthotropic	8
22	Thermal: time or temperature dependent orthotropic	16
31	Diffusion: linear orthotropic	9
32	Diffusion: time or temperature dependent orthotropic	18
41	Isotropic three-component charring and decomposing material	32
42	Isotropic time or temperature dependent three-component charring and decomposing material	
43	Orthotropic three-component charring and decomposing material	
44	Orthotropic time or temperature dependent three-component charring and decomposing material	

ORIGINAL PAGE IS
OF POOR QUALITY

***TITLE**

**TWO-DIMENSIONAL STEADY STATE HEAT TRANSFER
IN CONSTANT CONDUCTIVITY MEDIUM WITH INSULATED
AND ISOTHERMAL BOUNDARY CONDITIONS.**

1000	INSULATED									
	*	*	*	*	*	*	*	*	*	*
	37	38	39	40	41	42	43	44	45	
										0.25
	25	26	27	28	29	30	31	32		
924	*	*	*	*	*	*	*	*	*	*
	28	29	30	31	32	33	34	35	36	
	17	18	19	20	21	22	23	24		
707	*	*	*	*	*	*	*	*	*	*
	19	20	21	22	23	24	25	26	27	ZERO
										DEGREES
	9	10	11	12	13	14	15	16		
383	*	*	*	*	*	*	*	*	*	*
	10	11	12	13	14	15	16	17	18	
	1	2	3	4	5	6	7	8		
0	*	*	*	*	*	*	*	*	*	*
	1	2	3	4	5	6	7	8	9	
	ZERO DEGREES									
	- .25 -									
	*	2								

FIGURE 1 MODEL GEOMETRY SHOWINGS NODES (*), NODE NUMBERS 1 THROUGH 45,
ELEMENTS 1 THROUGH 32, AND BOUNDARY CONDITIONS

N88-15614-35

116715
298

1987

NASA/ASEE SUMMER FACUTLY RESEARCH FELLOWSHIP PROGRAM

MARSHALL SPACE FLIGHT CENTER
THE UNIVERSITY OF ALABAMA IN HUNTSVILLE

PATTERN RECOGNITION TECHNIQUES
FOR
FAILURE TREND DETECTION
IN
SSME GROUND TESTS

Prepared By:	A. Choudry
Academic Rank:	Professor
University and Department:	University of Alabama in Huntsville Applied Optics
NASA/MSFC:	
Laboratory:	Structures and Dynamics
Division:	Control Systems
Branch:	Mechanical Systems Control
NASA Colleague:	Harry A. Cikanek
Date:	August 31, 1987
Contract No:	NGT-01-008-021

Abstract

The Space Shuttle Main Engine (SSME) is a very complex power plant and plays a crucial role in Shuttle missions. To evaluate SSME performance 1200 hot-fire ground tests have been conducted, varying in duration from 0 to 500 secs. During the test about 500 sensors are sampled every 20ms to measure the various parameters. The sensors are generally bounded by 'red-lines' so that an excursion beyond the red-line could lead to premature shutdown by the operator. In 27 tests, guided by the red-lines, it was not possible to effect an orderly premature shutdown. These tests became major incidents where serious damage to the SSME and the test stand resulted. In this study we have investigated the application of pattern recognition techniques to detect SSME performance trends that lead to major incidents. Based on the sensor data a set of (n) features is defined. At any time, during the test, the state of the SSME is given by a point in the n-dimensional feature-space. The entire history of a given test can now be represented as a trajectory in the n-dimensional feature space. Portions of the 'normal' trajectories and the failed test trajectories would lie in different regions of the n-dimensional feature space. The feature space can now be partitioned into regions of normal-tests and failed tests. In this manner it is possible to examine the trajectory of a test in progress and predict if it is heading into the 'normal-region' or the 'failure-region' of the n-dimensional feature space. In this study we have developed techniques to extract features from ground test data, as supplied by Rocketdyne, and develop feature space trajectories for the tests. The initial results as presented here, look very promising.

Introduction

ORIGINAL PAGE IS
OF POOR QUALITY

The Space Shuttle Main Engine (SSME) based on Hydrogen-Oxygen combustion is a very complex power plant employing numerous pumps, valves and ducts as shown in Fig.1. During a ground test about 500 sensors are used to monitor the state of SSME. Some of these sensors are used for the close loop control of SSME and are connected to a Computer System 'Engine Controller' as shown in Fig.2.

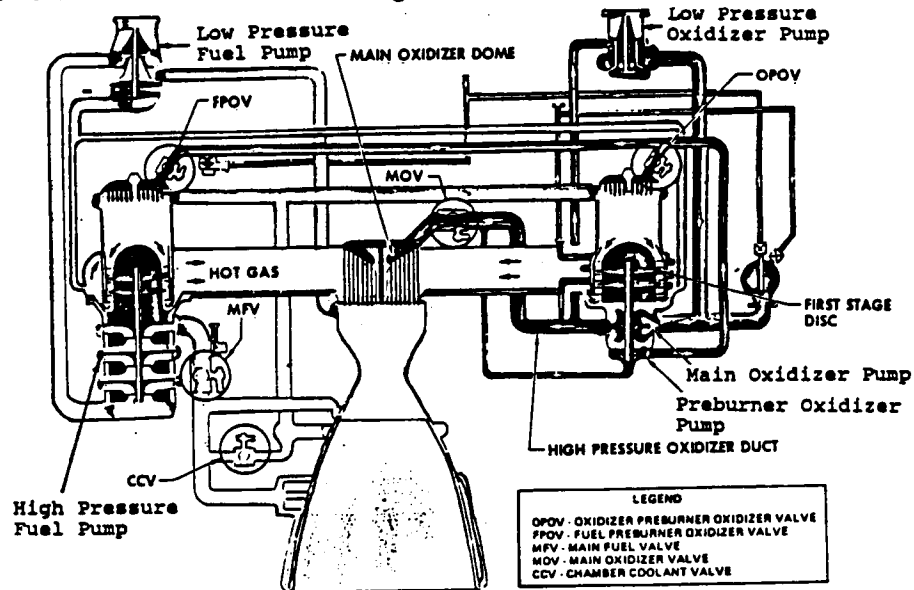


Fig. 1 SSME Propellant Flow Schematic

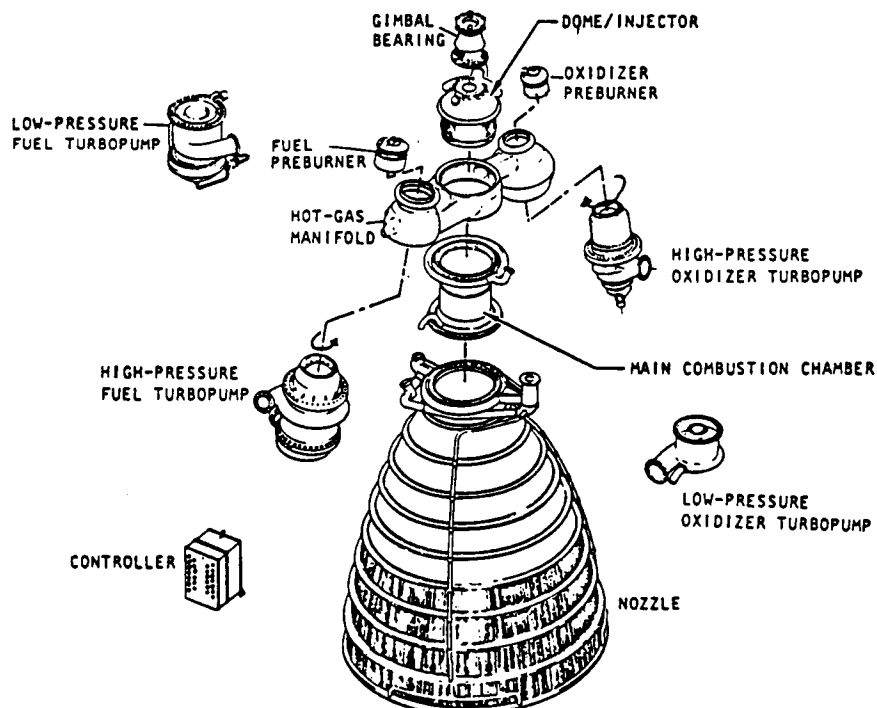


Fig. 2 Engine Controller & Hot Gas Manifold

There are 3 different data acquisition systems used to collect the sensor data (1,2), namely,

- Command and Data Simulator (CADS)
- Facility Recording (FR), and
- Analog High Frequency Recording (AHFR)

In Fig. 3, the salient points of these systems is shown. The engine controller uses 16 bit computations on 12-bit data words to perform close loop operation of the SSME. For the SSME Anomaly and Failure Detection (SAFD) analysis, as reported in (2), the CADS and FR data provide the bulk of the input.

In all about 1200 hot fire tests have been conducted on the SSME. In 27 tests the SSME went out of control and serious damage to the engine and the teststand resulted. A summary of some of the salient points of the ground tests is given in Table 1.

Considering that the replacement cost of an engine is ~\$50M, it is highly desirable to develop some technique for detecting failure trends which would allow an orderly shutdown of the SSME and thereby preventing a major incident (3). In (2) and (3) various techniques for failure detection have been suggested including the following,

- Generalized Likelihood Ratio (GLR)
- Generalized Likelihood Test (GLT)
- Voting
- Confidence Region Tests
- Kalman Filters
- Parameter Estimation
- Jump Processes
- Pattern Recognition.

The success of a technique will be determined by;

- detecting the fault fast enough to allow an orderly shutdown
- identifying the technical nature of the fault.

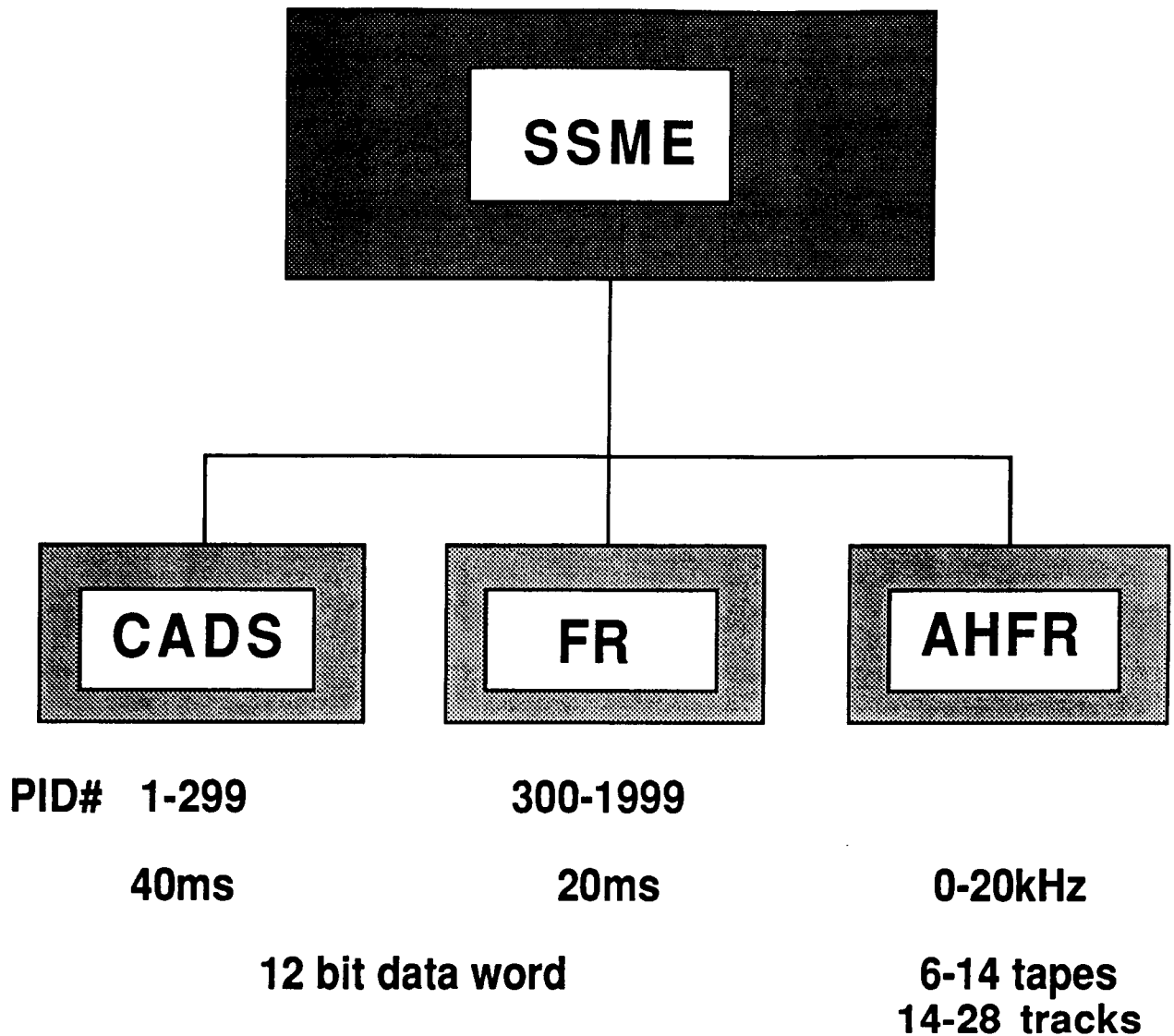


Fig. 3 SSME Data Acquisition System

TABLE 1. GROUND TEST SUMMARY

- -1200 HOT- FIRES**
- -27 MAJOR INCIDENTS**
- -TEST DURATION 0-500 SEC.**
- -300-500 SENSORS MONITORED**
- -SAMPLING RATE 50 Hz.**
- -DATA WORD 12 bits**
- -DATA TRANSFER RATE 0.5-1Mhz**
- -DATA VOLUME 0.1 - 1Gbits**

Associated criterion can best be described by the 'weighted truth-table' in Fig. 4 which shows the probability W for various actions.

		SAFD Decision	
		continue	shut-down
SSME Status	normal	$W1$	$W2$
	failure	$W3$	$W4$

Ideally, $W1=W4=1$ & $W2=W3=0$

Fig. 4 SAFD performance matrix.

Note that $W2$ being the probability of a false alarm should be zero, however, a small value, say 1%, may be acceptable. On the other hand $W3$ being the probability of a miss should indeed be zero, just as $W4$ should be 1. Various alternatives have been considered for implementing such a SAFD. We shall consider the use of Pattern Recognition (PR) techniques for SAFD. It should also be pointed out that much of the data processing in PR, as described below, can also be used for the other vital activities envisaged for the future systems, namely, real-time control, health assessment and condition monitoring (4,5).

Pattern Recognition (PR)

The fundamental premise for applying PR techniques is the observation that when systems fail due to internal causes there are always some warning signs that precede the event. Furthermore, the progression of a system from normal operating mode to anomalous (failure) mode does not happen at random but follows a pattern which can be analysed and explained. The object of PR technique, described here, is to identify the patterns that have led to failures and use this knowledge to look for warning signs in future tests and predict failures well in advance of their occurrence.

The current practice is based on red-lining the sensor outputs. The red-lining of n -sensors can be easily explained in terms of a polyhedron in n -dimensions as shown in Figs. 5(a,b,c). Each sensor is assigned a lower- and an upper-bound value for 'normal' operation and these define the two 'red-lines' for that sensor. For a 3-sensor case the state of the system, at a given time, can uniquely be defined by a point in the rectangular prismatic region of the S1-S2-S3 Space (S-Space), Fig. 5c. The collection of these state-points at successive times would define a trajectory in the S-Space. All the possible normal runs of the system would then be given by trajectories that lie entirely within the 'red-lined' rectangular prism as shown in Fig. 6. In principle, any trajectory that tends to approach a boundary and exit to the outside region is an indication of an imminent failure.

One can learn to detect the failure trends by examining the data of the 27 tests that resulted in failure and compare it with the normal test data. It is quite possible that the failure trajectories will reveal their different character (as compared to normal trajectories) even before coming close to the red-line polyhedron boundary as shown in Fig. 7.

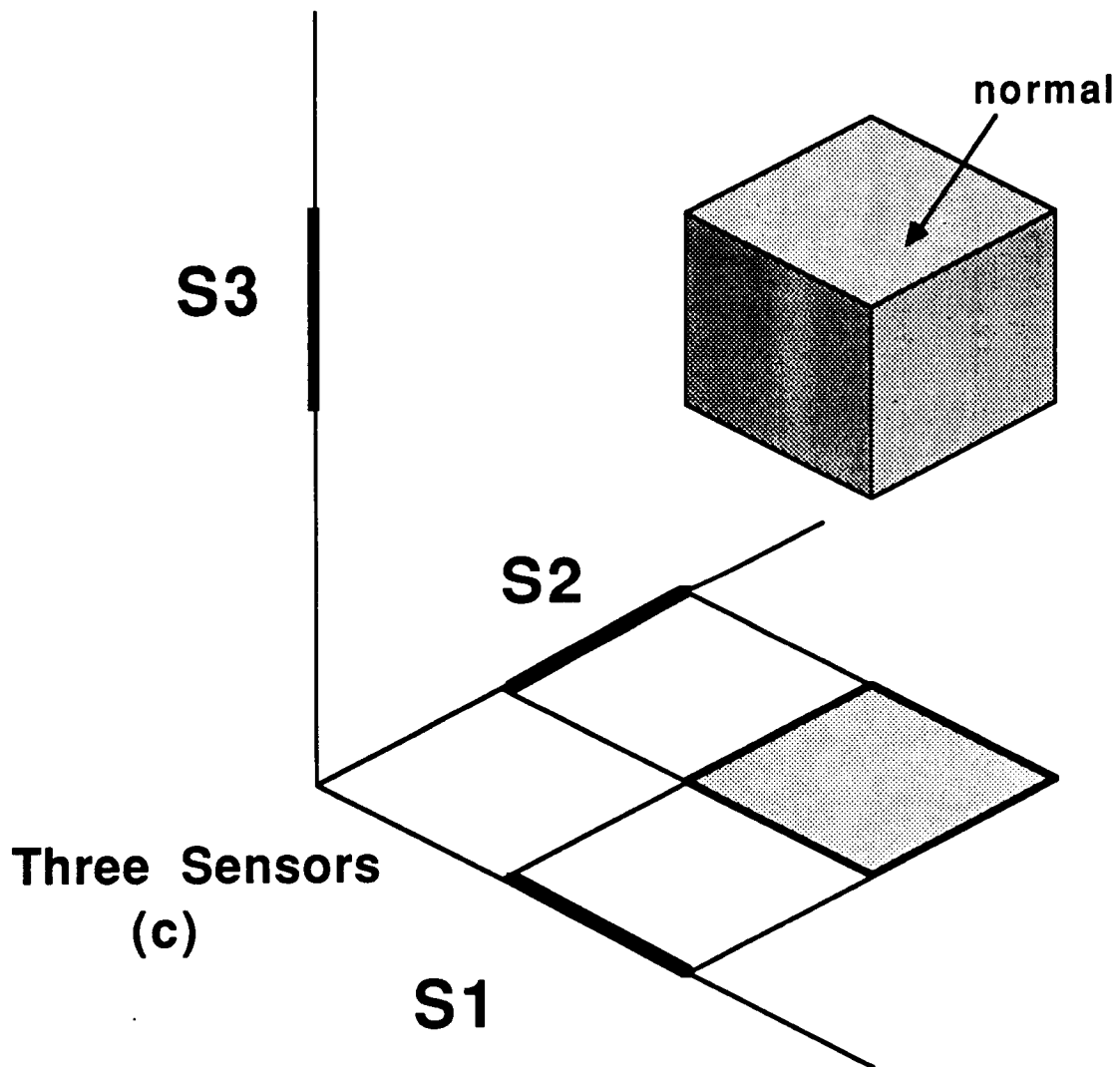
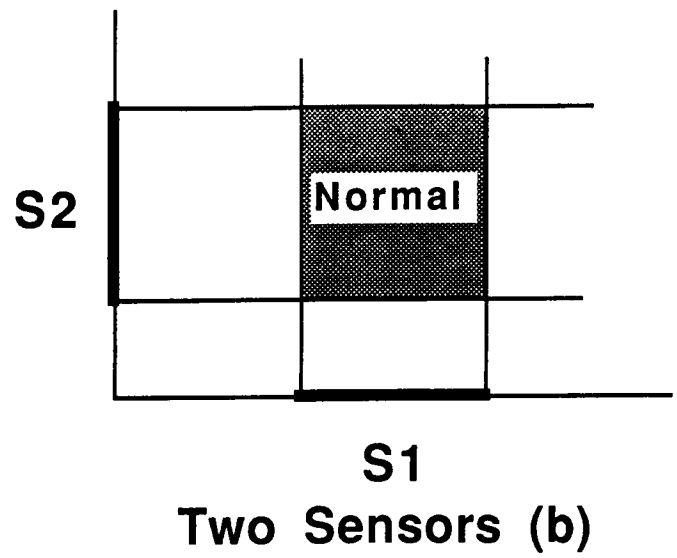
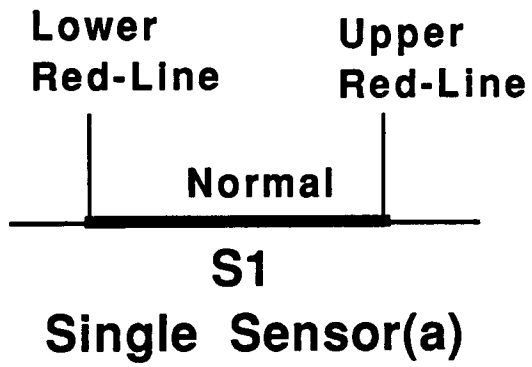


Fig. 5 Multi-Sensor Red-Lining

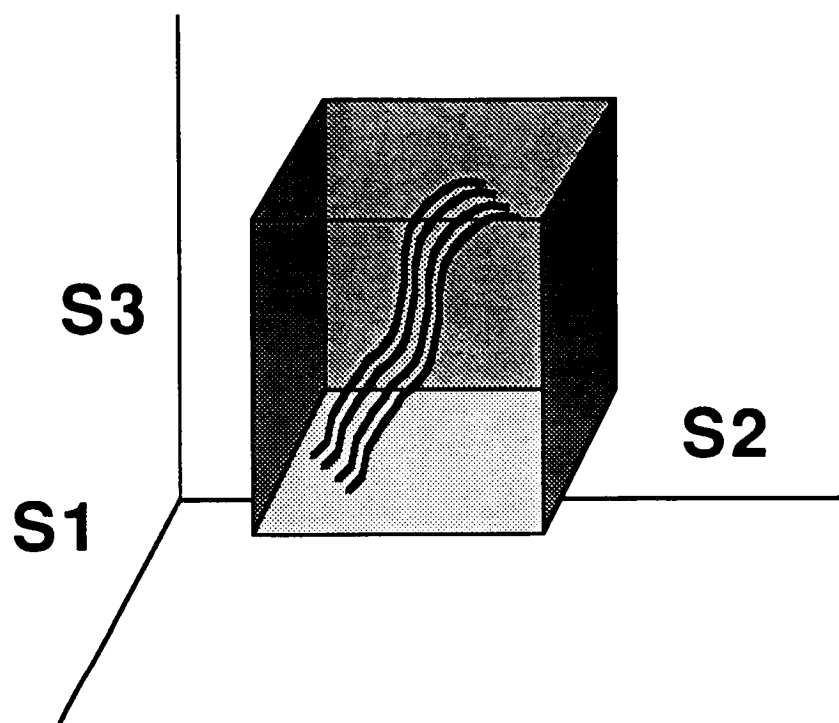


Fig. 6 System Trajectories in Sensor Space

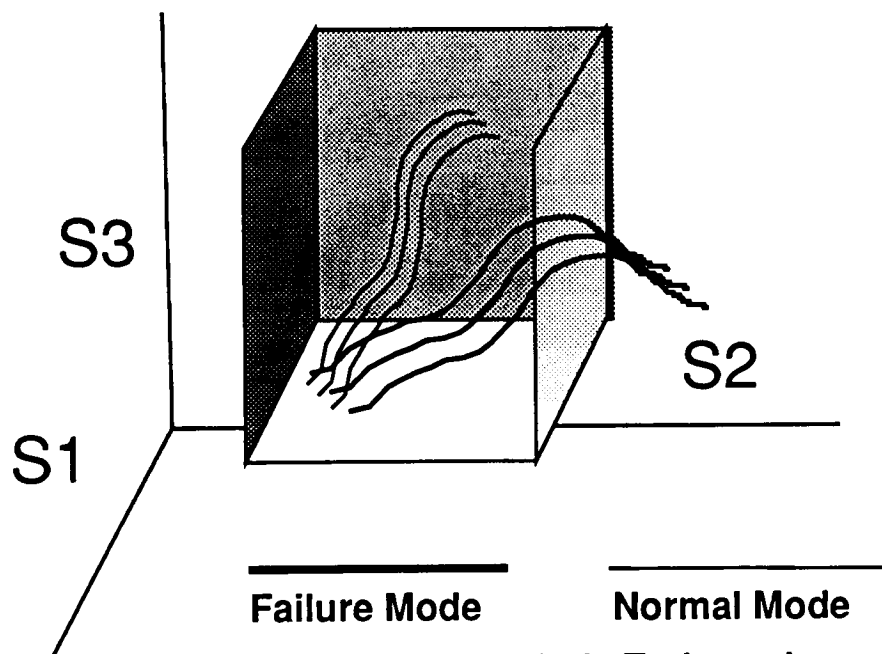


Fig. 7 Failure & Normal Mode Trajectories

There are two points that have to be considered in this context, namely,

1. The straight forward fixed red-lines for a sensor are adequate only for very special cases where no coupling among the sensors exists, i. e. the red-line for a given sensor is independent of the values of all the other parameters as measured by the rest of the sensors. Let r_k be the red-line for the k th sensor, then

$$r_k = c_k, \text{ where } c\text{'s are constants}$$

The software red-lines can be defined by replaing c 's by functions f_k so that,

$$r_k = f_k(S_1, S_2, \dots S_n), \text{ where } S_k \text{ is the } k\text{th sensor reading}$$

In real-time this implies that as the test is progressing the readings S_k are used to calculate the various r_k 's through f_k 's. This can become not only computationally quite cumbersome but the explicit form of f_k itself has to be known perhaps from a simulation model of the system. In principle, it is simple to build the simulation model in a modular manner (6), however, the ad hoc nature of such models leads to different control and real-time simulation models. By such models it is quite possible to determine most of the f_k 's, however, some crucial gaps may exist in this knowledge since not all the failure mechanisms are well understood.

2. Even if the f_k 's are known and the soft red-lines can be determined, there is yet another serious problem. In principle all red-lines, soft or otherwise, are based on a single time frame of the system without considering how the system got to the state represented by the time frame. Questions of the type; has the system reached its present state through a transient, slow drift, excessive noise or under a close-loop command etc., are not considered by red-line methods. The method proposed here considers the entire system trajectory and compares it with other trajectories to detect failure prone trajectories.

The PR technique we propose to employ here has two important steps,

- extension of the sensor-space into **Feature Space**
- **Segmentation** of the feature-space into normal- and failure-regions

Feature Space

The sensor space discussed above has two major drawbacks, namely,

-- For a truly multi-sensor system such as SSME the total amount of data is too large (about 100 Mbits) and can become too unwieldy for real-time processing.

On the other hand most of the data is of routine nature and a tremendous amount of data compression can be achieved by isolating and analysing only the deviations from the norm or the steady state. The norms can be defined as those values which can be calculated or predicted (assuming normal SSME operation) from a few key parameters e. g. power level, MCC pressure, throttle position etc. In the simplest case, only the deviations in sensor values, as compared to a moving average defined over a certain interval, are to be used for further analysis. This may even include deviations caused by closed- or open-loop control commands as may happen during throttling.

-- The sensor space, as based only on the sensor values, may not highlight the features important for SAFD.

This is based on the fact that the raw sensor readings, along with their red-lines, may themselves be not good indicators of impending failure. Further processing is often required to calculate features which are directly related to the failure modes. In Fig. 8 we show some of the features that can be defined for a given sensor. Starting with the raw value one can calculate first an average over a certain interval and then the deviation from it. From these one can also calculate the signal to noise ratio S/N which could be another feature. To detect drifts one can also calculate the local gradients as another feature. Similarly Fourier Transform of the signal (or the deviation), over a given time window, can be another feature, as shown in Fig. 8. One can also define 'compound' features involving data from more than one sensor. Thus, if needed, the net thermal flux, which may not be measured by a single sensor, can be calculated from the pressure, flow velocity and temperature as measured by sensors in the MCC and it can be used as a feature for failure detection.

Based on the above discussion, the sensor space is replaced by a feature-time space, where a feature is defined as the deviation from the norm or steady-state as calculated from some key parameters or by averaging over a specified interval. The state of SSME, at any given time will thus be represented by a state point in the feature space. In Fig. 9 a normal SSME run is shown in a two-feature space. In a normal run, all the state points cluster around the time axis as shown, since no large deviations are encountered.

S	F	Value	Devatn	S/N	Grad	FT(v')
		v	$v' = v - \langle v \rangle$		dv'/dt	
S1						
S2						
S3						
S..						
Sn						

Fig. 8 Sensor Values & Features

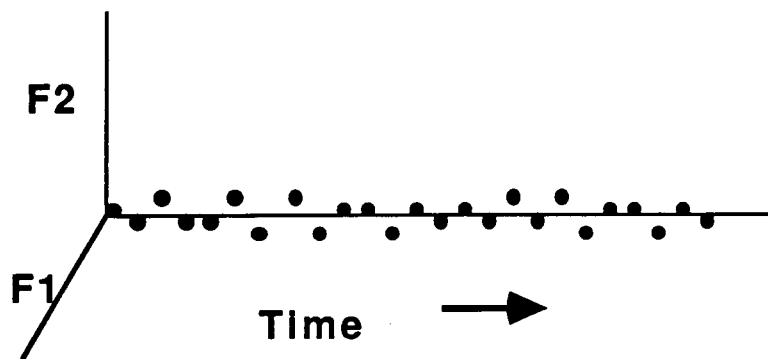


Fig. 9 Feature Space Representation of Normal SSME Test

Segmentation

Segmentation is the process of partitioning the feature space into clusters that can be identified with definite states of the system e. g. pre-failure or normal. An idealised illustration of this is shown in Fig.10 where the entire feature space has been projected along the time axis. All the points representing the normal runs should lie in a small region, cluster 1, around the origin. During normal runs there are large deviations caused by genuine excursions such as throttling etc. Such states of the system might show up as another region, cluster 2. It is anticipated that the deviations due to the failure modes will be of different nature and hopefully form another distinct region, cluster 3. An another form of the same situation is depicted in Fig.11 where an entire run is represented by a trajectory. A steady run trajectory would then lie entirely within cluster 1 whereas a controlled excursion in a run might cause the trajectory to migrate to cluste 2, but eventually return to cluster 1 after the steady state has been reached.

In practice, the situation may not be quite so clean cut, the clusters may not have so well defined boundaries and they may overlap. A number of powerful statistical techniques is available to locate cluster boundaries in such cases . It is also possible to assign to each state point, the probability of membership to a given cluster. One can also define a distance metric in the feature space to group points in clusters. In Table 2. (7) some of the commonly employed distance measures and the associated error bounds are shown.

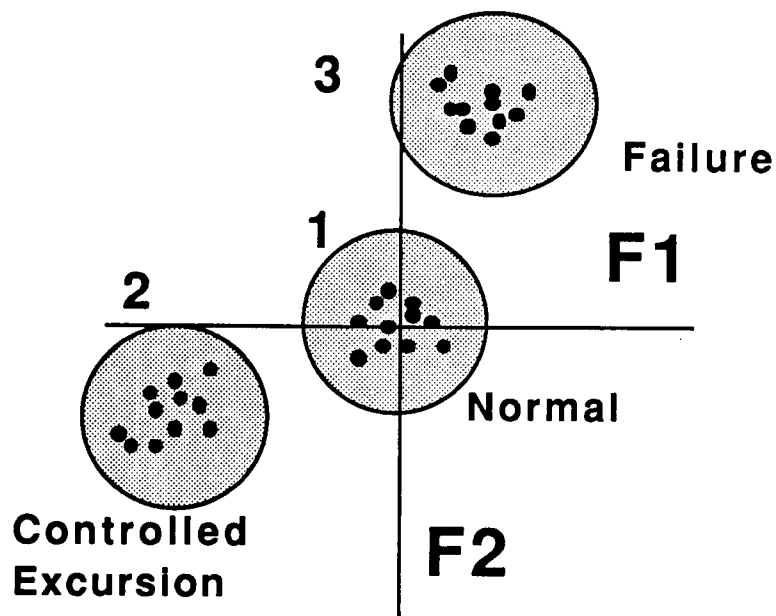


Fig. 10 Segmentation of the Feature Space

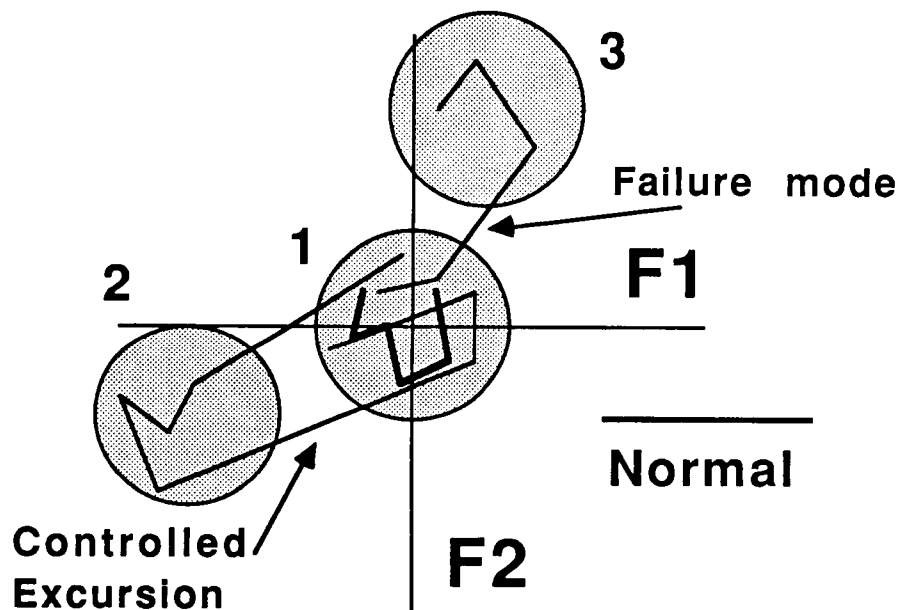


Fig. 11 Trajectories across the Clusters

Table 2. Distance Measure and Error Bounds

Name	Expression	Relationships
Bayes error probability	$P_e = 1 - \int_{S_n} \max_i [P_i p(X w_i)] dx$	<i>m Class Bounds</i>
1) Equivocation or Shannon entropy	$H(\Omega X) = E \left\{ - \sum_{i=1}^m P_i(w_i x) \log P_i(w_i x) \right\}$	$\frac{1}{2} [1 - B(\Omega X)]$
2) Average conditional quadratic entropy [Vajda (1970)]	$h(\Omega X) = E \left\{ \sum_{i=1}^m P_i(w_i x) [1 - P_i(w_i x)] \right\}$	$\leq [1 - \sqrt{B(\Omega X)}] \leq \frac{m-1}{m} \left[1 - \sqrt{\frac{mB(\Omega X) - 1}{m-1}} \right]$
3) Bayesian distance [Devijver (1974)]	$B(\Omega X) = E \left\{ \sum_{i=1}^m [P_i(w_i x)]^2 \right\}$	$\leq P_e \leq [1 - B(\Omega X)]$
4) Minkowski measures of non-uniformity [Toussaint (1973)]	$M_k(\Omega X) = E \left\{ \sum_{i=1}^m \left P_i(w_i x) - \frac{1}{m} \right ^{2k+1/2k+1} \right\}$	$= h(\Omega X) = R_{NN} = \frac{m-1}{m} - M_0(\Omega X);$ $P_e \leq \dots \leq R_{ENN} \leq \dots \leq R_{1NN} \leq R_{NN}$
5) Bhattacharyya bound [see Kailath (1967)]	$b(\Omega X) = E \{ [P_i(w_1 x) \cdot P_i(w_2 x)]^{1/2} \}$	[see Cover and Hart (1967) and Devijver (1974)]
6) Chernoff bound [see Kailath (1967)]	$C(\Omega X; s) = E \{ [P_i(w_1 x)^{1-s} \cdot P_i(w_2 x)^s] \}$	<i>Two Class Bounds</i> multicategory error: $P_e \leq \sum_{i=1}^m \sum_{j=i+1}^m P_i(w_i, w_j);$ $\frac{1}{2} [1 - [J_s(\Omega X)]^{1/s}] \leq P_e \leq \frac{1}{2} [1 - J_s(\Omega X)],$ for $s \geq 1;$ upper bound equals $[1 - B(\Omega X)]$, when $s = 2;$ $Q_{s+1} \leq Q_s; Q_0 = 1 - B(\Omega X);$
7) Kolmogorov variational distance [see Kailath (1967)]	$K(\Omega X) = \frac{1}{2} E \{ P_i(w_1 x) - P_i(w_2 x) \}$	
8) Generalized Kolmogorov distance [Devijver (1974), Lissack and Fu (1973)]	$J_s(\Omega X) = E \{ P_i(w_1 x) - P_i(w_2 x) ^s \}, 0 < s < \infty$	
9) A family of approximating functions [Ito (1972)]	$Q_s(\Omega X) = \frac{1}{2} - \frac{1}{2} E \{ [P_i(w_1 x) - P_i(w_2 x)]^{2(s+1/2s+1)} \}$	
10) The Matusita distance [see Kailath (1967)]	$\gamma = \left[\int_{S_n} (p(x w_1) - p(x w_2))^2 dx \right]^{1/2}$	γ gives the same bound as $b(\Omega X);$ two-class bound relations: $P_e \leq Q_s(\Omega X) \leq Q_0(\Omega X) \leq \frac{1}{2} H(\Omega X) \leq b(\Omega X)$ [see Ito (1972) and Hellman and Raviv (1970)]

Notation: $\Omega = (w_i, i = 1, 2, \dots, m; 2 \leq m < \infty)$ —a set of pattern classes; P_i is an *a priori* probability of class w_i ; X is a n dimensional vector random variable; S_n is a sample space of X ; $p(X|w_i)$ is a conditional probability density function; $P_i(w_i|X)$ is a posterior probability of class w_i conditioned on X ; $f(X) = \sum_{i=1}^m P_i p(x|w_i)$ —the mixture distribution; E is an expectation over S_n with respect to $f(X)$; R_{NN} is an m class infinite sample nearest-neighbor risk; R_{ENN} is a k nearest-neighbor risk.

the steps employed in the above technique are;

- definition of the features and construction of the feature space
- plotting of ground test data (of both normal and failure tests) as trajectories in the feature space
- segmentation of trajectories into failure and normal runs.

Implementation of these steps in practice is discussed below.

Results and Conclusions

the data from a run is stored on a number of magnetic tapes. the data for a short interval (10-100 sec.) and from a few important ssrs is combined into a single tape file. This tape file is read into a disk file which can be accessed by application programs. Fig. 12 shows the header, or the Run-Log, of the disk data file. This data, as can be seen from the first line, is for the time period 320 to 392 secs. of the run #901-364 which resulted in a failure. It also shows the srr PID#, the engineering unit used and the SSME component mnemonic.

9010364R*11		320.00000	392.15000
367	AP	MCC H.G. INJ PR	
940	GP	HPFP CLNT LN PR	
395	GP	MCC OX INJ PR	
410	AP	FPB PC NFD	
480	GP	OPB PC	
459	AP	HPFP DS PR NFD	
764	RM	HPFP SPD NFD	
854	GP	FAC OX FM DS PR	
858	GP	ENG OX IN PR 1	
878	GP	HX INT PR	
879	IC	HX INT T	
883	DP	HX VENT DP	

Fig. 12 Data File Header

An interactive, menu driven program has been written to process the data and extract the features. In Fig. 13 a beginning MENU of the program is shown. Various types of operations are available by choosing the appropriate code. these operations include both recursive and non-recursive filters, data compression, Logical Operations, FFT, Look-Up-Tables etc.

3	395	GP	MCC OX INJ PR
4	410	AP	FPB PC NFD
5	480	GP	OPB PC
6	459	AP	HPFP DS PR NFD
7	764	RH	HPFP SPD NFD
8	854	GP	FAC OX FM DS PR
9	858	GP	ENG OX IN PR 1
10	878	GP	HX INT PR
11	879	IC	HX INT T
12	883	DP	HX VENT DP

~ ~ TYPE SEQ#S OF COMPONENTS, END WITH 0

1

0

TYPE # OF DATA POINTS TO READ (LT.3000). 0=EXIT

3300

CHOOSE OPTION BY TYPING

DATA COMPRESS * * * * * =1

NON-REC FLTR * * * * * =2

RECURSIVE FILTER * * * * * =3

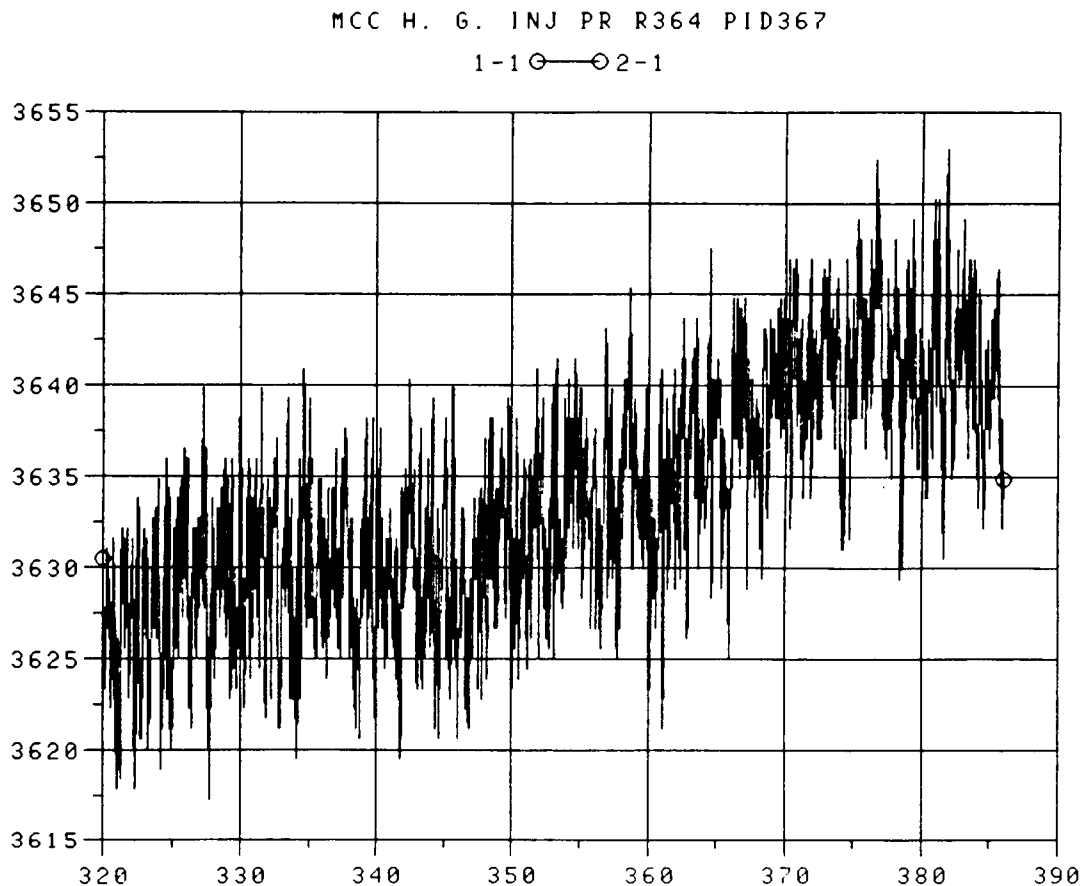
NRH-OPRNS * * * * * =4

FFT * * * * * =5

EXIT * * * * * =0

Fig. 13 Operations MENU

The first step is to read the raw data for a ssr by choosing the appropriate PID#. In Fig. 14 the data for PID#367, for the entire duration of 320 to 392 seconds is shown



FILES: 1=FOR001.DAT:486

Fig. 14. MCC H. G. INJ PR, PID #367, RUN 901-364

From the above figure it is clear that the data has some structure in the form of some distinct features, however, the noise level is fairly high to mask them. the first step we have taken is to reduce the 'observational sampling rate' through moving average. This is done in the following three steps;

C-4

1. Select a window size $N = 0, 1, 2, \dots$

$$\text{Let } M = 2N + 1$$

2. Form signal averages \underline{S}_k from the raw signal S_i

$$\underline{S}_k = \sum S_i / M ;$$

where $k = N+1, 2N+1, 3N+1, \dots, 2rN+1, \dots$ and

$$i = k-N, k-N+1, \dots, k+N$$

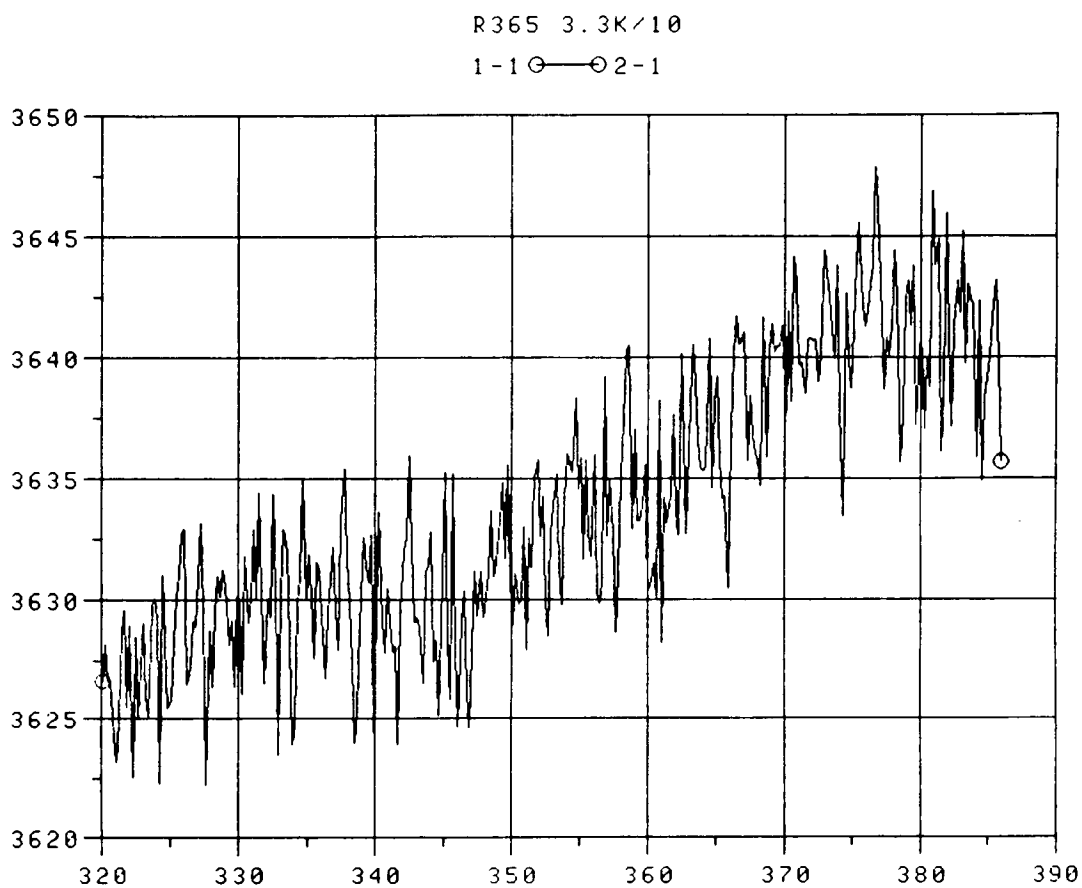
3. Replace the original signal S_i by \underline{S}_k . the sampling rate in the new signal, \underline{S}_k , is reduced by a factor of N .

In Fig. 15 the sampling rate of the data in Fig. 14 has been reduced by $N=9$, or compressed by a factor of 9. the program allows an interactive choice of N . the data in Fig. 15 still seems to have some noise which can be removed by various filtering techniques. As an illustration Fig. 16 shows the result of applying a non-recursive to the data of Fig. 15.

the data in Fig. 16 seems to have two distinct features, namely, a predominant frequency and a 'drifting background'. To separate these two components one can determine local averages over an interval larger than the hi-freq. wavelength as shown by the background line in Fig. 17. from this one can determine the zero-crossing points. A smooth curve can be fitted to these points to determine the background, as shown in Fig. 18.

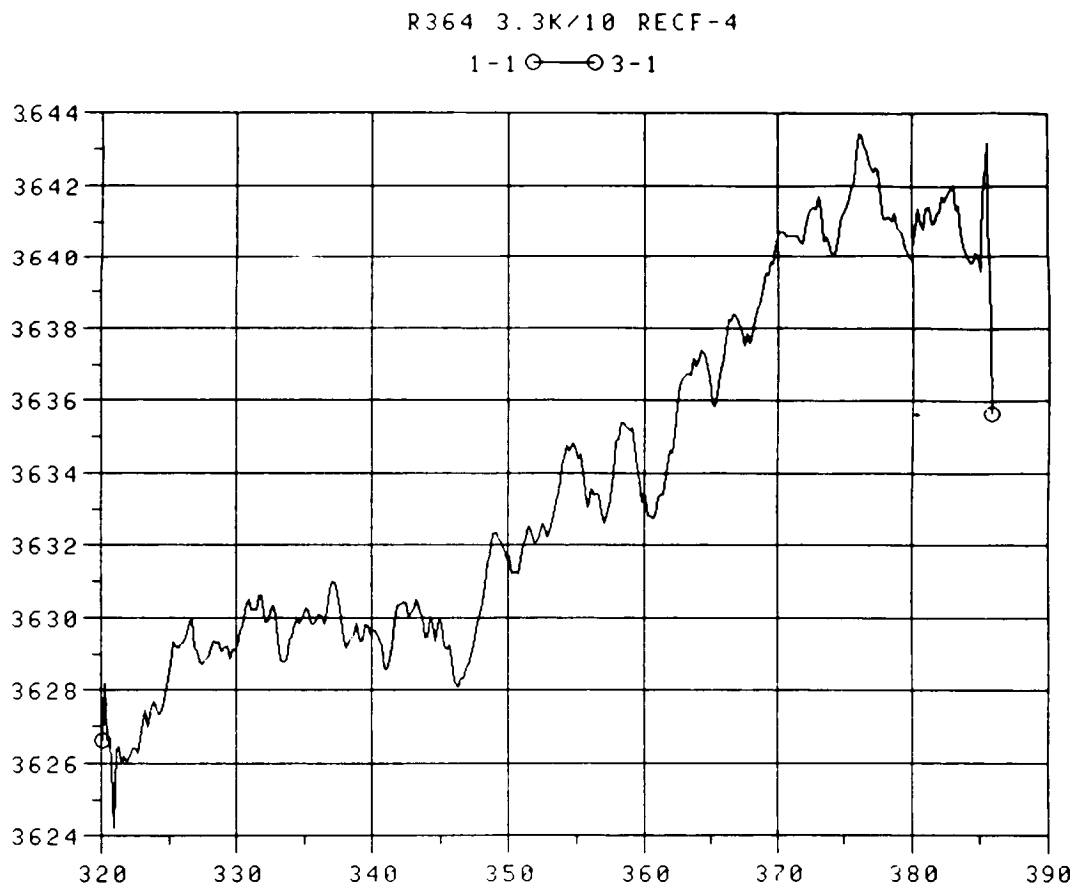
the background level, as found in Fig. 18 can now be subtracted from Fig.16 to give the hi-freq. component of the signal, as shown in Fig. 19. This signal can further be 'smoothed' to yield a 'cleaner' hi-freq. signal, as shown in Fig. 20.

Fig. 15 Reduced Sampling Rate Data, PID#367



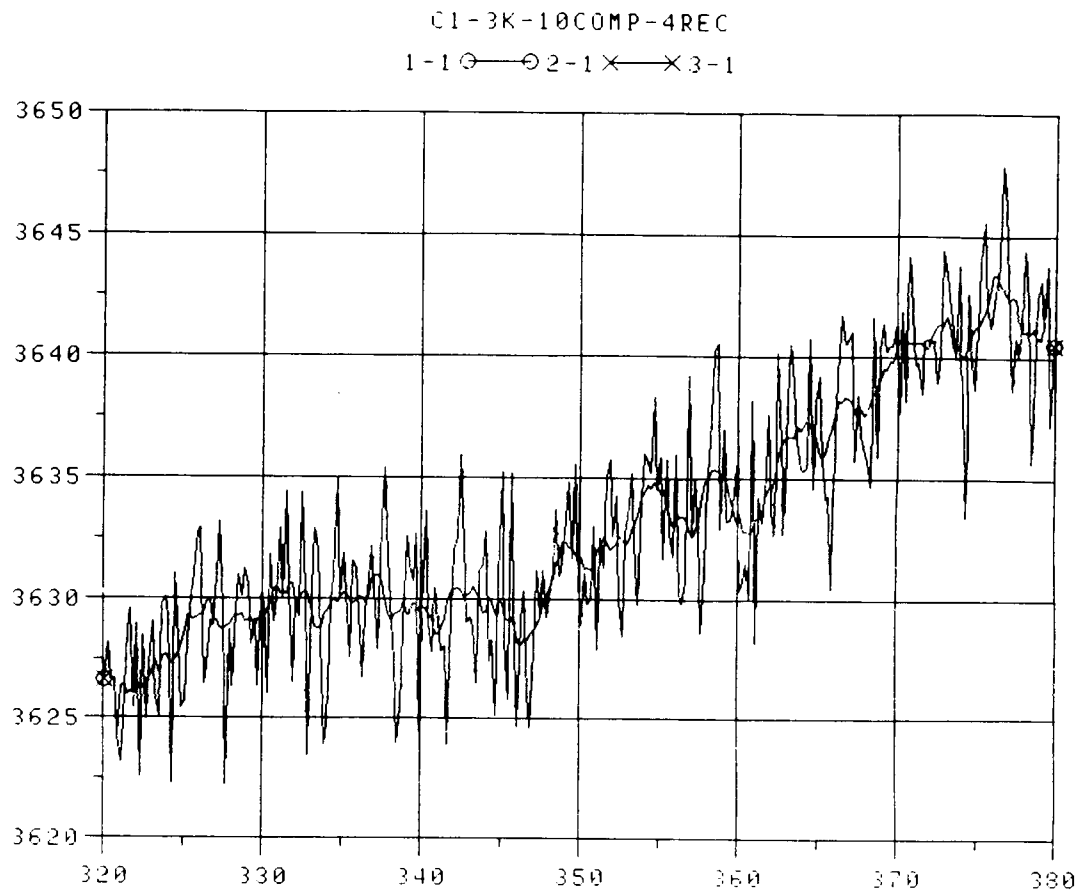
FILES: 1=FOR001.DAT:495

Fig. 16 High-Pass Filtered Data, PID#367



FILES: 1=FOR001.DAT:495

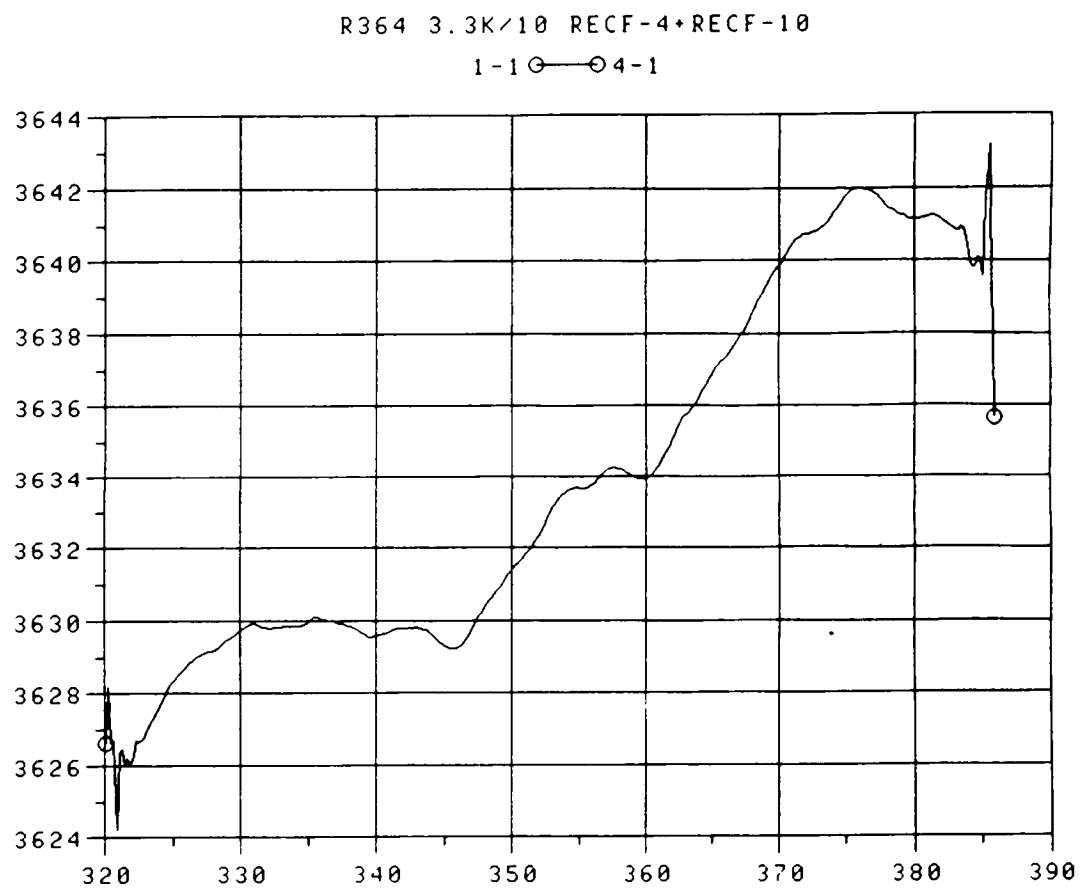
Fig. 17 Zero Crossing Points, PID#367



FILES: 1=FOR001.DAT;433

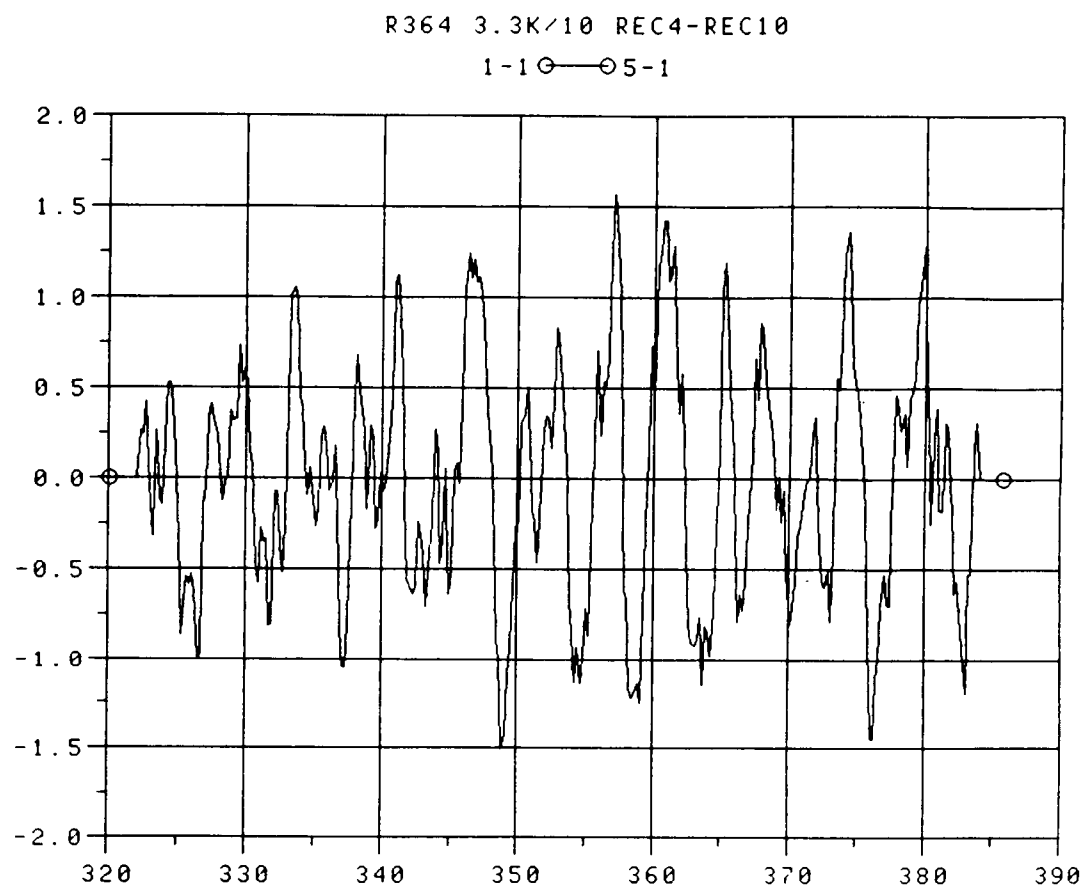
ORIGINAL PAGE IS
OF POOR QUALITY

Fig. 18 Background Trend, PID#367



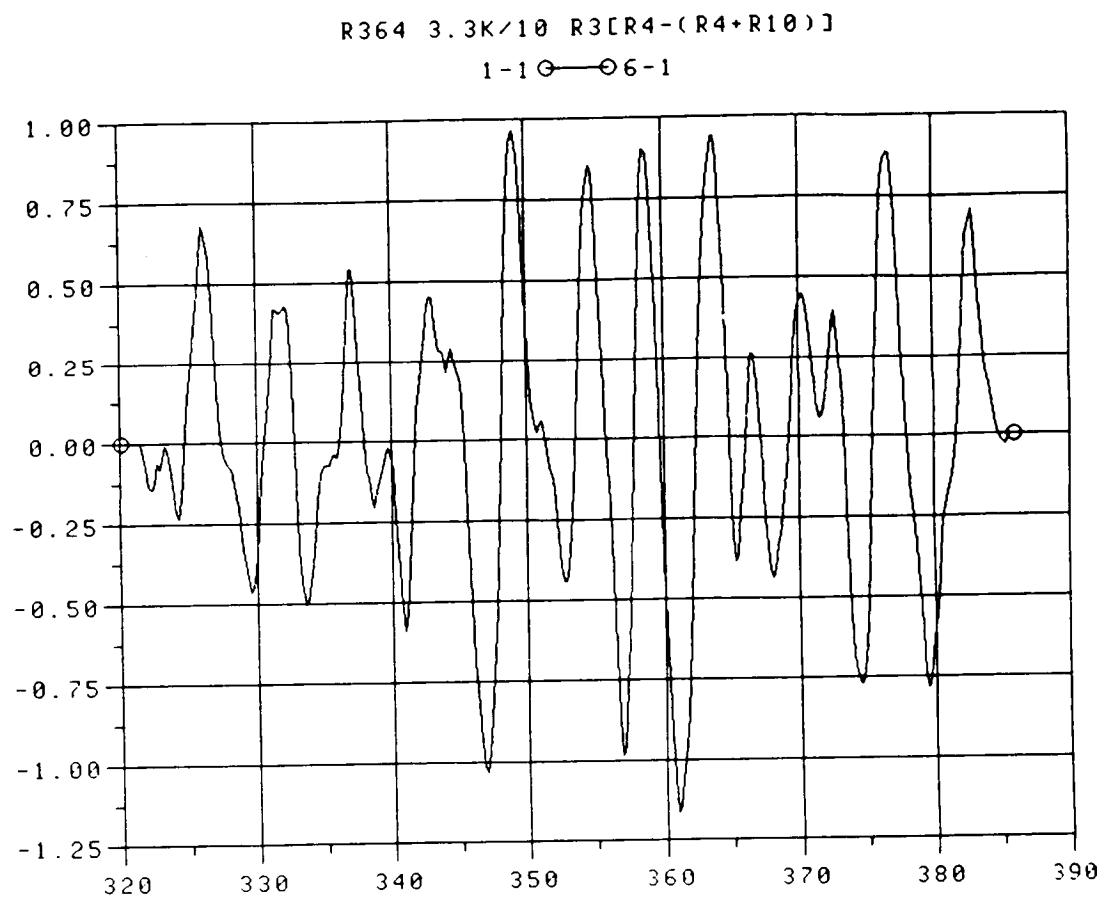
FILES: 1=FOR001.DAT:495

Fig. 19 High Frequency Data, PID#367



FILES: 1=FOR001.DAT:495

Fig. 20 Smoothed Hi-Freq Data, PID#367



FILES: 1=FOR001.DAT:497

the original signal of Fig. 14 can now be said to have two distinct features as represented by Figs. 18 & 20. the former is a slow drift with plateaus, whereas the latter is a high frequency jitter, which, if needed, can be Fourier analysed. This drift and the high frequency can now be taken as features for representation in the feature space as discussed earlier.

the above steps can now be repeated for the other sensors. the accumulation of all such ssrs and their features can be put in a single time-feature file to construct trajectories. the present computer facilities, with the limited memory allocation and the lack of on-line graphics, did not allow such implementation. A demonstration of this, however, was realised off-line at UAH facility and presented as a video film at MSFC.

From this study, the design of a comprehensive system to analyse the SSME ground test data has been made. the system should consist of;

1. A double density (6250/1600 bpi) tape drive interfaced to the host VAX/VMS environment.
2. An on-line RGB graphics display.
3. At least 20M disk memory.
4. A graphics kernel with hooks to application environment.
5. A two tiered version of software for interactive development and macro oriented operation.

Conclusions

- A feature space description of the SSME ground test data has been realised.
- An interactive program has been written to extract features from the ground test data.
- Techniques of pattern recognition have been identified to measure the deviations from the normal runs
- A design of a more comprehensive program has been made to;
 - A. Survey a large number of normal runs (about 50), and
 - B. Survey all the failed runs (27) and compare them with the above.
- Considering that an overall comprehensive review of neither the normal nor the failed runs exists it is highly recommended that an analysis environment of the type discussed above, be implemented.

References

1. SSME Controller
R. E. Mattox and J. B. White
GSFC/NASA Technical Paper. 1932 (1981)
2. Failure Control Techniques for the SSME.
Final Report, NAS8-36305, Rocketdyne Division.
3. 'SSME failure characteristics with regard to failure detection'
T. C. Evatt, L. R. Iwanicki, M. H. Taniguchi and H. A. Cikanek III
Adv. Earth-to-Orbit Propulsion Technology, NASA Conf. Proc. 2436
MSFC/NASA May 13-15, 1986
4. SSME Failure Detection
H. A. Cikanek III
Proc. Am. Control Conf. June 19-21(1985)282
5. Controls, Health Assessment and Condition Monitoring
H. A. Cikanek III
Proc. Am. Control Conf. June 18-20(1986)1943
6. 'DEAN: A program for dynamic engine analysis'
G. C. Sadler and K. J. Melcher
NASA TM 87033, July 1985
7. 'Patterns in Pattern Recognition'
L. Kanal
IEEE Trans IT-20(1974)697

N88-15615

514-60
116716
20P

1987

NASA/ASEE SUMMER FACULTY FELLOWSHIP PROGRAM

MARSHALL SPACE FLIGHT CENTER
THE UNIVERSITY OF ALABAMA

MICROPROCESSOR CONTROL AND NETWORKING FOR THE AMPS BREADBOARD

Prepared by:	Stephen A. Floyd
Academic Rank:	Assistant Professor
University and Department:	The University of Alabama - in Huntsville, School of Administrative Science Department of MIS/MSC
MSFC Colleague:	David J. Weeks
Date:	September 1, 1987
Contract No.	NGT-01-008-021 The University of Alabama in Huntsville

ABSTRACT

Future space missions will require more sophisticated power systems. This sophistication necessarily implies higher costs and more extensive crew and ground support involvement. In order to decrease this human involvement, as well as protect and most efficiently utilize this important resource, NASA has undertaken major efforts to promote progress in the design and development of autonomously managed power systems. Two areas being actively pursued within this effort are autonomous power system (APS) breadboards and knowledge-based expert system (KBES) applications. APS breadboards are viewed as a requirement for the timely development of knowledge-based systems. Not only will they serve as final testbeds for the various KBES applications within this domain, but they will in fact play a major role in the knowledge engineering phase of their development.

The current power system breadboard designs are of a distributed microprocessor nature. The distributed nature, plus the need to connect various external computer capabilities (i.e., conventional host computers and symbolic processors), places major emphasis on effective networking.

This paper presents the communications and networking technologies for the first power system breadboard/test facility in the agency. Primary emphasis is on the task of networking the host computer into the system.

ACKNOWLEDGEMENTS

The author wishes to express sincere appreciation to all those involved in the NASA/ASEE summer faculty program. Specifically I wish to thank Dr. Gerald Karr, Ms. Ernestine Cothran and Dina Engler for their professional administration of the program.

To all the employees of Marshall's Electrical Power Branch who made my summer a very enjoyable and rewarding one, I also express my sincere gratitude. In particular I wish to express my appreciation to Mr. Dave Weeks who sponsored me in the laboratory and also to Louis Lollar, Norma Dugal-Whitehead and Bryan Walls with whom I also interfaced on a regular basis. Appreciation is also extended to all the Branch and Laboratory personnel for their friendly and cooperative spirit.

INTRODUCTION

As the exploration of space continues missions become much more complex and much longer in duration. Future missions such as Space Station, spaced-based radar, communication and surveillance satellites, strategic defense initiative (SDI) systems and military aircraft will thus require more sophisticated and intricate electrical power systems (EPS). Space power is an extremely precious resource. The fact that almost every subsystem, especially those that support the human elements for manned missions, is dependent on power plus the fact that space power has historically cost about \$1000.00/KWH versus \$.05 per terrestrial KWH has placed space power high on NASA's priority list of research efforts. As was learned from Skylab, for which 15-18 ground support personnel were required to augment extensive crew involvement for an 8KW system, a major effort had to be directed toward autonomously managed electrical power systems.

Automating activities ordinarily performed by humans was seen as the primary means of reducing both airborne and ground support efforts and costs. Additionally, more fully autonomous power systems (as well as other subsystems) will be a necessity for deeper unmanned exploration of space where missions will require decisions and actions in "real-time". The time lags incurred with data transmission and remote intervention will not be acceptable in allocating and protecting the precious electrical power resources. In 1978, therefore, the Office of Aeronautics and Space Technology at NASA Headquarters directed NASA to undertake efforts towards accomplishing such autonomy. Since that directive various NASA efforts in conjunction with several contractors (including Martin Marietta, Rockwell/Rocketdyne, Boeing, TRW, Hughes and Ford Aerospace) and Universities (among them Auburn, University of Tennessee, Tennessee Tech., University of Alabama-Huntsville, Vanderbilt and Carnegie Mellon) have made much progress in the realm of space power automation.

It was realized early on in power system investigations that autonomous systems would require a certain amount of embedded intelligence to supplement the already proven more conventional computer approaches. Thus much of the current research effort is focussed on artificial intelligence techniques. More specifically these efforts are directed toward the application of expert and knowledge-based systems (ES/KBS) technologies in such application areas as: energy storage management, power management (i.e. generation, monitoring and allocation), load management (i.e. prioritization and scheduling) and fault management (i.e. prediction, detection and advisement/recovery) [1].

The term "expert system" (ES) refers to a software system which performs a complex, well defined task using the same input information and problem solving strategies as a human expert. Additionally, an

expert system possesses the capability to make accessible to the user the reasoning logic it uses to perform the task. It is implied that the expertise captured by such a system has its origins in the experience that one or more humans have accumulated while performing a given problem solving task. The term "knowledge-based system" (KBS) refers to a software system much like an expert system but which implements a body of problem solving knowledge which may come from any of several sources including text books, humans (in the form of expertise or more general experiential knowledge) or others.

It is important in the domain of space power system applications to draw the distinction between these two types of systems. The reason for this is that this is a very young domain and "experts" with experience managing space power systems do not exist. However, the experience of humans working in this arena coupled with more general knowledge about power subsystems and components make it possible to develop what for the purposes of this paper will be referred to as knowledge-based systems expert systems (KBES).

Though few doubt the important role that KBES approaches will play in space power automation the domain is one which offers more complex challenges than those to which the technology has already been successfully applied. One of the approaches to overcoming some of these challenges is the development and utilization of fairly realistic power system breadboards and test beds on which KBES technologies can be developed and validated. With such facilities many of the tasks of knowledge engineering can be performed and the archiving of expert problem solving knowledge necessary for autonomous operation can proceed at a much more rapid rate than through actual mission experience alone [2,3].

This report deals with the current efforts of the Electrical Power Branch at Marshall Space Flight Center to complete the operationalization of the Autonomously Managed Power System (AMPS). More specifically, it will be concerned with the networking of the various AMPS components with primary emphasis on networking the host computer system. It was these efforts in which the author participated while on the NASA/ASEE fellowship.

OBJECTIVES

The objectives of this work included:

1. Become familiar with the software and networking environments of the AMPS breadboard.
 - a. compile pertinent documentation available at MSFC for attaining such familiarity.
 - b. procure/request all additional documentation.
 - c. become familiar with proposed host computer system (i.e., hardware, operating system and networking capabilities).
2. Installation of NCR Tower communications board.
3. Evaluation of extent of previously perceived incompatibilities in connecting the NCR Tower host to the AMPS breadboard.
4. Proposal of solution strategy for software modification and development.
5. Undertake implementation of accepted solution strategy.

THE AUTONOMOUSLY MANAGED POWER SYSTEM (AMPS)

Amps Overview

The Space Power Distribution System Technology program commenced in 1978 as an overview study to define and assess multi-hundred kilowatt photovoltaic electrical power system concepts and technology development requirements. Based upon the study an integrated system-level approach to technology development was taken to encompass the following three tasks:

1. To define a reference 250 kilowatt electrical power system concept for low earth orbiting satellites which will be used to identify the related technology development needs and provide an investment criteria and payback assessment tool to guide the selection of technology development options.
2. To pursue the technology needs for the autonomous management of electrical power systems by developing selected controller hardware for a power management subsystem and the related algorithms of the power management subsystem.
3. To design, develop, and assemble a test bed that simulates a representative portion of the autonomously managed power system and the interfacing power sources, energy storage, and loads.

The result of these efforts has been the delivery, by the TRW Defense & Space Systems Group, of the autonomously managed power system test facility/broadboard (AMPS) to Marshall Space Flight Center Electrical Power Branch test facility [4,5].

The AMPS breadboard (Figure 1) is an end-to-end electrical power system with a power generation simulator, energy storage simulator and a power management and distribution system. AMPS is the result of direction by NASA Headquarters to address long-term, high power needs for future low earth orbit spacecraft. The system is representative of a multichannel, multikilowatt, utility-type power system and provides important new capabilities for demonstrating the feasibility of new technologies including knowledge-based expert systems. The power management portion of AMPS has three embedded micro-processor based controllers networked with Ethernet. This management area performs data collection and control functions required for autonomous operation and is therefore the area which will ultimately interface (via the Ethernet) with future ES/KBS developments. Potential ES/KBS include fault management, battery management, data reduction, trend analysis, state-

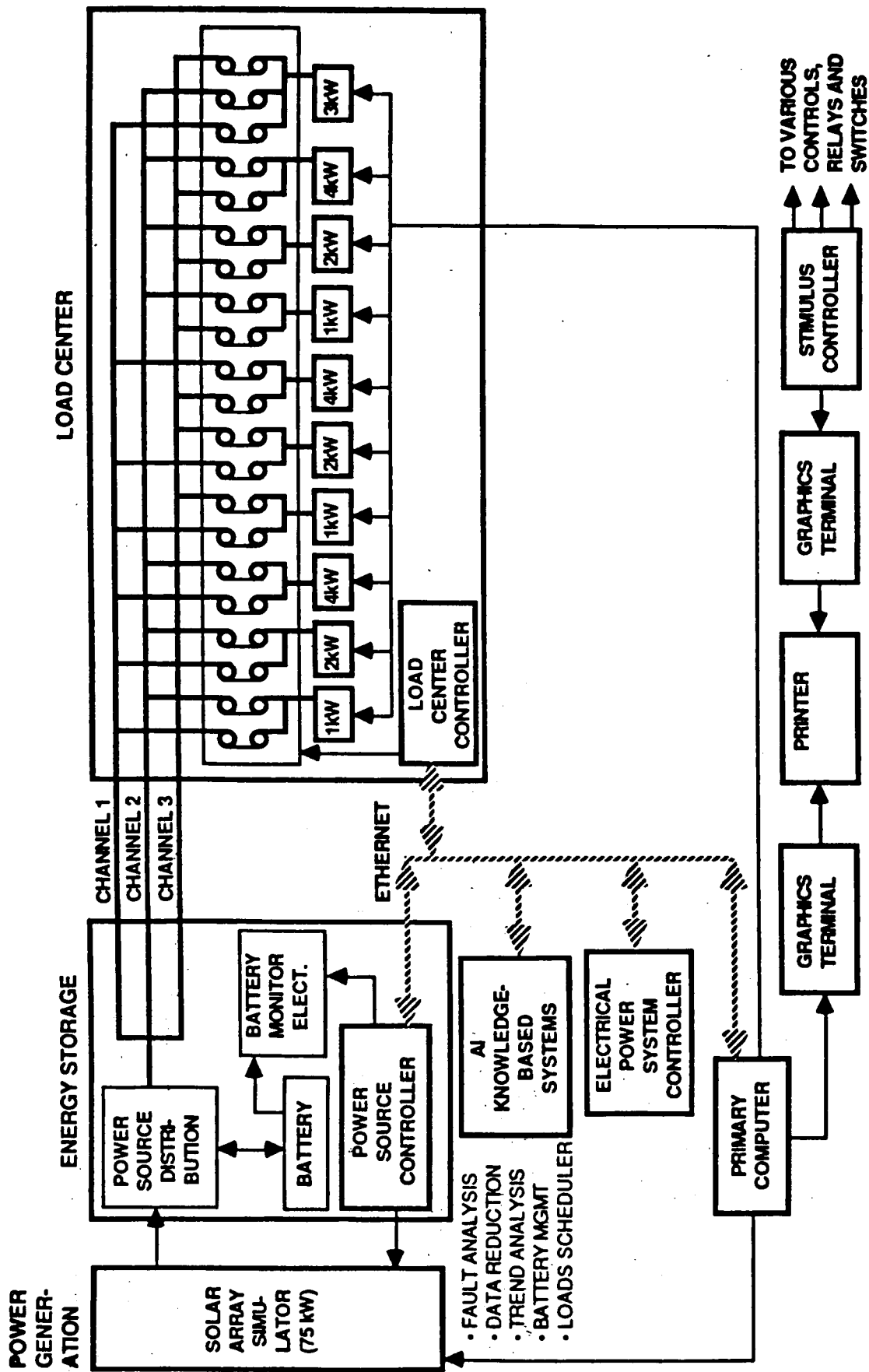


Figure 1 Autonomously Managed Power System

of-health monitoring and payload contingency scheduling. The breadboard is being connected to a host computer environment to include a graphics terminal and color ink-jet printer.

The current phase of the AMPS effort entails the actual development and testing of the proof-of-concept breadboard. The breadboard consists of:

- one 24 kilowatt load center;
- a 75 kilowatt solar array simulator (Power Generation);
- a 168 cell, 189 ampere hour, 240 volt nickel-cadmium battery with associated electronics (Energy Storage);
- a power management and distribution system consisting of three power channels (16 kilowatt total) and a load center with 21 load buses with associated switches and 24 kilowatts of load;
- a host computer system consisting of a primary computer (NCR Tower XP), two graphics terminals (Tektronics 4125P and 4105A), a color ink-jet printer (Tektronics 4691), and a stimulus controller (a second Tower XP);
- and the internal distributed controllers.

The Power Management System (PMS) is the "internal brains" of the actual breadboard and consists of three subsystem controllers and associated interface technology. The Power Source Controller (PSC) controls the power generation solar array simulator (SAS) and the energy storage system [6]. The Load Center Controller (LCC) is responsible for the load center while the Electrical Power System Controller (EPSC) functions as the breadboard interface to the outside world (host computer system) and is hierarchically above the PSC and the LCC [7,8]. The three internal controllers transmit all messages in the broadcast mode. These controllers utilize the FORTH computer language (using PolyForth) and are functional within their areas of domain as well as networked. At this time, no controller requests data or sends commands to the EPSC. Software for these controllers will continue to be developed in-house at MSFC and potentially by contractors.

Current efforts and those in which the author was involved under the summer fellowship are focused on attaching the NCR Tower XP multi-tasking host computer (which employs Multibus and has an installed ENP-30 communications board) to the Ethernet to allow the user to input commands to the breadboard for control and testing purposes and to receive data from the breadboard in order to monitor breadboard performance. The Tektronix 4125P graphics terminal, which functions as the user station, must be able to easily utilize the data received from the Tower and the Tower must be able to easily take data from the 4125P to send out over Ethernet. These two computers are currently physically

connected. The NCR Tower XP specifications are provided below:

- Processor/memory controller II (MC 68010 CPU)
- Seven Multibus I/O slots
- 1 MB error correcting RAM memory
- one 5-1/4" flexible disk drive (1 MB)
- one cartridge tape drive (45 MB)
- one 8-channel HPSIO controller
- Unix V operating system
- C compiler
- FORTRAN/77 compiler
- menu driven software for system reconfiguration

The next several sections of this report will be primarily concerned with providing a more detailed description of the microprocessor and communications hardware and software of the Power Management Subsystem. For a detailed discussion of the other hardware components and their configuration in the AMPS breadboard the reader is referred to references.

Power Management System

The power management subsystem (PMS) as presented in Figure 2 consists of three microprocessor based controllers that communicate by means of an Ethernet LAN and functions to monitor and control the complete electrical power system from generation to load. This allows efficient and predictable performance of monitoring, processing, controlling and recording functions. The PMS is a decentralized processing system consisting of the three microprocessor based controllers plus I/O circuitry, command and display interfacing hardware and a data bus. The power source controller (PSC) and the load center controller (LCC) each perform functions related to their respective centers. The PSC performs the processes and procedures required to operate the power source and energy storage devices and their associated power electronics hardware. The LCC collects load current, load voltage, switch status and switch temperature data from each remote power controller. The third controller, the electrical power system controller (EPSC), performs subsystem level functions such as energy planning and allocation, load assignments, and command and data interfacing to the host computer. The I/O circuitry connects the controllers to temperature, voltage, current and status sensors as well as to the various power control circuits.

The configuration of the elements in the PMS is shown in block diagram form in Figure 3. As can be seen each controller contains a microcomputer board and communication board. These boards are Motorola 68000 based and offer the availability of a high level language (FORTH). Additionally the PSC and LCC contain the necessary digital and analog I/O boards to accomplish their previously described functions. The controller components communicate via a parallel data bus which supports multiple processors and a large number of commercially available board level products. The communication board along with the data bus

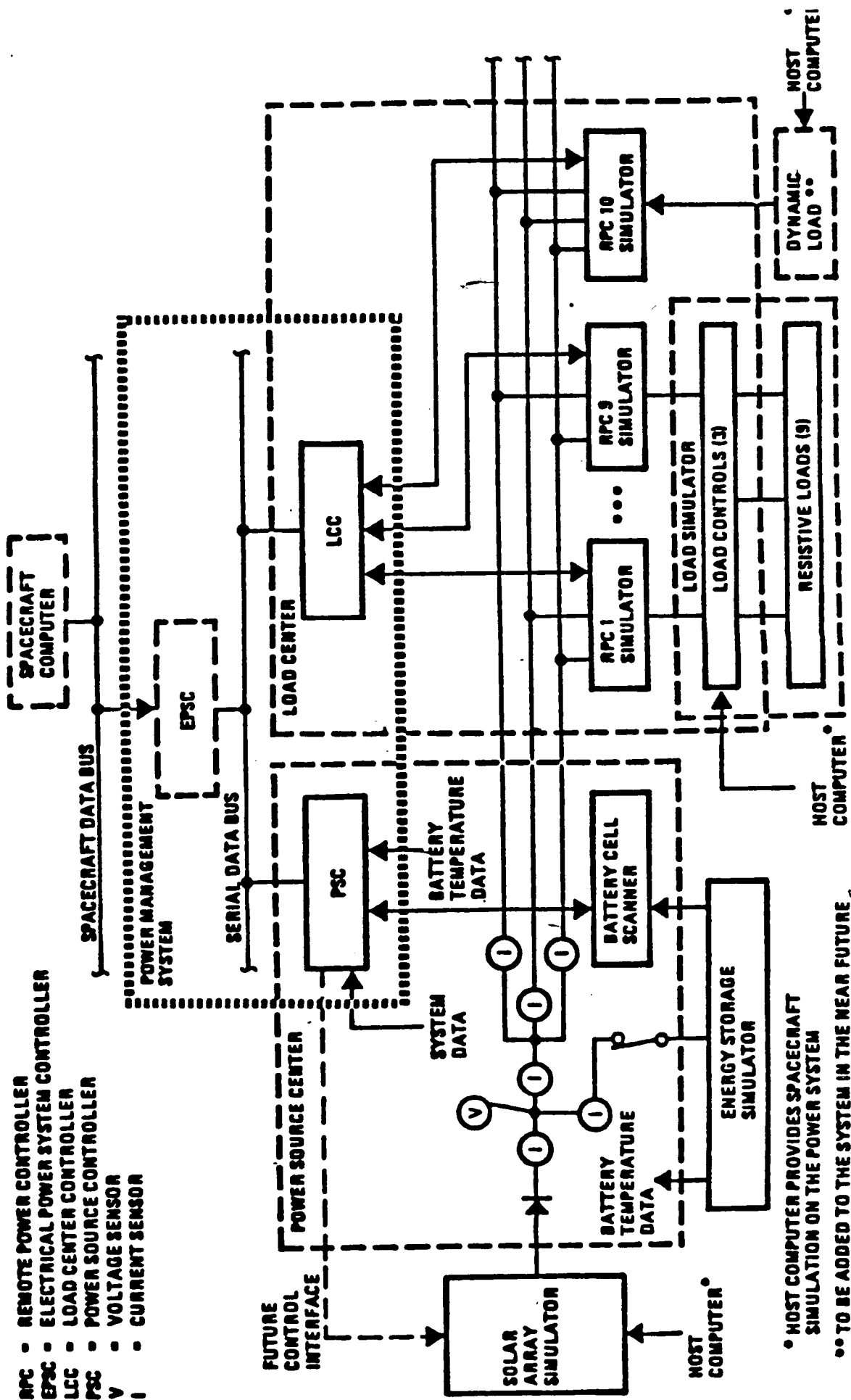
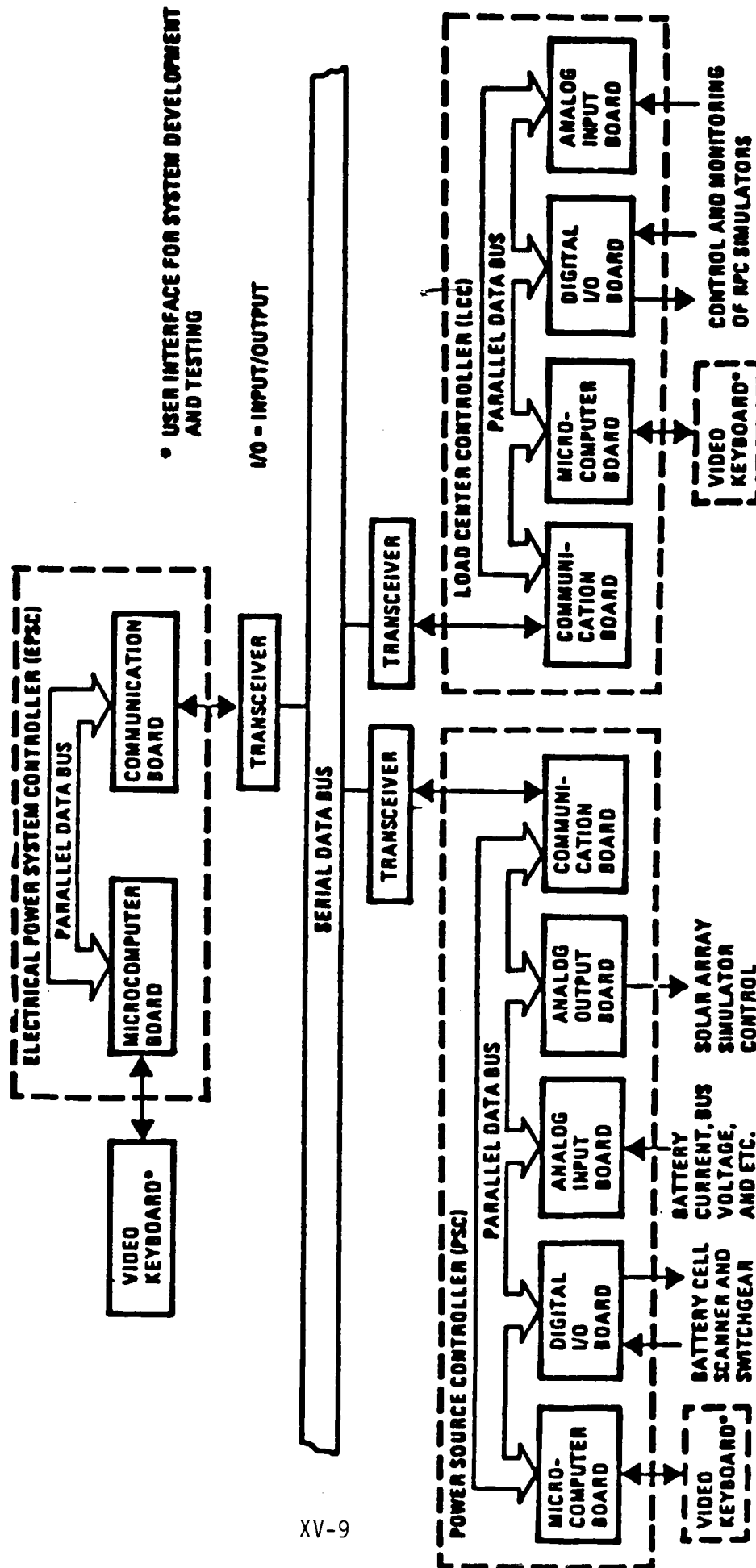


Figure 2 AMPS Hardware and Configuration



XV-9

Figure 3 Block Diagram of the Power Management System

transceiver provides the ability to exchange information between the controllers and host computer along the CSMA-CD serial data bus. In the current system all messages are broadcast and each controller determines applicability of messages by decoding.

The microprocessor is a Motorola 68000-R12 12.5 MHz (16/32 bit) MSBC1 processor. The board implements full address range (16 megabytes, 24 bits) and bus arbitration for single and multi-master systems and has been designed for compatibility with existing Multibus products. The board contains 256 Kbytes of dual-port RAM and 32 Kbytes of EPROM along with four serial I/O ports that can be used for interfacing with peripheral equipment.

Ethernet Node Processor

The Ethernet Node Processor communications board is a model ENP-30 manufactured by CMC and is a high performance communications processor[9]. It provides the physical interface and logic necessary for attaching information processing devices to the Ethernet LAN to allow a high speed exchange of information. The ENP30 provides the communication interface between the MSBC1 and the AMPS LAN. Functionally, the ENP30 in the EPSC must process messages that are generated and formatted in the MSBC1 and transmit these messages over the LAN. If a response to the LAN message is required, the ENP30 must process the incoming message from the LAN and deliver it to the MSBC1. Each ENP contains node-specific software, as well as industry standard protocol software for exchanging information throughout the network. The ENP architecture includes an MC68000 microprocessor unit (MPU), a local area network controller for Ethernet (LANCE), a 128 Kbyte dual-access DRAM for buffering in-coming and outgoing messages and application software, a 32 Kbyte EPROM for protocol processing and debug code, and a bus interface circuitry for connection to a host information processing system. The MPU responsibilities include moving commands and data to and from system memory, responding to and generating system bus interrupts, executing, upper layers of the selected protocol, and running the communications firmware, the KI Kernel [10]. The ENP30 communicates with the other PSC components through the IEEE-796 backplane. Communications to the Ethernet data bus is accomplished through a serial interface adapter (SIA) which performs encoding/decoding necessary for interfacing the LANCE to Ethernet. Features of the ENP-30 include:

- 10 MHz MC 68000 MPU
- 128k or 512 byte dual-access DRAM with parity and no wait states
- Up to 64 k bytes EPROM (2 sockets)
- MULTIBUS (IEEE 796) A24:D16 master and slave interface for Host to ENP communications
- Node address PROM contains a world-wide unique address issued by Xerox Corporation.
- A programmable interrupt for protocol software timing.
- Local Area Network Controller for Ethernet (LANCE)

- Buffer management structures in shared local RAM
- DMA to shared local RAM
- Line access protocol (CSMA/CD)
- Extensive diagnostics and error reporting
- Serial Interface Adaptor (SIA)
 - Manchester encoding/decoding
 - Transceiver cable interface
- Dual RS-232 Asynchronous Serial Communication Ports (DUART)
- MULTIBUS interrupt (NBVI)
- MULTIBUS to onboard processor interrupts

The software for each of the controllers resides in the MSBC1 and the ENP 30 boards and was developed in FORTH. Figure 4 provides a representative controller block diagram (in this case for the EPSC). The FORTH software required for system operation was burned into EPROM and resides on the MSBC1 board. The ENP30 and the MSBC1 boards execute concurrently and asynchronously. These two processor boards communicate to each other by placing command, addresses, data, etc. into a shared memory area called the global data area. This global data area is physically located on the MSBC1 board and is accessed by the ENP30 through the Multibus using TCP/IP protocols.

ENP30 Software Description

The major software elements in the ENP30 are shown in Figure 5. The KI Kernel software operates the local area network controller for Ethernet (LANCE) and performs the Ethernet protocols. As such, the Kernel and the LANCE provide the communications capability between the network's physical medium (the coaxial cable) and the ENP30 board. The remaining software in Figure 5 establishes the communications between the ENP30 and the MSBC1 and is referred to henceforth, as the applications protocol software. The applications protocol software (APS) which is available on the ENP-30 boards of the three PMS controllers is written in FORTH and performs TCP/IP protocols. The ENP-30 software performs the following functions: (1) manage received messages from the Kernel to the processor board (MSBC1). (2) Manage transmitted messages from the MSBC1 to the Kernel. (3) Manage MSBC1 network status request commands to the Kernel. (4) Manage the ENP-30 activity counter which allows the MSBC1 to determine if the ENP-30 software is executing.

The Kernel was supplied by the manufacturer and resides in firmware on the ENP30 board in MC68000 assembler code. The operation of the Kernel is to provide the function for interfacing the network media to the user application (ie., ENP30 software). The ENP Kernel is responsible for initializing LANCE and the application programs during startup. During ongoing operations the Kernel handles all communications between LANCE chips and the higher level ENP applications.

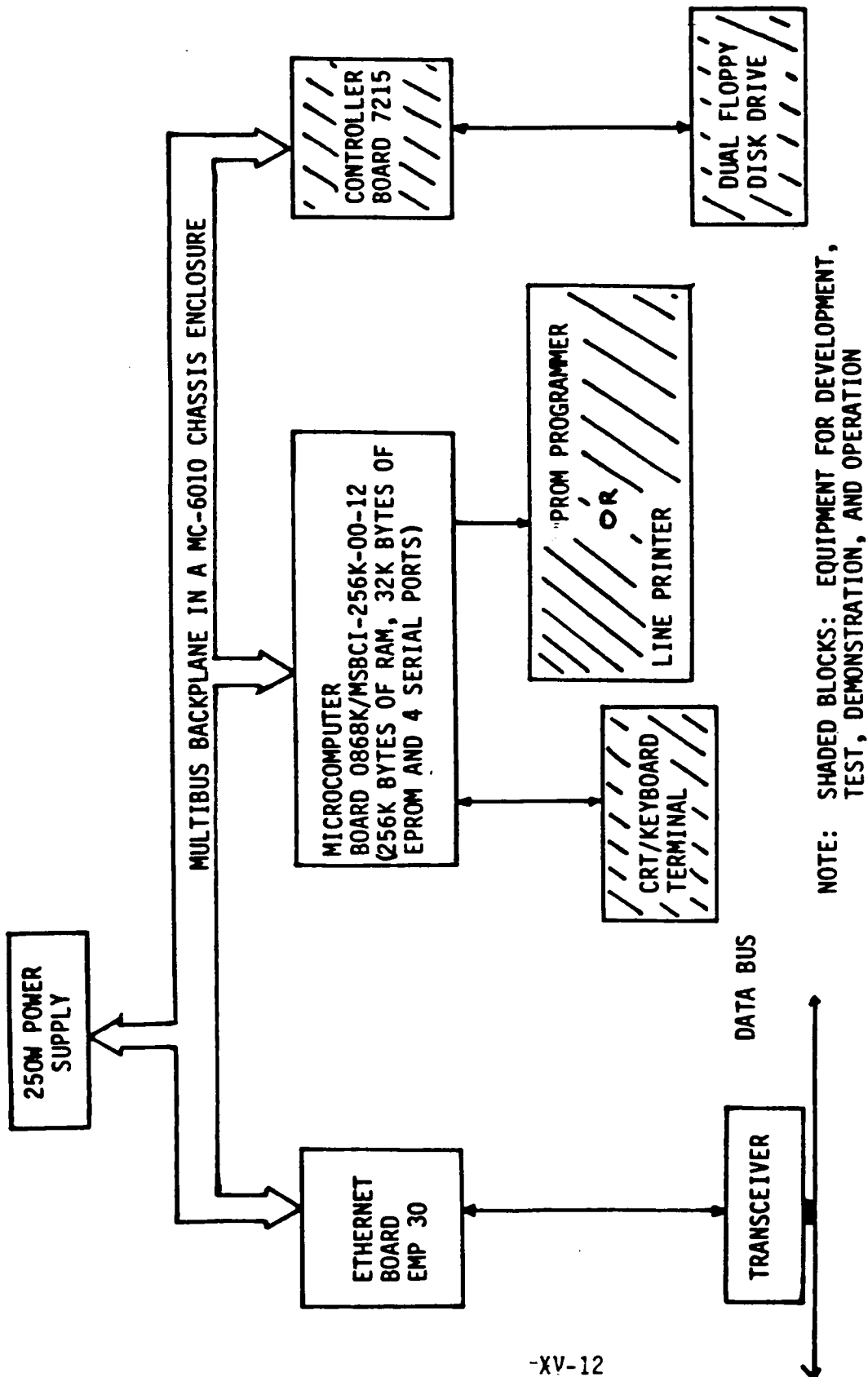


Figure 4 Electrical Power Subsystem Controller Block Diagram

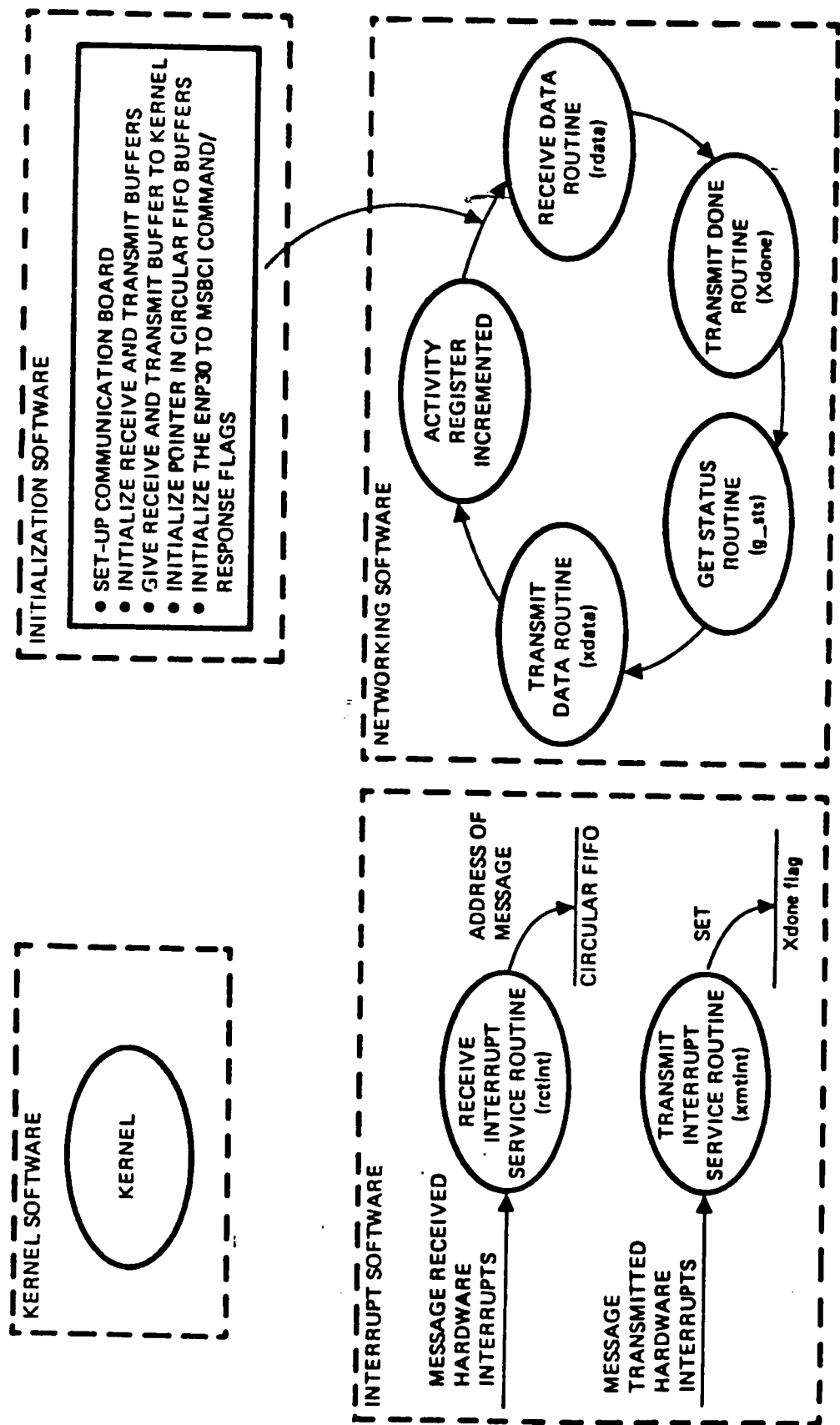


Figure 5 ENP30 Software

Networking the NCR Tower Host Computer

In order to connect the NCR Tower host to the network an ENP-30 communications board was procured from CMC and installed. The Tower ENP-30, like those in the FMS controllers, has the assembler language KI Kernel software resident in ROM. Consequently, the Tower ENP-30 can be Ethernetted to the AMPSW microprocessor. However, addressing incompatibilities must be overcome and additional software must be generated in order to use the Tower operating system as a host system. As can be seen from Figure 6 the Tower operating system uses 16 bit addressing while the LAN, ENP-30 boards and AMPS microprocessors use switchable 20/24 bit addressing. To overcome this problem software (NET.C) was developed to extend the Tower operating system with a 20/24 bit addressing environment. The software interrupts the suffix and prefix functions thus allowing the Tower to transmit and receive 20/24 bit data to and from the ENP-30. To allow the Tower to serve as the host computer for AMPS its ENP-30 must also mirror the TCP/IP APS protocol software. This capability must therefore be provided by developing the necessary software in RAM on the Tower ENP-30. This involves converting the TCP/IP software which was developed in FORTH by TRW into C for compatibility with the Tower environment. All necessary documentation has been obtained and these efforts have been initiated. Upon completion of these efforts a thorough test and debug effort will be conducted.

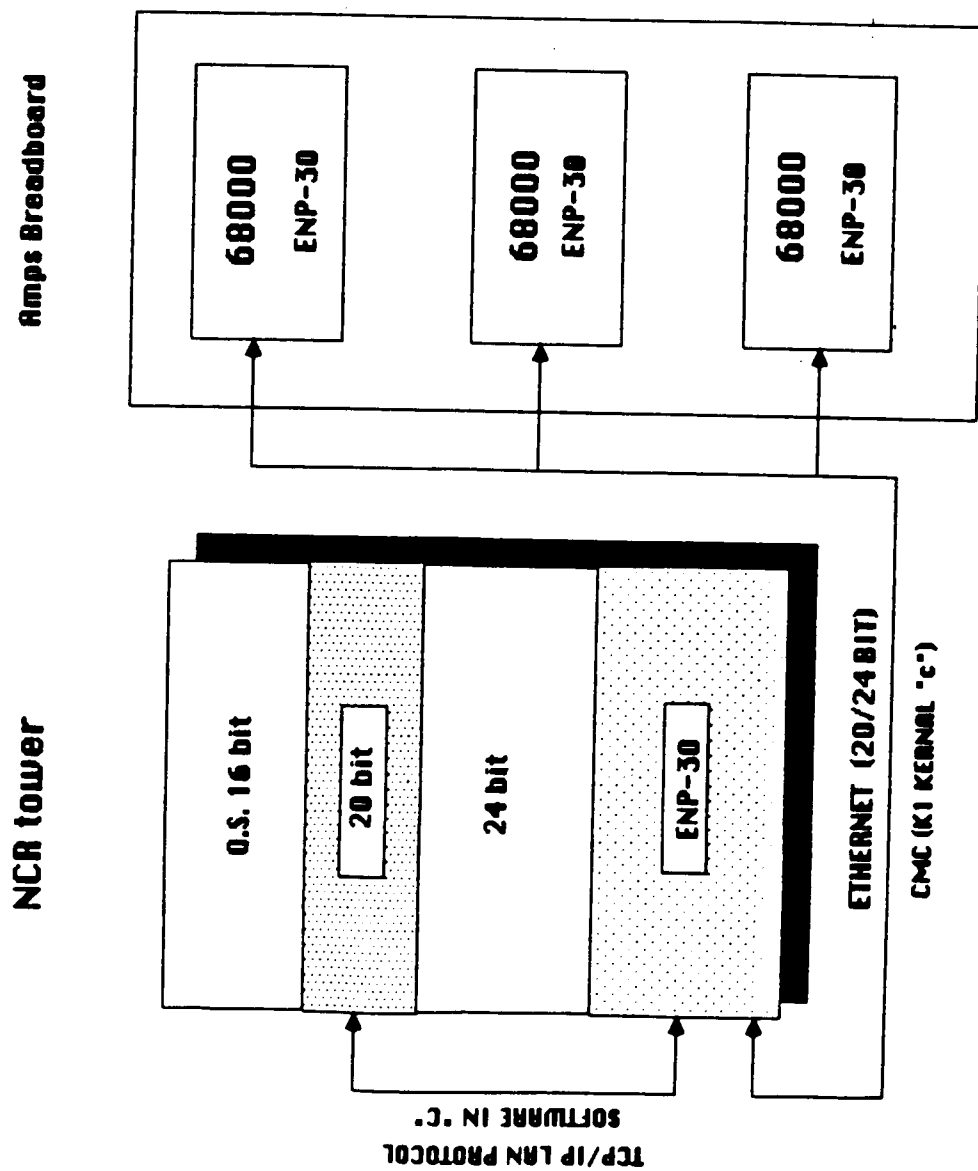


Figure 6 - NCR TOWER Reconfiguration

CONCLUSIONS AND RECOMMENDATIONS

Knowledge-based expert systems will play a major role in autonomous power systems for future space missions. Electrical power system breadboard and testbeds, in turn, will play a major role in the timely development of such systems. The ability to conduct knowledge engineering, validate reasoning mechanisms and update and expand knowledge bases requires the existence of realistic breadboards and testbeds. It will be necessary, therefore, for the various NASA agencies involved in these efforts to assure that the development of such realistic facilities is given prime consideration.

REFERENCES

1. Weeks, David J., "Expert Systems in Space", IEEE Potentials, Vol. 6, No. 2, 1987.
2. Lepisto, J.W. and Lin, W., "Autonomously Managed Electrical Power System", IECEC Conference Proceedings, p. 1780, 1986.
3. Weeks, David J. and Bechtel, Robert T., "Autonomously Managed High Power Systems", Proceedings of the 20th IECEC, p. 1132, 1985.
4. Space Power Distribution System Technology, Final Report, Vol. 3 Test Facility Design, TRW Defense & Space Systems Group, 1983.
5. Space Power Distribution System Technology, Final Report, Vol. 1, Autonomous Power Management - System Hardware Description, TRW Defense & Space Systems Group, 1987.
6. Space Power Distribution System Technology, Final Report, Vol. 2, Autonomous Power Management - Power Source Controller Software, TRW Defense & Space Systems Group, 1987.
7. Space Power Distribution System Technology, Final Report, Vol. 3 Autonomous Power Management - Load Center Controller Software, TRW Defense & Space Systems Group, 1987.
8. Space Power Distribution System Technology, Final Report, Vol. 4 Autonomous Power Management - Electrical Power System Software, TRW Defense & Space Systems Group, 1987.
9. Ethernet Node Processor ENP-30 User's Guide, Communication Machinery Corporation, 1985.
10. Ethernet Node Processor (ENP) Kernel Software Manual, Communication Machinery Corporation, 1984.

N88-15616 S15-20

116717
26P.

1987

NASA/ASEE SUMMER FACULTY RESEARCH FELLOWSHIP PROGRAM

MARSHALL SPACE FLIGHT CENTER
THE UNIVERSITY OF ALABAMA IN HUNTSVILLE

EQUILIBRIUM RETENTION IN THE NOZZLE
OF OXYGEN HYDROGEN PROPULSION SYSTEMS

Prepared By:	D. I. Ford
Academic Rank:	Associate Professor
University and Department:	LeTourneau College Natural Science
NASA/MSFC:	
Laboratory:	Propulsion
Division:	Component Devices
Branch:	Turbomachinery and Combustion Devices
NASA Colleague:	R. Eskridge

Abstract

Arguments are presented for the retention of vibrational equilibrium of species in the nozzle of the space shuttle main engine which are especially applicable to water and the hydroxyl radical. It is shown that the reaction $\text{OH} + \text{HH} \rightarrow \text{HOH} + \text{H}$ maintains equilibrium as well. This is used to relate OH to H, the temperature, and the oxidizer-to-fuel ratio.

EQUILIBRIUM RETENTION IN THE NOZZLE
OF OXYGEN-HYDROGEN PROPULSION SYSTEMS

D. I. Ford
LeTourneau College
Summer Faculty 1987
Marshall Space Flight Center
Huntsville, AL 35812

INTRODUCTION

Spectroscopic examination of the exhaust gases of liquid oxygen-hydrogen propulsion systems is currently being considered as a non-intrusive method to perform engine diagnostics. (1) Emission or absorption methods yield number densities for specific states and in some instances, rotational vibrational and electronic "temperatures." Knowing which processes are at equilibrium greatly facilitates the use of such data to calculate overall species concentrations by use of the Boltzmann distribution for internal states and equilibrium constants for the chemical reactions.

The most promising species for spectroscopic measurements is the hydroxyl radical, OH. If complete equilibrium were maintained at the exit plane, then the OH number density and rotational "temperature" which can be deduced from its band structure could be used to calculate all other species concentrations and the oxidizer-to-fuel mass ratio, (O/F). It is well known, however, that complete chemical equilibrium is not maintained. It is the purpose of this report to identify those processes which are expected to be at or near equilibrium.

Chemical Model

Typical combustion chamber and exit plane conditions are displayed in Fig. 1 for the Space Shuttle Main Engine (SSME). It is generally assumed that combustion is complete and total equilibrium is achieved in the combustion chamber before the combustion products begin their expansion through the throat and nozzle. Justification of such an assumption is based on the high collision frequencies of the various species under the chamber conditions of high temperature and pressure, along with a relatively long resident time in contrast to the opposite conditions in the nozzle. Computer codes for engine performance calculations use this initial equilibrium assumption and perhaps spectroscopic studies can shed some light as to the extent to which it is valid.

For fuelrich engines, the chemistry is described as follows: an initial equilibrium mixture of high enthalpy water vapor and molecular hydrogen (with about 4-7 percent of the dissociation products OH and H) is rapidly expanded through the nozzle. The temperature and pressure dropping rapidly, new conditions for equilibrium are established and the internal and chemical states change to accommodate the new Boltzmann distributions and equilibrium constants. These changes are rate processes and are governed by the collision frequencies between the various species and the probabilities for the individual collisions to produce a change.

Table 1 gives the typical number of collisions required for readjustment to take place for the various types of energy modes at 300K. (2) As a "rule of thumb" then, it is expected that equilibrium is achieved very fast for rotation, more slowly for vibration and ever slower yet for chemical reaction. However, it must be cautioned that these collision numbers have a strong temperature dependence and may overlap depending on the specific systems under consideration. In the following, each kinetic process will be examined separately as it applies toward the hydrogen-oxygen reaction.

Translational - Rotational Relaxation

Translational and rotational equilibrium is generally thought to be extremely rapid even in strong shock fronts. It is therefore safe to assume that the rotational "temperature" of the OH bands will be the same as the translational temperature at the exit plane. This temperature can be determined by comparing various rotational transitions which occur simultaneously with the electronic transition in the region of 280 to 340 nm for the OH radical.

Vibrational Relaxation

A significant amount of energy resides in the vibrational modes of the HH, and OH molecules in the high temperature environment of the combustion chamber. During expansion, the temperature drops and the vibrational energy begins to relax toward a new equilibrium state dictated by the local translational temperature. This again is a rate controlled process and occurs almost exclusively during molecular collisions. Present computer

codes assume that this relaxation process is fast and that vibrational equilibrium is maintained throughout the nozzle. At high expansion rotations, it is known that for molecules with long relaxation times such as N_2 , and CO_2 , and CO , significant deviations from the Boltzmann distribution can occur. (3) One approach that has been used to account for the final rate of vibrational relaxation along with the chemical reactions is to consider each vibrational state as a separate species. (3,4) There are, however, several serious difficulties with this approach:

1. The number of states goes up drastically. Present codes can handle effectively the kinetics of 150 to 250 species, but when each vibrational state is considered separately, the number of species increases to thousands instead of hundreds. This can be partially overcome by the somewhat arbitrary grouping of states.
2. Rate constants of the various vibrational relaxation processes have, for the most part, not been determined experimentally and theoretical predictions are at best tentative.
3. The most serious difficulty is that no one has been able to model the strong coupling which exists between the chemical reaction and the vibrational relaxation. It is known, for example, that molecular hydrogen in its first vibrationally excited state reacts with oxygen atoms 2600 times faster than hydrogen in the ground state at 300K. (5) Such data as this is sparse and then it is only given for one temperature. Also, the distribution of vibrational states among the newly formed products is

unknown except in some rather isolated cases.

In absence of a quantitative approach, we offer the following qualitative arguments for retention of vibrational equilibrium during the expansion of the exhaust gases of the liquid oxygen-hydrogen engines.

1. The vibrational modes of water are known to relax very rapidly - comparable to its rotational relaxation. (6) This is generally true of molecules which have large dipole movements. In contrast N_2 , CO_2 , and CO have zero or small dipole movements and relax much slower than water. As a rule, any strong intermolecular force assists vibrational relaxation. (7) Water forms hydrogen bonds which are very strong intermolecular forces.

(2) Water couples well with the other molecules present, OH and HH by forming hydrogen bonds.

3. The three vibrational frequencies of HOH are 1600, 3600 and 3760 $1/cm$. The vibrational frequency of hydroxyl, OH, is 3730 $1/cm$ which differs from the last frequency given for HOH by only 30 $1/cm$. Frequencies within 50 $1/cm$ are said to be "resonant" and equilibrate quickly. (8) In summary, the exhaust gases of liquid oxygen-hydrogen engines are much more likely to be at vibrational equilibrium than hydrocarbon engines because of the predominance of water in the former. This could be verified by the OH spectrum. If non-equilibrium is observed it could indicate:

1. The above vibrational relaxation mechanisms, though fast, are not fast enough.

2. Chamber equilibrium may not be established. For example, the liquid oxygen may not be fully dispresed before it makes it to the throat.
3. Secondary oxidation of the excess hydrogen with atmospheric oxygen in the vicinity of the exit plane may have to be excluded or allowed for in the data analysis.

Chemical Relaxation

Computer programs are available which compute the performance of rocket engines taken into account finite rate chemical reaction. (9) The results of such a calculation are shown in Fig. 2 where number density is plotted versus area ratio. Also shown are the number densities which would result if chemical equilibrium had been maintained during the expansion. It is seen that the concentrations of the minor components, OH, H, O and O₂ are orders of magnitude different when finite rate chemistry is used. The water and hydrogen gives essentially the same result whether or not chemical equilibrium is assumed. This is because only a small amount of each was dissociated in the combustion chamber. The major reactions taken place during the expansion are the following:



M is a third body required to dissipate the energy of the newly formed water or hydrogen molecule and is likely to be either a water or hydrogen molecule. It is known from the study of the chemistry of flames, that away from the flame front, the exchange reactions iii and iv maintain equilibrium while coupled to the recombination reactions, i and ii, which are not at equilibrium. (10) Since equilibrium relationships can relate species concentrations to one other, it is worthwhile to examine whether iii

and iv are in equilibrium in the nozzle expansion process as well.

The extent to which equilibrium is maintained is shown by comparing the equilibrium constant K_e to the quantity K . K has the same form as K_e but uses the prevailing partial pressures of the species of the reaction instead of those that occur at equilibrium. K_e is a function of temperature only and may be determined by the thermodynamic relation:

$$-\Delta G^0 = RT \ln K_e$$

and standard thermodynamic tables. K is calculated from the mole fraction and pressures computed at various area ratios using the NASA ODK code (9). Calculations were done for two engines. The smaller RL-10 engine has a 5 inch diameter throat, a chamber pressure of about 400 psi and a chamber temperature of about 3400K. The SSME has a 10 inch diameter throat, a chamber pressure of about 3000 psi and a chamber temperature of about 3400K.

Examination of Figs 3-8 shows that the exchange reactions iii and iv are essentially at equilibrium i.e. K/K_e is close to one. Reaction iii appears to be closer to equilibrium than iv. The exchange reactions i and ii quickly fall out of equilibrium as is evidence by the rapid decline of K/K_e to zero. Equilibrium is more persistent for the larger SSME engine than for the smaller engine, presumably as a result of higher operating pressures.

One should use the ODK number densities and corresponding K/K_e values with caution. They are based on rate constants which are in many cases uncertain by an order of magnitude. Also, it appears that the smaller number densities may suffer from "computational scatter" especially at the large expansion ratios. I would suggest that they be used in a "soft" fashion, that is, to demonstrate trends and qualitative behavior.

Relating OH to Other Quantities

Using reaction iii as being essentially at equilibrium and the known equilibrium constant $K_e(T)$, $[H]$ can be calculated from:

$$[H] = \frac{[OH] \times [HH]}{K_e(T) \times [HOH]} \quad \text{where}$$

UV absorption measurements can give $[OH]$ and T . $[HH] / [HOH]$ can be calculated using the relation:

$$(O/F) = 8.0 \times (1 + [HH]/[HOH])^{-1}$$

The last equation comes from conserving O and H atoms and recognizing that at the exit plane, essentially all of the exhaust gas is HH and HOH.

Alternately, if $[H]$ and $[OH]$ are both known, then (O/F) could be calculated.

However, accurate temperatures must be used as $K_e(T)$ is a strong function of temperature. (See table 2 and Fig 10.) A similar analysis can be made to estimate $[O]$ from $[OH]$ using reaction iv.

Fig. 9 shows how $[OH]$ at the exit plan varies with (O/F) . When (O/F) changes from 5 to 7, (8 being stoichiometric) $[OH]$ increases by a factor of 150. This suggests that the hydroxyl number density can be a sensitive measure of the oxidizer-to-fuel ratio. Note also in Fig. 10, that the temperature at the exit plan increases substantially as (O/F) increases.

Conclusion

Arguments are presented suggesting that equilibrium is substantially maintained in the nozzle of the SSME with the exception of certain chemical reactions, notably the recombination reactions. Reaction iii and iv will maintain equilibrium enough to be used to estimate [H] and [O] from the [OH] measurement. Accurate measurements of the absorption spectra of OH in the exit plane will yield valuable information for engine monitoring and verification of models employed in various computer codes in use to predict rocket engine performance. The measurement of OH in the test study environment is a challenging experimental and engineering problem with the potential for giving a wealth of information.

REFERENCES

1. Cikanek, H. A., Powers, W. T., and Eskridge, R., "Space Shuttle Main Engine Spectral Monitoring Preliminary Results," Paper 87-1792 at AIAA 23rd Joint Propulsion Conference, San Diego, Ca., June 29-July 2, 1987.
2. Lambert, J. D., "Vibrational And Rotational Relaxation In Gases," Clarendon Press, Oxford, 1977.
3. Limbaugh, C. C., "Vibrational Relaxation of CO₂ in High Area Ratio Rocket Engines," Paper 85-1082 at AIAA 20th Thermophysics Conference, Williamsburg, Va., June 19-21, 1985.
4. Nickerson, G. R., "Nonequilibrium Radiation Model For Exhaust Plumes," AFRPL-TR-74-74, March, 1975.
5. Light, G. C., J. Chem. Phys., 68, 1978, p. 2891.
6. Shin, H. K., J. Phys. Chem., 77, 1973, p. 346.
7. Kondrat'ev, V. N., "Chemical Kinetics of Gas Reactions," Pergamon Press, 1964, p. 378.
8. Ref. 2, p. 83 and Ref. 7, p. 377.
9. Nickerson, G. R., Dang, L. D. and Coats, D. E., "Two-Dimensional Kinetic Reference Computer Program," NASA contract no. NASA-35931, April, 1985.
10. Kaskan, W. E., J. Chem. Phys., 31, 1959, p. 944.

TABLE 1 - Collisions required for energy transfers.

Z(1-0) ----- vibrational to translational

Z(R) ----- rotational to translational

		T = 300 K	T = 2000 K
CO	Z(1-0)	1,000,000,000	100,000
	Z(R)	2	—
OO	Z(1-0)	100,000,000	10,000
	Z(R)	4	—
HH	Z(1-0)	10,000,000	10,000
	Z(R)	200	—
HOH	Z(1-0)	50	—
	Z(R)	4	—

TABLE 2 Equilibrium constants for various reactions of hydrogen and oxygen. K(x) is the equilibrium constant and x is the temperature in degrees Kelvin.

Reaction 1 ;	O + HH -> OH + H	Reaction 3 ;	OH + HH -> HOH + H	Reaction 5 ;	HH -> H + H		
Reaction 2 ;	O + HOH -> OH + OH	Reaction 4 ;	OO + H -> OH + O	Reaction 6 ;	HOH -> H + OH		
				Reaction 7 ;	OO -> O + O		
x	K1(x)	K2(x)	K3(x)	K4(x)	K5(x)	K6(x)	K7(x)
000.0	.79289669	.0016801417	471.92250	.0038066521	5.0808670e-18	1.0766316e-20	2.4392955e-20
050.0	.83259451	.0025534418	326.06755	.0056608269	6.4898589e-17	1.9903419e-19	4.4124681e-19
100.0	.87049220	.0037348662	233.07186	.0081113996	6.5951001e-16	2.8296424e-18	6.1454305e-18
150.0	.90668913	.0052838664	171.59577	.01254331	5.4925323e-15	3.2008552e-17	6.8176371e-17
200.0	.94128253	.0072603382	129.64720	.015181793	3.8426057e-14	2.9638940e-16	6.1976762e-16
250.0	.97436592	.0097230825	100.21163	.019979847	2.3057145e-13	2.3008453e-15	4.7279796e-15
300.0	1.0060282	.012728442	79.037812	.025726622	1.2076820e-12	1.5279800e-14	3.0883406e-14
350.0	1.0363533	.016329158	63.466427	.032491018	5.6050548e-12	8.8315272e-14	1.7572572e-13
400.0	1.0654198	.020573456	51.786135	.040331866	2.3349768e-11	4.5087874e-13	8.8389528e-13
450.0	1.0933012	.025504377	42.867198	.049297525	8.8277738e-11	2.0593307e-12	3.9804896e-12
500.0	1.1200659	.031159311	35.946426	.059425817	3.0583085e-10	8.5001765e-12	1.6226461e-11
550.0	1.1457774	.037569747	30.497342	.070744256	9.7912446e-10	3.2105240e-11	6.0454527e-11
600.0	1.1704949	.044761182	26.149776	.083270487	2.9179422e-09	1.1158575e-10	2.0758611e-10
650.0	1.1942730	.052753178	22.638882	.097012898	8.1472724e-09	3.5987962e-10	6.6181728e-10
700.0	1.2171625	.061559537	19.772120	.11197133	2.1434823e-08	1.0840933e-09	1.9718694e-09
750.0	1.2392107	.071188565	17.407440	.12813784	5.3406425e-08	3.0680203e-09	5.5223736e-09
800.0	1.2604610	.081643401	15.438614	.14549757	1.2658561e-07	8.1992859e-09	1.4612034e-08
850.0	1.2809541	.092922396	13.785203	.16402947	2.8657206e-07	2.0788381e-08	3.6696290e-08
900.0	1.3007277	.10501952	12.385581	.18370719	6.2187214e-07	5.0209365e-08	8.7829592e-08
950.0	1.3198167	.11792478	11.192022	.20449978	1.2977354e-06	1.1595183e-07	2.0107838e-07
1000.0	1.3382538	.13162464	10.167198	.22637243	2.6118599e-06	2.5689083e-07	4.4180939e-07
1050.0	1.3560691	.14610248	9.2816299	.24928718	5.0831250e-06	5.4765436e-07	9.3443460e-07
1100.0	1.3732911	.16133892	8.5118398	.27320348	9.5886989e-06	1.1265131e-06	1.9075824e-06
1150.0	1.3899460	.17731230	7.8389709	.29807878	.000017570010	2.2413669e-06	3.7679502e-06
1200.0	1.4060584	.19399897	7.2477625	.32386905	.000031334209	4.3232942e-06	7.2174670e-06
1250.0	1.4216515	.21137366	6.7257742	.35052920	.0000544848339	8.1009023e-06	.000013434043
1300.0	1.4367467	.22940981	6.2627956	.37801351	.0000925234006	.000014773499	.000024343259
1350.0	1.4513643	.24807982	5.8503925	.40627597	.00015367224	.000026266997	.000043017001
1400.0	1.4655232	.26735534	5.4815558	.43527059	.00024997430	.000045603531	.000074245295
1450.0	1.4792413	.28720749	5.1504271	.46495166	.000398768399	.00007424062	.00012533951
1500.0	1.4925352	.30760709	4.8520832	.49527398	.00062452464	.00012871268	.00020723854
1550.0	1.5054208	.32852480	4.5823657	.52619305	.00096129739	.00020978190	.00033600440
1600.0	1.5179129	.34993134	4.3377450	.55766523	.0014557024	.00033558967	.00053480975
1650.0	1.5300256	.37179759	4.1152113	.58964787	.0021706352	.00052747116	.00083653647
1700.0	1.5300256	.37179759	4.1152113	.58964787	.0021706352	.00052747116	.00083653647
1750.0	1.5417722	.39409476	3.9121865	.62209944	.0031899220	.00081538086	.0012871219
1800.0	1.5531652	.41679443	3.7264537	.65497959	.0046236113	.0012407537	.0019498062
1850.0	1.5642164	.43986871	3.5560984	.68824921	.0066147205	.0018601062	.0029104516
1900.0	1.5749372	.46329028	3.3994609	.72187051	.0093468537	.0027495106	.0042841188
1950.0	1.5853382	.48703245	3.2550978	.75580706	.013053225	.0040100870	.0062231009
2000.0	1.5954297	.51106922	3.1217487	.79002375	.018027059	.0057746569	.0089266265
2050.0	1.5954297	.51106922	3.1217487	.79002375	.018027059	.0057746569	.0089266265
2100.0	1.6052212	.53537533	2.9983099	.82448689	.024633484	.0082157900	.012652453

ORIGINAL PAGE IS
OF POOR QUALITY

FIG. 1 Representative conditions in the combustion chamber and exit plane of the SSME.

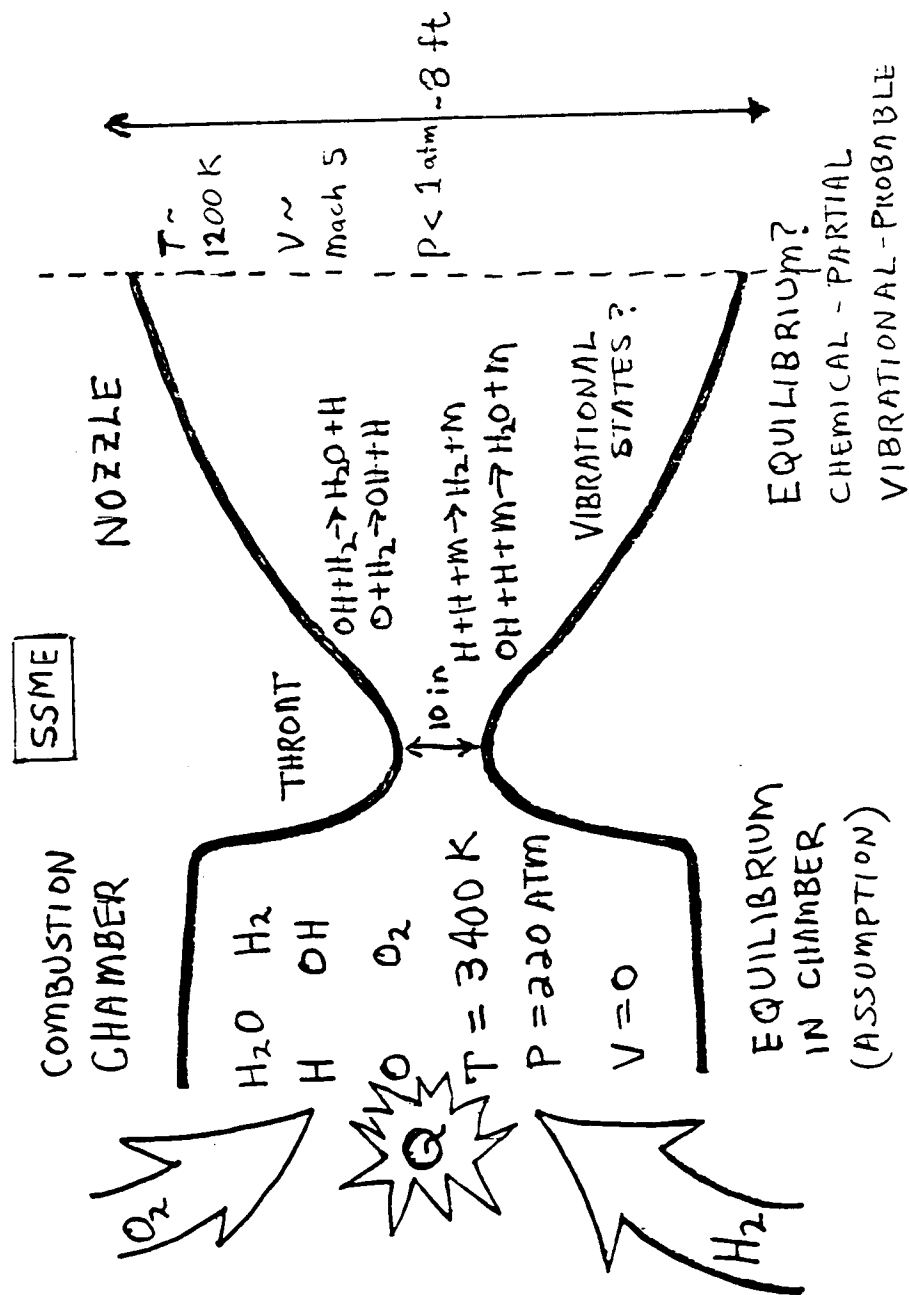


FIG. 2 Number density versus area ratio for RL-10 engine.
Solid lines are for finite rate chemistry and dotted lines are for equilibrium.

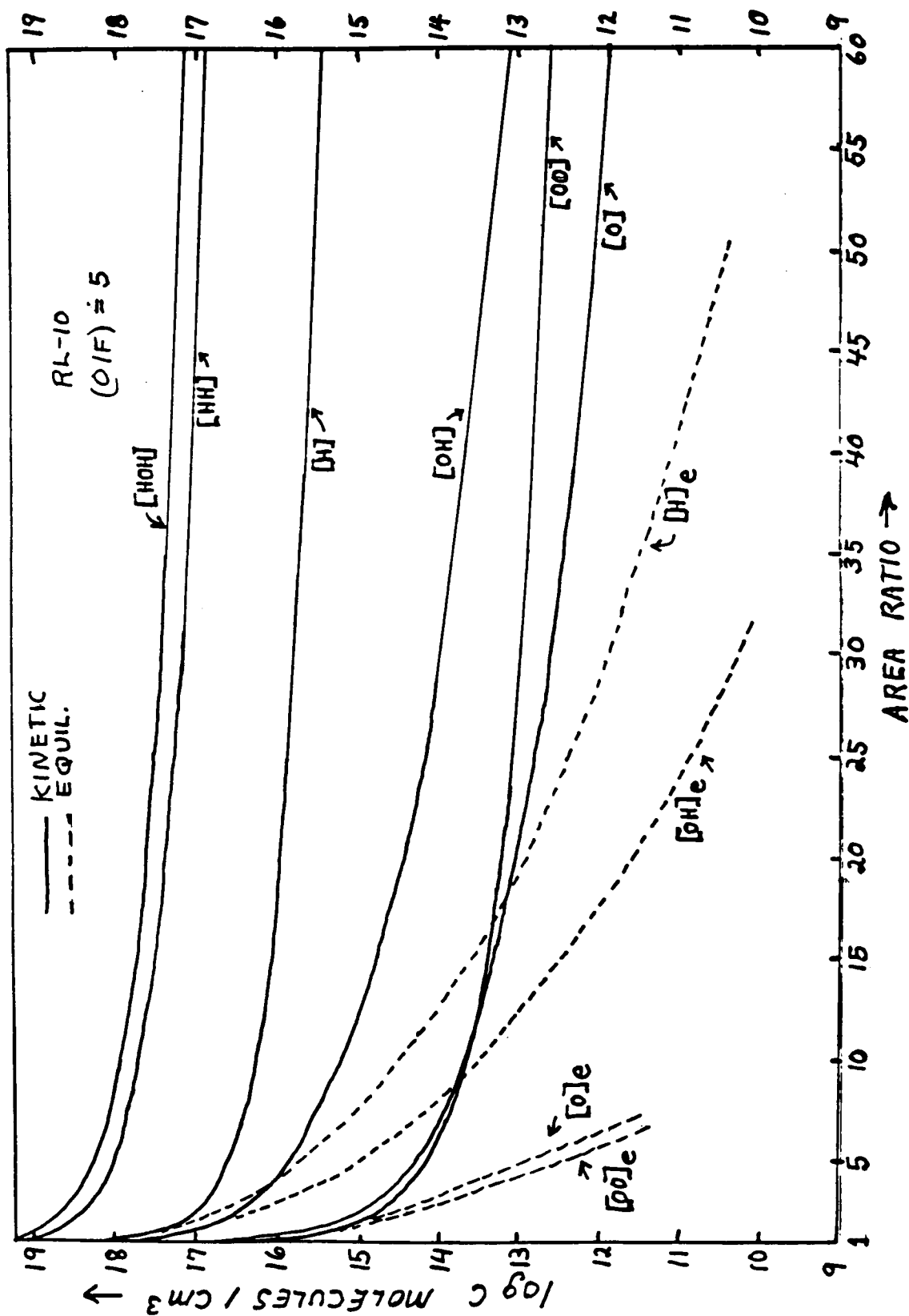


FIG. 3 K/Ke versus area ratio. Shows lack of equilibrium for



RL-10

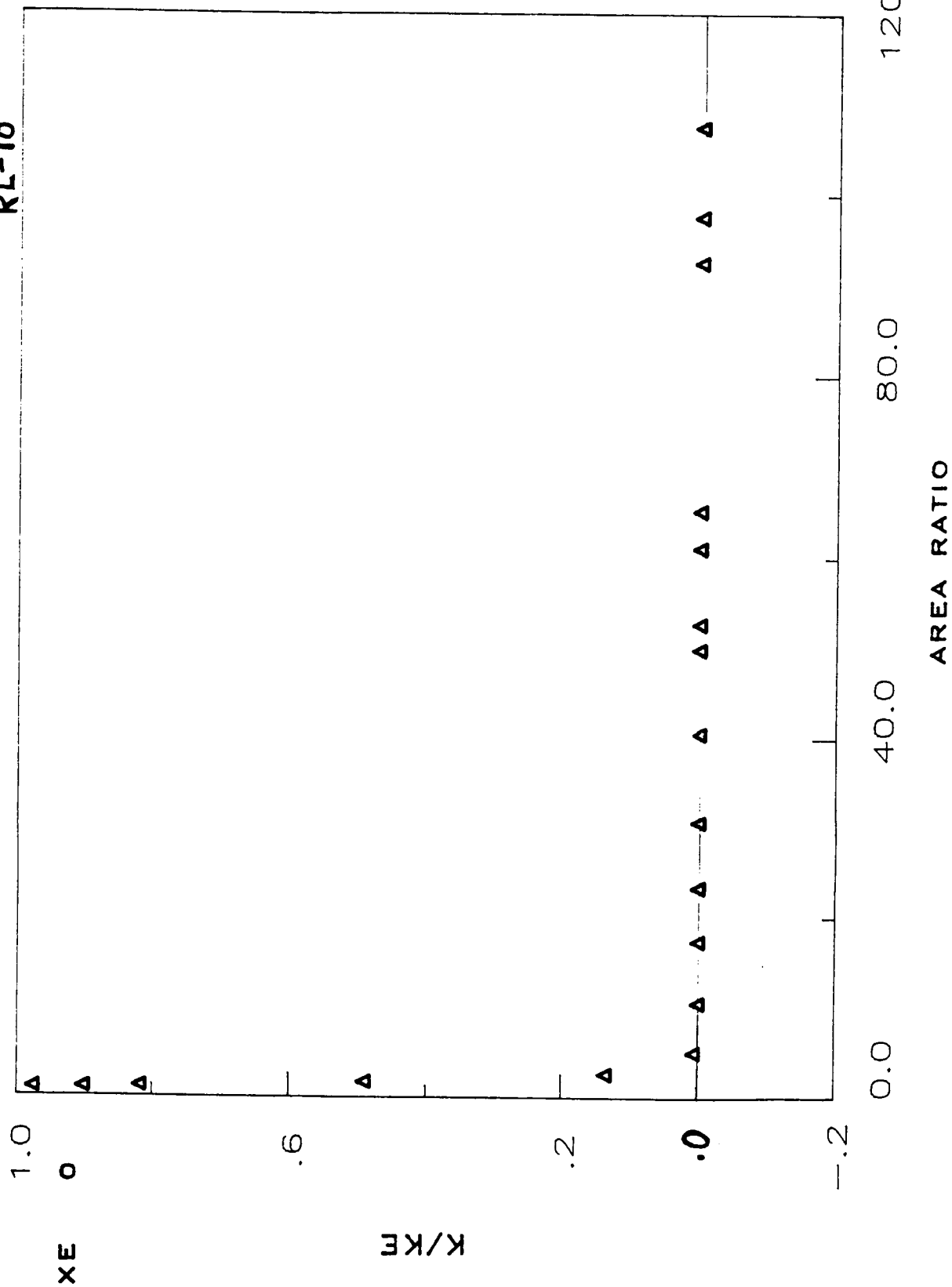
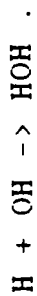


FIG. 4 K/Ke versus area ratio. Shows lack of equilibrium for



(O/F)=5

RL-10

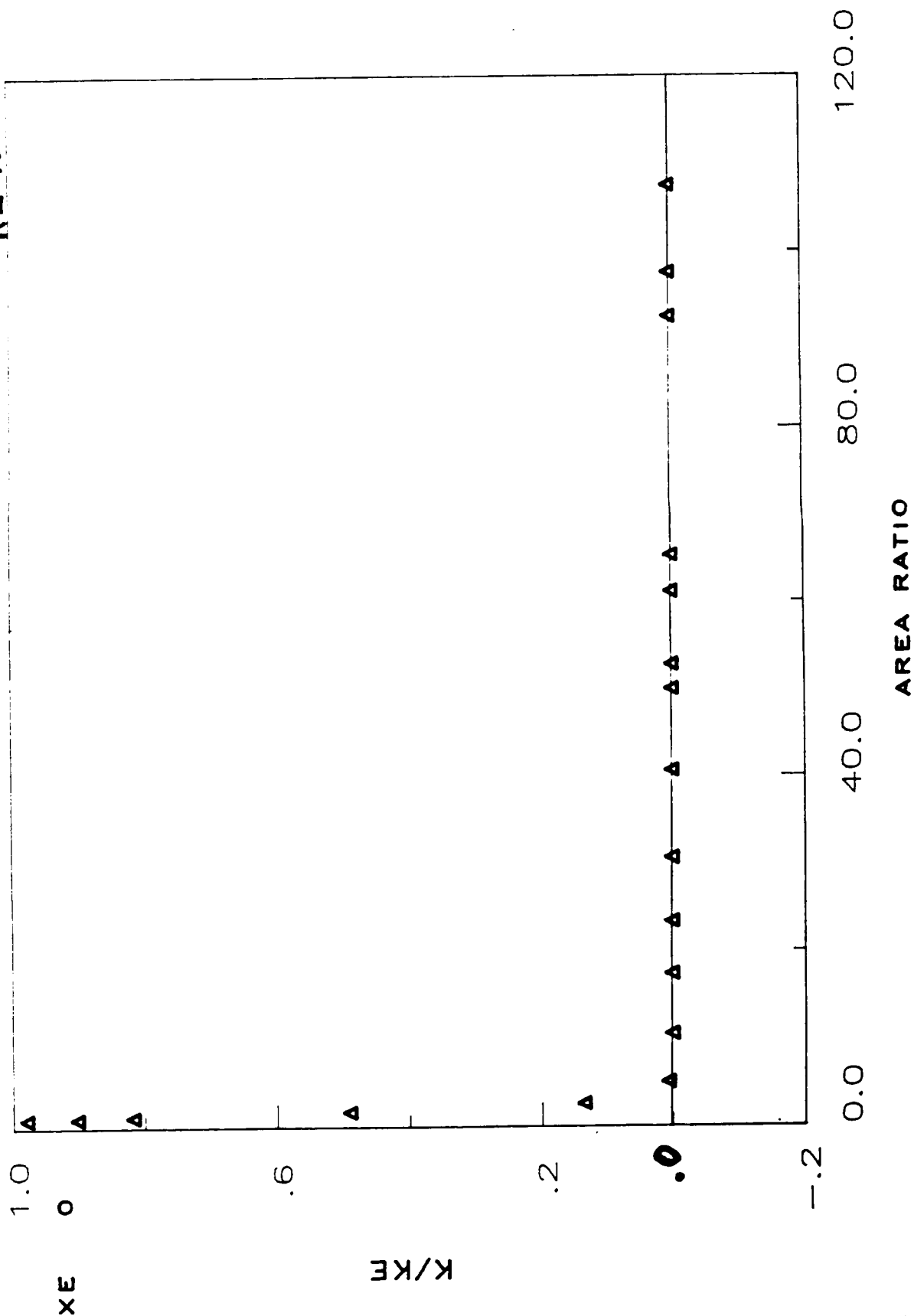
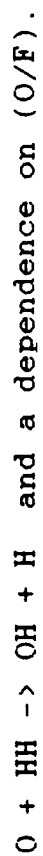


FIG. 5 K/Ke versus area ratio. Shows partial equilibrium for



$O + HH \rightarrow OH + H$ and a dependence on (O/F) . $(O/F) = 5 \text{ to } 7$

Rh-10

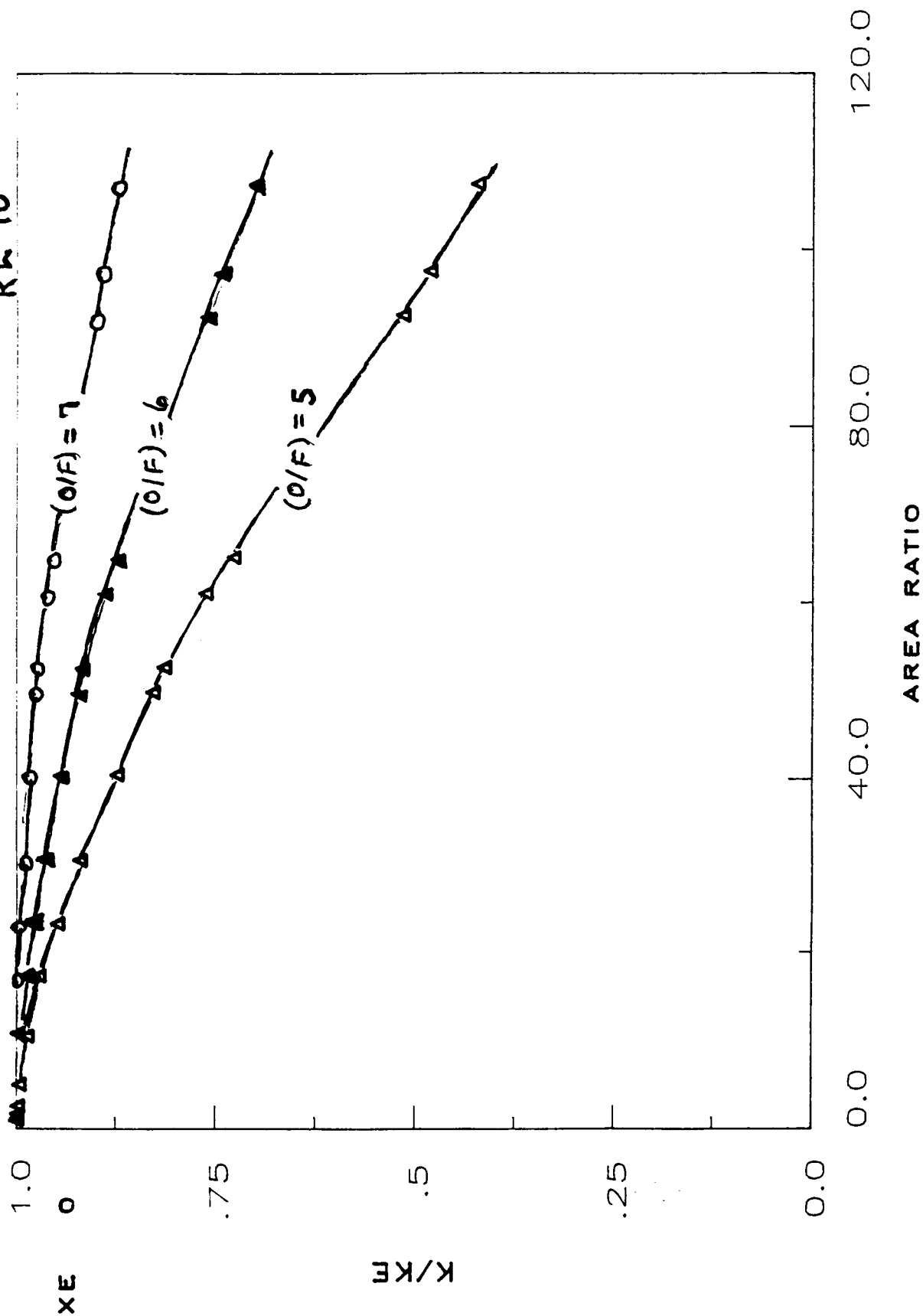
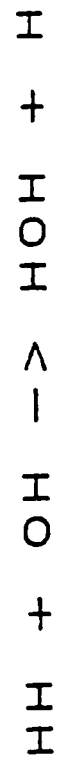


FIG. 6 K/Ke versus area ratio. Shows substantial equilibrium

for $HH + OH \rightarrow HOH + H$



$(O/F) = 6$

RL-10

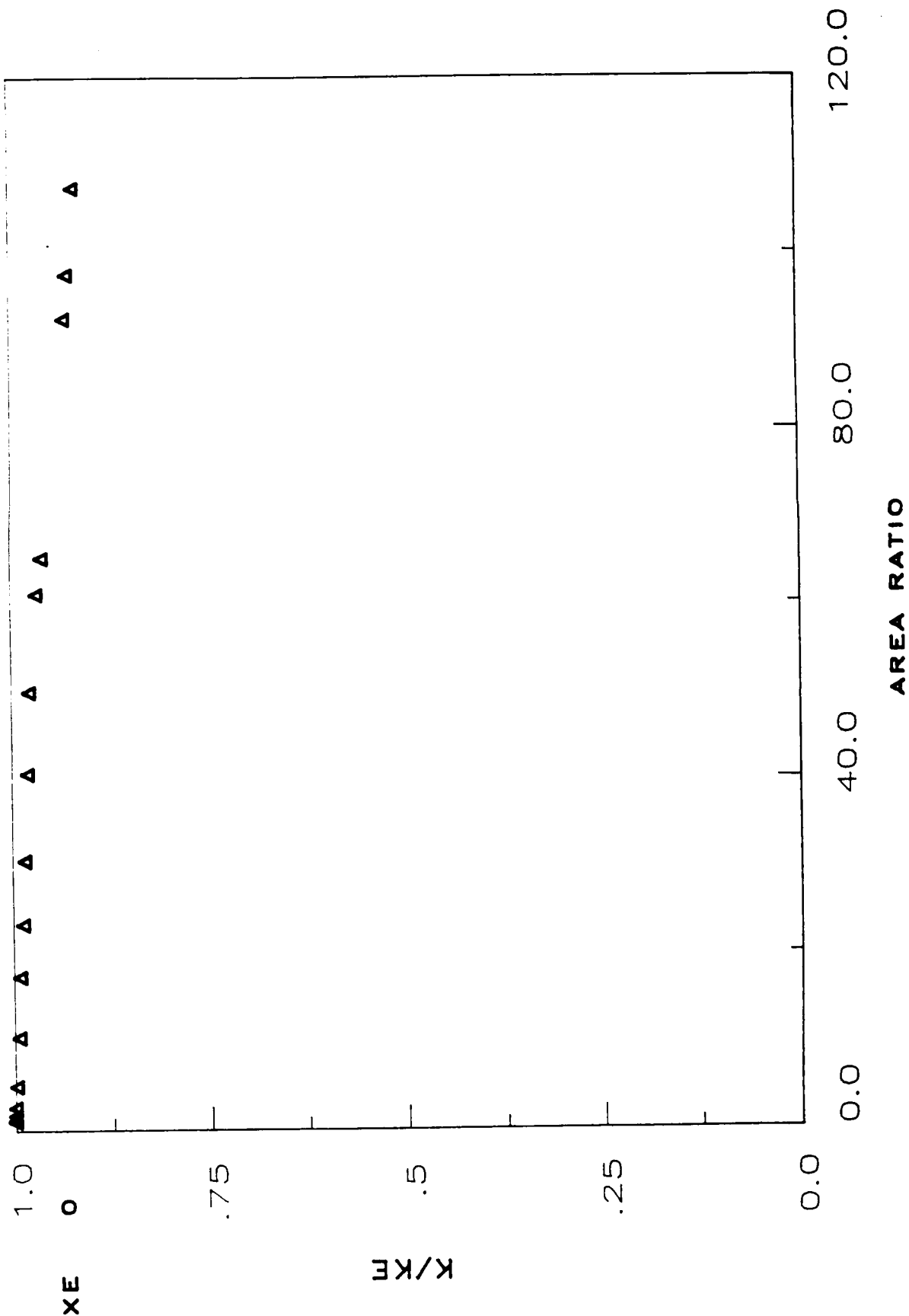


FIG. 7 K/Ke versus area ratio. Shows equilibrium for the

reaction $HH + OH \rightarrow HOH + H$ in the SSME.

$(O/F) = 6$

SSME

$HH + OH \rightarrow HOH + H$

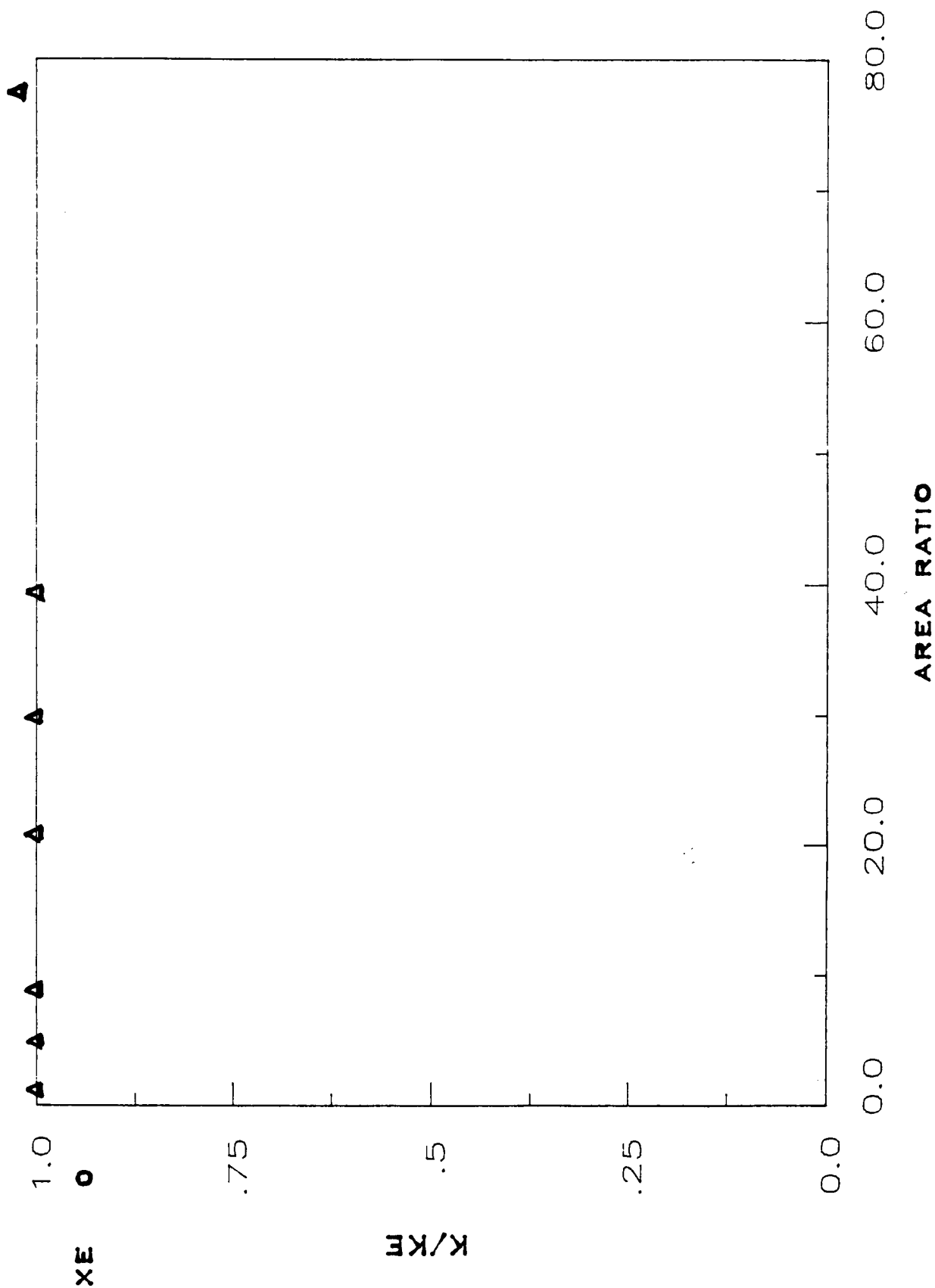


FIG. 8 K/Ke versus area ratio. Demonstrates a feeble attempt
to maintain equilibrium for the reaction $H + OH \rightarrow HOH$
in the SSME

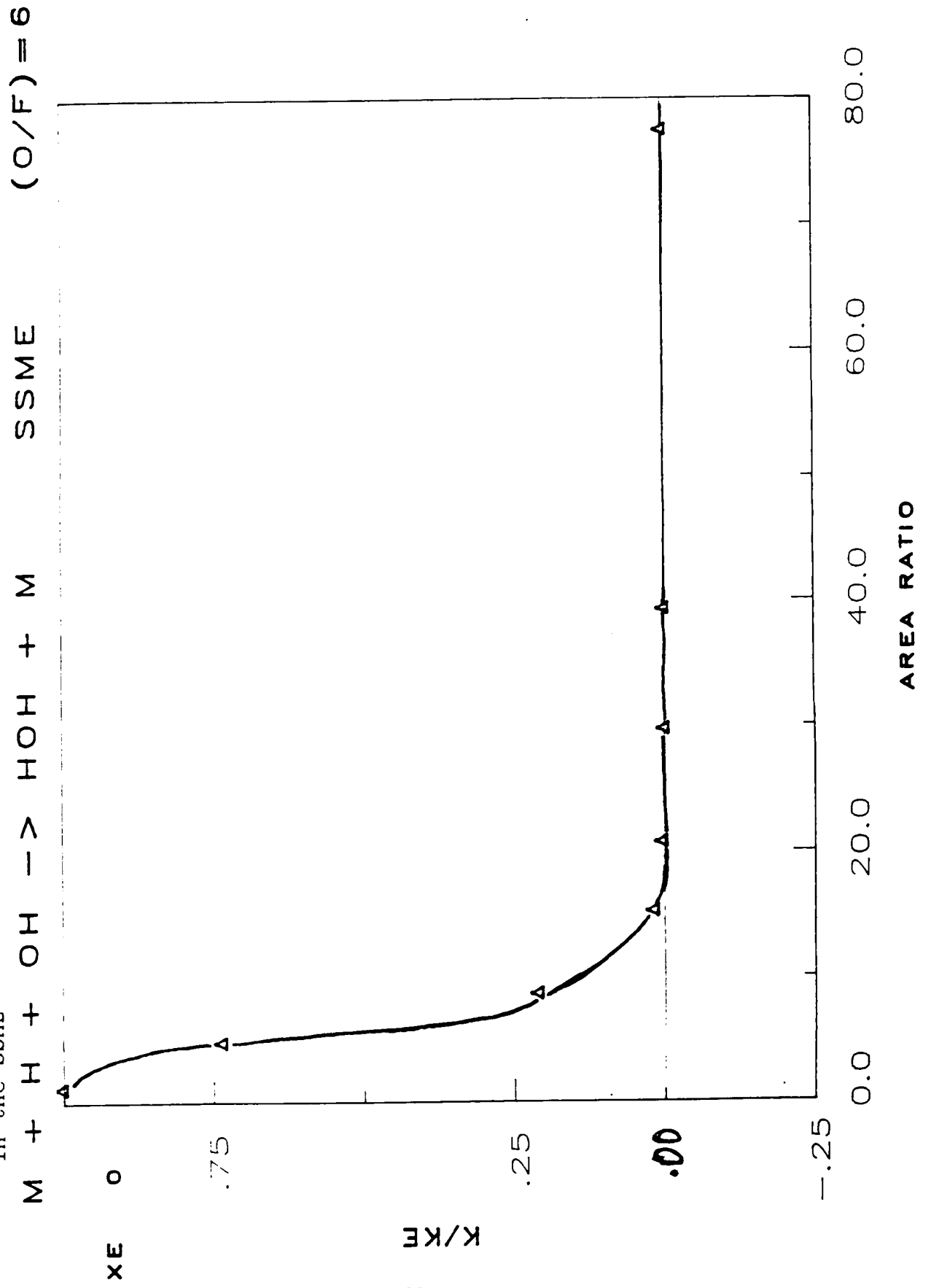


FIG. 9 Variation of $\log[\text{OH}]$ and other species with (O/F) .

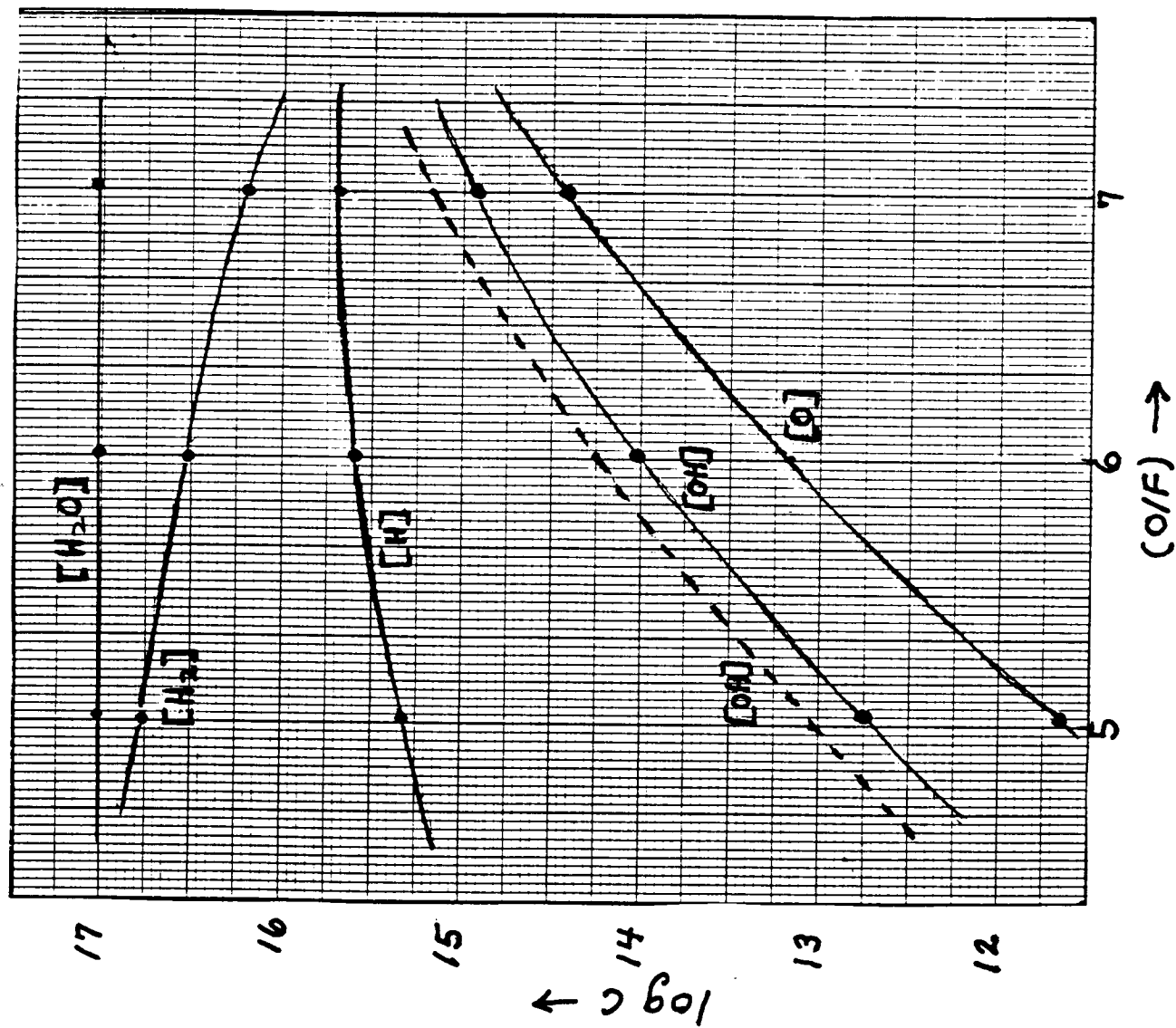
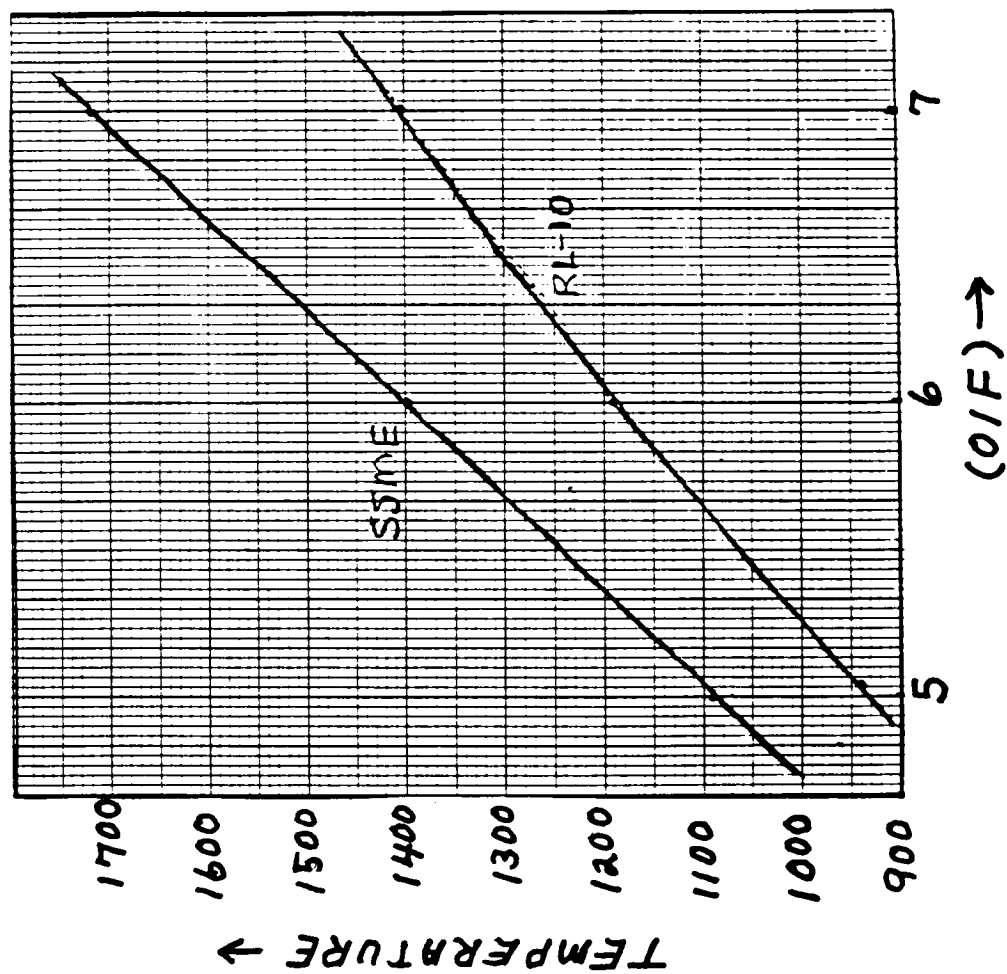


FIG. 10 Variation of the temperature (degrees Kelvin) at the exit plane with (O/F).



N88-15617⁵⁴⁶⁻²⁶

116718
282

1987

NASA/ASEE SUMMER FACULTY RESEARCH FELLOWSHIP PROGRAM

MARSHALL SPACE FLIGHT CENTER
THE UNIVERSITY OF ALABAMA IN HUNTSVILLE

ATOMIC OXYGEN EFFECTS ON METALS

Prepared by:	Albert T. Fromhold, Ph.D.
Academic Rank:	Professor
University and Department:	Auburn University Department of Physics
NASA/MSFC:	
Laboratory:	Materials and Processes
Division:	Engineering Physics
Branch:	Physical Sciences
MSFC Colleague:	Roger C. Linton
Date:	August 7, 1987
Contract No.:	The University of Alabama in Huntsville NGT-01-008-021

ATOMIC OXYGEN EFFECTS ON METALS

by

Albert T. Fromhold
Professor of Physics
Auburn University, AL 36849

ABSTRACT

The present work addresses the effect of specimen geometry on the attack of metals by atomic oxygen. This is done by extending the coupled-currents approach in metal oxidation to spherical and cylindrical geometries. Kinetic laws are derived for the rates of oxidation of samples having these geometries. It is found that the burn-up time for spherical particles of a given diameter can be as much as a factor of 3 shorter than the time required to completely oxidize a planar sample of the same thickness.

ACKNOWLEDGEMENTS

The author greatly appreciates the friendly hospitality extended to him by the personnel of the Materials and Processes Laboratory of Marshall Space Flight Center during his visit with them. He is grateful for the aid provided for him in the laboratory by his colleague, Roger C. Linton. He especially appreciates the help of John M. Reynolds in using the automated ellipsometer and Robert F. DeHaye in using the microprofiler. Several discussions with Ralph Carruth and Bruce Glick proved to be very helpful in setting up a program for continuation of the atomic oxygen studies. Finally, Dr. Gerald R. Karr, the UAH NASA/ASEE Summer Faculty Fellowship Program Director, and Mrs. Ernestine Cothran, Program Co-Director at MSFC, are to be highly commended for the outstanding seminars and activities which they carefully organized and subsequently supervised with such great flair.

INTRODUCTION

The failure of metal structures often occurs at cracks, corners, and crevices preferentially to planar surfaces. The present work addresses these geometric effects of the attack of atomic oxygen on metal surfaces.

OBJECTIVES

The objective of this work was to extend the coupled-currents approach for the oxidation of planar material surfaces to non-planar surfaces, specifically, surfaces having spherical and cylindrical symmetry.

CONCLUSIONS AND RECOMMENDATIONS

1. The burn-up rate can be significantly increased for non-planar geometries relative to planar geometries.
2. The theoretical development should be extended to include stress effects.

I. Concept of Steady-State Oxide Growth for Non-Planar Geometries

The focal point of this presentation is the effect of material sample geometry on the rate of oxidation. Because the oxidation rate is dependent upon the atom or ion current to the location where metal oxidation is occurring, it is necessary to evaluate the effects of sample geometry upon such currents. Frequently oxide formation occurs under fixed experimental conditions of ambient temperature and oxygen pressure, and in such situations the currents in the system are usually nearly steady-state.

The steady-state is a condition in which no change in the local value of the current takes place with time. Though thermodynamic equilibrium is a special case of the steady-state, the current then being uniformly zero, in general the steady-state differs from equilibrium.

To elaborate, current flows in response to driving forces, so currents are to be expected so long as the net driving force differs from zero. Currents may lead to a change in one or more components of the local driving force, in which case the net driving force may approach zero in time. Then the net current will approach zero in time, and a state of equilibrium is thereby attained. This evolution of the system can be expected for many, but not all, situations. A specific counter example is that of an externally-applied driving force and a closed-loop circuit around which the current can be sustained practically indefinitely, so the equilibrium state is not approached with time. In fact, there will be initial transients when the current is established, and it is the steady-state which is approached with time. Thus for some systems the long-time asymptotic limit on a laboratory time scale can be the steady-state, in contrast to equilibrium.

In the steady-state limit, the actual values of the local currents will depend directly upon the local values of the conductivity, as well as upon the local driving forces. The critical distinction between the steady-state and equilibrium, however, is in actuality one of net local driving force rather than actual value of the local current, even though in practice it may well be the measurable current that is used as the threshold criterion for equilibrium. Theoretically the values of the net local driving force must be zero everywhere in the system at equilibrium, and this naturally leads to the condition of zero current everywhere in the system, regardless of the value of the local conductivity.

The space-dependence of the current is likewise pertinent. For non-steady-state situations, the current can certainly vary locally with position. In the steady-state, however, the situation is not quite so intuitively clear. The local driving force or the local conductivity may vary with position initially, but the local driving force may adjust to compensate for the spatial variation of the conductivity. Care must be taken in the analysis of such cases. The critical aspect of the problem is that the spatial variation of the

current in the limit of the steady-state must be such that neither electric charge nor diffusing species concentrations build up or deplete anywhere within the system as the flow is maintained. This requires that the net current flowing into any region of space be equal to the net current flowing out of that region of space. Thus there must be no time-dependence of the local concentration of the mobile species. In vector terminology, the divergence of the current J in question must be zero,

$$(1) -\partial C/\partial t = \nabla \cdot J = 0 ,$$

where C is the local mobile species concentration at time t . This condition will be shown to lead to the conclusion that even in the steady-state, the current can vary locally with position, depending on the geometry in question. Our attention is directed entirely to cases of thermal oxidation for which Eq. (1) represents a reasonably good approximation.

II. Ionic Current and Oxide Growth Rate

If the steady-state ionic current density J_i can be evaluated for the geometry in question, then the value of that i current at the location where the chemical reaction of metal oxidation is occurring (usually one of the oxide interfaces) will enable a determination of the oxidation rate. Specifically, the ionic particle current density J_i at the reaction interface leads to an increase in the oxide film thickness L at that interface. The local oxide thickness formation rate at that location can be written as

$$(2) \frac{dL}{dt} = R_i J_i ,$$

where R_i is the volume of oxide formed per transported particle of ionic species labeled i . The volume V_{oxide} of oxide being formed because of this oxide thickness increase is given by the product of the thickness increase with the area, summed over the reaction zone where oxide film formation is occurring. Assuming this to be either the interface between the sample and the oxide (designated the *metal-oxide interface*) or else the interface between the oxide and the oxygen being utilized for the reaction (designated the *oxide-oxygen interface*), then the oxide volume formation rate is given by

$$(3) \frac{dV_{\text{oxide}}}{dt} = R_i \int_{\text{Reaction Interface}} J_i \cdot dA .$$

Note that the surface integral involves the vector dot product between the current density vector J_i and the differential area vector dA on the reaction interface. The current density vector is parallel to the motion of the species, and the differential area vector is locally perpendicular to the surface area where the current density vector is being evaluated. The effect of taking the vector dot product is to obtain the product of the current density flow perpendicular to the surface area with that surface area in order to obtain the total particle flow through the surface.

III. Sample Geometry

A. Domain of Application

Since the oxidation rate of materials is dependent upon the ionic currents through the protective oxide covering the material, it is necessary to evaluate the effects of sample geometry upon such currents. Our attention is now directed to the spatial variation of the steady-state current for cases of spherical and cylindrical symmetry. Spherical symmetry should well characterize the oxidation of spherical particles and should yield an approach to the oxidation within spherical cavities in materials. Cylindrical symmetry should well represent the oxidation of wires, and should model reasonably well the oxidation of edges formed by intersection of two planar surfaces.

B. Spherically-Symmetric Case

Consider a uniform radial flow of current density J_s of species s between two concentric metal spheres having radii a and b , with $a < b$, which can be called the inner and outer electrodes. If none of the species concentrations C_s change at any vector position r with time t , the condition necessary for the steady-state, then the total current I_s of species s given by

$$(4) \quad I_s = \int_{\substack{\text{Symmetry} \\ \text{Sphere of} \\ \text{Radius } r}} J_s(r) \, dA = J_s(r) [4\pi r^2]$$

must be the same when evaluated over any imagined sphere concentric with the spherical electrodes, assuming $a < r < b$. The spherical symmetry insures that J_s is independent of the position of the area element dA on the sphere of radius r . That is, there is no preferred radial direction of flow in a spherically-symmetric situation such as this, so the current density is uniform over the surfaces of symmetry consistent with the physical system. This allows the ready evaluation of the surface integral in Eq. (4).

The fact that the total current I_s is independent of the radius r of the chosen sphere in Eq. (4) means that for a spherical shell volume element bounded by two such spherical surfaces, the current out of the volume element will equal the current into the volume element. Thus there will be no build-up or depletion of the concentration of the species within the volume element, as required by the steady-state condition.

The conclusion to be derived from Eq. (4) is that the steady-state radial current density for the case of spherical symmetry varies inversely with the square of the distance r ,

$$(5) \quad J_s(r) \propto 1/r^2.$$

C. Cylindrically-Symmetric Case

If the two metal electrodes are concentric cylinders instead of being concentric spheres, then the current will likewise be radial if the medium between the two electrodes is uniform. Equation (4) is then replaced by

$$(6) \quad I_s = \int_{\substack{\text{Symmetry} \\ \text{Cylinder of} \\ \text{Radius } r}} J_s(r) \, dA = J_s(r) [2\pi r h] ,$$

where h is the length of the concentric cylindrical electrodes having radii a and b ($a < r < b$). The steady-state in this case likewise requires that I_s be independent of r , where in this case r is the radius of any imagined cylinder of symmetry with the electrodes ($a < r < b$). The symbol dA in this case is the area element on the cylinder of radius r . The uniformity of the current density J_s , which because of the electrode symmetry is in the radial direction and has the same value at any point on a given symmetry cylinder, leads to the ready evaluation of the surface integral as shown in Eq. (6). There is no need to consider the flat ends of the imagined cylinder in Eq. (6), since there would be no contribution to I_s from a surface integral over those regions because there is no current perpendicular to the flat ends of the cylinder. The separation distance h between the ends of the imagined cylinder does enter into Eq. (6) because the surface area of the curved portion of the cylindrical surface through which the current flows depends upon the length of the cylinder.

The independence of the total current I_s on radius r of the chosen cylinder in Eq. (6) means that for a cylindrical shell volume element bounded by two such cylindrical surfaces, the current out of the volume element will be equal to the current into the volume element. Thus there will be no build-up or depletion of the concentration of the species within the volume element, as required by the steady-state condition.

The conclusion to be derived from Eq. (6) is that the steady-state radial current density for the case of cylindrical symmetry varies inversely with the distance r ,

$$(7) \quad J_s(r) \propto 1/r .$$

D. Planar-Symmetric Case

For completeness, let us carry out the above analysis for two metal electrodes which are symmetrically-located parallel planes separated by some distance L . The current will be perpendicular to the electrodes if the medium between the two electrodes is uniform. Equation (4) is then replaced by

$$(8) \quad I_s = \int_{\substack{\text{Symmetry} \\ \text{Rectangle at} \\ \text{Position } x}} J_s(x) \, dA = J_s(x) A ,$$

where A is the total area of the rectangle. The steady-state in this case also requires that I_s be independent of x , where x is the distance to the rectangle, as measured perpendicularly from one of the electrodes.

The symbol dA in this case is the area element on the rectangle. The uniformity of the current density J_s , which because of the electrode symmetry is in the perpendicular direction and has the same value at any point on a given symmetry rectangle, leads to the easy

evaluation of the surface integral as shown in Eq. (8). There is no dependence of I_s on the position x of the rectangle, as noted from Eq. (6). In addition, there is no dependence on the electrode separation distance L .

The independence of the total current I_s on position x of the rectangle in Eq. (8) means that for a parallelepiped volume element bounded by two such rectangular surfaces, the current out of the volume element will be equal to the current into the volume element. There would be no current through the four ends of the parallelepiped because the current density is parallel to those planar ends. Thus there will be no build-up or depletion of the concentration of the species within the volume element, as required by the steady-state condition.

The conclusion to be derived from Eq. (8) is that the steady-state current density for the case of planar symmetry does not vary with the position x in the medium,

$$(9) \quad J_s \propto \text{Constant, independent of position } x.$$

To summarize, the steady-state current density is independent of position for planar geometry, it decreases inversely as the radial position r for cylindrical symmetry, and it decreases inversely as the square of the radial distance for spherical symmetry.

E. More Formal Treatment

We can treat the problems of spherical, cylindrical, and planar symmetry more formally by introducing the corresponding vector forms for the divergence operator in the appropriate orthogonal coordinate systems.

The divergence operator in the spherical polar coordinate system is given by

$$(10) \quad \nabla \cdot \mathbf{J} = \frac{1}{r^2 \sin \theta} \left[\sin \theta \frac{\partial}{\partial r} (r^2 J_r) + r \frac{\partial}{\partial \theta} (\sin \theta J_\theta) + r \frac{\partial}{\partial \phi} (J_\phi) \right]$$

where the vector

$$(11) \quad \mathbf{J} = \hat{\mathbf{r}} J_r + \hat{\boldsymbol{\theta}} J_\theta + \hat{\boldsymbol{\phi}} J_\phi$$

in spherical polar coordinates r , θ , and ϕ has the components J_r , J_θ , and J_ϕ , with $\hat{\mathbf{r}}$, $\hat{\boldsymbol{\theta}}$, and $\hat{\boldsymbol{\phi}}$ being the unit vectors in that coordinate system. Because in our application, \mathbf{J} represents the current which is entirely radial and moreover is a function of r only, $J_r = J_r(r)$, $J_\theta = 0$, and $J_\phi = 0$. Equation (10) for the divergence reduces in this case to

$$(12) \quad \nabla \cdot \mathbf{J} = \frac{1}{r^2} \frac{\partial}{\partial r} (r^2 J_r).$$

Applying the steady-state condition in the form of Eq. (1) then leads to

$$(13) \quad \frac{\partial}{\partial r} [r^2 J_r(r)] = 0,$$

which integrates to yield

$$(14) \quad r^2 J_r(r) = \mathcal{K}_{sph}$$

with \mathcal{K}_{sph} being the constant of integration. Thus we obtain $J \propto 1/r^2$ for this case, in accordance with Eq. (5) previously deduced. By comparing this result with Eq. (4) we see that $\mathcal{K}_{sph} = I_S/4\pi$.

The divergence operator in the cylindrical polar coordinates is given by

$$(15) \quad \nabla \cdot \mathbf{J} = \frac{1}{r} \frac{\partial}{\partial r}(r J_r) + \frac{1}{r} \frac{\partial}{\partial \theta}(J_\theta) + \frac{\partial}{\partial z}(J_z),$$

where the vector

$$(16) \quad \mathbf{J} = \hat{r} J_r + \hat{\theta} J_\theta + \hat{z} J_z$$

in cylindrical polar coordinates r , θ , and z has the components J_r , J_θ , and J_z , with \hat{r} , $\hat{\theta}$, and \hat{z} being the unit vectors in that coordinate system. However, in cylindrical symmetry cases, the current density vector is radial. Therefore, in cylindrical polar coordinates, the component J_r is the only non-zero component of the vector; the components J_θ and J_z are zero. Moreover, J_r is a function of r only. Thus we can write

$$(17) \quad \nabla \cdot \mathbf{J} = \frac{1}{r} \frac{\partial}{\partial r}(r J_r).$$

Applying the steady-state condition in the form of Eq. (1) then leads to

$$(18) \quad \frac{\partial}{\partial r} [r J_r(r)] = 0,$$

which integrates to give

$$(19) \quad r J_r(r) = \mathcal{K}_{cyl},$$

with \mathcal{K}_{cyl} being the constant of integration. Thus we obtain $J \propto 1/r$ for this case, in accordance with Eq. (7) previously deduced. By comparing this result with Eq. (6) we see that $\mathcal{K}_{cyl} = I_S/2\pi h$.

For completeness, let us also carry out the above analysis for planar symmetry, where any variation is considered to occur in the x -direction, with the system being entirely uniform in the y and z -directions. The divergence operator in rectangular cartesian coordinates is given by

$$(20) \quad \nabla \cdot \mathbf{J} = \frac{\partial J_x}{\partial x} + \frac{\partial J_y}{\partial y} + \frac{\partial J_z}{\partial z}$$

where the vector

$$(21) \quad \mathbf{J} = \hat{x} J_x + \hat{y} J_y + \hat{z} J_z$$

in rectangular cartesian coordinates x , y , and z has the components J_x , J_y , and J_z , with \hat{x} , \hat{y} , and \hat{z} being the unit vectors in that coordinate system. However, in the presently-considered case, the current density vector is in the x direction and moreover is at most a

function of the x-coordinate. Thus

$$(22) \quad \nabla \cdot \mathbf{J} = \frac{\partial J_x(x)}{\partial x} .$$

Applying the steady-state condition in the form of Eq. (1) then leads to

$$(23) \quad \frac{\partial J_x(x)}{\partial x} = 0 .$$

which integrates to yield

$$(24) \quad J_x(x) = \mathcal{K}_{\text{plane}} ,$$

with $\mathcal{K}_{\text{plane}}$ being the constant of integration. Thus we obtain J_x independent of x for this case, in accordance with Eq. (9) previously deduced.

In the following section we show how to proceed in obtaining the values of the total current. This is tantamount to evaluating the integration constants obtained above.

IV. Driving Forces and Currents

The general vector relation for the current density \mathbf{J}_s for species s in terms of the electrochemical potential \tilde{u}_s for species s is determined by the vector gradient,

$$(25) \quad \mathbf{J}_s \propto - C_s \nabla \tilde{u}_s ,$$

where C_s is the concentration of species s . The form for the gradient operator ∇ is specific to the symmetry of the physical problem to be treated. It can be expressed, for example, in rectangular, spherical, and cylindrical coordinates, or in a more general form which applies to any orthogonal curvilinear coordinate system. In spherical polar coordinates,

$$(26) \quad \nabla \tilde{u}_s = \hat{r} \frac{\partial \tilde{u}_s}{\partial r} + \hat{\theta} \frac{1}{r} \frac{\partial \tilde{u}_s}{\partial \theta} + \hat{\phi} \frac{1}{r \sin \theta} \frac{\partial \tilde{u}_s}{\partial \phi} ,$$

while in cylindrical polar coordinates,

$$(27) \quad \nabla \tilde{u}_s = \hat{r} \frac{\partial \tilde{u}_s}{\partial r} + \hat{\theta} \frac{1}{r} \frac{\partial \tilde{u}_s}{\partial \theta} + \hat{z} \frac{\partial \tilde{u}_s}{\partial z} .$$

Denoting the proportionality factor for Eq. (25) by \mathfrak{B}_s , and using the standard form for the electrochemical potential,^s

$$(28) \quad \tilde{u}_s = u_s^0 + k_B T \ln C_s + q_s V ,$$

where u_s^0 is the reference state value of the chemical potential u_s , k_B is Boltzmann's constant, T is the absolute temperature, q_s is the charge per particle of species s , and V is the electrostatic potential, Eq. (25) becomes

$$(29) \quad \mathbf{J}_s = - \mathfrak{B}_s C_s \nabla \tilde{u}_s = - k_B T \mathfrak{B}_s \nabla C_s + q_s \mathfrak{B}_s \mathbf{E} C_s ,$$

where E is the electric field given by

$$(30) \quad E = - \nabla V .$$

Comparison with the usual linear diffusion equation

$$(31) \quad J_s = - D_s \nabla C_s + \mu_s E C_s ,$$

shows term-by-term agreement, with the diffusion coefficient being given by

$$(32) \quad D_s = k_B T \mathfrak{B}_s$$

and the mobility being given by

$$(33) \quad \mu_s = q_s \mathfrak{B}_s .$$

The ratio of the two coefficients gives the Einstein relation

$$(34) \quad \mu_s / D_s = q_s / k_B T .$$

The electric field is of course zero in the above equations if the diffusing species giving rise to the oxidation process are uncharged. With this choice, the equations in our development for the rate of oxidation yield also the growth rate for non-planar geometries for the diffusion of uncharged particles. In this limit the results can be compared to those deduced by Wilson and Marcus.¹ Generally the diffusing species are charged, however, in which case the full treatment is required.

V. Electric Fields

A. General Relations and Zero-Space-Charge Limit

For charged particle diffusion, the driving force of the electric field is as important as the concentration gradient, both being included as part of the gradient in the electrochemical potential.² For cases of high symmetry, Gauss' law provides the easiest approach to finding the value and position-dependence of the field. A closed imaginary surface having the symmetry of the physical problem is used for carrying out a surface integral of the electric field,

$$(35) \quad \int_{\text{Imaginary Surface}} \epsilon E \cdot dA = Q$$

where Q is the net charge within the closed surface that is chosen for the integration. The parameter ϵ is the electric permittivity of the medium.

The relationship between the electric field E and the electric potential difference V_{ab} between points b and a is given by the line integral

$$(36) \quad V_{ab} = - \int_a^b E \cdot dr ,$$

which is in accord with Eq. (30). The magnitude of the potential difference between two electrodes is usually called the applied voltage.

There can be space-charge contributions to the field as well as surface-charge contributions, but for diffusing defect densities below $10^{16}/\text{cm}^3$, for example, the space-charge contributions may be neglected for oxide thicknesses below 1000 Å or so.³ Because the space charge is a complexity in itself, in the present development we choose to neglect it. The present development is therefore restricted to the zero space-charge limit, so that the electric field is due to surface charge only. In the case of planar oxides, the zero space-charge limit leads to electric fields which are independent of position x within the oxide, and for this reason it has been designated² the "homogeneous-field approximation". At the moment, we restrict our consideration to the zero space-charge limit in order to focus more intensely on the purely geometric effects which is the subject of this presentation.

B. Spherical Geometry

Consider specifically the spherical geometry case with concentric spherical electrodes of radius a and b , with $a < b$. The electric field does not require the existence of electrodes, but it is helpful to imagine that they are present. Radial symmetry and zero space charge in the uniform medium leads to a ready evaluation of Gauss' law for this case,

$$(37) \quad \epsilon E_r 4 \pi r^2 = Q_a, \quad (a < r < b)$$

where Q_a is the charge on the inner electrode a . The radial component of the field is the only nonzero component, as can be argued convincingly from the symmetry of the physical problem.

The corresponding electric potential difference evaluated at some arbitrary position r between the electrodes is given by

$$(38) \quad V(r) - V(a) = - \int_a^r E_r dr = \frac{Q_a}{4\pi\epsilon} \left(\frac{1}{r} - \frac{1}{a} \right)$$

The total built-in electric potential across the oxide is given by this expression evaluated at $r = b$,

$$(39) \quad V_{\text{built-in}} = V(b) - V(a) = \frac{Q_a}{4\pi\epsilon} \left(\frac{1}{b} - \frac{1}{a} \right).$$

With no space charge, the charge Q_b at b is the negative of Q_a ,

$$(40) \quad Q_b = - Q_a.$$

The specific evaluation of $V_{\text{built-in}}$ will be carried out subsequently.

C. Cylindrical Geometry

Consider concentric cylindrical electrodes of radius a and b , with $a < b$. Gauss' law leads to

$$(41) \quad \epsilon E_r 2 \pi r h = Q_a \quad (a < r < b)$$

where the total charge Q_a on electrode a is determined by the charge λ per unit length of that electrode,

$$(42) \quad Q_a = \lambda h .$$

Conservation of charge and the absence of space charge allows writing

$$(43) \quad Q_b = - Q_a .$$

As in the spherical geometry case, the radial component is the only nonzero component of the field.

The electric potential $V(r)$ for this cylindrically-symmetric case is given by

$$(44) \quad V(r) - V(a) = - \int_a^r E_r dr = -(\lambda/2\pi\epsilon)\ln(r/b) .$$

The total built-in electric potential across the oxide is given by this expression evaluated at $r = b$,

$$(45) \quad V_{\text{built-in}} = V(b) - V(a) = -(\lambda/2\pi\epsilon)\ln(b/a) .$$

D. Planar Symmetry

For completeness, let us give the analogous results for planar geometry. For the metal-oxide interface at a and the oxide-oxygen interface at b, the oxide thickness is given by $L=b-a$. Planar symmetry and zero space charge leads to a ready evaluation of Gauss' law,

$$(46) \quad \epsilon E_x A = Q_a ,$$

where $\tau = Q_a/A$ is the charge per unit area. The corresponding electric potential is given by

$$(47) \quad V(x) - V(a) = (\tau/\epsilon)(x - a) .$$

Evaluation of this expression at $x = b$ gives the potential difference across the oxide.

E. More Formal Treatment

A more formal treatment can be based on Poisson's equation

$$(48) \quad -\nabla^2 V = \rho/\epsilon ,$$

where ρ is the local volume charge density and ϵ is the electric permittivity of the oxide. For zero space charge, $\rho=0$. Employing $E = -\nabla V$, this leads to

$$(49) \quad -\nabla^2 V = -\nabla \cdot \nabla V = \nabla \cdot E = 0 .$$

In spherical polar coordinates this becomes

$$(50) \quad \frac{1}{r^2 \sin \theta} \left[\sin \theta \frac{\partial}{\partial r}(r^2 E_r) + r \frac{\partial}{\partial \theta}(\sin \theta E_\theta) + r \frac{\partial E_\phi}{\partial \phi} \right] = 0 ,$$

while in cylindrical polar coordinates this relation is

$$(51) \quad \frac{1}{r} \frac{\partial}{\partial r}(r E_r) + \frac{1}{r} \frac{\partial E_\theta}{\partial \theta} + \frac{\partial E_z}{\partial z} = 0 .$$

Due to the spherical and cylindrical symmetry assumed in the respective cases, only the radial component of the field is nonzero. Furthermore, $E_r = E_r(r)$ only, since, with the specified symmetries, there is no cause for variation of the field in the other directions. Thus we obtain in the spherically-symmetric case

$$(52) \quad \frac{\partial}{\partial r}(r^2 E_r) = 0 ,$$

while for the cylindrically-symmetric case we obtain

$$(53) \quad \frac{\partial}{\partial r}(r E_r) = 0 .$$

These expressions are readily integrated. Thus for spherical symmetry,

$$(54) \quad E_r \propto \frac{1}{r^2} ,$$

while for cylindrical symmetry,

$$(55) \quad E_r \propto \frac{1}{r} ,$$

in accordance with the above results obtained using Gauss' law. The planar case is just as simple, since for zero space charge,

$$(56) \quad \nabla \cdot \mathbf{E} = \frac{\partial E_x}{\partial x} + \frac{\partial E_y}{\partial y} + \frac{\partial E_z}{\partial z} = 0 .$$

For symmetry over planes perpendicular to \hat{x} , we expect that $E_y=0$ and $E_z=0$, and that E_x will be independent of y and z . Thus

$$(57) \quad \frac{\partial E_x}{\partial x} = 0 ,$$

and

$$(58) \quad E_x = \text{Constant} .$$

The electrical potentials follow from a line integral of the electric field in the usual way, as already shown above.

VI. Coupled Currents for Spherical and Cylindrical Symmetries

A. Coupled-Currents Condition

Let us consider the interface between the material being oxidized (usually a metal) and the oxide layer to be located by the radius a . This is the metal-oxide interface. Then the opposite interface of the oxide, which is the oxide-oxygen interface in contact with the attacking oxygen phase, is considered to be located by the radius b . As the oxide film grows, both a and b change. In spherical,

cylindrical, and planar geometries, the oxide film thickness L is given by the difference between a and b , so $a = a(t)$ and $b = b(t)$.

The electrochemical potential difference between the metal-oxide and the oxide-oxygen interfaces provides the driving force for the currents, as outlined above. At any position in the oxide layer, the existing electric field will aid transport of the ionic or the electronic species, and oppose transport of the other. The currents can themselves lead to a net charge transport, which changes the field since Q_a will be modified. Careful analysis² has shown that the net charge transported through the oxide layer of thickness L over any time increment is generally much smaller than the charge transported by either the ions or the electrons individually. Were this not the case, the electric fields produced within the system would reach catastrophic values very quickly, with dielectric breakdown occurring. The fundamental point is that a monolayer of charged particles can produce an incredibly large electric field, so that the net charge setting up the surface-charge field requires only a tiny imbalance in positive and negative charge. The difference between the positive and negative charge transport during the building of a layer of oxide can represent at most only a tiny fraction of the total particles in that layer.

The coupled-currents condition

$$(59) \quad q_1 J_1 + q_2 J_2 = 0$$

represents a state of zero net charge transport, since the charge current $q_1 J_1$ of the ionic species (species 1) is nullified by the charge current $q_2 J_2$ of the electronic species (species 2). This presumes the specific situation where there is one dominant diffusing ionic species and one dominant diffusing electronic species, which is the simplest case for growth by charged particles.

The coupled currents condition has been used widely in the evaluation of planar oxide growth², but to date it has not been applied to the growth of non-planar oxides. For the spherical and the cylindrical symmetries, the currents $J(r)$ given by Eqs. (4) and (8) respectively, can be substituted into Eq. (59) above to obtain the following form for the coupled-currents condition,

$$(60) \quad q_1 I_1 + q_2 I_2 = 0 .$$

This is the most useful form for present purposes.

B. Differential Equation for the Current

The current density J_s of species s is given in general, by Eq. (29). The geometry in question determines the form of the gradient operator ∇ and the functional form of the electric field E . In both the spherical and the cylindrical geometries, C_s varies only radially, so that $C_s = C_s(r)$. The gradient operation in both geometries [see Eqs. (26) and (27)] then reduces to the especially simple form

$$(61) \quad \nabla C_s = \hat{r}(dC_s/dr) ,$$

where \hat{r} is the unit vector in the radial direction. In both geometries the electric field is radial, so that

$$(62) \quad \mathbf{E} = \hat{r} E_r .$$

Substituting these two relations into Eq. (29) yields the current

$$(63) \quad \mathbf{J}_s = \hat{r} J_s$$

which is totally radial, with J_s given by

$$(64) \quad J_s = -k_B T \varpi_s \frac{dC_s}{dr} + q_s \varpi_s E_r C_s .$$

VII. Solution of Problem for Spherical Symmetry

A. Concentration Profile and Steady-State Current

The electric field for spherical symmetry given by Eq. (37) can be substituted into Eq. (64) for the current, and in addition Eq. (4) can be used to replace the position-dependent current density J_s by the position-independent quantity I_s . Thus we obtain

$$(65) \quad \frac{I_s}{4\pi r^2} = -k_B T \varpi_s \frac{dC_s}{dr} + q_s \varpi_s C_s \frac{Q_a}{4\pi \epsilon r^2} .$$

Rearranging this equation to separate variables yields the integral form

$$(66) \quad \int_{C_s(a)}^{C_s(r)} \frac{(4\pi \epsilon k_B T \varpi_s) dC_s}{(q_s \varpi_s Q_a) C_s - \epsilon I_s} = \int_a^r \frac{dr}{r^2} .$$

These integrals are readily evaluated to give the concentration profile,

$$(67) \quad C_s(r) = (\epsilon I_s / q_s \varpi_s Q_a) + \left[C_s(a) - (\epsilon I_s / q_s \varpi_s Q_a) \right] P_s(r) ,$$

where

$$(68) \quad P_s(r) = \exp \left[\alpha_s \left[(1/a) - (1/r) \right] \right] ,$$

with

$$(69) \quad \alpha_s = q_s Q_a / 4\pi \epsilon k_B T .$$

The total particle current I_s for species s then follows by evaluating the concentration profile expression at $r=b$,

$$(70) \quad I_s = (q_s Q_a \varpi_s / \epsilon) \left[\frac{C_s(b) - C_s(a) P_s(b)}{1 - P_s(b)} \right] .$$

Thus I_s is given in terms of Q_a and otherwise known parameters of the system for any species s .

The subsequent algebraic details are simplified by introducing the parameter Γ defined by

$$(71) \quad \Gamma = \exp \left[\alpha_0 \left[(1/a) - (1/b) \right] \right],$$

where

$$(72) \quad \alpha_0 = eQ_a / 4\pi\epsilon k_B T,$$

with e representing the electronic charge magnitude. Expressing the charge q_s per particle of species s as

$$(73) \quad q_s = Z_s e,$$

the quantity $P_s(b)$ appearing in Eq. (70) becomes

$$(74) \quad P_s(b) = \Gamma^{Z_s},$$

since

$$(75) \quad \alpha_s = Z_s \alpha_0.$$

B. Built-in Potential

To determine Q_a , we now invoke the coupled currents condition. Substituting Eq. (70) for I_s (with $s=1$ and $s=2$) into Eq. (60) and utilizing Eqs. (73)-(74) yields

$$(76) \quad \frac{Z_1^2 \mathfrak{R}_1 [C_1(a)\Gamma^{Z_1} - C_1(b)]}{\Gamma^{Z_1} - 1} + \frac{Z_2^2 \mathfrak{R}_2 [C_2(a)\Gamma^{Z_2} - C_2(b)]}{\Gamma^{Z_2} - 1} = 0.$$

This represents an algebraic equation for Γ , and the solution yields the quantity Q_a because that is the only variable quantity in the definition of Γ , as can be noted from Eqs. (71) and (72). This in turn is sufficient to evaluate $V_{\text{built-in}}$ by means of Eq. (39). Thus

$$(77) \quad V_{\text{built-in}} = -(k_B T/e) \ln \Gamma.$$

The details of solving the algebraic equation for Γ hinges upon the ratio Z_1/Z_2 , but this is a technical problem only. The important point is that the solution will yield a value for Γ which depends upon the fixed parameters of the system but which under normal circumstances will be independent of the values of the radii a and b . Thus Γ will not depend upon the thickness of the oxide, and hence the built-in potential $V_{\text{built-in}}$ will be fixed during growth of the oxide. This is a very important result for the kinetics of oxidation for the case of spherical geometry.

At this point it is worthwhile to find the explicit forms for the built-in potential for some specific situations. Consider first the ionic species to be monovalent cation interstitials, in which case $Z_1 = 1$, with the attendant electronic species being electrons, so $Z_2 = -1$. The solution of Eq. (76) is readily obtained,

$$(78) \quad \Gamma = [\mathfrak{R}_1 C_1(b) + \mathfrak{R}_2 C_2(a)] / [\mathfrak{R}_1 C_1(a) + \mathfrak{R}_2 C_2(b)], \quad (Z_1=+1; Z_2=-1)$$

and the built-in potential follows immediately from Eq. (77).

Since this result is independent of the radii a and b , it follows that it must also give the corresponding value for the built-in potential in the planar limit where $L=(b-a)$ is small relative to a . [Refer to ch. 7, §3 in Ref. 2 for the planar treatment].

For the converse case of monovalent cation vacancies and electron holes, $Z_1 = -1$ and $Z_2 = +1$. The same form of equation results, but with Γ replaced by $1/\Gamma$. Thus the solution for Γ for this case is the reciprocal of the right-hand side of Eq. (78) above. The built-in potential will then have the same magnitude but will be of opposite sign.

Whenever the ionic species is divalent, the ratio Z_1/Z_2 will have the value -2 . This case may involve cation interstitials ($Z_1=+2$) with electrons, or else cation vacancies ($Z_1=-2$) with electron holes. In either case a quadratic equation for Γ emerges, but this is readily solved by the quadratic formula. The value of Γ will be independent of the thickness of the oxide, so the built-in potential given by Eq. (77) will be independent of oxide thickness.

C. Ionic Current for Spherical Samples

The total ionic current I_1 is readily evaluated at this point, since the evaluation of Γ is sufficient to yield $P_s(b)$ from Eq. (74) above, and also sufficient to yield α_0 and hence Q_a from Eqs. (71)-(72),

$$(79) \quad Q_a = (4\pi\epsilon k_B T/e) \left(\frac{1}{a} - \frac{1}{b} \right)^{-1} \ln \Gamma.$$

Thus the charge on the metal changes with the radii a and b as the oxide grows. This technically is a violation of the coupled-currents condition, but it can be shown to provide only a minor perturbation on the final result.

Utilizing the above result for Q_a , we obtain from Eq. (70) for I_1 the following expression for the total ionic current,

$$(80) \quad I_1 = 4\pi Z_1 R_1 k_B T \ln(\Gamma) \left(\frac{1}{a} - \frac{1}{b} \right)^{-1} \left[\frac{C_1(b) - C_1(a)\Gamma^{Z_1}}{1 - \Gamma^{Z_1}} \right].$$

Alternatively, the total current may be expressed in terms of the constant built-in potential,

$$(81) \quad I_1 = -4\pi q_1 R_1 \left(\frac{1}{a} - \frac{1}{b} \right)^{-1} V_{\text{built-in}} \times \left[\frac{C_1(b) - C_1(a)\exp[-Z_1 e V_{\text{built-in}}/k_B T]}{1 - \exp[-Z_1 e V_{\text{built-in}}/k_B T]} \right].$$

For the positive monovalent ionic species case, the evaluation of $V_{\text{built-in}}$ given by Eqs. (77)-(78) can be inserted directly into this expression to obtain an alternate form, if desired.

D. Oxide Growth and Particle Burnup Rate Laws for Spherical Samples

Because I_1 gives the total current flowing through any symmetry sphere, as defined in Eq. (4), and moreover is independent of the

radius of the sphere chosen, it represents the value of the integral appearing in Eq. (3) for the volume rate of oxide formation. Thus we can write

$$(82) \quad \frac{dV_{\text{oxide}}}{dt} = R_1 I_1 ,$$

where I_1 is the total ionic current as evaluated above. Since I_1 is given in terms of the time-dependent radii a and b , it is necessary to relate these quantities to V_{oxide} before the growth law can be evaluated.

Let us next define the volume expansion parameter σ ,

$$(83) \quad \sigma = \frac{\text{Volume of oxide formed}}{\text{Volume of metal used in oxide formation}}$$

Since the volume of metal which has been utilized at any time t is given by

$$(84) \quad V_{\text{metal}} = \frac{4}{3} \pi a_o^3 - \frac{4}{3} \pi a^3 ,$$

where a_o is the radius of the metal sphere at $t=0$, the corresponding volume of oxide which has been formed is given by

$$(85) \quad V_{\text{oxide}} = \left(\frac{4}{3} \pi b^3 - \frac{4}{3} \pi a^3 \right) - \left(\frac{4}{3} \pi b_o^3 - \frac{4}{3} \pi a_o^3 \right) ,$$

where b_o locates the oxide-oxygen interface at $t=0$. If no initial oxide is present, then $b_o = a_o$, and the above expression simplifies accordingly. The volume expansion parameter thus can be written as

$$(86) \quad \sigma = \frac{(b^3 - b_o^3) + (a_o^3 - a^3)}{a_o^3 - a^3} = 1 + [(b^3 - b_o^3)/(a_o^3 - a^3)] ,$$

which provides the following relation between b and a ,

$$(87) \quad b = \left(b_o^3 + (\sigma - 1)(a_o^3 - a^3) \right)^{1/3} .$$

Whenever the volume of oxide exceeds the volume of metal consumed in forming the oxide, σ exceeds unity. For a negligible expansion in volume upon oxide formation, σ would be unity and b would maintain its $t=0$ value b_o . Since in general

$$(88) \quad V_{\text{oxide}} = \sigma V_{\text{metal}} ,$$

we obtain from Eq. (84),

$$(89) \quad \frac{dV_{\text{oxide}}}{dt} = \sigma \frac{dV_{\text{metal}}}{dt} = -4\pi\sigma a^2 \frac{da}{dt}$$

Setting this equal to $R_1 I_1$ in accordance with Eq. (82) above gives

$$(90) \quad -\sigma a^2 \frac{da}{dt} \left(\frac{1}{a} - \frac{1}{b} \right) = \Omega ,$$

where Ω is the constant quantity

$$(91) \quad \Omega = - R_1 \mu_1 V_{\text{built-in}} \left[\frac{C_1(b) - C_1(a) \exp[-Z_1 e V_{\text{built-in}} / k_B T]}{1 - \exp[-Z_1 e V_{\text{built-in}} / k_B T]} \right] ,$$

with μ_1 being the ionic mobility defined by Eq. (33). Next we can utilize Eq. (87) for b in terms of a , and integrate the above differential equation from $t = 0$ to arbitrary time t ,

$$(92) \quad \frac{1}{2} \sigma [a_0^2 - a^2] + \sigma \mathcal{J}_1(a) = \Omega t ,$$

where

$$(93) \quad \mathcal{J}_1(a) = \int_{a_0}^a \frac{a^2 da}{[b_0^3 + (\sigma - 1)(a_0^3 - a^3)]^{1/3}} .$$

The integral $\mathcal{J}_1(a)$ is easily evaluated,

$$(94) \quad \mathcal{J}_1(a) = - \frac{1}{2(\sigma - 1)} \left[(b_0^3 + (\sigma - 1)(a_0^3 - a^3))^{2/3} - b_0^2 \right]$$

We note in passing that $\mathcal{J}_1(a)$ can likewise be written in terms of b ,

$$(95) \quad \mathcal{J}_1 = - \frac{1}{2(\sigma - 1)} [b^2 - b_0^2] .$$

Combining the integrated form for $\mathcal{J}_1(a)$ with Eq. (92) yields the rate law for the time-rate of change of the radius $a(t)$ of the metal particle.

Next let us deduce the corresponding rate law for the variation of the outer radius b with time. From Eq. (87) which relates b to a we obtain by differentiation

$$(96) \quad a^2 da = -(\sigma - 1)^{-1} b^2 db .$$

Substituting this relation into Eq. (90) yields

$$(97) \quad \left(\frac{\sigma}{\sigma - 1} \right) \left[\frac{b^2}{a} \frac{db}{dt} - b \frac{db}{dt} \right] = \Omega .$$

Integrating this equation from $t=0$ to arbitrary time t yields the rate law for the outer radius $b(t)$,

$$(98) \quad \left(\frac{\sigma}{\sigma - 1} \right) \left[\mathcal{J}_2(b) - \frac{1}{2} [b^2 - b_0^2] \right] = \Omega t ,$$

where, employing Eq. (87),

$$(99) \quad \mathcal{J}_2(b) = \int_{b_0}^b \frac{b^2 db}{[a_0^3 - (\sigma - 1)^{-1}(b^3 - b_0^3)]^{1/3}}$$

This integral is readily evaluated to obtain

$$(100) \quad \mathcal{J}_2(b) = - \frac{1}{2} (\sigma - 1) \left[(a_0^3 - (\sigma - 1)^{-1}(b^3 - b_0^3))^{2/3} - a_0^2 \right]$$

Note that $\mathcal{J}_2(b)$ can likewise be written in terms of a ,

$$(101) \quad \mathcal{J}_2 = - \frac{1}{2} (\sigma - 1) [a^2 - a_0^2]$$

Combining the integrated form for $\mathcal{J}_2(b)$ with Eq. (98) yields the rate law for the time-rate of change of the radius $b(t)$ of the metal

particle. This result also can be obtained by substituting directly Eq. (87) into Eq. (92) and utilizing Eq. (95).

Next let us ask whether or not it is possible to obtain any expressions for the time-dependence of the oxide thickness L and the volume of oxide. Because $L=b-a$, the above expressions relating b and a to t provide a method to obtain $L(t)$ numerically. More directly, combining Eqs. (84), (85), and (88), the obtained relation

$$(102) \quad V_{\text{oxide}} = \sigma \left(\frac{4}{3} \pi (a_o^3 - a^3) \right) = \left(\frac{4}{3} \pi (b^3 - a^3) \right) - \left(\frac{4}{3} \pi (b_o^3 - a_o^3) \right),$$

serves to yield V_{oxide} directly in terms of a and also provides a ready way to obtain L in terms of a . Substituting $b=L+a$ into this relation and solving for L yields

$$(103) \quad L = \left[(1 - \sigma)(a^3 - a_o^3) + b_o^3 \right]^{1/3} - a.$$

Numerically the problem can then be evaluated as follows. A sequence of values of a is substituted into Eqs. (92) and (94) to obtain the corresponding sequence of time values. Next the corresponding sequences of values for b , V_{oxide} , and L are obtained from the sequence of values of a by using Eqs. (87), (102), and (103). The results can then be plotted as individual curves, namely, $a(t)$ vs t , $b(t)$ vs t , $V_{\text{oxide}}(t)$ vs t , and/or $L(t)$ vs t , as desired.

There will eventually be a point in time where $a(t)$ decreases to zero. Since the metal particle will then have been converted totally to oxide, we designate this as the burn-up time t_{burnup} . The $a(t) \rightarrow 0$ limit of Eqs. (92) and (94) yields the time required for the complete oxidation of the spherical particles,

$$(104) \quad t_{\text{burnup}} = (\sigma/2\Omega) \left[a_o^2 - \frac{1}{(\sigma - 1)} \left[(b_o^3 + (\sigma - 1)a_o^3)^{2/3} - b_o^2 \right] \right].$$

This can be written in an alternative form involving the quantity b_{max} defined as the value b approaches as $a \rightarrow 0$. Then the total quantity of oxide is given by

$$(105) \quad \frac{4}{3} \pi b_{\text{max}}^3 = \left(\frac{4}{3} \pi b_o^3 - \frac{4}{3} \pi a_o^3 \right) + \sigma \left(\frac{4}{3} \pi a_o^3 \right)$$

$$(106) \quad b_{\text{max}} = \left[\sigma a_o^3 + (b_o^3 - a_o^3) \right]^{1/3}.$$

Thus Eq. (104) can be expressed in the form

$$(107) \quad t_{\text{burnup}} = (\sigma/2\Omega) \left[a_o^2 - \frac{1}{(\sigma - 1)} (b_{\text{max}}^2 - b_o^2) \right].$$

Due to the complexity of the above rate laws, little can be deduced from a cursory inspection. Three methods suggest themselves for obtaining physical understanding of the result, viz., numerical evaluations using the scheme outlined above, series expansions, and simplifying approximations. Although we have used all three, at the moment it is most informative to adopt the latter approach. One simplifying assumption which can be made is that the volume expansion

of the oxide is relatively small. In the limit that no expansion of the metal occurs upon formation of the oxide, the volume expansion parameter σ will be unity. The differential equation for $a(t)$ given by Eq. (90) then reduces to

$$(108) \quad -a^2 \frac{da}{dt} \left(\frac{1}{a} - \frac{1}{b_0} \right) = \Omega ,$$

since the location of the oxide surface $b(t)$ will then be unchanged with the degree of oxidation, having the initial value b_0 . Integration of this expression gives

$$(109) \quad [a_0^2 - a^2] - (2/3b_0)[a_0^3 - a^3] = 2 \Omega t .$$

Since $a_0 < a$ for spherical particles, and $b_0 > 0$, the second bracketed term tends to cancel the first bracketed term on the left-hand side of this equation. Furthermore, the value of the second term will always be smaller than the first term, so that the expression is well-behaved as time increases. The observation to be made is that the time required to reach any given $a(t)$ will be shorter due to the presence of the second bracketed term. As shown later, the first bracketed term expresses the entire planar-limit result for which the radii a and b are much greater than the oxide thickness $L=b-a$.

The simplified equation above yields the following result for the burn-up time for spherical metal particles,

$$(110) \quad t_{\text{burnup}} = a_0^2 / 6\Omega ,$$

where for simplicity we have now assumed there exists no initial oxide (viz., at $t=0$, $b_0 = a_0$).

It is interesting to derive the corresponding result for the oxide thickness $L(t)$ as a function of the oxidation time t . Again assuming $\sigma = 1$, we have

$$(111) \quad b = b_0 = a + L ,$$

so that

$$(112) \quad da = -dL .$$

Equation (108) takes the form

$$(113) \quad [1 - (L/b_0)] L dL = \Omega dt ,$$

which is readily integrated to obtain the oxide growth rate law for the oxidation of spherical particles,

$$(114) \quad \frac{1}{2} [L^2 - L_0^2] - \frac{1}{3b_0} [L^3 - L_0^3] = \Omega t .$$

Often it can be assumed that $L_0 = 0$. The cubic term in L is always smaller than the quadratic term, since $L < b_0$, so this equation represents a well-behaved rate law. Furthermore, the cubic term

subtracts from the quadratic term, so a shorter time t is required to reach a given oxide thickness L because of the presence of the cubic term.

It is interesting to compare this result with the corresponding result for planar geometry. The planar limit is achieved by assuming that $L \ll b_0$, so that (L/b_0) can be neglected relative to unity. The differential equation for growth [Eq. (113)] then reduces to the approximate form

$$(115) \quad L \, dL = \Omega \, dt ,$$

which is integrated readily to yield the planar growth law,

$$(116) \quad L^2 - L_0^2 = 2 \, \Omega \, t .$$

Comparison of this planar result with Eq. (114) for spherical samples shows that the cubic term contains all of the effects of the spherical geometry.

If a metal plate having an initial thickness $2a_0$ is attacked by oxygen from both sides, then a comparison between the planar result and Eq. (114) above for spherical samples shows that the burn-up time for bare spherical particles of initial radius a_0 is only 1/3 the burn-up time required for the plate. Moreover, if the plate is attacked on only one side, the time required for the oxide to reach a thickness on the plate which is equal to the spherical particle diameter would be a factor of 12 larger than the burn-up time of the spherical particle. This simplified example thus serves to illustrate that geometrical effects on the rate of metal oxidation can be quite pronounced.

A numerical computation has been carried out to illustrate the functional form of the simplified rate law [Eq. (114)]. The numerical values used for the several parameters are listed in Table 1. The results of the computation for oxide film thickness L vs time t are shown in Fig. 1. For comparison, the planar result given by Eq. (116) is also plotted in Fig. 1. The faster burn-up of the spherical particles relative to the planar sample as the oxide thickness approaches the value of the initial radius a_0 of the metal particle is to be noted in the figure, corresponding to the factor of 3 deduced analytically above. In addition, the rapid increase in the rate as the oxide thickness approaches the value of the initial radius a_0 of the metal particle, corresponding to the burn-up point where the radius of the spherical metal particle approaches zero, is of major significance.

References

1. Lynn O. Wilson and R. B. Marcus, "Oxidation of Curved Silicon Surfaces," J. Electrochem. Soc. 134, 481-490 (1987).
2. A. T. Fromhold, Jr., Theory of Metal Oxidation. Vol. I -- Fundamentals (North Holland Publishing Company, Amsterdam, 1976), ch. 7.
3. A. T. Fromhold, Jr., Theory of Metal Oxidation. Vol. II -- Space Charge (North Holland Publishing Company, Amsterdam, 1980), ch. 13.

TABLE 1 -- Values used for the parameters in computing Fig. 1.

$$\mu_1 = -1 \times 10^{-8} \text{ cm}^2/\text{V-sec}$$

$$\mu_2 = 1 \times 10^{-6} \text{ cm}^2/\text{V-sec}$$

$$C_1(a) = 1 \times 10^{14} \text{ /cm}^3$$

$$C_1(b) = 5 \times 10^{17} \text{ /cm}^3$$

$$C_2(a) = 1 \times 10^{17} \text{ /cm}^3$$

$$C_2(b) = 5 \times 10^{17} \text{ /cm}^3$$

$$R_1 = -2.0 \times 10^{-22} \text{ cm}^3$$

$$T = 900 \text{ K}$$

$$Z_1 = -1$$

$$Z_2 = 1$$

$$a_o = 1 \times 10^{-4} \text{ cm} = 10,000 \text{ Å}$$

$$b_o = 1 \times 10^{-4} \text{ cm} = 10,000 \text{ Å}$$

$$\sigma = 1$$

$$k_B = 1.3806 \times 10^{-23} \text{ J/K}$$

$$e = 1.6022 \times 10^{-19} \text{ C}$$

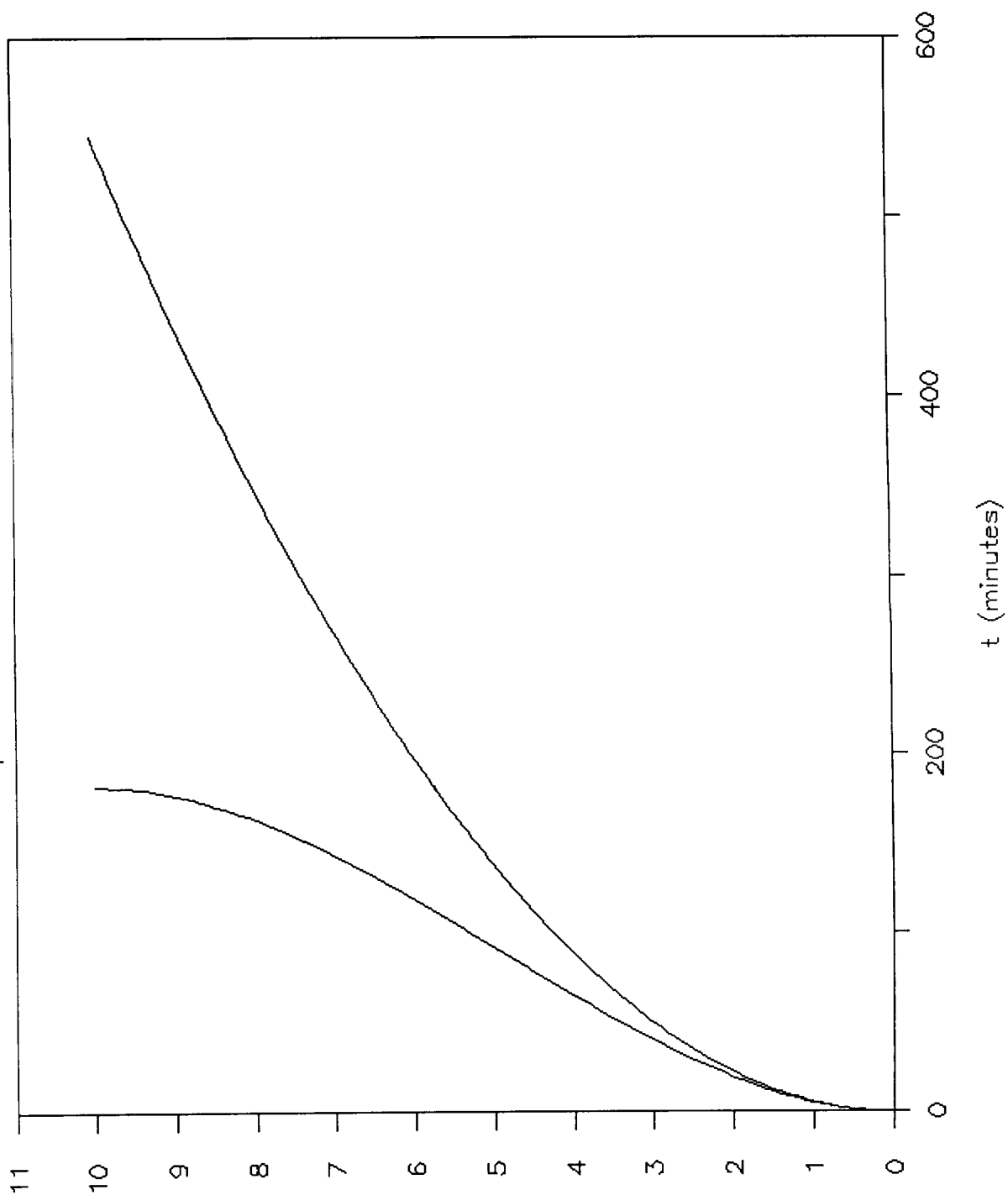
Computed Results:

$$V_{\text{built-in}} = -0.1210 \text{ Volts}$$

Fig. 1. Oxidation rate law for spherical particles (upper curve) with growth by anion interstitial or cation vacancy diffusion coupled with electron-hole diffusion. The corresponding parabolic law [$L^2 \propto t$] for planar samples (lower curve) is shown for comparison.

Metal Oxidation Kinetics

Spherical & Planar Geometries



L (Angstroms)
(Thousands)

N88-15618⁵¹⁷⁻⁶¹

116719

22P

1987

NASA/ASEE SUMMER FACULTY FELLOWSHIP PROGRAM

MARSHALL SPACE FLIGHT CENTER

THE UNIVERSITY OF ALABAMA IN HUNTSVILLE

THE FEASIBILITY OF USING TAE AS THE UIL FOR THE SPACE STATION
AND FOR OTHER INTERNAL NASA TASKS AND PROJECTS

Prepared By:	Esther Naomi Gill, Ed.D.
Academic Rank:	Associate Professor
University & Department:	Oakwood College Huntsville, AL 35896 Business & Information Systems Management
NASA/MSFC:	
Laboratory:	Information & Electronic Systems
Division:	Software & Data Management
Branch:	Systems Software
NASA Colleagues:	Robert L. Stevens and John W. Wolfsberger
Date:	August 21, 1987
Contract No.:	The University of Alabama in Huntsville NGT 01-008-021

2.0 ACKNOWLEDGEMENTS

My thanks go again to the Information and Electronic Systems Laboratory, W. C. Bradford, Director, Gabe Wallace, Assistant Lab Director; Software and Data Management Division, Jack Lucas, Chief; Systems Software Branch, Walter Mitchell, Chief; and colleagues Robert L. Stevens and John W. Wolfsberger who for the third year opened their laboratory, shared their facilities, and gave of their expertise and time which provided the necessary atmosphere and pleasant surroundings for this research effort.

Early in the summer, Cathy White shared her library of current TAE happenings, and Bob Stevens briefed me on the area of research I was to address for which I am grateful. Terry Brown made sure that the partitions were removed from the hard disk of my computer which permitted me to gain access and save and revise my findings and eliminated early frustrations of entering text and not being able to save it. To John Wolfsberger who invited Elfrieda Harris from the TAE Support Office, and co-editor of the TAE News, NASA/Goddard Space Flight Center, Greenbelt, MD 20771 to conduct a TAE workshop for the Systems Software Branch and me, in particular, on my topic --I'm grateful. Kaye Langford and Brenda Sparks aided in getting my viewgraphs together for my oral presentation--thanks ladies. Without the amenities and the cooperation of the aforementioned persons, this effort would have been futile.

Last, but not least, highest praise goes to ASEE, the designers of the Summer Faculty Fellowship Program; The University of Alabama, Huntsville, sponsors, Dr. Gerald R. Karr, University Program Co-Director; Mrs. Dina Engler, Dr. Karr's secretary, for your untiring efforts in keeping us informed of program happenings and for always being available to answer questions and offer assistance; Mrs. Ernestine Cothran, NASA/MSFC Assistant for University Relations and NASA/MSFC Program Co-Director; and NASA/Marshall Space Flight Center for cooperating and sharing in the implementation of the Summer Faculty Fellowship Program (SFFP) over the years.

THE FEASIBILITY OF USING TAE AS THE UIL FOR THE
SPACE STATION AND FOR OTHER INTERNAL NASA TASKS AND PROJECTS

By

Esther Naomi Gill, Ed.D.
Associate Professor of Computer Science
Oakwood College
Huntsville, AL 35896

3.0 A B S T R A C T

This description of Transportable Applications Executive (TAE) is intended to serve as a determination of the feasibility of its use as the Space Station User Interface Language (SSUIL). TAE was developed by the Space Data and Computing Division, Space and Earth Sciences Directorate of the NASA/GSFC (Goddard Space Flight Center) and by Century Computing, Inc. in 1980.

TAE is an executive program that ties a system of application programs into a single easily operated whole & supports users' operations of programs through a consistent friendly and flexible interactive user interface. TAE also supplies the interface between the user and the various application programs in a particular computer system. It appears to be an effective user interface for infrequent as well as for expert users.

The UIL will support software development, on board and on ground operations, tests & diagnoses, and a family of languages (Ada, Assembly, BASIC, C, COBOL, FORTRAN, Pascal). Prospective users of the SSUIL are Requirement and Specification Engineers, Coding and Testing Engineers; Experimenters; Software Designers and Developers; Maintenance Engineers, and Crewpersons.

For most applications, the various elements of the system are so complex that users cannot communicate directly with the operational programs, but must manage the system through intermediate interfaces. An applications executive is a master program which unifies the many subprograms of the system.

TAE uses everyday terminology, is almost 100 per cent machine independent, is NASA owned, imposes no restrictions on the type of application programs supporting TAE, permits the prototyping of systems without writing any code, and can interface with FORTRAN, C, and Ada programming applications.

TAE is primarily a text-based user interface management system utilizing programs that acquire parameters or a command language which is not appropriate for all SS applications needing solutions. TAE is neither in use for real-time operations nor integration and tests which are primary UI functions.

Nevertheless, since there are more pros than cons for the use of TAE as the UIL for the SS and other NASA internal tasks and projects, I say, why not give it a try with nothing to lose and possibly everything to gain, as it is already a NASA owned/maintained interfacing programming tool.

4.0 TABLE OF CONTENTS

	Page
1.0 TITLE PAGE.	
2.0 ACKNOWLEDGEMENTS.	i
3.0 ABSTRACT.	ii
4.0 TABLE OF CONTENTS	iii
5.0 PREFACE	1
5.1 OVERVIEW	1
5.2 BACKGROUND	1
6.0 TAE FEATURES.	4
6.1 FUNCTIONS AND COMMANDS	4
6.2 MODES, PROCS, AND PARAMETERS	5
6.2.1 Modes (Managerial).	5
6.2.1.1 Using Menu Mode.	5
6.2.1.2 Using Command Mode	9
6.2.2 Procs and Parameters (Operational).	9
6.2.2.1 Procs.	9
6.2.2.2 Parameters	10
6.3 HELP (INFORMATIONAL/INSTRUCTIONAL)	10
6.4 TAE COMMAND LANGUAGE (TCL)	10
7.0 PROS.	12
8.0 CONS.	14
9.0 SUMMARY, CONCLUSIONS AND RECOMMENDATIONS.	15
10.0 REFERENCES.	16
11.0 LIST OF ACRONYMS.	18

5.0 PREFACE

5.1 OVERVIEW

This description of TAE is intended to serve as a determination of the feasibility of using TAE for the User Interface Language (UIL) of the Space Station (SS). This treatise is not an exhaustive examination of TAE's capabilities; details on TAE can be found in the Reference section of this document.

The Transportable Applications Executive (TAE) was developed by the Space Data and Computing Division, Space and Earth Sciences Directorate, of the NASA/Goddard Space Flight Center (GSFC) and by Century Computing, Inc., in 1980 to give programmers developing applications a standardized portable user interface.

The (TAE) is an executive program that ties a system of application programs into a single easily operated whole and supports users operations of programs through a consistent friendly and flexible interactive user interface. It was developed to better serve the needs of the end user, the application programmer, and the systems designer.

TAE also supplies the interface between the various application programs in a particular computer system and the user. TAE communicates with the human operator through menu and command interfaces, information displays, parameter prompting, error reporting, and on-line help.

It appears to be an effective user interface for infrequent as well as for expert users. It is highly portable (87% of code), supports system extendability and provides common interactive user interface to application programs.

5.2 BACKGROUND

The permanently manned Space Station calls for one of the most demanding arrays of software capabilities that any project to date has been required to provide. NASA, therefore, established a common software support environment that all contributing entities must use in the production of customized software; and it finally recommended that one language be designated for the production of all Space Station Application Software--specifically, Ada was recommended. MSFC has mission responsibility to produce the software to be used during the life-cycle phases of the Space Station for such elements as the habitation, laboratory, and logistics modules. Since these elements will include software packages provided by other work packages, the MSFC software manager is developing plans to integrate and test

software provided by other centers. This as well as those developed by MSFC will require MSFC developed software to be integrated into a total Space Station package at the same time software packages from other sources must be mated and integrated into the MSFC packages for subsequent verification of the total Space Station system.

The UIL will support software development, on-board and ground operations, tests and diagnostics, and a family of languages (Ada, Assembly, COBOL, FORTRAN, BASIC, Forth, Pascal, C, etc.). It should be device independent and transparent (friendly) to the user.

The prospective users of the Space Station User Interface Language (SSUIL) are described as:

- Requirement/Specification Engineers
- Software Designers and Developers
- Coding and Testing Engineers
- Experimenters
- Maintenance Engineers
- Managers
- Crewpersons (Astronauts, Scientists, Flight
and Ground Controllers, Payload Operators,
and Application Customers)

The users will be utilizing the UIL to support such Space Station (SS) operations as:

- Planning and Scheduling
- Interacting with Real-time Modular/Payload Satellites
- In-Orbit Checkout, Repairing, Processing & Servicing, Controlling & Monitoring Space
- Environment Control and Life-Support Systems (ECLSS)
- Communicating with other Languages
- Detecting and Diagnosing Equipment Malfunctions
- Interacting with Configuration Management Malfunctions
- Monitoring On-Going Systems and Making Adjustments or Troubleshooting where Needed
- Examining and Updating Databases
- Monitoring and Recording Observations
- Interacting and Communicating with Ground Systems, Interpreting, Recording, and Presenting of data
- Communicating with Payloads
- Forecasting Potential Conditions and Making Contingency Analyses
- Validating Systems Performance

- Creating and Describing Graphics Displays
- Evaluating Program's Performance
- Monitoring Users' Use of UIL

On an interactive computer system, the user gives directions for the machine's operation. For most applications, the various elements of the system are so complex that users cannot communicate directly with the operational programs, but must manage the system through an intermediate interface.

An applications executive is a master program which unifies the many subprograms of the system. In general, an executive should facilitate the user's interaction with the computer by:

1. Standardizing the Users interface to application programs.
2. Shielding the user from the host operating system.
3. Providing a congenial environment.

6.0 TAE FEATURES

TAE consists of two distinct bodies of software: the TAE Monitor (TM) and the subroutine library. The monitor handles all user-computer communications and manages the execution of application programs. The subroutine library provides several packages of commonly needed services for application programs. TAE isolates application programs from both the interactive user interface and the host operating system. The isolation of programs from host-dependent services facilitates the porting of applications among TAE-based hosts.

6.1 FUNCTIONS AND COMMANDS

To get an idea of TAE as a system, keep in mind three basic concepts:

1. Management__mode, which refers to the methods used to address the system's aggregate of resources and services.
2. Procs__(processes or procedures) and parameters, refers to the resources and services of the system and how you select a feature and adapt it for a specific situation.
3. On-line__help, refers to the various kinds of information--available interactively--to aid you, either on an individual topic or in the use of the system as a whole.

6.1.1 TAE Model

To build a model of TAE, we'll consider the three major types of activities carried out by the executive system and the components associated with each. Table 1 summarizes these relationships:

Table 1 - TAE FUNCTIONS AND COMPONENTS

<u>FUNCTION</u>	<u>COMPONENT</u>	<u>DESCRIPTION</u>
Managerial	Modes	Methods of addressing the operational components which will accommodate the user's individual level of experience with TAE.

Operational	Procs & Parameters	A collection of programs which perform the analytical and housekeeping activities necessary to complete required tasks.
Informational/ Instructional	Help	A means of supplying both supplemental information on a single topic and a systematic teaching tool for the new user.

6.2 MODES PROCS AND PARAMETERS

The user sees TAE as an interface having two modes: menu and command. Novice or casual users make their way through the system by means of menus, augmented by extensive on-line help. Experienced users have a powerful language for commanding the system and controlling the environment. Both menu and command users have online explanations of the system. In either mode, the user's ultimate purpose is the same: to execute the application functions of the system.

6.2.1 Modes (Managerial)

With TAE you may send directions to the computer in one of two modes:

1. Menu Mode where you select an operation from a numbered list presented on the screen.
2. Command Mode where you communicate with the system through the TAE Command Language (TCL).

The mode selected depends on the task to be performed and familiarity with the features of the system and with one's confidence in using TAE.

6.2.1.1 Using Menu Mode--In Menu Mode, TAE communicates with the user by means of four types of displays: (1) Menu, (2) Tutor, (3) Help, and (4) Messages.

In all four types, the screen shows two different kinds of material:

1. Contents: the instructions, information, or data you need to know at that time.

2. Prompt-Line Options: A set of choices to manage your task session.

(1) Menu: A TAE menu is normally a CRT display containing numbered entries (arranged vertically on the screen) and menu prompt-line options (arranged horizontally at the bottom of the screen above the prompt line). See Figure 1 for TAE menu example.

(2) Tutor: Once a user reaches a proc, he or she is "tutored" to enter the desired parameter values. In a tutor session, the user sees a screen containing a formatted list of parameter names and either their previously established values or their defaulted values. These values can be changed easily through the tutor session. With a tutor display, users may set new values or edit old values. Users may also save sets of parameter values for future restoration. Figure 2 shows a typical tutor screen.

Unless you are using a hard copy terminal, a TAE menu is normally a CRT display containing numbered entries (arranged vertically on the screen) and menu prompt-line options (arranged horizontally at the bottom of the screen near the prompt line). See Menu Illustration which follows for an example.

On most TAE systems, you log on as a menu user and are given a "root" menu and a menu question mark (?) prompt, which appears at the lower left-side of the screen. You then have two choices to make:

1. You can make a selection from the numbered entries.
2. You can give a prompt line option.

(3) Help: To be an effective interface, an executive must be self-contained. That is, it should be able to inform the user of its resources and give instructions for their use. TAE provides the user with help in five categories: a proc or a TAE command, a menu, the operation of a mode, the parameters of a proc, and a TAE message.

A typical TAE help display may have several screens, each of which contains context-specific explanatory information (usually in sentence form and appearing in the top part of the frame) and standard help options (arranged horizontally across the bottom of the screen).

(4) Messages: A message display is used to report an error or a piece of information to a user. It consists of a single

MENU "ROOT", LIBRARY "TAE\$MENU"

* TAE DELIVERY SKELETON ROOT MENU *

- 1) DEMONSTRATION ENTRY: NO MENU EXISTS FOR THIS ENTRY
- 2) SUBMIT SUGGESTIONS, COMPLAINTS, COMMENTS TO
TAE DEVELOPERS (SUGGEST)
- 3) MENU OF TAE UTILITIES [UTIL]
- 4) MENU OF TAE DEMONSTRATION PROGRAMS [DEMO]
- 5) MENU OF TAE TEST PROGRAMS [TESTS]

ENTER: SELECTION NUMBER, HELP, BACK, TOP, MENU, COMMAND, OR LOG OFF
?

* NOTE - IF NUMBERED ENTRY NAME IS IN PARENTHESES, THE SELECTION WILL GIVE YOU A
PROC. IF IT IS IN BRACKETS, IT WILL GIVE YOU ANOTHER MENU.

FIGURE 1

Tutor: Proc "XPTTEST," library "SYS\$USER:[Esther]"

<u>Part</u>	<u>Description</u>	<u>Value</u>
FILE	File name of image to test. [THIS PARAMETER HAS QUALIFIERS]	"IMAGE15"
THRESHLD	Probability threshold	2.45983E-04

Enter: parm=value,HELP, PAGE, QUALIFY, SHOW, RUN, EXIT, SAVE, RESTORE,
Return to page.

Figure 2
SAMPLE TUTOR PARAMETER DISPLAY

comment line that appears on the current display screen. The user may then choose from the options appearing on the prompt line of that particular screen. Messages may come from TAE itself, or from procs through TAE. A typical message has the form:

[WHOSE-WHAT] description

where WHOSE identifies the source of the message (e.g., TAE, ADIPS, BISHOP) and WHAT is a key (e.g., NOSUCHFILE). Any message may be supplemented by additional help, which a user accesses by typing " ? " when the message occurs.

6.2.1.2 Using Command Language Mode--Users who employ the TAE Command Language (TCL) can freely direct system activities. Unlike menu users, who have a limited set of possible actions and very little to remember at any one time, TCL users are bound only by the breadth of the system and their ability to recall how to use the various resources.

Like menu users, command users are primarily interested in executing the application and utility procs of a system. In a simple command statement, the user enters the name of a proc and parameter values, either positively or by keyboard. Command users also have access to help and messages. In addition, they may tutor on a proc or switch to menu mode at any time.

Users may also set up standard sequences of commands by creating command procedures -- collections of TAE commands, executed as a single, named function. For this purpose, the language contains control directives (e.g., LOOP, IF-THEN-ELSE) typically found in a procedural language. Other features; such as, global and local variables, substitution, assignments, input and output parameters and expression evaluation support programming through procedures.

A simple on-line command editor allows users to recall and edit or resubmit previous commands.

In TAE command mode, a user operates through a classic command line interpreter. There is a command in menu mode to enter command mode, and a command in command mode to enter menu mode.

6.2.2 Procs and Parameters (Operational)

6.2.2.1 Procs: A proc executes one of two things: (1) A requested application or (2) A utility feature. Application procs usually perform analytical tasks. Utility procs usually perform service functions.

6.2.2.2 Parameters: Once you invoke the proc you want, you may adapt it to your own use. Each proc has a parameter or set of parameters which may be given different values when the program is run for a specific reason.

Defaulted Parameters--In many cases, a parameter will have a predefined value (based on what is most convenient or most commonly used). This value is the "default;" if you do not replace it with another value, the program executes using this value. Whether you are working in Menu Mode or in Command Mode, you will have the option of entering parameter data or accepting a default value before activating the proc.

6.3 HELP (INFORMATIONAL/INSTRUCTIONAL)

Unlike some systems, help instructions for TAE will not appear of their own accord when the computer detects that the operator is making mistakes at the terminal. You must request help--on-line help is available at all times during your TAE sessions.

Help is available in several different forms on TAE. No matter what mode you are in, the system can provide you with assistance on almost any item.

6.4 TCL (TAE COMMAND LANGUAGE)

The TAE command language (TCL) is a classic command language based on Digital's DCL, the IBM System/38 command language, the UNIX shell and C shell, and the deliberations of the ANSI committee standardizing Operating System Command and Response Languages.

A TCL command line consists of the name of a proc or a TCL intrinsic command, followed by command or proc parameter values. Parameter values for any proc and most intrinsic commands are given by the user either positionally or by associating the value with the name of the parameter.

As an example, assume we have a proc named DOIT, with two integer parameters named A and B, and a string parameter named C. Assume further that the PDF for DOIT specifies that the order of the parameters is A, B, C. One may specify the initial value of the proc in any of the following ways:

```
DOIT 1, 4, hello
DOIT 1, C = hello, B = 4
DOIT C = hello, A = 1, B = 4
```

Command lines may be continued past the end of the physical terminal line; the number of continuations depends on the host facility. Comments may be appended to any command line, including continued command lines.

If the definition of a parameter specifies a default value and the user gives no value for the parameter on the command line, then the default value will be assumed. If the PDF did not specify a default value, then the TAE command line interpreter will respond with a message indicating to the user which parameters require values.

In addition to executing TAE procs, a TAE command mode user may execute a TCL intrinsic command. An intrinsic command is a built-in command, that is, a command executed by the command line interpreter. TCL provides intrinsic commands to:

- abort an executing proc;
- define an acronym for an arbitrary string of characters;
- create, delete or assign values to TCL variables;
- set the library search order;
- start or stop session logging;
- start or stop logging all terminal I/O;
- obtain help information on a TAE intrinsic command, on a proc or proc parameters, on a menu, or on a TAE message;
- save or restore a set of TCL variables;
- initiate a tutor session;
- abort or get status on TAE async or batch jobs;
- log out of TAE.

TCL supports real, integer, and string type variables, and implicit conversion on mixed-type arithmetic operations. A value is assigned to a variable when the variable is created, or through the LET statement. TCL provides addition, subtraction, division, and multiplication arithmetic operators, a concatenation string operator, and the logical operators NOT, AND, and OR. To save the global variables to a file use the TCL SAVE command.

7.0 PROS

The advantages of using TAE to prototype the UIL are as follows:

1. Many elements of TAE's terminology are also words with everyday meanings (such as, "HELP").
2. TAE accepts upper or lower case for user input; for example, "HELP" is the same as "help".
3. Commands and keywords may be abbreviated, even down to a single letter, so long as they are unique.
4. TAE allows for portability of itself and applications (87% of Code).
5. TAE is cost effective as it is an in-house development owned by NASA and its contractors.
6. The ability to browse TAE -- The HELP is an instructional tool and is especially valuable to intermediate learners because it allows you to request information on the topics.
7. Users of TAE on different host computers find almost identical user interfaces.
8. There are no restrictions on the type of application programs supporting TAE.
9. Programmers who write application systems to run under TAE do not have to invent their own control language or provide logic in their programs for interfacing with the user.
10. The physical appearance of TAE helps the user learn the system quickly.
11. TAE has the ability to prototype a system without writing a single line of application code.
12. TAE is able to interface with FORTRAN, C, and, most recently (see Smith Advanced Technology, Inc. Senior Systems Analysts' comments in the Reference Section of this paper) Ada programs.

13. TAE provides easily learned user-computer interface with power, flexibility, and consistency in managing application systems.
14. TAE lowers cost of software development thru savings in development efforts, reduced maintenance overhead, and decreased upgrade time.
15. TAE facilitates building a system by supplying tools for developing and customizing, interactive analysis in any discipline, and convenient implementation.

8.0 CONS

The disadvantage for using TAE for prototyping the Space Station (SS) User Interface Language (UIL) are as follows:

1. TAE graphics interface has been recently added and is not yet operationally error free.
2. TAE is primarily a text-based user interface management system utilizing programs that acquire parameters or a command language, which is not appropriate for all SS applications needing solutions.
3. Multiple users of TAE cannot communicate during shared sessions.
4. TAE does not run on a 16-bit machine at least without some function loss.
5. TAE's 87% portability claims may be overstated and therefore not good enough when one moves from machine to machine.
6. TAE is neither in use for real-time operations (some speed penalty) nor for integration and tests which are primary user interface functions.

9.0 SUMMARY, CONCLUSIONS AND RECOMMENDATIONS

Many computer activities use multiple programs to perform a task. For some applications, these programs are numerous, complex, and interrelated. Thus the user needs help in managing the various operations.

The TAE executive system provides an interface between the user and the programs in a particular computer application.

As a system, TAE contains 3 functional domains: (1) Informational/Instructional, (2) Managerial, and (3) Operational. The Informational/Instructional domain provides explanation and training on the system through the HELP component. The Managerial domain allows the user to give directions to the system through the MENU and COMMAND MODE components. The Operational domain supplies the analytical and service features of the system through the PROC and PARAMETER component.

At the least, I see TAE as a prototyping tool to be utilized by designers for the various Space Station operations as well as other internal NASA projects and tasks.

At the most, I see program designers using TAE to develop expert systems that join together various new and previously written and maintained programs which in turn will be utilized by users (of both advanced and novice types) to get answers to questions, to supply data, to control and monitor on-going systems and operations, to make adjustments where needed, to maintain, interact, and communicate with Ground Systems, to examine performances, and to detect, diagnose, and correct malfunctions, to communicate with other programming languages, etc. mentioning only some of the operations that need to be performed on the Space Station.

In order for all of these and more operations to be performed successfully, the designers will need to build user friendliness or simplicity of use into the system by keeping as many details as possible transparent to the user.

Also, since TAE can be used to interface with and develop Ada programs, it seems that this program developing tool could be included with the Ada compilers for the Micro/VAXII/VMS or UNIX disk operating systems.

I highly recommend as feasible the use of TAE as a development tool already owned by the Government for prototyping, program development, and interfacing with the numerous simple, compound and complex Space Station operations/tasks and with other NASA internal projects.

10.0 REFERENCES

"Application Programmer's Reference Manual for the Transportable Applications Executive Version 1.4," Century Computing Document Number 82-TAE-PGMV1H, March 31, 1987.

"C Programmer's Reference Manual for the Transportable Application Executive (Version 1.4)," Century Computing Document Number 84-TAE-CPGMV1B, March 31, 1987.

"Primer for the Transportable Application Executive (Version 1.0)" by Patricia A. Carlson, Carmen Ana Emmanuelli, Elfrieda L. Harris, and Dorothy C. Perkins, January, 1984.

Promotional Brochure TAE was developed by the Space Data & Computing Division, Space & Earth Sciences Directorate of the NASA/GSFC, Greenbelt, MD 20771, and by Century Computing, Inc., 1100 West Street, Laurel, MD 20707.

"Release Notes for the Transportable Applications Executive (Version 1.4) (VAXstation II/GFX [VMS] TAE Facelift)," Century Computing Document Number 87-TAE-GFXPLV1, February 27, 1987.

"Release Notes for the Transportable Applications Executive (Version 2.1) (UNIX Implementation)," Century Computing Document Number 84-TAE-UNIX-RELV21, June 22, 1987.

"Space Station Software Challenge to MSFC," by John W. Wolfsberger, SSE and TMIS Committee Member, August, 1987, and to be published in an ISEE upcoming issue.

"System Manager's Guide for the Transportable Application Executive (Version 1.4) (VAX/VMS Implementation)," Century Computing Document Number 82-TAE-SYSV1F, March 31, 1987.

"TAE News Release--August, 1987," by Albert E. Horn and Morris C. Harwell, Senior System Analysts for Smith Advanced Technology, Inc., 2009 Gallatin Street, Huntsville, AL 35802, NASA Contractors for the Space Station Operating System Study. They have recently successfully implemented and tested two methods to interface DEC VAX Ada applications with TAE. For more details, call Al or Morris at AC 205 - 533-3822 if you are a can't-wait-to-try TAE/Ada user and/or read your October, 1987, issue of TAE News.

"TAE Tutorial," Conducted July 28, and 29, 1987 at NASA/MSFC, Information & Electronic Systems Laboratory, Software and Data Management Division, Systems Software Branch by Mrs. Elfrieda L. Harris, Co-editor, TAE Newsletter, published tri-annually (February, June & October)--the Newsletter contains updates on TAE

users--TAE News is published by the TAE Support Office, Image Analysis Facility, Code 635, NASA/GSFC, Greenbelt, MD 20771 and is free to users.

"User Interface Prototype (UIP) Program Plan," by John T. Ellis, TRW87-281, March, 1987.

"User-Programmer Dialogue: Guidelines for Designing Menus and Help Files for Interactive Computer Systems" by Patricia A. Carlson, NASA Technical Memorandum 84980, February, 1983.

"User's Reference Manual for the Transportable Applications Executive (Version 1.4)," Century Computing Document Number 82-TAE-USRV1H, March 31, 1987.

11.0 LIST OF ACRONYMS USED

ASEE	American Society for Engineering Education
BASIC	Beginners All Purpose Symbolic Instruction Code
C	A revision to the B Programming Language
COBOL	Common Business Oriented Language
CRT	Cathode Ray Tube
ECLSS	Environmental Control and Life Support System
FORTTRAN	FORmula TRANslator or TRANslation
GSFC	Goddard Space Flight Center, Greenbelt, MD
MSFC	Marshall Space Flight Center, Huntsville, AL
NASA	National Aeronautics and Space Administration
PDF	Process or Procedure (PROC) Definition File
PROCS	TAE PROCesseS or PROCedureS
SFFP	Summer Faculty Fellowship Program
SS	Space Station
SSE	Software Support Environment
SSUIL	Space Station User Interface Language
TAE	Transportable Applications Executive
TCL	TAE Command Language
TM	TAE Monitor
TMIS	Technology Management Information System
UIL	User Interface Language

ORIGINAL PAGE IS
OF POOR QUALITY

N88-15619³¹⁸⁻⁷⁶
116720
298

1987

NASA/ASEE SUMMER FACULTY RESEARCH FELLOWSHIP PROGRAM

MARSHALL SPACE FLIGHT CENTER
THE UNIVERSITY OF ALABAMA IN HUNTSVILLE

A NUMERICAL STUDY OF TRANSIENT HEAT AND MASS TRANSFER
IN CRYSTAL GROWTH

Prepared By:	Samuel Sang-Moo Han
Academic Rank:	Associate Professor
University and Department:	Tennessee Tech University Department of Mech. Eng.
NASA/MSFC:	
Laboratory:	Structures and Dynamics
Division:	Earth and Atmospheric Science
Branch:	Fluid Dynamics
NASA Colleague:	Charles F. Schafer Cheryl Morroni
Date:	August 14, 1987
Contract No:	The University of Alabama in Huntsville NGT-01-002-021

ABSTRACT

A numerical analysis of transient heat and solute transport across a rectangular cavity is performed. Five nonlinear partial differential equations which govern the conservation of mass, momentum, energy and solute concentration related to crystal growth in solution, are simultaneously integrated by a numerical method based on the SIMPLE algorithm.

Numerical results showed that the flow, temperature and solute fields are dependent on thermal and solutal Grashoff number, Prandtl number, Schmidt number and aspect ratio. The average Nusselt and Sherwood numbers evaluated at the center of the cavity decrease markedly when the solutal buoyancy force acts in the opposite direction to the thermal buoyancy force. When the solutal and thermal buoyancy forces act in the same direction, however, Sherwood number increases significantly and yet Nusselt number decreases.

Overall effects of convection on the crystal growth are seen to be an enhancement of growth rate as expected but with highly non-uniform spatial growth variations.

ORIGINAL PAGE IS
OF POOR QUALITY

ACKNOWLEDGEMENT

I would like to thank Dr. Gerald Karr, Co-Director of NASA/ASEE MSFC program for extending me an invitation to participate in this program.

Dr. Charles Schafer deserves a special recognition for suggesting an interesting research topic and providing me with continuing guidance and encouragement. Ms. Cheryl Morroni and Dr. Ramachandran, distinguished members of microgravity working group, gave me strong encouragement and support.

There are many friends who made my stay at MSFC much easier and enjoyable through their hospitality: Drs. Nate Reynolds, Yemo Fashola, Y. S. Chen, Rand Decker and Tim Miller. John Parker, Karen Parker and Alan Johnston helped me with computer use and graphics. I thank them for their help.

My family had a very rough time living in a make-shift arrangement throughout ten weeks. They deserve more than thanks from me. They deserve a vacation. Thanks, Kee, Michael and Alex. You are the best bunch!

NOMANCLATURE

a	=H/L=aspect ratio of the cavity
A, B	species A and B
Cv, Cp	specific heat at constant volume and constant pressure
D _{AB}	diffusion coefficient of A through B
E	internal energy, Eqn (3)
g	gravitational acceleration
Gr _T	$= \frac{g\beta\Delta T H^3}{\nu^2}$ = thermal Grashof number
Gr _M	$= \frac{g\alpha_A \Delta W_A H^3}{\nu^2}$ = solutal Grashof number
H	cavity height
L	cavity width
Le	$= \nu/D_{AB}$ = Lewis number
N	buoyancy ratio, Eqn (18)
Nu	Nusselt number, Eqn (10)
P	dynamic pressure
Pr	$= \nu/\alpha$ = Prandtl number
Q _H	net energy flux, Eqn (11)
Q _M	net mass flux, Eqn (15)
S	source terms, Table 1
Sc	$= \nu/D_{AB}$ = Schmidt number
Sh	average Sherwood number, Eqn (14)
Ra _T	=Gr _T x Pr = thermal Rayleigh number
Ra _M	=Gr _M x Sc = solutal Rayleigh number
t	time
T	temperature
u, v	flow speed in x- and y-direction
u _o	$= \nu/H$ = residence velocity
x, y	horizontal and vertical coordinates
W _A	$= \rho_A/\rho$ = mass fraction of species A

Greek Symbols

ρ	= $\rho_A + \rho_B$ = density
μ	dynamic viscosity
ν	kinematic viscosity
α	$= K/\rho c_p$ = thermal diffusivity
K	thermal conductivity
$\delta x_i, \delta y_j$	control volume size in x and y
δt	time step
δ_T, δ_c	thermal and concentration boundary layer thickness
α_A	solutal expansion coefficient
β	thermal expansion coefficient
ΔT	= T _H - T _C = temperature difference
ΔW_A	= W _{AH} - W _{Ac} = mass fraction difference

Super Scripts

~	nondimensional quantities
o	initial conditions

I. INTRODUCTION

ORIGINAL PAGE IS
OF POOR QUALITY

Single crystals are solid with the most uniform atomic structure that can be attained. This uniformity is the basis for a wide range of technological applications of single crystals. The most important feature of crystal is that it allows the transmission of acoustic, electromagnetic and charged particle with a minimal scattering. In particular, this transparency can be selectively modified by the controlled addition of impurities (dopants) to produce semi-conductor materials.[1]

Crystals are made from carefully controlled phase changes that involve solidification of a high temperature melt (melt growth), growth from low temperature mixture (solution growth) and condensation of a vapor (vapor growth). In all of these methods, the the nutrient materials are in either liquid or vapor phase. The physical transport mechanism at the interface between a nutrient fluid and the solid surface of growing crystal is controlled by mass diffusion. The solute gradient at the interface is , however, critically dependent upon the solute and thermal distribution of the nutrient fluid far away from the interface. This far-field flow behavior is controlled by the convection which is produced by various physical mechanism. Convection can be generated by the density gradients in a gravitational field (natural convection), or by an externally applied pressure (forced convection) or by both (mixed convection). In a low gravity environment, surface tension driven convection can be important when the nutrient fluid is allowed to have a free surface. Thus, in general, the growth of crystals is a coupled process of heat and mass transport, fluid flow , phase transformation and chemical reactions.

Even though the technology of crystal growth is well grounded in physical chemistry and materials science, the treatment of transport processes sometimes have been rudimentary and qualitative. To improve the quality of crystals, it is apparent that the flow characteristics at the growing interface must be understood so that one can control whatever influences the convection might have on the quality of crystals. Significant attempts have been made in recent years by fluid dynamicists to understand the complex interactions among various transport and physical processes in crystal growth. [1,2,3,4]

II. OBJECTIVES OF THE PRESENT RESEARCH

Much of the earlier works on the study of convection in crystal growth were based on the premise that convection is deleterious and therefore should be kept minimum at all cost. Materials processing in a space environment would provide a low gravity environment which will reduce buoyancy induced natural convection significantly. It is not likely however to create a completely acceleration free environment. A space station in which materials processing would occur is subject to microgravity due to near earth orbit and viscous drag force. Diffusion

processes in crystal growth are usually extremely slow and natural convection created by transient microgravity could be in the same order of magnitude. Surface tension driven natural convection, which is usually insignificant in terrestrial conditions, becomes very important in low gravity environment when the crystals are made by a containerless process.[2]

The purpose of the present research is to initiate a development of a numerical model which can be used to simulate crystal growth in realistic space environments. The thermal and solutal fields encountered in crystal growth from solution are, in general, three-dimensional and time-dependent. Transport properties, such as thermal diffusivity, mass diffusivity and fluid viscosity are general functions of solute concentration and fluid temperature of the mixture. Solidification processes usually involve liberation of latent heat at the interface. Also, rate of solidification depends on segregation (distribution) coefficient, which in turn depends on fluid temperature. A full scale three-dimensional model which accounts for all these physical conditions is not warranted until sufficient analyses of simplified two-dimensional situations are performed.

As a first step, a two-dimensional, time-dependent natural convection driven by both thermal and solutal buoyancy forces is selected in this research. Even though this physical model is far simpler than the actual processes, it should provide insights into the complex interactions between thermal and solutal convections encountered in crystal growth. Detailed descriptions on the physical model and appropriate equations are presented in section III. Numerical results are presented in section IV followed by conclusions and recommendations in section V.

III. FORMULATIONS

Two-dimensional thermal and solutal convection across a rectangular cavity is depicted in Figure 1. The vertical walls are maintained at isothermal and uniform mass-fraction of component A and the horizontal walls are assumed to be adiabatic and impermeable to mass diffusion. The fluid in the cavity is made of two components of liquid (say, A and B) with different molecular weights. Heat transfer occurs from the high temperature surface (left wall) to the low temperature surface (right wall). Mass transfer of species A also occurs from the left surface where the mass concentration of A is higher than at the right surface. It is assumed that all surfaces are impermeable to species B. One might consider species A to be a dopant in melt growth or crystal material in vapor or solution growth. Relative location of higher temperature wall and higher concentration surface is immaterial.

Thermal conduction occurs from the hot surface to the fluid and the temperature of the fluid increases over its initial value. Since the volume of most fluid expands as increasing

temperature, density of the fluid becomes less than its surrounding fluid. Lighter fluid elements rise up when the gravity acts along downward. This buoyancy force sets the convective flow motion within the cavity. Buoyancy force will act along the downward direction next to the cold surface at the right. Unless the initial temperature difference between the walls and fluid is large, the amount of heat transfer is small and the density change is almost negligible. This is known as the Boussinesq approximation. Mass diffusion from the left surface to the fluid will have similar effects on the flow field. Suppose species A has higher molecular weight than species B. Then diffusion of species A into the fluid will increase the density of the mixture and the solutal buoyancy force will act downward near the left wall. If the molecular weight of species A is lower than B, the solutal buoyancy force will be in the opposite direction. Since the mass diffusion through liquid is extremely slow, Boussinesq approximation can be invoked for mass transfer as well.

Governing Equations

The governing equations for the conservation of mass, momentum, energy and species A can be expressed by a generalized transport equation of the form

$$\frac{\partial \rho \phi}{\partial t} + \frac{\partial}{\partial x} \left[\rho u \phi - \Gamma \frac{\partial \phi}{\partial x} \right] + \frac{\partial}{\partial y} \left[\rho v \phi - \Gamma \frac{\partial \phi}{\partial y} \right] = S. \quad (1)$$

Table 1 contains appropriate expressions for ϕ , Γ and S for each equations.

Buoyancy forces due to thermal and solutal convections are included in the vertical direction momentum equation. All transport coefficients are assumed to be constants. No latent heat liberation is considered. The pressure appearing in the momentum equation represents only dynamic pressure. Static pressure is eliminated by using the density variation given by the Boussinesq approximation, i. e.,

$$\rho = \rho^0 [1 - \alpha_A (w_A - w_A^0) - \beta (T - T^0)]. \quad (2)$$

It is assumed that the mass concentration of species A of the liquid at the right vertical wall is equal to the mass concentration of species A at the solid. This assumption amounts to having a unit segregation coefficient at the growing surface. It is also assumed that the interfacial mass flux of species A at the vertical walls is negligible. (Interfacial mass flux can be calculated at these walls and the mass averaged flow velocities in the horizontal direction should be imposed at these walls for a more accurate boundary treatment.) Internal energy of the fluid is given by

$$E = C_v (T - T^0). \quad (3)$$

ORIGINAL PAGE IS
OF POOR QUALITY

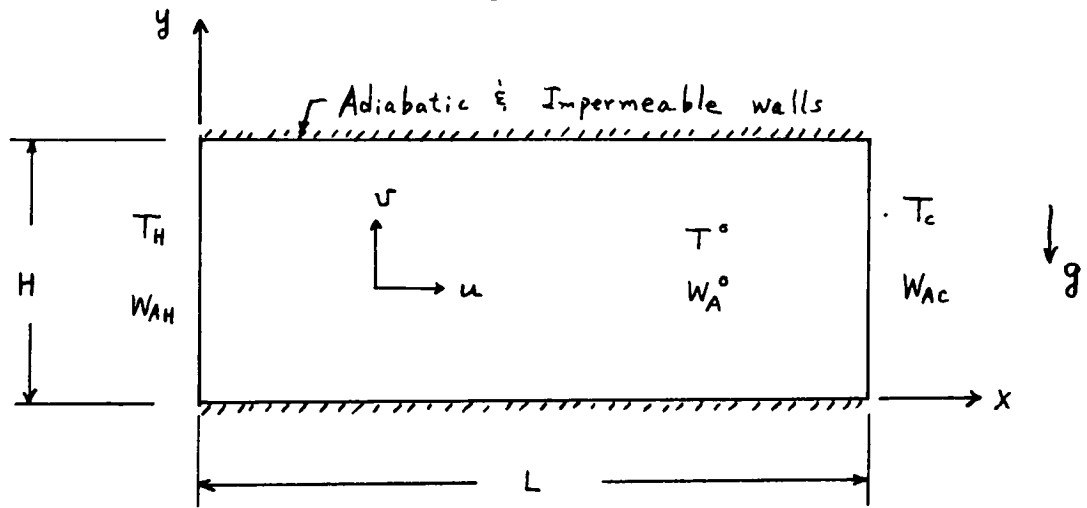


Figure 1. Geometry of the cavity

Table 1. Components of governing equations

	ϕ	Γ	S
Mass	1	0	0
x-momentum	u	μ	$-\frac{\partial p}{\partial x}$
y-momentum	v	μ	$-\frac{\partial p}{\partial y} + \rho g \beta (T - T^\circ) + \rho g \alpha_A (W_A - W_A^\circ)$
Energy	E	k/c_v	0
Concentration (Mass)	W_A	ρD_{AB}	0

Initial and Boundary Conditions

Initial and boundary conditions depend on the physical problems under consideration. Two types of initial conditions are considered; one corresponds to a static equilibrium condition and the other corresponds to a steady-state thermally driven natural convection. For the static initial conditions

$$\begin{aligned} u(x, y, t=0) &= v(x, y, t=0) = 0 \\ \rho(x, y, t=0) &= \rho^0 \\ T(x, y, t=0) &= T^0 \\ W_A(x, y, t=0) &= W_A^0 \end{aligned} \quad (4)$$

Boundary conditions are fixed for all numerical results reported in this paper. They are

$$\begin{aligned} T(x=0, y, t) &= T_H, \quad T(x=L, y, t) = T_C \\ W_A(x=0, y, t) &= W_{AH}, \quad W_A(x=L, y, t) = W_{AC} \\ \left. \frac{\partial T}{\partial y} \right|_{x, y=0, t} &= \left. \frac{\partial T}{\partial y} \right|_{x, y=H, t} = \left. \frac{\partial W_A}{\partial y} \right|_{x, y=0, t} = \left. \frac{\partial W_A}{\partial y} \right|_{x, y=H, t} = 0 \end{aligned} \quad (5)$$

Nondimensional Parameters

The present numerical method utilizes primitive variables in dimensional forms. It is convenient, however, to introduce appropriate flow characteristics into the governing equations to obtain important nondimensional parameters which govern the flow. Numerical and experimental data presented in nondimensional parameters are universal and can be used to infer other similar problems with different fluid properties and physical geometries.

Nondimensional variables are defined by

$$\begin{aligned} \tilde{x} &= \frac{x}{H} ; \quad \tilde{y} = \frac{y}{H} ; \quad \tilde{t} = \frac{t}{H/u_0} ; \quad \tilde{u} = \frac{u}{u_0} \\ \tilde{v} &= \frac{v}{u_0} ; \quad \tilde{T} = \frac{T - T^0}{\Delta T} ; \quad \tilde{W}_A = \frac{W_A - W_A^0}{\Delta W_A} \end{aligned} \quad (6)$$

Introducing these nondimensional variables into the governing

equations (1), it can be readily shown that nondimensional equations contain five nondimensional parameters. They are; aspect ratio (a), thermal Grashoff number (Gr), solutal Grashoff number (Gr), Prandtl number (Pr), and Schmidt number (Sc). Numerical results will be presented in terms of nondimensional quantities.

VI. ANALYSIS

Numerical Method

The numerical method used for the present study is a finite volume method based on the SIMPLE algorithm.[5] Since a detailed description on the essence of SIMPLE can be found in a reference [5], it will not be discussed in this report.

The SIMPLE method, in principle, can be applied to both high speed flow as well as low speed flow by using a proper equation of state and including the density variations due to the pressure change. These modifications were added to the original SIMPLE method and the revised method were successfully applied to a transient acoustic wave propagation in a water hammer [6] and a transient natural convection in a square cavity [7].

Physical and Numerical Parameters

Physical and numerical parameters used for the present study are listed in Table 2. Physical properties are selected only to give representative thermal and solutal Grashof numbers, Prandtl and Schmidt numbers encountered in solution growth under terrestrial conditions. Thus these values may not represent any actual crystal growth environment. Numerical parameters are selected (by trial and error) such that either the solution approaches to the true solution (if exists) or converges to steady or quasi-steady solution within a reasonable computing time.

Numerical Results

Four different cases are simulated to investigate the effects of thermal and solutal convections and their interactions.

CASE 1: Thermal convection : Nondimensional parameters used for this case are

$$\begin{aligned} Gr_T &= 9 \times 10^5 ; Gr_M = 0 ; Pr = 7.07 ; a = 0.53 \\ Ra_T &= 6.36 \times 10^6 \end{aligned} \quad (7)$$

This case is studied first to check the accuracy of the numerical code developed. Thermally driven natural convection in

rectangular geometries are extensively studied and the present results can be easily checked against existing data.

Numerical accuracy and computational economy depend on the choice of computational mesh arrangement. Since the driving force for the present convection comes from the vertical walls. The resulting buoyancy driven convection will form thermal and momentum boundary layers. It is therefore necessary to have fine grids near the vertical walls. Invoking scale analysis for the boundary layer regime [8], the thermal boundary layer thickness is

$$\delta_T \sim H Ra_T^{-1/4} \approx 2.07 \times 10^{-3} \text{ m.} \quad (8)$$

The mesh size at the vertical walls therefore should be small enough that at least one computational mesh should be placed within this boundary layer. The mesh arrangement along the x-direction is given by

$$\delta x_{i+1} = \delta x_i (1 + \Delta x_{\text{per}}) \quad (9)$$

, where δx_i is the first mesh size and Δx_{per} is the percent increment. The mesh arrangement near the horizontal walls need not be as small walls since the horizontal walls are adiabatic and the momentum boundary layer is thicker than the thermal boundary layer ($Pr > 1.0$). Grid expansion along the y-direction is similar to x-direction. Number of trial runs were made before settling to the mesh arrangement as shown in Figure 4a. Total 26 (X-direction) by 20 (Y-direction) meshes were used in all subsequent computations. (Actually, the first mesh size near the vertical walls are much larger than the thermal boundary layer thickness. However, solutal boundary layer thickness, discussed later, dictates this size.)

Figure 2 shows transient behavior of rate of energy transfer across the cavity evaluated at the center of the cavity. Nusselt number is defined by

$$Nu_L = \frac{Q_H}{H \frac{\kappa}{L} \Delta T} \quad (10)$$

where Q_H represents the total energy flux given by

$$Q_H = \int_0^H \left[\rho u c_p (T - T^0) - \kappa \frac{\partial T}{\partial x} \right]_{x=\frac{L}{2}} dy. \quad (11)$$

Table 2. Physical and Numerical Parameters

Parameters	Values	Dimension
C_v, C_p	1.0	$\text{m}^2/\text{s}^2 \cdot \text{K}$
μ	$8.55\text{E}-3$	$\text{kg}/\text{m} \cdot \text{s}$
ρ^0	1000	kg/m^3
g	9.81	m/s^2
β	$6.0\text{E}-4$	K^{-1}
α_A	+0.276 -0.276	dimensionless
K	5.0	$\text{kg} \cdot \text{m}/\text{K} \cdot \text{s}^3$
T^0	300	K
W_A^0	0.9	dimensionless
ΔT	10	K
ΔW_A	0.2	dimensionless
D_{AB}	$4.0\text{E}-9$	m^2/s
H	0.10384	m
L	0.19526	m
$\delta x_i, \delta y_i$	0.0005 - 0.028	m
δt	0.1 - 5.0	s
ϵ	$1.0\text{E}-3$	dimensionless

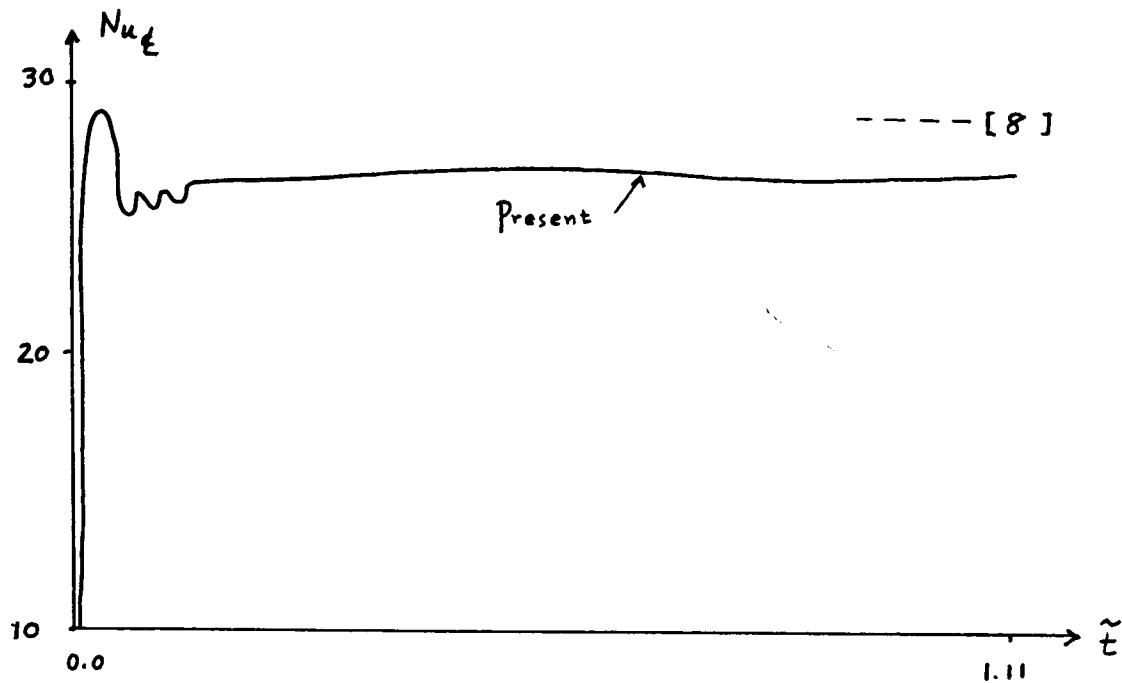


Figure 2. Transient Nusselt Number (Case 1)

Nusselt number increases rapidly as the hot and cold fluid intrude the top and bottom portions of the cavity. Energy transfer is at the maximum when the convection velocity reaches the maximum at this early stage of transient convection. Numerical solution exhibits oscillatory horizontal flow speed. These oscillations are mainly responsible for the oscillatory Nusselt number. Oscillatory energy transfer across a square cavity was theoretically predicted by Patterson and Imberger [9] and was numerically confirmed. [7,9] Oscillation periods and amplitudes for the present case ($a=0.53$) are different from those for $a=1.0$ reported in ref[7,9].

Steady-state Nusselt number computed by the present simulation is about 27. Bejan [8] obtained the analytical solutions for the boundary layer regime with $Pr > 1$. Figure 3 shows the average Nusselt number obtained by his solutions. Using his results, the average Nusselt number for the present case is about 29, which is in reasonable agreement with the computed value.

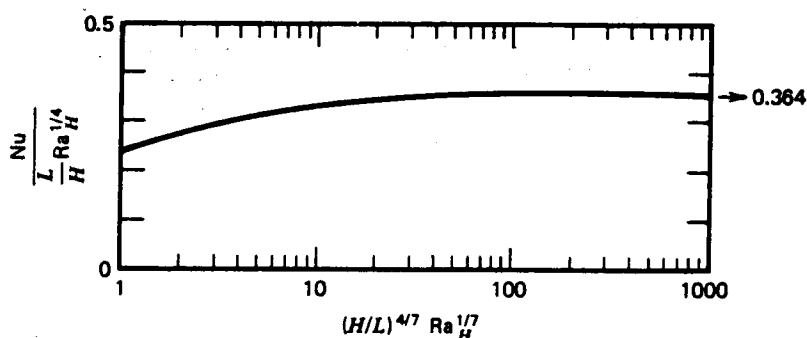


Figure 3. Nusselt number correlations [8]

Figure 4 shows the global view of steady-state flow and temperature fields for Case 1. Very thin thermal and momentum boundary layers are developed at the vertical walls. Temperature in the core regions are highly stratified and isotherms are almost parallel. Most of the fluid in the core is relatively stagnant.

Figure 5 shows the temperature and velocity profiles at two selected spatial locations in the cavity. Figure 5a shows the vertical velocity and fluid temperature at a horizontal plane located at the mid-height of the cavity. Thermal boundary layer is located within the momentum boundary layer and the over-all boundary layer thickness is in the order of % of the cavity width. Figure 5b shows the horizontal velocity and temperature of the fluid at the vertical plane located at the mid-width of the cavity. Magnitude of horizontal velocity and temperature distribution at this plane as shown in Figure 5b determines the energy transfer rate across the cavity. Note that the vertical velocity is order of magnitude higher than the horizontal velocity.

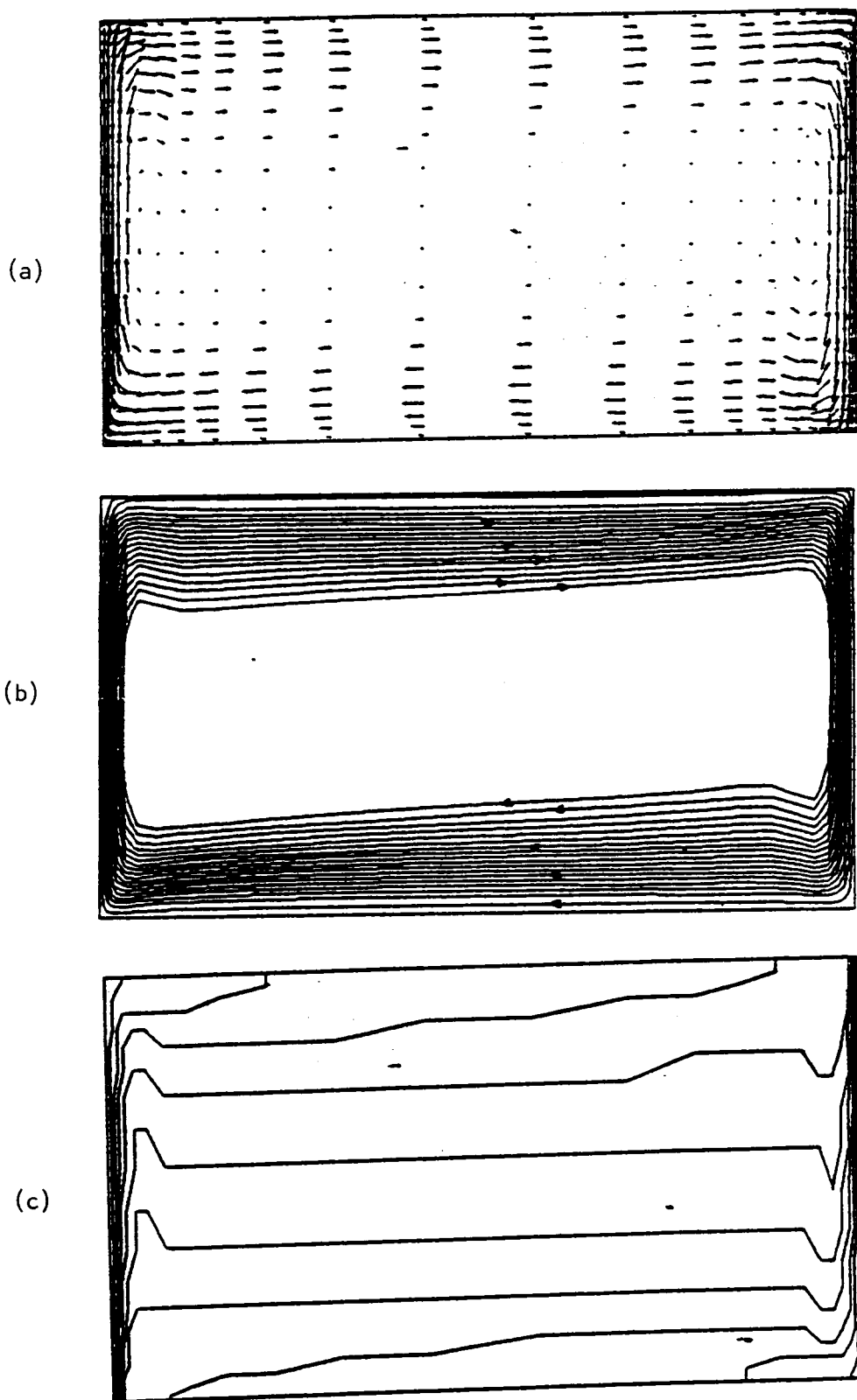


Figure 4. Steady-state velocity vector (a), stream lines (b) and isotherms (c) for Case 1

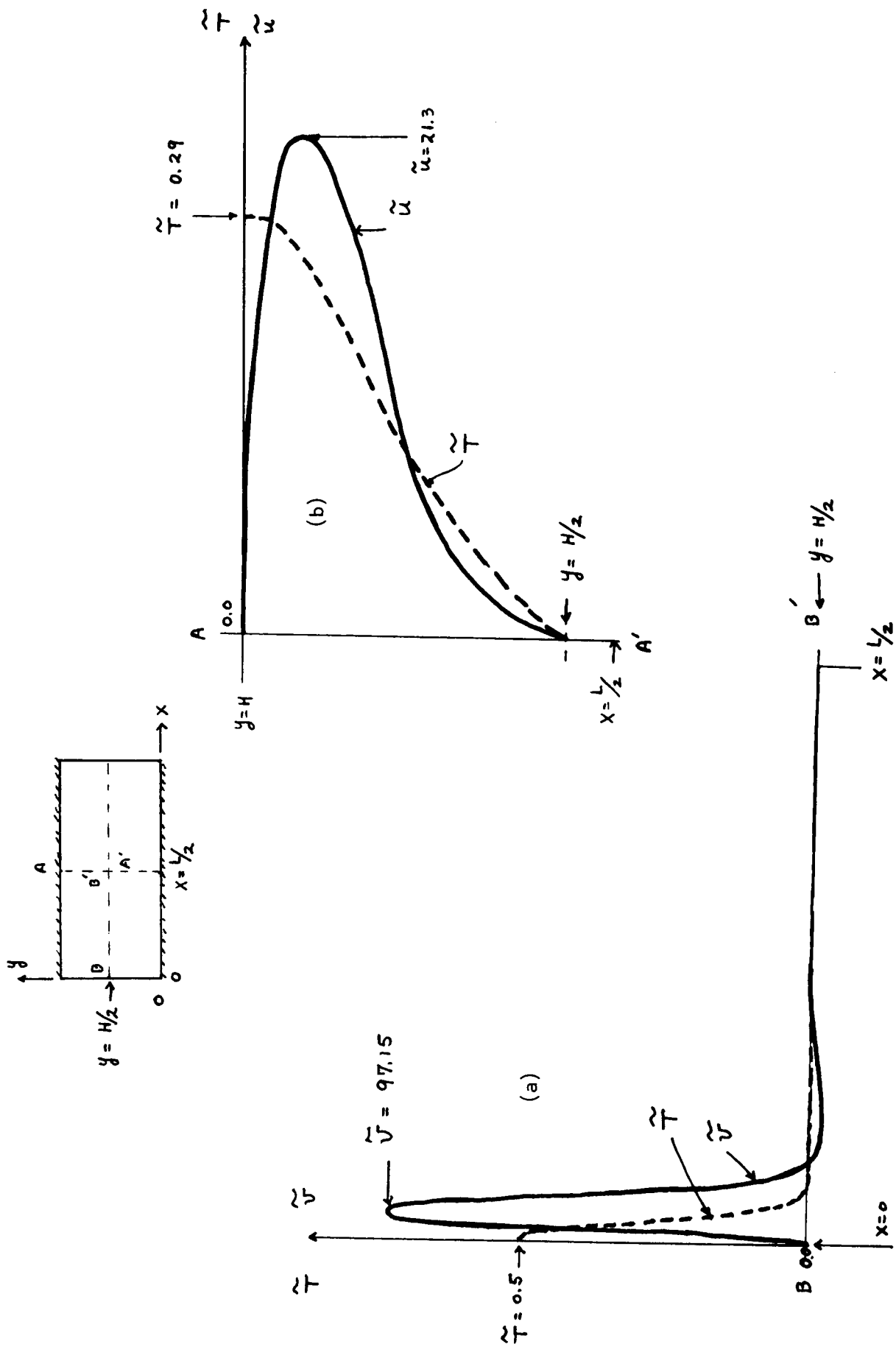


Figure 5. Velocity and temperature profiles at selected planes

CASE 2: Solutal convection: Nondimensional parameters used for this case are

$$\begin{aligned} Gr_M &= -8.3 \times 10^6 ; Gr_T = 0 ; Sc = 2140 ; A = 0.53 \\ Ra_M &= 1.78 \times 10^{10} \end{aligned} \quad (12)$$

Nondimensional solute concentration equation is identical to the nondimensional energy equation except the Schmidt number appears in place of the Prandtl number. By virtue of this analogy between equations, average mass transfer of species A across the cavity can be determined by using the Nusselt number correlations with simple replacement of nondimensional parameters such as

$$Pr \rightarrow Sc \quad Gr_T \rightarrow Gr_M \quad Nu \rightarrow Sh \quad (13)$$

Using the results of Nusselt number correlation as shown in Figure 3, the average steady-state Sherwood number corresponding to the given mass Rayleigh number is approximately 226.

Figure 6 shows the computed transient Sherwood number evaluated at the center of the cavity defined by

$$Sh_c = \frac{Q_M}{\rho D_{AB} \frac{H}{L} \Delta W_A} \quad (14)$$

where Q_M is the net mass transfer of species A at the center of the cavity and given by

$$Q_M = \int_0^H \left[\rho u (W_A - W_A^0) - \rho D_{AB} \frac{\partial W_A}{\partial x} \right]_{x=\frac{L}{2}} dy. \quad (15)$$

Mass transfer increases sharply as the convection current reaches the center of the cavity and undergoes a weak oscillation before approaching the steady value of about 222. This is in excellent agreement with the analytical result.

Using the analogy, solutal boundary layer thickness can be computed as

$$\delta_c \sim H Ra_M^{-1/4} \approx 2.84 \times 10^{-4} \text{ m}. \quad (16)$$

This implies that the center of the control volume next to the vertical wall should be less than 2.84×10^{-4} m. The present grid system ($\delta x_1 = 0.0005$) does satisfy this requirement. When the grid size of the control volume next to the vertical walls was doubled ($\delta x_1 = 0.001$) the steady Sh number was 170 and when $\delta x_1 = 0.002$, $Sh = 97$.

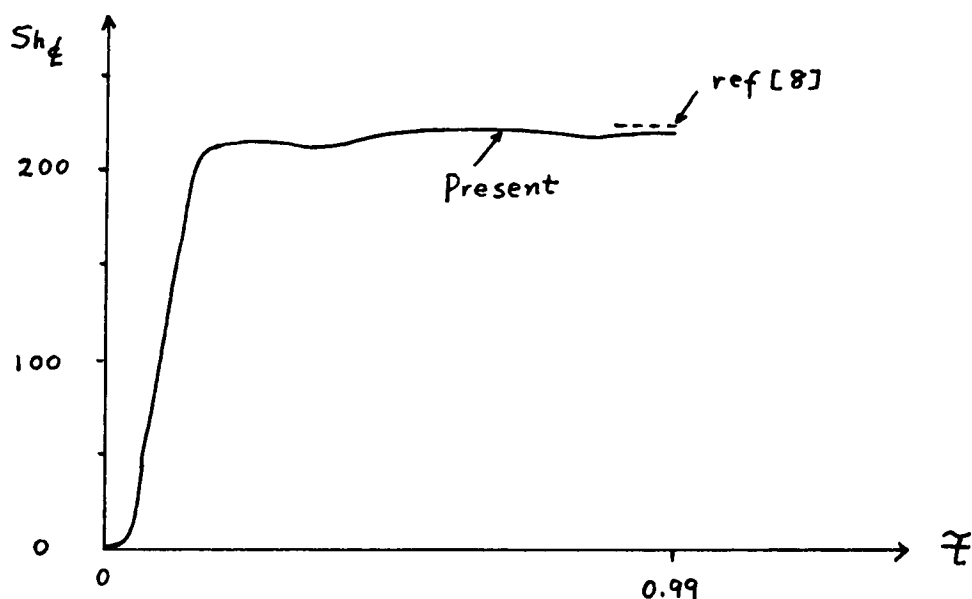


Figure 6. Transient Sherwood number variations (Case 2)

The amplitude and frequency of Sherwood number oscillations are much smaller than the Nusselt number oscillations as shown in Figure 2. This is due to extremely high Schmidt number (2140) used in Case 2 compared with a smaller Prandtl number (7.0) used in Case 1. Viscous damping is more pronounced in Case 2.

Figure 7 shows the steady-state flow, temperature and concentration field for Case 2. Note that the solutal buoyancy force acts along the negative y -direction near the left wall. The magnitude of convection is much smaller than the Case 1 and the momentum boundary layer thickness is much smaller than Case 1. Furthermore, solutal boundary layer on the vertical walls (Figure 7c) are confined within one computational cells along the vertical walls.

The most peculiar aspect of the flow field in Case 2 is two-distinct horizontal convection layers along the horizontal walls. There are relatively dead flow zones between these horizontal convection currents. Figure 8 shows these peculiarity more clearly. Figure 8a shows the vertical velocity and concentration profiles at a horizontal plane at the cavity mid-height. Figure 8b shows the horizontal velocity and concentration profiles at a vertical plane at the mid-width of the cavity. Horizontal velocity distributions have double humps. Mass transfer across the cavity is however mainly contributed by the convection current near the horizontal walls since the mass concentration remains mostly at the initial value around the second velocity maximum.

Layered convection could occur, for example, when a stable water (saturated with salt) is heated from the side wall. Heat transfer to water occurs from the wall by conduction. Heated

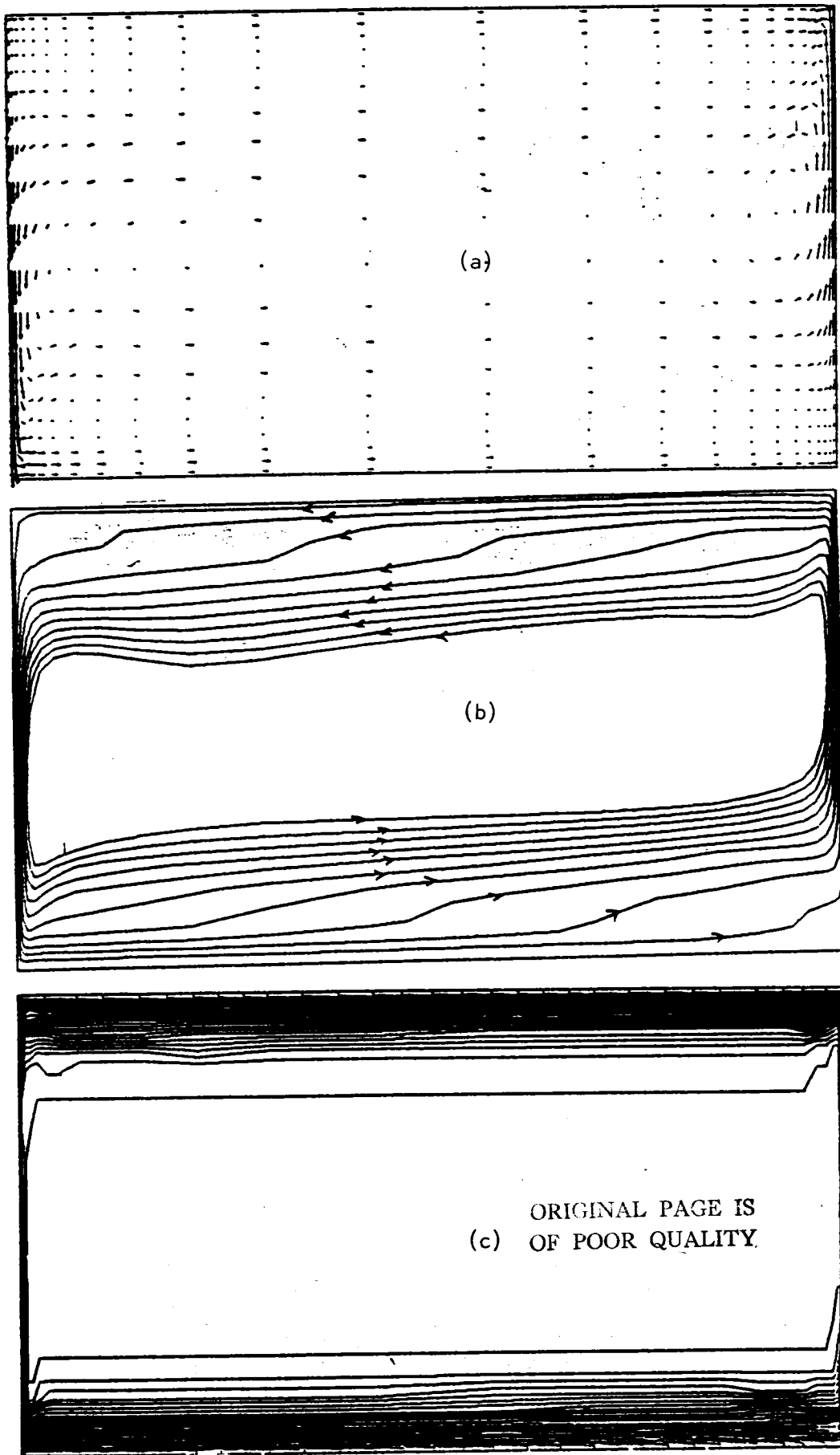


Figure 7. Steady-state velocity vectors (a), stream lines (b) and iso-concentrations for Case 2

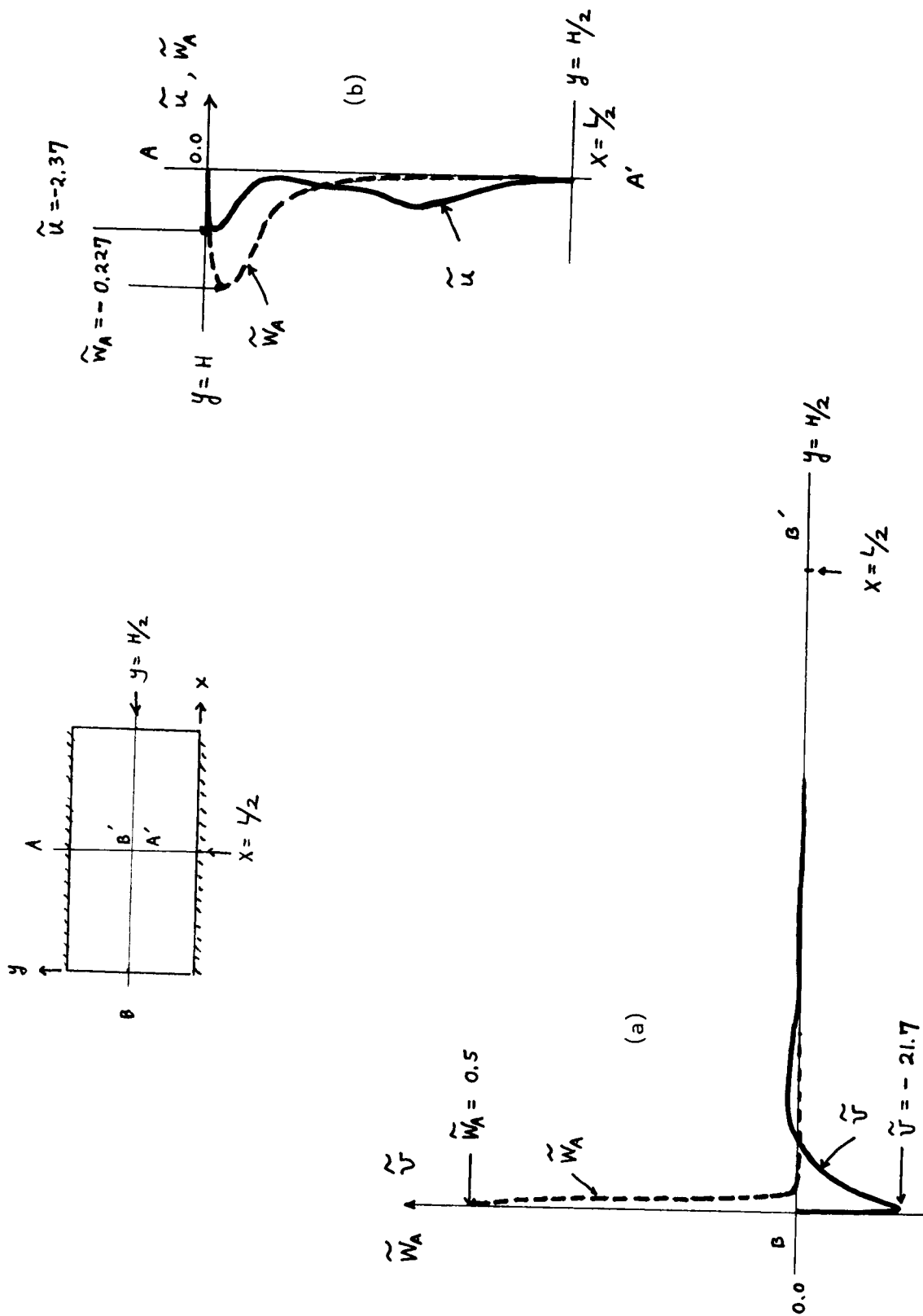


Figure 8. Velocity and mass concentration profiles at selected planes for Case 2

water expands and rises up to the level where its density matches the surrounding density and flows horizontally away from the hot wall. If the mass diffusivity of salt through water is equal to the thermal diffusivity, density change due to heat transfer and mass transfer can cancel each other. In this case, layered convection can not occur. Double-diffusive flow involves two distinct diffusion processes with different diffusion coefficients. The present results are somewhat similar to double-diffusive flow situation even though mass transfer is the only available diffusion mechanism. No satisfactory physical explanation can be offered at present moment to explain the layered convection in Case 2.

CASE 3. Opposing combined convection: In this case both thermal and solutal buoyancy effects are considered. The initial flow and temperature fields are those obtained in Case 1. Solutal buoyancy force acts in the opposite direction to the thermal buoyancy force. Nondimensional parameters are

$$\begin{aligned} Gr_T &= 9 \times 10^5 ; Gr_M = -8.3 \times 10^6 ; Pr = 7.07 ; Sc = 2140 ; \\ \alpha &= 0.53 ; Ra_T = 6.36 \times 10^6 ; Ra_M = 1.78 \times 10^{10} \end{aligned} \quad (17)$$

Two additional nondimensional parameters are defined in order to compare the thermal and solutal effects. They are Lewis number and the buoyancy ratio

$$Le = \frac{Sc}{Pr} = 302 ; N = \frac{\alpha_A \Delta W_A}{\beta \Delta T} = -9.27 \quad (18)$$

Figure 9 shows the average Nusselt and Sherwood number variations as a function of time for the combined convection. The

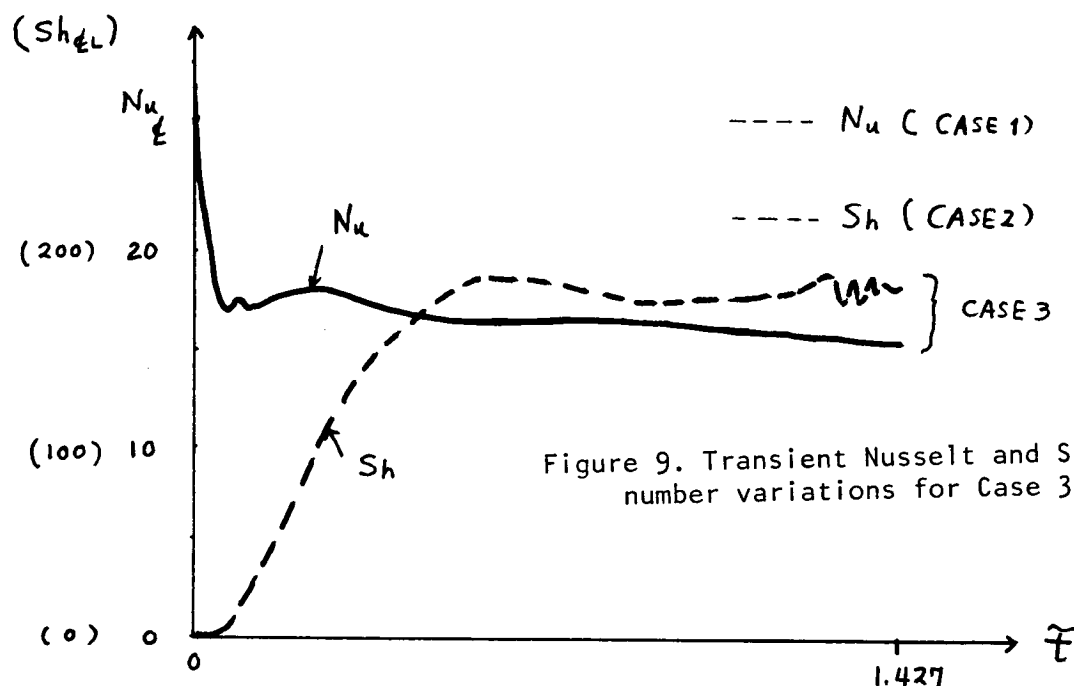


Figure 9. Transient Nusselt and Sherwood number variations for Case 3

ORIGINAL PAGE IS
OF POOR QUALITY

steady state Nusselt number for Case 1 and Sherwood number for Case 2 are also indicated for comparison. Due to the opposing buoyancy effects, energy and mass transfer rates are markedly dropped compared with a pure thermal and a pure solutal cases. Numerical solutions at the end of computations were not steady-state. Small fluctuations in Sherwood number are due to fluctuating velocity field. Qualitatively similar fluctuations were observed in experiments. [1]

Figure 10 shows the quasi-steady state flow, temperature and concentration fields at the end of computation. Two convection loops can be identified: a slow counter clockwise circulation near the solid walls due to solutal effects and a dominant clockwise circulation in the rest of the cavity. Overall flow characteristics are determined by the thermal effects because of high Lewis number. Temperature inversion (hotter fluid on top of cold) occurs at the lower left and top right corner of the cavity (Fig 10c) due to solutal effects.

CASE 4. Aiding combined convection: In this case, solutal buoyancy force and the thermal buoyancy force are acting along the same direction. Nondimensional parameters are identical to those of Case 3 except the change in sign for the buoyancy ratio. Initial conditions are again provided by Case 1.

Figure 11 shows the transient heat and mass transfer rate across the cavity for the aiding case in comparison with a pure thermal and a pure solutal cases. Numerical solutions, in particular the mass transfer rate, exhibit the mild fluctuations toward the end of computations as Case 3. Quasi-steady-state Sherwood number for the aiding case increased markedly over Case 2. However, Nusselt number is decreased below that of Case 1. This unexpected result is a consequence of thermal and solutal interactions, which is explained in a later section.

Figure 12 shows the quasi-steady velocity, temperature and concentration fields for Case 3. Over-all features are similar to case 1 (Figures 12a, 12b and 12c) and Case 2 (Figure 12d).

Thermal and Solutal Interactions

To analyse the thermal and solutal interactions more closely, detailed flow profiles at a horizontal plane located at the mid-height of the cavity are presented in Figure 13. It can be seen that opposing solutal buoyancy forces result in the negative vertical velocity near the left vertical wall and reduced vertical velocity compared with the pure thermal case. Temperature and concentration gradients at the left wall are also reduced compared with pure convection cases.

For the aiding case, vertical velocity is increased near the vertical wall due to the solutal buoyancy force as expected. However, vertical velocity is actually smaller than that of Case 1 in most of the remaining velocity boundary layer. Temperature gradient at the wall remains almost identical to Case 1. But

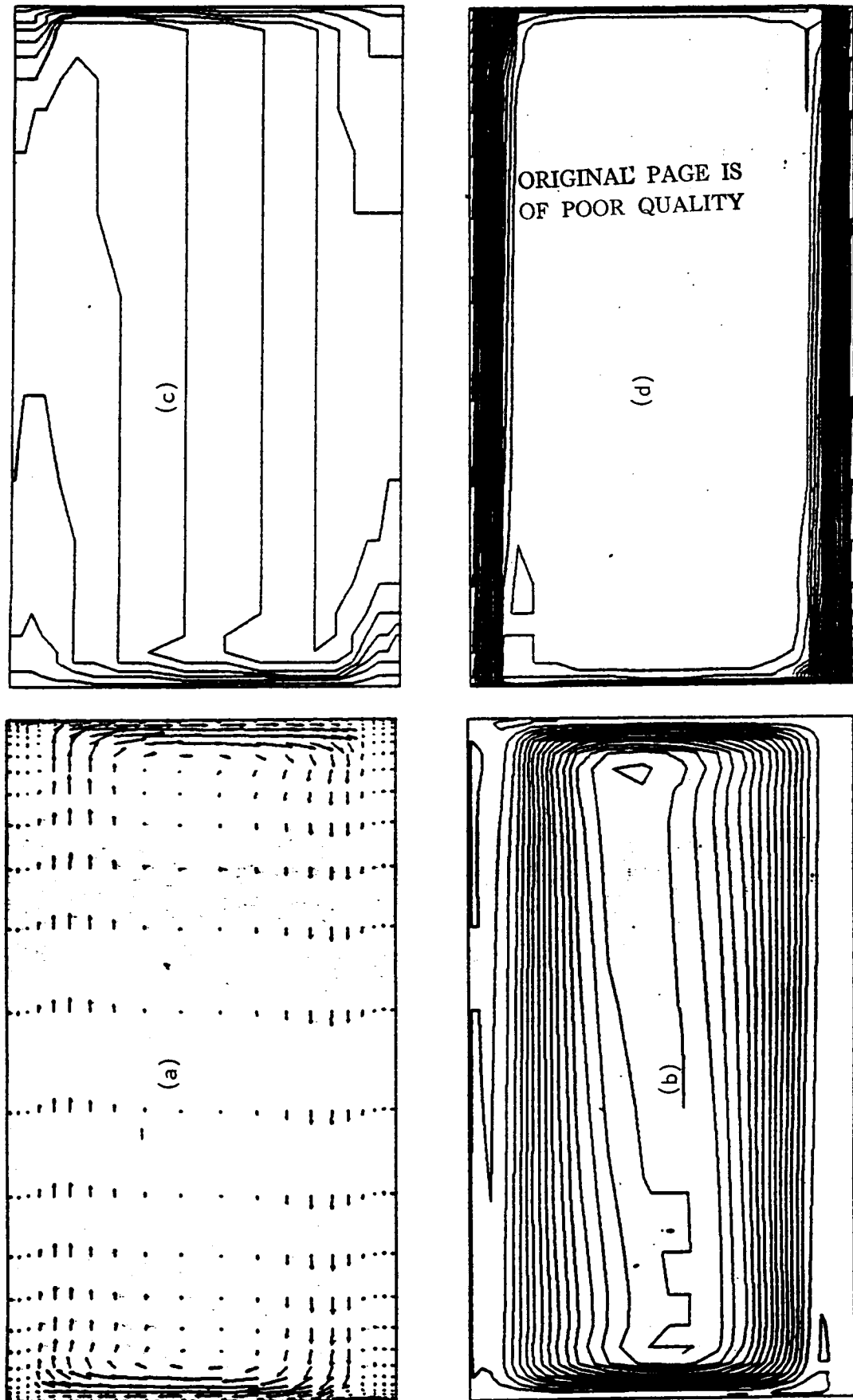


Figure 10. Quasi-steady-state velocity vectors (a), stream lines (b), iso-mass concentrations for Case 3

ORIGINAL PAGE IS
OF POOR QUALITY

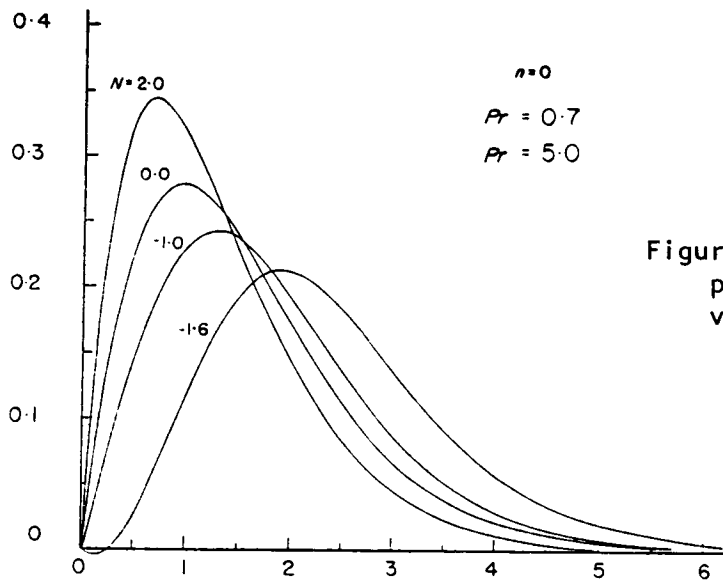


Figure 14. Vertical velocity profiles at an infinite vertical plane [11]

concentration gradient is much higher than that of Case 2 due to the increased vertical flow speed compared with Case 2. Consequently, Nusselt number for this aiding case is slightly lower than Case 1 but the Sherwood number is much higher than Case 2.

The velocity profiles shown in Figure 13a are similar to similarity solutions [11] over a vertical flat plate, except the aiding case. (Figure 14) Direct one to one comparison is not possible since two problems differ in geometry and nondimensional parameters.

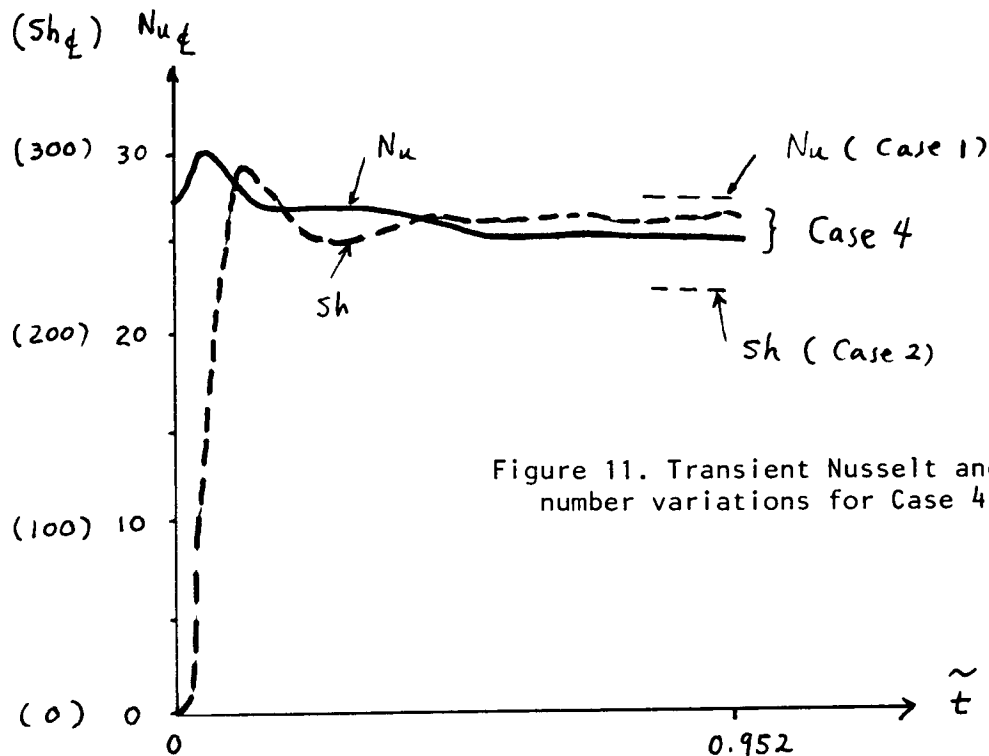


Figure 11. Transient Nusselt and Sherwood number variations for Case 4

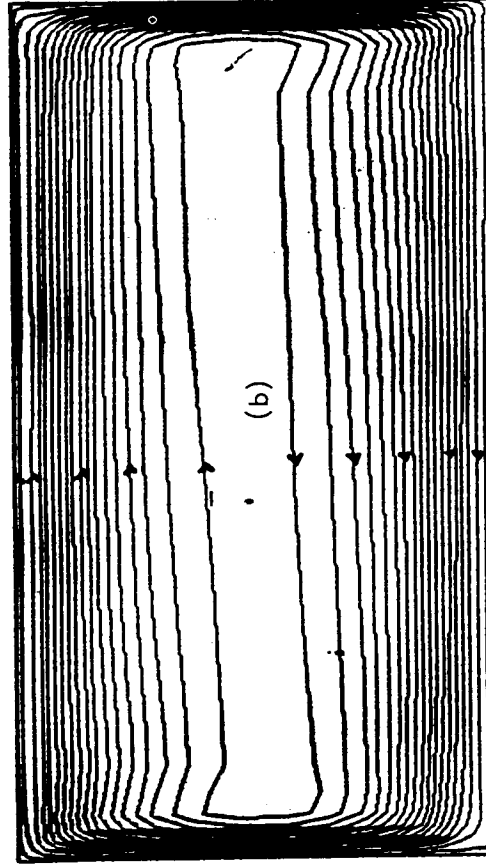
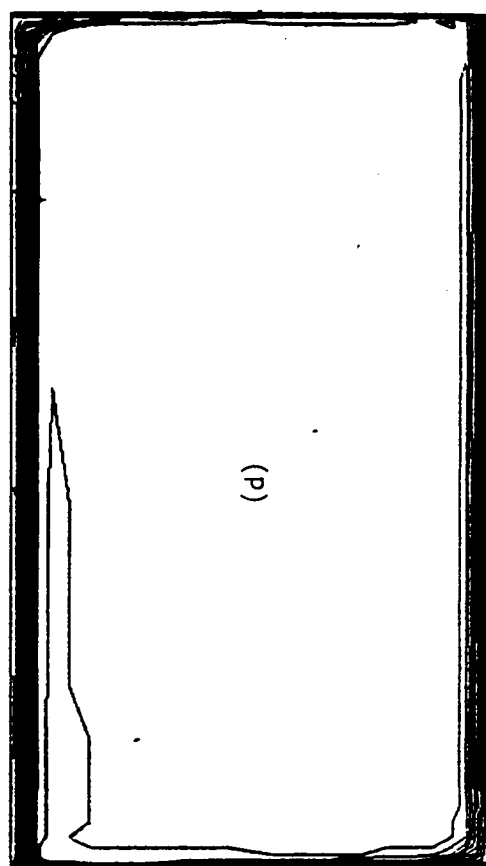
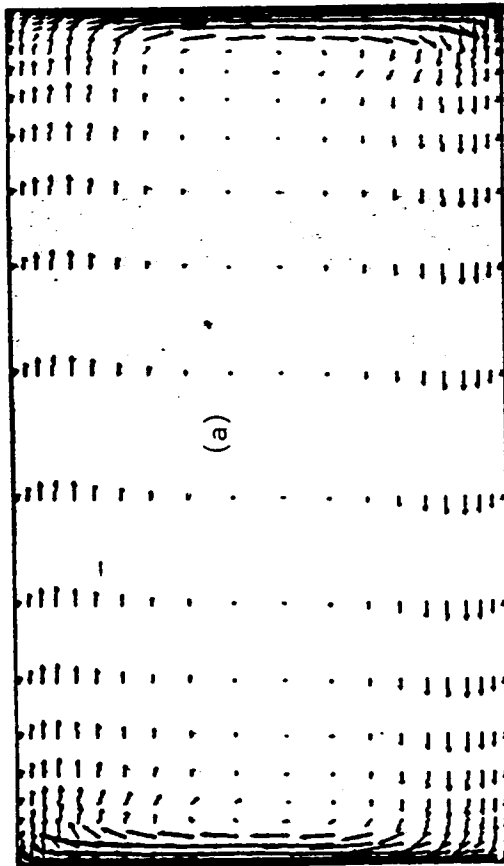
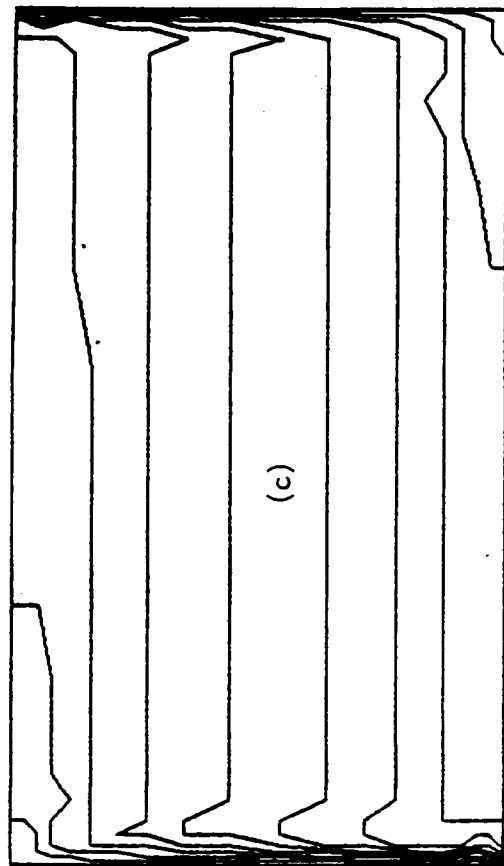


Figure 12. Quasi-steady-state velocity vectors (a), stream lines (b), isotherms (c) and iso-mass concentrations (d) for Case 4

ORIGINAL PAGE IS
OF POOR QUALITY

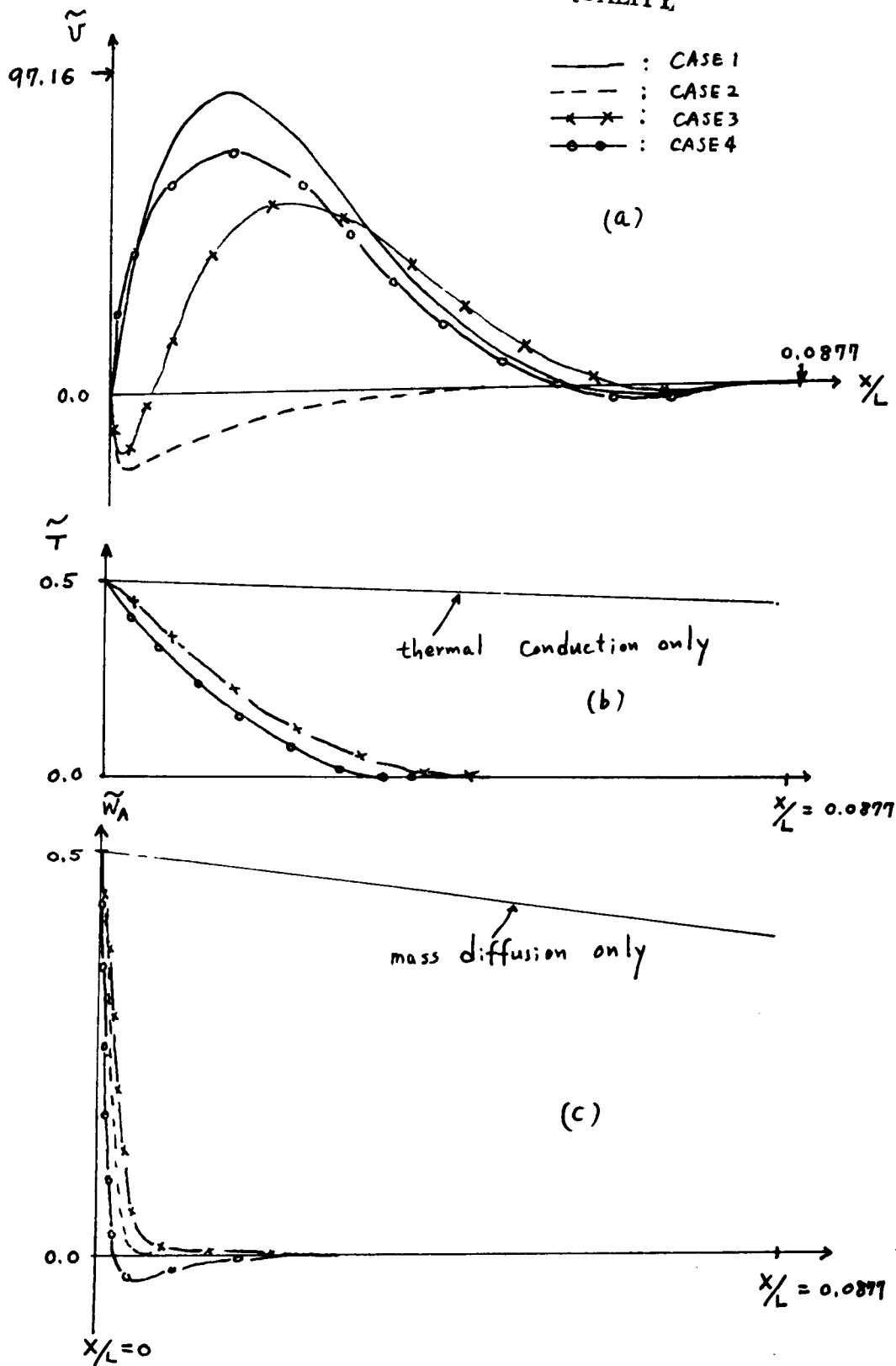


Figure 13. Vertical velocities (a), temperatures (b) and mass concentrations (c) distributions in boundary layers at the left vertical wall at the mid-height of the cavity

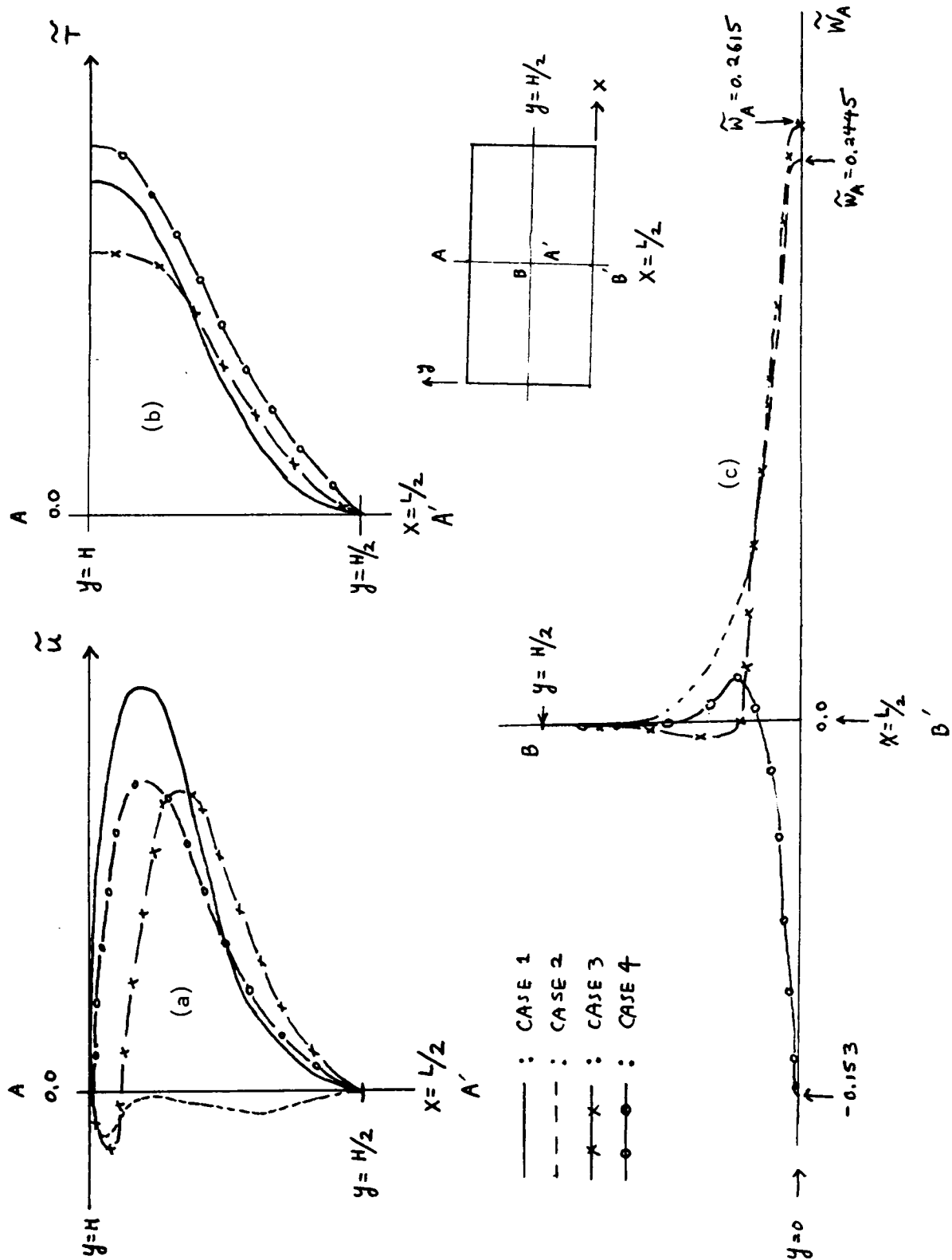


Figure 15. Horizontal velocity (a), temperature (b) and mass concentration distributions at a vertical plane located at the mid-width of the cavity

Figure 15 shows the horizontal velocity, temperature and concentration profiles at a vertical plane located at the mid-width of the cavity. These results again show that the mass and heat transfer across the cavity are strongly dependent on the interactions between the thermal and solutal convections and that opposing and aiding effects can have unexpected influences on the transport mechanisms.

Effects on Crystal Growth

Figure 16 shows the temperature and concentration at the center of the control volumes next to the right vertical wall, which might represent the growing surface of a crystal. Highly nonuniform temperature and concentration profiles there imply an uneven heat transfer and crystal growth rate. As expected, convection enhances the rate of crystal growth significantly over the pure diffusion cases but with detrimental effects on the crystal structure.

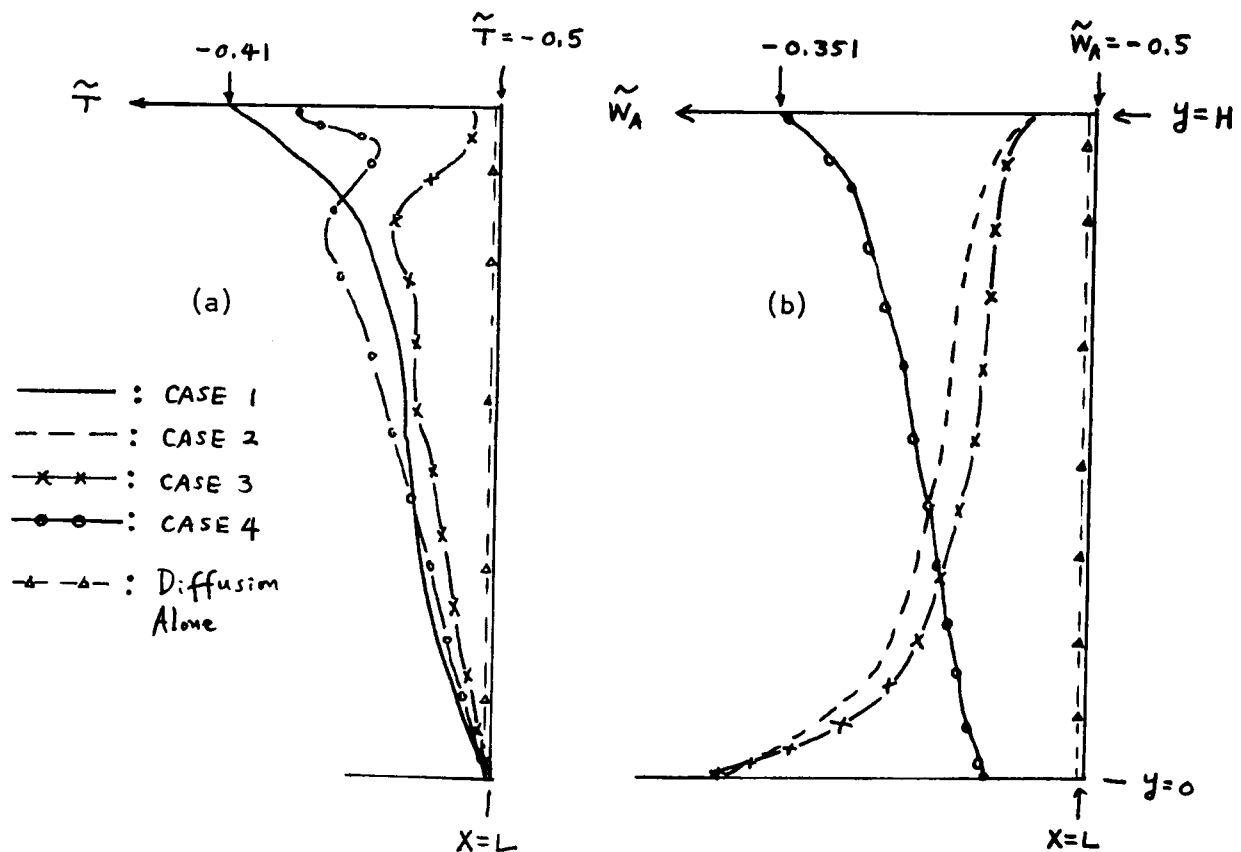


Figure 16. Temperature and mass concentration profiles along the vertical coordinate at the control volumes next to the right vertical surface

V. CONCLUSIONS AND RECOMMENDATIONS

Numerical simulations of thermal and solutal buoyancy driven convections in a rectangular cavity are performed by a numerical model based on the SIMPLE algorithm. Physical parameters are chosen to represent a possible crystal growth from solution.

Numerical results for a pure thermal convection were found to agree reasonably well with a known solution. Numerical results for a pure solutal convection also agree well with an analytic solution in terms of the average Sherwood number. However, the velocity field for the pure solutal convection exhibits a peculiar feature which can not be explained. Relatively large solutal Rayleigh number ($1.67E+10$) and an extremely large Schmidt number (2140) combination might have produced the nonphysical solutions. This has to be checked more carefully through further numerical experimentations.

Overall energy and mass transfer rates are seen to depend strongly on the interactions between the thermal and solutal effects. These interactions are highly nonlinear and the steady-state conditions may not exist for certain combined convections. To arrive at the more conclusive and quantitative correlations, however, experiments covering wide range of nondimensional parameters are required.

To investigate the double-diffusive effects on the flow, a non-uniform initial solutal distribution in the cavity is needed before the commencement of heat transfer from side walls. (The initial solute concentration was assumed constant for present analysis.) This can be easily accomplished by assigning any non-uniform solute distribution in the cavity.

After performing the recommended refinements and verifications as discussed above, one can relax the constraints on the problem formulations, such as the interfacial velocity, segregation effects and the temperature boundary conditions.

ORIGINAL PAGE IS
OF POOR QUALITY

REFERENCES

1. Ostrach, Simon, "Fluid Mechanics in Crystal Growth-The 1982 Freeman Schler Lecture," J. Fluid Eng., Vol 105, 5-20, 1982.
2. Ostrach, Simon, "Low-Gravity Fluid Flows," Ann. Rev. Fluid Mech., Vol. 14, 313-345, 1982.
3. Extremet, G., Roux B., Bontoux P., and Elie F., "Two-dimensional Model for Thermal and Solutal Convection in Multizone Physical Vapor Transport," J. Crystal Growth, Vol. 82, 761-775, 1987.
4. Napolitano, L. G., "Recent Advances in Microgravity Fluid Dynamics," Annal New York Academy of Science, 278-298, 1983.
5. Patankar, S. V., Numerical Heat Transfer and Fluid Flow, McGraw-Hill, 1980.
6. Han, S. M., "A Generalized Implicit Finite Difference Method for Transient Analysis of Compressible and Incompressible Fluid Flows," Numerical Methods for Fluid Transient Analysis, ASME FED-Vol 4, 17-21, 1983.
7. Han, S. M., "A Transient Numerical Analysis of High Rayleigh Number Convection in a Differentially Heated Square Cavity," ASME Paper 84-HT-57, 1984.
8. Bejan, A., Convection Heat Transfer, Wiley and Sons, 1984.
9. Patterson, J. and Imberger, J., "Unsteady Natural Convection in a Rectangular Cavity," J. Fluid Mech., Vol. 100, Part 1, 65-80, 1980.
10. Turner, J. S., "Double-Diffusive Phenomena," Ann. Rev. Fluid Mech., Vol. 6, 37-56, 1974.
11. Gebhart, B. and Pera, L., "The Nature of Vertical Natural Convection Flows Resulting From the Combined Buoyancy Effects of Thermal and Mass Diffusion," Int. J. Heat Mass Transfer, Vol. 14, 2025-2050, 1971.

1987

519-27
N88-15620/6721

NASA/ASEE SUMMER FACULTY RESEARCH FELLOWSHIP PROGRAM 88

MARSHALL SPACE FLIGHT CENTER
THE UNIVERSITY OF ALABAMA IN HUNTSVILLE

USE OF HYDROPHILIC POLYMER COATINGS FOR CONTROL OF ELECTROOSMOSIS
AND PROTEIN ADSORPTION

Prepared by: J. Milton Harris
Academic Rank: Professor
University and Department: Univ. Alabama Huntsville
Chemistry

NASA/MSFC:

Laboratory: Space Science
Division: Low Gravity Science
Branch: Biophysics

NASA/Colleague: Robert Snyder

Date: September 3, 1987

ABSTRACT

The purpose of this project was to examine the utility of polyethylene glycol (PEG) and dextran coatings for control of electroosmosis and protein adsorption; electroosmosis is an important, deleterious process affecting electrophoretic separations, and protein adsorption is a factor which needs to be controlled during protein crystal growth to avoid multiple nucleation sites. Performance of the project required use of X-ray photoelectron spectroscopy to refine previously developed synthetic methods. The results of this spectroscopic examination are reported. Measurements of electroosmotic mobility of charged particles in appropriately coated capillaries reveals that a new, one-step route to coating capillaries gives a surface in which electroosmosis is dramatically reduced. Similarly, both PEG and dextran coatings were shown by protein adsorption measurements to be highly effective at reducing protein adsorption on solid surfaces. These results should have impact on future low-g electrophoretic and protein crystal growth experiments.

INTRODUCTION

This work involves use of organic polymer coatings to control electroosmosis and protein adsorption. Before giving details of the experiments that were performed it is useful to provide a brief review of some background concepts.

Electroosmosis can be described as movement of a conducting liquid relative to a stationary charged surface, which results when an electric field is applied to the liquid. Generally, clean surfaces will be negatively charged, so that application of an electric field will produce movement of the positive counterions toward the negative electrode. This electroosmotic flow reduces the effectiveness of electrophoretic processes and thus tends to eliminate the benefits achieved by performing electrophoresis in low g where thermal and concentration driven convection is eliminated.

We have previously shown that polyethylene glycol (PEG) coatings are effective at reducing electroosmosis (1). Apparently this reduction results from the hydrophilic polymer coating acting as a wetted viscous layer (a "kelp forest") over the charged surface. The goal of the present work is to simplify the coating chemistry by preparing a PEG-silane that can be directly applied to glass surfaces. The previous technique required three steps: preparation of an activated PEG, amination of the glass surface, and coupling of the activated PEG to the aminated surface.

The second part of this project is concerned with examining the ability of hydrophilic polymer coatings (PEG and dextran) for their ability to reject proteins (i.e., their biocompatibility). The coatings are tethered to the surface by a single covalent linkage (the kelp forest analogy) and would be expected to exclude proteins from the surface simply by waving around. This phenomenon has been used to explain the ability of covalently-linked PEG to render proteins nonimmunogenic. In this work we have attached PEG and dextran to glass slides and measured the extent of fibrinogen I-125 adsorption. Controlling protein adsorption is important in protein electrophoresis and in protein crystal growth experiments where it is desirable to avoid multiple nucleation sites.

An important aspect of all this work is utilization of X-ray photoelectron spectroscopy (XPS) to characterize our surfaces. This technique provides a direct elemental analysis of surfaces. By using it we should have a more quantitative and direct means of following chemistry on the surfaces. Previously, we have used wet chemical techniques that give averages of surface chemistry. With XPS we can study surface homogeneity and we can work with small slides having too little surface area to use the wet chemical methods previously applied.

OBJECTIVES

The objectives of this work are as follows:

- (1) to prepare a PEG silane and couple it to glass
- (2) to measure the electroosmotic mobility of a polystyrene microsphere in a PEG-silane coated glass capillary
- (3) to improve our glass amination procedures by use of X-ray photoelectron spectroscopy
- (4) to measure the extent of protein (fibrinogen) adsorption on dextran- and PEG-coated glass using improved amination procedures to coat the glass

Results of X-Ray Photoelectron Spectroscopic (XPS) Surface Analysis

Our first goal was to use XPS to examine coating chemistry. The first step in the standard coating procedure is to aminate the glass surface using trimethoxyaminopropylsilane, 1. Previously we examined the efficiency of this process by conducting the reaction on porous glass (with a large surface area) and titrating the amine groups with acid. With XPS we can directly determine the percentage of nitrogen on the surface of slides actually used in the protein adsorption experiments. Nitrogen has a relatively small cross section, so we have fluorinated the surface by reacting the aminated surface with pentafluorobenzaldehyde. Thus we can check the nitrogen results by measuring the percentage of fluorine, an element having a much larger cross section.

In a typical amination procedure the glass substrate is immersed in a 5% solution of 1 in water for 24 hours at 80 degrees, and then cured dry at 110 degrees for four hours; after curing, the glass is exhaustively washed with distilled water. Surfaces prepared in four different ways were examined. The four routes are: (1) treatment with 1 followed by washing with water before curing; (2) as in example 1, but done twice; (3) treatment with 1 followed by curing without washing; (4) as in example 3, but done twice. The results of these experiments, using two different XPS instruments (a Perkin-Elmer at UAH and a Surface Science at University of Washington), are given in Table 1.

Table 1. Measurement of percent nitrogen and fluorine on aminated glass slides (prepared four ways as described in text) treated with pentafluorobenzaldehyde on an Perkin-Elmer XPS and a Surface Science XPS.

	Method			
	#1	#2	#3	#4
%N (Perkin-Elmer)	0.98	1.98	2.30	2.37
%N (Surface-Sci.)	1.66	1.95	2.75	5.09
%F (Surface-Sci.)	4.49	5.45	4.17	7.17

The data show that higher percentages of nitrogen are obtained if the surface is not washed before curing. Also a higher nitrogen coverage is obtained if the process is repeated. It is noteworthy that significant different values for percent nitrogen were measured with the two instruments. The Perkin-Elmer machine is new and uncalibrated, so it is likely that the Surface Science data are more trustworthy. Further comparison of the two machines with known substrates will be done. Also, the %F does not parallel the trends in %N. This result has two possible explanations. First, it is known that the XPS probes the first 5 nm of the surface, and the fluorines are applied directly onto the surface; so the nitrogen and fluorine measurements are actually made on different layers of surface. A second possibility is that the pentafluorobenzaldehyde liquid alters the surface in some way. We are now exploring a vapor-phase

fluorination procedure with trifluoroacetic anhydride to avoid this second possibility.

RESULTS OF ELECTROOSMOSIS EXPERIMENTS

As noted above, the goal of this segment of the project is to attach PEG to glass capillaries in a single step by reaction with a PEG-silane. The PEG-silane was synthesized by reacting PEG with trimethoxysilylpropyl isocyanate in methylene chloride. The reaction could be followed on IR by monitoring the isocyanate absorbance. Reaction of the PEG-silane with quartz electrophoresis capillaries was performed as described above. Electroosmotic mobilities were then determined for uncoated, standard two-step coated, and silane coated capillaries; standard coating involves the two-step process with amination and reaction with activated PEG described above. In both cases, the PEG used was the monomethyl ether of PEG 5000. Details on electroosmosis measurements are available in reference 1.

Measured electroosmotic mobilities (in $\mu\text{m/s cm/V}$ at pH 5.78, 7.5 mM NaCl) were: uncoated, 1.7; standard coated, 0.3; and silane coated, 0.7. This result shows that the single-step, silane coating is effective at reducing electroosmosis, although it is not as effective as the standard two-step procedure. It will be very interesting to follow up on these results by doing XPS experiments to determine the extent of PEG coverage using the two methods. Also it will be interesting to determine the pH dependence of the two different coatings, since we earlier concluded that the two-step procedure left some uncoupled amine groups which could show a large response to pH variation.

RESULTS ON PROTEIN ADSORPTION

The final set of experiments were to measure the extent of protein adsorption on PEG- and dextran-coated surfaces. The actual measurement was extent of fibrinogen I-125 adsorbed onto the materials. The results are presented in Table 2.

Table 2. Fibrinogen I-125 adsorption of PEG coated glass slides

substrate	protein adsorbed ($\mu\text{g/cm}^2$)
glass	0.420
glass-amine	0.683
glass -PEG200	0.540
-PEG400	0.468
-PEG1000	0.382
-PEG3000	0.206
-PEG8000	0.104
-PEG20000	0.072

As can be seen from Table 2, there is a dramatic drop in protein adsorption with the PEG MW. Presumably the larger PEGs have a larger exclusion volume and are thus better able to "sweep" the protein from the surface. We have also examined dextran coatings. Although the experiments are preliminary, we do have qualitative data showing that dextran is even more effective than PEG at reducing protein adsorption. The dextran was attached by reductive amination of aminated glass by the reducing end of the polysaccharide.

CONCLUSIONS

The goals of the proposed work have been met. Polymer coating chemistry was improved by use of XPS, and the PEG-silane was synthesized. PEG coatings attached to electrophoresis capillaries by means of the PEG-silane are effective at reducing electroosmosis, although they are not as effective as those coatings applied by the standard two-step procedure. Finally, PEG and dextran coatings are very effective at reducing protein adsorption onto glass, and thus these coatings offer potential for controlling nucleation sites in protein crystal growth. Future work will involve refinement of coating chemistry using fully calibrated XPS spectrometers and examination of dextran coatings for control of protein adsorption and electroosmosis.

REFERENCES

- (1) B. J. Herren, S. G. Shafer, J. M. Van Alstine, J. M. Harris, and R. S. Snyder, "Control of Electroosmosis in Coated Quartz Capillaries," J. Colloid Interface Sci., **115**, 46-55 (1987).

ACKNOWLEDGEMENTS

Assistance in obtaining electroosmosis measurements was provided by J. M. Van Alstine and Todd Williams. Assistance in use of the XPS was provided by Mike Edgell and Wayne Gombotz. Wayne Gombotz also provided protein adsorption data. Financial assistance of this work by NASA is gratefully acknowledged.

1987

NASA/ASEE SUMMER FACULTY FELLOWSHIP PROGRAM

MARSHALL SPACE FLIGHT CENTER
THE UNIVERSITY OF ALABAMA

FURTHER STUDY OF INVERSION LAYER MOS SOLAR CELLS

Prepared by:	Fat Duen Ho, Ph.D
Academic Rank:	Associate Professor
University and Department:	The University of Alabama in Huntsville Department of Electrical and Computer Engineering
NASA/MSFC:	
Laboratory:	Information and Electronic Systems
Division:	Electrical
Branch:	Electrical/Electronic Parts
MSFC Colleague:	Michael D. Martin and Teddy M. Edge
Date:	October 15, 1987
Contract No.:	The University of Alabama in Huntsville NGT-01-008-021

520-44
N88-15621 116722
16P

FURTHER STUDY OF INVERSION LAYER MOS SOLAR CELLS

by

Fat Duen Ho
Associate Professor of Electrical and Computer Engineering
The University of Alabama in Huntsville
Huntsville, Alabama

ABSTRACT

A group of inversion layer MOS solar cells has been fabricated. The highest value of open-circuit voltage obtained for the cells is 0.568V. One of the cells has produced a short-circuit current of 79.6 mA and an open-circuit voltage of 0.54V. It is estimated that the actual area AMO efficiency of this cell is 6.6% with an assumed value of 0.75 for its fill factor. Efforts made for fabricating an IL/MOS cell with reasonable efficiencies are reported. Future work for 4 cm² IL cells and 25 cm² IL cells is discussed

ACKNOWLEDGEMENTS

The author wishes to express his gratitude to Mr. M. D. Martin and Mr. T. M. Edge for their continuous support and encouragement for this research. He wishes to acknowledge Mr. P. D. McManus for his work with the fabrication of the IL/MOS solar cells. He would like to thank Mr. O. A. Norton, Sr., for helping test the devices, Mr. J. B. Farner for bonding the IL cells into packages, Mr. C. Bahr for his assistance in metalization using the vacuum systems and Mr. P. Belcher for doing some machine shop work for the project. He would like to express his appreciation to Mrs. M. S. McCartney for her help. He is grateful to Ms. Georgann Ricks for her assistance and for her typing of this manuscript. His thanks also go to Dr. Gerald Karr, Ms. Ernestine Cothran, and other members of the 1987 NASA/ASEE coordinating team for their work for this program.

LIST OF TABLES

<u>Table Number</u>	<u>Title</u>	<u>Page</u>
1	Experimental results of the IL/MOS solar cells fabricated in Run 2	XXI-8
2	Experimental results of the IL/MOS solar cells fabricated in Run No. 3	XXI-9
3	Experimental results of the IL/MOS solar cells fabricated in Run No. 4	XXI-10

INTRODUCTION

In the previous report (1), we presented the experimental results for three IL/MOS solar cells fabricated in the NASA/MSFC laboratory in 1986. The best open-circuit voltage recorded then was 0.465V for one of the cells, while its short-circuit current only had a value of 0.02 mA. In the same report (1), we pointed out that the reasons of getting low short-circuit currents were probably due to (1) the thin interfacial oxide formed by sputtering was too thick and (2) the thermal oxide became too thin at the edge of aluminum to strongly invert the surface.

Efforts have been made to control more accurately the thickness of the thin layer of oxide between aluminum and silicon of the MIS contacts. Using the furnace with 450°C, an oxide layer about 20Å can be grown on a <111> p-type silicon wafer in 20 minutes. This process has improved the open-circuit voltages and the short-circuit currents of the IL cells substantially. One of the 4 cm² cells in the fourth run of the experiments has produced 79.6 mA short-circuit current and a value of 0.54V for the open-circuit voltage. An actual area (3.56 cm²) AMO efficiency of 6.6% has been achieved with the assumption that the fill factor equals 0.75.

OBJECTIVES

The objectives of this study are (1) fabrication of 4 cm² IL/MOS solar cells with good efficiencies (13% AMO efficiency or better), (2) development of a simple, inexpensive, low-temperature process for fabricating high-efficiency IL solar cells and (3) preliminary study of large-area (25 cm²) IL/MOS solar cells and arrays.

BACKGROUND AND OVERVIEW

The operational principle and the design consideration of IL/MIS solar cells have been discussed in some details in other papers and reports (1)-(7). Here, only a brief review is given.

A. Advantages of the IL Cells

The advantages of IL/MIS solar cells are that the processing is mainly of low temperature and the diffusion-induced crystal damage inherent in diffused p-n junction cells can be avoided. In IL cells, very shallow junctions are formed with high electric field which helps to collect electron-hole pairs generated by short-wavelength light. There is no "dead layer" in this kind of cells. Therefore, their responses for the ultraviolet light are better than those of diffused cells. The IL cells may be possible to have nearly ideal diode properties, which in turn can produce a larger value of open-circuit voltage. The cost of producing the cells can be cut down by using the low temperature processing technology.

B. Design Consideration of IL cells

To have the highest possible efficiency, the structure of an IL cell must be optimized. The most important parameters of the cells for design consideration are (1) the resistivity of the substrate,

(2) the fixed charge in the oxide or other insulators, (3) the number of grids per unit length (usually per cm), and (4) the thickness of the interfacial layer of the thin oxide in an MIS diode.

For an IL cell, the substrate must be p-type with the $\langle 111 \rangle$ orientation. The wafers should be doped properly. If it is doped too heavily, it may have difficulty to invert the thin inversion layer beneath the oxide or other insulator; and if it is too lightly doped, the sheet resistance of the inversion layer would be too large. The sheet resistance of the inversion layer can be reduced by increasing the number of grid lines. But too many grid lines would cover too large an area, which would reduce the area exposed to the sunlight. A compromise between these two parameters should be reached by balancing their opposite effects. The thickness of the thin oxide in the MIS contacts plays a very critical role in processing the IL cells. The insulator must be thin enough to guarantee the tunneling effect is sufficient (8). But too thin interfacial layer of the oxide would lead to low open-circuit voltages and would affect the general performance of the cell. Therefore, the thickness of the insulating thin layer should be optimized.

C. Fabrication Process

The fabrication procedures of the IL cells are summerized as follows:

- (1) Thermal oxide with a thickness of approximately 1500\AA is grown on p-type silicon substrate with $\langle 111 \rangle$ crystal orientation.

- (2) Metal contact regions are defined using the first mask.
- (3) Aluminum is deposited on the back surface and sintered.
- (4) The thin oxide in an MIS contact is grown using 450°C furnace for 20 minutes.
- (5) Aluminum is evaporated onto the front part of the sample.
- (6) Aluminum grid patterns are defined using a second mask.

RESULTS AND DISCUSSION

There were three runs of experiments for the IL cells in the ten weeks period of the 1987 Summer Faculty Fellowship Program. The fourth run was ended on September 15, 1987, about one month after the program was over. The results of the first run were poor due to the accidental etching of the aluminum on the backs of the wafers. In addition the thin layers of oxide in MIS contacts may be too thick because there was no accurate control of the thin oxide at that time. The results of the second run are listed in Table 1 while those of the third run are in table 2.

Both open-circuit voltages and short-circuit currents are much better in the third run than those corresponding values obtained in the first and second runs. In the third run, the aluminum on the back sides was also accidentally etched. The worsening contacts in the back sides of the IL cells definitely contributed the bad effects on the short-circuit currents, which are even smaller than their counterparts in the cells fabricated in 1986.

The fourth run was much more successful. The open-circuit voltage of one of the cells equals 0.54V while having a short-circuit current of 79.6 mA. The total area of the cell is about 4 cm^2 . The measurements are done under AMO illumination. An actual area (3.56 cm^2) efficiency of 6.8% was estimated with an assumed value of 0.75 for the fill factor of the cell. The result are listed in Table 3.

Note that the oxidation processes with HCl gettering and those without HCl gettering did not make significant difference for the performance of the cells. Therefore, from Run #4 on, we have been using HCl gettering in all oxidation processes.

TABLE 1: EXPERIMENTAL RESULTS OF THE IL/MOS SOLAR CELLS
FABRICATED IN RUN NO. 2

<u>Cell No.</u>	<u>Type and Resistivity of Substrate</u>	<u>Number of Grids per cm</u>	<u>Oxide</u>	<u>I_{SC} (mA)</u>	<u>V_{OC} (V)</u>
1A	P <111> 1.19 Ω -cm	121	1544Å (Thermal)	0.002	0.27
1B	P <111> 1.19 Ω -cm	121	1545Å (Thermal)	0.001	0.29
2A	P <111> 1.19 Ω -cm	121	1218Å (Sputtering)	0.005	0.32
2B	P <111> 1.19 Ω -cm	121	1227Å (Sputtering)	0.005	0.002

TABLE 2: EXPERIMENTAL RESULTS OF THE IL/MOS SOLAR CELLS
FABRICATED IN RUN NO. 3

<u>Cell No.</u>	<u>Type and Resistivity of Substrate</u>	<u>Number of Grids per cm</u>	<u>Oxide</u>	<u>I_{SC} (mA)</u>	<u>V_{OC} (V)</u>
3	P <111> 1.19 Ω -cm	121	1435Å (With HCl gettering)	0.752	0.539
4	P <111> 1.19 Ω -cm	121	1845Å (With HCl gettering)	0.388	0.283
5	P <111> 1.19 Ω -cm	121	1460Å (With HCl gettering)	0.814	0.568

TABLE 3: EXPERIMENTAL RESULTS OF THE IL/MOS SOLAR CELLS
FABRICATED IN RUN NO. 4

<u>Cell No.</u>	<u>Type and Resistivity of Substrate</u>	<u>Number of Grids per cm</u>	<u>Oxide</u>	<u>I_{SC} (mA)</u>	<u>V_{OC} (V)</u>
W1-1	P <111> 1.1 Ω -cm	69	1530Å (With HCl Gettering)	79.6	0.54
W1-2	P <111> 1.1 Ω -cm	69	1535Å (With HCl Gettering)	75.2	0.56
W2-2	P <111> 17 Ω -cm	41	1506Å (With HCl Gettering)	1.6	0.38
W2-3	P <111> 17 Ω -cm	41	1409Å (With HCl Gettering)	52.6	0.482

CONCLUSION AND RECOMMENDATION

A. Conclusion

A group of IL/MOS solar cells have been fabricated in the NASA/MSFC laboratory. One of the cells has a short-circuit current of 79.6 mA and an open-circuit voltage of 0.54V. The actual area (3.56 cm^2) AMO efficiency is estimated to be 6.6% with an assumed value of 0.75 for its fill factor. We conclude that the thin oxide in MIS contacts of the cells has been playing a very critical role to improve the short-circuit currents and even the open-circuit voltages. More efforts, therefore, should be made to control the thickness of the thin oxide (less than 20\AA) more accurately. We also conclude that HCl purge is irrelevant to the inversion layer induced in IL cells. Hence, HCl purge is recommended for all oxidation processes.

B. Recommendations:

The future work for the IL cells is recommended as follows:

1. Improvement of the performance of the IL cells so that the 4 cm^2 cells with about 13% AMO efficiency or better could be fabricated. In addition, the cells using sputtering SiO_2 or chemical vapor deposition (CVD) of SiO_2 should be made to get higher oxide charge densities. Also, we have planned to use other insulators such as SiO and Si_3N_4 to establish the inversion layer of an IL cell.

2. Study of smaller area (1 cm^2) IL cells for comparison.

3. Study of large-area (25 cm^2) IL cells and arrays. It is believed that the large area cells can provide large area arrays at lower assembly cost. To study the feasibility of IL/MIS cells for large-scale application, the ability to scale up to large areas for these cells must be explored. Up to now, to the best of our knowledge, there is no literature which has dealt with large-area IL/MIS cells, and the IL cells fabricated are no larger than 4 cm^2 . It is believed that our efforts will be significant in developing large silicon solar cells in general and in designing IL/MIS solar cell arrays in particular.

4. Study the large-area IL/MOS solar cell array for space application. The work on 4 cm^2 and 25 cm^2 cells will lay the groundwork of the research for IL solar cell arrays.

REFERENCES

1. F. D. Ho. Research Reports for 1986 NASA/ASEE Summer Fellowship Program, XXii (1986).
2. G. C. Salter and R. E. Thomas, Proceedings, 11th Photovoltaic Specialists Conference, Arizona, 364 (1975).
3. P. van Halen, R. E. Thomas, R. Mertens, and R. van Overstraeten, "Proceedings, 12th IEEE Photovoltaic Specialists Conference, 907 (1976).
4. G. C. Salter and R. E. Thomas, Solid State Electronics 20, 95 (1977).
5. C. E. Norman and R. E. Thomas, IEEE Transactions on Electronic Devices, ED-27, 731 (1980).
6. D. K. Yeh and T. A. DeMassa, Solid State Electronics 27, 283 (1984).
7. R. Hezel and R. P. Vollersten, Proceedings, 5th E. C. Photovoltaic Solar Energy Conference, 1113 (1983).
8. R. Godfrey and M. Green, IEEE Transactions on Electronic Devices, ED-27, 737 (1980).

N 8 8 - 1 5 6 2 2

521-61
116723
228

1987

NASA/ASEE SUMMER FACULTY RESEARCH FELLOWSHIP PROGRAM

**MARSHALL SPACE FLIGHT CENTER
THE UNIVERSITY OF ALABAMA IN HUNTSVILLE**

**CAN SPACE STATION SOFTWARE
BE SPECIFIED THROUGH ADA?**

Prepared By:	Arthur Knoebel
Academic Rank:	Professor
University and Department:	New Mexico State University Mathematical Sciences
NASA/MSFC:	
Laboratory:	Information and Electronic Systems
Division:	Software and Data Management
Branch:	Systems Software
NASA Colleagues	John W. Wolfsberger Robert L. Stevens
Date:	August 20, 1987
Contract No.:	The University of Alabama in Huntsville NGT-01-008-021

ABSTRACT

Programming of the Space Station is to be done in Ada. A breadboard of selected parts of the work package for Marshall Space Flight Center is to be built, and programming this small part will be a good testing ground for Ada. One coding of the upper levels of the design brings out several problems with top-down design when it is to be carried out strictly within the language. Ada is evaluated on the basis of this experience, and the points raised are compared with other people's experience as related in the literature. Rapid prototyping is another approach to the initial programming; several different kinds of prototypes are discussed, and compared with the art of specification. Some solutions are proposed and a number of recommendations presented.

ACKNOWLEDGEMENTS

Many thanks are due many people. Without attempting to mention everyone, I will simply express my gratitude to John Wolfsberger, Robert Stevens and David Aichele for making it possible for me to be here another summer, and to Ellen Williams and Catherine White for their help in learning to use the computers in the Language Laboratory.

TABLE OF CONTENTS

- I. Introduction
 - The Problem
 - Results
 - Overview
 - Ada as a Stimulant
- II. Background
 - Space Station
 - Request for Proposal
 - Breadboard
 - Specifying versus Prototyping
- III. Programming
 - Philosophies and Styles
 - A Program
 - Another Approach
 - Comments
- IV. Critique
 - In Praise of Ada
 - Software Difficulties
 - Hardware Specifications
- V. Solutions
 - Recommendations
 - Specification
 - Prototyping Language
 - Other
- VI. Summary
- References

I. INTRODUCTION

The Problem. The Space Station is to be programmed in Ada. How well will this relatively new and untried language fare? Selected parts of the Space Station are to be built on a breadboard. Now may be the time to start programming this model to see how well Ada will work out. In particular, can Ada be used to specify or prototype the software? If not, when should Ada be introduced into the life cycle?

Results. Separate compilation of the specifications and bodies of subprograms in Ada makes possible top-down design of the Space Station software. However, one is not free to cut off the coding for a procedure or the declaration of a data type indiscriminately. Thus to go a ways in the coding, one needs to know something of the configuration of the computers on which the software is to run. Moreover, one needs to know something of the data flow and the nature of the data types to be used for input and output. Since this information was not available, only a little bit of code could be produced. Crucial to obtaining good coding is knowing when to start programming on such a large project. From this viewpoint this summer project is premature.

The Ada library, into which compiled units go, has no explicit structure. There are implicit dependencies of one unit on others, but the programmer needs help from the software development environment to keep all this straight.

Connected with this is what style of programming should be used: should it be hierarchical, with a deep tree structure, or should it be like an alphabet soup with a large number of separate tasks and subprograms?

The fundamental recommendation is to defer coding in Ada until after the traditional techniques of specification and design have gotten the software organized.

Overview. We review the background of the Space Station, where the project is now, and the role of Ada in it. Next is presented several philosophies of programming,

particularly as regards Ada. One of these is illustrated by a sample program.

Out of this we present a critique of Ada and compare our observations with those already presented in the literature. A number of solutions to problems with Ada are given.

Ada as a Stimulant. This introduction closes with a comment about this writer's experience with Ada this summer and his reaction to it. More controversy surrounds Ada than any other programming language. Much has been written about its merits and demerits, as well as more generally about what language features and combinations of them are really feasible. Quite possibly, its eventual value will be seen more in the high quality discussions and debates it has engendered and in the resulting clarification of software issues rather than in its use in coding. This leads this writer to suggest that every ten to twelve years a new truly general purpose language should be designed, building on recent software experience and on projected advances in hardware. Of necessity no one person can be an expert in all features; hence the need for a panel again to design it and achieve a consensus to ensure widespread use.

II. BACKGROUND

Space Station. President Reagan, proposed in his State of the Union message in 1984 a permanently manned earth satellite orbiting the earth. Congress approved this, phases A and B are completed, and now NASA is reviewing the proposals for phases C and D to determine which contractors will design it in detail and build it. The work is split into four work packages, each the responsibility of a separate NASA site. Marshall Space Flight Center is to oversee the Laboratory, Logistics and Habitation modules, plus related work. For these contracts, Boeing and Martin-Marietta have submitted bids.

Ada has been mandated as the programming language for the Space Station.

Request for Proposal. In the Request for Proposal for phases C and D we find the Software Requirements Specification of the Laboratory Module. To give a flavor of the detail now known in the Space Station so we can illustrate in the next section the extent to which this can be converted to Ada code, we show a small section of this document [RFP] where it outlines ECLSS, the Environmental Control and Life Support System. We quote from pp. 18-22 and indicate by ellipsis those interior portions which we are omitting.

"3.4.7 ECLSS Temperature & Humidity Control (THC)

...

3.4.8 ECLSS Atmosphere Control and Supply (ACS)

...

3.4.9 ECLSS Atmospheric Revitalization (AR)

3.4.9.1 Inputs

The ECLSS AR software shall accept the following input:

- a. atmospheric makeup range limits for carbon dioxide and contaminants in the module atmosphere.
- b. atmospheric makeup sensor data for carbon dioxide and contaminants in the module atmosphere.

- c. AR equipment performance and status sensor data.
- d. requests for subsystem initiation, control, and reconfiguration.

3.4.9.2 Processing

...

3.4.9.3 Outputs

...

3.4.10 ECLSS Fire Detection and Suppression (FDS)

...

3.4.11 ECLSS Water Recovery and Management (WRM)

...

Breadboard. Even though the contracts for the detailed design and construction have yet to be let out, a breadboard of selected features of the Space Station is under design now in the Systems Analysis and Integration Laboratory in building 4610. The Software supporting it will be written by the Information and Electronic Systems Laboratory.

Three computers are to be used: A Microvax II for the Data Management System, a Sun Workstation for displays and user interaction, and a third for the simulator of the physical systems.

Specifying versus Prototyping. At their extremes these two very different choices for top-down design are described in the article [BGS]:

Specifying: Develop a requirements specification for the product. Develop a design specification to implement the requirements. Develop the code to implement the design. Again, rework the resulting product as necessary.

Prototyping: Build prototype versions of parts of the product. Exercise the prototype parts to determine how best to implement the operational product. Proceed to build the operational product, and again rework it as necessary."

The authors of this stimulating article go on to describe an experiment conducted to compare these two modes of software design. They conclude that prototyping is definitely cheaper but tends to produce less functional code. In more detail, to again quote them on the relative merits, they cite these benefits of prototyping:

"products with better human-machine interfaces;
always having something that works."
Three negative effects of prototyping were:
"proportionally less effort planning and
designing, and proportionally more testing and fixing;
more difficult integration due to lack of
interface specifications;
a less coherent design."

See also section 7 of the paper [HI] for more
trade-offs.

There are two species of prototyping: vertical and
horizontal. The vertical does only selected parts of the
project but does those in detail. The horizontal does
something on all tasks but only crudely. It is important
to know at the outset which style one wishes to follow.

The book of R. J. A. Buhr has a description in section
1.2 of the software life cycle initiated by specification.
Clearly the life cycle will be different for prototyping.

III. PROGRAMMING

Philosophies and Styles. While Ada encourages and even enforces good programming practices, there is much leeway left as to how an individual programmer may develop his coding from initial conception to finished product. Since NASA's Space Station is definitely a collective and not an individual effort, considerable attention should be paid to formulating a common style of top-down design of software which is compatible with Ada.

First consider two philosophies. The first is to make use of the facility in Ada for separate compilation. In Ada specifications and bodies of subprograms may be compiled individually as they are written. This allows the deferral of decisions while at the same time coding may be started. It also allows, to some extent, the top-down specification of the software with no modification of code already produced.

The second philosophy is to allow for modification of existing code in order to fill out packages and subprograms with tasks. This requires new compilation, not only of the particular unit being recompiled, but also of all units which depend upon it. This is one its disadvantages. The obvious advantage is that more structure can be exhibited within the code itself.

We illustrate the second style of programming extensively, and then comment on the first.

A Program. We illustrate the second philosophy by following quite closely the portion of the Request for Proposal that was excerpted in the previous chapter. Our top-most package for the Environmental Control and Life Support System is simplicity itself.

```
package ECLSS is
end ECLSS;
```

This is compilable. We introduce the components of ECLSS by adding more packages inside this one.

```
package ECLSS is
```

```
    package TRC is
```

```

end TRC;

package ACS is
end ACS;

package AR is
end AR;

package FDS is
end FDS;

.
.
.

end ECLSS;

```

We recompile to check syntax. By way of example on how to proceed, we will refine the package AR. As the RFP lists three parts: INPUT, PROCESSING. AND OUTPUT, these are entered as packages within AR in the obvious way.

Let's refine INPUT, ignoring the other packages. We could proceed by introducing more packages, but it is seems appropriate now to introduce tasks, since we want concurrent activity of some parts of INPUT.

```

package AR is

    package INPUT is
        task ATMOS_RANGE_LIMITS;
        task ATMOS_SENSOR;
        task STATUS;
        task REQUESTS;
    end INPUT;

    package PROCESSING is
    end PROCESSING;

    package OUTPUT is
    end OUTPUT;

end AR;

```

Again this compilable, i.e., syntactically correct.

The RFP goes a bit beyond this in detail, but I don't think we can refine what we already have any further without losing compilability. To see how it might look, we refine, as best we can, the task ATMOS_SENSOR.

```

task ATMOS_SENSOR is
    entry CO2_DATA;
    entry CONTAMINANT_DATA;
end ATMOS_SENSOR;

task body ATMOS_SENSOR is
    CO2: fixed
    CONTAMINANTS: ARRAY (1..S) of fixed;
begin
    select
        accept CO2_DATA
            do get (CO2);
        end CO2_DATA;
    or
        accept CONTAMINANT_DATA
            do get (CONTAMINANTS);
        end CONTAMINANT_DATA;
    end select;
end ATMOS_SENSOR;

```

At this point we begin to see some of the limitations of Ada for software specification and prototyping. We are told by the RFP that there are contaminants to worry about, but no details about what they might be, or even their number. Thus we must introduce a variable *S* for their number which is to be filled in later. Also we are assuming we need only one number, a component of the array *CONTAMINANT_DATA*, to specify the extent of a particular contaminant.

Here are some comments about the coding for tasks. Ada makes provisions for a rendezvous so that concurrently running tasks may communicate with each other. We are assuming that there are some kind of lines or other input into the central processor bringing in signals telling how much carbon dioxide there is, etc. The 'select' statement chooses between the two 'accept' statements; in what sense it alternates at random between the two depends on the particular implementation of Ada; with additional coding one can make this more precise and independent of the implementation. Finally, the command get is not standard Ada and needs to be defined further.

Another Approach. Following the first philosophy that once coded, a package or subprogram should not have to be recompiled, barring mistakes, we could rewrite the preceding code. We would need to redo it as a flat horizontal design using procedures with body stubs. The idea is to specify declarations without having to write the bodies, which will be filled in later. Since the RFP is so limited in detail,

this did not seem worthwhile to pursue. Those familiar with Ada will readily see how this can be done.

Comments. This style of programming raises a number of questions which must be answered before full scale coding is undertaken. Should one use procedures or packages? (At least one procedure is needed to start execution, according to Ada rules.) This last comment centers around the question alluded to earlier. How should the Ada library of packages and subprograms be organized and extended: by units which are compiled once and more units added on down the road, or with units that are to be continually recompiled?

Clearly many more tasks are going to have to be created to accommodate all the simultaneous sensing, controlling and potential alarming that must be done. But before this can be done, we need to know the configuration of computers and the processes to be run on each.

Now this configuration may well be specified by data flow diagrams. This is something Ada does not support, and it is perhaps the most serious drawback to using Ada as a specification language. See [Buhr] pp. 83-86 and pp. 94-101 for an extended discussion of this important issue.

IV. CRITIQUE

In this chapter we address problems encountered in attempting to code immediately the specification and prototyping of the software for the breadboard. We break these up into software and hardware difficulties. First though we recall some of the strengths of Ada.

In Praise of Ada. Of the four ways to evaluate languages set forth in my earlier report [Kno1], only one, the method of qualitative matrices, has been done in depth for more than a few languages. For each of the various language features needed in the matrix for the Space Station, Ada generally does as well or better than any of the other languages surveyed.

Ada solely by itself would be hard to use. Within a good support environment it becomes a productive tool. The article by Vittorio Frigo has much praise for the VAX Ada tools written by the Digital Equipment Corporation, otherwise known as APSE, and was written after the author had written and debugged an application program. Frigo had minor complaints about the trickiness of dealing with syntax in the language-sensitive editor and the difficulty of learning the debugger. But overall he was impressed by DEC's software support.

Software Difficulties. We present four problem areas.

Separate compilation of specifications and bodies of subprograms is a powerful feature of Ada which encourages modularization. Clearly it should make possible top-down design of the software. However there are limits. In the Ada library, units can be compiled separately, and linked together according to their dependencies. Unfortunately these dependencies are not made explicit by the Ada library. A programmer must keep a separate log of these dependencies together with what has been compiled.

In Ada there are lots of data types and woe to the programmer who attempts to violate the strong typing constraints. Data has to be typed and declared to some extent in Ada. Unfortunately, many times in the initial stages of specification we would like not to do this, and instead only say that some kind of unspecified data is to be

passed. The difficulty here is that initially we may not know enough to satisfy the typing requirements of Ada. For example, contaminants are mentioned in the RFP. But not how many or how they are to be measured so that suitable ranges for their values may be specified. Thus we are stymied in our attempt to sketch out the overall structure of the software directly in Ada code.

Another nice feature of Ada is the provision for stubs in subprocedures. When a procedure Q within another procedure is incompletely known, we can simply write:

```
procedure Q is separate;
```

When finally Q is figured out, we can write the appropriate compilable package. The shortcoming of this feature is that partial information about the procedure can not be written in; we must keep it on a separate piece of paper. We can not simply work on the procedure until our fund of knowledge for it exhausted, stop and then compile. This is perhaps natural in terms of designing a workable compiler but it has the disadvantage of forcing a certain coarse granularity into the specification process.

Hardware Specifications. The last point concerns when coding should start vis-a-vis the specification and design of the hardware. Ada programming can start earlier than with most languages. But it is premature to start programming now, as was attempted in this project. To proceed further at this point we need further information on both the hardware and software to be designed. And on projects in general when should programming start? There needs to be a substantial understanding of the specific computers to be used, their configuration, the input and output to each and the data flow among them, before code can be committed to the library and hence before high-level specification can begin. Also we must decide how to organize the upper levels of the tree of packages and procedures, and how to manage the library.

V. SOLUTIONS

Recommendation. Our principal finding is that it is premature to start programming in Ada right away. We can either try some of the specification tools extending Ada, described below, or better yet employ the old fashion solution of a good English exposition of the specifications. When used correctly, concisely and accurately, our mother tongue can serve us well. Fuzzy thinking and poorly planned hardware of course will get in the way. But this is not the fault of the Queen's English. As the specification moves along, gathering up more and more detail, appropriate mathematical and technical jargon should be introduced as necessary to clarify. Then program in Ada.

Specification. SSE. Lockheed has been awarded the contract to build a Software Support Environment for the Space Station. The requirements specification for this package will be available soon. There will be four subpackages (re)programmed in Ada. These package will be designed around the Apollo work stations.

This SSE will greatly affect how we proceed. In particular how will it contribute to top-down design? Into the SSE should be incorporated a scheme for managing and structuring the Ada library. Also there should be provisions for simulating the stubs in the subprograms so that the software can be run, even though it is not completed.

TAGS. Teledyne-Brown is developing the design tool called Technology for the Automatic Generation of Software. This promises to generate code automatically from detailed diagrams of data flow. It is hierarchically organized so that the design can be done top-down directly from the engineering specifications of the hardware whose software is to be coded.

We see at least three problems if this computer-aided specifier were to be used to produce Ada coding for the Space Station. First the emphasis is on detailed flow charts; but the detail may not be initially available. Also many computer scientists do not consider flow charting the best way to organize a program in order to show the tree structure of dependencies of its various parts.

Nevertheless this points up to the need for the specification of data flow at an early stage, which Ada, because of its strong typing, inhibits. Recommendation: into the SSE incorporate the specification early on of data flow.

TAGS seems to be making an end run around Ada by inventing a quite different language for the specification of the software, and only when this is completed in detail do we see Ada code generated. It would seem better to extend Ada as necessary to generate high-level specifications so that one eases naturally into the finished coding, all done in Ada.

Finally, not all features of Ada will be used in the automatic generation of the final code. This raises serious questions. Does this take full advantage of Ada? Is this really subsetting in disguise? Does it satisfy the mandate to program the Space Station in Ada?

In this connection we mention the book of Buhr, which has in chapter 3 a scheme of pictures, reminiscent of the flow charts of TAGS for notating data flow.

Prototyping Language. What is proposed here is a high-order language to be used for both specification and prototyping of software. It should be superimposed on top of Ada. Presumably it would be part of the SSE.

Anna. An example of this is the extensive project [LNR] now under way at Stanford university to develop what they call a wide spectrum language. In their words, "a wide spectrum language is a notation for describing the intended behavior of a system and the implementation of that behavior. The notation for intended behavior is usually based on a formal logic or algebra and describes what the system will do in formal terms. The implementation notation is usually concerned with efficiency of execution on hardware, and describes how the system will operate in great detail."

There are two major components of their system: Anna, a language for specifying Ada software; and TSL, Task Sequencing Language, a language for specifying distributed Ada systems. There were four principal considerations for Ada. In their words, "constructing annotations should be easy for the Ada programmer Anna should provide language features that are widely used in the specification and documentation of programs. Anna should provide a

framework within which the various established theories of formally specifying and verifying programs may be applied to Ada. Annotations should be equally well suited for different applications during the life cycle of a program."

These brief excerpts do not do justice to this excellent and ambitious project; there are several parts and many more auxiliary tools not mentioned here. It is highly recommended that NASA get the latest documentation to study this system in more detail.

Algebra. There is a rigorous theory of the algebra of abstract data types, on which are based a number of languages, some already in existence and some still on paper. This is another approach to prototyping since in the algebraic theory one need not give algorithms for the operations to be performed in a procedure but, for the purposes of prototyping, one may simply give a short but complete set of properties or relationships which they must satisfy.

One such language is UMIST OBJ, outlined in the paper [GC]. As all such languages are, it is based on equational logic, given in axioms (i) to (v) of the paper. However to express the typical properties needed in computer science it is necessary to accommodate conditionals, i.e., implications and partial operations, which will encompass such things as popping empty stacks.

Unfortunately the authors of this paper seem to forget that the axioms they give must be considerably modified and extended to include these more general statements or pseudoequations. Nevertheless, it is known how to set things up to include these more general specifications (See [Kno3] and [Kno4]).

Along these same lines is the prototyping system of B. Belkhouche [Bel]. He describes a system for translating abstract data types into actual code. He was heading for code in the language PL/1 but his source output file in Appendix A has an uncanny resemblance to Ada syntax. So Ada generics could have been used here to generate compilable code better than his PL/1 code.

Other. In this last section are collected an assortment of miscellaneous suggestions for capitalizing on Ada.

Expertise. Marshall S. F. C. should develop an expertise in Ada. Several local people should learn it well and become familiar with its many facets and the literature describing and documenting the controversial issues surrounding this large and extensive language.

In this connection, an Ada library should be developed and include selected books, journals, video courses, and reports from our sister NASA sites.

Information. More information on the breadboard needs to be known. Have written down what the scope of the breadboard is to be; what it is to accomplish; and what is to be learned. Have written down the scope of the programming effort.

Miscellaneous. It almost goes without saying, do strong typing, and even make it stronger than Ada demands.

In the article [ACGE] are solutions to some common problems with Ada:

To reduce the depth of nesting, see p. 142;

Whether to decompose large programs into library units or subunits, see p. 161;

For how Ada may affect the specification phase in the life cycle, see p. 176.

In designing the breadboard, gain practice and experience in recognizing where (see [ACGE]) generics can be used to avoid duplicating common code.

Final observation. To anticipate changes in 'maintenance', modularize according to accepted concepts in the field of application.

VI. SUMMARY

This study reports on exercises done to see how well the programming language Ada supports high-level specification and prototyping. The conclusion to be drawn so far is that while Ada has a number of strong modularization features which allow for some incompleteness in coding, its strong typing prevents it from being used at the very start of a project, and most programmers will want some assistance with data flow, which Ada does not provide. The recommendation is to use English as the specification language as in the past, and perhaps extend Ada so that some of the detailed design is possible within an essentially Ada context.

Afterthought

Let me close with a philosophical thought. I sometimes think that my counterparts here feel that after an easy year in academia, we fellows should be made to do some honest work during the summer. On the other side of the coin, many fellows will agree with the sentiment found back home in our departments that, after working hard during the academic year, its nice for you fellows to get a paid vacation at NASA. With this in mind, I leave you with this quote.

"It is impossible to enjoy idling thoroughly unless one has plenty of work to do."

J. K. Jerome

Postscript

(Added in press) At several places in this report it has been noted that further coding was stymied by a lack of knowledge of the breadboard for the core module, apparently due to its nonexistence. Surprisingly, and unknown to this fellow during most of the time while he was engaged in this project, there are two working models of the common module in building 4755. The module being built by NASA already has two units to recover carbon dioxide and an oxygen generator.

The core module built by Martin-Marietta is extensive.

In addition to carbon dioxide recovery and oxygen generation, there are also power handling units at three different frequencies, heat removal and automatic balancing, human waste disposal and a trash compactor. There is model software, originally written in C and recently transported to Ada! A user interface is provided.

What has been learned from designing, constructing, programming and operating these two modules should be compared with this report.

If information on these core modules had been provided to this faculty fellow early in the summer, this report would definitely be different.

REFERENCES

- [ACD] **Architectural Control Document -- Data Management System.** Space Station Program Office, Johnson Space Center, NASA. Jan. 1987.
- [ACGE] Christine N. Ausnit; Norman H. Cohen; John B. Goodenough & R. Sterling Eanes. **Ada in Practice.** Springer-Verlag, 1985.
- [Bran] A. E. Brandli. **Operations Management System (OMS).** Viewgraphs, prepared in the Avionics Systems Division, Johnson Space Center, NASA. Aug. 1986.
- [Belk] Boumediene Belkhouche. Compilation of Specification Languages as a Basis for Rapid and Efficient Prototyping. **Third International Workshop on Software Specification and Design**, Aug. 26-27, 1985, London. IEEE Computer Science Press. 1985.
- [BGS] Barry W. Boehm; Terence E. Gray & Thomas Seewaltdt. Prototyping versus specifying: a multiproject experiment. **IEEE Transactions on Software Engineering**, SE-10 (May 1984), pp. 290-302.
- [Buhr] R. J. A. Buhr. **System Design with Ada.** Prentice-Hall, 1984.
- [Frigo] G. Vittorio Frigo. Evaluation of the VAX Ada compiler and APSE by means of a real program. **Ada Letters** 7 (May, June 1987), pp. 94-106.
- [GC] R. M. Gallimore & D. Coleman. Algebra in Software Engineering. **Third International Workshop on Software Specification and Design**, Aug. 26-27, 1985, London. IEEE Computer Science Press. 1985.
- [HI] S. Hekmatpour & D. C. Ince. Rapid software prototyping. In **Oxford Surveys in Information Technology** 3, F. I. Zorkoczy, ed., Oxford Univ. Press, 1986. pp. 37-76.
- [IEEE] IEEE Computer Society. **Ada as a Program Design Language.** IEEE Standard 990-1987. (To appear 1987).
- [LNR] David C. Luckham; Randall Neff & David S. Rosenblum. An environment for Ada software development

based on formal specification. **Ada Letters** 7 (May, June 1987), pp. 84-93.

[Kno1] Arthur Knoebel. Analysis of high-order languages for use on the Space Station application software, in **Research Reports -- 1985 NASA/ASEE Summer Faculty Fellowship Program**. NASA CR-178709, Jan. 1986.

[Kno2] " " Benchmarks of programming languages for special purposes in the Space Station, in **Research Reports -- 1986 NASA/ASEE Summer Faculty Fellowship Program**. NASA CR-178966, Nov. 1986.

[Kno3] " " A tripartite specification of abstract data types. (Article submitted).

[Kno4] " " The Algebraic Theory of Abstract Data Types. (Book in preparation).

[NW] John Nissen & Peter Wallis. **Portability and Style in Ada**. Cambridge Univ. Press, 1984.

[RFP] Request for Proposal. **Software Requirements Specification, Attachment A for the Space Station United States Laboratory Module**. SS-SPEC-0002, Marshall Space Flight Center, 15 Dec. 1986.

[Rog] M. W. Rogers. **Ada: Language, Compilers and Bibliography**. Cambridge Univ. Press, 1984.

522-37
N88-15623 116724
238

1987

NASA/ASEE SUMMER FACULTY RESEARCH FELLOWSHIP PROGRAM

MARSHALL SPACE FLIGHT CENTER
THE UNIVERSITY OF ALABAMA IN HUNTSVILLE

THE DETERMINATION OF EQUIVALENT BEARING LOADING FOR THE
BSMT THAT SIMULATE SSME HIGH PRESSURE OXIDIZER TURBOPUMP
CONDITIONS USING THE SHABERTH/SINDA COMPUTER PROGRAMS

Prepared By: Gary H. McDonald, Ph.D.
Academic Rank: Assistant Professor
University and Department: The University of Tennessee
at Chattanooga
Mechanical Engineering --
Mechanics

NASA/MSFC:

Laboratory Propulsion
Division: Component Development
Branch: Turbomachinery and Combustion
Devices

NASA Colleague: Henry P. Stinson /
James Cannon

Date: August 8, 1987

Contract No.: NGT-01-008-021
The University of Alabama in
Huntsville

THE DETERMINATION OF EQUIVALENT BEARING LOADING
FOR THE BSMT THAT SIMULATE SSME HIGH PRESSURE OXIDIZER
TURBOPUMP CONDITIONS USING THE SHABERTH/SINDA COMPUTER
PROGRAMS

by

Gary H. McDonald
Assistant Professor of Engineering
in Mechanical--Mechanics
The University of Tennessee at
Chattanooga
Chattanooga, Tennessee

ABSTRACT

The MSFC bearing seal material tester (BSMT) can be used to evaluate the SSME high pressure oxygen turbopump (HPOTP) bearing performance. The four HPOTP bearings have both an imposed radial and axial load. These radial and axial loads are caused by the HPOTP's shaft, main impeller, preburner impeller, turbine and by the LOX coolant flow through the bearings respectively. These loads coupled with bearing geometry and operating speed can define bearing contact angle, contact Hertz stress and heat generation rates. The BSMT has the capability of operating at HPOTP shaft speeds, provide proper coolant flowrates but presently, can only apply an axial load. Due to the inability to operate the bearings in the BSMT with an applied radial load, it is important to develop an equivalency between the applied axial load and the actual HPOTP loadings.

In this study, the objective was to use the SHABERTH/SINDA (shaft-bearing-thermal) computer code to simulate the BSMT bearing-shaft geometry and thermal-fluid operating conditions. This study was performed at two shaft speeds using two coolants, LN2 and LOX. A simulation of the HPOTP was also generated by SRS/System Division using current operating conditions from the SSME HPOTP. Then, a comparison of the bearing contact stresses and heat generation rates of these two simulations was attempted to establish the equivalence between the BSMT axial load and the HPOTP loads.

ACKNOWLEDGEMENTS

There have been several individuals that have provided valuable contributions in this author's NASA/ASEE fellowship project. I would first like to thank Dr. Gerald R. Karr, director of the MSFC NASA/ASEE fellowship program and Ms. Ernestine Cothran, director of MSFC university relations, for their diligent efforts in the organization of the seminars, tours, the general administration of this program and the opportunity for this author to participate this summer.

I would especially like to thank my colleagues Mr. Henry P. Stinson and Mr. James P. Cannon who were valuable in formulating this project and providing the necessary technical assistance. A special appreciation is extended to Mr. Fredrick Bachtel and Mr. Glenn E. Wilmer of NASA/MSFC who greatly assisted in the author's operation and understanding of the SHABERTH/SINDA codes and provided the necessary technical background resources.

Also, a grateful appreciation is extended to Mr. Joe Cody of SRS/System Division, whose notes provided needed information for the program's input file, and Mr. Dave Marty of SRS/System Division, whose interest in the project constantly aided this author with the parametric study. Dave also performed execution of SHABERTH/SINDA, the construction of the appropriate files and the execution of the HPOTP simulation.

A special thanks to Ms. Sandra Gallik of Boeing Computer Support Services, who assisted the author in the use of the SPERRY/UNIVAC computer and to Ms. Gloria Gideon who diligently typed this manuscript. I would like to thank Mr. Loren Gross and all members of his Turbomachinery and Combustion Devices Branch for making this an enjoyable and productive summer experience.

INTRODUCTION

In the Space Shuttle Main Engine (SSME) High Pressure Oxygen Turbopump (HPOTP), four ball bearings support a turbopump shaft, a main impeller, preburner impeller and turbine. Throughout the flight history of the SSME, these bearings have been subject to various degrees of damaging wear. Two possible causes for this wear are insufficient lubrication resulting in frictional heat generation and large contact (Hertz) stresses between the balls and the inner and outer races due to loading and bearing geometry variations. Even though these causes will be addressed in this study, numerous scenario's based on test data can be formulated to address the HPOTP bearing wear problem. The main source of test data is from instrumentation measurements of the HPOTP. However, due to the expense of this process, viable alternatives to predict bearing behavior must be established. One alternative is the use of the NASA-Marshall Space Flight Center (MSFC) Bearing Seal Material Tester (BSMT). Another relatively inexpensive alternative is to develop a computer model to simulate the bearing environment. A general program called SHABERTH (Shaft-Bearing-Thermal) developed originally by SKF Industries and later greatly modified by SRS Technologies/System Division exists and will be used to attempt this simulation. In addition to SHABERTH which analyzes the bearings and shaft, a code named SINDA (System Improved Numerical Differencing Analyzer) will be coupled to SHABERTH to perform the temperature calculations. Thus, this code will be referred to as SHABERTH/SINDA.

The major unknown in this study of bearing behavior is loading. From experimental studies on the HPOTP, Figure 1 shows the best estimate of the loads applied to the shaft due to the preburner impeller, main impeller and turbine that the bearings support. In addition to these radially applied loads, there also exists axially applied loads due to the pressure*area (PA loads) of the liquid oxygen (LOX) coolant that flows through the bearings. These PA loads are of particular importance when the turbopump throttles its speed.

Figure 2 shows a schematic of the bearing-shaft arrangement and the flow paths through the BSMT. To reproduce HPOTP conditions at this time is not possible since the tester has a different flow path than the HPOTP, the working fluid in the tester is LN2 (liquid nitrogen) not LOX, and most importantly, there can be only an applied axial load in the tester to simulate PA loading and preloading. Thus, presently, no radially load can be applied to simulate the radial HPOTP loads.

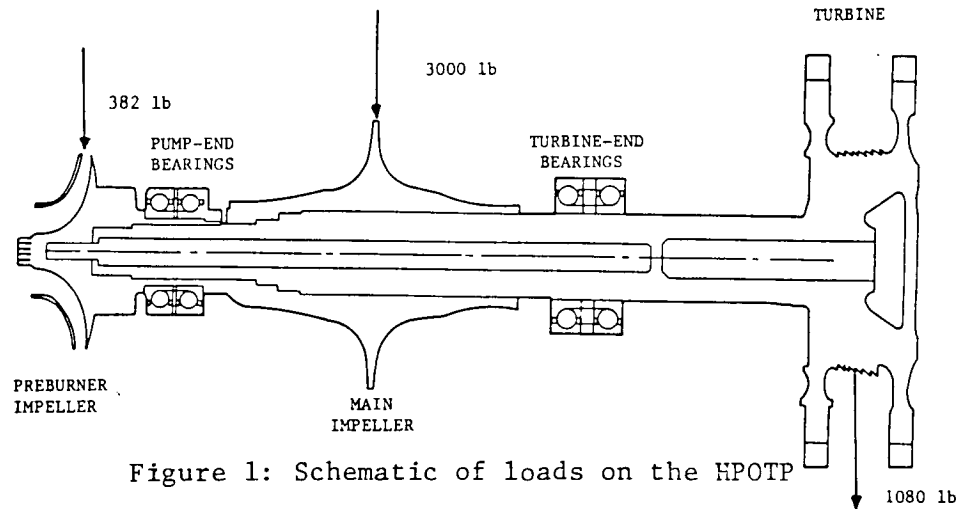


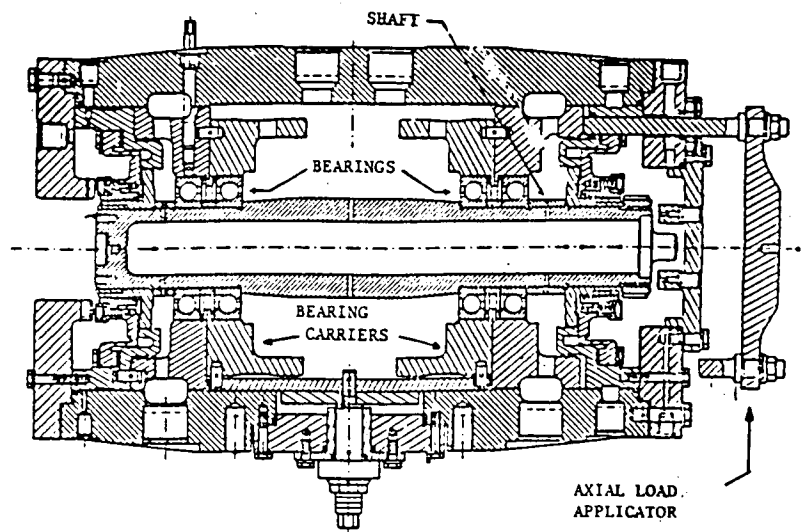
Figure 1: Schematic of loads on the HPOTP

The purpose of this study is to attempt to use SHABERTH/SINDA programs to model the BSMT. This model will only have applied axial loads on the shaft and will be used in conjunction with a model of the HPOTP that was conducted by Spectra Research Systems (SRS) to compare heat generation rates and Hertzian stresses. Hopefully, this study will establish which applied axial loads for the BSMT model corresponds to the combined radial and axial loads for the SRS HPOTP model. From the comparison of heat generation rates and contact stresses, a so-called "equivalent" load can be stated for the BSMT based on HPOTP loading cases. Note that several important parameters as coolant flow rate, bearing geometry changes, coefficient of friction, coolant inlet temperature and pressure drop will be held fixed in this study. This was done to limit the problem's scope not to infer the insignificance of these parameter's affect on bearing behavior. In this study, only shaft speed will be varied along with type of coolant used (LOX vs. LN2). Recall, LOX is the coolant of the HPOTP, however LN2 is the current working fluid for the BSMT. The BSMT is currently undergoing redesign changes to eventually use LOX as the working fluid again. So, equivalent loads will be established using both fluids for the BSMT to simulate HPOTP loading.

OBJECTIVES

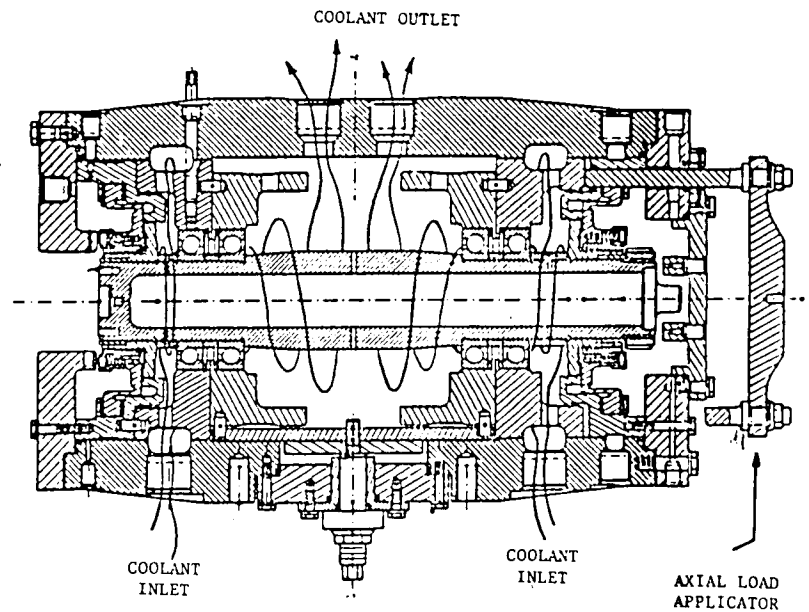
As previously stated, the purpose of this project is to simulate the BSMT conditions using the SHABERTH/SINDA computer code. Using this model of the tester and a turbopump simulation using SHABERTH/SINDA performed by SRS, a comparison of the heat generation rates and Hertz stresses will be made to attempt to correlate the axial load applied

ORIGINAL PAGE IS
OF POOR QUALITY



CURRENT BSMT LN2 (002) BUILD .1 CONFIGURATION

The Bearing Seals and Materials Tester



CURRENT BSMT LN2 (002) BUILD .1 CONFIGURATION

. The BSMT flow paths

Figure 2: The current BSMT and its flow paths

in the tester model to the axial-radial load combination that exists in the turbopump simulation. The objectives of this project were.

1. To develop the input data necessary for modelling the BSMT using LN2 and LOX and perform a parametric study.
2. To obtain SHABERTH/SINDA models of the turbopump from SRS/System Division.
3. To compare for two different shaft speeds for both LN2 and LOX, the heat generation rates and contact Hertz stresses of two models to correlate the loadings applied to the tester simulation to those applied in the turbopump simulation.

SHABERTH/SINDA Computer Models

The SHABERTH program is structured in four sections: thermal, bearing dimensional equilibrium, shaft-bearing system load equilibrium and bearing rolling element and cage load equilibrium. A detailed account of these sections, bearing equations that are used, flowcharts of program structure, and sample input and output are described in reference (3). The bearing theory used in this problem is based on reference (1) by Harris. When SHABERTH was modified for the HPOTP by SRS, it was decided not to use the SHABERTH thermal model but to replace it with SINDA. SHABERTH uses an assumed set of temperatures given by a user then calculates all the bearing forces and moments, Hertz stresses, bearing geometry changes and heat generation rates. SINDA uses the calculated heat generation rates from SHABERTH to compute a temperature distribution. A UNIVAC computer runstream which controls the program flow replaces the assumed temperatures with the newly calculated SINDA temperatures. These temperatures that are being compared are of the shaft, inner ring, inner race, ball, outer race, outer ring, housing, bulk fluid temperature respectively. This iteration process between SHABERTH and SINDA continues until thermal convergence to 2° F occurs, or thermal runaway to 1000° F diverges the solution or when 15 iterations occur usually related to an oscillating solution. Maximum runtime or maximum number of pages usually is associated with a divergence or oscillating solution. A good indicator of this type solution is when SINDA cannot reach an energy balance. For these cases of divergence, the SHABERTH/SINDA simulation will terminate. For convergence,

[illegible]

XXIII-5

the SHABERTH/SINDA simulation usually iterates 4 to 7 times depending on values of the initial temperatures assumed in SHABERTH. The computer run time of a converged solution is from 45 minutes to 1 hour.

The input data to the SHABERTH model in general is discussed in reference (3). The Appendices to this reference are particularly helpful since it shows the formatting and structure of the input information and a listing of typical output. The input data that SRS added for their modifications to SHABERTH is described in (14). Much effort was expended to learn and verify analytically many of the inputs to SHABERTH and the source data in SINDA. However, some of inputs are based on experimental tester data. For instance, shaft dimensions and bearing locations, shown schematically in Figure 3, were found from the BSMT drawings. Fluid properties used for LN2 were found by interpolating at 480 psia, the tester pressure, using reference (5). In the same manner, fluid properties for LOX were found using reference (6). Cage load and viscous heat generation inputs were extensively calculated by myself based on J.C. Cody's notes from SRS Technologies. These calculations are based on the theory in reference (12). Cage heat generation rates based on the cage loads are found in a table in reference (14) as a function of coefficient of friction.

In the Appendices of this report, a representative listing of SHABERTH input and references to the lines of SINDA code that are to be changed by the user are given for both LN2 and LOX. When shaft speed was varied, the inputs that must be varied were viscous heat generation rates for bearings 3 & 4 (VQBRG1, VQBRG2), shaft speed (SHAFTS), cage speed (CAGESP), ball spin (BSPEED), and ball spin speed (BALLSP). If other parameters as coolant inlet temperature, cage load, pressure drop, and coolant flowrate need to be varied, reference (14) states the affected inputs to SHABERTH/SINDA that must also be varied. These parameters will be considered fixed in this study.

The SHABERTH inputs indicate a four-bearing system being modeled. However, due to the arbitrarily chosen small initial contact angle α_0 to be $+ 5^\circ$ and zero diametrical clearance, bearings 1 & 2 are dummy bearings in this model. Since the BSMT has four 57 mm bearings shown schematically in Figure 2, symmetry was used and only 2 of the 4 bearings are actually analyzed by SHABERTH. Therefore, bearings 1 and 2 (the pump end bearings for HPOTP) are the dummy bearings and bearings 3 and 4 (the turbine end bearings for HPOTP) are analyzed. The SINDA model was written only for

bearing #3. The grid generation and nodal numbering was performed similiar to the process shown in (8,9 and 13) for the 45 mm pump-end bearings. The user need only be concerned with SINDA's coolant inlet and saturation temperatures (lines 697-709), cage heat (line 757), half of the viscous heat generation rates for bearing #4 (lines 760-761 for nodes 2 and 3) and for bearing #3 (lines 763-764 for nodes 5 & 6) and coolant flowrate per ball (lines 2228-2236). Also, specific heat vs. temperature lines 2293-2300 of SINDA, must be changed when using different coolants. Notice in the initial nodal temperature guess in the SHABERTH input, only the 3rd line representing bearing #3 has been deviated from an initial value of -170°F . These temperatures represent the shaft, inner ring, inner race, ball, outer race, outer ring, housing and fluid bulk temperatures. These initial temperatures will change with each iteration of SHABERTH/SINDA until either convergence or divergence occurs. Also, change the modulus of elasticity and thermal expansion coefficients to match the initial temperatures of bearing #3. They will also be updated in the iteration process.

Axial preload can be included by setting the diametrical clearance of bearing #3 and #4 to a non-zero value. In the Appendices, a table is presented relating the amount of axial preload to the diametrical clearance. This was generated by running SHABERTH only at steady state temperature and denoting the F_x (x force reaction) in the output. Therefore, the amount of diametrical clearance inputted is related to the F_x force reaction which is the axial preload on bearings #3 and #4. These results are independent of coolant used and flowrate based on the simulation.

In this study, the coefficient of friction was set at 0.2, tester pressure was 480 psia, saturated temperature for LN2 was -233.8°F and for LOX was -200.8°F and the coolant flowrate was 6.4 lbm/sec. The axial preload was set at 1000 lbs by setting the diametrical clearance input to be 0.013 mm on bearings #3 and #4.

RESULTS

Due to input parameter problems and UNIVAC down-time, the study of the BSMT axial load variation producing heat generation rates and contact stresses that were compared to a HPOTP simulation was abandoned at a shaft speed of 20,000 rpm. At 30,000 rpm, a coolant flowrate of 4.6 lbm/sec was used initially for both the BSMT LN2 and LOX simulations.

This was the coolant flowrate used in the HPOTP simulation. At this flowrate for both LN2 and LOX coolants, the solutions diverged. The range of applied axial loads were from 1000 lbs to 3000 lbs with a fixed preload of 1000 lbs for these cases. As the axial load increased, the ball temperature accelerated toward 1000°F in 3 to 4 iterations before divergence was declared. Based on these initial results, it was decided to increase the coolant flowrate to 6.4 lbm/sec for both LN2 and LOX BSMT models. In this process, however, several errors were found in the SINDA source data. Specifically, lines 2293-2300 were not changed in the LOX SINDA file. These lines list the specific heat vs. temperature of the coolant used. So, the LOX SINDA file was still using LN2 data. Also, in the SHABERTH input file, the LN2 fluid properties of specific heat, thermal conductivity, and Prandtl number had to be adjusted at the saturated temperatures. Since the tester operating pressure of 480 psi is near the critical pressure of LN2 of 493 psi, the variation in these properties were held at a constant value at the saturation temperature. This should stabilize the heat transfer conductance calculations according to SRS. So, these two problems could have played a part in the divergence of the solution at a flowrate of 4.6 lbm/sec.

The above changes were made to the SHABERTH/SINDA input files and with the coolant flowrate value changed to 6.4 lbm/sec, another series of program executions were performed. From this series of computer runs, Tables 1 and 2 show the converged results of the heat generation rates and Hertz stresses in bearings 3 & 4. As shown, for both heat generation rates and Hertz stresses, there is no significant difference between using LN2 or LOX coolants for the range of axial loads. From Table 1, for bearing #3, there is a reasonable agreement between the BSMT and HPOTP simulations. For bearing #4, the BSMT simulation under predicts the HPOTP simulation by a factor of 1/2. This effect may be caused by the HPOTP simulation having a SINDA model of both bearings 3 & 4 whereas, the BSMT model only has bearing #3 thermally modelled. In Table 2, again, there is no significant difference in Hertz stress for bearings #3 and #4 due to the coolant used in the BSMT model. The results from Table 2 show a reasonable agreement of outer and inner race Hertz stresses for the BSMT and HPOTP simulation for bearing #3; however, the BSMT model again underestimates Hertz stresses by about one-fourth compared to the HPOTP simulation. From these results, it is difficult to predict how much axial load could exactly predict the HPOTP simulation results. Further studies are necessary to attempt to establish an equivalent load relationship.

Table 1: Total Heat Generation Rates of the BSMT & HPOTP Simulations (Preload 1000 lbs)
in Watts

Axial Load	<u>BSMT Simulation</u>				<u>HPOTP Simulation</u>			
	<u>LN2</u>				<u>LOX</u>			
	<u>N</u> (lb)	Bearing 3	Bearing 4	Bearing 3	Bearing 4	Bearing #3	Bearing #4	
2223.3 (500)		4489	1978	5018	2288			
3334.9 (750)		5389	2009	5877	2275	5396	4833	
4446.5 (1000)		7311	2541	6898	2330			

Table 2: Hertz Contact Stresses of the BSMT & HPOTP Simulation (Preload-1000 lbs)
in N/mm^2

Axial Load N (lb)	<u>BSMT Simulation</u>				<u>HPOTP Simulation</u>			
	<u>LN2</u>		<u>LOX</u>					
	<u>Bearing 3</u>	<u>Bearing 4</u>	<u>Bearing 3</u>	<u>Bearing 4</u>	<u>Bearing 3</u>	<u>Bearing 4</u>	<u>Bearing 3</u>	<u>Bearing 4</u>
	Outer	Inner	Outer	Inner	Outer	Inner	Outer	Inner
2223.8 (500)	2074	2284	1787	1720	2126	2370	1826	1810
3334.9 (750)	2159	2422	1791	1729	2197	2487	1825	1807
4446.5 (1000)	2307	2656	1858	1878	2276	2609	1832	1822

CONCLUSIONS AND RECOMMENDATIONS

Based on my limited results, no relationship can be established at this time between the BSMT simulation and the HPOTP simulation loadings. In the BSMT simulation, no axial load above 1000 lbs (4446.5N) would result in a stable thermally converging solution at a shaft speed of 30,000 rpm. Based on this study, several recommendations for future research in this area are as follows.

1. The continuation of this study at a lower shaft speed to determine it's effect on the comparison of heat generation rates contact stresses and on enabling the use of higher axial loads.
2. The study of the effects of coolant flowrates and coefficient of friction on the comparison between BSMT simulation axial loads and HPOTP simulation loads.
3. The investigation of other bearing parameters that need be included besides heat generation rates and contact stress in the equivalency of BSMT and HPOTP loading.
4. The correlation of BSMT simulation axial load results to actual BSMT tester data for both LN2 and coolants.

Hopefully, from these recommendations, an equivalency between BSMT axial loads and HPOTP loadings can be found. However, the possibility exists that an applied axial load only may never produce equivalent HPOTP conditions in the bearing tester. So, the logical alternative may be to incorporate a workable radial load capability to the bearing tester and to the SHABERTH BSMT simulation. The alternative would lead to a matching of both axial and radial load conditions between the tester and turbopump to hopefully generate the same mechanical and thermal environment for the bearings.

For SHABERTH's results to be a reliable predictor of bearing performance, it must have reliable inputs based upon both experimental data and analytical formulation. SHABERTH is also constantly being modified and updated by SRS to make it more versatile in its simulation of a shaft bearing system by including more bearing theory. Eventually, SHABERTH could become an important analytic tool for both the current HPOTP or BSMT configuration and for any future alternative configurations that may be developed.

REFERENCES

1. Harris, Tedric A., Rolling Bearing Analysis, 2nd edition. A Wiley-Interscience Publication of John Wiley and Sons, New York, NY, 1984.
2. Eschmann, Hasbargen, and Weigand, Ball and Roller Bearings; Theory, Design and Application. John Wiley and Sons, New York, NY, 1985.
3. Crecelius, W.J. and J. Pirvics, Computer Program Operation Manual on SHABERTH Computer Program for the Analysis of the Steady State and Transient Thermal Performance of the Shaft-Bearing Systems. Technical Report AFAPL-TR-76-90, (SKF report AL76P030), Air Force Aero Propulsion Laboratory and Naval Air Propulsion Test Center, October 1976.
4. Bisson, E.D. and W.J. Anderson, Advanced Bearing Technology, NASA SP-38 National Aeronautics and Space Administration, Washington, D.C., 1964.
5. Jacobsen, R.T., R.B. Stewart, R.D. McCarty, H.J.M. Hanley, Thermophysical Properties of Nitrogen from the Fusion Line to 3500°R (1944°K) for Pressures to 150,000 psia (10342×10^5 N/m²). U.S. Department of Commerce, National Bureau of Standards, NBS-TN-648, December 1973.
6. McCarty, R.D. and L.A. Weber, Thermophysical Properties of Oxygen from Freezing Liquid Line to 600°R for Pressures to 5000 psia. NBS-TN-384, U.S. Department of Commerce, National Bureau of Standards, July 1971.
7. Sherman, A.L. and R. Gershmann, J.T. Osugi, Fluid Properties Handbook, MDC G0814, McDonnell Douglas Astronautics Company, October 1970.
8. "Assessment of the Operating Characteristics of the SSME LOX Turbopump Pump-End Bearings - Final Report", SRS/STD-TR85- 009, SRS Technologies - System Technology Division, Huntsville, AL, December 1984.
9. "Space Shuttle Main Engine (SSME) LOX Turbopump Pump-End Bearing Analysis - Final Report", SRS/STD-TR86-007, SRS Technologies - System Technology Division, Huntsville, AL, January 1986.

10. "Bearing Tester Data Compilation, Analysis, and Reporting and Bearing Match Modeling - Annual Report", SRS/STD-TR86-014, SRS Technologies - System Technology Division, Huntsville, AL, January 1986.
11. Lowry, S.A., "BSMT LN₂ D.C.C. Test Series Final Report Review Team Members Assessments, Internal NASA/MSFC Memorandum EP26(85-100), NASA/MSFC, Huntsville, AL, June 27, 1985.
12. Thlodorein, Theodore and Arthur Regier, "Elements on Drag of Revolving Disks, Cylinders, and Streamline Rods at High Speeds", NACA Report No. 793, Langley Memorial Aeronautical Laboratory, National Advisory Committee for Aeronautics Langely Field, VA, April 24, 1944.
13. "SRS Technologies Bearing Model Summary Description", SRS Technologies - System Technology Division, Huntsville, AL, September 22, 1986.
14. "Latest Bearing Thermal Models", OL87-647, SRS Technologies - System Technology Division, Huntsville, AL, March 16, 1987. (a memo to Rick Bachtel NASA/MSFC)

SHABERTH/SINDA INPUTS
FOR LN₂

Bearing #1

Bearing #2

Bearing #3

Bearing #4

Initial
TemperaturesXXIII-14

ORIGINAL PAGE IS
OF POOR QUALITY

```
60 1 1 67.40 38.10 0 38.10 57.33 2.346E5
61 1 1 100.00 38.10 57.33 72.40 2.346E5
62 1 1 100.00 38.10 57.33 72.40 2.346E5
63 1 1 150.00 38.10 72.40 72.40 2.346E5
64 1 1 200.00 38.10 72.40 72.40 2.346E5
65 1 1 229.40 38.10 72.40 57.33 2.346E5
66 1 1 236.80 38.10 57.33 0 2.346E5
67 2 26.81 0 0
68 2 58.05 0
69 2 238.75 0
70 2 269.99 0
71 3 34.04 0000.0 0 0 0 0000.0
72 3 224.50 0000.0 0 0 0 2223.3
73 3
74
75
76 THE ADDITIONAL DATA IS FOR THE CONDUCTANCE CALCULATIONS (SRS)
77 $BRGHUM
78 LOUT=3
79 $END
80 $CONDAT
81 IDENT='57MM', SHAFTS=3141.59, CAGESP=1365.0, FILM=TRUE, DELP=32.,
82 DIA=.0417, HFI=-28.384, HS2=0.573, HFC=7.73, IFA=-274., TSI=-228.3,
83 HSI=8.73, CAGEH=169.3, HFG2=25.61, VOBREG1=2842.1, VOBREG2=752.5
84 $END
85 $COOLNT
86 FLUID='LN2', FLOW=6.40
87 TFLUID=-300., -255., -245., -240., -234., -233., -232., -231.,
88 VISCOW=8.23E-5, 2.43E-5, 1.34E-5, 1.04E-5, 0.78E-5, .945E-5, 1.29E-5,
89 1.87E-5, 1.92E-5,
90 SHEATF=0.493, 0.633, .782, .997, 1.40, 1.40, 1.40, 1.40, 1.40
91 $END
92 $OUTER
93 HCDEI=1, PRESS=480., TSAT=-233.8,
94 TEMPO=-300., -240., -230., -229., -225., -100., 100., 500., 1000.,
95 DENS=47.61, 32.35, 22.63, 17.62, 10.91, 5.19, 3.32, 2.10, 1.46,
96 SHEATO=493, 1.24, 1.400, 1.400, 1.400, .341, .281, .259, .256,
97 KO=.0684, .0352, .0750, .0710, .0168, .0111, .0129, .0171, .0220,
98 VISCOW=8.23E-5, 2.43E-5, 1.34E-5, 1.04E-5, 0.811E-5, 0.82E-5, 1.01E-5,
99 1.35E-5, 1.72E-5,
100 PRO=2.13, 2.48, 2.48, 2.48, 2.47, 0.90, 0.778, 0.735, 0.720,
101 VARO1=0.0, 0.0, 0.0, 0.0, 0.0, 0.0, 0.0, 0.0, 0.0,
102 VARO2=0.0, 0.0, 0.0, 0.0, 0.0, 0.0, 0.0, 0.0, 0.0,
103 $END
104 $INNER
105 HCDEI=1, PRESS=480., TSAT=-233.8,
106 TEMPI=-300., -240., -230., -229., -225., -100., 100., 500., 1000.,
107 DENS=47.61, 32.35, 22.63, 17.62, 10.91, 5.19, 3.32, 2.10, 1.46,
108 SHEATI=493, 1.24, 1.400, 1.400, 1.400, .341, .281, .259, .256,
109 KI=.0684, .0352, .0750, .0710, .0168, .0111, .0129, .0171, .0220,
110 VISCOW=8.23E-5, 2.43E-5, 1.34E-5, 1.04E-5, 0.811E-5, 0.82E-5, 1.01E-5,
111 1.35E-5, 1.72E-5,
112 PRI=2.13, 2.48, 2.48, 2.48, 2.47, 0.90, 0.778, 0.735, 0.720,
113 VARI1=0.0, 0.0, 0.0, 0.0, 0.0, 0.0, 0.0, 0.0, 0.0,
114 VARI2=0.0, 0.0, 0.0, 0.0, 0.0, 0.0, 0.0, 0.0, 0.0,
115 $END
116 $BALL
117 BSPEED=130., BALLSP=9425., HCDEB=3,
118 TEMPB=-300., -240., -230., -229., -225., -100., 100., 500., 1000.,
119 DENS=47.61, 32.35, 22.63, 17.62, 10.91, 5.19, 3.32, 2.10, 1.46,
```

Shaft Dimensions

Axial Load

Outer Race
Fluid Properties

Inner Race
Fluid Properties

```

120 SHEATB= .493, 1.24, 1.400, 1.400, 1.400, .341, .281, .259, .256,
121 KB = .0684, .0352, .0750, .0710, .0168, .0111, .0129, .0171, .0220,
122 VISCOS=8.23E-5, 2.43E-5, 1.34E-5, 1.04E-5, 0.81E-5, 0.82E-5, 1.01E-5,
123 1.95E-5, 1.72E-5,
124 PRB = 2.13, 2.48, 2.48, 2.48, 2.47, 0.90, 0.778, 0.735, 0.720,
125 VARB1= 0.0, 0.0, 0.0, 0.0, 0.0, 0.0,
126 VARB2= 0.0, 0.0, 0.0, 0.0, 0.0,
127 $END

```

Ball
Fluid Properties

•XOT SHABOLD.RUNTESTER

•ADD.P SHABOLD.SHAB57DUMP

SINDA inputs

```

lines 697-709
coolant inlet temperatures
saturation temperature

```

-274 F nodes 1-8,998,-999,-997,-993
-233.8 F node 19

```

line 757
cage heat (note:  $\frac{1}{2}$  the value is in
SHABERTH,  $\frac{1}{2}$  is in SINDA)
total: 338.6 Btu/hr

```

169.3 Btu/hr

```

lines 760-761
add together = VQBRG1 in SHABERTH

```

1421.1 Btu/hr ball
1421.1 Btu/hr ball

```

lines 763-764
add together = VQBRG2 in SHABERTH

```

376.3 Btu/hr ball
376.3 Btu/hr ball

```

lines 2228-2236
coolant flowrate

```

1772.3 lb/hr ball
(nodes 12,23,34,45,56,67,78,9981,9999998)

flowrate = $6.4 \frac{\text{lb}}{\text{sec}} \cdot 3600 \frac{\text{sec}}{\text{hr}} = 23040 \text{ lb/hr}$ / 13 balls in a bearing = 1772.3 lb/hr ball

```

lines 2296-2301
specific heat vs temperature at 480 psia for LN2 at node 27 (see reference (5))

```

ORIGINAL PAGE IS
OF POOR QUALITY

ORIGINAL PAGE IS
OF POOR QUALITY

XIII-17

ORIGINAL PAGE IS
OF POOR QUALITY

```
60 1 38.10 0 38.10 57.33 2.346E5
61 1 67.40 38.10 57.33 72.40 2.346E5
62 1 100.00 38.10 72.40 72.40 2.346E5
63 1 150.00 38.10 72.40 72.40 2.346E5
64 1 200.00 38.10 72.40 72.40 2.346E5
65 1 229.40 38.10 72.40 57.33 2.346E5
66 1 296.80 38.10 57.33 0 2.346E5
67 2 26.81 0 0 0 0
68 2 58.05 0 0 0 0
69 2 238.75 0 0 0 0
70 2 269.99 0 0 0 0
71 3 34.04 0000.0 0 0 0 0000.0
72 3 224.50 0000.0 0 0 0 2223.3
73 3
74 3
75
76
77 $BRGNUM
78 LOUT=3
79 $END
80 $CONDAT
81 IDENT=-.57MM , SHAFTS=3141.59, CAGESP=1365.0, FILM=TRUE, DELP=32.,
82 DIA=.0417, HFI=-.41,228,HS2=-.13,150,HFG= 47.40,TF=-260.,TS1=-196.,
83 HS1=-11.34 , CAGEH=169.3,HFG2=50.01, VOBRI1=4973.1, VOBRI2=910.44
84 $END
85 $COOLNT
86 FLUID='LOX', FLOW=6.40
87 TFLUID=-230.,-220.,-210.,-201.,-200.,-195.,-190.,-185.,
88 VISCOW=14.22E-5,7.23E-5,4.29E-5,1.18E-5,1.21E-5,1.29E-5,1.47E-5,
89 1.56E-5,1.63E-5
90 SHEATF=0.475,0.516,.587,.774,.702,.546,.470,.423
91 $END
92 $OUTER
93 HCODED=1, PRESSO=480., TSATO=-200.8,
94 TEMPO=-300.,-250.,-201.,-200.,-100.,-50.,50.,100.,450.,
95 DENSQ= 72.06, 62.69, 47.89, 9.13, 5.55, 4.89, 4.02, 3.71, 2.46,
96 SHEATO= 401, 434, 774, 702, 303, 285, 253, 246, 231,
97 KQ = .0897, .0681, .0429, .0158, .0128, .0131, .0138, .0142, .0176,
98 VISCOW=14.22E-5,7.23E-5,4.29E-5,1.17E-5,1.14E-5,1.17E-5,1.25E-5,
99 1.295E-5,1.61E-5,
100 PRO = 2.29, 1.66, 2.79, 1.88, 0.969, 0.896, 0.826, 0.807, 0.757,
101 VARO1= 0.0,0.0,0.0,0.0,0.0,0.0,
102 VARO2= 0.0,0.0,0.0,0.0,0.0,0.0,
103 $END
104 $INNER
105 HCODEI=1, PRESSI=480., TSATI=-200.8,
106 TEMPI=-300.,-250.,-201.,-200.,-100.,-50.,50.,100.,450.,
107 Densi= 72.06, 62.69, 47.89, 9.13, 5.55, 4.89, 4.02, 3.71, 2.46,
108 SHEATI= 401, 434, 774, 702, 303, 285, 253, 246, 231,
109 KI = .0897, .0681, .0429, .0158, .0128, .0131, .0138, .0142, .0176,
110 VISCOW=14.22E-5,7.23E-5,4.29E-5,1.17E-5,1.14E-5,1.17E-5,1.25E-5,
111 1.295E-5,1.61E-5,
112 PRI = 2.29, 1.66, 2.79, 1.88, 0.969, 0.896, 0.826, 0.807, 0.757,
113 VARI1= 0.0,0.0,0.0,0.0,0.0,0.0,
114 VARI2= 0.0,0.0,0.0,0.0,0.0,0.0,
115 $END
116 $BALL
117 BSPEED= 130., BALLSP= 9425., HCODEB=3,
118 TEMPB=-300.,-250.,-201.,-200.,-100.,-50.,50.,100.,450.,
119 DENS8= 72.06, 62.69, 47.89, 9.13, 5.55, 4.89, 4.02, 3.71, 2.46,
```

Shaft Dimensions

Axial Load

Outer Race
Fluid Properties

Inner Race
Fluid Properties

ORIGINAL PAGE IS
OF POOR QUALITY

```

120 SHEATB= .401, .434, .774, .702, .303, .285, .253, .246, .231,
121 KB = .0897, .0681, .0429, .0158, .0128, .0131, .0138, .0142, .0176,
122 VISCOS=14.22E-5, 7.23E-5, 4.29E-5, 1.17E-5, 1.14E-5, 1.17E-5, 1.25E-5,
123 1.295E-5, 1.61E-5,
124 PRB = 2.29, 1.66, 2.79, 1.88, 0.969, 0.896, 0.826, 0.807, 0.757,
125 VARB1= 0.0, 0.0, 0.0, 0.0, 0.0, 0.0, 0.0, 0.0, 0.0,
126 VARB2= 0.0, 0.0, 0.0, 0.0, 0.0, 0.0, 0.0, 0.0, 0.0,
127 $END

```

Ball
Fluid Properties

•XOT SHABOLD.RUNTESTER

•ADD.P SHABOLO.SHAB57DUMP

SINDA inputs

lines 697-709

coolant inlet temperatures
saturation temperature

-260 F nodes 1-8,998,-999,-997,-993
-200.8 F node 19

line 757

cage heat (note: $\frac{1}{2}$ the value is in
SHABERTH, $\frac{1}{2}$ is in SINDA
total: 338.6 Btu/hr

169.3 Btu/hr

lines 760-761

add together = VQBRC1 in SHABERTH

2486.5 Btu/hr ball
2486.5 Btu/hr ball

lines 763-764

add together = VQBRC2 in SHABERTH

455.2 Btu/hr ball
455.2 Btu/hr ball

lines 2228-2236

coolant flowrate

1772.3 lb/hr ball
(nodes 12,23,34,45,56,67,78,9981,999998)

flowrate = $6.4 \frac{\text{lb}}{\text{sec}} \cdot 3600 \frac{\text{sec}}{\text{hr}} = 23040 \text{ lb/hr}$ / 13 balls in a bearing = 1772.3 lb/hr

lines 2296-2301

specific heat vs temperature at 480 psia for LOX at node 27 (see reference (6))

Diametrical Clearance vs Axial Preload

Diametrical Clearance Input to SHABERTH (mm)	(N)	Axial preload on bearing pair (lb)
0.0043	5137	1155.3
0.009	4750	1068.3
0.013	4450	1000.8
0.0148	4315	970.4
0.025	3651	821.1
0.05	2466	554.6

523-72
N88-15624 116725
258

1987

NASA/ASEE SUMMER FACULTY RESEARCH FELLOWSHIP PROGRAM

MARSHALL SPACE FLIGHT CENTER
THE UNIVERSITY OF ALABAMA IN HUNTSVILLE

ANALYSIS OF RELATIVISTIC NUCLEUS-NUCLEUS INTERACTIONS
IN EMULSION CHAMBERS

Prepared By:	Stephen C. McGuire
Academic Rank:	Associate Professor
University and Department:	Alabama A&M University Department of Physics
NASA/MSFC:	
Laboratory:	Space Science
Division:	Astrophysics
Branch:	High Energy Astrophysics
NASA Colleague:	Thomas A. Parnell
Date:	August 7, 1987
Contract No.:	The University of Alabama in Huntsville NGT-01-008-021

TABLE OF CONTENTS

	Page No.
ABSTRACT	ii
ACKNOWLEDGEMENTS	iii
LIST OF FIGURES	iv
I. INTRODUCTION	1
II. OBJECTIVES	3
III. EXPERIMENT DESCRIPTION	4
IV. DATA REDUCTION METHODS	5
a. Determination of Emission Angles	5
b. Calculation of Linear Momenta	7
V. SOFTWARE DEVELOPMENT	9
VI. CONCLUSIONS AND RECOMMENDATIONS	10
VII. REFERENCES	11
APPENDIX A	16

ABSTRACT

We report on the development of a computer-assisted method for the determination of the angular distribution data for secondary particles produced in relativistic nucleus-nucleus collisions in emulsions. The method is applied to emulsion detectors that were placed in a constant, uniform magnetic field and exposed to beams of 60 and 200 GeV/nucleon ^{16}O ions at the Super Proton Synchrotron (SPS) of the European Center for Nuclear Research (CERN). Linear regression analysis is used to determine the azimuthal and polar emission angles from measured track coordinate data. The software, written in BASIC, is designed to be machine independent, and adaptable to an automated system for acquiring the track coordinates. The fitting algorithm is deterministic, and takes into account the experimental uncertainty in the measured points. Further, a procedure for using the track data to estimate the linear momenta of the charged particles observed in the detectors is included.

ACKNOWLEDGEMENTS

The author expresses his appreciation to Thomas A. Parnell and James H. Derrickson for serving as technical monitors during his appointment as a NASA/ASEE Summer Faculty Fellow. Thanks also go to Yoshiyaki Takahashi for helpful discussions regarding the construction and performance characteristics of the emulsion detectors, to Fred Berry for assistance with the computer system, and to Taka Tabuki for providing experimental data for testing the software. Lastly, the financial support of the NASA/ASEE Summer Faculty Fellowship Program, Gerald F. Karr, director and Ernestine Cothran, co-director, is gratefully acknowledged.

LIST OF FIGURES

	Page No.
Figure 1. Sketch of the experimental arrangement showing the approximate dimensions of the detector	12
Figure 2. Cross sectional view of the chamber configuration designated as 5A2 for the EMU05 experiment	13
Figure 3. Coordinate system diagram illustrating the use of track coordinates to obtain emission angles.	14
Figure 4. Schematic diagram used to show how the radius of curvature is related to the measured distances, Δx_i	15

I. INTRODUCTION

In this paper we report on the development of a data analysis method for the rapid determination of the azimuthal and polar emission angles of particles produced in nucleus-nucleus collisions observed in emulsion chambers exposed to relativistic 160 beams. The method makes use of the track coordinate (x,y,z) data that is presently obtained by visual inspection of the developed emulsion plates, using scanning microscopes. Although our initial application focusses on studying charged pions, the method is applicable to data for any emitted particle. The results of this work will be applied to the analysis of heavy ion cosmic ray interactions that are observed in emulsion chambers flown at high altitudes¹. Events from these cosmic ray experiments are especially valuable since they often occur at energies that are substantially greater than those readily achievable with present-day particle accelerators.

The angular distributions of secondary particles, generated in the collision of two nuclei, contain information on the dynamics of the nuclear interaction process. Events that are characterized by large numbers of secondary particles and large transverse momenta are likely candidates to exhibit new fundamental phenomena. One such phenomenon is a new state of matter, the quark-gluon plasma (QGP), that is expected to occur in relativistic collisions that involve unusually high energy densities². Another example rests in the idea that, if the collisions are simple superpositions of proton-like collisions, the produced particles are expected to be emitted isotropically in the center-of-mass frame. In each of these cases, it is very important to examine and understand the angular distributions of particles produced in high energy nuclear interactions, specifically with respect to non-statistical structure that may contain signatures of new physics^{3,4}.

Emulsion chambers are well established as a tool for observing nuclear interactions involving energetic charged projectiles. They have the advantages of being relatively durable and easy to prepare. They can be used to accurately measure the charge and energy of the primary projectile, in addition to the emission angles associated with fragments

and secondary particles produced for the highest energy nuclear interactions. However, being passive detectors, they require a lengthy and somewhat involved set of developing and scanning procedures in order to obtain the raw data needed for analyzing the events they record. Even after the emulsion plates are developed, considerable laboratory work is needed to obtain angular distribution data.

II. OBJECTIVES

The primary objective of this project is to analyze secondary particle distribution data, recorded in emulsions from the EMU05 experiment⁵, for the existence of non-statistical structures. To accomplish this objective, it was necessary to develop appropriate computer software that could be used to find the azimuthal and polar emission angles from particle track coordinate data. The software includes error analysis, and it has been tested successfully with data for which the results are known. In particular, the angular distributions of charged pions, observed in the EMU05 experiment, are to be examined for deviations from isotropy in the center-of-mass frame.

III. EXPERIMENT DESCRIPTION

For the EMU05 experiment, pulsed beams of ^{16}O with energies of 60 and 200 GeV/nucleon were provided by the Super Proton Synchrotron (SPS) at the European Center for Nuclear Research (CERN). The pulse duration was 2s with a total intensity of 3×10^3 ions/cm² pulse. The integrated exposure given to a chamber was 10^4 ions. The beam size was 2.54cmx2.54cm (1 sq. in.) and each chamber was exposed to beam spills shifted laterally from each other by 1 cm. Proportional counter measurements at the chamber, located 30 cm downstream from the beamline end, indicated the beam to be 98% pure.

The chamber used in this work consisted of stacked emulsion plates separated by layers of lead, CR39 plastic and polystyrene. A sketch of the experimental arrangement, showing the approximate dimensions of the chamber, is provided in figure 1. The chamber was placed inside a uniform, 1.8 Tesla magnetic field. A cross sectional view of the detector configuration for which our analysis method was developed, is provided in figure 2. In this case, each emulsion plate had a 70 μm base coated on both sides with 50 μm of emulsion. The separation between the emulsion plates is not constant, but gradually increases in the direction of the beam. This facilitates the measurement of the track curvature, the identification of the charge of the emitted particle, and places an upper limit of 10 GeV on the energy of the secondary particles that can be analyzed. Also, lead plates are placed near the front of the detector where the density of emulsion plates is greater to increase the likelihood of collisions there. This feature also improves the accuracy with which the position of the collision vertex and the track angles can be determined.

IV. DATA REDUCTION METHODS

IV.a. Determination of Emission Angles

The method employed to find the polar and azimuthal emission angles consists essentially of fitting the set of position coordinates, (x_i, y_i, z_i) , for a given track, to the equation of a straight line⁶. The situation is illustrated in figure 3. The vector \mathbf{d} points in the initial direction of motion of the emitted particle. Since the paths are curved, it is recognized from the outset that this approach can be used to obtain a good estimate of the initial direction of motion of the outgoing particle, at the point of collision. Consequently, only those points closest to the collision vertex are used in the calculation.

First, a fit to the line $y = a + bx$ is found using the set of points, (x_i, y_i) , in the x-y plane. The azimuthal angle, ϕ , is then simply obtained from

$$\phi = \tan^{-1}(b) \quad , \quad (1)$$

where b is the slope of the line. The procedure is repeated for the set of points, (r_i, z_i) , in the r-z plane where

$$r_i = \sqrt{(x_i)^2 + (y_i)^2} \quad , \quad (2)$$

and $z = c + mr$. The angle θ is then obtained from

$$\theta = \tan^{-1}(m) \quad . \quad (3)$$

This procedure is performed for each track associated with the event.

Values for b and m are obtained by the minimization of a chi-square quantity given by

$$\chi^2(a,b) = \sum_{i=1}^N \left(\frac{y_i - y(x_i; a, b)}{\sigma_i} \right)^2, \quad (4)$$

where σ_i is the experimental uncertainty in the i th point. The resulting conditions,

$$\frac{\partial \chi^2}{\partial a} = 0$$

and (5)

$$\frac{\partial \chi^2}{\partial b} = 0,$$

must be satisfied, and in doing so yield two equations in two unknowns that are readily solvable for the constants $a(c)$ and $b(m)$. An estimate of the probable uncertainties in the constants can be obtained if the data are treated as independent with each contributing its own bit of uncertainty to the parameters. Consideration of the propagation of errors shows that the variance, σ_f , in the value of any function will be

$$\sigma_f^2 = \sum_{i=1}^N \sigma_i^2 \left(\frac{\partial f}{\partial y_i} \right)^2 \quad (6)$$

where $f = a(c), b(m)$.

If, however, the individual measurement errors of the points σ_i , are not known, then a more accurate estimate of the probable uncertainties in the parameters $a(c)$ and $b(m)$ can be obtained via the following procedure. Set $\sigma_i = 1$ in equations (4), (5), and (6), and multiply the values of σ_f by the additional factor,

$$\sqrt{\chi^2 / (N-2)},$$

where χ^2 is computed by (4). In essence, this latter procedure is equivalent to assuming that one obtains a good fit.

IV.b Calculations of the Linear Momenta

As suggested in the introduction, it is important to identify those events in which a large amount of linear momentum of the incident projectile is transferred to the target nucleus. This may be done by careful examination of the linear momenta reaction products⁷.

The radius of curvature of the path of a secondary particle is related directly to its linear momentum. To show this, consider the motion of a charged particle in a magnetic field. The magnetic force on the particle is given by

$$\mathbf{F} = q(\mathbf{v} \times \mathbf{B}) , \quad (7)$$

where q is the charge on the particle, \mathbf{v} is its velocity, and \mathbf{B} is the magnetic field. In the present case, \mathbf{B} is assumed to be uniform and oriented in the positive y -direction. Thus, the magnitude of the force can be written as

$$F = qvB\sin(\theta') , \quad (8)$$

where θ' is the angle between \mathbf{v} and \mathbf{B} , and the direction of \mathbf{F} is everywhere perpendicular to the plane formed by \mathbf{v} and \mathbf{B} . The curved motion is described in terms of a centripetal acceleration so that,

$$qvB\sin(\theta') = mv^2/R , \quad (9)$$

where m is the mass of the particle and R is its radius of curvature. Since $p = mv$ is the linear momentum of the particle, we have

$$p = qBR\sin\theta' . \quad (10)$$

For convenience, equation (10) may be expressed as⁸

$$p(\text{GeV}/c) = 0.29979 \, q \, B(\text{T}) \, R(\text{cm}) \, \sin\theta' , \quad (11)$$

where q takes on the value ± 1 for pions.

We can derive an estimate of R from the measured track coordinates using the scheme illustrated in figure 4. From the figure,

$$L_i = R \sin \alpha_i \quad (12)$$

where L is the distance along the symmetry axis of the detector, in this case the z -direction, to the i th emulsion plate. Also, note that

$$\Delta x_i = R(1 - \cos \alpha_i) \quad (13)$$

The quantity Δx_i is the perpendicular distance from the beam direction. These last two equations can be combined to give

$$R = \Delta x_i / (1 - \cos(\sin^{-1}(L_i/R))) \quad (14)$$

Since we are interested in obtaining a solution to this last, non-linear equation for R in terms of Δx_i , this may best be done by approximating the $\cos(x)$ and $\sin^{-1}(x)$ functions by their series forms, i.e.,

$$\cos(x) = 1 - \frac{x^2}{2!} + \frac{x^4}{4!} - \frac{x^6}{6!} + \dots + |x| < \infty$$

$$\sin^{-1}(x) = x + \frac{x^3}{2 \cdot 3} + \frac{1 \cdot 3 \cdot x^5}{2 \cdot 4 \cdot 5} + \dots \quad |x| < 1$$

Using only the first order terms, we obtain

$$R \approx (L_i)^2 / 2\Delta x_i$$

Clearly, this approximation is best suited for measurements involving the coordinates of the first few emulsion plates nearest the interaction vertex, and for reaction products with large p values.

V. SOFTWARE DEVELOPMENT

A computer code that makes use of the analysis methods described in the previous section was written for the Commodore AMIGA⁹ computer. The code is written in BASIC and is designed to be machine independent. It is expected that the code will be executed under the BASIC interpreter supplied with the computer. For input, the program requires files that contain the track coordinate (x,y,z) data that have been obtained for each event by scanning the developed emulsion plates. At present, the program returns the corresponding angles, θ and ϕ for each track, and it also has a provision for estimating the linear momenta of the emitted particles, based upon the track radius of curvature and the magnetic field. Early tests, employing idealized track data, as well as actual track data from a few plates, indicate that the code is operating correctly. A current source listing, to be regarded as preliminary, is provided in Appendix A along with a logic diagram for the code. A detailed description will appear elsewhere, after finalization of the software.

VI. CONCLUSIONS AND RECOMMENDATIONS

Initial development work on the computer software for determining the emission angles and estimating the linear momenta of particles emitted in nucleus-nucleus collisions observed in emulsions has been completed. The software has been tested successfully for correct operation using idealized track data and partial data from the EMU05 experiment. Further testing of the code with complete track data for EMU05 events is recommended to confirm the accuracy of the calculations.

Additional heavy ion experiments involving emulsion chambers of the 5A2 design are planned for the SPS accelerator. The first will employ a ^{32}S beam and is scheduled for September, 1987. Another will use a ^{208}Pb beam that is anticipated being available during the Fall of 1989. Also, the High Energy Astrophysics Branch of SSL has been involved over the past 10 years in a collaborative research program, the Japanese American Collaborative Emulsion Experiment (JACEE), the purpose of which is to study charge particle cosmic ray interactions in emulsion chambers flown at high altitude. To date, seven balloon flights have been conducted and data analysis has been completed for five of these. In view of the large amount of data anticipated to be available from these two efforts, it is recommended that an automated system of coordinate data recording be incorporated with the code development work presently underway in order to reduce the time between plate scanning and final analysis of the angular distributions. Such a system will be especially valuable for analyzing events having high multiplicities.

The present method of calculating the emission angles will work best when data are available for a few closely spaced plates near the interaction vertex of the event. It is therefore of interest to explore alternative means of fitting the track data that make use of functions that better represent the curved path. An initial approach would include using higher order polynomial function approximations to the path, and finding the tangent to the curve at the interaction vertex.

VII. REFERENCES

1. R. W. Austin et al., Papers at the 18th ICRC, T2-15, (1983).
2. J. Rafelski and M. Danos, NBS Report No. NBSIR 83-2725, June 1983.
3. H. A. Gustafsson et al., Phys. Rev. Lett., 52, 1590 (1984) and G. Buchwald et. al., Phys. Rev. Lett., 52, 1594 (1984).
4. S. C. McGuire, NASA CR No. 4054, March 1987.
5. CERN Experiment Proposal No. CERN/SPS 85-50, SP SC/P165, Oct. 15, 1985.
6. W. H. Press et al., Numerical Recipes, The Art of Scientific Computing, Cambridge University Press, New York, 1986, pp. 504-508.
7. T. H. Burnett et al., Phys. Rev. Lett., 57, 3249 (1986).
8. Private Communication with Y. Takahashi.
9. AMIGA is the Commodore trade name for this computer.

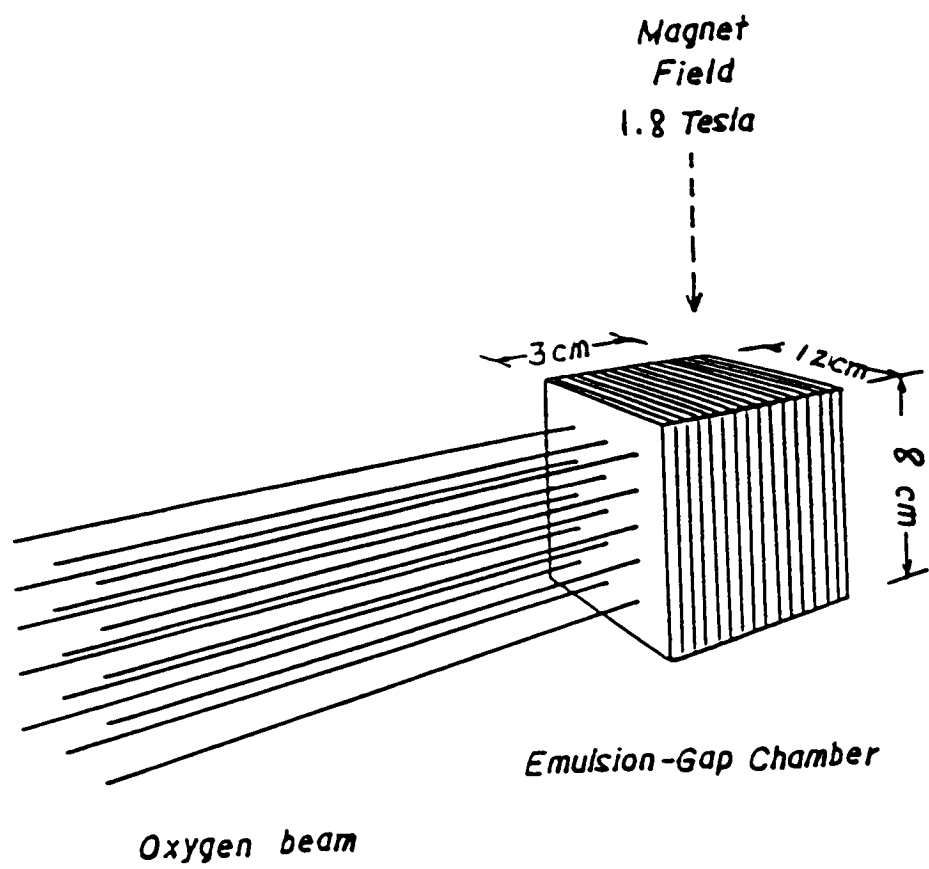


FIGURE 1.

ORIGINAL PAGE IS
OF POOR QUALITY

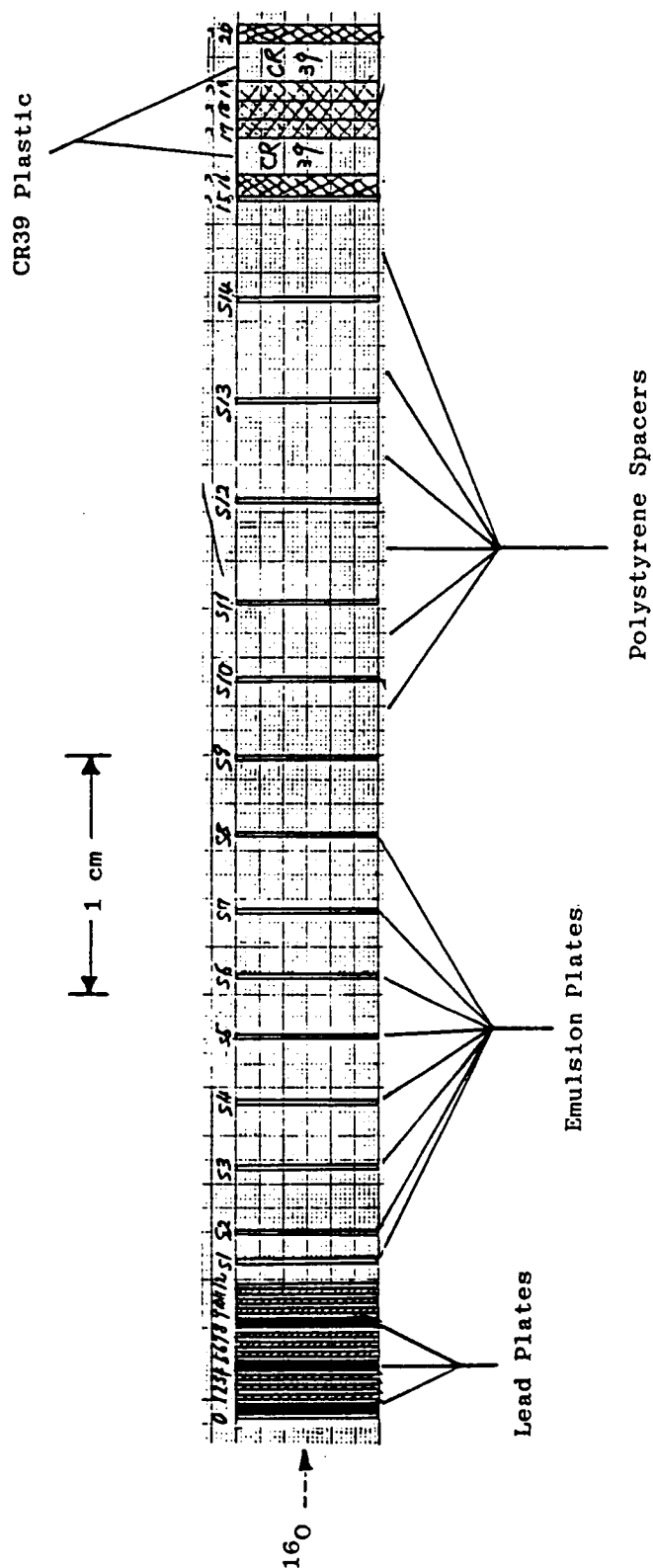


FIGURE 2.

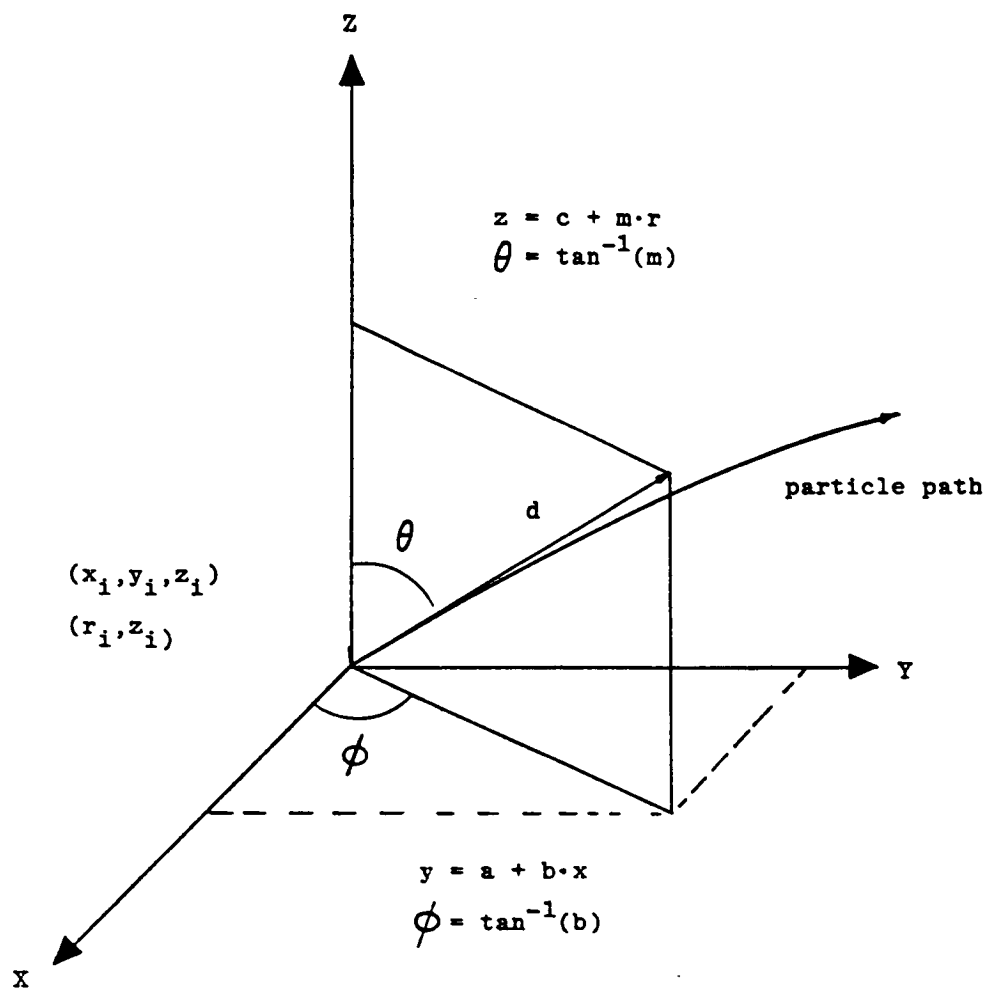


FIGURE 3.

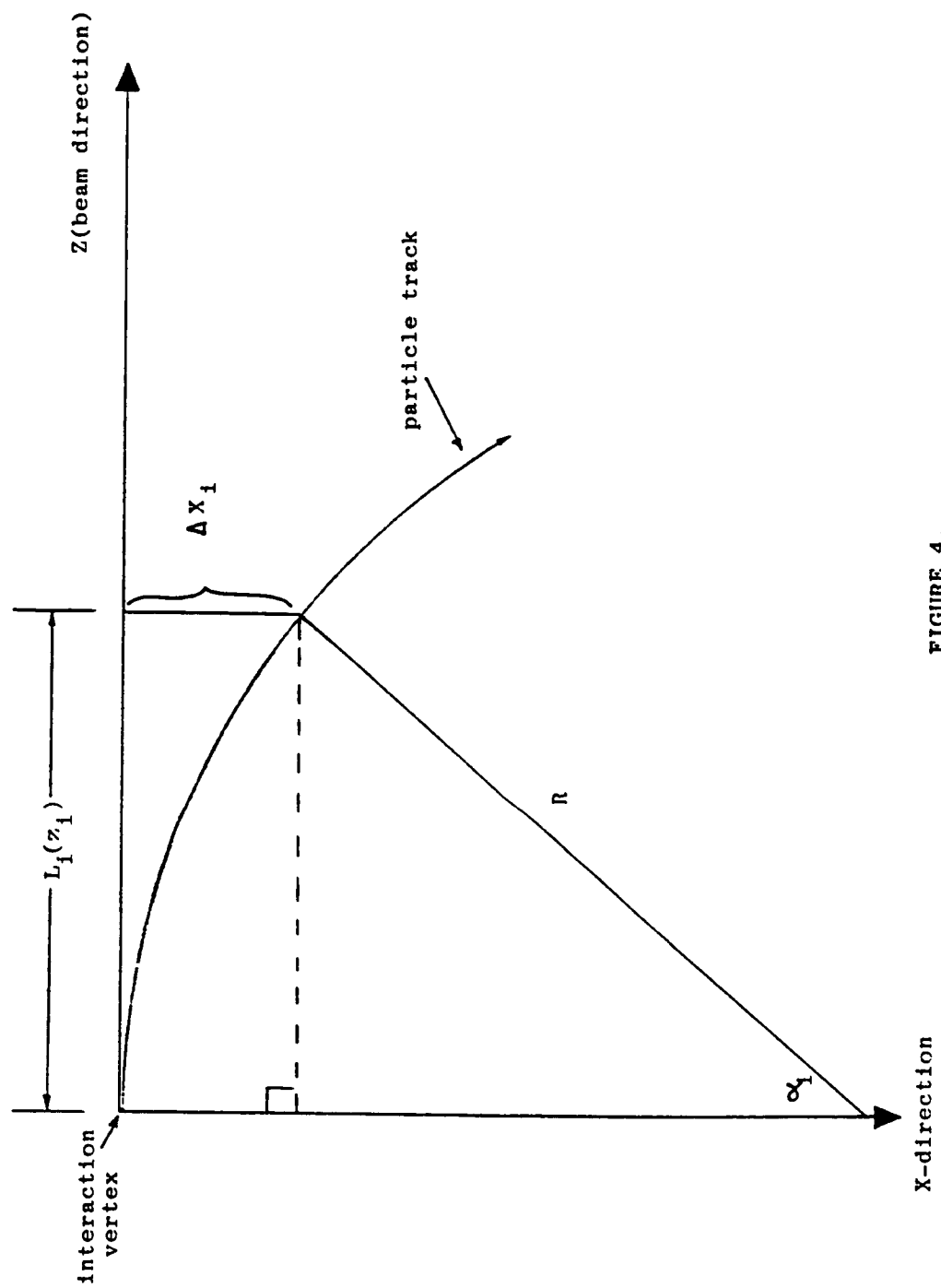
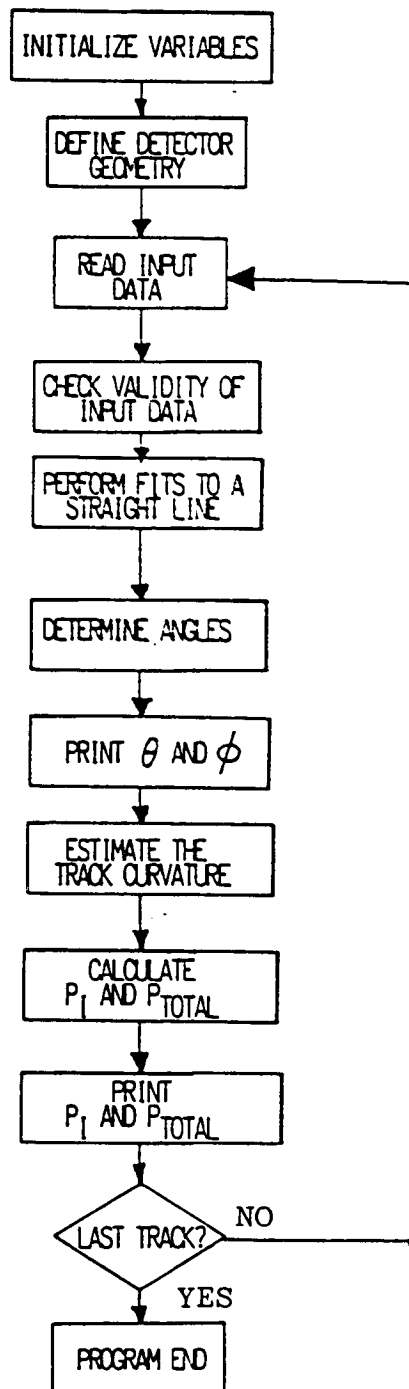


FIGURE 4.

APPENDIX A

Logic Diagram and Source Listing of the Track Coordinate
Analysis Program



```

10 REM****PROGRAM TO CALCULATE THE AZIMUTHAL AND POLAR EMISSION***
20 REM ANGLES FROM THE EMU05 EXPERIMENT DATA.*****
30 REM*****EMU05B.BAS*****
40 DIM A(4),X(50),Y(50),Z(50),SIG(50),R(50)
50 XMAX=80000!:YMAX=80000!:ZMAX=47680!
60 ANGFACT=(180!/3.14159):PFAC%=1
80 CONST = .29979: BFIELD = 1.8
90 QP = 1!: QN = -1!
100 REM*****READ IN THE TRACK DATA.*****
110 REM*****UNITS SHOULD BE MICRONS*****
200 INPUT "FILENAME= ",FILENAM$
210 OPEN FILENAM$ FOR INPUT AS 1
212 LPRINT "DATA FILE = ", FILENAM$
215 REM *****
217 LPRINT
220 REM*****
225 INPUT #1, NRAY%
227 LPRINT " NRAY= ",NRAY%
228 REM*****
230 PPR = 0!: PFL = 0!:PPRTOT=0!:PPLTOT=0!
240 FOR J% = 1 TO NRAY%
245 LPRINT " -----INPUT TRACK DATA FOLLOWS-----"
246 LPRINT
250 NPTS% = 0
260 FOR K% = 1 TO 40
270 NPTS% = NPTS% + 1
275 REM*****
280 INPUT #1, X(K%),Y(K%),Z(K%),SIG(K%)
295 R(K%) = SQR(X(K%)*X(K%) + Y(K%)*Y(K%))
290 LPRINT USING "#####.##"; X(K%),Y(K%),Z(K%),R(K%),SIG(K%)
300 IF X(K%) = -1! THEN NPTS% = NPTS% - 1: GOTO 320
305 REM END INNER LOOP
310 NEXT K%
320 REM*****PERFORM FIT TO A STRAIGHT LINE AND*****
330 REM ***BASED ON THE FITTED DATA , FIND THE EMISSION ANGLES.*****
332 LPRINT " -----EMISSION ANGLES FOLLOW-----"
335 GOSUB 1000
340 REM*****
345 GOTO 510
350 REM*****BASED ON ITS ESTIMATED RADIUS OF CURVATURE, DETERMINE
351 REM THE LINEAR MOMENTUM OF THE TRACK.*****
360 FOR IR% = 1 TO NPTS%
370 RI = Z(IR%)*Z(IR%)
380 RI = RI/(2!*X(IR%))
390 R = R + RI
400 NEXT IR%
410 FLN=NPTS%:AVR = R/FLN:AVR=AVR/10000!
420 PMOM = CONST*QP*BFIELD*AVR
430 PPR = PMOM*SIN(THETA)
440 PFL = PMOM*COS(THETA)
450 PPRTOT = PPRTOT + PPR
460 PPLTOT = PPLTOT + PFL
470 REM*****
480 LPRINT USING "#####.##"; PMOM,PPR,PPRTOT,PPL,PPLTOT
490 REM****
500 LPRINT
510 REM ****GET DATA FOR THE NEXT TRACK, OR
530 REM END OUTER LOOP.*****
540 NEXT J%
545 REM*****
550 CLOSE #1
560 REM*****
570 END

```

ORIGINAL PAGE IS
OF POOR QUALITY

```

580 REM
1000 REM***SUBPROGRAM TO PERFORM A BEST FIT TO STRAIGHT LINES;
1005 REM IN THE X-Y AND R-Z PLANES. THESE FITS WILL BE*****
1010 REM** TO DETERMINE THE AZIMUTHAL AND POLAR EMISSION ANGLES*****
1012 REM NOTE:** Y = B*X + A IS THE FORM OF THE STRAIGHT LINE.*****
1015 REM*****FIRST CONSTRUCT THE SUMS OVER THE DATA POINTS
1020 REM NEEDED FOR THE CALCULATION OF THE CONSTANTS.*****
1030 SX=0:SY=0:S=0:SXX=0:SY=0
1045 REM*****USE ONLY A FRACTION OF THE AVAILABLE POINTS.*****
1050 NPTSH% = NPTS%/PFAC%
1060 FOR J2% = 1 TO NPTSH%
1070 SIGSQR = SIG(J2%)*SIG(J2%)
1070 SXY = SXY + X(J2%)*Y(J2%)/SIGSQR
1100 SXX = SXX + X(J2%)*X(J2%)/SIGSQR
1120 SX = SX + X(J2%)/SIGSQR
1130 SY = SY + Y(J2%)/SIGSQR
1150 S = S + 1!/SIGSQR
1160 NEXT J2%
1170 REM*****
1180 REM***THE NEXT STEP IS TO CALCULATE THE VALUES
1190 REM OF THE PARAMETERS A AND B FOR THE AZIMUTHAL ANGLE.*****
1200 DELTA = S*SXX - SX*SX
1210 APhi = (SXX*SY - SX*SXY)/DELTA
1220 BPhi = (S*SXY - SX*SY)/DELTA
1230 REM *****FIND THE UNCERTAINTY IN THE A AND B.*****
1240 SIGMAA = SXX/DELTA:SIGMAA = SQR(SIGMAA)
1250 SIGMAB = S/DELTA:SIGMAB = SQR(SIGMAB)
1260 REM*****
1270 REM*****CALCULATE A CHISQUARE VALUE FOR THE FIT.*****
1280 REM AND RE-ESTIMATE THE UNCERTAINTIES IN A AND B.***
1290 SRES=0!
1300 FOR I% = 1 TO NPTSH%
1310 YP = BPhi*X(I%) + APhi
1320 RESI = (Y(I%) - YP)/SIG(I%)
1330 RESI = RESI*RESI
1340 SRES = SRES + RESI
1350 NEXT I%
1360 CHISQR = SRES
1370 EFAC = CHISQR/(NPTSH% - 2)
1380 EFAC = SQR(EFAC)
1390 REM*****REESTIMATE THE UNCERTAINTY IN THE FITTED CONSTANTS.*****
1400 SIGMAA = SIGMAA*EFAC
1410 SIGMAB = SIGMAB*EFAC
1412 REM*****NEXT, CALCULATE THE ANGLE PHI.*****
1415 PHI = ATN(BPhi):PHI = ANGFACT*PHI
1417 LPRINT "      A      SIGMAA      B      SIGMAB      PHI"
1420 REM*****
1424 IF (X(1) < 0! AND Y(1) < 0!) THEN PHI = PHI + 180!:GOTO 1929
1425 IF X(1) < 0! THEN PHI = PHI + 180!: GOTO 1929
1426 IF Y(1) < 0! THEN PHI = PHI + 360!: GOTO 1929
1429 REM *****
1430 LPRINT USING "*****.###";APhi,SIGMAA,BPhi,SIGMAB,PHI
1440 LPRINT
2000 REM***NOW DO THE SAME FOR THE POLAR ANGLE*****
2005 REM *****X --> R AND Y --> Z.*****
2010 SR=0:SZ=0:SRR=0:SRZ=0:S=0
2005 FOR J1% = 1 TO NPTSH%
2002 SIGSQR = SIG(J1%)*SIG(J1%)
2010 SR = SR + R(J1%)/SIGSQR
2015 SZ = SZ + Z(J1%)/SIGSQR
2020 SRR = SRR + R(J1%)*R(J1%)/SIGSQR
2030 SRZ = SRZ + R(J1%)*Z(J1%)/SIGSQR
2035 S = S + 1!/SIGSQR
2040 NEXT J1%
2042 REM*****FIND THE FITTED CONSTANTS, A AND B FOR THE DETERMINATION OF
2043 REM THE ANGLES.*****

```



```

2045 DELTA = S*SRR - SR*SR
2047 ATHETA = (SRR*SZ - SR*SRZ)/DELTA
2050 BTHETA = (S*SRZ - SR*SZ)/DELTA
2052 REM***NOW FIND THE UNCERTAINTIES IN THE FITTED CONSTANTS.*****
2055 SRES = 0!
2056 SIGMAA = SQR(SRR/DELTA): SIGMAB = SQR(S/DELTA)
2057 FOR IX = 1 TO NPTSH%
2060 ZP = BTHETA*R(IX) + ATHETA
2062 RESI = (Z(IX) - ZP)/SIG(IX)
2065 RESI = RESI*RESI
2067 SRES = SRES + RESI
2068 NEXT IX
2070 CHISQR = SRES
2072 EFACT = CHISQR/(NPTSH% - 2)
2075 EFACT = SQR(EFACT)
2077 SIGMAA = SIGMAA*EFACT
2080 SIGMAB = SIGMAB*EFACT
2081 REM *****NEXT, FIND THE ANGLE THETA.*****
2082 THETA = ATN(1/BTHETA):THETA = ANGFACT*THETA
2083 IF Z(1) < 0! THEN THETA = THETA + 180!
2084 LPRINT "      A      SIGMAA      B      SIGMAB      THETA"
2085 LPRINT USING "*****.##";ATHETA, SIGMAA,BTHETA,SIGMAB,THETA
2086 LPRINT
2090 REM*****
2270 REM *****
2290 RETURN

```

524-25
116726
388
N88-15625

1987

NASA/ASEE SUMMER FACULTY RESEARCH FELLOWSHIP PROGRAM

GEORGE C. MARSHALL SPACE FLIGHT CENTER
THE UNIVERSITY OF ALABAMA IN HUNTSVILLE

RAMAN SPECTROSCOPIC INVESTIGATIONS OF Hg-Cd-Te MELTS

Prepared by:	Anny Morrobel-Sosa
Academic Rank:	Assistant Professor
University and Department:	The University of Alabama Department of Chemistry
NASA/MSFC Laboratory: Division: Branch:	Space Science Laboratory Low-Gravity Science Crystal Growth
NASA Colleagues:	Frank R. Szofran Sandor L. Lehoczky
Date:	August 24, 1987
Contract No.:	The University of Alabama in Huntsville NGT-01-008-021

ABSTRACT

Raman scattering measurements are reported for a series of $\text{Hg}_{1-x}\text{Cd}_x\text{Te}$ (with $x \leq 0.2$) materials from 295K (room temperature) to 1126K (up to and above their liquidus temperatures), and for $\text{Hg}_{1-x}\text{Cd}_x\text{Te}$ ($x = 0.3$) at 295K. The samples were contained in high-temperature optically-flat fused silica cell. Variable temperature measurements were effected in a three-zone, high-temperature furnace equipped with optical windows, and monitored externally by three independently programmable temperature controllers. All studies were made in the backscattering geometry using the 5145 Å line of an Ar^+ ion laser, with incident power less than 250 mW, as excitation source. An intensity enhancement is observed for a mode in each of the compositions studied. The frequency of this mode varies with composition, 142 cm^{-1} for HgTe , and 128 cm^{-1} for both the $\text{Hg}_{1-x}\text{Cd}_x\text{Te}$ ($x = 0.053$ and 0.204) samples. In addition, a shift to lower frequency as a function of temperature is observed in all samples. This shift is most prominent for the $x = 0.053$ sample. The temperature dependence of these modes as the liquidus temperatures are achieved and surpassed for these samples is presented as being associated with a structural transition in the Hg-rich compositions of the $\text{Hg}_{1-x}\text{Cd}_x\text{Te}$ series. To our knowledge this is the first reported study of Raman scattering by phonons in the melts of these materials.

ACKNOWLEDGEMENTS

The author wishes to thank the NASA/ASEE Summer Faculty Fellowship Program, its Directors, Dr. Gerald R. Karr of UAH and Ms. Ernestine Cothran of NASA/MSFC, and staff for their enthusiastic support of the Program and its objectives.

Utmost gratitude is due to both of my NASA colleagues, Dr. Frank R. Szofran and Dr. Sandor L. Lehoczky of the Space Science Laboratory/Low-Gravity Science Division/Crystal Growth Branch for their sponsorship and support of this project; their help and guidance was invaluable. Particular thanks are also due to Mr. Ronald P. Harris for his assistance in providing quick solutions to unexpected problems. The efforts and kindness of all members of the Crystal Growth Branch are also acknowledged.

The support of Prof. Drury S. Caine, Chairman of the Department of Chemistry at The University of Alabama, is greatly acknowledged for allowing me to pursue the opportunity provided in the participation of this program.

INTRODUCTION

The $\text{Hg}_{1-x}\text{Cd}_x\text{Te}$ alloy system has received considerable attention in recent years, as can be attested to by several reviews¹⁻³ on the subject, for their use as infrared detector devices.⁴ The energy gap in these materials increases continuously (almost linearly) with cadmium composition, ranging from -0.3 eV (for $x = 0$, HgTe) to +1.6 eV (for $x = 1$, CdTe) and zero-gap crossover at 4.2K for $x = 0.15$. The corresponding spectral range can thus be tuned with alloy composition from 0.8 μm to 50 μm . In particular, the $x = 0.20$ alloy has an atmospheric window of 8 μm to 14 μm at 77K. These materials have therefore been mostly considered for military, space and commercial applications. It is then not surprising to note that a significant proportion of past and present research efforts has been dedicated to the advancement of photodetector technologies and of crystal growth techniques.^{2,5-7} These studies have, in turn, generated enormous interest in the characterization of basic physical properties for this pseudo-binary alloy system.

Recent reports of variations in the thermal conductivities between the solid and melt,⁶⁻⁸ changes in the melt thermal conductivity as a function of temperature and composition,^{9,10} and increases in the thermal diffusivity with temperature,^{10,11} are of particular interest to the work presented here, for they suggest possible chemical or structural changes in the melt structure near and/or above the liquidus temperatures. Optical studies of these materials are of clear significance since they reflect the nature of their electronic and vibrational structure. These efforts have concentrated on three spectroscopic techniques: infrared,¹²⁻²¹ Raman,²¹⁻²⁶ and resonance Raman²⁷⁻²⁹ scattering. The temperatures at which these studies were made range between 1.7K to 300K, the maximum temperature. All of the Raman studies have included the materials with $0 < x < 0.3$ composition; yet, none of the resonance Raman scattering investigations fall within this range. These reports have revealed a "two-mode"³⁰ behavior in the alloys arising from HgTe -like and CdTe -like modes which exhibit composition-dependent frequency shifts. Clustering and defect modes have also been detected²³⁻²⁶ suggesting that surface morphology, such as structural dislocations, composition gradients, and surface preparation, can be studied by these techniques.

In this report we present what to our knowledge is the first study of Raman scattering by phonons in $\text{Hg}_{1-x}\text{Cd}_x\text{Te}$ melts. We have performed these studies on alloy

compositions of $x = 0$, 0.05 , and 0.20 , from room temperature, 22°C (295K), up to and above their liquidus temperatures, 670°C (943K), 703°C (976K), and 794°C (1067K), respectively. We also report the room temperature spectrum for $x = 0.30$ as the first step in a similar investigation to be performed on this alloy composition. The most salient feature in our study is the observation of an intensity enhancement of a phonon mode in each sample composition near and above its liquidus temperatures. We believe this mode to be indicative of a structural phase transition as suggested by others.⁶⁻¹¹ The mechanism for this transition has not yet been identified, though these results, preliminary as they are, do not indicate a soft phonon mechanism as being responsible for the structural transition.

OBJECTIVES

The primary purpose of this effort is the characterization of the liquid structure of $\text{Hg}_{1-x}\text{Cd}_x\text{Te}$ ($x \leq 0.30$) near and above the liquidus temperatures of each alloy composition by means of Raman scattering spectroscopy. The project was motivated by previous observation⁶⁻¹¹ as discussed earlier. The technique of Raman scattering was chosen to perform this study for it probes lattice vibrations, phonons, and is very sensitive to the local structural environment. In what follows is a brief theoretical introduction and description of the technique and its relevant parameters. It is suggested that other authors be consulted for a detailed treatment of the phenomenon,³⁴⁻³⁶ and in particular, for the case of semiconductors.^{27,37-41}

The Raman effect⁴² results from the inelastic scattering of light (of a given frequency, ω_0) by the molecular vibrations and lattice vibrations (in the case of dense media) of a medium. The scattered light consists of several frequency components, ω_j , and their corresponding frequency shifts, $\Delta\omega_j = \omega_0 - \omega_j$, are characteristic of the material and independent of the choice of incident light frequency (except for the case of resonance light scattering). This frequency spread is identified by two regions, Stokes scattering ($\Delta\omega_j > 0$) and anti-Stokes scattering ($\Delta\omega_j < 0$). Since the populations are governed by the Bose-Einstein relationship, the intensities of the Stokes components are usually greater than those of the anti-Stokes components, they are the ones most frequently measured in Raman spectroscopy.

In the simplest case of an isolated, free, atom or molecule, the total intensity of scattered light for an optical transition from a state m to a state n is given by:

$$I_{mn} = \frac{27 \pi^5}{32 c^4} I_0 (\nu_0 \pm \nu_{mn})^4 \sum_{k,l} |(\alpha_{kl})_{mn}|^2$$

in the Kramers-Heisenberg-Weisskopf formalism. The incident radiation intensity and frequency are I_0 and ν_0 , respectively. $(\nu_0 \pm \nu_{mn})$ is the scattered light frequency, where $\nu_{mn} = \nu_m - \nu_n$, and k and l are molecular fixed coordinates that characterize the scattered and incident light, respectively. $(\alpha_{kl})_{mn}$ is a complex, non-centrosymmetric polarizability tensor defined⁴³ as:

$$(\alpha_{kl})_{mn} = \frac{1}{h} \sum_r \frac{(\langle n | \hat{M}_k | r \rangle \langle r | \hat{M}_l | m \rangle + \langle n | \hat{M}_l | r \rangle \langle r | \hat{M}_k | m \rangle)}{(\nu_{rm} - \nu_0 + i \Gamma_r)} + \frac{(\langle n | \hat{M}_l | r \rangle \langle r | \hat{M}_k | m \rangle)}{(\nu_{rn} + \nu_0 + i \Gamma_r)}$$

where: $\hat{\mu}_k$ and $\hat{\mu}_l$ are electric dipole moment operators in the k th and l th polarization, respectively, and Γ_r is the damping constant for the intermediate state(s), accounting for its finite width(s). The wavefunctions $|m\rangle$, $|n\rangle$, and $|r\rangle$ are eigenfunctions of the total Hamiltonian. The summation is performed over all the vibronic states of the molecules, including m and n , so as to consider the contributions from all electronic levels and their corresponding vibrational levels. In this treatment the wavefunctions are usually expanded in terms of the transition moments and generalized coordinates to obtain final expressions for the intensities of the Raman fundamentals and overtones.

Recently, extensions of the theoretical developments by Hayes and Loudon³⁴ have been presented for the specific case of Raman and resonance Raman scattering in semiconductors.^{27,38-41} In this case, and for a similar experimental configuration as used in our study, the rate of scattered photons "inside" the sample per unit solid angle is given by:

$$\frac{dR_s^{\text{in}}}{d\Omega} = \frac{I_0}{\hbar \omega_0} \frac{d\sigma}{d\Omega}$$

where R_s^{in} is the scattered photon rate (photons/sec) inside the sample, Ω , is the unit solid angle and $d\sigma/d\Omega$ is the differential cross-section. The corresponding scattering rate "outside" the sample, which are experimentally measured as the area of the observed Raman peaks, can then be expressed in terms of the polarizability tensor^{27,39,40} as:

$$R_s^{\text{out}} = \frac{T_o T_s P_o \omega_s^3}{(a_o + a_s) \eta_o \eta_s} \frac{\Delta\Omega^{\text{out}} N(\omega_{\text{ph}}) + 1}{2 c^4 \omega_{\text{ph}} M V_c} |\alpha_{os}|^2$$

where T_o and T_s are the incident and scattered transmission coefficients, a_o and a_s are the absorption coefficients at the incident and scattered frequencies, and η_o and η_s are the indices of refraction at the incident and scattered frequencies. (It is important to note that these parameters are temperature dependent). P_o is the incident laser power, ω_{ph} is the observed phonon frequency and $N(\omega_{\text{ph}})$ is the phonon occupation number. ω_s is the scattered photon frequency, $\Delta\Omega^{\text{out}}$ is the constant collection solid angle, and α_{os} is the Raman polarizability tensor. M and V_c are the reduced mass of the unit cell and the primitive cell volume, respectively.

While this analysis has been applied successfully for resonance Raman scattering in $\text{Hg}_{1-x}\text{Cd}_x\text{Te}$ ($x = 0.966$) at

100K,²⁷ only one study has been performed at high temperatures, for Si.³⁹ In this latter case, the data show a decrease in Raman signal intensities with increased temperature, while a resonance enhancement is observed with temperature dependent shifts and broadenings.

It is of interest to extend this theoretical treatment to the Raman scattering at high temperatures for $\text{Hg}_{1-x}\text{Cd}_x\text{Te}$ of $x \leq 0.3$ to aid in the elucidation of the melt structures. The experimental studies reported here are the initial efforts in such a study.

EXPERIMENTAL

The samples used for this study were provided by NASA from a series of previously prepared materials (see Table 1).⁹ Each alloy was prepared from purified elements and loaded in-situ (inside a rocking-furnace to provide homogenization) into specially designed high-temperature, high-pressure, optically flat, fused silica cells (see Figure 1).⁴⁴ The last four sample cells listed in Table 1 (numbers 5, 6, 7, and 8) were selected for these measurements based on the quality of the cell surface. The cell configuration and the high reflectivity of the samples were among the factors considered in the determination of the optical configuration to be used.

Variable temperature measurements were performed with a three-zone, high-temperature furnace designed and built at NASA.⁴⁵ A cross-section of this furnace is shown in Figure 2.⁴⁶ The sample is attached to or placed in a sample holder and located in the middle zone. Optical access is effected through coated heat rejection windows.

Each zone is independently controlled and its temperature monitored by a programmable temperature controller (Barber-Colman model no. 570). These three controllers allow for the establishment of sequential programming (up to eight sequences within each of four possible programs) of a desired starting temperature, an end temperature (both in degrees Centigrade) and sequence duration (in fractions or multiples of minutes or hours). Any program-sequence can be initiated, held constant or stopped at any given time.

The sample cells were handled with polyethylene gloves and thoroughly cleansed with ethanol (99.9%) prior to placing inside the furnace cavity. This is required to avoid cell cracking or damage due to dust or excess sodium. Since the alloys expand upon freezing, every effort was made to maintain a temperature gradient throughout the zones. For all temperatures, other than at or very near room temperature, the top zone was maintained at temperatures hotter than the middle zone and it, in turn, kept hotter than the bottom zone. All samples were heated at a rate of approximately 1 °C/min., allowing for the temperature differences. Each zone was also allowed to achieve equilibrium by holding the temperatures constant at several intervals. It was during these intervals, which lasted between thirty and ninety minutes, that the spectra were recorded. After the alloys were completely liquefied, the samples were rapidly quenched (by cutting-off all electrical

Figure 1:
SAMPLE CELLS

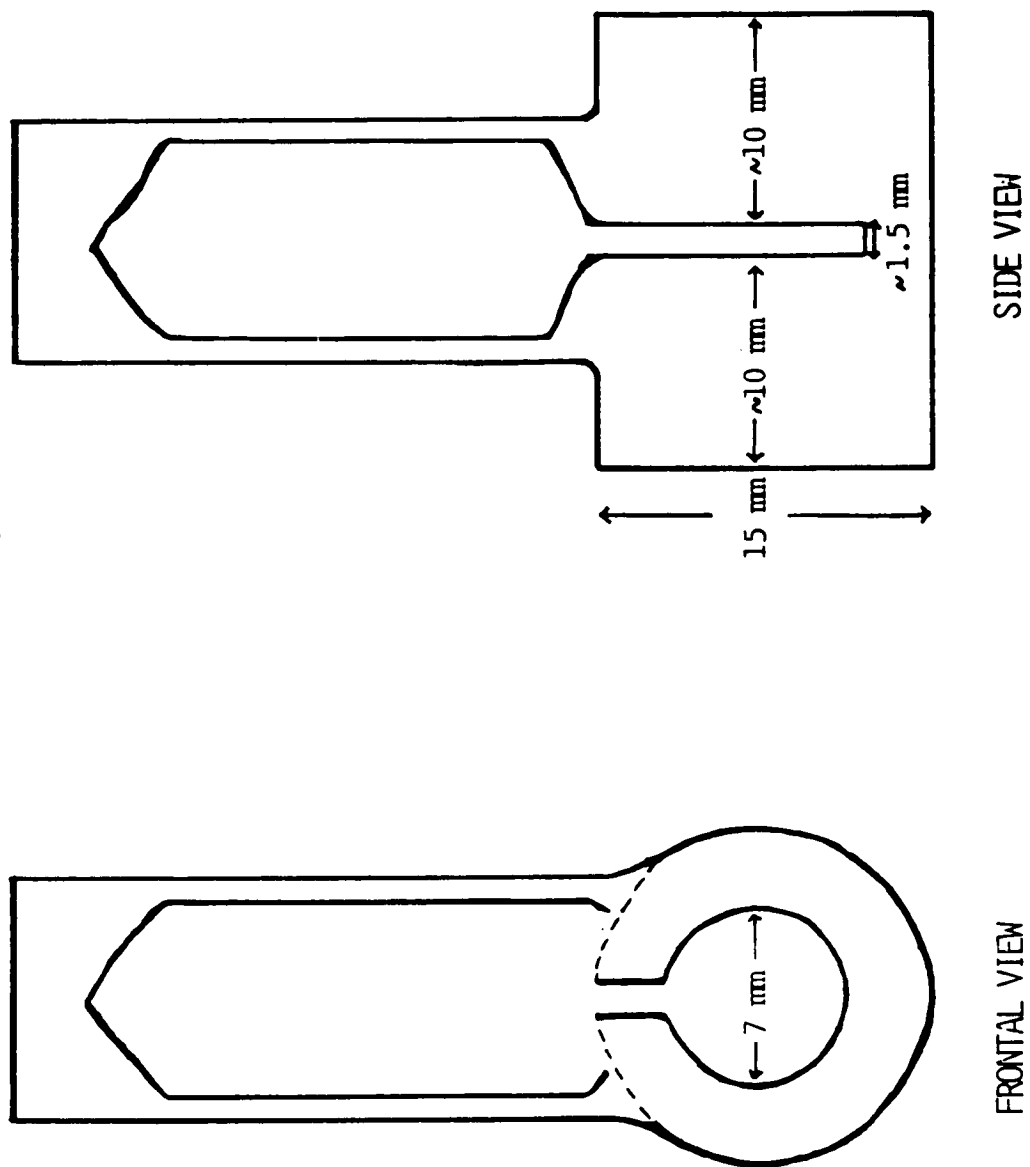
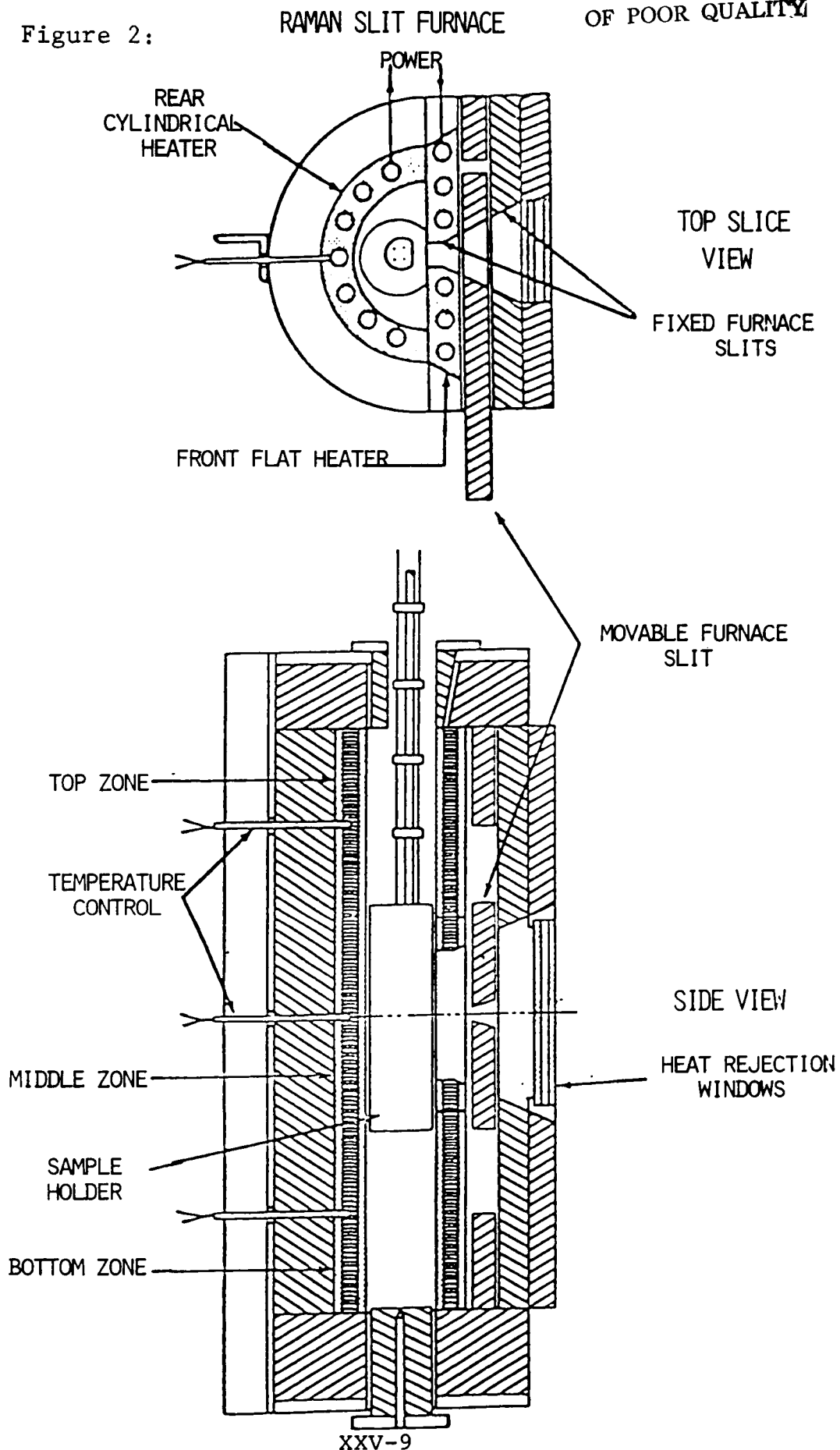


Table 1

<i>f</i>	<i>x</i>	Solidus (°C)	Liquidus (°C)	Thickness (mm)
1	0.205	707	794	1.371
2	0	670	670	1.797
3	0.051	679	702	1.341
4	0.107	689	731	1.412
5	0.301	727	841	1.485
6	0.204	707	794	1.438
7	0	670	670	1.161
8	0.053	679	703	1.221

Figure 2:



power to the furnace) to avoid CdTe segregation in samples where $x > 0$.

The cells were fixed in place by the sample holder. Two different sample holders were used during the course of this work (see Figures 3,⁴⁶ and 4), each with at least three type-K (chromel-alumel) thermocouples used to monitor either the three zone temperatures, or the top, middle and bottom of the cells, respectively. The thermocouple outputs were connected to a data acquisition/control unit (Hewlett-Packard model no. 3497A) via a 20-channel thermocouple acquisition plug-in assembly (Hewlett-Packard model no. 44422A). The HP-3497A was interfaced to a personal computer (Hewlett-Packard model no. 85B). A computer program, originally developed by F. R. Szofran and modified for these purposes, was used to evaluate voltage-to-temperature conversions with respect to an internal reference, and plot temperatures, from various channels, versus selected acquisition time intervals. Temperature stability was maintained to an uncertainty of $\pm 2^\circ\text{C}$.

The experimental configuration used for the measurements reported here is shown in Figure 5. The 5145 Å line of a continuous-wave argon ion laser (Spectra Physics model no. 165) was used as the excitation source. The positioning optics consisted of a double-mirror combination to raise the laser beam to the same plane as the spectrometer slit, an iris and an optical filter that rejects all but the 5145 Å line. The incident laser beam was then focused with a cylindrical lens (focal length of 300 mm), reflected by a small front-surface mirror into the furnace and onto the sample. This focuses the beam into a rectangular cross-section, or line image, parallel to the spectrometer entrance slit. The incident laser power was maintained at or below 250 mW to further diminish background scattering from entering the spectrometer. This is best achieved by operating the laser in the light (power-stabilized) mode.

The scattered light is then collected and focused by a double lens assembly (focal length of 300 mm), placed immediately behind the small mirror, and a single lens (focal length of 254 mm). This lens combination (see Figure 6) offered a good match with the spectrometer optics. The 0.85 m double monochromator (Spex model no. 14018) was equipped with 1800 grooves/mm gratings. The spectrometer slit settings are very important in determining the experimental resolution; but, another equally important factor is the total amount of signal collected and used for detection. Since the use of the backscattering geometry technique, in which both the incident and scattered light

Figure 3:

ISOTHERMAL SAMPLE HOLDER

ORIGINAL PAGE IS
OF POOR QUALITY

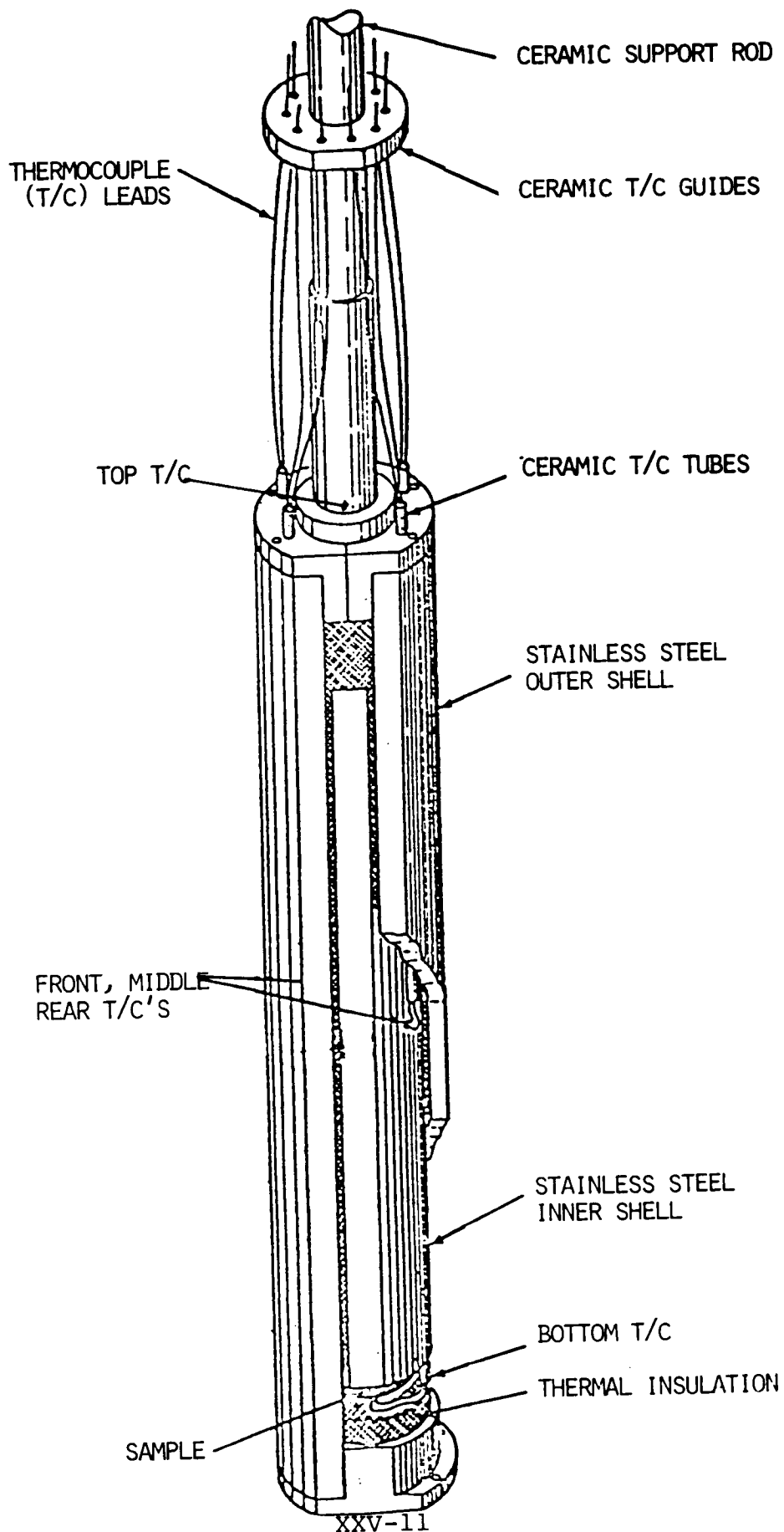


Figure 4:

SAMPLE HOLDER

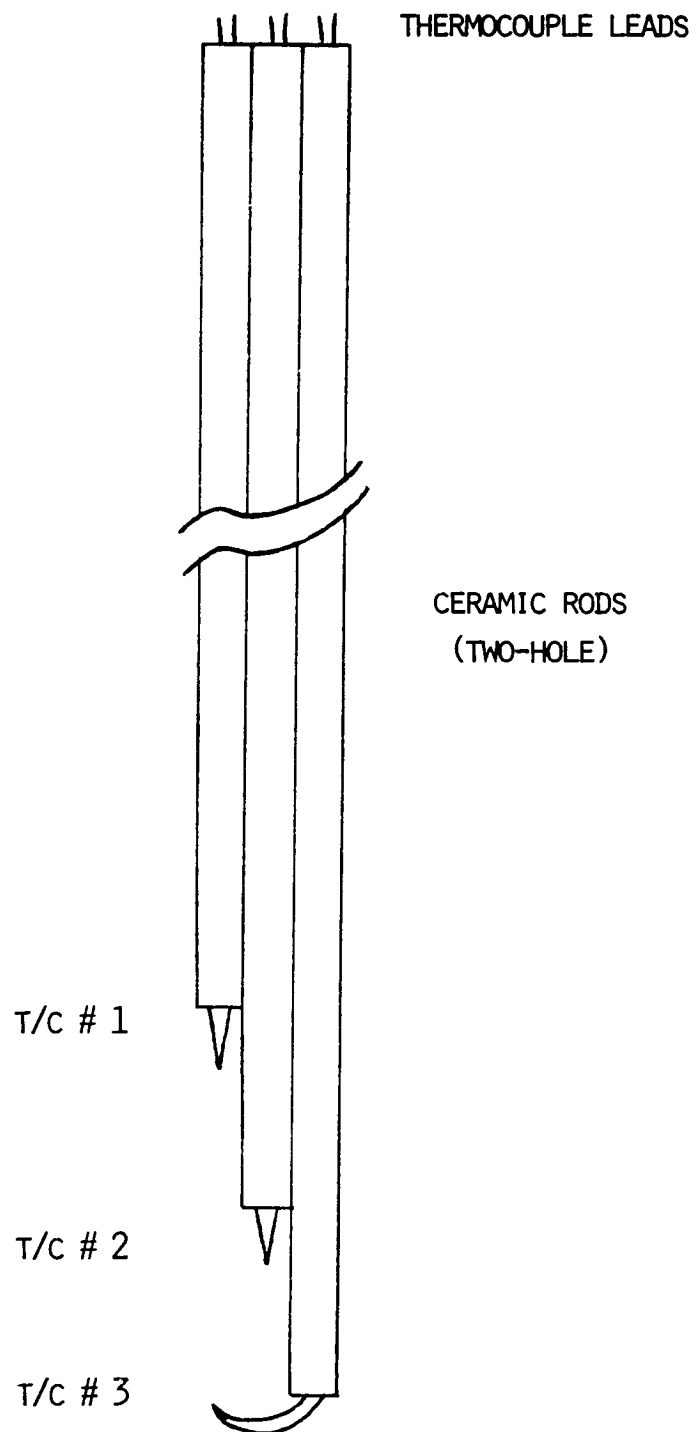


Figure 5: SCHEMATIC OF EXPERIMENTAL CONFIGURATION

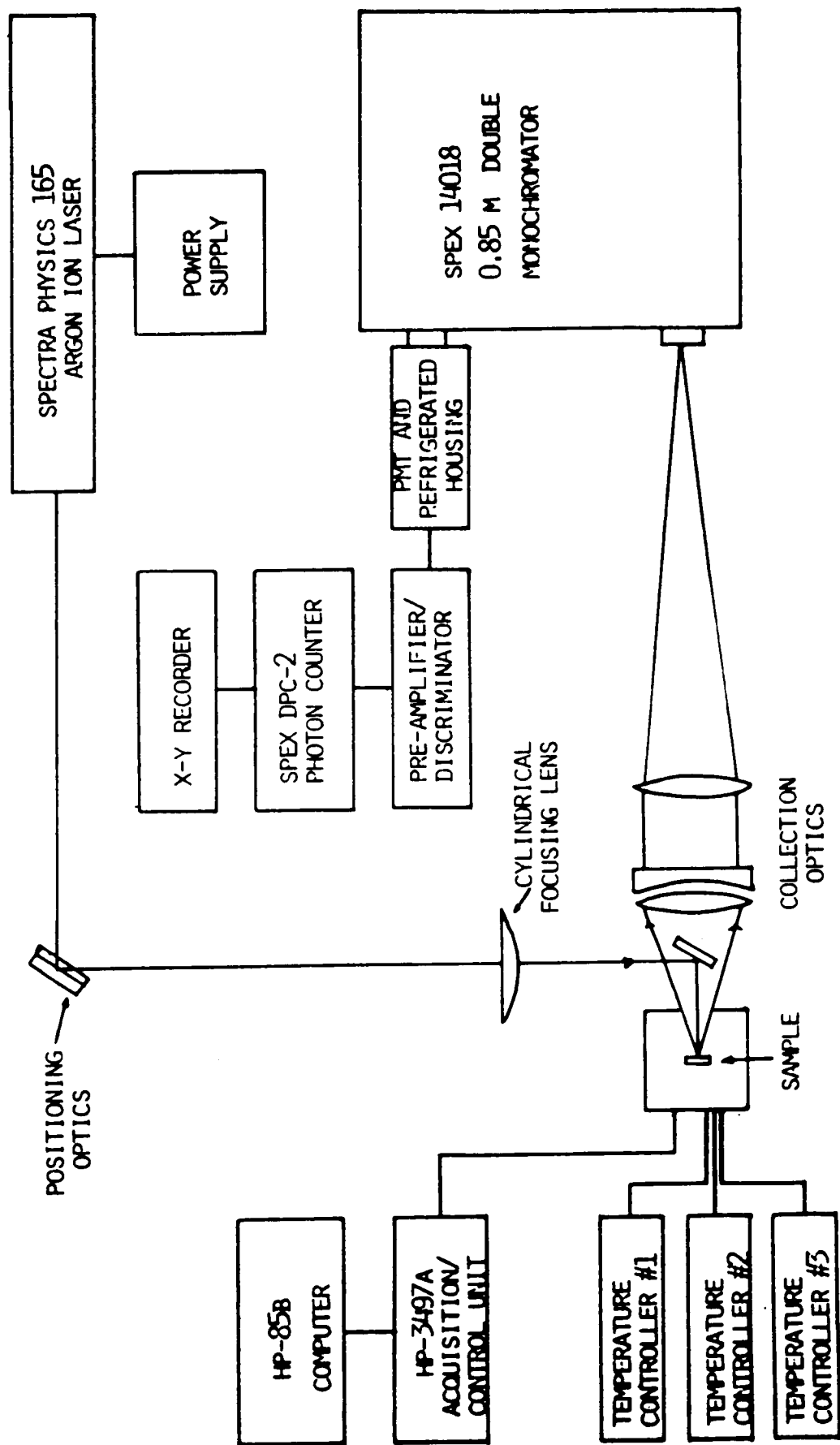
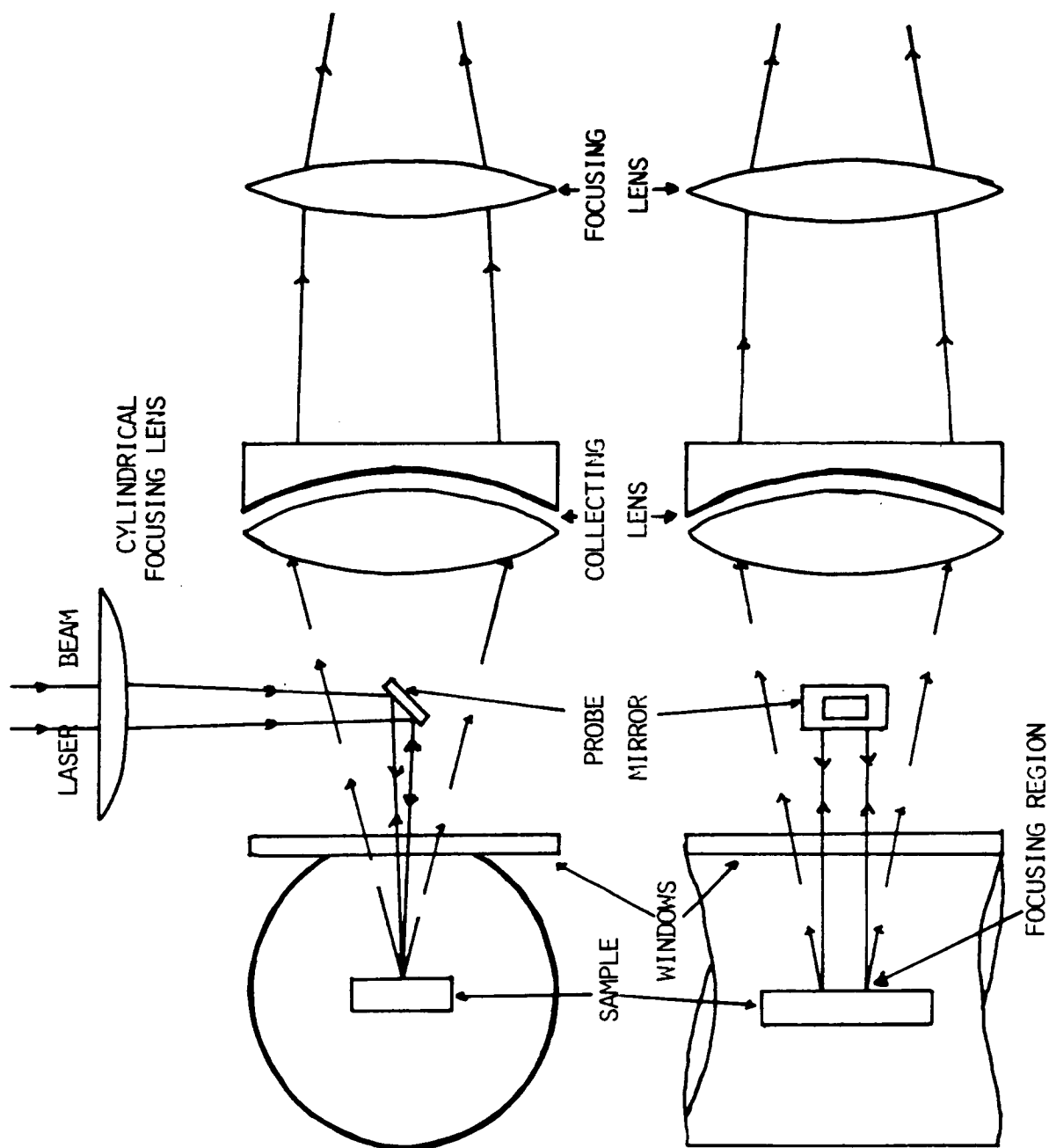


Figure 6: SCHEMATIC OF LASER PROBE AND BACKSCATTER COLLECTION OPTICS



are co-linear, also allows for a line image focus onto the spectrometer slit. The entrance slit was kept at settings that would allow for a maximum collection of the scattered light. Typical settings were 0.5 mm - 1.0 mm - 0.5 mm slit widths for the three spectrometers slits and fully opened (2 cm) slit-height. Thus, a major portion of the scattered signal is collected at the sacrifice of increased spectral bandpass (approximately $5\text{-}6\text{ cm}^{-1}$).

The advantages and disadvantages of the backscattering technique have been describe by others.⁴⁷⁻⁴⁹ The primary concerns for this work are excitation/collection from only one, reflective sample surface, vertical line focus and minimization of local heating. It should be noted that caution is required to prevent direct laser beam reflection into the spectrometer and detector. This can cause unwanted laser-line ghosts, swamp the Raman signals in addition to possible damage to the detector.

The signals were detected by a refrigerated ($-45\text{ }^{\circ}\text{C}$) photomultiplier tube (EMI tube model no. 9658 RAM, and housing model no. CH-25). The output is fed into a pre-amplifier/discriminator and into a digital photon counter (Spex model no. DPC-2). Typical dark counts were less than 200 counts/sec, while signals were on the order of 10^5 counts/sec. The spectra were then recorded by scanning the spectrometer ($0.2\text{ cm}^{-1}/\text{sec}$) and displayed on an X-Y recorder (Hewlett-Packard model no. 7034A or 7044A).

A series of preliminary procedures were undertaken prior to the performance of the experiments discussed here so as to ensure a successful outcome. The double monochromator was calibrated with a 200W Hg-Xe arc lamp (Oriel model no. 8500). Optical alignments of the experimental configuration was effected by removing the photomultiplier tube and replacing it wiht a low-power He-Ne laser (Spectra Physics model no. 155A). This back-alignment procedure was used to determine and optimize the optical path to be used for the optics and sample positions relative to the Ar^+ ion laser beam. To confirm that this optical arrangement was feasible for detection of Raman signals, carbon tetrachloride (CCl_4) was loaded into a sample cell similar to those used in these experiments and placed inside the furnace in a manner typical of the configuration to be used later. The expected Raman bands (~ 214 , 314 , and 460 cm^{-1}) were easily detected. Subsequently, preliminary runs with all the samples at room temperature were performed. Adequate safety precautions were also taken. A vented plexi-glass enclosure was designed around the upper part of the furnace, and near the working station. This

provides adequate operator safety in the event of a sample cell explosion.

RESULTS

The results are reported not in chronological order, but in order of increasing Cd composition for clarity. Preliminary measurements were performed on all samples to discern the most likely candidate for which strong Raman scattering signals could be obtained. Once this was established we proceeded in order of increasing liquidus temperatures. All temperature measurements were performed for one sample at a time.

A. HgTe

The Raman spectra of the HgTe sample for various temperatures are shown in Figures 7, 8, and 9. All spectra were recorded with increasing temperature and a spectral bandpass of 5 cm^{-1} . The most salient features are the decrease in intensity and shift towards lower frequency of the room temperature 128 cm^{-1} peak, the shift towards lower frequency of the very broad (18 cm^{-1}) band centered around 254 cm^{-1} , and the appearance of a strong broad (8 cm^{-1}) peak centered around 142 cm^{-1} with increasing temperature. The intensity enhancement of this latter band is most evident in the region between 700°C and 751°C . The difference between the two spectra recorded at 700°C (see Figure 9) is that the uppermost spectrum was taken after a refocusing of the optics for the lower spectrum. This effect was also noticed for all other recorded Raman spectra as the liquidus temperatures were approached from below and surpassed. This may be due to an actual sample shift or settling in the molten state.

B. $\text{Hg}_{0.95}\text{Cd}_{0.05}\text{Te}$

The Raman spectra as a function of temperature for the 5% Cd composition sample are shown in Figures 10 through 14. As in the previous examples, all spectra were obtained with a spectral bandpass of 5 cm^{-1} . The 128 cm^{-1} peak observed in the HgTe sample is also detected here, but the shift towards lower frequency as well as the decrease in intensity with increasing temperature is most prominent in this sample. The shift is about 35 cm^{-1} . This is equally true for all features observed in the spectra. It should be noted that during the heating and detection sequence for this sample several adjustments in the optical focus had to be made. This may account for the different lineshapes observed for the same features, and for the almost disappearance of any detectable signal between 597°C and 704°C .

Figure 7

HgTe

$\lambda_{\text{exc.}} = 5145 \text{ \AA}$

1.0 M PC/s

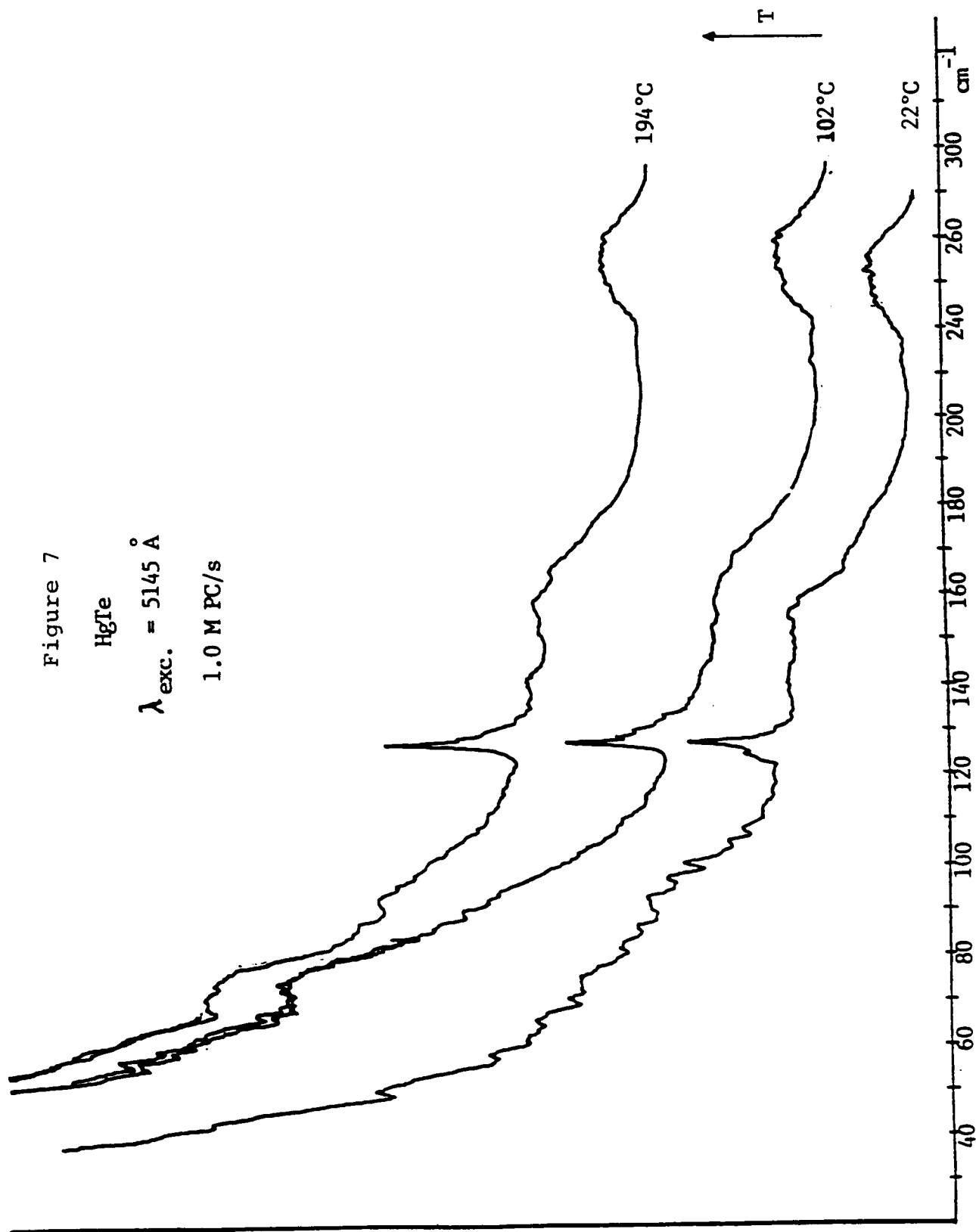


Figure 8

HgTe

$\lambda_{\text{exc.}} = 5145 \text{ \AA}$

1.0 M PC/s

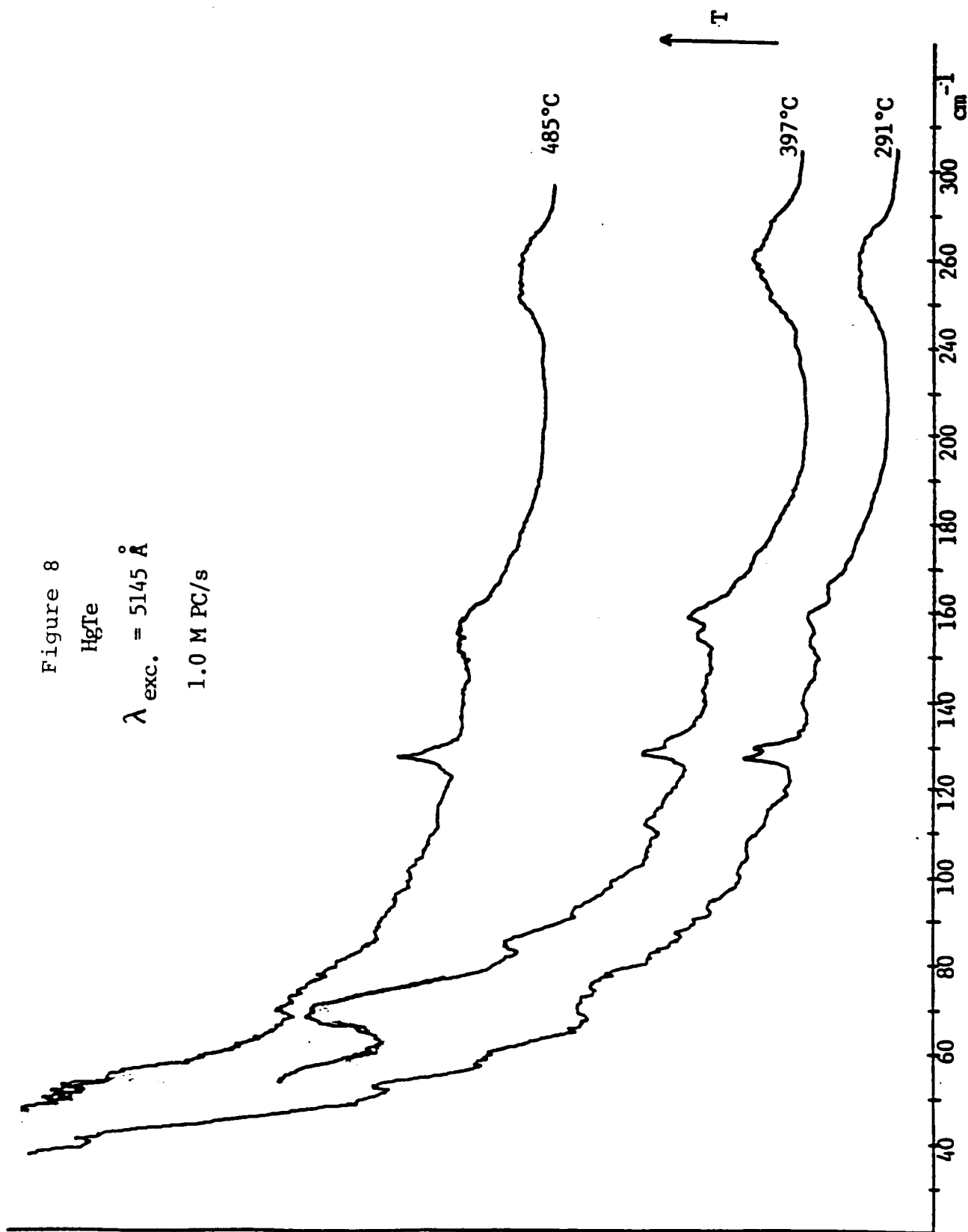
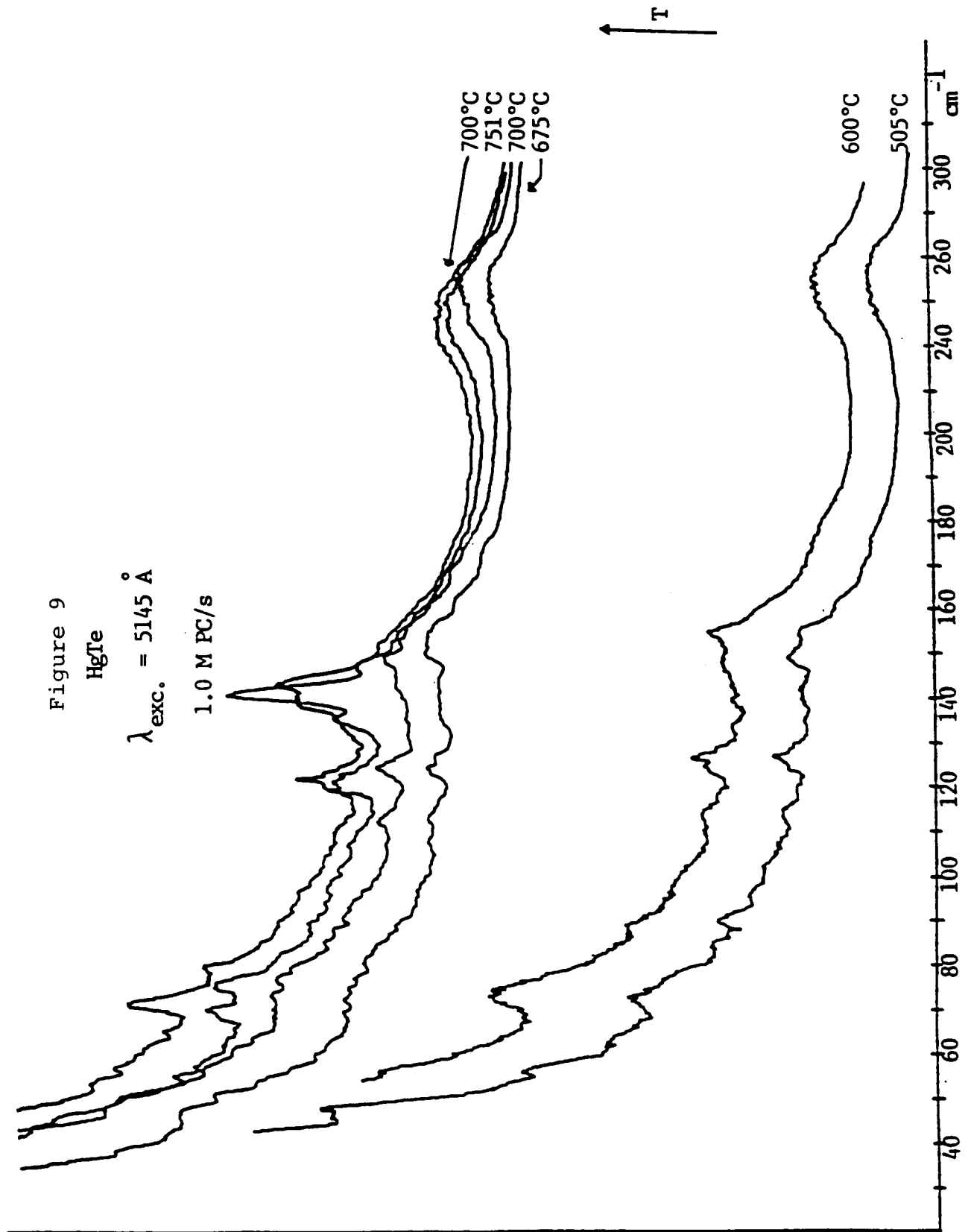


Figure 9

HgTe

$\lambda_{\text{exc.}} = 5145 \text{ \AA}$

1.0 M PC/s



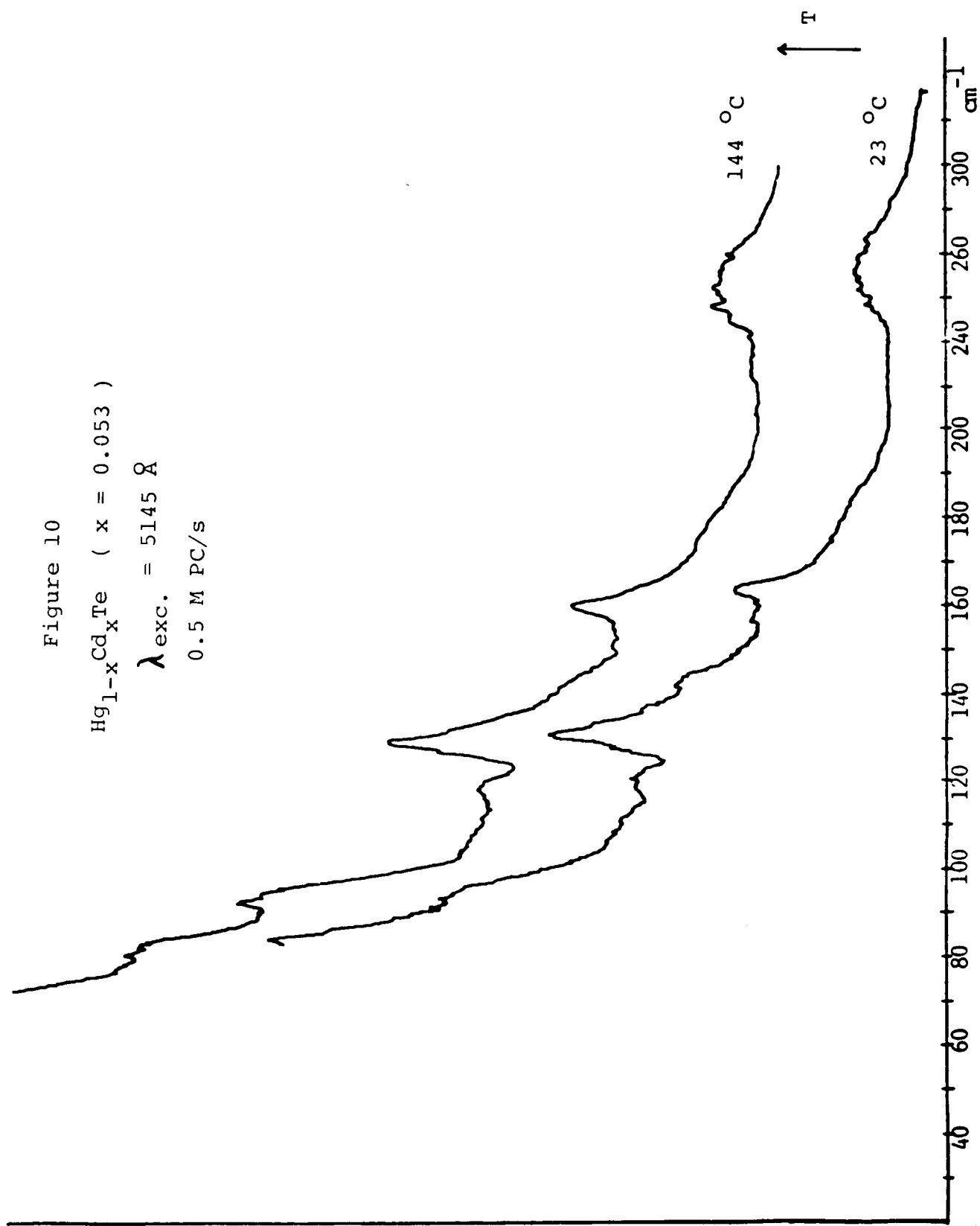


Figure 10

$\text{Hg}_{1-x}\text{Cd}_x\text{Te}$ ($x = 0.053$)

$\lambda_{\text{exc.}} = 5145 \text{ \AA}$

0.5 M PC/s

Figure 11

$\text{Hg}_{1-x}\text{Cd}_x\text{Te}$ ($x = 0.053$)

$\lambda_{\text{exc.}} = 5145 \text{ \AA}$

1.0 M PC/s

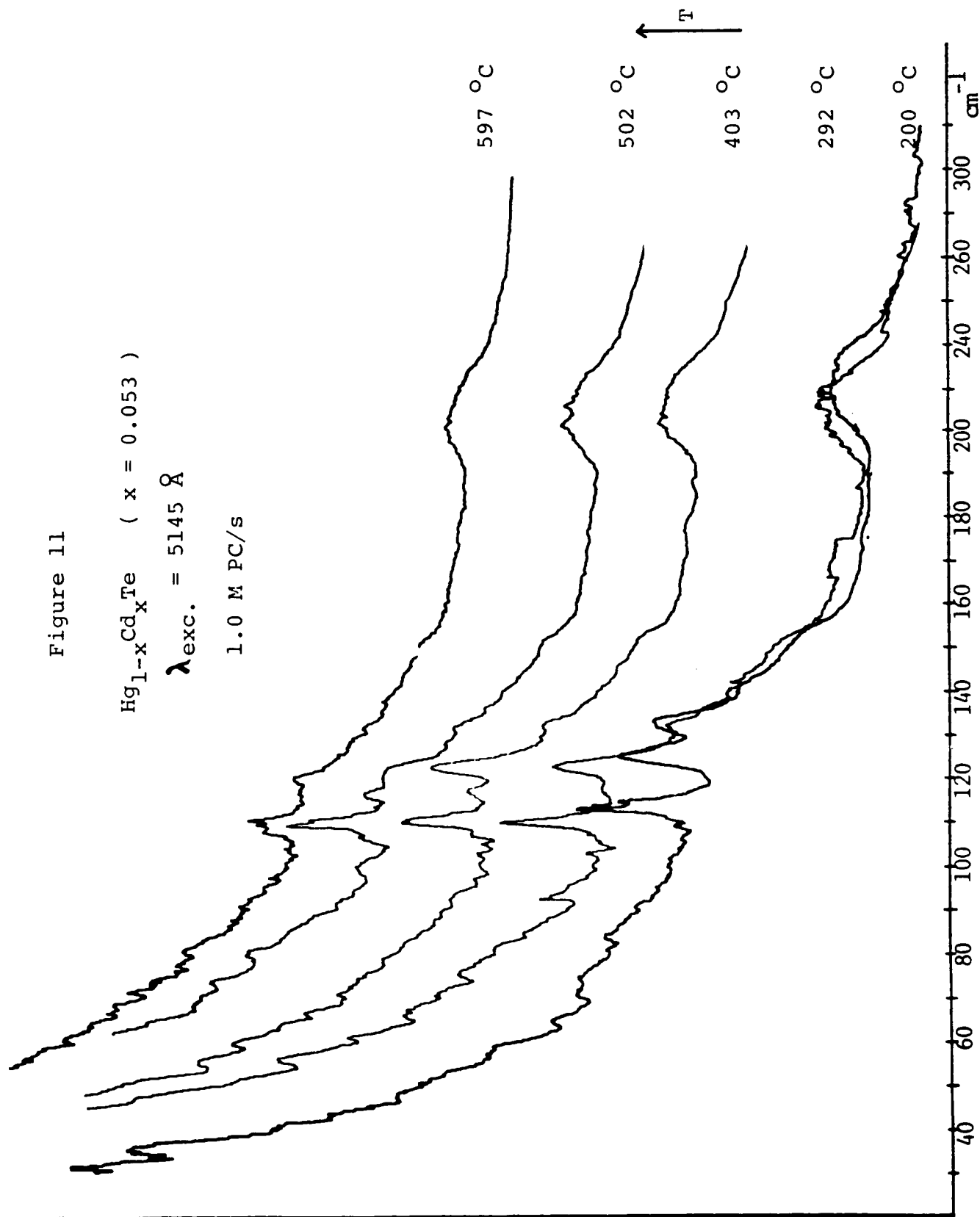


Figure 12

$\text{Hg}_{1-x}\text{Cd}_x\text{Te}$ ($x = 0.053$)

$\lambda_{\text{exc.}} = 5145 \text{ \AA}$

1.0 M PC/s

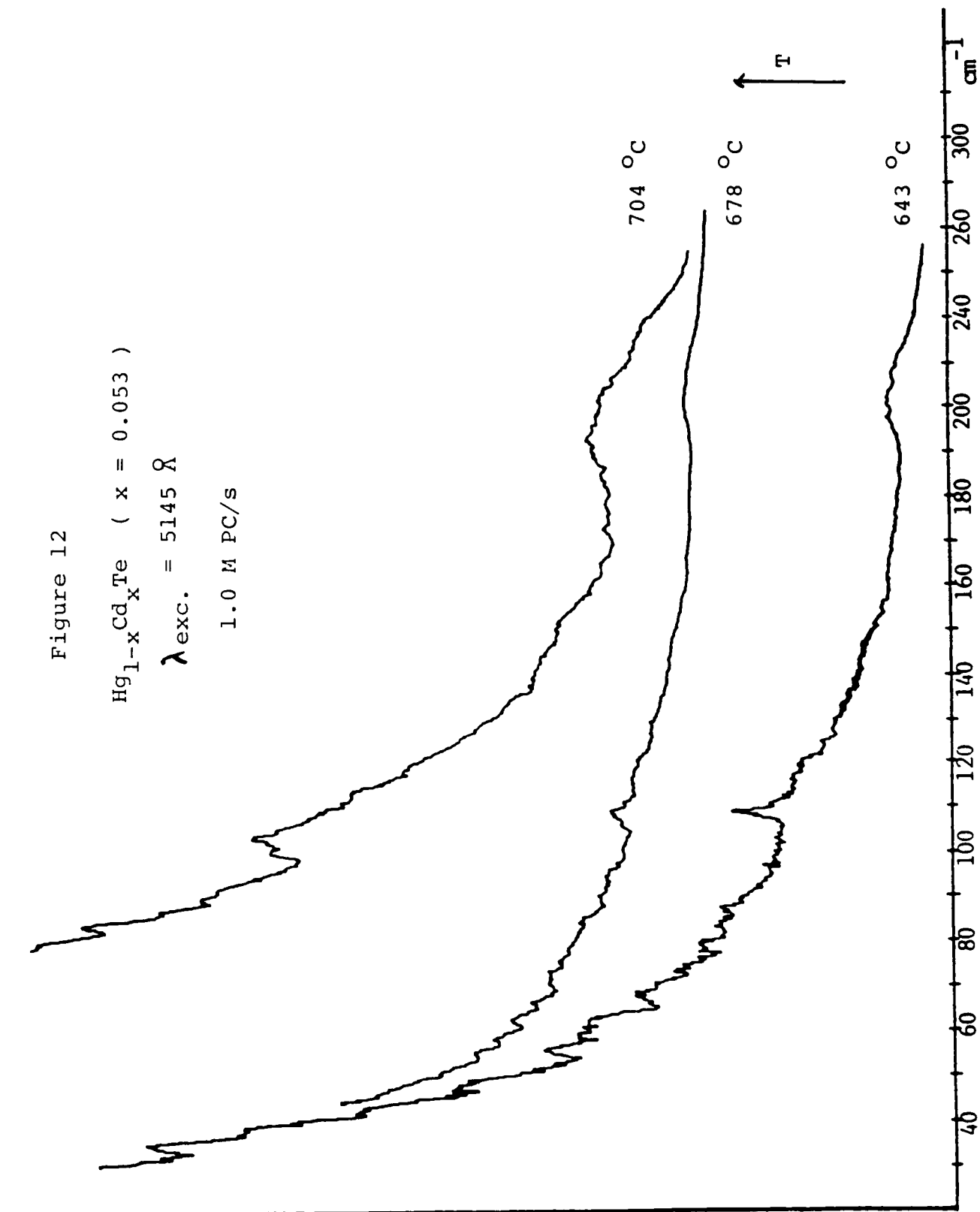


Figure 13

$\text{Hg}_{1-x}\text{Cd}_x\text{Te}$ ($x = 0.053$)

$\lambda_{\text{exc.}} = 5145 \text{ \AA}$

1.0 M PC/s

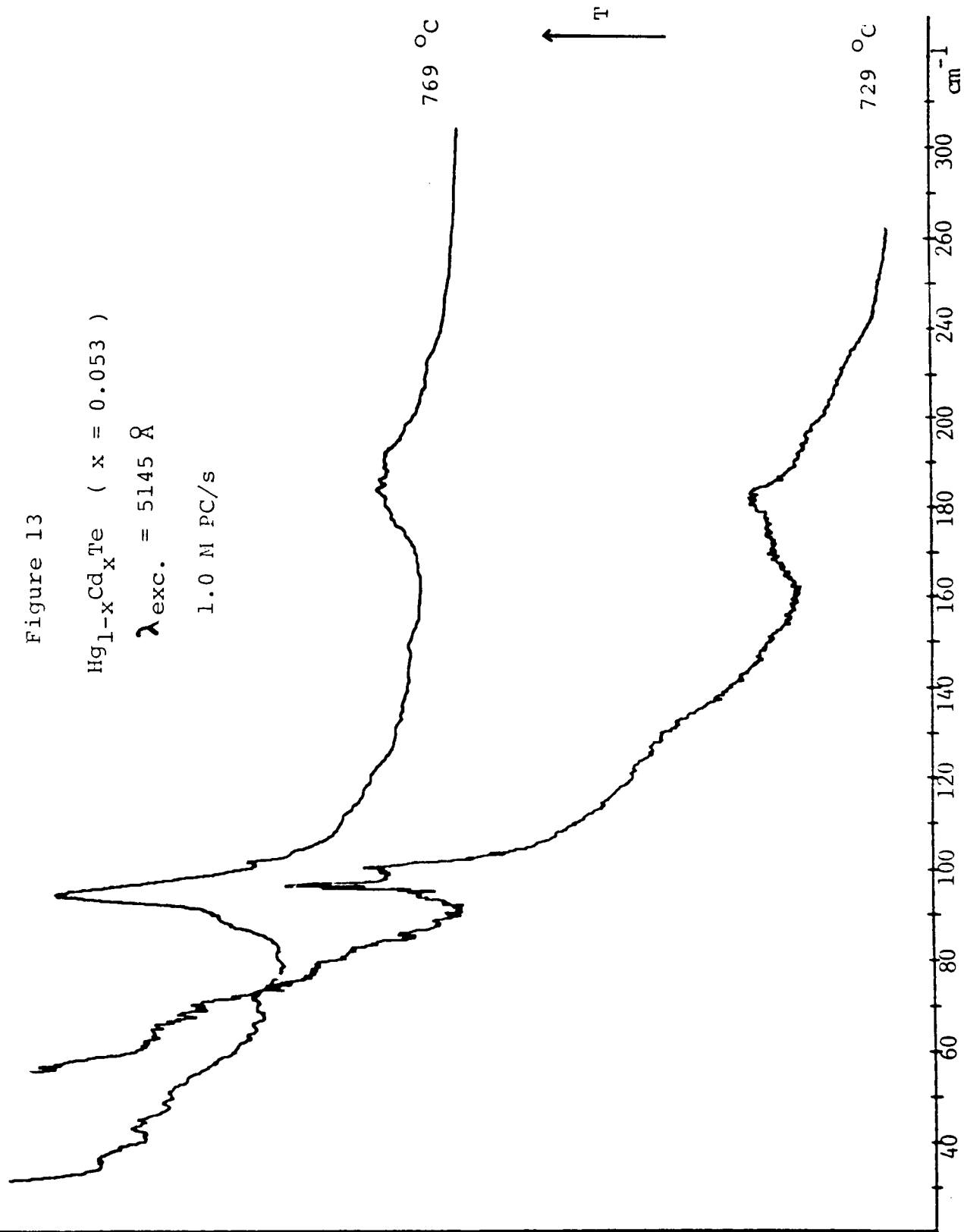
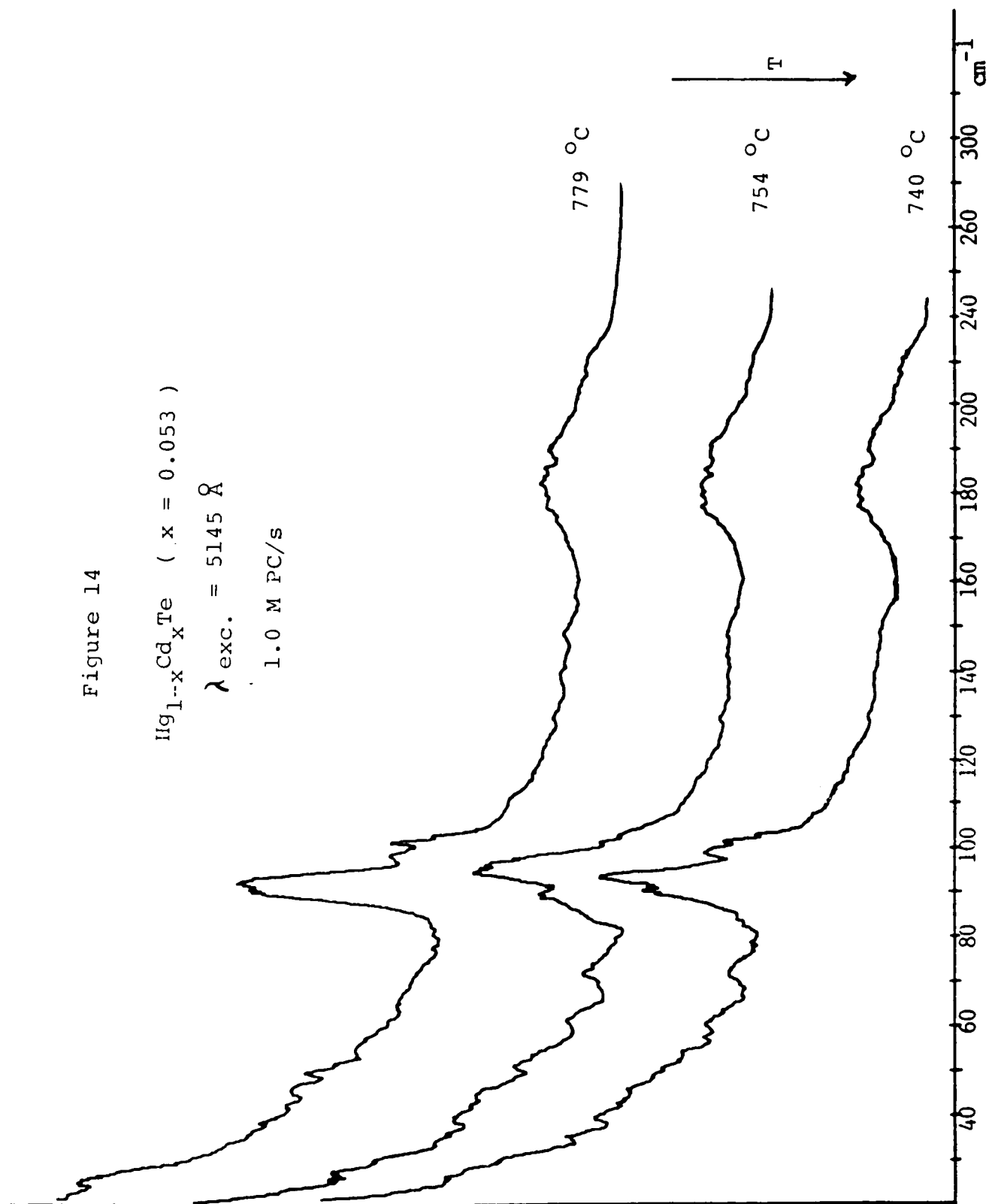


Figure 14

$\text{Hg}_{1-x}\text{Cd}_x\text{Te}$ ($x = 0.053$)

$\lambda_{\text{exc.}} = 5145 \text{ \AA}$

1.0 M PC/s



C. $\text{Hg}_{0.796}\text{Cd}_{0.204}\text{Te}$

The Raman spectra as a function of temperature for this 20% Cd composition sample are presented in Figures 15 through 18. Chronologically, this was the first sample on which the series of experiments were performed; it also produced the most dramatic signal enhancements with increased temperature. The spectra shown in Figure 15 were recorded with a spectral bandpass of 2.5 cm^{-1} and an incident laser power of 400 mW. The Raman signals were not easily detected as the temperature of the sample was increased, particularly for the series of spectra recorded between 106°C and 500°C . During this run we observed the first shifts in the scattered signal light relative to the entrance slit. Because these shifts caused significant decreases in the total collected signal, it was deemed necessary to maximize this amount (by increasing the slit widths) at the expense of a greater spectral bandpass. All subsequent spectra were then recorded under the same conditions. As seen in Figure 17, the intensity of the band at 128 cm^{-1} increases between 765°C and 853°C , decreases in intensity when the temperature is lowered to 750°C , and does so by a factor of two when a temperature of 691°C is attained.

D. $\text{Hg}_{0.70}\text{Cd}_{0.30}\text{Te}$

Only room temperature spectra were recorded for this alloy composition. The only difference between the room temperature spectra of the 20% sample and this 30% sample is that the latter exhibits weaker intensities for the same signals. Consequently, it was the last sample to be run for the series and not fully completed.

Figure 15

$\text{Hg}_{1-x}\text{Cd}_x\text{Te}$ ($x = 0.204$)

$\lambda_{\text{exc.}} = 5145 \text{ \AA}$

20.0 K PC/s

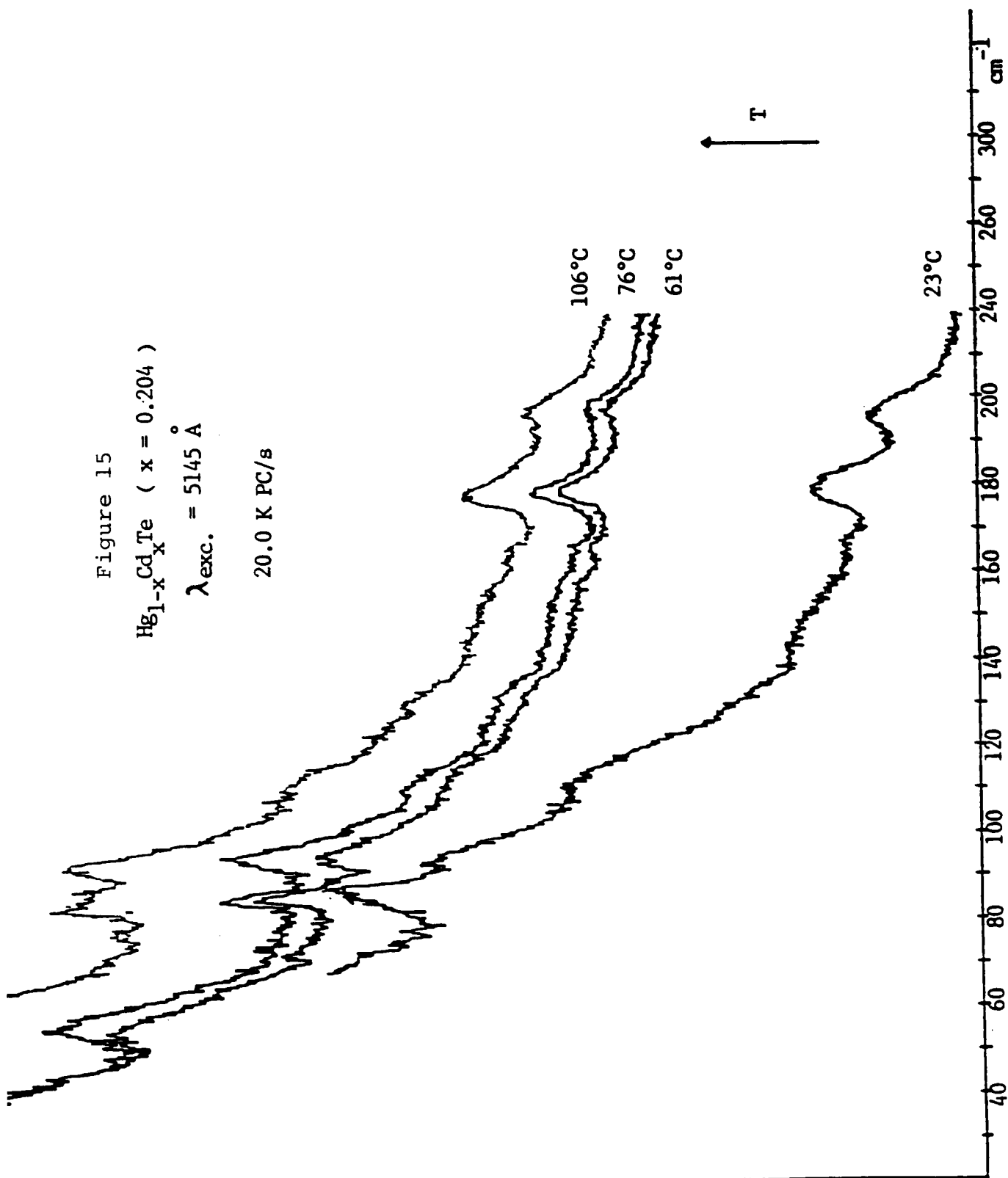
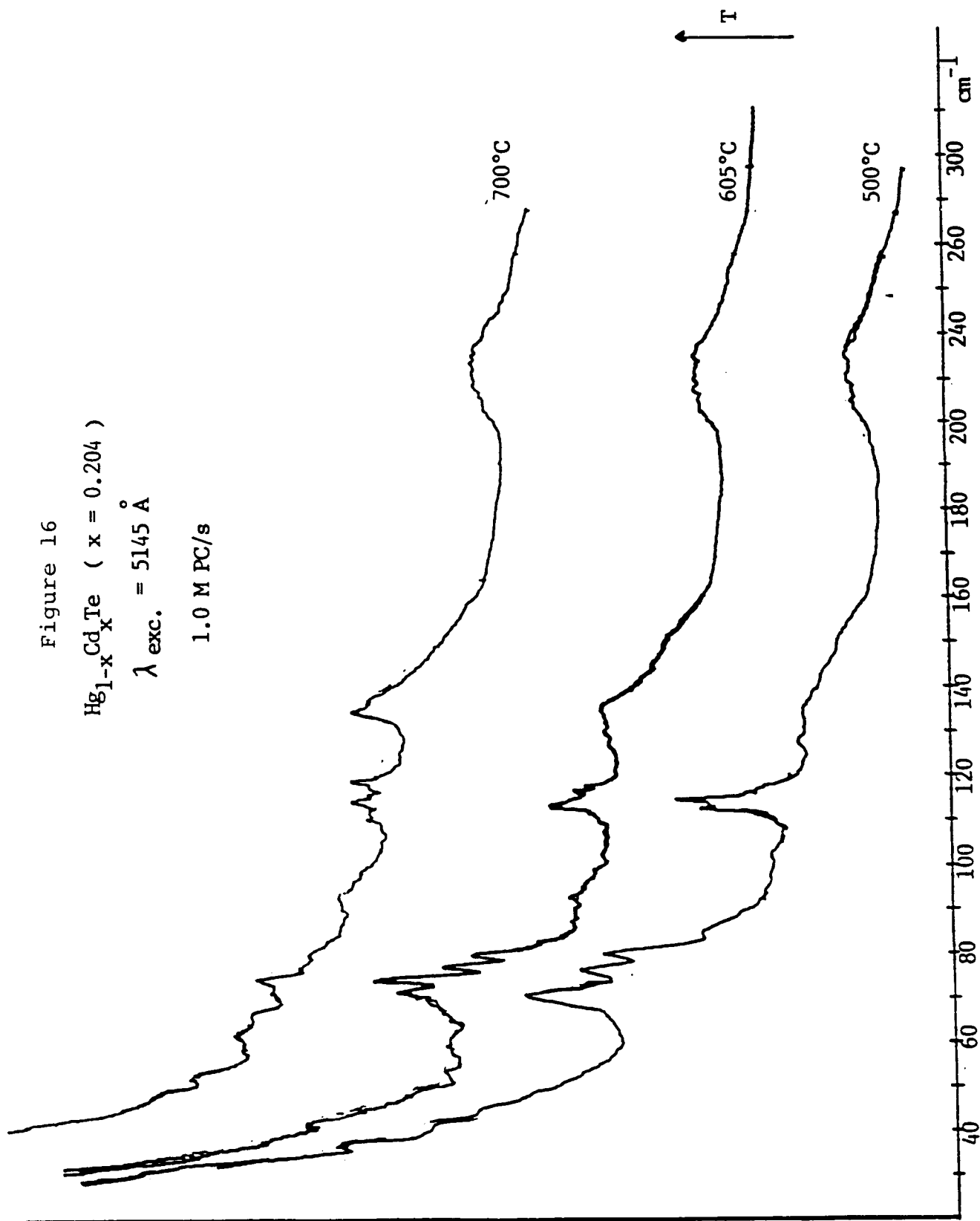


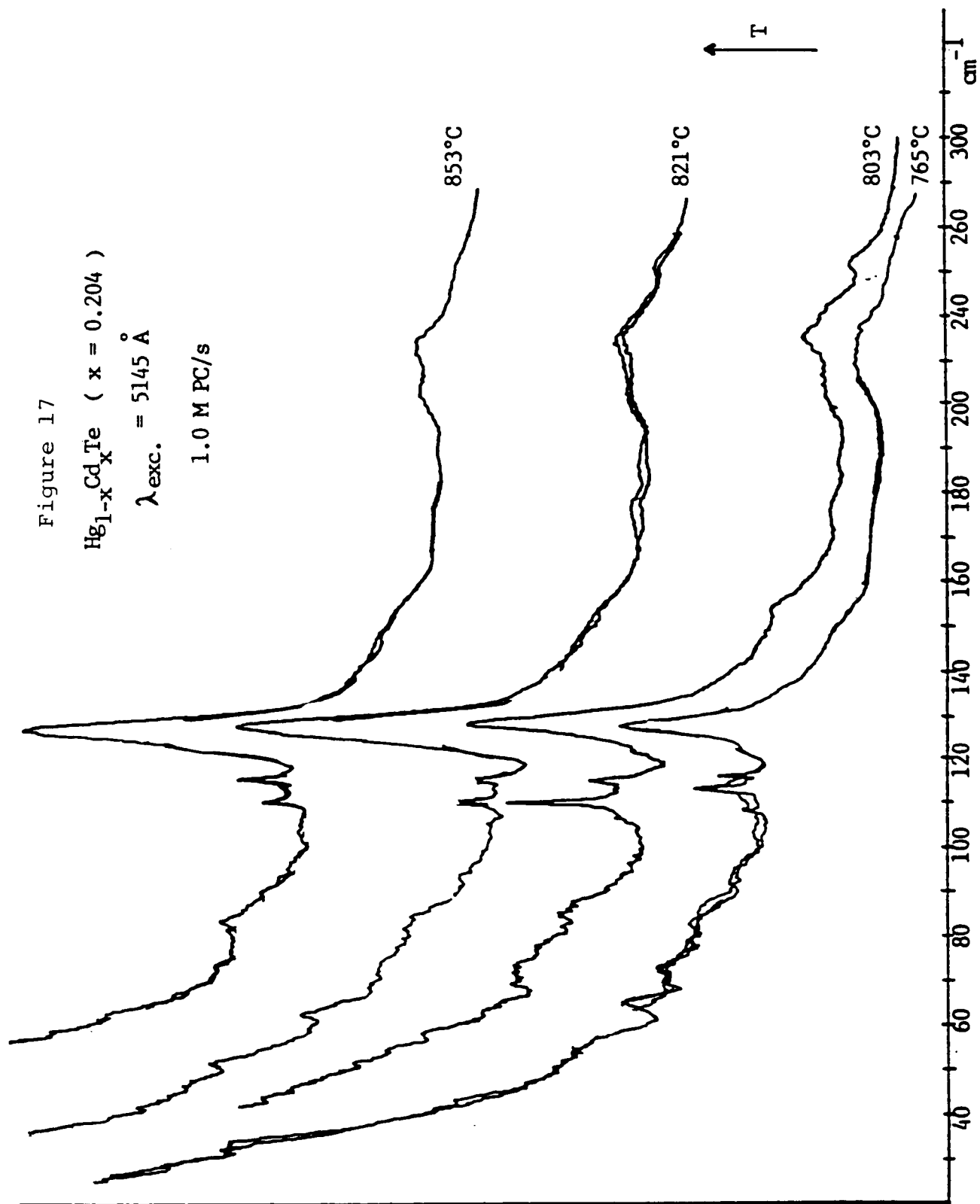
Figure 16

$\text{Hg}_{1-x}\text{Cd}_x\text{Te}$ ($x = 0.204$)

$\lambda_{\text{exc.}} = 5145 \text{ \AA}$

1.0 M PC/s





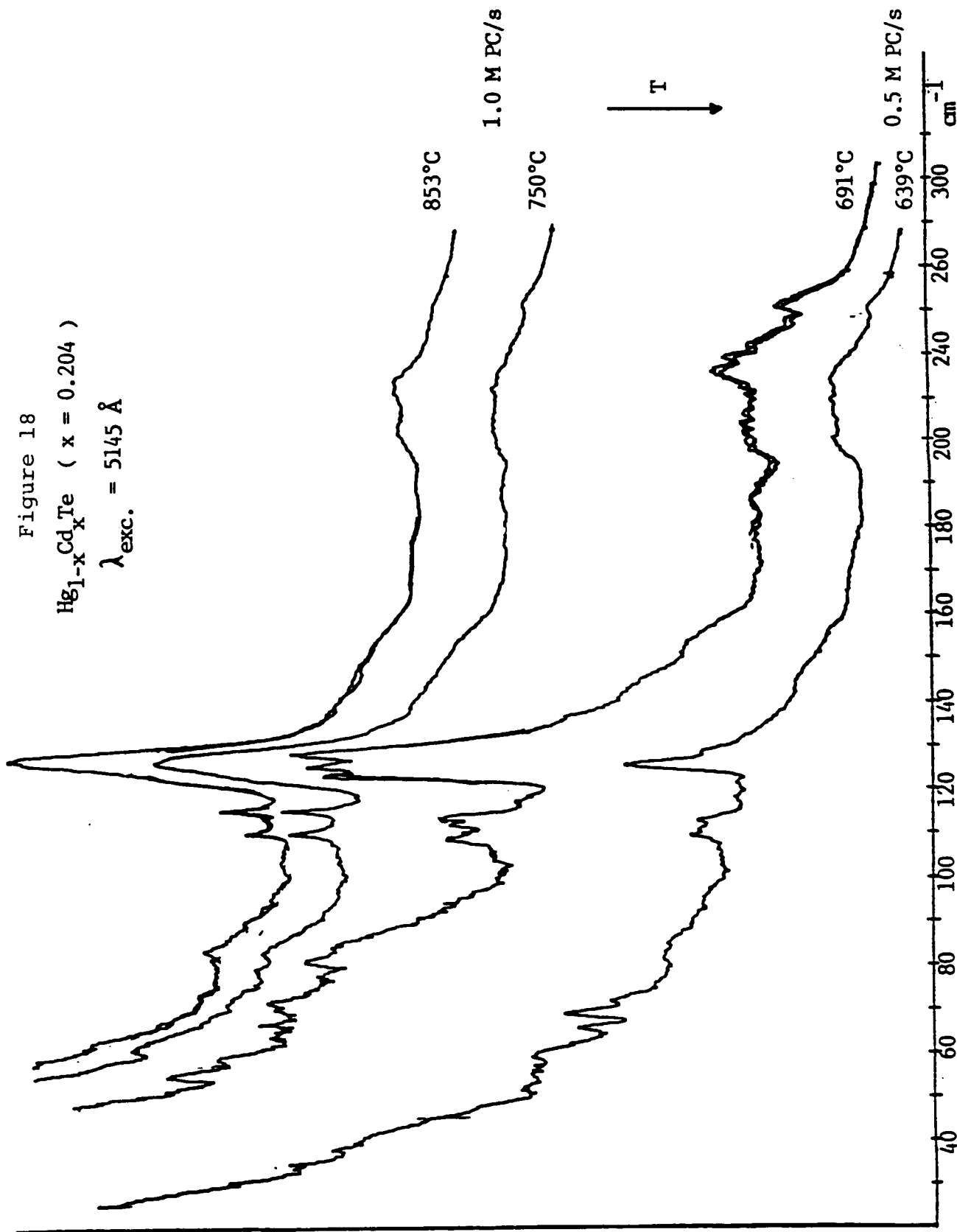


Figure 18
 $\text{Hg}_{1-x}\text{Cd}_x\text{Te}$ ($x = 0.204$)
 $\lambda_{\text{exc.}} = 5145 \text{ \AA}$

CONCLUSION

We have presented Raman scattering data for Hg-rich $\text{Hg}_{1-x}\text{Cd}_x\text{Te}$ melts. The spectra exhibit dramatic intensity enhancements for modes which can be associated with structural phase transitions for each sample composition studied. This argument is consistent with those previously suggested by others⁶⁻¹¹ to explain changes in thermal conductivities,⁶⁻¹⁰ and in thermal diffusivity.^{10,11} The measurements performed thus far do not indicate a soft-phonon mediated mechanism for this transition, although a 35 cm^{-1} shift to lower frequency was detected for the 5% Cd composition sample near its liquidus temperature.

These results are indeed very encouraging, but more needs to be done to complete the study. These measurements should be repeated for the same samples under similar conditions with shorter temperature intervals. This would aid in establishing the temperature width of the transition. In addition, the same experiments should also be performed for different excitation frequencies to confirm the phonon mode frequencies. This can be achieved by using the 4880 Å line of the Ar^+ ion laser used for these experiments. If this option is used, every precaution must be taken to assure that a direct change of excitation frequency from the laser does not alter the optical path of the incident light. A better solution would be to use a completely different laser source, such as a He-Ne or Kr^+ laser, which can be positioned such that the optical paths are not disturbed other than by switching one mirror to reflect either one of the two incident beams.

These changes do not affect an important element in the detection and analysis of the data, and that is the strong background scattering that is observed for all of these materials. A computer data acquisition/control interface to the digital photon counter and program should help in the analysis of the data. The scattered background can then be digitally subtracted from the recorded spectrum leaving only the relevant part of the spectrum.

In conclusion, the preliminary results presented here are important for they represent the first observation of Raman scattering in Hg-Cd-Te melts. These efforts need to be enhanced with the above suggestions to confirm the observed phonon frequencies associated with the structural transitions, and to develop theoretical arguments to interpret the data within the framework of those previously presented for resonance Raman studies in these materials²⁷.

REFERENCES

1. R. Dornhaus and G. Nimtz, in "Springer Tracts in Modern Physics, Solid State Physics", vol. 78, ed. by G. Hohler, Springer-Verlag, Berlin, 1976, P. 1 and references therein.
2. R. K. Willardson and A. E. Beer, eds., "Semiconductors and Semimetals", vol. 18, Academic Press, New York, 1981.
3. R. Dornhaus and G. Nimtz, in "Narrow Gap Semiconductors", Springer Tracts in Modern Physics, vol. 98, ed. by G. Hohler and E. A. Niekish, Springer-Verlag, Berlin, 1983, p. 119 and references therein.
4. W. D. Lawson, et. al., J. Phys. Chem. Sol. 9 (1959) 325.
5. S. L. Lehoczky, F. R. Szofran, and B. G. Martin, "Advance Methods for Preparation and Characterization of Infrared Detector Materials, Part I", NASA CR-161598, 1980, and references therein.
6. S. L. Lehozcky and F. R. Szofran, "Advanced Methods for Preparation and Characterization of Infrared Detector Devices, Part II", NASA CR-161949, 1981, and references therein.
7. S. L. Lehoczky and F. R. Szofran, in "Materials Processing in the Reduced Gravity Environment of Space", ed. by G. E. Rindne, North-Holland Publishing, Amsterdam, 1982, p.409.
8. P. Capper, et. al., J. Cryst. Growth 63 (1983) 154.
9. L. R. Holland, "Space Processing of Electronic Materials", NASA CR-170653, 1982.
10. L. R. Holland and R. E. Taylor, J. Vac. Sci. Technol. A1 (1983) 1615.
11. F. R. Szofran and S. L. Lehoczky, J. Cryst. Growth 70 (1984) 349.
12. D. L. Carter, M. A. Kinch, D. D. Buss, in "The Physics of Semimetals and Narrow-Gap Semiconductors", ed. by D. L. Carter and R. T. Bate, Pergamon Press, Oxford, 1971, p.273.
13. J. Baars and F. Sorger, Solid State Commun. 10 (1972) 875.

14. R. S. Kim and S. I. Narita, J. Phys. Soc. Japan **31** (1971) 613.
15. A. Polian, R. LeToullec and M. Balkanski, Phys. Rev. **B13** (1976) 3558.
16. M. Odet, et. al., Phys. Stat. Solidi **b92** (1979) 545.
17. S. P. Kozyrev, L. K. Vodopyanov and R. Triboulet, Solid State Commun. **45** (1983) 383.
18. S. P. Kozyrev, L. K. Vodopyanov and R. Triboulet, Sov. Phys. Solid State **25** (1983) 361.
19. S. C. Shen, J. H. Chu and H. J. Ye, in "Proceedings of the 17th International Conference on the Physics of Semiconductors", ed. by J. D. Chadi and W. A. Harrison, Springer-Verlag, New York, 1984, p. 1189.
20. D. N. Talwar and M. Vandevyver, J. Appl. Phys. **56** (1984) 1601.
21. L. K. Vodopyanov, et. al., in "Proceedings of the 17th International Conference on the Physics of Semiconductors", ed. by J. D. Chadi and W. A. Harrison, Springer-Verlag, New York, 1984, p. 947.
22. A. Mooradian and T. C. Harman, in "The Physics of Semimetals and Narrow-Gap Semiconductors", ed. by D. L. Carter and R. T. Bate, Pergamon Press, Oxford, 1971, p. 297.
23. P. M. Amirtharaj, et. al., in "Proceedings of the 17th International Conference on the Physics of Semiconductors", ed. by J. D. Chadi and W. A. Harrison, Springer-Verlag, New York, 1984, p. 1397.
24. P. M. Amirtharaj, K.-K. Tiong, and F. H. Pollak, J. Vac Sci. Technol. **A1** (1983) 1744.
25. K.-K. Tiong, et. al., Solid State Commun. **50** (1984) 891.
26. P. M. Amirtharaj, et. al., J. Vac Sci. Technol. **A3** (1985) 226.
27. J. Menendez, M. Cardona, and L. K. Vodopyanov, Phys. Rev. **B31** (1985) 3705.
28. D. J. Olego, J. P. Faurie, and P. M. Raccah, Phys. Rev. Lett. **55** (1985) 328.

29. Y. A. Aleshchenko and L. K. Vodopyanov, *Sov. Phys. Solid State* **28** (1986) 1623.
30. G. Lucovsky, M. H. Brodsky and E. Burstein, *Bull. Am. Phys. Soc.* **15** (1970) 382.
31. C. V. Raman and T. M. K. Nedungadi, *Nature* **145** (1940) 147.
32. J. F. Scott, *Rev. Mod. Phys.* **46** (1974) 83.
33. D. M. Hanson, *J. Chem. Phys.* **63** (1975) 5046.
34. W. Hayes and R. Loudon, "Scattering of Light by Crystals", Wiley-Interscience, New York, 1978.
35. A. Anderson, ed., "The Raman Effect", Marcel-Dekker, New York, vol. 1, 1971, and vol. 2, 1973.
36. *Advances in Raman Spectroscopy* **1** (1971) and subsequent volumes of this periodical.
37. M. Balkanski, in "Narrow-Gap Semiconductors: Physics and Applications", ed. by W. Zawadzki, *Lecture Notes in Physics*, vol. 133, Springer-Verlag, Berlin, 1980, p. 67.
38. M. Cardona, in "Light Scattering in Solids II", ed. by M. Cardona and G. Guntherodt, Springer-Verlag, Heidelberg, 1982, p. 19.
39. A. Compaan and H. J. Trodahl, *Phys. Rev.* **B29** (1984) 793.
40. J. Menendez and M. Cardona, *Phys. Rev.* **B31** (1985) 3696.
41. W. Kauschke and M. Cardona, *Phys. Rev.* **B35** (1987) 9619.
42. C. V. Raman and K. S. Krishnan, *Nature* **121** (1928) 501.
43. J. Behringer, in "Molecular Spectroscopy", ed. by R. F. Barrow, D. A. Long and D. J. Millen, *Specialist Periodical Reports*, vol. 2,, The Chemical Society, London, 1974, p. 100.
44. L. R. Holland, R. P. Harris and R. Smith, *Rev. Sci. Instrum.* **54** (1983) 993.
45. J. M. Zwiener, personal communication.

46. G. L. Workman, "Vapor Transport Mechanisms", Final Report, NASA Contract NAS8-31731, 1978.
47. R. C. Hawes, et. al., Anal. Chem. 38 (1966) 1842.
48. J. R. Scherer, G. F. Briley and S. Kint, Anal. Chem. 43 (1971) 1917.
49. D. F. Shriver and J. B. R. Dunn, Appl. Spec. 28 (1974) 319.

525-31

116727

268

N88-15626

1987

NASA/ASEE SUMMER FACULTY FELLOWSHIP PROGRAM

MARSHALL SPACE FLIGHT CENTER
THE UNIVERSITY OF ALABAMA

COMPUTER-AIDED ANALYSIS FOR THE
MECHANICS OF GRANULAR MATERIALS (MGM) EXPERIMENT, PART 2

Prepared by:	Joey K. Parker, Ph.D.
Academic Rank:	Assistant Professor
University and Department:	The University of Alabama Mechanical Engineering Department
NASA/MSFC:	
Laboratory:	Systems Dynamics
Division:	Atmospheric Sciences
Branch:	Fluid Dynamics
MSFC Colleague:	Nicholas C. Costes, Ph.D.
Date:	July 17, 1987
Contract No.:	The University of Alabama in Huntsville NGT-01-008-021

Abstract

Computer vision based analysis for the MGM experiment is continued and expanded into new areas. Volumetric strains of granular material triaxial test specimens have been measured from digitized images. A computer-assisted procedure is used to identify the edges of the specimen, and the edges are used in a three-dimensional model to estimate specimen volume. The results of this technique compare favorably to conventional measurements. A simplified model of the magnification caused by diffraction of light within the water of the test apparatus was also developed. This model yields good results when the distance between the camera and the test specimen is large compared to the specimen height. An algorithm for a more accurate three-dimensional magnification correction is also presented. The use of composite and RGB color cameras is discussed and potentially significant benefits from using an RGB camera are presented.

Acknowledgements

The author would like to thank his NASA colleague, Dr. Nicholas C. Costes for the opportunity to conduct this research, and for his help during the last two summers. Thanks are also due for his associate, Dr. C. J. Shin of the University of Colorado, for his many useful suggestions and assistance with the experimental apparatus.

Introduction

Civil engineers have conducted triaxial tests on soil specimens for many years. These tests are used to determine stress-strain relationships as well as specimen volume changes during axial compression or extension. The mechanical behavior of soils and other granular materials is important in the design of building foundations, bridges, dams, and other civil engineering applications. Another important characteristic of soils is their behavior during earthquakes.

One limitation of current triaxial testing methods is that the uniform confining pressure applied to a cylindrical soil specimen must be above a level of approximately 7-13 kPa (1-2 psi). Below this pressure threshold the weight of the specimen causes non-uniform stresses and deformations from the top to the bottom. However, during an earthquake the confining pressure can drop to essentially zero. One purpose of the Mechanics of Granular Materials Experiment (MGM) is to use the micro-gravity environment of the Space Shuttle to allow triaxial testing of granular materials under low confining pressures of less than 7 kPa (1 psi). Conventional measurements of axial loads and displacements, confining pressure, and pore pressure of the granular material specimen will be regularly recorded during a Shuttle flight. Video recordings of three views of the specimen uniformly spaced around the periphery will also be made. The video recordings have three major uses:

- 1) give visual confirmation of the presence (or absence) of "shear bands" in the specimen,
- 2) allow the precise tracking of several "tracer" particles scattered throughout the granular material, and
- 3) provide an alternate means for determining volume changes within the specimen.

This project is primarily concerned with the last two uses given above. Work conducted last summer [Parker, '86] concentrated on the tracking of individual tracer particles. That effort is continued in this report, and the measurement of volume changes is also considered.

Computer vision is used to perform these additional analyses for triaxial tests on granular materials. A "frame grabber" is used to digitize the recorded video signal for subsequent computer processing. A set of interactive computer programs has been written to assist the data analyst in evaluating the experiments.

Objectives

The primary objective of this project is to develop techniques for analyzing digitized images of granular material triaxial tests. Within this primary objective are several specific objectives:

- 1) continue development of tracer bead tracking,
- 2) develop a means for detecting and analyzing tracer beads that "touch" one another,
- 3) generate procedure to correct for magnification of the test specimen due to diffraction of light within the water/confining chamber system, and
- 4) measure volumetric strain from the digitized images.

A secondary objective is to develop methods for generating hardcopies of the digitized images.

Hardware & Equipment

The computer vision system uses an Imaging Technology PCVision Frame Grabber accessory board. The frame grabber is installed in an IBM PC AT microcomputer (with a 6 MHz Intel 80286 microprocessor). The PCVision board effectively digitizes a standard RS-170 television signal into a 512 column by 480 row pixel (picture element) matrix with a resolution of 8 bits ($2^8 = 256$ gray levels). A standard composite color camera (JVC #BY-110) and an electronic CCD (charge coupled device) camera (Micro-Technica #M-852) were both used for viewing the experimental setup. The CCD camera delivered both composite color output and separate RGB (red-green-blue) outputs.

Several different granular material specimens were used. Most were from 0.05 to 0.1 m (2 to 4 inches) in diameter and from 0.08 to 0.15 m (3 to 6 inches) tall. The granular materials used were either 3 mm diameter glass beads, "Ottawa" sand, or #20 silica sand. All specimens are constrained by a thin translucent latex membrane which tends to blur the details of the specimen. The specimen is placed inside a clear plastic pressure chamber cylinder of approximately 0.15 m (6 inch) inside diameter. The annular region between the specimen and the clear outer cylinder is filled with water, which is externally pressurized to maintain a constant confining pressure. Figure 1 shows a photograph of the test apparatus. The test specimen in Figure 2 consists of red and blue 3 mm diameter glass beads.

Volume Change Measurement

One of the important measurements desired from a triaxial test is the per cent volume change as a function of axial strain. Test specimens are carefully compacted to a uniform desired density prior to testing. Density is calculated from the measured volume and weight of the specimen. The standard method for determining volume changes during the test is to measure the amount of water displaced from the confining chamber. With a known initial volume the per cent volume change can then be determined.

There are two potential sources of error with this conventional method for determining volumetric strain. The volume of the specimen can change slightly (2-3%) between the time of density measurement and actual testing. Since the maximum per cent volume change during the test is approximately 7-10%, an alternative procedure is desired. Also, during an undrained triaxial test with a saturated specimen (voids between granular material are filled with water) the phenomenon of "membrane penetration" can occur. The pressure of the confined water in the test specimen increases when the specimen compacts during axial compression. This increased pressure causes the membrane to separate from the test specimen. The water displaced from the confining chamber depends on the volume inside the membrane, and no longer accurately represents the specimen volume change. If the video system can directly measure the specimen volume, this source of error may be eliminated.

Since volume is a three-dimensional property of the specimen, using two-dimensional video images for measurement causes some problems. First, since only a projection of the surface of the specimen is viewed, a model must be selected for mapping this projection into a three-dimensional volume. The results of the image-based volume measurement depend greatly on how well the conditions of the model are satisfied by the actual specimen throughout the test. Secondly, the magnification effects caused by the diffraction of light in the water between the specimen and the confining chamber must be accounted for. Both of these considerations are discussed along with several comparisons to data obtained from the conventional measurement technique.

Three-dimensional Model

The model chosen for mapping the two-dimensional image to a three dimensional solid is a series of circular disks stacked one atop the other. Only the diameter and height of each disk must be known in order to determine volume. The

height of each disk was assumed to be one vertical pixel in the observed image. The model does not require that the disks form a concentric stack. Therefore, the diameter for each disk can be determined if the left and right edges of the specimen are found at each vertical pixel location.

One way to determine the edges of the specimen is to manually trace them with a pointer on the screen. A simple program to accomplish this was written and evaluated. A "mouse" was used to move a cursor which overlaid the specimen image on the video screen. The cursor left a "trail" of black pixels marking the edge. This process was very tedious and prone to errors after a few images were analyzed. The main benefit is that the operator can be quite confident that the exact edge of the specimen is marked, if sufficient care and patience are used.

Computer detection of edges in digitized images has been studied for several years by many researchers. An overview of edge detection techniques is given in [Pratt, '78] and [Abdou and Pratt, '79]. Most of these techniques produce a new image in which edge pixels are enhanced and non-edge pixels are suppressed. The Robert's operator [Roberts, '65] is a relatively simple 2x2 nonlinear cross operation for sharpening edges. The Sobel [Duda and Hart, '73], Prewitt [Prewitt, '70] and the Kirsch [Kirsch, '71] operators all use 3x3 nonlinear operations and give similar performance in detecting edges. All of these operators use small regions (3x3 pixels or less) and are essentially first derivative approximations. They are also quite sensitive to noise, i.e., an image with spot noise will produce many false edges.

The trend in edge detection for the last several years has been to use larger areas to reduce the effects of noise. The Marr-Hildreth zero crossing of Laplacian [Marr and Hildreth, '80] and the 11x11 directional derivative operator [Haralick, '84] are both second derivative operations. These operators have one benefit in that thresholding is replaced by zero crossing for edge detection. The fact that they use large areas (11x11 pixels) makes them computationally slow and difficult. The six operators of the linear feature extraction algorithm [Nevatia and Babu, '80] use 5x5 areas and appear to strike a good compromise between noise rejection and computational ease. The latest in edge detection is the blur-minimum morphologic edge operator [Lee, Haralick, and Shapiro, '87] which uses either 3x3, 5x5, or larger areas. Figure 3 shows an application of this operator to the typical specimen image. The primary benefit of this operator is good noise rejection even with small regions.

Observation of Figure 3 indicates a major problem for the detection of the edges of the granular material specimen: too many "edges" are found. All of the edge operators developed to date use a localized operator which manipulates pixel intensities to locate regions of high contrast. Unfortunately, the digitized images of the specimens have many areas where relatively high contrast can occur due to shadows, uneven lighting, tracer beads, etc. The problem becomes especially acute during the latter stages of the triaxial test when the latex membrane starts to buckle and fold creating many false edges.

To overcome these problems a program was developed (ASSIST.PAS) which combines features of both manual and computerized edge detection. The program presents the digitized image on the screen with cursors for manually identifying the top and bottom edges of the specimen with straight line segments. These line segments are placed in the center of the specimen to clearly indicate the maximum height. After placing the cursor at the upper left hand edge of the specimen, two options are available to the analyst. Pressing either outside button on the mouse provides manual edge tracing. Pressing the center button causes the computer to go into a search mode. The six edge maps of the linear feature extraction method [Nevatia and Babu, '80] are applied to five pixels on the row immediately below the current edge. Of the five pixels, there are two pixels to the left, one below, and two to the right of the current column. Of these five pixels, the one with the largest edge strength (greatest magnitude from the six edge detectors) is identified as the new edge. This process continues while the center button on the mouse is depressed. If at any time this algorithm begins to trace a false edge, the analyst can stop by releasing the center button. An erase function is also available by depressing either outside button and moving the cursor upwards along the current edge.

This computer-assisted edge tracing method has been very successful in identifying edges of the granular material specimens. The search mode of the computer is much faster than manual tracing, but is still subject to override by the analyst. During the early stages of a triaxial test, when the edges are relatively straight, the search mode can usually identify 95-100% of an edge. In the later stages, the search mode usually identifies 80-90% of the edge. Manual tracing is used to trace the edge in regions of uncertainty where the search method identifies a false edge. This computer-assisted edge finding technique is not an elegant computer vision process, but it is quite successful in determining volume changes in the triaxial test specimens.

Magnification Correction

The presence of the water between the specimen and the confining chamber of Figure 1 creates an apparent magnification of the specimen. This magnification effect is caused by the different indices of refraction of light in the water and the plastic chamber wall. The cylindrical geometry of the test specimen and the confining chamber also requires a nonlinear mapping from the three-dimensional specimen to the two-dimensional image plane. The required mapping function is best described by an algorithm, which will be described later. The major drawback to this algorithm is that it is computationally expensive. In order to accurately map 300 rows by 200 columns in the image plane requires 60,000 passes through the algorithm, once for each pixel. Of course a smaller number of pixels could be mapped and curve fitting used, but this also requires additional computation.

Fortunately a simpler, two-dimensional model can also be developed. The physics of the test apparatus are shown in Figure 4. This model assumes that the camera can be modeled as a pinhole and there are no three-dimensional effects. Figure 4 is a true model in the plane of the pinhole camera, but is only an approximation elsewhere. Experimental results will be shown that confirm these assumptions when the distance L is "large" compared to the height of the specimen. The "image plane" is selected at the front of the confining chamber because the horizontal and vertical "inches per pixel" calibrations are easily determined at this location. The appropriate equations for the simplified model from the geometry of Figure 4 are:

$$\theta_1 = \tan^{-1}\left(\frac{X}{L}\right) \quad (1)$$

$$\theta_a = \sin^{-1}\left(\frac{(r_3 + L) \sin(\theta_1)}{r_3}\right) \quad (2)$$

$$\theta_2 = \theta_a - \theta_1 \quad (3)$$

$$\theta_{1a} = \sin^{-1}\left(\frac{n_a \sin(\theta_a)}{n_1}\right) \quad (4)$$

$$\theta_{1w} = \sin^{-1}\left(\frac{r_3 \sin(\theta_{1a})}{r_2}\right) \quad (5)$$

$$\theta_w = \sin^{-1}\left(\frac{n_1 \sin(\theta_{1w})}{n_w}\right) \quad (6)$$

$$\theta_4 = \sin^{-1}\left(\frac{r_2 \sin(\theta_w)}{r_1}\right) - \theta_w \quad (7)$$

$$\theta_3 = \theta_{lw} - \theta_{la} \quad (8)$$

$$\theta_5 = \theta_2 + \theta_3 + \theta_4 \quad (9)$$

In these equations the indices of refraction of light in the various materials are assumed to be $n_a=1$ (air), $n_l=1.51$ ("Lucite"), and $n_w=1.33$ (water). Equations 1 to 9 relate the geometrical parameters of the system to an observed horizontal position at the front of the chamber. Figure 5 shows a plot of angular position versus observed horizontal position for a value of $L=24$ inches. The plot shows that for small angles, i.e., near the center of the specimen, the relationship is nearly linear. Also, note that for this particular geometry it is possible to "see" an angle greater than 90 degrees. The diffraction of light in the water is responsible for this phenomenon.

In order to use Equations 1 to 9 the true specimen radius r_1 must be known. This can be determined from the observed maximum horizontal position (or edge) in Figure 4. When the angle $(\theta_4 + \theta_w)$ reaches a maximum of 90 degrees, the edge appearing in the image plane (r_1'') is related to the true radius r_1 by the following equations:

$$\theta_w = \sin^{-1}\left(\frac{r_1}{r_2}\right) \quad (10)$$

$$\theta_4 = 90 - \theta_w \quad (11)$$

$$\theta_{lw} = \sin^{-1}\left(\frac{n_w \sin(\theta_w)}{n_l}\right) \quad (12)$$

$$\theta_{la} = \sin^{-1}\left(\frac{r_2 \sin(\theta_{lw})}{r_3}\right) \quad (13)$$

$$\theta_3 = \theta_{lw} - \theta_{la} \quad (14)$$

$$\theta_a = \sin^{-1}(n_l \sin(\theta_{la})) \quad (15)$$

$$\theta_1 = \sin^{-1}\left(\frac{r_3 \sin(\theta_a)}{r_3+L}\right) \quad (16)$$

$$\theta_2 = \theta_a - \theta_1 \quad (17)$$

$$\theta_5 = \theta_2 + \theta_3 + \theta_4 \quad (18)$$

$$r_1'' = L \tan(\theta_1) \quad (19)$$

Figure 6 shows a plot of the calculated radius, r_1'' versus the true specimen radius, r_1 , along with five experimental points. The experimental values match the calculated ones

closely. Also, the relationship between true and observed radius is essentially linear in the region of specimen radii of interest (1 to 2 inches). Figure 7 shows a plot of observed radius versus true radius for several different distances L.

The two simplified models given above correct for horizontal magnification of the image. Another small correction is required for the specimen in the vertical direction. Figure 8 shows a side view of the specimen and the pinhole camera. With a large distance L the diffraction effects over the height of the specimen are small, so they are ignored in this simple model. The specimen has height h_f at the front, and height h_s along the side (where the edge is detected by the ASSIST.PAS program). By geometry the following relationship can be derived:

$$\frac{h_s}{h_f} = \frac{L + r_3 - r_1}{L + r_3} \quad (20)$$

This correction has application in the calculation of specimen volume. Height of the specimen is best measured at the front (h_f), whereas diameter is measured along the sides. The edge tracing program identifies an edge between h_s and h_f that does not belong to the specimen (it is usually part of the platen). The pixels corresponding to this extraneous edge are discarded during the determination of specimen volume.

The development of the two-dimensional cases above will make the three-dimensional algorithm more understandable. The three-dimensional model also makes use of a pinhole camera assumption. The confining chamber is assumed to be perfectly cylindrical and oriented perpendicularly to the axis of the pinhole camera. In the algorithm given below, terms in curly braces, $\{X, Y, Z\}$ are vectors in a right-handed, rectangular coordinate system. This coordinate system is rigidly attached to the confining chamber, as shown in Figure 9. According to this figure, the sequence for the algorithm is:

- 1) The origin of the pinhole camera is at $\{0, L, 0\}$, the image plane is at $\{0, r_3, 0\}$ and is perpendicular to the Y axis.
- 2) Select mapping points on image plane, $\{X_{ip}, r_3, Z_{ip}\}$.
- 3) Extend line from origin $\{0, L, 0\}$ through image plane at $\{X_{ip}, r_3, Z_{ip}\}$ to outer wall using direction cosines. The equation for outer wall points is: $X_{ow}^2 + Y_{ow}^2 = r_3^2$. This forms line #1. (The points $\{X_{ip}, r_3, Z_{ip}\}$ would normally be chosen at each pixel in the image).

- 4) The normal to the outer wall at the point of intersection is the line from the point $\{0, 0, Z_{ow}\}$ to the point $\{X_{ow}, Y_{ow}, Z_{ow}\}$. This forms line #2.
- 5) Lines #1 and #2 form Plane #1-2, and the angle between the lines in this plane is θ_a .
- 6) Angle θ_{1a} is found by the diffraction equation:

$$n_a \sin \theta_a = n_1 \sin \theta_{1a}.$$
- 7) Line #3 begins at $\{X_{ow}, Y_{ow}, Z_{ow}\}$, lies in Plane #1-2, and is at angle θ_{1a} from Line #2 in this plane.
- 8) Line #3 extends to the inner wall to the point $\{X_{iw}, Y_{iw}, Z_{iw}\}$. The equation for inner wall points is:

$$X_{iw}^2 + Y_{iw}^2 = r_2^2.$$
- 9) The normal to the inner wall at the point of intersection is the line from the point $\{0, 0, Z_{iw}\}$ to the point $\{X_{iw}, Y_{iw}, Z_{iw}\}$. This forms line #4.
- 10) Lines #3 and #4 form Plane #3-4, and the angle between the lines in this plane is θ_{lw} .
- 11) Angle θ_w is found by diffraction equation:

$$n_w \sin \theta_w = n_1 \sin \theta_{lw}.$$
- 12) Line #5 begins at $\{X_{iw}, Y_{iw}, Z_{iw}\}$, lies in Plane #3-4, and is at angle θ_w from Line #4 in this plane.
- 13) Line #5 extends to the specimen surface to the point $\{X_{sp}, Y_{sp}, Z_{sp}\}$. The equation for inner wall points is:

$$X_{sp}^2 + Y_{sp}^2 = r_1^2.$$
- 14) The maximum angular position observable on the specimen surface occurs when condition #13 is just barely satisfied, i.e., Line #5 is perpendicular to the specimen surface.

The point $\{X_{sp}, Y_{sp}, Z_{sp}\}$ determines the true angular position of the bead located on the image plane at the point $\{X_{ip}, r_3, Z_{ip}\}$.

Experimental Results

A series of three granular material triaxial tests were conducted to evaluate the computer vision measurement of volumetric strain. The results of these tests are given in Figures 10, 11, and 12. In each figure data from the conventional method for determining volumetric strain (measurement of displaced water) is plotted. Computer vision measurements were obtained from two different cameras, a front view and a side view (about 120 degrees apart). Parameters for the granular material test specimens are given in Table 1.

Table 1
Specimen Parameters

Test date	Figure 10 6/16/87	Figure 11 6/18/87	Figure 12 6/25/87
Specimen height :	6.402"	6.612"	6.460"
Specimen diameter :	2.805"	2.805"	2.805"
Initial void ratio :	0.697"	0.637"	0.651"
Material :	3 mm glass beads		
Confining pressure :	0.2 psi		
Deformation rate :	0.021"/minute		

Figure 10 shows the worst correlation between the conventional and computer vision techniques. In the latter stages of the test the computer vision data shows a shift of approximately 1.5% volumetric strain. However, the slopes of the three sets of data do show similar trends. The digitized images of the test corresponding to Figure 10 were the lowest quality of the three experiments, possibly explaining some of the discrepancy with the conventional technique.

Figures 11 and 12 show much better agreement between the conventional and computer vision techniques. In Figure 11 the front and side view data agree within approximately 1% of volumetric strain, with the exception of one set of points at the 75 minute mark. In Figure 12 the data points before the 55 minute mark agree closely, but begin to diverge at this point. There are two possible explanations for this type of uniform divergence. First, the specimen can begin to dilate non-symmetrically, thus violating the round disk assumption of the computer vision model. Secondly, the upper platen begins to penetrate the sample at

approximately the 50 minute mark. The volume measuring algorithm assumes that the top of the specimen is stationary, so platen penetration introduces a small error in the measurement.

RGB vs. Composite Video Cameras

Two different types of color video cameras are available, RGB (red-green-blue) and composite. An RGB camera generates three RS-170 (television) signals that can be separately digitized. In a composite color camera using the NTSC standard, signals from the red, green, and blue sensors are combined to form a single RS-170 compatible output signal. The composite video signal is therefore of somewhat lower quality, since there is three times as much information available from an RGB camera. This often leads to a patterning effect when the composite video signal is displayed in "shades of gray." This patterning appears as diagonal and/or horizontal lines running across the image.

Composite video systems are also known to have some peculiarities with certain colors, notably red. Red objects appear to have a noticeable "cross-hatch" pattern associated with them. This cross-hatch pattern has been used in the bead tracing software for the identification of red tracer beads [Parker, '86]. Passing a Laplacian convolution filter over a digitized composite video image enhances the appearance of these cross-hatch patterns by converting them into vertical black and white bands. Unfortunately, the Laplacian also enhances some of the other patterns generated by the composite video signal. Careful selection of lighting and non-tracer bead color is required to successfully use this method for locating tracer beads. In particular, blue non-tracer beads give the best performance in bead tracing. However, many of the planned experiments for the granular materials project require the use of sand particles, which are an off-white color. It is difficult to "see" the red tracer beads in the white sand, even when the tracers are on the surface of the specimen.

Another problem occurs when the analyst desires to do bead tracing and volume change measurement from the same digitized image. With red tracer and blue non-tracer beads, a light background gives the best contrast for finding the specimen edges, and thusly the volume. If red tracer beads are used in white sand, then a relatively dark background would be required to give a good contrast for edge tracing. Since these experiments will (hopefully) eventually be conducted in a rarely attended, confined area of the Space Shuttle, two different backgrounds are not desirable.

The use of RGB color cameras may provide a solution to this problem. Under the right conditions, tracer beads can appear at significantly different intensities (shades of gray) in the three images from an RGB camera. Therefore lighting and background color can be optimized for specimen edge tracing and another technique used for finding the tracer beads. As an example, Figures 13 and 14 show the same region of a red and blue bead specimen. The histograms of pixel intensities in these figures have been "equalized", i.e., there are approximately the same number of pixels at each of eight gray levels. In Figure 13 most, but not all, of the light regions are red tracer beads. In Figure 14 there are significantly fewer light regions, and most of these correspond to glare from the lighting.

One way to use the two color images of the same scene is to subtract one image from the other. Figure 15 is the difference between the original images of Figures 13 and 14 (before equalizing). Note that seven tracer beads are separated and clearly identified in this figure. Another group of five touching tracer beads are also discernable. The major advantage to the subtraction method for identifying tracer beads is that it is relatively insensitive to lighting. There is a temptation to simply threshold the image of Figure 13 to find the red beads, i.e., all pixels above a certain brightness are set to white and all others to black. However, the correct threshold value would depend on carefully controlled lighting, and could vary from region to region in the image. The glare in the center of Figure 14 has been eliminated in the subtracted image of Figure 15. With simple thresholding of a single image this type of glare reduction would be difficult to accomplish.

Using RGB cameras does present a few small problems. If only two of the RGB signals are recorded (red and green for example), then twice as many video recorders or multiplexer channels will be required for the Shuttle flight hardware. Also, images to be subtracted must be from the same point in the two recordings, i.e., they must be images of the same scene. Lastly, the video systems must be well synchronized such that a point in the scene occurs at the same vertical and horizontal pixel locations in the two digitized images. Some type of registration marks could be used to correct for this type of error. Even with these additional problems, the use of RGB cameras is highly recommended.

Miscellaneous

Several miscellaneous programs have been written for use in this project. All programs using image data require the full 512x480 pixel image to be in the ImageAction non-compressed file format (*.IMG). One of the most useful is the program for printing images at eight shades of gray on the Hewlett-Packard LaserJet Plus printer (LASER_PR.PAS). This program uses the same 8x8 dot patterns defined by HP in their technical reference manual, but does not use the advanced graphics capabilities of the LaserJet (they are too slow). The program allows the user to print any selected portion of an image, up to approximately 43,000 pixels (215 columns by 200 rows). This limitation is due to the graphics limitations of the LaserJet Plus printer. Other limits are 300 columns or 360 rows due to the physical size of the paper.

Another printing program (HP_THR.PAS) prints black and white (thresholded) images in three different sizes. This program can print an entire 512x480 pixel image, provided there are not too many long vertical columns of black pixels (another limitation of the LaserJet Plus printer). One program (FULL_SIZ) can "shrink" a full 512x480 pixel image to an equivalent 213x200 pixel image and print it within the limitations of the LaserJet Plus. This program maps each 12x12 area of the original image into an equivalent 5x5 area before printing, so some details such as lines can be lost. A program for generating color pictures on the 8 pen HP 7550 plotter is also available (IMG_PLOT.PAS), but requires more than one hour of plotting time for most images.

One useful program (COLLECT.PAS) allows the user to "grab" frames at specified time intervals, either directly from the camera or from a video cassette recorder. A histogram printing program (HISTGRAM.PAS) generates a printer-plot of the pixel intensity histogram for an image. Histograms are useful for evaluating the quality of lighting used in the video system. Most computer vision algorithms perform best on an image with "good" contrast. The histogram of such an image will be spread over the entire range of pixel intensities. If the histogram is grouped near either end of the pixel intensity scale, then changes in lighting conditions are usually needed. Another program (OVERLAY.PAS) allows the user to overlay specimen edges (from a *.WID file) onto the original image. This can be useful as a subsequent check on the validity of the edge detection procedure.

Results

Most of the objectives of this project have been met. A methodology for determining volumetric changes during a granular materials triaxial test has been developed. A computer-assisted edge tracking program is used with a circular disk model to estimate the specimen volume from a digitized image. Results from this computer vision based technique show generally good correlation to conventional volumetric strain measurements.

Two models for determining the magnification effects produced by the diffraction of light in the test apparatus have been developed. The simpler of these two methods generates two linear correction factors, one each for the horizontal and vertical directions. This simplified model is adequate when the distance between the camera and the test specimen is "large" compared to the specimen height. Experimental data is provided to substantiate this claim. An algorithm is also given for generating a more accurate three-dimensional correction. The drawback to this algorithm is computational expense, but it is necessary if the camera is "close" to the test specimen.

Tracer bead tracking requires a final conversion from the two-dimensional data of the image plane to true three-dimensional position. The relationship between the observed horizontal position and the true angular position of the object depends on the local specimen diameter. Therefore, specimen diameter must be determined before this final correction can be applied (specimen diameter is estimated in the volumetric strain measurement process). Previous efforts in the tracer bead tracking effort required the use of a composite color video image of the specimen. Red tracer beads created "cross-hatch" areas that were detected by the bead locating and tracking procedures. Preliminary investigations with RGB (red-green-blue) camera signals indicate that a different method for tracer bead detection might have significant advantages. Subtracting one color image from another (green from red for example) can provide tracer bead location that is relatively insensitive to ambient lighting. Therefore lighting can be optimized for the edge tracking process.

No significant progress has been made in the evaluation of two or more "touching" beads. Initially this objective was considered a high priority. However, a different method for generating the test specimen ("raining" versus vibration) allows fairly precise placement of the tracer

beads on the surface of the specimen. Therefore few tracer beads will contact one another during the test. Work on this topic was deferred to a later date.

Recommendations

Testing of the computer vision system in a full-scale mockup of the "double locker" (17" x 20" x 20") of the Space Shuttle should be done soon. One of the critical components of any computer vision system is lighting. The current procedure to detect the edges of the specimen is especially dependent on lighting. The best system for lighting the test apparatus, the best choice of camera lenses, and the effects of background and tracer bead colors can only be determined in a full-scale system. The full three-dimensional magnification correction algorithm can also be tested in this system.

A significant difference is apparent in the quality of images digitized from a VCR (video cassette recorder) and directly from a video camera. Current VCR's have approximately half the vertical resolution of a video camera. A new generation of VCR's ("Super VHS") with approximately the same vertical resolution as a video camera is being introduced to the marketplace. If the claims are true, then this newer VCR technology should be used both in the flight mission and during ground testing.

RGB cameras offer potentially significant advantages over composite color cameras for the tracer bead tracking process. At a cost of twice as much video recording, an additional measure of independence between the requirements for "good" bead tracking and specimen edge detection can be had.

A series of tests to precisely evaluate the volumetric strain measurement procedure should be conducted. Several cylindrical specimens of well-known dimensions can be measured by the computer vision system. This would establish an absolute error baseline for this technique. There are ambiguities in the conventional measurement of volumetric strain (determination of initial specimen volume and measurement of small volumes of displaced chamber water), and this uncertainty needs to be evaluated.

Finally, a procedure for tying the two parts of the analysis (bead tracking and volumetric strain measurement) together should be developed. In particular, the specimen diameter information generated in the volumetric strain measurement analysis is needed in bead tracking for correction to true bead angular and radial position.

References

- Abdou, I. E. and W. K. Pratt, "Quantitative Design and Evaluation of Enhancement/Thresholding Edge Detectors", Proceedings of the IEEE, Vol. 67, No. 5, May 1979, pp. 753-763.
- Duda, R. O. and P. E. Hart, Pattern Classification and Scene Analysis, Wiley, New York, 1973.
- Haralick, R. M., "Digital Step Edges from Zero Crossing of Second Directional Derivatives", IEEE Transactions on Pattern Analysis and Machine Intelligence, Vol. PAMI-6, No. 1, January, 1984, pp.58-68.
- Haralick, R. M., "Edge and Region Analysis for Digital Image Data", Computer Graphics and Image Processing, Vol. 12, 1980, pp. 60-73.
- Kirsch, R. "Computer Determination of the Constituent Structure of Biological Images", Computers and Biomedical Research, Vol. 4, No. 3, 1971, pp. 315-328.
- Lee, J. S., R. M. Haralick, and L. G. Shapiro, "Morphologic Edge Detection", IEEE Journal of Robotics and Automation, Vol. RA-3, No. 2, April 1987, pp. 142-156.
- Marr, D. and E. Hildreth, "Theory of Edge Detection", Proceedings of Royal Society of London, Vol. 207, 1980, pp. 187-217.
- Nevatia, R. and K. R. Babu, "Linear Feature Extraction and Description", Computer Graphics and Image Processing, Vol. 13, 1980, pp. 257-269.
- Parker, J. K. "Image Processing and Analysis for the Mechanics of Granular Materials Experiment", Proceedings of the 19th Southeastern Symposium on System Theory, IEEE Cat. #TH0180-0, March, 1987
- Pratt, W. K., Digital Image Processing, Wiley, New York, 1978, pp. 478-513.
- Prewitt, J. M. S., "Object Enhancement and Extraction", in Picture Processing and Psychopictorics, B. S. Lipkin and A. Rosenfeld, Eds., Academic Press, New York, 1970.
- Roberts, L. G., "Machine Perception of Three-Dimensional Solids", in Optical and Electro-Optical Information Processing, J. T. Tippett et al., Eds., M.I.T. Press, Cambridge, MA, 1965, pp. 159-197.

ORIGINAL PAGE IS
OF POOR QUALITY



Figure 1 - Triaxial Test Apparatus

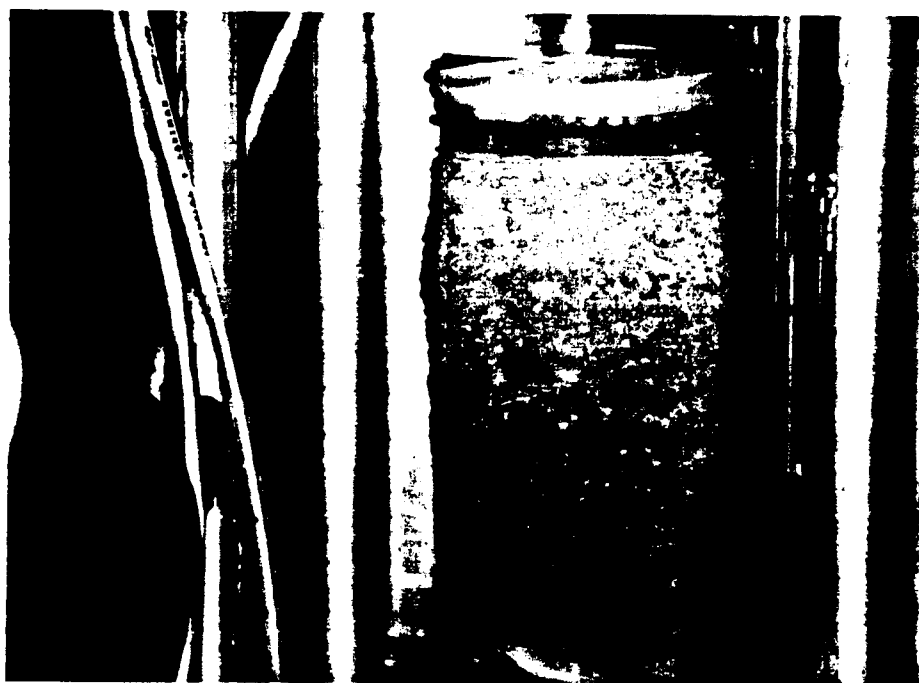


Figure 2 - Triaxial Test Specimen

ORIGINAL PAGE IS
OF POOR QUALITY



Figure 3 - Computer Vision Edge Detection

ORIGINAL PAGE IS
OF POOR QUALITY

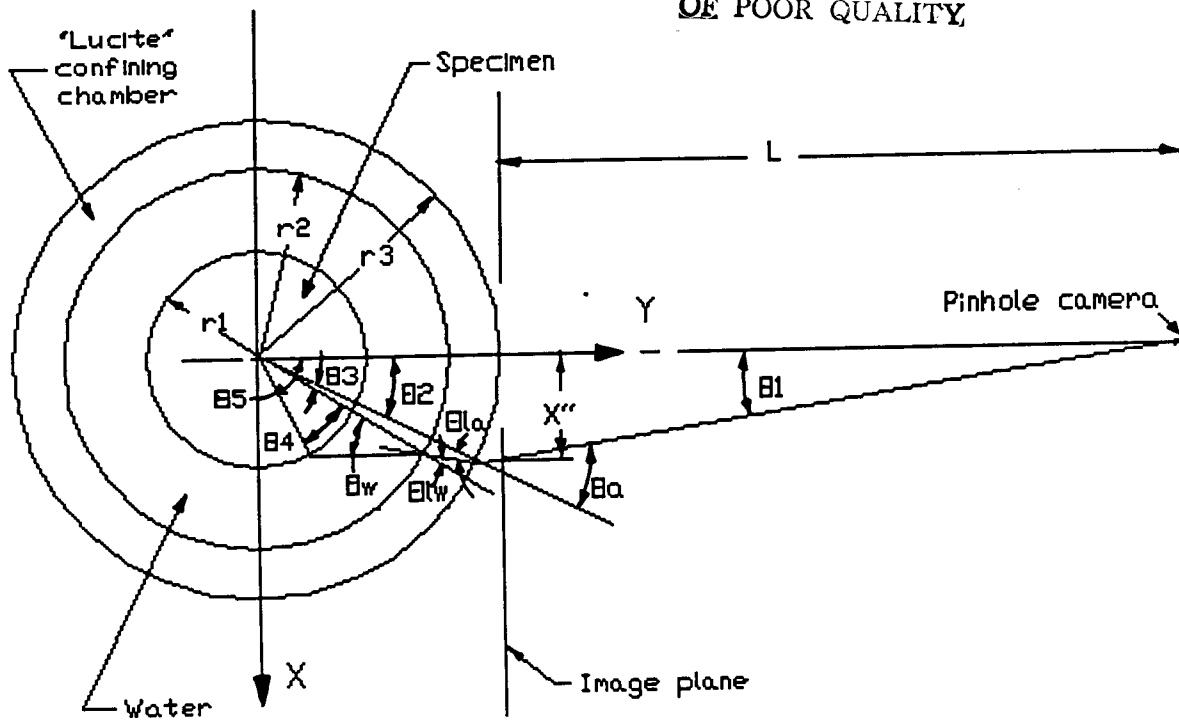


Figure 4 - Two Dimensional System Model

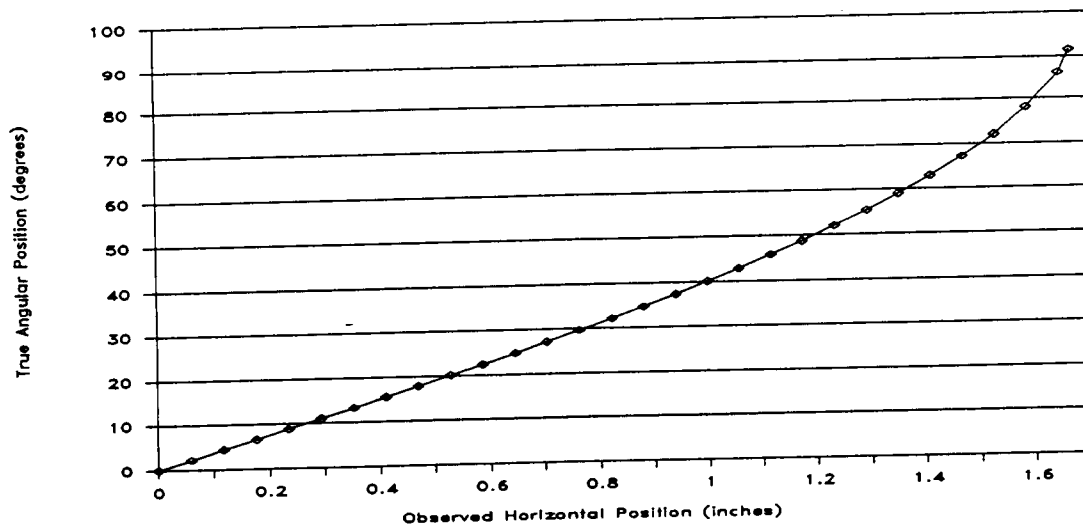


Figure 5 - True Angular Position from Observed Position

ORIGINAL PAGE IS
OF POOR QUALITY

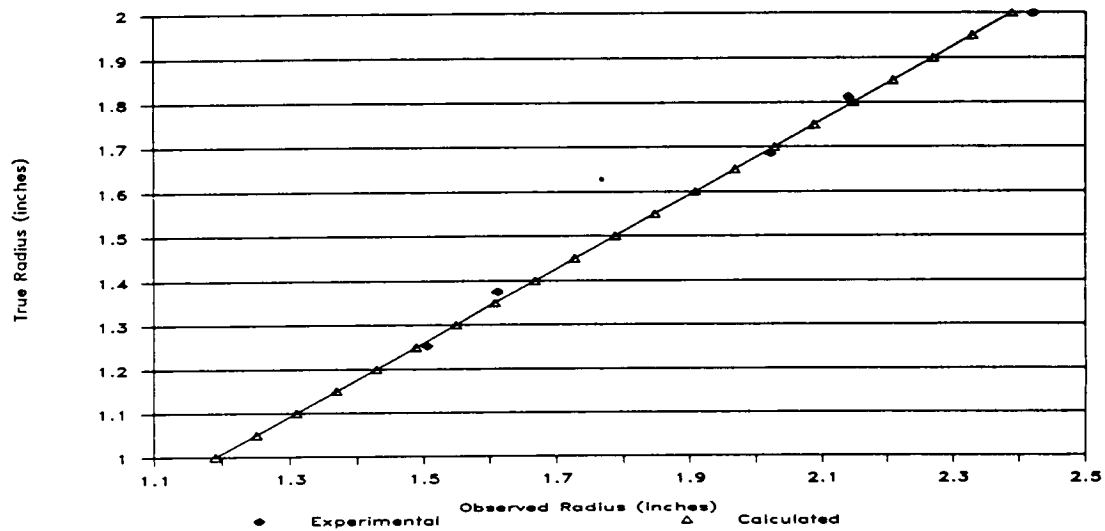


Figure 6 - Experimental and Calculated Specimen Radii

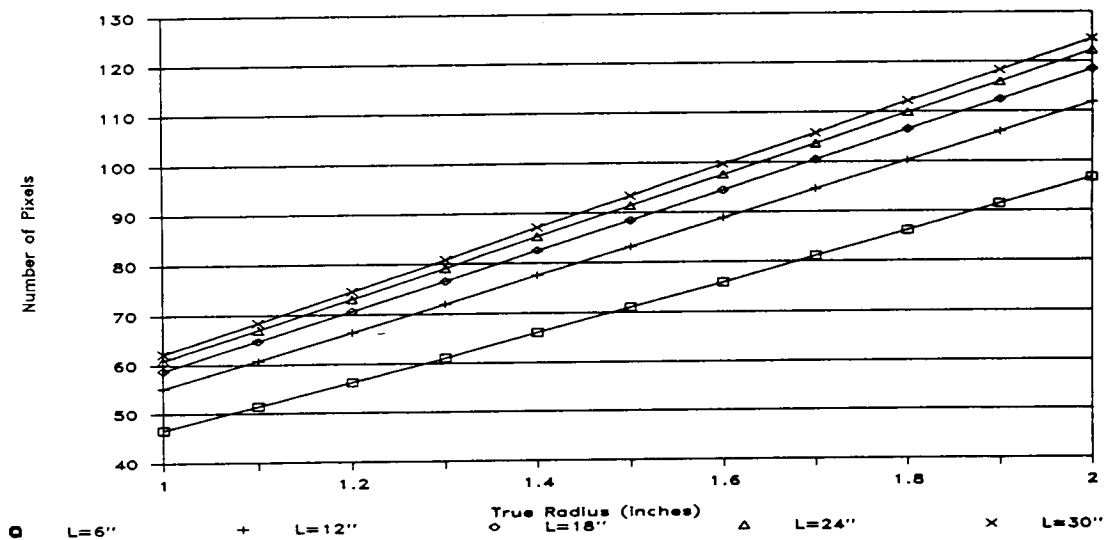


Figure 7 - True Specimen Radius from Observed Radius

ORIGINAL PAGE IS
OF POOR QUALITY

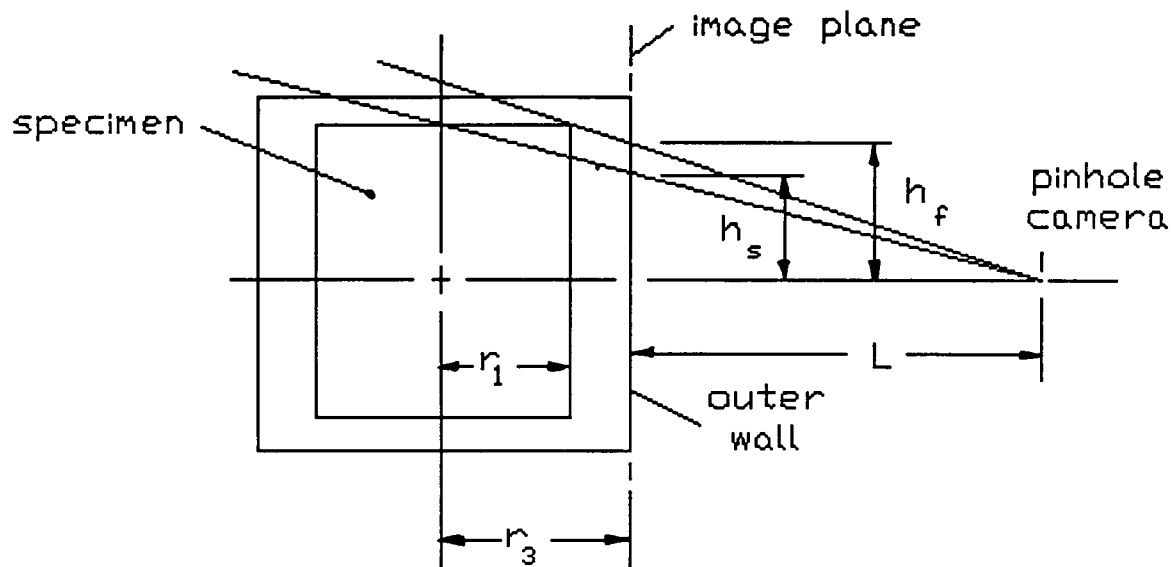


Figure 8 - Vertical Correction Model

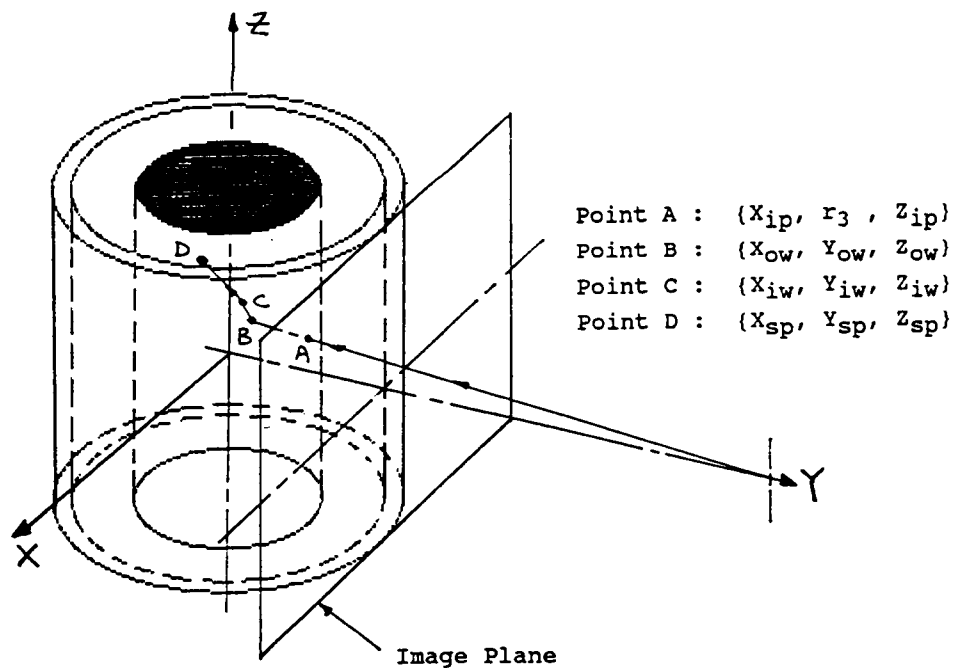


Figure 9 - Three-dimensional Magnification Correction

ORIGINAL PAGE IS
OF POOR QUALITY

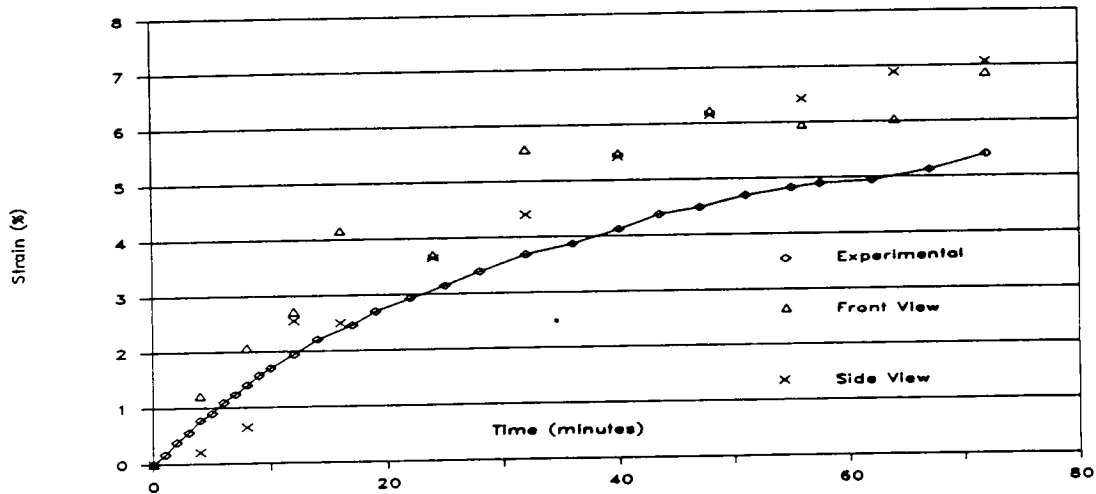


Figure 10 - Volumetric Strain Measurement (6/16/87)

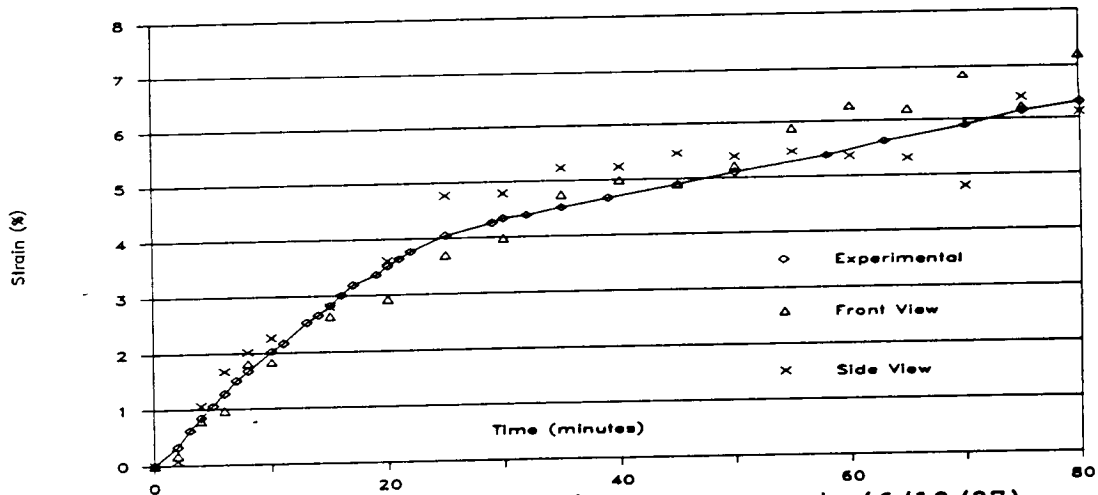


Figure 11 - Volumetric Strain Measurement (6/18/87)

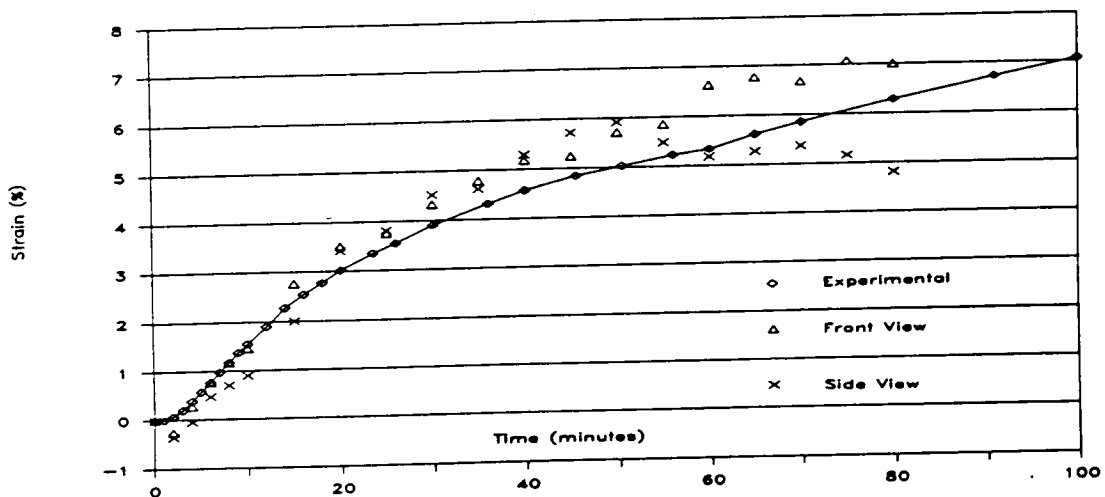


Figure 12 - Volumetric Strain Measurement (6/25/87)

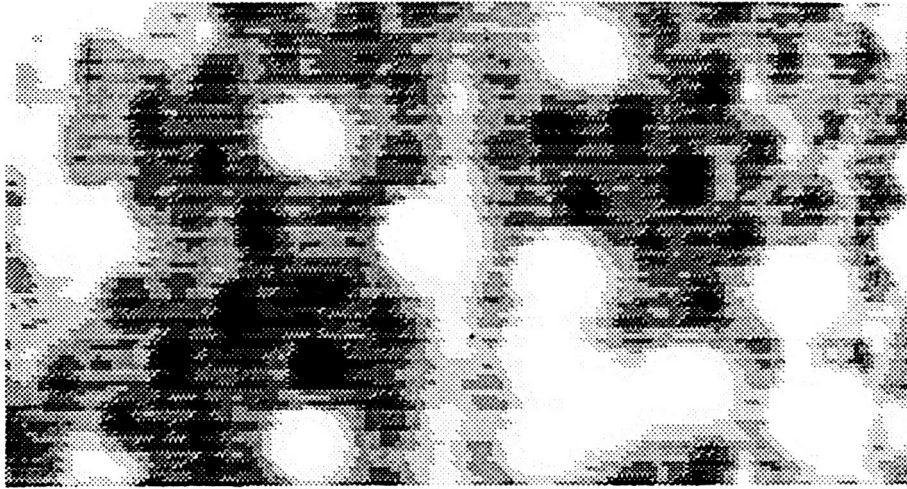


Figure 13 - Partial Image from Red Sensor

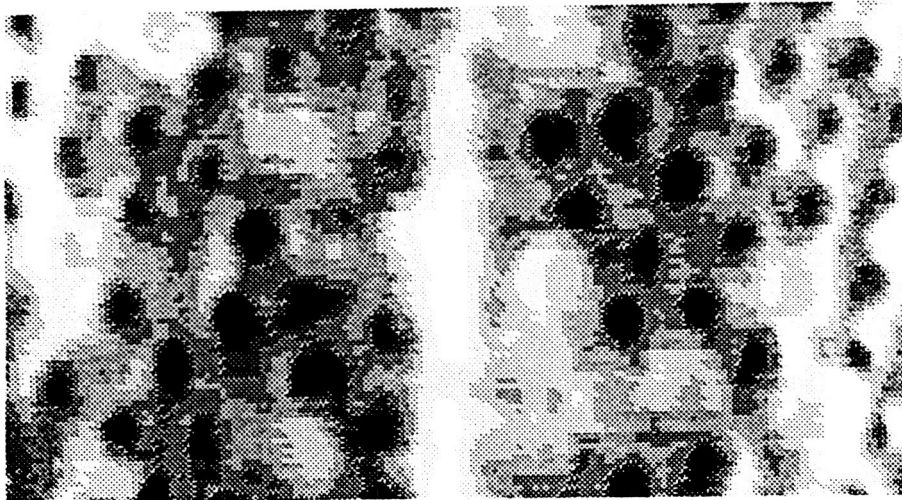


Figure 14 - Partial Image from Green Sensor

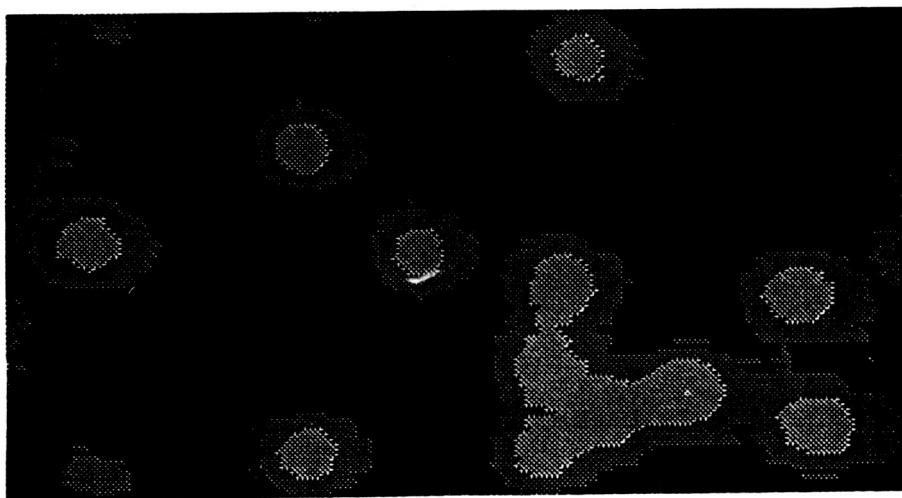


Figure 15 - Subtracted Partial Images

526-76
N88-15627 116728
288

1987

NASA/ASEE SUMMER FACULTY RESEARCH FELLOWSHIP PROGRAM

MARSHALL SPACE FLIGHT CENTER
THE UNIVERSITY OF ALABAMA IN HUNTSVILLE

Improving the Method of Calculating Electronic Properties of
Narrow Bandgap Semiconductors

Prepared By: James D. Patterson
Academic Rank: Professor
University and Department: Florida Institute of Technology
Physics/Space Science

NASA/MSFC

Laboratory: Space Science
Division: Low-Gravity Science
Branch: Crystal Growth

NASA Colleague: Sandor L. Lehoczky

Date: August 21, 1987

Contract No: The University of Alabama in
Huntsville
NGT-01-008-021

ABSTRACT

A previously developed code for calculating the mobility of charge carriers in narrow bandgap semiconductors does not predict the correct temperature dependence in all cases. It is thought that this is due to the way the electronic screening of the carriers is treated in the model. The objective of this research is to improve the handling of the screening by going beyond the current first Born approximation. Much of this work is directly related to the alloy semiconductor $\text{Hg}_{1-x}\text{Cd}_x\text{Te}$ which is important for infrared detectors and is a good candidate for microgravity crystal growth. The principal conclusion, so far, is that the major difficulty is probably the treatment of short range screening at higher temperatures.

ACKNOWLEDGEMENTS

The author wishes to acknowledge the NASA/ASEE Summer Faculty Fellowship Program, along with Gerald Karr the UAH University Program Co-Director.

To NASA Colleagues and sponsors Sandor (Alex) Lehoczky and Frank Szofran of the Crystal Growth Branch, Low-Gravity Science Division, thanks for help is expressed.

A further thanks is due Ernestine Cothran, MSFC Program Co-Director.

Finally, the author is grateful to Shirley A. Buford, of the Crystal Growth Branch, for typing of this manuscript.

1. Introduction

$\text{Hg}_{1-x}\text{Cd}_x\text{Te}$ is a mixed pseudo-binary semiconductor. Its energy gap can be "tuned" from 0.0 to 1.6 eV as x varies from $x = 0$ to $x = 1$ at zero degrees (Dornhaus, Nimtz and B. Schlicht, 1983, p. 148). This variation of band gap with x allows one to optimize for infrared detection (Long and Schmit, 1970, Kruse, 1981). Because of difficulties with producing compositionally uniform crystals due to gravity driven convective effects, $\text{Hg}_{1-x}\text{Cd}_x\text{Te}$ is a good candidate for production in the reduced gravity environment of space (Lehoczky and Szofran, 1981, 1982).

Semiconductors with small gaps tend to have small effective masses and hence high mobilities (Kruse, 1981). The band structure of these materials is now understood from Kane's three level band model and k.p perturbation calculation (Kane, 1957) which leads to non parabolic band structure. See appendix A.5.

Since these semiconductors are polar, scattering by the optical modes is important. The energy of the optical phonons is comparable to the energy of the electrons and hence the electrons are not scattered elastically. This means a relaxation time approximation is not valid (Howard and Sondheimer, 1953; Dingle, 1956) and therefore variational methods are used to solve the Boltzmann equation (Ehrenreich, 1957). The Boltzmann equation must contain all appropriate scattering terms and the narrow band gap means that thermally excited electrons will screen the carriers in certain scattering interactions (Ehrenreich, 1959 - two papers). We attempt to improve the calculation of the scattering by improving the treatment of screening (see Appendix A.1). There are several contributions to the scattering of electrons in $\text{Hg}_{1-x}\text{Cd}_x\text{Te}$ and hence to the determination of electron mobility (Lehoczky, Szofran and Martin, 1980; Lehoczky, Summers, Szofran and Martin, 1982). These include longitudinal - optic phonon interactions (LO), acoustic phonon scattering (ac), ionized impurity scattering (ii), electron hole scattering (eh), compositional disorder scattering (dis) and neutral defect (nd) scattering. Screening is involved in (LO), (ii), and (eh). At temperatures above approximately liquid nitrogen temperatures, LO scattering is easily the most important. See Appendix A.6 for a discussion of the basic interaction term in the Hamiltonian. The LO modes are important rather than the TO modes because it is only the LO modes that have strong electric fields which accompany their vibration

2. Objectives

In alloy semiconductors, such as $\text{Hg}_{1-x}\text{Cd}_x\text{Te}$, there is a strong polar coupling of the carriers to the^x optic modes. In describing this interaction, one must properly account for the screening by use of a suitable dielectric function (Ziman, 1972; Mahan, 1981; Whitsett et al., 1981, see also appendix A.2). The dielectric function depends on several factors (Lehoczky et al. 1974, Nelson et al, 1978) among which is the Fermi Thomas wave vector or its reciprocal which is essentially the screening length. Previous calculations of electron mobility considering, among other factors, the scattering of carriers by optical phonon modes have yielded electron mobilities which are too high (Lehoczky et al, 1982). We aim to improve these calculations by using the Friedel sum rule and the second Born approximation (Joachain, 1975) for the phase shifts to calculate a better screening length (Stern, 1967; Agarwal and Singh, 1983).

A second objective is to fill in the necessary background material by use of a suitable set of appendices (some reviews are by Zawadski, 1974; Chattopadhyay and Queisser, 1981; Chattopadhyay and Nag, 1974; Nag, 1980; Nag, 1975; Rode, 1975).

It is essential in all our calculations to take into account the fact that the energy bands are non parabolic, although they may still be assumed to be spherically symmetric (Szymanska and Dietl, 1978; Pfeffer and Zawadzki, 1978). The non parabolicity of the band is a major complicating feature.

3. The Calculation

The background details and the definitions can be found in the appendices. Here we outline the calculation. The idea is to choose a form for the screened potential of a charged impurity and then to use the Friedel sum rule to place a constraint on this potential which involves the screening length. From Appendix A.3, the Friedel sum rule is

$$2/\pi \sum_l (2l+1) \int_0^\infty \frac{d\delta_l}{dE} f(E) dE = Z. \quad (1)$$

From Appendix A.4 the phase shifts δ_l can be determined, at least to second order Born approximation accuracy, by

$$\tan \delta_l = - \frac{k A_l}{1 - B_l/A_l}, \quad (2)$$

where

$$A_l = \int_0^\infty j_l^2(kr) U(r) r^2 dr, \quad (3)$$

$$B_l = \int_0^\infty dr \int_0^\infty dr' j_l(kr) U(r) G(r, r') U(r') j_l(kr') r^2 r'^2, \quad (4a)$$

$$\text{with } U(r) = (2m^*/\hbar^2) V(r), \quad (4b)$$

and $V(r)$ is the customary screened Coulomb potential (see Appendix A.1)

$$V(r) = -Za e^{-r/L}/r, \quad (5)$$

with L being the screening length.

$$G(r, r') = k j_\ell(kr_<) \eta_\ell(kr_>),$$

with $r_<, r_>$ being the smaller and the larger of r and r' and j_ℓ, η_ℓ are the spherical Bessel functions.

Since $\tan \delta_\ell \cong \delta_\ell$ through second order we can write Eq. (2) as

$$\delta_\ell \cong -k \left[A_\ell + \frac{B_\ell}{1 - B_\ell/A_\ell} \right]. \quad (6)$$

Since $\sum_\ell (2\ell+1) j_\ell^2(x) = 1$,

we can easily show

$$\sum_\ell A_\ell (2\ell+1) = -Za L^2. \quad (7)$$

If we assume $(kr) \ll 1$ for $r \leq L$ where L is the screening length in the spherical Bessel functions of Eqs. (3) and (4) (see Appendix A.7 for a discussion of the validity of our approximations) then we find

$$A_\ell = -Za k^{2\ell} \frac{2\ell!!}{(2\ell+1)!!} L^{2(\ell+1)}, \quad (8)$$

$$B_\ell = -(Za)^2 k^{2\ell} \frac{(2\ell)!}{[(2\ell+1)!!]^2} L^{2\ell+3} \frac{2}{2^{2(\ell+1)}}. \quad (9)$$

Following Agarwal and Singh (1983) (also see Appendix A.7), we approximate Eq. (6) as

$$\delta_\ell \cong -k \left[A_\ell + \frac{B_\ell}{1 - B_\ell/A_\ell} \delta_\ell^c \right]. \quad (10)$$

The screening length in the first Born approximation is $L_{(1)}$ where

$$L_{(1)}^{-2} = \left\{ 2b\pi\hbar^2 \int_0^\infty \left(-\frac{\partial f}{\partial E} \right) \rho(E) dE \right\}, \quad b = a/m^* \quad (11)$$

(see e.g. Szymanska and Dietl, 1978) This expression is good even for non parabolic bands (See Appendix A.8 for different ways of expressing the density of states). We find

$$\left(L / L_{(1)} \right)^2 = 1 - \frac{a Z L}{2}, \quad (12)$$

where m^* has been treated as constant in the factor multiplying δ_ρ^0 in Eq. (2).

Eq. (12) is readily solved with the following results

$$\left(L / L_{(1)} \right) = \sqrt{1 + A^2} - A,$$

which gives with $A = \frac{a Z}{4} L_{(1)}$

the following numbers.

A	$L/L_{(1)}$
-1	2.41
-.5	1.62
0	1
.5	.62
1	.41

4. Conclusions and Recommendations

The results of the previous section were derived with the following approximations applied to the correction term to the first Born approximation [$B_2 / (1 - B_2/A_2)$ of Eq. (6)]

- a. A constant effective mass can be used beyond the first Born approximation,
- b. $kL \ll 1$ where L is the screening length
- c. need only the $\ell = 0$ term.

We have discussed this approximation in A.7. In Appendix A.9 we note that improvements are not so easy and it is not clear our results are valid at higher temperatures.

The major comment to make about this result is that it disagrees with that of Agarwal and Singh (1983) who in my notation get

$$\begin{aligned} (L / L_0)^2 &= (1 - L \partial Z)^{-1} \\ &\cong 1 + L \partial Z. \end{aligned} \quad (13)$$

Both Eq. (12) (my result) and Eq. (13) assume $|L \partial Z| \ll 1$. It should be noted that my result differs qualitatively from Agarwal and Singh. They predict corrections to the first Born approximation increase L (for donors, $Z > 0$) whereas I predict they decrease L . The literature seems to be divided as to which qualitative effect to expect (D. Chattopadhyay and H.J. Queisser, 1981). It should be mentioned that a decrease in L would mean more screening, less scattering and hence higher mobility - the opposite result from what we expected.

We can also obtain the results of Agarwal and Singh if we use their expression for the second Born approximation but this expression does not appear to agree with standard sources (Joachain, 1975).

It remains to be seen whether better treatment of corrections to the first Born approximation would lower the mobilities and yield better agreement with experiment. This would be the first thing we would recommend investigating as our low energy approximation are suspect at higher temperatures. As shown in Appendix A.9, going beyond $\ell = 0$ in the correction term quickly yielded equations that must be solved numerically for L .

Also if we drop the assumption that $kL \ll 1$, then the integrals may still be doable, but they certainly are not convenient.

Experimentally the calculations of the mobility are off by a factor of perhaps 2. If the corrections to the first Born approximation were enough to bring agreement with experiment it is likely that we would have cause to suspect the convergence of our procedure.

Our recommendations would stress the positive aspects of the calculation which has already been done. The calculation is so complex that it is remarkable that qualitative and in some cases perhaps quantitative agreement with experiment can be achieved. It would appear that a review of the whole calculation is in order. It could be that the lack of agreement with experiment might not reflect just one error but perhaps several, none of them particularly serious by themselves.

The error at high temperature should mean that close in scattering is overscreened by this model. Whatever the approach it seems this basic problem should be fixed. We also need to take into account that in general more than one type of carrier can contribute to electric current and to screening. There is also the troublesome problem of antiscreening which can occur in polar optic mode scattering when the electrons don't move fast enough to "follow the charge motion due to lattice waves (Ehrenreich, 1959).

5. References

5.1.1 Most Relevant Papers

1. D.J. Howarth and E.H. Sondheimer, "The Theory of Electronic Conduction in Polar Semiconductors", Proc. Roy. Soc. A219, 53 (1953).
2. R.B. Dingle, "The Concept of Formal Relaxation Times in the Theory of Electronic Conductors at Low Temperatures", Physica XXII, 698 (1956).
3. H. Ehrenreich, "Electron Scattering in InSb", J. Phys. Chem. Solids 2, 131 (1957).
4. H. Ehrenreich, "Screening Effects in Polar Semiconductors", J. Phys. Chem. Solids 8, 130 (1959).
5. H. Ehrenreich, "Transport of Electrons in Intrinsic InSb", J. Phys. Chem. Solids 9, 129 (1959).
6. F. Stern, "Friedel Phase-Shift Sum Rule for Semiconductors", Phys. Rev. 158, 697 (1967).
7. B.K. Agarwal and Narendra Singh, "Friedel Sum Rule in the Second Born approximation", Phys. Letters 95A, 319 (1983).

5.1.2 Generally Relevant Papers

1. Evan O. Kane, "Band Structure of Indium Antimonide", J. Phys. Chem Solids 1, 249 (1957).
2. D. Chattopadhyay and B.R. Nag, "Mobility of Electrons in $\text{Hg}_{1-x}\text{Cd}_x\text{Te}$ ", J. Applied Phys. 45, 1463 (1974).
3. W. Zawadzki, "Electron Transport Phenomena in Small Gap Semiconductors", Adv. Phys. 23, 435 (1974).
4. W. Szymanska and T. Dietl, "Electron Scattering and Transport Phenomena in Small-Gap Zinc-Blende Semiconductors", J. Phys. Chem. Solids 39, 1025 (1978).
5. P. Pfeffer and W. Zawadzki, "Inelastic Scattering of Electron by Optic Phonons in InSb-Type Semiconductors", phys. stat. sol. (b) 88, 247 (1978).

6. D. Chattopadhyay and H.J. Queisser, "Electron Scattering by Ionized Impurities in Semiconductors", Rev. Mod. Phys. 53 (4), 745 (1981).

5.1.3 Papers Directly Related To Relevant Compounds With Mercury

1. S.L. Lehoczky, J.G. Broerman, Donald A. Nelson, and Charles R. Whitset, "Temperature-Dependent Electrical Properties of HgSe", Phys. Rev. B9, 1598 (1974).

2. D.A. Nelson, J.G. Broerman, C.J. Summers, and C.R. Whitset, "Electron Transport in the $\text{Hg}_{1-x}\text{Cd}_x\text{Se}$ Alloy System", Phys. Rev. B18 (4), 1658 (1978)

3. S.L. Lehoczky, F.R. Szofran, B.G. Martin, "Advanced Methods for Preparation and Characterization of Infrared Detector Materials, Part I", NASA CR-161598, July 5, 1980.

4. S.L. Lehoczky and F.R. Szofran, "Advanced Methods for Preparation and Characterization of Infrared Detector Materials, Part II", NASA CR-161949, Sept. 30, 1981.

5. S.L. Lehoczky and F.R. Szofran, "Directional Solidification and Characterization of $\text{Hg}_{1-x}\text{Cd}_x\text{Te}$ Alloys", in Materials Processing in The Reduced Gravity Environment of Space, Guy E. Rindone, Ed., Elsevier, Amsterdam, 1982.

6. S.L. Lehoczky, C.J. Summers, F.R. Szofran, and B.G. Martin, "Electrical Characterization of $\text{Hg}_{1-x}\text{Cd}_x\text{Te}$ Alloys", Materials Processing in The Reduced Gravity Environment of Space, Guy E. Rindone, Ed., Elsevier, Amsterdam, 1982.

5.2 Books

1. J.M. Ziman, "Principles of The Theory of Solids", 2nd Edition, Cambridge at The University Press, 1972.

2. B.R. Nag, "Theory of Electrical Transport in Semiconductors", Pergamon Press, 1972.

3. J. Joachain, "Quantum Collision Theory", North Holland, Amsterdam, 1975.

4. B.R. Nag, "Electron Transportation Compound Semiconductors", Springer-Verlag, Berlin, 1980.

5. Gerald D. Mahan, "Many-Particle Physics", Plenum Press, New York, 1981.

6. R. Dornhaus, G. Nimtz and B. Schlicht, "Narrow-Gap Semiconductors", Springer-Verlag, 1983, Vol. 98, Springer. Tracts in Modern Physics, see especially R. Dornhaus and G. Nimtz, "The Properties and Applications of the $\text{Hg}_{1-x}\text{Cd}_x\text{Te}$ Alloy Systems".

7. R.K. Willardson and Albert C. Beer (Eds.) Semiconductors and Semimetals, Academic Press, New York.

a. Vol. 5, Infrared Detectors, 1970, Ch. 5, "Mercury-Cadmium Telluride and Closely Related Alloys", by Donald Long and Joseph L. Schmit.

b. Vol. 10, Transport Phenomena, 1975, Ch. 1, "Low-Field Electron Transport", by D.L. Rode.

c. Vol. 16, Defects, $(\text{HgCd})\text{Se}$, $(\text{HgCd})\text{Te}$, 1981, Ch. 2, "Crystal Growth and Properties of $\text{Hg}_{1-x}\text{Cd}_x\text{Se}$ Alloys", by C.R. Whitsett, J.G. Broerman, and C.J. Summers.

d. Vol. 18, Mercury Cadmium Telluride, 1981, Ch. 1, "The Emergence of $\text{Hg}_{1-x}\text{Cd}_x\text{Te}$ as a Modern Infrared Sensitive Material" by Paul W. Kruse.

Appendix A.1 Screening

We present here the basic ideas (Ziman, 1972) without putting in the details. A key idea we wish to mention is the difference between screening by free electrons and by band electrons which are described by Bloch Wave functions.

For a free electron gas (with a uniform positive background) the applied potential can be written

$$V(\vec{r}, t) = \iint V(\vec{q}, \omega) e^{i(\vec{q} \cdot \vec{r} + \omega t)} d\vec{q} d\omega, \quad (\text{A.1.1})$$

with \vec{r} being the space coordinate, t the time, \vec{q} and ω are the usual wave vector and frequency. The Fourier components of the effective potential is then $V(\vec{q}, \omega)$ divided by the dielectric function.

The Lindhard or Random Phase Approximation dielectric function is the Fourier component of the displacement vector divided by the Fourier component of the electric field and it comes out;

$$\epsilon(\vec{q}, \omega) = 1 - \frac{4\pi e^2}{V q^2} \sum_{\vec{k}, \sigma} \frac{f(\vec{k}) - f(\vec{k} + \vec{q})}{E_{\vec{k}} - E_{\vec{k} + \vec{q}} + \hbar\omega - i\delta}, \quad (\text{A.1.2})$$

where f is the Fermi Function and $E_{\vec{k}}$ is the electron energy at wave vector \vec{k} .

It is particularly interesting to examine this for the static case ($\omega = 0$) when \vec{q} is near zero. For then (assuming one band)

$$E_{\vec{k}} - E_{\vec{k} + \vec{q}} \cong - \vec{q} \cdot \vec{\nabla}_{\vec{k}} E_{\vec{k}}, \quad (\text{A.1.3})$$

$$f(\vec{k}) - f(\vec{k} + \vec{q}) \cong - \vec{q} \cdot \vec{\nabla}_{\vec{k}} E_{\vec{k}} \left(\frac{\partial f}{\partial E_{\vec{k}}} \right). \quad (\text{A.1.4})$$

The static dielectric constant then comes out

$$\epsilon(\vec{q}, 0) = 1 + k_{TF}^2 / q^2, \quad (A.1.5)$$

where k_{TF} is the Thomas-Fermi screening wave vector and it is given by

$$k_{TF}^2 = 4\pi e^2 \int \left(- \frac{\partial f}{\partial E} \right) \rho(E) dE, \quad (A.1.6)$$

where $\rho(E)$ is the density of states including spin.

The significance of k_{TF} is not hard to find. If we have a bare Coulomb potential energy

$$V(\vec{r}) = e^2 / r, \quad (A.1.7)$$

then its Fourier transform is

$$V(q) = 4\pi e^2 / q^2, \quad (A.1.8)$$

and the effective Fourier transform of the screened Coulomb potential is

$$U(q) = \frac{V(q)}{\epsilon(q, 0)} = \frac{4\pi e^2}{q^2 + k_{TF}^2}. \quad (A.1.9)$$

By inversion, we can then show that this leads to the following effective potential energy

$$U(r) = \frac{e^2}{r} e^{-k_{TF} r}. \quad (A.1.10)$$

Many authors have shown for Bloch Wave functions referred to band n , that

$$\epsilon(\vec{q}, \omega) = 1 - \frac{4\pi e^2}{Vq^2} \sum_{\vec{k}, n, n'} \frac{| \langle \vec{k}, n | e^{-i\vec{q} \cdot \vec{r}} | \vec{k} + \vec{q}, n' \rangle |^2 (f_{\vec{k} + \vec{q}, n'} - f_{\vec{k}, n})}{E_{\vec{k} + \vec{q}, n'} - E_{\vec{k}, n} + \hbar\omega - i\alpha} \quad (A.1.11)$$

For non parabolic but still spherical energy surfaces the Fermi-Thomas wave vector is still given by Eq. (A.1.6) (Szymanska and Dietl, 1978) with

$$\rho(\epsilon) = (k^2/\pi^2) \frac{dk}{d\epsilon}, \quad (\text{A.1.12})$$

(see Appendix A.8).

Appendix A.2 Dielectric Function

We have already discussed the dielectric function and given an expression for a semiconductor. Here we want to summarize the results for the band structure of $\text{Hg}_{1-x}\text{Cd}_x\text{Te}$. Similar material is discussed by Whitsell (1981).

It is usual to start by dividing the dielectric constant into two parts, one part from the ionic lattice via its polarizability (lat) and the other part from the electrons (el) due to inter and intra band effects.

$$\epsilon(\vec{q}, \omega) = \epsilon_{\text{lat}}(\vec{q}, \omega) + \epsilon_{\text{el}}(\vec{q}, \omega) \quad (\text{A.2.1})$$

The lattice part shows two mode behavior, but can be analyzed with no particular difficulty and reference can be made to the literature. The electronic part is rather complicated but has been well summarized by Lehoczky, Broerman, Nelson and Whitsett (1974), Nelson, Broerman, Summers and Whitsett (1978) and Lehoczky, Szofran and Martin (1980). The later paper gives a summary of how screening and the Thomas-Fermi cruve vectors enter into the longitudinal-optical phonon scattering and in ionizing impurity and electron-hole scattering. Generally speaking we write,

$$\begin{aligned} \epsilon(\vec{q}, \omega) &= \epsilon_b + \frac{k(q)}{q^2} k_{\text{TF}}^2 = \epsilon_b \left(1 + \frac{k_{\text{TF}}^2}{\epsilon_b} \frac{f(q)}{q^2} \right) \\ &= \epsilon_b \left(1 + \frac{f(q)}{L^2 q^2} \right), \end{aligned} \quad (\text{A.2.2})$$

where ϵ_b and $f(q)$, are chosen appropriately according to the scattering mechanism (and notice with $\epsilon_b \neq 1$ we have $\epsilon_b L^{-2} = k_{\text{TF}}^2$) and, depending on the circumstances, more complicated frequency dependent forms may be necessary.

Appendix A.3 Friedel Sum Rule

The Friedel sum rule relates phase shifts δ_ℓ (see Joachain, 1975 for a definition of phase shifts) of partial waves of angular momentum ℓ scattered from a spherically symmetric potential to the charge of the scattering center. At large distances, the scattering center is screened and so the charge of this center also equals the magnitude of the charge of the total number of electrons which are attracted to or repelled from it.

The Friedel sum rule as customarily written (Ziman, 1978) is

$$Z = 2/\pi \sum_\ell (2\ell+1) \delta_\ell(k_F), \quad (\text{A.3.1})$$

where k_F is the Fermi wave vector and Z is the charge of the scattering center (in units of the magnitude of the electron charge).

For the conduction electrons in a semiconductor we write (Stern, 1967);

$$Z = 2/\pi \sum_\ell (2\ell+1) \int_0^\infty f(E) \frac{d\delta_\ell}{dE} dE, \quad (\text{A.3.2})$$

where $f(E)$ is the Fermi function. Assuming a sharp Fermi surface, the first equation follows from the second.

The usual form for the screening length (Eq. A.1.6) can be derived from the Friedel sum rule and the first Born approximation. The Friedel sum rule is thought to be exact (Mahan 1981, p. 236).

Appendix A.4
The First and Second Born Approximation

Here we are concerned with the Born series for the phase shifts of partial waves. The development of the appropriate mathematics can be obtained from standard references such as Joachain (1975). The equations we need are

$$\tan \delta_l = -k \int_0^\infty j_l(kr) U(r) R_l(k, r) r^2 dr, \quad (\text{A.4.1})$$

and

$$R_l(k, r) = j_l(kr) + \int_0^\infty G_l(r, r') U(r') R_l(k, r') r'^2 dr', \quad (\text{A.4.2})$$

$$G_l(r, r') = k j_l(kr_<) \eta_l(kr_>), \quad (\text{A.4.3})$$

where $r_>$ and $r_<$ are the greater and lesser of r and r' respectively and j_l , η_l are the spherical Bessel and Neuman functions.

One iteration yields the first Born approximation for the phase shifts

$$\tan \delta_l^{(1)} = -k A_l, \quad (\text{A.4.4})$$

(see Eq. 2).

Two iterations yield the second Born approximation

$$\tan \delta_l^{(2)} = \tan \delta_l^{(1)} - k B_l, \quad (\text{A.4.5})$$

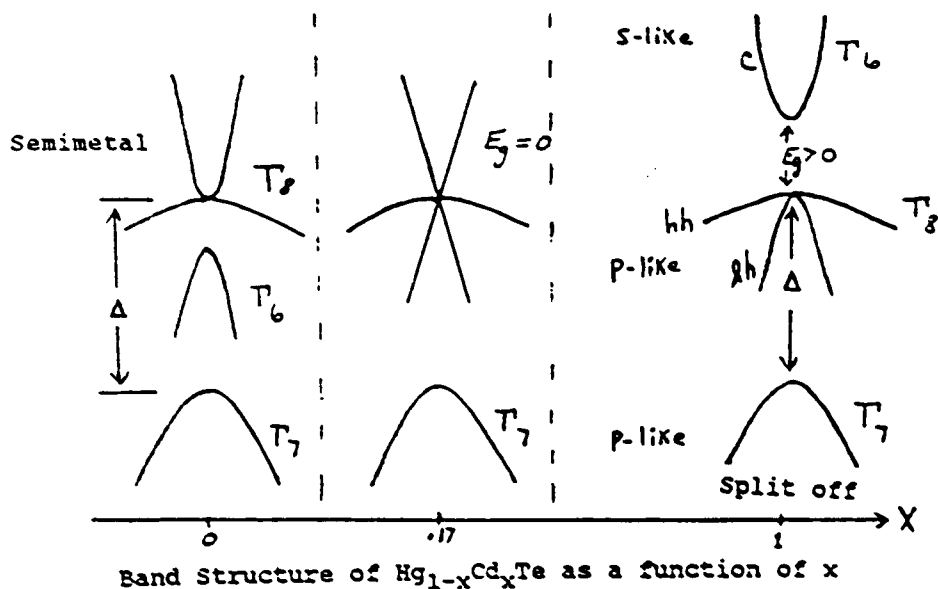
(see Eq. 4).

Variational methods can yield even better approximations (Joachain, ch. 10, 1975). The following agrees with the Born series through second order.

$$\frac{\tan \delta_l}{k} = -k \frac{A_l^2}{A_l - B_l} \quad (\text{A.4.6})$$

Appendix A.5
Band Structure of $\text{Hg}_{1-x}\text{Cd}_x\text{Te}$
The Three Level Model

It is customary to neglect the bands not shown.



The $\vec{k} \cdot \vec{p}$ Hamiltonian is solved with this model (Kane, 1957) near the Γ point ($k = 0$). The equation describing the conduction band (c), the light hole (lh) band and the split off band is

$$E^3 + (\Delta - E_g)E^2 - (E_g\Delta + P^2k^2)E - \frac{2}{3}\Delta P^2k^2 = 0, \quad (\text{A.5.1})$$

where P is a momentum matrix element. The heavy hole (hh) band is described by a simple parabolic band. The spin-orbit interaction mixes mixed spin functions and the $\vec{k} \cdot \vec{p}$ interaction mixes s and p functions. The dispersion relations are non parabolic and the electron effective masses are typically small.

Whitsett (1981) gives a two and a half page summary of Kane's band theory and discusses the band structure of the similar compound $\text{Hg}_{1-x}\text{Cd}_x\text{Se}$. For $x > x_0 \cong .17$ (the cross over point) the band structure^x is like InSb. Γ_6 and the light hole

part of π_g are coupled by the $\vec{k} \cdot \vec{p}$ interaction and this "inverts" them. For $\chi < \chi_0$, π_6 becomes a valence band and $\pi_g(lh)$ becomes a conduction band. The degeneracy of these two below χ_0 causes the energy gap to vanish.

Appendix A.6 The Fröhlich Hamiltonian

In $\text{Hg}_{1-x}\text{Cd}_x\text{Te}$, at not too low temperatures, the scattering of current carriers by polar longitudinal optic phonons is particularly important. The Fröhlich Hamiltonian describes this interaction. As given by Mahan (1981, p. 487) it is

$$H = \sum_{\mathbf{p}} \frac{\mathbf{p}^2}{2m} c_{\mathbf{p}}^{\dagger} c_{\mathbf{p}} + \sum_{\mathbf{q}} \hbar \omega_{\mathbf{q}} a_{\mathbf{q}}^{\dagger} a_{\mathbf{q}} + \sum_{\mathbf{q}, \mathbf{p}} f(\mathbf{q}) c_{\mathbf{p}+\mathbf{q}}^{\dagger} c_{\mathbf{p}} (a_{\mathbf{q}} + a_{-\mathbf{q}}^{\dagger}), \quad (\text{A.6.1})$$

where $c_{\mathbf{p}}^{\dagger}$, $c_{\mathbf{p}}$, $a_{\mathbf{q}}^{\dagger}$, $a_{\mathbf{q}}$ are the customary creation and annihilation operators for electrons and phonons and $f(\mathbf{q})$ which is proportional to the effective charge for interaction (Ehrenreich, 1956) is defined by Mahan. This coupling is not effective for transverse modes because these do not create strong electric fields. It is usual to approximate $\omega_{\mathbf{q}}$ by two modes (for HgTe and CdTe).

In order to discuss screening properly, one needs to add to this Hamiltonian electron-electron interactions. Screening affects the way the lattice interacts and so it affects the phonon energies. Screening also affects the electron-phonon interactions (Ehrenreich, 1959). Screening is included by insertion of the correct dielectric function (Zawadski, 1974, Lehoczky et al, 1974, Whisett, 1981 p. 98).

Appendix A.7
Approximations

We first give an order of magnitude estimate for the quantity LaZ which we have assumed to be small.

$$\text{If } L = 1\text{\AA}$$

$$Z = 1$$

$$a = \frac{2m^*}{\hbar^2} \frac{e^2}{4\pi\epsilon_0} \quad (\text{MKS})$$

$$m^* = .025m_e$$

then we find

$$LaZ = .1$$

Although L might be larger, we also should correct the above by dividing by a static dielectric constant so the estimate may not be too far off. If the electron has an energy of 1 electronvolt and a mass as given above we estimate (on a parabolic band assumption) that

$$k \cong 8 \times 10^8 \text{ m}^{-1},$$

thus if L is 1\AA then

$$kL = .08.$$

The following simple argument picks out what ℓ 's should be important. If b is the impact parameter we expect

$$kb \sim \ell.$$

Now if $b > L$ then there should be no scattering for those values of ℓ for which

$$b = \ell/k > L.$$

Thus if $kL < 1$,

we would only expect the $\ell = 0$ terms to be important.

Joachain (1975 p. 172) notes that at zero energy ($k = 0$) the Born series converges if

$$\int_0^{\infty} r |U(r)| dr < 1, \quad (\text{for } l=0). \quad (\text{A.7.1})$$

Substituting and evaluating the integrals we find this requires
 $L a z < 1$.

Thus our basic approximations would appear to be O.K. provided kL and $L a z$ are both small, which would at least be true at low temperature.

Appendix A.8
Density of States
and
Screening Length

If $\rho(E)$ is the density of states per unit volume, several authors give the screening length as

$$L_{(1)}^{-2} = k_{TF}^2 / \epsilon_b, \quad (A.8.1)$$

where a background dielectric constant ϵ_b is included and Eq. A.1.6 gives k_{TF} (with A.1.12). As we have seen, this can also be called the screening length in the 1st Born approximation. This expression is still valid for non parabolic bands provided they are spherical.

Now

$$\rho(E) dE = \frac{2}{(2\pi)^3} 4\pi k^2 dk, \quad (A.8.2)$$

for spherical energy surfaces using the usual factor of $(2\pi)^{-3}$ for the number of states per unit volume in real and k space and the factor of 2 comes from spin. This implies

$$\rho(E) = \frac{k^2}{\pi^2} \frac{dk}{dE}. \quad (A.8.3)$$

Sometimes the momentum effective mass (m^*) is used. For m^* ,

$$m^* v = \hbar k$$

$$v = \frac{1}{\hbar} \frac{dE}{dk}$$

so

$$\rho(E) = \frac{k m^*}{\hbar^2 \pi^2}. \quad (A.8.4)$$

Appendix A.9 Better Approximations

If we are to make better approximations we must eliminate the three approximations we made; namely,

(a) m^* in $V(r)$ a constant for corrections to the first Born approximation

(b) $kL \ll 1$

(c) only need $l = 0$ term.

We first indicate what happens when we relax (a) and (c). It is convenient to redo the derivation a bit to see how things fit together.

We assume $a \propto m^*$ is not a constant. In order to get agreement with previous results for the screening length, m^* is interpreted as the momentum effective mass as in Eq. A.8.4. If we assume

$$\delta_l f(E) \Big|_0^\infty = 0,$$

the Friedel sum rule can be written

$$2/\pi \sum_l (2l+1) \int_0^\infty \delta_l \left(- \frac{\partial f}{\partial E} \right) dE = Z. \quad (A.9.1)$$

With A_l and B_l defined as previously

$$\delta_l = -k \left[\int_0^\infty j_l^2(kr) U(r) r^2 dr + B_l (1 - B_l/A_l)^{-1} \right], \quad (A.9.2)$$

If we let $a = m^*b$ where now m^* is considered a function of k , putting the expression for δ_l into the Friedel sum rule and using

$$j_l(z) = \frac{z^l}{(2l+1)!!} \quad (A.9.3a)$$

and

$$\eta_l(z) = - \frac{(2l-1)!!}{z^{l+1}} \quad (A.9.3b)$$

as long as $|Z| \ll 1$, we find

$$\frac{L^2}{L_{(1)}^2} = 1 - \frac{2Zb^2}{\pi} \sum_l \left[2^{-(2l+1)} (2l)!! / (2l+1)!! \right] L^{2l+3} \int \frac{k^{2l+1} m^*^2 \left(-\frac{\partial f}{\partial E} \right) dE}{1 - \frac{bZ}{2l+1} 2^{-(2l+1)} m^* L}, \quad (\text{A.9.4})$$

where as before $L_{(1)}$ is the screening length in the first Born approximation. This is obviously not a simple equation to solve.

To see what happens if we do not assume $kL \ll 1$, it is instructive to evaluate A_0 .

$$\begin{aligned} A_0 &= \int_0^\infty j_0^2 U(r) r^2 dr \\ &= - \int_0^\infty \frac{\sin^2(kr)}{(kr)} (Za) r e^{-r/L} dr. \end{aligned} \quad (\text{A.9.5})$$

We easily obtain

$$A_0 = - \frac{Za}{k} \left[\frac{1}{4} \ln(1 + 4k^2 L^2) \right]. \quad (\text{A.9.6})$$

If $kL \ll 1$ we obtain,

$$A_0 = - (LaZ) L \left[1 - 2 (kL)^2 \right], \quad (\text{A.9.7})$$

which goes over to our previous results when $(kL)^2$ is negligible compared to 1. Similar results can be obtained for B_o , but they do not appear to be particularly transparent.

N88-15628

527-63
116729
176

1987

NASA/ASEE SUMMER FACULTY RESEARCH FELLOWSHIP PROGRAM

MARSHALL SPACE FLIGHT CENTER
THE UNIVERSITY OF ALABAMA IN HUNTSVILLE

EXPERT SYSTEM TECHNOLOGY

Prepared by:	Mary Ellen Prince, M.S.
Academic Rank:	Instructor
University and Department:	University of Alabama in Huntsville Department of Computer Science
NASA/MSFC:	
Laboratory:	Space Sciences
Division:	Astrophysics
Branch:	X-ray Astronomy
MSFC Colleague:	Martin C. Weisskopf
Date:	August 21, 1987
Contract No.:	The University of Alabama in Huntsville NGT 01-008-021

OBJECTIVES

The objectives of my research this summer were

1. To present a series of informal talks covering general topics in the area of artificial intelligence.
2. To concentrate in particular on the subject of expert systems, with an emphasis on their possible usefulness and practicality in scientific applications

This report will summarize some of the findings on expert systems.

INTRODUCTION

The emergence in recent years of expert systems as a new kind of computational tool is a trend that deserves close examination by every organization that uses computers for problem solving. To evaluate the utility of expert systems prospective users must understand what these systems are, how they are structured, and when they can produce beneficial results.

Briefly stated, an expert system is a computer program that attempts to reproduce the problem-solving behavior of an expert. Experts do not generally rely on domain axioms and principles when solving a problem. Instead, they tend to employ ready-made or empirical "know-how", compiled from past experience. They are able to view problems from a broad perspective and arrive at conclusions rapidly, using intuition, shortcuts, and analogies to previous situations. This experiential knowledge is called heuristic knowledge, and is what differentiates the expert from the merely competent.

Expert systems are a departure from the usual artificial intelligence approach to problem solving. Researchers have traditionally tried to develop general models of human intelligence that could be applied to many different situations. Expert systems, on the other hand, tend to rely on large quantities of domain specific knowledge, much of it heuristic. The reasoning component of the system is relatively simple and straightforward. For this reason, expert systems are often called knowledge based systems.

The body of this paper will attempt to expand on the ideas outlined above. Section 1 will explain the architecture of a typical expert system. Section 2 discusses the characteristics that make a problem a suitable candidate for expert system solution. Section 3 surveys current technology, describing some of the software aids that are available for expert system development. Section 4 discusses the limitations of this technology. The concluding section will attempt to predict future trends.

1. EXPERT SYSTEM COMPONENTS

Expert systems have three major components: a working memory, which contains facts about the current problem; the knowledge base, an integrated body of domain facts, heuristics, and relationships; and the inference engine, which is the reasoning and control mechanism. This organization is derived from earlier studies of production system models, which were originally proposed as a general computational mechanism. [Davis and King, 84] Production systems consist of a data base, a set of rules, and a rule interpreter. They have been used for a variety of purposes, including compiler construction, formal language theory, and psychological modeling of human cognitive processes. Early expert system designers saw production systems as an elegant formalism for representing the mental activity of expert problem solvers.

Working Memory

Working memory corresponds in some ways to the data storage area of conventional programs. It is empty until a problem is proposed. At that time, the initial problem description and data are entered, perhaps by means of a consultation between the program and the user. As the program works toward a solution, additional facts are inferred or provided by the user. These are stored in working memory as well, as are any intermediate results concluded by the reasoning process.

Knowledge Base

The knowledge base is arguably the most important part of an expert system. Its structure is more complex than that of the working memory and its development is a collaborative effort between the domain expert and a knowledge engineer. The knowledge engineer is a trained professional whose responsibility is to help the expert express his know-how verbally. This is a difficult task, since one characteristic of expertise is the ability to solve problems without following a conscious step-by-step procedure. Once the knowledge is verbalized it must be encoded in some form and run on sample problems. If the solutions do not agree with the expert's solutions to the same problems, the knowledge must be modified. Thus, development of the knowledge base is an iterative procedure.

How the knowledge is represented is an important consideration. Heuristics are most commonly described by a set of production rules which have the format IF (condition) THEN (action). Rules are a convenient method of encoding "chunks" of knowledge, and are thought by many cognitive scientists to reflect the way the human brain organizes information. Rules are "triggered" when their conditions are satisfied by facts from the working memory. Once triggered, a rule may be "fired" by the inference engine. When a rule fires, its action causes a change in working memory, possibly triggering other rules in the process.

Domain facts can be represented in a number of different ways. Object-attribute-value (O-A-V) triples were used in many of the early systems. An object can be either a physical entity or a concept. Attributes are the general characteristics that describe an object, and values identify a specific instance of the object. For example the object "ball" might have attributes "size", "shape", and "color". A specific ball could then have descriptive attribute values such as "size" = "large".

Frames or units provide another way to describe objects. A single frame represents an object and contains a number of "slots". Slots are similar to, but more general than, the attributes in O-A-V triples. Two special slot types, superclass and subclass, provide a method of structuring factual information into a hierarchy. The object "ball" might be a member of the super-class "toys" and have as subclasses "baseball", "football", "golfball", etc. In the absence of knowledge about a particular object's attributes, values may be inherited, or passed down by default, from the frame which defines that object's superclass.

Logic programming languages such as PROLOG are another approach to knowledge representation. Rules are expressed as logical propositions and facts as assertions. Built-in language features are then able to reason with this knowledge.

Inference Engine

The inference engine's reasoning processes are based on formal logic. In a simple production rule system the inference strategy is usually a variation of the modus ponens principle, which states that if

the conditions of a rule are satisfied, then it may be inferred that the result is also true. To illustrate, assume that a knowledge base contains the rule "If a person is a secretary then that person can type" and that the working memory contains the fact "Martha is a secretary". From this it is logical to conclude that Martha can type.

Systems which are built on logic programming languages use more sophisticated proof techniques based on the predicate calculus. These techniques are provided as standard control mechanisms in the language, much as DO-LOOPS are provided by FORTRAN.

Human experts often solve problems in situations where information is missing or uncertain. Consequently, inference engines should also be able to operate with incomplete data. To provide this capability most systems include facilities which allow users and knowledge engineers to tag facts and rules with certainty factors. Special combining rules enable the system to infer conclusions which are similarly qualified.

The control portion of an inference engine determines which rules will fire and the order of their firing. There are two basic control strategies: backward chaining, or goal directed, and forward chaining, or data driven. Both depend on the fact that the rules in a rule-based system form a hierarchical structure, with paths through the hierarchy from initial facts and conditions to conclusions.

Backward chaining is appropriate when a problem has a few well defined solutions (goal states). The system selects a tentative goal or hypothesis, perhaps based on some external priority, and examines its conditions. If working memory contains these conditions as facts, then the goal is established. Otherwise, the conditions will in turn be the goals of other rules and the system will try to establish them. By following this procedure repeatedly, the inferencing process can work backwards to the initial facts of the case. If the first goal selected cannot be proved, the system will select another and try again.

Forward chaining is a more complex procedure but is appropriate when there are many possible goal states, or when the goals are poorly or incompletely defined, as in planning situations. In this strategy

the rule hierarchy is traversed from initial facts to goals. The contents of working memory are compared to the condition clauses of rules and those rules whose conditions are satisfied are eligible to fire, thus modifying the contents of working memory. Repeated applications of this "recognize-act" cycle will eventually produce a solution.

An immediate consequence of the system architecture outlined above is that expert systems are relatively easy to modify. Because the knowledge base is completely separate from the control structure it can be developed incrementally. As knowledge in a domain increases or changes, rules can be added or modified. In fact, it is feasible to replace the entire knowledge base with one from another domain, since the inference engine is not problem dependent. This is the basic principle underlying the concept of expert system shells. The algorithmic structure of conventional programs, on the other hand, does not lend itself so readily to change. Knowledge and control are closely integrated in the program code and changes in one facet of the program frequently require changes in the other.

User Interface

One final aspect of expert system design is the user interface. Most expert systems are based on a consultation paradigm, where the user supplies the initial problem parameters in response to a series of questions proposed by the program. At certain points during execution the system may ask for additional information. Under ideal circumstances this dialogue would be conducted in natural language, but since natural language processing is not yet a mature technology it is more common to find restricted forms of communication based on menus or one word responses. A few systems are able to process English language responses within a very limited area, but this is the exception rather than the rule.

Explanation facilities are included in many expert systems. If the user wonders why a particular question was asked or how a conclusion was reached, he can interrogate the system directly. Explanations are usually little more than straightforward translations of the rules which are currently under consideration, and do not attempt to offer a deeper

rationale. Nevertheless, the ability of an expert system to justify its own actions is considered by many people to be a valuable feature, and is one of the characteristics that distinguishes expert systems from traditional programs.

2. APPROPRIATE PROBLEMS

Not every problem is a good candidate for expert system solution. Conventional computational techniques are still preferable in situations where clearly defined procedures, or algorithms, are available. Expert system technology should only be considered when one or more of the following conditions is present:

The task to be performed is usually handled by an expert who uses heuristic rather than algorithmic techniques.

The task is combinatorily explosive. There are so many conditions and complex interactions involved that even experienced human experts have difficulty considering all of them.

The task is qualitative rather than quantitative, involving symbolic rather than numerical manipulations. Solutions may be subjective or judgmental in nature.

In addition to the above factors which characterize the problem domain, the current state of expert system technology imposes further restrictions. There must be at least one person, expert in the task domain, who is able to explain his expertise and problem solving techniques. The domain itself must be relatively narrow and well defined. Improvements in machine learning and knowledge acquisition methods may at some future date enable these restrictions to be relaxed.

Successful expert systems have been developed in a variety of fields, from medicine to engineering. An examination of the task domains reveals that the applications fall into a few broad categories, identified by function. A discussion of several of these categories will further serve to illustrate the range and applicability of expert system technology.

Diagnosis/Classification

Problems in this area try to identify a particular object or situation as being a specific instance from a set of possible situations. Identification is based on a group of "symptoms" provided by the user. Many diagnostic programs prescribe remedial action once the situation is identified. Typical applications include medical diagnosis and fault diagnosis in various kinds of systems.

MYCIN, developed as part of the Heuristic Programming Project at Stanford University, [Buchanan and Shortliffe, 84] is an excellent example of a medical diagnostic program. Its purpose is to identify bacterial infections and then prescribe an appropriate antibiotic treatment. This is a hard task, even for experienced diagnosticians. The physician must first decide if a significant infection is present and then identify the particular organism (or set of possible organisms) which is responsible for the infection. Finally, a suitable combination of drugs must be chosen to treat the disease. It is frequently necessary to make these decisions based on fuzzy and incomplete data; thus, good judgment is an essential component of the decision process.

MYCIN works as a backward chaining system. An initial hypothesis, based on preliminary patient data, is selected and guides the program in its consultation with the physician. Once the most likely organisms are identified, the program prescribes a drug treatment. Certainty factors attached to the action portion of rules enable the system to reproduce the judgmental behavior of domain experts.

DELTA (Diesel-Electric Locomotive Troubleshooting Aid) [Harmon and King, 85] was developed by the General Electric Company, Schenectady, New York, to assist railroad personnel in the maintenance of diesel-electric locomotives. In addition to locating mechanical faults DELTA provides diagrams showing the faulty components and can, if requested, show training films which instruct maintenance personnel in the necessary repair procedures.

Planning

Planning problems are constructive in nature, unlike diagnostic programs, which have a fixed set of possible solutions built in. Plan generation may be

described briefly as follows: Given a task and the current situation, decide how to perform the task. [Charniak and McDermott, 85, p. 487] By decomposing the initial problem into subtasks, perhaps down through several levels, the system eventually identifies a set of elementary tasks whose solution plans are built into the system. It can then construct a master plan based on these subplans. Usually, constraints of various kinds must be incorporated into the planning process.

One of the best known planning programs is R1, sometimes known as XCON. R1 was developed by John McDermott [McDermott, 81]. It is used regularly by Digital Equipment Corporation to configure VAX computer systems. There are no standard VAX systems; instead, customers choose from a list of several hundred components which must then be arranged to conform to physical constraints imposed by the components themselves, the size of the area in which the system is to be installed, and other considerations. Due to the complexity of the systems and frequent modifications to the data base, the problem is difficult and time consuming even for experienced personnel. R1 has reduced system configuration time from hours to minutes, with a savings to the company which is measured in millions of dollars.

The MOLGEN programs are equally successful in an entirely different domain. Their purpose is to design experiments for molecular geneticists to use for analyzing DNA molecules. Originally developed at Stanford University, MOLGEN has evolved into GENESIS, a package of several expert systems available from IntelliCorp (formerly IntelliGenetics). Users have the option of accessing GENESIS through a time sharing system or as a program to run on a LISP machine. [Harmon and King, 85]

Intelligent Instruction

Traditional computer-aided instruction consists of little more than an electronic textbook or training manual supplemented by question and answer drills. In contrast, intelligent assistance can be provided by embedding the knowledge bases of expert systems into larger programs. In addition to expert domain knowledge, intelligent tutors must contain teaching expertise and some way of interacting with the student.

GUIDON, developed by William Clancey at Stanford, was an early attempt to adapt an expert system for

instructional purposes. [Clancey, 82] It uses the knowledge base from MYCIN augmented by some two hundred additional rules which outline teaching strategies, methods of communicating with students, and explanation techniques. GUIDON has been used experimentally to train medical students at the Stanford School of Medicine.

Other instructional programs, notably STEAMER [Harmon and King, 85] and SOPHIE [Brown, 82], while not true expert systems, are still able to provide intelligent guidance to students by employing many of the techniques of knowledge engineering. STEAMER is being developed by the Naval Research Personnel Development Center in conjunction with Bolt Beranek and Newman. Its purpose is to train naval officers to run the steam propulsion plants in naval ships. SOPHIE tutors students in the art of troubleshooting electronic devices. Both programs use sophisticated simulation models of the systems being taught. Students are allowed to change the simulations interactively and observe what happens as results of the changes are propagated through the model.

Search

Occasionally expert systems are used in domains where algorithms are also available. Typically, these are "generate-and-test" algorithms. They provide a method of systematically enumerating candidate solutions, each of which must then be tested to determine if it matches the problem statement. Expert systems use heuristics to limit the number of possible solutions generated, thus reducing significantly the amount of time spent in testing.

DENDRAL, developed at Stanford, is a good example of a heuristic search program. The task is to determine the structure of a particular molecule when given information about its component atoms and its mass spectra. [Barr and Feigenbaum, 82] Heuristics provided by expert chemists act as constraints, ruling out certain structural features and requiring the presence of others. The program is reported to perform at a level consistent with, or better than, domain experts.

This is by no means a comprehensive survey of expert system applications. As with any rapidly developing technology, new uses appear on the scene regularly. Some involve small systems which may not even deserve the name "expert". Nevertheless they are useful in many situations as an extension of or replacement for human involvement. Monitoring industrial equipment and processes is an example of this kind of application.

3. DEVELOPMENT AIDS

The earliest expert systems were developed using high level languages intended specifically for artificial intelligence applications, notably LISP. LISP provides a great deal of flexibility in the way information can be organized and is expressly designed to perform symbolic manipulations. Other AI languages such as PROLOG have also been used. Conventional programming languages (FORTRAN, for example) are oriented toward numerical processing and do not contain many of the features which simplify the job of the AI programmer.

In recent years the trend has been to provide even more assistance than is available from special purpose languages. Software tools developed expressly for expert system development are now being marketed for all size machines and in all price ranges. Most commercially available expert system tools are LISP-based, although some are written in PROLOG or PASCAL. Tools are in general less flexible than high level languages, but compensate for this loss of flexibility by offering a variety of special features which simplify the job of the knowledge engineer. Typically, these features would include an inference engine, various aids to knowledge acquisition and knowledge representation, and utilities to help with the development and debugging of the knowledge base.

Small expert system shells are designed to run on personal computers and support the development of systems containing a few hundred rules. Most of these tools are based on the diagnostic model, use backward chaining as the primary control strategy, and represent facts as O-A-V triples. Interaction with the user is through menus or a question-and-answer format. Little support is provided for knowledge engineering. Knowledge bases are typically created outside of the system using a word processor, although a few systems prompt for knowledge entry. Some provide trace features that let the user watch the rules as they fire. This is a useful method of debugging the knowledge base. Examples of this class of tools are ES/P ADVISOR (Expert Systems International), M.I (Teknowledge, Inc.), and Personal Consultant (Texas Instruments).

Large system building tools are much more powerful than the simple aids discussed above. They run on large computers or special LISP workstations and can be used to

construct systems with several thousand rules. Instead of offering a single paradigm, they provide an array of features that can be used to customize a program to the application. System builders can choose from several different control strategies. Most common knowledge representation schemes are available, including O-A-V triples, frames, inheritance and certainty factors. Sophisticated graphics capabilities aid in debugging and the design of special screens. Such flexibility does not come without a price, however. The knowledge engineer must be skilled in the use of the tool and must be thoroughly familiar with the task domain in order to choose the most suitable methods out of the many that are offered. Software vendors usually provide workshops or on-site consulting to train programmers in the use of the tool. Examples of large expert system tools are ART (Automatic Reasoning Tool) from Inference Corp. and KEE (Knowledge Engineering Environment) from IntelliCorp.

Expert system developers may employ different tools at different stages. An initial prototype, which serves as a proof-of-concept, might be built quickly with one of the smaller expert system shells. The final prototype expands on this preliminary version by augmenting the knowledge base, providing graphic interfaces, and adding other features. A large tool is typically required at this point. For additional information on factors to consider in choosing a tool see Citrenbaum, Geissman and Schultz. Surveys of some of the current commercial tools are available from Harmon and King, and Gevarter..(See references)

4. LIMITATIONS

The advantages of expert systems have been widely advertised. They solve problems that have previously been intractable to computer solution, using programs that can evolve to keep pace with changes in the problem domain. They provide expert advice and assistance to an entire community of users, allowing human experts the freedom to work on new problems. They reduce computationally explosive tasks to a manageable size. The benefits of expert system technology should not, however, blind potential users to its limitations.

The heart of an expert system is its knowledge base and this is also the source of many of its limitations. Knowledge acquisition is a costly and time-consuming process, requiring months on the part of expert and knowledge

engineer alike. Once the knowledge base is built, the problem becomes one of truth maintenance. As rules are added over time, it becomes increasingly likely that contradictions and inconsistencies will be introduced. Size is also a problem; even modest systems may require many hundreds of rules. One practical consequence of all this is the necessity to restrict expert systems to narrow, well-understood task domains. Current technology does not support building the enormous knowledge bases that would be needed to handle problems with a broader scope.

Reliability is also of critical concern. Most systems employ a form of "shallow" reasoning; that is, inferences are based on heuristics and empirical data rather than being derived from domain axioms and principles. As a result, such systems tend to perform poorly when confronted with unexpected situations which were not anticipated in the original design.

Other problems are a result of the need to interface the system to humans, both during the building and operational phases of its lifetime. Ideally, one would like to be able to enter rules and describe problems in English, but in fact most systems still require the use of a stylized and sometimes obscure knowledge representation language.

Explanation facilities are limited in their ability to justify system behavior. A typical explanation consists of English translations of the rules involved in reaching that conclusion. Definitions of terms, causal relationships, and other potentially helpful information cannot be presented since it is not represented in the knowledge base.

An even more fundamental problem concerns the basic nature of expertise. Many skeptics question whether IF-THEN rules can fully capture the essence of an expert's know-how. [Dreyfus, 86] They claim that while rule based systems may be able to perform credibly in some situations, true expertise operates on many levels and cannot be reduced to an analytic process.

CONCLUSION

In the last five to ten years interest in artificial intelligence has increased dramatically. Established companies are developing AI departments, government agencies are investing enormous sums in AI research, and private software firms specializing in AI products are proliferating. Most of this activity centers on expert systems and related technology. Although there are still relatively few workable systems in use today, many prototypes are currently undergoing development and refinement.

It is reasonable to project that within the next five years small, special purpose expert systems will become common. Implemented on personal computers or as specially designed micro chips, these systems could perform reliably in many situations. Programs to monitor instruments and industrial machinery, to serve as intelligent procedure manuals or training aids, and to retrieve information from data bases are within the reach of current technology. Many of these small systems will be more appropriately called "competent" rather than "expert". When (and whether) large, truly expert systems will become widespread depends on the progress made by AI researchers in a number of areas.

First, there must be significant improvements in techniques of knowledge representation and knowledge acquisition. New methods for incorporating causality and domain principles into the reasoning process will enable systems to handle novel situations and to better justify their actions. Current research in computer learning techniques offers great promise for the future. A system which can learn domain rules by analyzing examples provided by an expert will greatly simplify the process of knowledge acquisition. Extrapolating even further, one can imagine a system provided with basic domain knowledge which will enable it to generate solutions by trial-and-error; and which, by observing the results, is able to derive its own rules independent of expert assistance. Methods of incorporating general world knowledge and common sense knowledge would provide even more human-like performance.

Currently there are ongoing research projects in all of these areas. Although advances have been made there is still much that remains to be done before significant

results will appear. There are some who think that order-of-magnitude improvements will not be possible unless new computer architectures are developed. They argue that today's sequential processing machines do not model the working of the human brain closely enough to successfully simulate intelligent behavior.

Regardless of whether expert systems are truly intelligent or can be considered accurate models of human expertise, it is becoming increasingly apparent that they can, in fact, be an important aid to computational problem solving. Existing systems have demonstrated the ability to perform reliably when used in an appropriate context and without unrealistic expectations. System designers who are aware of the weaknesses of expert system technology as well as of the advantages will be able to realize its full potential.

REFERENCES

- Barr, Avron and Feigenbaum, Edward A., eds., "Applications-oriented AI Research: Science", in The Handbook of Artificial Intelligence, Vol. II, William Kaufmann, Inc., Los Altos, California (1982).
- Brown, J. S., Burton, R., and deKleer, J., "Pedagogical, Natural Language and Knowledge Engineering Techniques in SOPHIE I, II, and III", in Intelligent Tutoring Systems, Sleeman, D. and Brown, J. S., eds., Academic Press, Cambridge, Mass., (1982).
- Buchanan, Bruce G. and Shortliffe, Edward H., Rule Based Expert Systems, Addison-Wesley Publishing Company, Reading, Mass. (1984).
- Charniak, E., and McDermott, D., Introduction to Artificial Intelligence, Addison-Wesley Publishing Company, Reading, Mass., (1985).
- Citrebaum, Ronald, Geissman, James R., and Schultz, Roger, "Selecting a Shell", AI Expert, Vol. 2, No. 9, 30-39, (1987).
- Clancey, W. J. "Tutoring Rules for Guiding a Case Method Dialogue", Intelligent Tutoring Systems, Sleeman, D. and Brown, J. S., eds., Academic Press, Cambridge, Mass. (1982).
- Davis, Randall, and King, Jonathan J., "The Origin of Rule-Based Systems in AI", in Rule Based Expert Systems, Buchanan, Bruce and Shortliffe, Edward H., Addison Wesley Publishing Co., Reading, Mass. (1984).
- Dreyfus, Hubert and Stuart, "Why Expert Systems Do Not Exhibit Expertise", IEEE Expert, Vol. 1, No. 2, 86-90, (1986).
- Gevarter, W.B., "The Nature and Evaluation of Commercial Expert System Building Tools", IEEE Computer, Vol. 20, No. 5, 24-41, (1987).
- Harmon, Paul, and King, David, Expert Systems: Artificial Intelligence in Business, John Wiley and Sons, New York, NY (1985).
- McDermott, J. "R1: The Formative Years", AI Magazine, Vol. 2, No. 2, 21-29 (1981).

528-39
N88-15629/16730
30P

1987

NASA/ASEE SUMMER FACULTY RESEARCH FELLOWSHIP PROGRAM

MARSHALL SPACE FLIGHT CENTER
THE UNIVERSITY OF ALABAMA IN HUNTSVILLE

AN INVESTIGATION OF
OBLIQUE HYPERVELOCITY IMPACT

Prepared By:	William P. Schonberg
Academic Rank:	Assistant Professor
University and Department:	The University of Alabama in Huntsville Mechanical Engineering
NASA/MSFC:	
Laboratory:	Materials and Processes
Division:	Engineering Physics
Branch:	Laboratory Support
NASA Colleague:	Roy Taylor
Date:	August 17, 1987
Contract No:	The University of Alabama in Huntsville NGT-01-008-021

ABSTRACT

This report describes the results of an experimental investigation of phenomena associated with the oblique hypervelocity impact of spherical projectiles on multi-sheet aluminum structures. A model that can be employed in the design of meteoroid and space debris protection systems for space structures is developed. The model consists of equations that relate crater and perforation damage of a multi-sheet structure to parameters such as projectile size, impact velocity, and trajectory obliquity. The equations are obtained through a regression analysis of oblique hypervelocity impact test data. This data shows that the response of a multi-sheet structure to oblique impact is significantly different from its response to normal hypervelocity impact. It was found that obliquely incident projectiles produce ricochet debris that can severely damage panels or instrumentation located on the exterior of a space structure. Obliquity effects of high-speed impact must, therefore, be considered in the design of any structure exposed to the hazardous meteoroid and space debris environment.

INTRODUCTION

All spacecraft with a mission duration of more than a few days are susceptible to impacts by meteoroid and pieces of orbiting space debris. These impacts occur at high speeds and can damage flight-critical systems of a spacecraft. This damage can in turn lead to catastrophic failure of the spacecraft. Therefore, the design of a spacecraft for a long-duration mission must take into account the effects of such impacts on the spacecraft structure and all of its exposed subsystem components, such as solar arrays and instrumentation units.

Until recently, meteoroid impact was better understood and believed to be more serious than the impact of orbital space debris. However, recent studies and workshops on orbital debris have determined that orbital debris is becoming an increasingly serious hazard to long-duration near-earth space missions (see, e.g., Kessler and Su, 1985; Reynolds, et.al., 1983; and, Kessler, 1981). In certain regions of earth orbit the threat of orbital debris impact now exceeds the threat posed by meteoroid impact. It is evident from these and other studies that the orbital debris problem is serious, and that the probability of collision is rising as the orbital population increases. Protective systems must be developed in order to insure the safety of a spacecraft hull and its occupants, as well as the integrity of its exterior subsystems when encountering the meteoroid and space debris environment.

The design of meteoroid/space debris protection systems depends largely on the ability to predict the behavior of a variety of structural components under conditions of meteoroid or space debris impact. Forty years ago it was suggested that 'meteoroid bumpers' could be used to minimize the damage caused by the high-speed impact of meteoroids (Whipple, 1947). Since then, numerous experimental and analytical investigations have been performed to determine the resistance of multi-sheet structures to hypervelocity impact (see, e.g., Swift, 1983; Wilkinson, 1969; Lundeborg, et.al., 1966; Maiden and McMillan, 1964; and, Wallace, et.al., 1962). In the majority of the experimental studies, the trajectories of the high-speed projectiles were normal to the surface of the structures. However, it has become increasingly evident that most meteoroid or space debris impacts will not occur normal to the surface of a spacecraft. Unfortunately, information on oblique hypervelocity impact is relatively scarce so that it is difficult to assess the severity of such impacts on a structure or subsystem component. Studies of oblique impact that have been performed typically do not discuss the possibility of ricochet damage to external systems (see, e.g., Johnson, 1969; McMillan, 1968; Burch, 1967; and, Summers, 1959).

OBJECTIVES

To increase the understanding of phenomena associated with oblique hypervelocity impact, a program of research was developed at the Marshall Space Flight Center. The objective of this program was to generate and analyze oblique hypervelocity impact test data. The results of this research program are presented in this report.

In the first section, a review of the experimental procedure used in the oblique hypervelocity impact testing of multi-sheet structures is presented. In the next section, impact test results are reviewed qualitatively. In the following sections, the test data obtained are reduced and analyzed. The analysis indicates that perforation and ricochet trajectories, as well as bumper hole dimensions, can be correlated as functions of the impact parameters of the original projectile and the geometrical properties of the projectile/multi-sheet specimen system. A preliminary investigation of ricochet damage is performed to determine probable sizes and velocities of ricochet particles. In the final section, conclusions are made based on the analysis of the data and visual inspection of the damaged specimens. Recommendations for future experimental and analytical investigations of oblique hypervelocity impact are also presented.

EXPERIMENTAL PROCEDURE AND RESULTS

The oblique hypervelocity impact testing of multi-sheet specimens was done at the Space Debris Simulation Facility of the Materials and Processes Laboratory at the Marshall Space Flight Center. The Facility consists of a light gas gun with a 12.7 mm launch tube capable of launching 2.5 - 12.7 mm projectiles of mass 4 - 300 mg at velocities of 2 - 8 km/sec. Projectile velocity measurements were accomplished via pulsed X-ray, laser diode detectors, and a Hall photographic station. The light gas gun has three target tanks with interior volumes of 0.067, 0.53, and 28.5 cubic meters. The multi-sheet specimen set-up is shown in Figure 1. The specimens and the conditions of impact were chosen to simulate the conditions of space debris impact as closely as possible and still remain within the realm of experimental feasibility.

In each test, an spherical projectile of diameter D impacted a bumper plate of thickness t_B with a velocity V and at an angle of obliquity θ . The projectile was shattered upon impact and created an elliptical hole in the bumper plate. Some secondary projectile and bumper plate fragments were sprayed upon the pressure wall plate a distance S away while some fragments ricocheted and struck the ricochet witness plate (thickness t_R). The angles θ_1 and θ_2 are 'perforation angles' and denote the trajectories of bumper and 'in-line' projectile fragments, respectively. The angles α_c and α_{99} are 'ricochet angles' and denote the trajectory of the center of mass of the ricochet fragments and the angle below which lie 99% of the ricochet fragments, respectively.

The projectiles used were solid 1100 aluminum spheres of diameter 4.75 mm, 6.35 mm, and 7.95 mm. The bumper, pressure wall, and ricochet witness plates were made of 6061-T6, 2219-T87, and 2219-T6 aluminum, respectively. Their thicknesses were held constant at 1.5875 mm, 3.175 mm, and 2.54 mm, respectively. The angles of obliquity ranged from 30 to 75 degrees, and the test impact velocities ranged from 5.0 to 7.5 km/sec. The bumper and pressure wall plates were separated by a constant distance of 10.16 mm. A total of 22 test specimens were used to study the penetration and ricochet phenomena.

The results of the test firings are presented in Table 1. The angles θ_1 and θ_2 were obtained by estimating the locations of the centers of mass of the bumper fragments and 'in-line' projectile fragments on the pressure wall plate. The angle α_c was obtained by determining the vertical location of the center of mass of the ricochet debris based on the vertical distribution of the holes, craters, etc. formed by the debris. The angle α_{99} was determined based on the height below which lay 99% of the holes, craters, etc. formed by the ricochet debris. The minimum and maximum dimensions of the bumper plate hole, D_{min} and D_{max} , respectively, were measured directly from the bumper plate. Examples of damaged test specimens for various angles of obliquity are presented in Figures 2 through 5. Visual inspection of these and other test plates

revealed several interesting features in each of three obliquity regimes.

Low Obliquity Regime ($0\text{-deg} < \theta < 45\text{-deg}$)

For the impact tests in which the angle of obliquity was 30 degrees, there was extensive damage to the pressure wall plate but virtually no damage to the ricochet witness plate (Figures 2b and 2c). The pressure wall plate damage strongly resembled the damage observed during normal impact. Furthermore, the trajectory of the center of mass of the projectile fragments was very close to the original impact trajectory. The hole in the bumper plate was elliptical, with an eccentricity close to 1.0 (Figure 2a).

Medium Obliquity Regime ($45\text{-deg} < \theta < 60\text{-deg}$)

The damaged pressure wall plates shown in Figures 3b and 3c are typical of test specimens in which the trajectory obliquity of the original projectile was greater than 45 degrees. Two distinct areas of damage are discernable on the plates. The damage areas on the left contain craters and holes that are nearly circular, which is characteristic of normal impact. The craters in the damage areas on the right are oblong, indicating that they were formed by oblique impacts. From these considerations, it became possible to differentiate between pressure wall plate damage caused by bumper plate fragments (circular craters and holes) and damage caused by projectile fragments (oblong craters and holes). As the trajectory obliquity of the original projectile was increased, the trajectories of the bumper plate and projectile fragments were observed to separate even more. The trajectory of the bumper fragments began to approach the normal line between the bumper and pressure wall plate while the trajectory of the projectile fragments, although no longer 'in-line' with the original trajectory, was still relatively close to it. The bumper plate hole was still elliptical with a steadily increasing eccentricity (see Figures 3a and 4a).

High Obliquity Regime ($60\text{-deg} < \theta < 75\text{-deg}$)

With further increases in obliquity, an increasing amount of cratering and perforation was observed on the ricochet witness plates. Up to a certain critical angle, the most serious damage was still observed on the pressure wall plate, with the ricochet witness plate sustaining a relatively low level of damage (Figures 3b,c and 4b,c). However, once the critical angle was exceeded, the ricochet witness plate began to exhibit excessive cratering and perforation while the damage to the pressure wall plate decreased dramatically (Figure 5c). This critical angle is estimated to have a value between 60 and 65 degrees. At obliquities beyond this critical angle, the trajectory of the shield fragments was virtually normal to the pressure wall plate and the trajectory of the projectile fragments was severely departed from the original trajectory of the impacting projectile (Figure 5b). The bumper plate hole, although still elongated, ceased to be elliptical and developed a flattened end at the end nearest to the ricochet witness plate (Figure 5a). This indicates that a projectile incident at a high angle of obliquity will tear, as well as shatter, the bumper plate upon impact.

BUMPER PLATE HOLE ANALYSIS

Elastodynamic theory predicts that as a hypervelocity projectile impacts a protective bumper plate, the projectile and the portion of the plate surrounding the impact site will break up into many fragments (Cour-Palais, 1979). In order to be able to predict the damage capability of these fragments, it is necessary to know the volume of debris that will be produced as a result of the impact. A good estimate of the volume of bumper plate fragments can be obtained by calculating the area of the hole created during the impact. Inspection of the test specimens revealed the bumper plate hole to be elliptical with the elongation along the horizontal projection of the original projectile trajectory (Figures 2a, 3a, 4a, and, 5a). The bumper plate hole area can be, therefore, approximated as the area of an ellipse having major and minor axes equal to the maximum and minimum transverse hole dimensions, respectively. The objective of this analysis was to obtain empirical equations that relate these hole dimensions to impact parameters such as velocity, angle of obliquity, and projectile diameter.

Inspection of the hole size data in Table 1 reveals several interesting features. First, the size of the minimum dimension, D_{min} , appears to be relatively independent of the angle of obliquity. The maximum dimension, D_{max} , however, appears to be strongly dependent on trajectory obliquity.

Based on these observations, the first task in the analysis was to determine whether existing equations that predict bumper hole diameters in normal high-speed impacts could be used to predict either dimension of the holes formed in oblique impact. A survey of the literature revealed six equations for hole diameter under normal impact. They are listed in the Appendix. The equations developed by Maiden, et.al. (1963) for normal impact were found to predict the minimum hole dimension under oblique impact rather well (See Table 2). However, no single equation was able to accurately predict the maximum hole dimension, even for small trajectory obliquities. This is not surprising considering the strong dependence of D_{max} on the initial trajectory obliquity of the projectile.

The second task undertaken was to independently derive empirical equations for the maximum and minimum hole dimensions as functions of the projectile diameter, impact velocity, and angle of obliquity. Because the minimum hole dimension is relatively independent of trajectory obliquity, an obliquity correction term was included only in the equation for the maximum hole dimension. The equations were obtained through standard multiple linear regression techniques with the following results:

$$D_{min}/D = 2.794 (V/C)^{0.962} (t_s/D)^{0.895} + 1.120 \quad (1)$$

$$D_{\max}/D = 4.575 (V/C)^{0.450} (\sin \theta)^{1.303} (t_S/D)^{0.672} + 1.470 \quad (2)$$

where C is the speed of sound in the bumper plate material. The average prediction errors and correlation coefficients of the regression model are presented in Table 3 (columns 1 and 2, respectively). The equations are a fairly good fit to the hole dimension data and have a small average prediction error. It should be noted that these equations are valid only for projectiles and plates made of the same material.

PERFORATION ANGLE ANALYSIS

The perforation angles θ_1 and θ_2 were obtained by estimating the locations of the centers of mass of the bumper fragment sprays and the 'in-line' projectile fragment sprays on the pressure wall plates of the impacted specimens. Empirical expressions for θ_1 and θ_2 were obtained first as functions of the bumper plate hole dimensions, and then as functions of projectile diameter, impact velocity and trajectory obliquity. The equations were obtained through standard multiple linear regression techniques with the following results:

As functions of bumper hole dimensions:

$$\theta_1 / \theta = 0.697 (V/C)^{0.277} (D_{\min}/D)^{0.246} (D_{\max}/D)^{-1.463} \quad (3)$$

$$\theta_2 / \theta = 1.518 (V/C)^{0.034} (D_{\min}/D)^{-0.733} (D_{\max}/D)^{-0.105} \quad (4)$$

As functions of original impact parameters:

$$\theta_1 / \theta = 0.085 (V/C)^{0.149} (\sin \theta)^{-1.744} (t_s/D)^{-0.233} \quad (5)$$

$$\theta_2 / \theta = 0.427 (V/C)^{-0.318} (\sin \theta)^{-0.225} (t_s/D)^{-0.436} \quad (6)$$

The average prediction errors and correlation coefficients are presented in Table 4. Inspection of the correlation coefficients reveals that the θ_2 data did not regress as well as the θ_1 data. This is in part due to the fact that the 'in-line' trajectory angle, θ_2 , is not a single-valued function of trajectory obliquity, θ . It can be seen in Figure 6 that θ_2 varies directly with θ up to a critical value, θ_{cr} , between 60 and 65 degrees and then decreases with further increases in θ . This reversal at $\theta = \theta_{cr}$ corresponds to a change in the location of the most severe damage from the pressure wall plate for $\theta < \theta_{cr}$ to the ricochet witness plate for $\theta > \theta_{cr}$. This multi-valued behavior of θ_2 and its effect on the behavior of θ_1 will be examined at a future time. As such, equations (3) through (6) are applicable only for angles of obliquity between 0 and 65 degrees. It should again be noted that these equations are valid only for projectiles and plates of the same material. Furthermore, the data used in the regression analysis itself may have an error of ± 1 or ± 2 percent due to the difficulty in determining the exact locations on the pressure wall plate of the centers of mass of the particle sprays.

RICOCHET ANGLE ANALYSIS

The ricochet angle α_c was obtained by determining the vertical location of the center of mass of the ricochet debris based on the vertical distribution of the holes, craters, etc., formed by the debris on the ricochet witness plate. The angle α_{99} was determined based on the height below which lay 99% of the holes, craters, etc. formed by the ricochet debris. Empirical expressions for α_c and α_{99} were obtained as first as functions of the bumper plate hole dimensions, and then as functions of projectile diameter, impact velocity and trajectory obliquity. The equations were obtained through standard multiple linear regression techniques with the following results:

As functions of bumper hole dimensions:

$$\alpha_c/\theta = 2.196 (V/C)^{1.079} (D_{\min}/D)^{-0.288} (D_{\max}/D)^{-2.295} \quad (7)$$

$$\alpha_{99}/\theta = 2.381 (V/C)^{0.465} (D_{\min}/D)^{0.185} (D_{\max}/D)^{-1.762} \quad (8)$$

As functions of original impact parameters:

$$\alpha_c/\theta = 0.030 (V/C)^{0.898} (\sin \theta)^{-2.892} (t_s/D)^{-0.685} \quad (9)$$

$$\alpha_{99}/\theta = 0.169 (V/C)^{0.431} (\sin \theta)^{-2.072} (t_s/D)^{-0.291} \quad (10)$$

The average prediction errors and correlation coefficients are presented in Table 5, which shows that the regression of the ricochet angle data was quite good. These equations are valid only for projectiles and plates of the same material, and for angles of obliquity, θ , between 45 and 65 degrees.

RICOCHET PARTICLE SIZE AND VELOCITY ANALYSIS

The next step in the analysis of the oblique impact test specimens was to use crater and hole damage on the ricochet witness plates to determine the sizes and velocities of ricochet debris particles. The following observations were made during inspection of ricochet witness plate damage.

1) Crater dimensions, such as diameter and depth, were found to increase with increasing trajectory obliquity. Penetration depths were observed to decrease with increasing projectile diameter and to increase with increasing original impact velocity.

2) Craters and holes found on ricochet witness plate were approximately circular in shape with very little elongation. This was not very surprising since it had been previously observed that 99% of the impacts occurred at angles of less than 30 degrees with respect to the plane of the bumper plate.

3) Hole diameters were found to increase with increasing trajectory obliquity, and with increasing projectile diameter.

4) The ricochet plates exhibited an excessive amount of dimpling, spalling, and perforation, especially at larger angles of obliquity and higher impact velocities. This damage was concentrated within an angle of 15 degrees with respect to the plane of the bumper plate.

Based on observation (2), it was assumed that normal impact equations for crater depths in thick plates and hole diameters in thin plates could be used in subsequent analyses. However, based on observation (4), it was concluded that equations for penetration depths in thick plates could not be used routinely in the analyses. These equations are, by definition, valid only when there is no spalling or dimpling on the reverse side.

Examination of existing hole diameter equations (ie. those in the Appendix) revealed a strong coupling between particle size and velocity effects. That is, the same size crater can be produced by a small particle travelling at a high speed or by a larger particle travelling at a slower speed. This ambiguity makes exact calculation of ricochet particle sizes and speeds extremely difficult.

However, it was possible to estimate the range of probable ricochet velocities based on an assumed range of probable particle diameters. These velocities were calculated by using the normal impact equations for hole diameters to solve for velocity in terms of all the other quantities. The lower limit of the particle diameter range was set by the limit of applicability of the equations. In most cases, this value was equal to 1.25 mm. For the purposes of this investigation, the upper

limit on the particle size was assumed to be equal to 1/2 of the original projectile diameter. Substitution of appropriate parameters and analysis of the results led to the conclusion that ricochet velocities can exceed 10 km/sec for the smaller particles, but can be as low as 0.5 km/sec for the larger particles. Thus, there is a good probability that some of the the larger ricochet debris particles travel at low velocities. These large low-speed particles can be expected to inflict more serious damage than the smaller ones travelling at higher velocities. In order to understand this phenomenon more fully, further tests will have to be made in which little or no perforation of the ricochet witness plate is allowed to occur. Under these conditions, ballistic limit equations, as well as penetration depth equations, can be used to obtain better estimates of ricochet particle sizes and velocities.

CONCLUSIONS AND RECOMENDATIONS

Several conclusions can be drawn from the analysis of key components in the problem of oblique hypervelocity impact on multi-sheet specimens. These conclusions can have a wide range of consequences on the design of spacecraft meteoroid and space debris protection systems.

First, there exists a critical angle of obliquity. Projectiles with angles of obliquity less than this critical angle produce significant damage to the interior pressure wall and little damage to the ricochet witness plate. Projectiles with trajectory obliquities greater than the critical angle produce little damage to the pressure wall plate, but produce ricochet debris that causes major damage to the ricochet witness plate. This critical angle is estimated to have a value between 60 and 65 degrees. The existence of such an angle has serious consequences on the design and placement of external subsystems such as instrumentation units on spacecraft that are developed for long-duration missions in the meteoroid and space debris environment.

Second, the damage potential of ricochet debris is difficult to extrapolate from existing damage data due to coupling effects of ricochet particle size and velocity. Initial investigations reveal that the velocities of small ricochet debris particles can exceed the original projectile impact velocity while the velocities of larger particles can enter the dangerous low velocity regime. Damage produced by the larger, slower particles was found to be more serious than that produced by the smaller, faster projectiles.

Third, the most serious ricochet damage was found to occur at angles less than 15 degrees with respect to the plane of the bumper plate. For original trajectory obliquities of greater than 60 degrees, the ricochet plate was completely perforated at the bumper plate/ricochet witness plate interface. In general, ricochet damage was found to increase with increases in original trajectory obliquity, original impact velocity, and the size of the original incident projectile.

Fourth, additional experimental and analytical studies are needed in order to be able to more accurately assess the extent of ricochet damage that can be expected to occur as the result of an oblique hypervelocity impact. Several specifics of these future studies are outlined below.

The following recommendations are made for future investigations of oblique hypervelocity impact phenomena.

- 1) It would be instructive to know at which angles the ricochet particles causing the largest holes or deepest craters strike the witness plate. A preliminary investigation of these angles was performed, but the results were inconclusive. Knowledge of these angles would enable a designer to estimate critical exterior locations and avoid them in the

placement of exterior subsystem components.

2) Future experimental testing of oblique impact should be conducted with ricochet witness plates sufficiently thick so that little or no perforation occurs. In this manner, virtually all the crater damage produced by ricochet particles can be used with thick plate equations to estimate ricochet velocities and particle sizes.

3) A more precise value of the critical angle of obliquity should be made. In order to accomplish this, a more sophisticated damage criterion is needed. It should also be determined whether or not this critical angle is dependent on any material, geometric, or impact parameters.

4) Future experimental investigations should be conducted with projectiles and specimen plates made from different materials. In this manner, the testing will better simulate on-orbit impacts of meteoroids or pieces of space debris with spacecraft materials. Use of a wide variety of materials, including composites, will also serve to improve and expand the applicability of the empirical expressions of the current model.

5) More testing should be done at higher angles of obliquity to complement the large number of tests that have been performed at smaller angles (ie. less than 45 degrees). In light of the existence of a critical obliquity angle near 60 degrees, these tests are essential to be able to fully understand the oblique impact process.

6) Further analyses of spray angles and damage areas due to projectile, bumper plate and ricochet debris particle sprays need to be performed. The inclusion of a thickness term in equations (3) and (4) should be investigated as should the inclusion of an obliquity correction term in equation (1). Information on the scatter of the predictions of the regression equations should also be provided.

7) Extensive analytical investigations of the phenomena involved in oblique hypervelocity impact are strongly recommended. Such investigations would achieve several important goals. First, they would provide verification of the empirical model developed in this study. Second, they would provide reliable means of predicting ricochet damage through accurate estimates of ricochet particle sizes and velocities. Third, they would yield damage criteria that would be applicable in a variety of impact situations.

In conclusion, a preliminary investigation of oblique hypervelocity impact has been successfully performed. A set of empirical equations that can be used to estimate the extent of structural damage due to such an impact has been derived. There is, however, a need for further combined experimental testing and analytical study of the mechanisms involved in oblique hypervelocity impact phenomena. Such investigations would result in more reliable design methodologies for meteoroid and space debris protection systems for future long-duration spacecraft, such as the space station.

REFERENCES

Burch, G.T., 1967, "Multi-plate Damage Study", AF-ATL-TR-67-116, Air Force Armament Library, Elgin Air Force Base, Florida.

Cour-Palais, B.G., 1979, "Space Vehicle Meteoroid Shielding Design", Proceedings of the Comet Halley Micrometeoroid Hazard Workshop, N. Longdon, ed., ESA SP-153, Paris, France, p. 85.

Johnson, W.E., 1969, "Oblique Impact Calculations Using a 3-D Eulerian Code", Proceedings of the AIAA Hypervelocity Impact Symposium, AIAA Pap. No. 69-353.

Kessler, D.J., 1981, "Sources of Orbital Debris and the Projected Environment for Future Spacecraft", J. Spacecraft, v. 18, n. 4, p. 357.

Kessler, D.J., and Su, S.Y., 1985, Orbital Debris, NASA CP 2360, Washington, D.C.

Lundeberg, J.F., Lee, D.H., and Burch, G.T., 1966, "Impact Penetration of Manned Spacecraft", J. Spacecraft, v. 3, n. 2, p. 182.

McMillan, A.R., 1968, "Experimental Investigations of Simulated Meteoroid Damage to Various Spacecraft Structures", NASA CR 915, Washington, D.C.

Maiden, C.J., and McMillan, A.R., 1964, "An Investigation of the Protection Afforded a Spacecraft by a Thin Shield", AIAA Journal, v. 2, n. 11, p. 1992.

Reynolds, R.C., Fisher, N.H., and Rice, E.E., 1983, "Man-Made Debris in Low Earth Orbit - A Threat to Future Space Operations", J. Spacecraft, v. 20, n. 3, p. 179.

Summers, J.L., 1959, "Investigation of High Speed Impact: Regions of Impact and Impact at Oblique Angles", NASA TN D-94, Washington, D.C.

Swift, H.F., Bamford, R., and Chen, R., 1983, "Designing Space Vehicle Shields for Meteoroid Protection: A New Analysis", Adv. Space Res., v. 2, n. 12, p. 219.

Wallace, R.R., Vinson, J.R., and Kornhauser, M., 1962, "Effects of Hypervelocity Particles on Shielded Structures", ARS Journal, p. 1231.

Whipple, E.L., 1947, "Meteorites and Space Travel", Astron. Journal, v. 52, p. 5.

Wilkinson, J.P.D., 1968, "A Penetration Criterion for Double-Walled Structures Subject to Meteoroid Impact", AIAA Journal, v. 7, n. 10, p. 1937.

APPENDIX

Thin Plate Hole Diameter Equations for Normal Hypervelocity Projectile Impact

Maiden, Gehring, and McMillan (1963):

$$D/d = 0.45 V (t_s/d)^{0.666} + 0.90 \quad (A-1)$$

$$D/d = 2.40 (V/C) (t_s/d)^{0.666} + 0.90 \quad (A-2)$$

Sawle (1970):

$$D/d = 3.2 [(\rho_p/\rho_T)(V/C)]^{0.222} (t_s/d)^{0.666} + 1.0 \quad (A-3)$$

Nysmith (1968):

$$D/d = 1.32 (t_s/d)^{0.45} V^{0.50} \quad (A-4)$$

Lundeberg, Stern, and Bristow (1965):

$$D/d = 3.4 (t_s/d)^{0.333} (V/C)^{0.333} (1.0 - 0.0308 \rho_T/\rho_P) \quad (A-5)$$

Rolsten, Wellnitz, and Hunt (1964):

$$D/d = [2.0 + (\rho_T/\rho_P)^{0.50}]^{0.50} \quad (A-6)$$

Notation

D ... hole diameter
d ... projectile diameter
V ... impact velocity
C ... longitudinal wave speed in
bumper plate material
 t_S ... bumper plate thickness
 ρ_P ... projectile material density
 ρ_T ... bumper plate material density

Additional References

Lundeberg, J.F., Stern, P.H., and Bristow, R.J., 1965, "Meteoroid Protection for Spacecraft Structures", NASA CR 54201, Washington, D.C.

Maiden, C.J., Gehring, J.W., and McMillan, A.R., 1963, "Investigation of Fundamental Mechanism of Damage to Thin Targets by Hypervelocity Projectiles", GM-DRL-TR-63-225, General Motors Defence Research Laboratory, Santa Barbara, California.

Nysmith, C.R., 1968, "Penetration Resistance of Double Sheet Structures at Velocities to 8.8 km/sec", NASA TN D-4568, Washington, D.C.

Rolsten, R.F., Wellnitz, J.N., and Hunt, H.H., 1964, "An Example of Hole Diameter in Thin Plates Due to Hypervelocity Impact", J. Appl. Physics, v. 33, n. 3, p. 556.

Sawle, D.R., "Hypervelocity Impact on Thin Sheets and Semi-Infinite Targets at 15 km/sec", AIAA Journal, v. 8, n. 7, p. 1240.

Acknowledgements

The author wishes to acknowledge the support of the NASA/ASEE Summer Faculty Fellowship Program along with Gerald Karr, the UAH Director, and Ernestine Cothran, the MSFC Program Co-Director.

The author's gratitude is extended to Roy Taylor, Chief of the Laboratory Support Branch of the Engineering Physics Division of the Materials and Processes Laboratory for his support and guidance.

Test No.	V (km/sec)	D (mm)	θ (deg)	D_{min} (mm)	D_{max} (mm)	Eccentricity	θ_1 (deg)	θ_2 (deg)	α_c (deg)	α_{gg} (deg)
EH1A	7.07	7.95	30	16.0	17.0	1.06	****	24.8	****	****
EH1B	6.96	7.95	45	16.5	20.0	1.22	10.9	38.1	15.5	29.2
EH1C	7.14	7.95	60	16.5	24.9	1.51	9.6	50.0	11.2	27.6
EH1D	7.18	7.95	75	14.5	36.1	2.49	4.7	26.9	7.9	27.1
EHCP	7.58	4.75	75	10.0	18.0	1.82	4.7	20.9	8.2	25.6
135C	6.76	6.35	30	13.2	14.2	1.08	****	24.0	****	****
135D	6.93	6.35	30	13.2	14.2	1.08	****	27.0	****	****
136A	6.25	6.35	55	14.0	18.3	1.31	10.7	43.5	8.7	23.3
136B	7.30	6.35	55	14.0	20.1	1.44	10.1	41.8	11.9	28.3
136C	6.67	6.35	55	13.5	17.0	1.26	11.0	38.2	12.9	28.4
150A	7.08	6.35	45	14.2	18.0	1.26	10.0	39.0	11.0	24.0
157A	7.40	4.75	60	13.7	17.3	1.26	9.3	36.0	8.0	22.0
162A	6.49	4.75	30	11.9	14.0	1.18	****	21.0	****	****
162B	5.03	4.75	30	9.9	11.7	1.17	****	27.0	****	****
206F	6.24	4.75	45	11.7	13.5	1.16	8.0	31.0	8.0	21.0
208E	6.48	6.35	65	13.0	21.0	1.61	9.0	47.0	8.0	20.0
209D	7.40	6.35	65	14.5	19.6	1.36	****	****	11.0	27.0
230C	5.16	6.35	45	12.4	16.0	1.28	10.0	34.0	11.0	26.0
230D	5.59	6.35	45	13.5	16.3	1.22	10.0	37.0	10.0	25.0
230E	6.62	6.35	45	14.2	17.5	1.25	10.0	32.0	12.0	25.0
231C	6.59	7.95	65	16.5	31.0	1.87	8.7	55.7	8.4	20.4
231D	7.26	7.95	65	16.5	25.9	1.57	10.2	49.7	9.7	23.0

Table 1 -- Impact Test Data

	Maiden et.al.		Sawle	Nysmith	Lundeberg et.al.	Rolsten et.al.
	(A-1)	(A-2)	(A-3)	(A-4)	(A-5)	(A-6)
Average Error (%)	-4	-1	+14	-16	+7	-15
Standard Deviation (%)	6	6	17	5	9	14

Table 2 -- Minimum Hole Dimension Predictions,
Normal Impact Equations

	$\% \epsilon_{avg}$	$100R^2$
D_{min}/D	-0.001	78.7
D_{max}/D	0.000	75.2

Table 3 -- Regression Analysis of Bumper Hole Dimension Data
Error Summary

		$\% \epsilon_{avg}$	$100R^2$
As functions of hole parameters	θ_1/θ	0.236	86.5
	θ_2/θ	0.269	50.2
As functions of imp. parameters	θ_1/θ	0.312	82.1
	θ_2/θ	0.226	57.7

Table 4 -- Regression Analysis of Penetration Angle Data
Error Summary

		$\% \epsilon_{avg}$	$100R^2$
As functions of hole parameters	α_c/θ	0.968	77.5
	α_{99}/θ	0.463	81.1
As functions of imp. parameters	α_c/θ	0.779	81.9
	α_{99}/θ	0.548	77.6

Table 5 -- Regression Analysis of Ricochet Angle Data
Error Summary

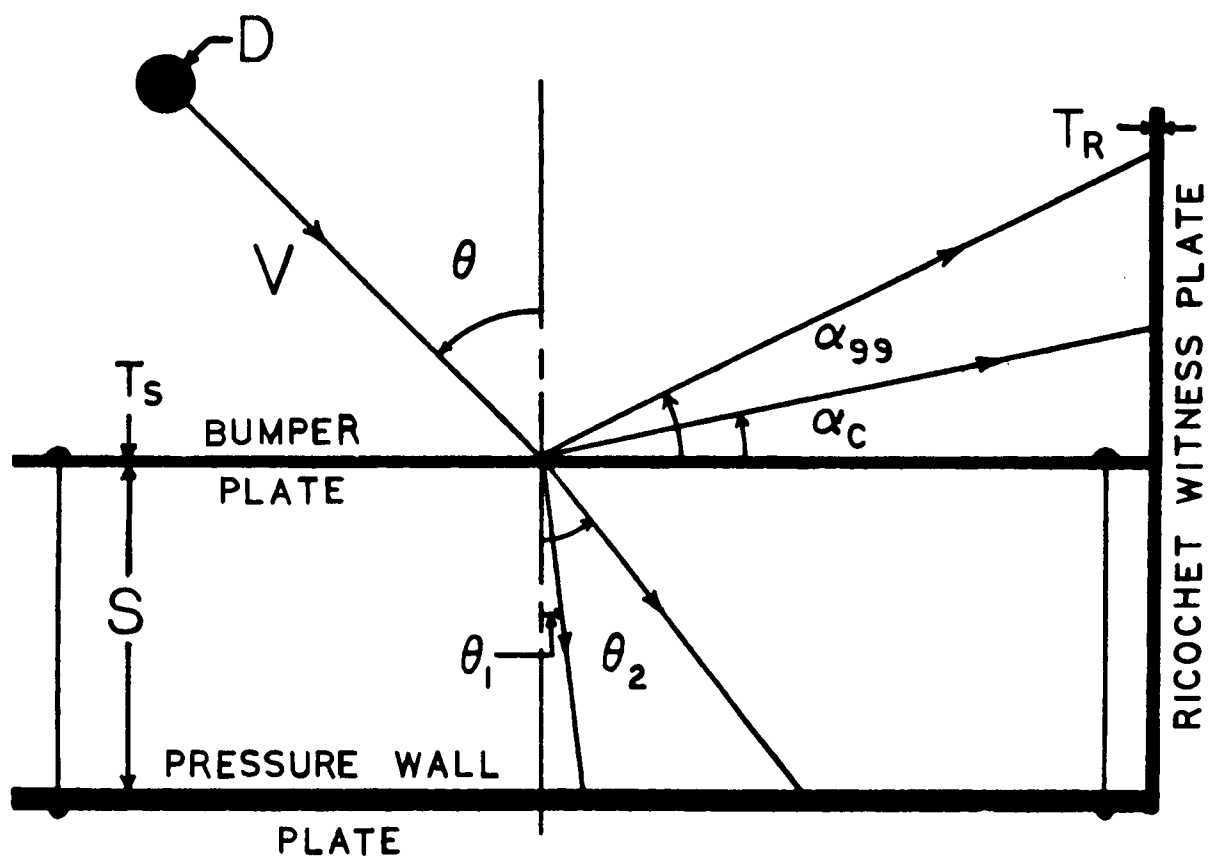


Figure 1 -- Test Configuration and Definitions

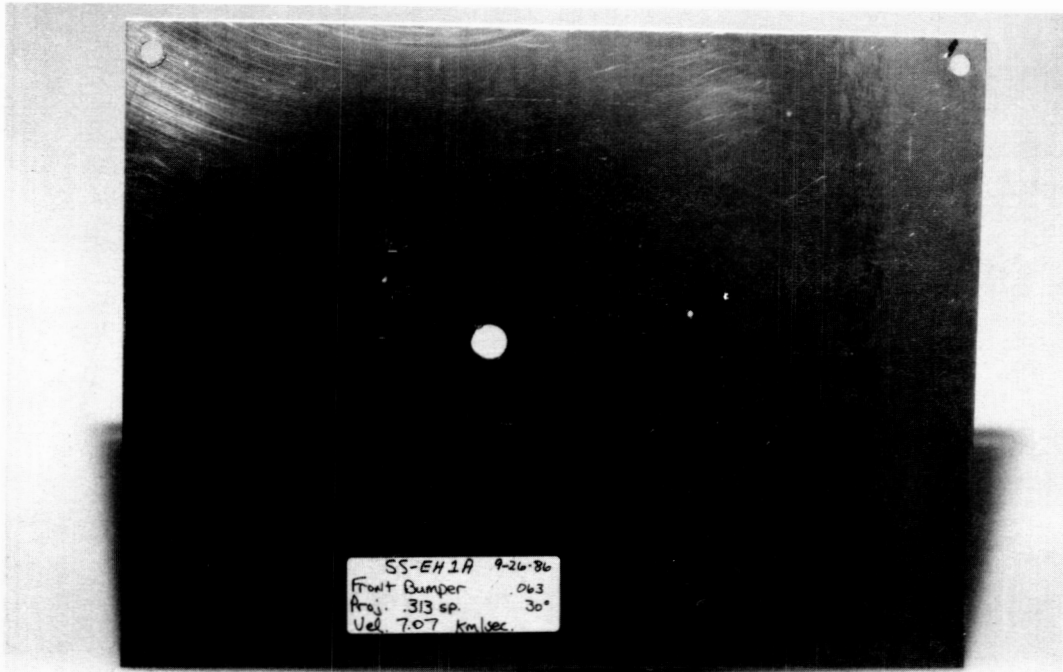


Figure 2a

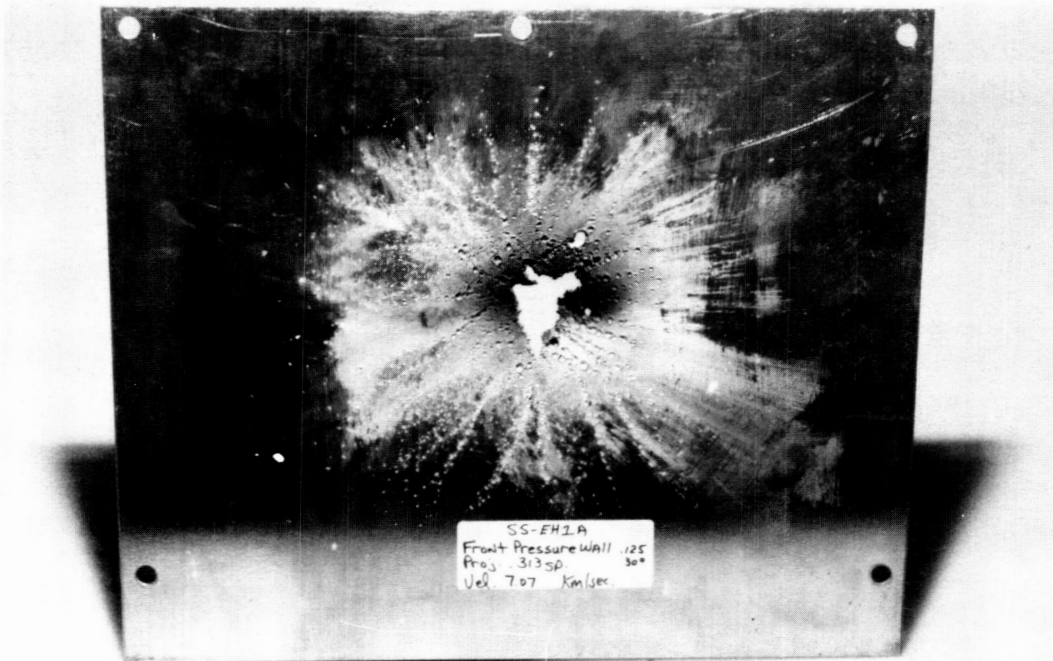


Figure 2b

ORIGINAL PAGE IS
OF POOR QUALITY

ORIGINAL PAGE IS
OF POOR QUALITY



Figure 2c

Figure Captions

Figure 2a -- 30-deg Impact (EH1A)
Bumper Plate

Figure 2b -- 30-deg Impact (EH1A)
Pressure Wall Plate

Figure 2c -- 30-deg Impact (EH1A)
Ricochet Witness Plate

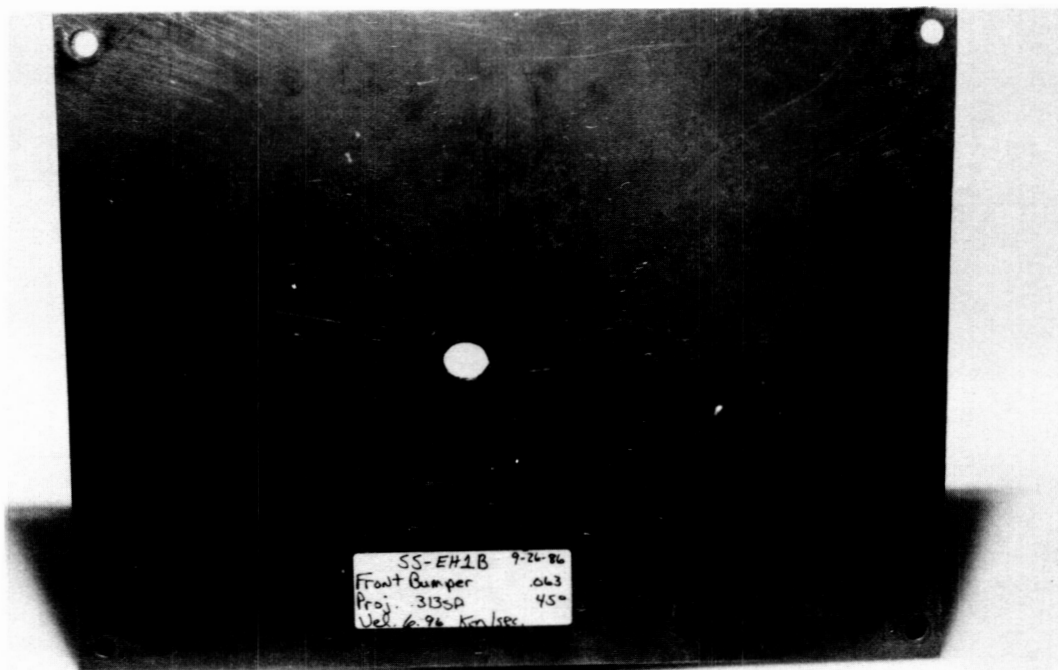


Figure 3a



Figure 3b

ORIGINAL PAGE IS
OF POOR QUALITY

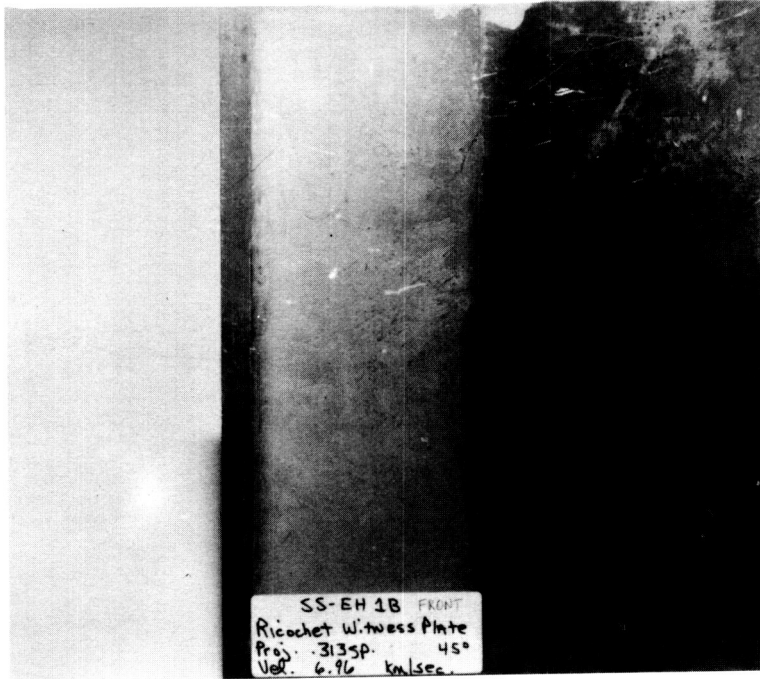


Figure 3c

Figure Captions

Figure 3a -- 45-deg Impact (EH1B)
Bumper Plate

Figure 3b -- 45-deg Impact (EH1B)
Pressure Wall Plate

Figure 3c -- 45-deg Impact (EH1B)
Ricochet Witness Plate

ORIGINAL PAGE IS
OF POOR QUALITY

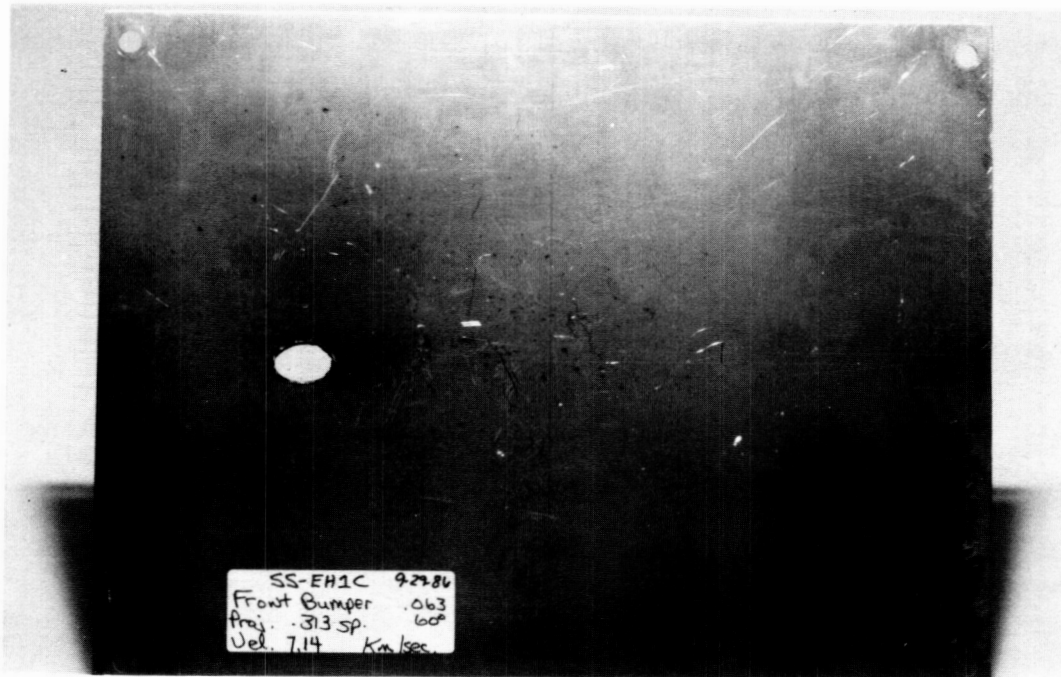


Figure 4a

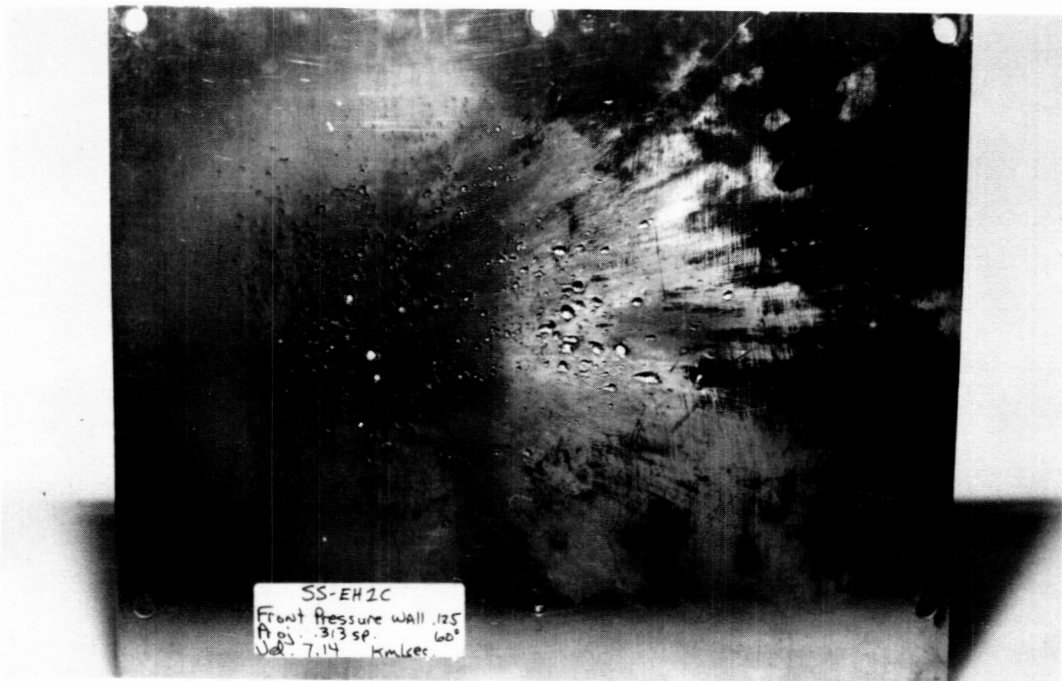


Figure 4b

ORIGINAL PAGE IS
OF POOR QUALITY



Figure 4c

Figure Captions

Figure 4a -- 60-deg Impact (EH1C)
Bumper Plate

Figure 4b -- 60-deg Impact (EH1C)
Pressure Wall Plate

Figure 4c -- 60-deg Impact (EH1C)
Ricochet Witness Plate

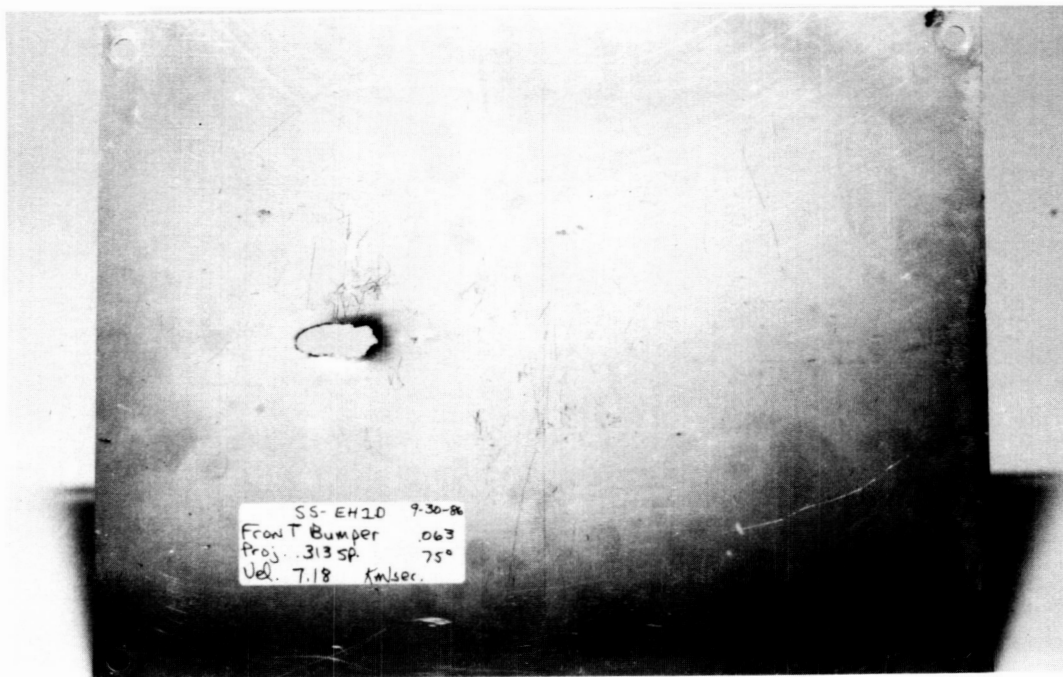


Figure 5a



Figure 5b

ORIGINAL PAGE IS
OF POOR QUALITY

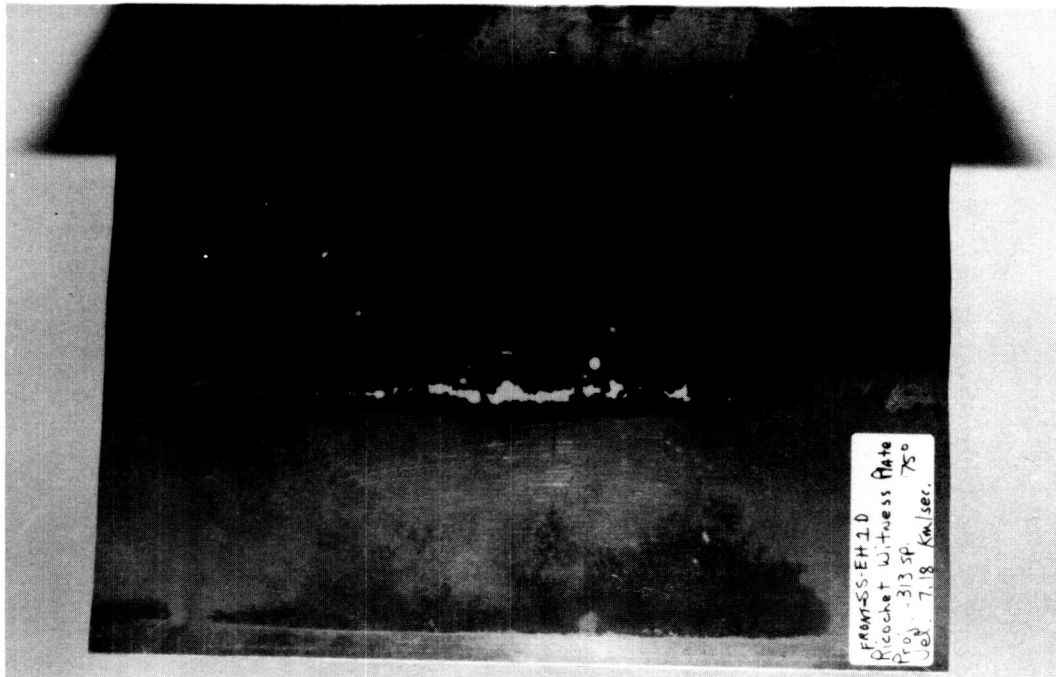


Figure 5c

Figure Captions

Figure 5a -- 75-deg Impact (EH1D)
Bumper Plate

Figure 5b -- 75-deg Impact (EH1D)
Pressure Wall Plate

Figure 5c -- 75-deg Impact (EH1D)
Ricochet Witness Plate

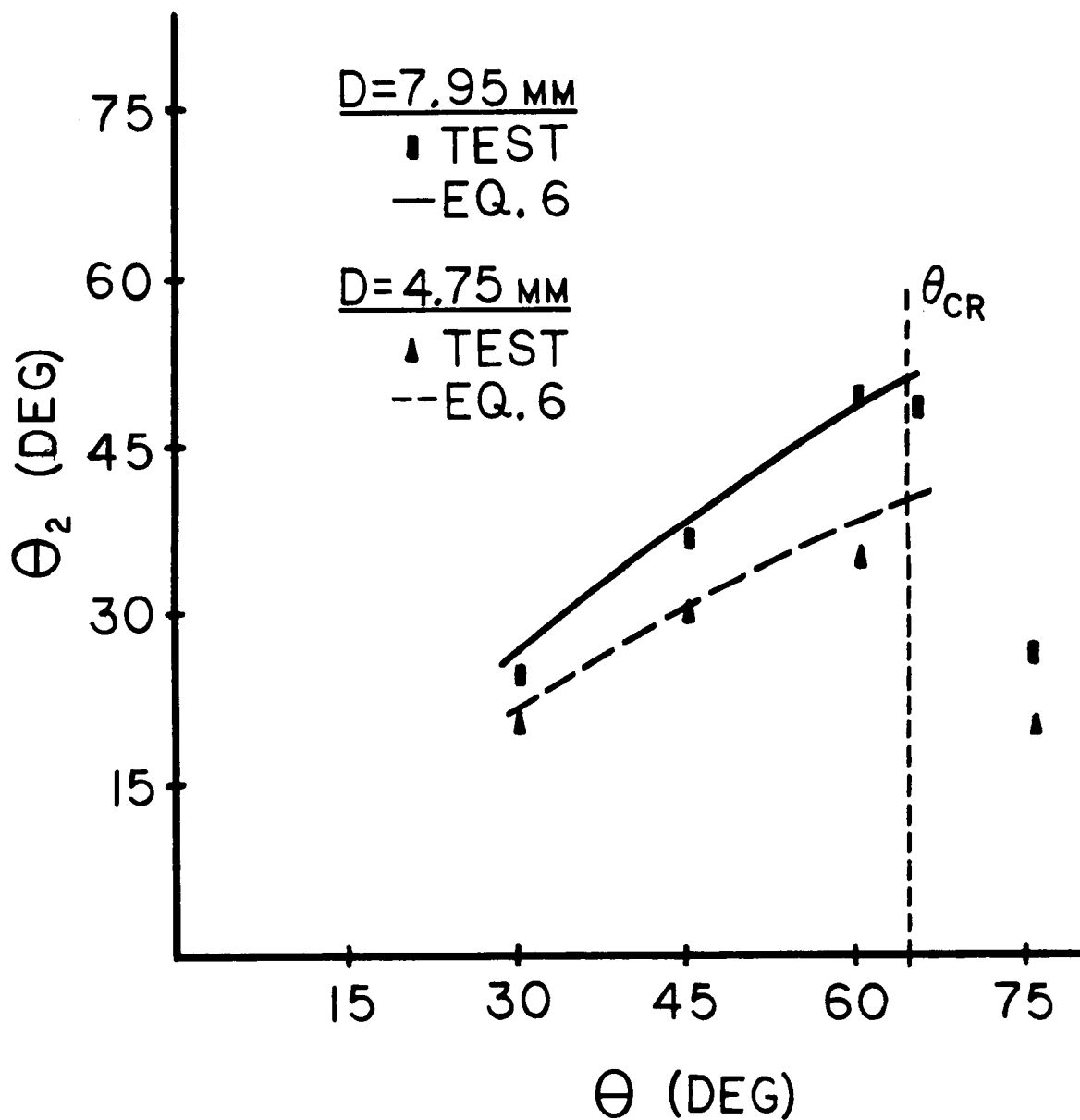


Figure 6 -- 'In-Line' Projectile Particle Trajectory:
 Test Data Compared With
 Regression Equation Predictions
 ($V=7$ km/sec)

N88-15630

529-39
116731
258

1987

NASA/ASEE SUMMER FACULTY RESEARCH FELLOWSHIP PROGRAM

MARSHALL SPACE FLIGHT CENTER
THE UNIVERSITY OF ALABAMA IN HUNTSVILLE

EVALUATE THE APPLICATION OF MODAL TEST AND ANALYSIS
PROCESSES TO STRUCTURAL FAULT DETECTION IN
MSFC - STS PROJECT ELEMENTS

Prepared By: William T. Springer
Academic Rank: Assistant Professor
University and Department: University of Arkansas
Mechanical Engineering

NASA/MSFC:

Laboratory: Test
Division: Structural Test
Branch: Dynamic Test

NASA Colleague: A. D. Coleman

Date: August 7, 1987

Contract No.: The University of Alabama
in Huntsville
NGT-01-008-021



XXX

ABSTRACT

The Space Transportation System (STS) is a very complex and expensive flight system which is intended to carry very unique payloads into low earth orbit and return. A catastrophic failure of the STS (such as experienced in the 51-L incident) results in the loss of both human life as well as very expensive and unique hardware. One impact of this incident has been to re-affirm the need to do everything possible to insure the integrity and reliability of the STS is sufficient to produce a safe flight.

One means of achieving this goal is to expand the number of inspection technologies available for use on the STS. The purpose of the activity reported here was to begin to evaluate the possible use of modal analysis and test techniques for the purpose of assessing the structural integrity of STS components for which Marshall Space Flight Center (MSFC) has responsibility. This entailed reviewing the available literature and determining a low-level experimental program which could be carried out by MFSC and would help establish the feasibility of using this technology for structural fault detection.

ACKNOWLEDGEMENTS

The author wishes to express his appreciation to the NASA/ASEE Summer Faculty Fellowship Program for the opportunity to participate in this program. In addition, he would like to specifically thank Gerald Karr, Dina Engler, Ernestine Cothran, and Billie Swinford for the support and guidance they provided this summer.

To NASA Colleagues A. D. Coleman and C. A. Kirby (Chief) of the Dynamics Test Branch, and G. B. Waggoner, Chief of the Structural Test Division, the author wishes to extend his gratitude for their interest and encouragement.

Finally, to G. D. Johnston (former Chief, Dynamics Test Branch) of Vibration and Acoustics, Inc., thanks are due for his support and assistance, both past and present.

INTRODUCTION

During recent years it has become increasingly necessary to assess the integrity of existing structural systems so as to determine their suitability for continued use. Examples of these structural systems include commercial and military aircraft, offshore oil platforms, commercial buildings in earthquake prone regions, and bridges. All of these examples are structures which represent a significant initial capital investment and/or the potential for harm to either human occupants or the environment or both if they fail.

Recently, the Space Transportation System (STS) has been added to this list. The STS has many components which are reuseable, and the Orbiter Vehicle is the most recognizable of these. In addition to the usual problems encountered in inspecting and evaluating the condition of a typical aerospace structure, the STS has several unique requirements which must be accommodated. These include exposure to an extremely hostile and wide ranging environment, the need to significantly reconfigure the vehicle for each flight, and a very tight schedule of access to the vehicle between flights.

The technology currently used to assess the integrity of the orbiter and other pieces of flight structure requires direct access to the areas to be inspected. Additionally, these technologies (such as ultrasonics, acoustic emissions, dye penetrants, and others) require the surface of the component to be inspected to be clean, and in many instances, the component must be physically removed from the structure. The result is an extremely localized inspection program which requires the expenditure of large amounts of time and labor, and can result in a degradation of the structural integrity just do to the disassembly-reassembly cycle involved. The DC-10 crash on take-off in Chicago a few years ago is a dramatic example of this possibility.

Less tragic but equally costly results can be produced by simple mistakes such as a bearing being improperly installed after an inspection of a large piece of equipment in the petrochemical or power generation industry. Therefore, any inspection scheme which either eliminates the need for or reduces the frequency of this type of detailed inspection process without sacrificing the quality of the inspection

can provide significant savings to the industry using it.

This approach has been used successfully in many process related industries and is referred to as "preventive maintenance". By monitoring such things as machine vibrations and the chemical composition of lubricants on a regular basis, it is possible to keep a running log of the condition of important pieces of equipment without removing them from service. In this manner, down-time and equipment outages can be controlled and scheduled to coincide with other related activities.

The purpose of the work performed under this program was to begin the evaluation of modal analysis methods for use as a structural fault detection tool. The major advantages this method has over those currently in use are that it is a global inspection technique, and does not require disassembly of the structure to be inspected. It may also be possible to extend the application of this technology to a point where it can function in a preventive maintenance role. However, the current interest in this technology centers around its global measurement capability, and the fact that it can be utilized without requiring any disassembly of the structure.

PROJECT DESCRIPTION

As mentioned earlier, modal analysis and testing techniques have two major benefits to offer as a Non-Destructive Evaluation (NDE) method. These are 1) the global nature of the evaluation and 2) the fact that the evaluation can be performed without disassembling the structure. However, there are some significant questions which must be investigated before it will be possible to determine the extent of the usefulness of this method as an NDE tool.

These questions concern themselves with such things as the type of fixturing, if any, required, the amount and type of data to be taken, the accuracy and repeatability required for the data, the type of data processing to be used, the manner in which the data should be presented, the rationale for interpreting the data, and so forth. While this list is far from complete, it serves to illustrate the complexity of this issue.

Therefore, it was decided that the best approach to take in the present effort was to review the literature available on this topic, and then establish a low-level test program that could be carried out by the Dynamic Test Branch at MFSC. This test program would serve to familiarize their personnel with the use of modal test methods for NDE purposes, demonstrate the level of accuracy and repeatability which is needed, allow some preliminary evaluation of various data processing and presentation methods, and to generally illustrate how typical aerospace structural systems will behave when damage is present. The results of these preliminary investigations will provide the basic information required to determine how best to proceed with a more advanced and ambitious evaluation program.

Literature Survey

The fact that the frequency content of a vibrating system changes as the physical characteristics of the system change has been used to advantage in several areas. These range from the above mentioned application to preventive maintenance and troubleshooting as described by Downham and Woods [5], Glew and Watson [6], Cempel [82], and Mutch and Russell [86] to the determination of the elastic properties of structural adhesives as explained by Adams and Crippendale [81].

One does not have to expend much effort to discover that this concept has been applied in many different forms to many different problems. This is demonstrated by the set of references listed at the end of this report. While this list is by no means complete, it does serve to illustrate the point quite well. In particular, these articles can be divided into several general categories, and they will be described in this manner.

Two areas which have received considerable attention in recent years are civil engineering structures and offshore oil platforms. Yao and his colleagues [11,15,16,78-80] have published extensively on the subject of inspecting civil engineering structures. The goal being to define a method of assessing the integrity of these structures after their exposure to some situation such as an earthquake which could severely damage a structure without causing it to collapse. The outcome of this work has been a probabilistic method to quantify the damage as either minor or moderate or severe coupled with an attempt to computerize the evaluation process. Inputs range from subjective evaluations made by inspectors to actual empirical data. There is no indication of how successfully the system works.

Krauthammer [9] has suggested a numerical evaluation plan similar in intent to that of Yao. Matzen and Hardee [10] have demonstrated a numerical method based on the Hessian matrix for determining if an element in an FEM model has a value of stiffness equal to zero. The ability of the method to determine a value other than zero was not studied. Sparks, Jeary and de Souza [17] are but one set of investigators that have examined the use of ambient excitation to determine the dynamic properties of a building. Kopff [21] has attempted to set down a rationale for inspecting large natural convection cooling towers also using ambient excitation. All of these investigations are lacking both experimental verification and a method of correlating the presence of damage to changes in dynamic properties.

Another type of structure which has received a fair amount of attention is the offshore oil platform. This class of structure is both unique and extremely expensive. Also, a sudden failure of such a structure can have a tremendous impact on the environment as well as the potential loss of human life. The two main obstacles faced by investigators in this area are both related to economics. The first is the general need to find an answer quickly when structural damage is suspected coupled with the lack of interest on the part of the petroleum industry in supporting fundamental

research on this topic. The second is the fact that the platform cannot be casually taken out of service at any time during its life. The cost of putting these structures into service and then keeping them operating is enormous. Therefore, any NDE which must be performed on these structures must take place while the platform is operating. This can complicate the measurement and analysis process to the point where it is virtually fruitless.

Loland, Mackenzie, Begg and Bendat [8,14,19] have highlighted some of these difficulties. One of the most significant of these is determining an adequate model of the platform which can be used with modal analysis procedures to determine structural integrity. This is not a simple problem. Kummer, Yang and Dagalakakis [13] have applied the "log decrement" technique to simple structures to detect the presence of fatigue cracks with an eye to applying the results to offshore platforms. This application to real structures has yet to be accomplished. Vanduerzen, Leuridan and Doucet [28] have also applied modal analysis techniques to an offshore platform. Again, the model of the platform used was extremely simple and made it difficult to determine the precise condition of the structure.

Large rotating equipment has also received attention. The concern in these papers is the ability to avoid an unexpected catastrophic failure of these extremely large and expensive pieces of equipment. In addition, if the need to disassemble this equipment unnecessarily can be avoided, the financial benefits to the owner are significant. This concern results from the fact that the materials used in these large pieces of equipment are not, typically, very damage tolerant. Therefore, a relatively small crack can be devastating. References 59 to 63 and 67 describe several different variations of this problem. In all cases, no clear choice for an obvious monitoring scheme is identified.

There has also been much written in way of what can be termed general application of vibration analysis to damage detection or the detection of structural changes. The amount of published literature is extensive and References 20, 22, 23, 25-27, 29, 30, 43-58, 64-72, 84, 85 and 88 constitute a small but representative sample of the work in this area. Virtually all of this work concentrates on examining very simple structures or structural elements and, again, it is unclear whether this information can be applied to real structural systems.

There have also been a number of theses and dissertations written on this general subject, and References 31 to 41 are

reflective of this work. Of this body of work, only the contributions of Haisty [40] and Duerr [41] have addressed the need of providing the analyst as well as the experimentalist with the capability of evaluating the effect damage will have on the dynamic properties of a structure. In the long term, this will be an important feature of this technology. Again, none of this work has been applied to large structural systems.

One method which seems to be finding some favor is to force an FEM model to exhibit the measured structural vibration characteristics. Typically, this approach uses some type of optimization routine to determine the final configuration. Most of the work which falls into this category is either proprietary or else just developing. More of this work should be coming to publication in the near future.

Present Investigation

The need to monitor the structural integrity of aerospace structures is well established. The number of these systems in commercial service alone is staggering. Recent estimates put the number of departures and arrivals in excess of 26,000 per day. Each of these flights carries a large number of passengers and operates, at least a portion of the time, in areas of high population density. These facts all combine to produce a situation that would result in the loss of a large number of human lives if a catastrophic structural failure should occur.

In addition to this pressure, the military also has a tremendous inventory of aircraft of all types. While, in general, these aircraft carry fewer passengers and crew than those in civilian service, the sheer number of aircraft in the military inventory establishes an economic imperative, if nothing else, to keep them in the best possible health. However, it is not at all clear how the needed inspections should be accomplished. This situation is well documented by Sproat and Rowe [87]. They point out how the existence of all the competing inspection technologies complicate the issue even more. This reference details a four year test program carried out by Lockheed-Georgia for the Air Force which was intended to evaluate all of these competing methods. But, as stated earlier, everyone agrees that inspections are needed.

One approach to this problem has been to measure the strain experienced by the structural component or assembly of interest and use this data to make a determination of its integrity. An early attempt to implement this strategy is

documented by Bochniak and Garcia [42]. This report describes a twelve channel strain measurement and recording system which was developed for the Navy, and intended for use as an aircraft structural integrity monitoring device. There is no information concerning the success of the monitoring program.

A more recent attempt to accomplish the same goal is presented by Bruinsma et al. [3], and details the use of fiber-optic strain measurements to provide information concerning the structural integrity of composite materials. Again, this reference describes only the data acquisition strategy and no information is presented concerning an actual application of this device in a real system.

The investigation presented here resulted, in part, from the interest generated by a Level II Change Request and PRCBD #S40155 titled "Orbiter Structural Inspection Via Modal Processes." This request was initiated by Mr. Walter M. West Jr., JSC-ES4, as a possible solution to the problem of inspecting components of the shuttle which cannot practically be inspected using other technologies. The particular items of concern are control surfaces. These components are typically built-up structures and can sustain internal damage which cannot be detected by conventional NDE methods without removal of the component's aluminum skin.

The prime motivation for this concern resulted from an acoustic test of the body flap of the Space Shuttle. Cheng, Dunham and Joanides [83] have documented the basic test procedure and expected test results. After the completion of this evaluation program on the body flap, a modal survey revealed that some of its dynamic characteristics had changed. West determined that damage had accumulated in the body flap by reviewing the vibrational mode shapes.

Later, West [74-76] developed a technique for locating damage in structures using a modal vector correlation coefficient. The structure is partitioned into several components and the correlation coefficient between baseline and post-service mode shapes are calculated. For components in which no change has occurred, the correlation coefficient is near unity, while in damaged segments the value of the correlation coefficient is less than one. The procedure was applied to Space Shuttle test specimens with success.

Haisty, West and Mitchell [77] applied West's technique to the Space Shuttle Orbiter body flap test specimen with good results. Several damage sites were correctly identified using this technique which were not detected by conventional

NDE techniques. While this technique can locate damage in structures reasonably well, it is unable to determine the extent of the damage.

As an extension of these activities, work has recently begun at JSC to apply this technique to a small Cessna airframe. The goal is to inspect the control surfaces while they are installed in the airplane. The initial damaged placed in the structure will be used to evaluate the concept of using local modes (i.e. modes primarily attributed to the subsystem only) to detect damage in the control surfaces. While this work is still in progress, the preliminary results are favorable.

Further support for the use of modal analysis procedures as an NDE tool has been provided by the Structural Dynamics Research Corporation [73]. SDRC has reported cases in which damage in spacecraft and airplanes has been diagnosed as the result of routine modal tests. They conclude that modal analysis can be readily adapted to the identification of structural failures, that frequency response functions can quickly give an indication of whether or not damage has occurred in the structure, and the mode shapes can provide information about where the structural problem has occurred. This work also stops short of quantifying the damage present.

In addition to the work underway at JSC and the interest in evaluating this technology for use by MSFC-ET53, there are additional groups within NASA with similar problems. The first of these is MSFC-PD22. This group is working on development programs utilizing new materials which will have very unique properties. Because of this, it will be extremely important to have reliable, efficient, and economic NDE methods available for use on these systems. The propulsion group at MSFC also has interest in using measured quantities to determine the condition of the SSME and other related hardware. Many of the problems associated with these activities are similar, at least in form, to those reviewed in this report. Last, there is an apparent interest at the Langley Research Center in evaluating the application of modal analysis methods to the problem of assessing acoustic fatigue damage.

Existing Problems

The following problems currently exist and must be solved in order to make modal analysis an effective and useful NDE method:

1. Measurement noise.
2. Available excitation techniques for certain situations may limit the usefulness of the data.
3. Best methods for data presentation and processing are unclear.
4. Measurement accuracy and repeatability requirements are unknown.
5. Interpretation of data to yield damage level and/or location values not yet clearly possible.
6. Quantity of data required to make an accurate damage assessment is unknown.
7. Low cost transducer development is needed.
8. Very little understanding of damage/structure interaction.
9. Much information on this general topic is available in the literature but its usefulness is not clear.
10. Expense of hardware and software required for data acquisition and analysis is still high.
11. Desire to apply this technology to NDE of new materials before simple structures are understood.
12. Uniqueness of the predicted damage location and/or level values may be questionable.
13. Fixturing needed to insure reproduceable test conditions is unclear and may be extensive.

The problem of measurement noise is being addressed by Wicks and Mitchell [1,2,24], and their work seems to be bringing this problem under control. Concern over the available excitation methods is of less importance in the aerospace industry than in the other application areas mentioned earlier because of the control one has over the test article during the inspection process.

In the future, on the other hand, if this method is to be expanded to include in-service responses in the evaluation process as well, the information contained in these measurements will have to be examined very closely to insure that it will produce useful estimates of the integrity of

the structure. It is possible that the measurement sites selected for use in the modal test which would be done when the system is out of service may not provide the best possible information from the in-service measurements.

Another issue is the number of in-service measurement sites needed. This number will have a significant impact on not only the quality of the data but on the cost of the monitoring system as well. Therefore, it will be very important to select the measurement sites with great care and deliberation.

The need to develop low cost transducers stems from the desire to eventually be able to install the required instrumentation in the vehicle as a part of the construction process. In this way considerable effort and expense can be avoided during the service life of the vehicle by eliminating the need to install and remove large numbers of transducers each time a structural integrity assessment was to be made. At the same time, adequate instrumentation would still be available to permit a complete inspection to be performed.

Obviously, how this technology is applied by the general public and the cost of the data acquisition and analysis equipment are items which cannot be controlled. However, these are two issues which will play a significant role in the development and utility of this technology for NDE purposes.

The remainder of the items listed above will have to be addressed through comprehensive research efforts.

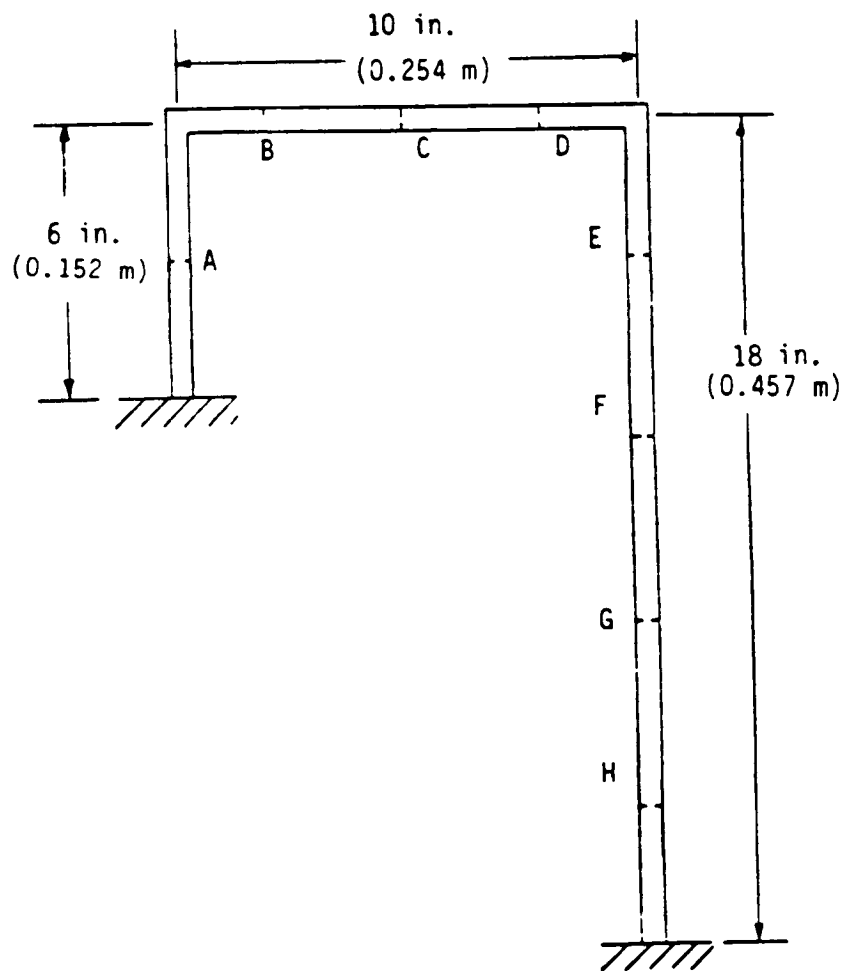
CONCLUSIONS AND RECOMMENDATIONS

The ability of modal analysis methods to provide information which can be used for the NDE of structural systems is clear. However, many issues concerning the efficient and accurate utilization of this data for NDE purposes are unresolved. These include, but are not limited to, the amount of data needed, how accurate and repeatable the data must be, how this data should be processed and presented, and how the damage interacts with the dynamic characteristics of the structure. A comprehensive research effort will be required to successfully address these concerns.

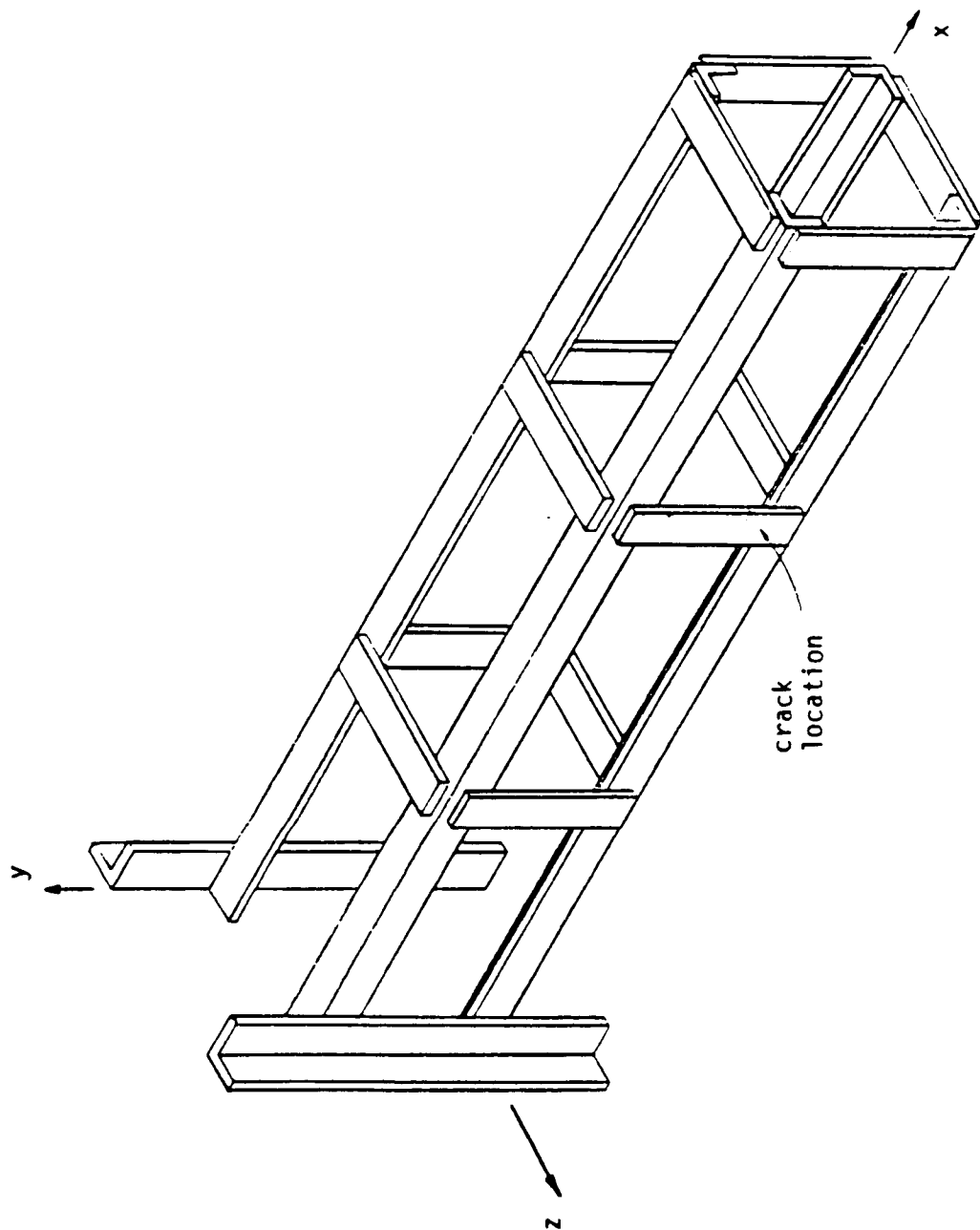
Proposed Test Program

To familiarize the personnel of MSFC-ET53 with the application of modal analysis methods to NDE problems, the test program described below is proposed. This program takes advantage of existing test data and, thereby, provides a means of comparison so that any questions which may arise can be easily resolved.

1. Repeat the longitudinal and transverse beam experiments of Springer and Reznicek which used free-free samples. This will serve to illustrate the effects of temperature and mass loading on the measured data, and the difficulty of damage magnitude and location prediction on systems which can be solved analytically.
2. Repeat the tests carried out by Haisty and Duerr on unequal length U-frame structures. These test items featured fixed end conditions and will serve to demonstrate the application of the MAC for purposes of damage detection. Also, test data is available for comparative purposes and the structure is easily modeled using FEM methods.
3. Repeat the tests of Haisty and West on a box-beam structure. This structure is a three dimensional cantilever beam arrangement which was well documented in the earlier work. These test activities will demonstrate the effect of damage in both primary and secondary structural elements as well as the difficulties resulting from the use of typical mechanical fasteners. This structure is also easily modeled using FEM techniques.



U-frame Structure



Boxbeam Structure

BIBLIOGRAPHY

1. Wicks, A. L. and Mitchell, L. D., "A New Means of Estimation of Frequency Response Functions in the Presence of Uncorrelated Signals, Part I," Proceedings of the Spring Meeting of the Society for Experimental Mechanics, 1987, pp. 629-634.
2. Wicks, A. L., "Frequency Response Function Estimation and Quality Statistic," Proceedings of the Spring Meeting of the Society for Experimental Mechanics, 1987, pp. 517-523.
3. Bruinsma, A. J. A., et al., "Fibre-Optic Strain Measurement for Structural Integrity Monitoring," Proceedings of the Second International Conference on Optical Sensors, 1984, pp. 399-402.
4. Rakshin, A. F. and Sidorov, O. T., "Determination of the Degree of Defectiveness in Structural Components," Soviet Journal of Nondestructive Testing, Vol. 18, No. 3, November 1982, pp. 158-161 (Translation).
5. Downham, E. and Woods, R., "The Rationale of Monitoring Vibration on Rotating Machinery in Continuously Operating Process Plant," ASME Paper No. 71-Vibr-96, 1971.
6. Glew, C. A. W. and Watson, D., "Vibration Analysis as a Maintenance Tool," Transactions of the Institute of Marine Engineers, Canadian Division, Supp. No. 32, June 1968, pp. 18-29.
7. Petroski, H. J. and Glazik, J. L., Jr., "The Response of Cracked Cylindrical Shells," Journal of Applied Mechanics, Trans. ASME, Vol. 47, June 1980, pp. 444-446.
8. Loland, O. and Mackenzie, A. C., "On the Natural Frequencies of Damaged Offshore Oil Platforms," Mech. Res. Comm., Vol. 1, 1974, pp. 353-354.
9. Krauthammer, T., "A 'Numerical Gauge' for Structural Assessment," Shock and Vibration Bulletin, No. 56, Part 1, 1986, pp. 179-194.
10. Matzen, Vernon Charles and Hardee, Joseph Earlton, Jr., "Mathematical Modelling of Indeterminate Trusses," Proceedings of the Second Specialty Conference on Dynamic

Response of Structures, 1981, pp. 687-697.

11. Yao, J. T. P., "Damage Detection Using System Identification," Proceedings of the Spring Meeting of the Society for Experimental Mechanics, 1987, pp. 383-384.

12. Liu, Dahsin, Sun, C. T. and Malvern, L. E., "Structural Degradation of Impacted Graphite/Epoxy Laminates," Shock and Vibration Bulletin, No. 56, Part 2, 1986, pp. 51-60.

13. Kummer, E., Yang, J. C. S. and Dagalakis, N., "Detection of Fatigue Cracks in Structural Members," Proceedings of the Second Speciality Conference on Dynamic Response of Structures, 1981, pp. 445-461.

14. Loland, O., Mackenzie, A. C. and Begg, R. D., "Integrity Monitoring of Fixed, Steel Offshore Oil Platforms," BSSM/RINA Joint Conference of Measurement in the Offshore Industry, 1975.

15. Liu, Shih-Chi and Yao, James T. P., "Structural Identification Concept," Journal Of The Structural Division, ASCE, Vol. 104, ST12, December 1978, pp. 1845-1858.

16. Yao, James T. P., "Damage Assessment of Existing Structures," Journal Of The Engineering Mechanics Division, ASCE, Vol. 106, No. EM4, August 1980, pp. 785-799.

17. Sparks, P. R., Jeary, A. P. and de Souza, V. C. M., "A Study of the Use of Ambient Vibration Measurements to Detect Changes in the Structural Characteristics of a Building," Proceedings of the Second Speciality Conference on Dynamic Response of Structures, 1981, pp. 189-200.

18. Cole, Henry A., Jr., "On-Line Failure Detection and Damping Measurements of Aerospace Structures by Random Decrement Signatures," NASA CR-2205, 1973, 75 pages.

19. Begg, R. D. and Bendat, J. S., "Instrumentation and Analysis Techniques for the Monitoring of Offshore Structures," Petroleum Times, October 1, 1976, pp. 29 and 35.

20. Wang, J. T. S., Liu, Y. Y. and Gibby, J. A., "Vibrations of Split Beams," Journal of Sound and Vibration, Vol. 84, No. 4, 1982, pp. 491-502.

21. Kopff, Paul, "Experimental Modal Analysis for Structural Damage Assessment: The Case of Natural Convection Cooling Towers," Proceedings of the Fifth International Modal

Analysis Conference, 1987, pp. 122-126.

22. Lai, Hsin-Yi, "Computer Aided Fault Diagnosis of Crank Systems Using Engine Vibration Data," Proceedings of the Fifth International Modal Analysis Conference, 1987, pp. 248-253.

23. Brown, T. A., "The Identification of Spatial Parameter Changes Via Modal Analysis," Proceedings of the Fifth International Modal Analysis Conference, 1987, pp. 267-273.

24. Mitchell, L. D., et al., "An Unbiased Frequency Response Function Estimator," Proceedings of the Fifth International Modal Analysis Conference, 1987, pp. 364-373.

25. Hopton, Gregory W. and Deblauwe, Filip, "Relationships Between Analysis Errors and Complex Mode Shapes," Proceedings of the Fifth International Modal Analysis Conference, 1987, pp. 381-388.

26. Afolabi, D., "An Anti-Resonance Technique for Detecting Structural Damage," Proceedings of the Fifth International Modal Analysis Conference, 1987, pp. 491-495.

27. Wang, Wei Ji and Zhang, Azhou, "Sensitivity Analysis in Fault Vibration Diagnosis of Structures," Proceedings of the Fifth International Modal Analysis Conference, 1987, pp. 496-501.

28. Vandeuren, U., Leuridan, J. and Doucet, Y., "Structure Monitoring Using a Diagnosis Technique Based on Combined Use of FEA and Test," Proceedings of the Fifth International Modal Analysis Conference, 1987, pp. 1338-1346.

29. Springer, W. T., Lawrence, K. L. and Lawley, T. J., "The Effect of a Symmetric Discontinuity on Adjacent Material in a Longitudinally Vibrating Uniform Beam," Experimental Mechanics, SEM, To appear.

30. Springer, W. T., Lawrence, K. L. and Lawley, T. J., "Damage Assessment Based on the Structural Frequency Response Function," Experimental Mechanics, SEM, To appear.

31. Bourne, C. A., Material Damping As A Means Of Quantifying Fatigue Damage, Masters Thesis, Air Force Institute of Technology, 1978.

32. Chen, S. H., System Identification And Damage Assessment Of Existing Structures, Ph.D. Dissertation,

Purdue University, 1980.

33. Toussi, S., System Identification Methods For The Evaluation Of Structural Damage, Ph.D. Dissertation, Purdue University, 1982.

34. Stephens, J. E., Structural Damage Assessment Using Response Measurements, Ph.D. Dissertation, Purdue University, 1985.

35. Tsai, Wen-Hu, Detecting And Locating Damages In Complex Structures By The System Identification Technique, Ph.D. Dissertation, University of Maryland, 1985.

36. Springer, W. T., The Vibrational Characteristics of Uniform Bars Containing a Symmetric Discontinuity in Stiffness Applied to Structural Integrity Monitoring, Ph.D. Dissertation, University of Texas at Arlington, 1982.

37. Reznicek, M. E., The Transverse Vibrational Characteristics of Symmetrically Damaged Bars, Masters Thesis, University of Arkansas, 1984.

38. Haisty, B. S., Damage Assessment Using the Longitudinal Vibrational Characteristics of Uniform Bars, Masters Thesis, University of Arkansas, 1984.

39. Moshrefi, N., The Transverse Vibrational Behavior of a Peripherally Cracked Pipe and a Uniformly Corroded Pipe, Masters Thesis, University of Arkansas, 1985.

40. Haisty, B. S., Development and Application of a Cracked-Beam Finite Element and a Cracked-Beam Modal Element for Assessing the Effects of Damage on the Modal Properties of Mechanical Systems, Ph.D. Dissertation, University of Arkansas, 1986.

41. Duerr, R. R., Development and Evaluation of a Dynamic Transfer Matrix for a Damaged Uniform Beam, Masters Thesis, University of Arkansas, 1987.

42. Bochniak, J. and Garcia, R., Structural Integrity Monitoring System, Report No. NADC-77101-30, 1979, 82 pages.

43. Hetenyi, M., "Deflection of Beams of Varying Cross Section," Trans. ASME, Vol. 59, March 1937, pp. A-49-A-52.

44. Kirmser, P. G., "The Effect of Discontinuities on the Natural Frequencies of Beams," Proceedings of the ASTM, Vol. 44, pp. 897-904.

45. Thomson, W. T., "Vibration of Slender Bars With Discontinuities in Stiffness," Journal of Applied Mechanics, Trans. ASME, Vol. 6, June 1949, pp. 203-207.
46. Adams, R. D., et al., "A Vibration Technique for Non-Destructively Assessing the Integrity of Structures," Journal of Mechanical Engineering Science, Vol. 20, No. 2, 1978, pp. 93-100.
47. Cawley, P. and Adams, R. D., "The Location of Defects in Structures From Measurements of Natural Frequencies," Journal of Strain Analysis, Vol. 14, No. 2, 1979, pp.49-57.
48. Cawley, P. and Adams, R. D., "Defect Location in Structures by a Vibration Technique," ASME Paper No. 79-DET-46, 1979.
49. Ju, F. D., et al., Diagnosis of Fracture Damage in Simple Structures, Bureau of Engineering Research, Report No. CE-62(82) AFOSR-993-1, October 1982.
50. Ju, F. D., Wong, E. T. and Lopez, T. L., "Modal Method in Diagnosis of Fracture Damage in Simple Structures," Productive Applications of Mechanical Vibrations, Applied Mechanics Division, Vol. 52, ASME, 1982, pp. 113-125.
51. Gudmundson, P., "Eigenfrequency Changes of Structures Due to Cracks, Nothches or Other Geometrical Changes," Journal of Mech. Phys. Solids, Vol. 30, NO. 5, 1982, pp. 339-353.
52. Gudmundson, P., "Changes in Modal Parameters Resulting From Small Cracks," Proceedings of the Second International Modal Analysis Conference, 1984, pp. 690-697.
53. Gudmundson, P., "The Dynamic Behavior of Slender Structures With Cross-Sectional Cracks," Journal of Mech. Phys. Solids, 1983.
54. Reznicek, M. E. and Springer, W. T., "Damage Assessment of Transversely Vibrating Uniform Beams Containing a Symmetric Discontinuity," Proceedings of the Spring Meeting of the Society for Experimental Mechanics, 1985, pp. 404-409.
55. Haisty, B. S. and Springer, W. T., "Identification of Multiple Discontinuities in a Uniform Beam Using Longitudinal Vibration Properties," Proceedings of the 40th Mechanical Failures Prevention Group, National Bureau of Standards, 1985.

56. Haisty, B. S. and Springer, W. T., "The Longitudinal Vibration Characteristics of a Uniform Bar Containing Two Symmetric Discontinuities," Proceedings of the Spring Meeting of the Society for Experimental Mechanics, 1985, pp. 389-393.
57. Moshrefi, N., Sreshta, H. A. and Springer, W. T., "The Transverse Vibration Characteristics of an Externally Damaged Pipe," Vibration Analysis to Improve Reliability and Reduce Failure, Applied Mechanics Division, Vol. , ASME, 1985, pp. 23-30.
58. Al-Ansary, M. D. and Azagem, K. M., "A Modal Model for Fatigue Crack Non-Destructive Testing," Proceedings of the Fourth International Modal Analysis Conference, 1986, pp. 202-208.
59. Henry, T. A. and Okah-Avae, B. E., "Vibrations in Cracked Shafts," Proceedings of the First International Conference of Vibrations in Rotating Machinery, I. Mech. E., Vol. 9, No. C162/76, 1976, pp. 15-19.
60. Mayes, J. W. and Davies, W. G. R., "The Vibrational Behaviour of a Rotating Shaft System Containing a Transverse Crack," Proceedings of the First International Conference of Vibrations in Rotating Machinery, I. Mech. E., Vol. 9, No. C168/76, 1976, pp. 53-64.
61. Gasch, R., "Dynamic Behavior of a Simple Rotor With a Cross-Sectional Crack," Proceedings of the First International Conference of Vibrations in Rotating Machinery, I. Mech. E., Vol. 9, No. C178/76, 1976, pp. 123-128.
62. Grabowski, B., "Vibrational Behavior of a Turbine Rotor Containing a Transverse Crack," Journal of Mechanical Design, Trans. ASME, Vol. 102, No. 1, January 1980, pp. 140-146.
63. Rauch, A., "Shaft Cracking Supervision of Heavy Turbine Rotors by FEM Method," Proceedings of the Third International Modal Analysis Conference, 1985, pp. 714-722.
64. Chondros, T. G. and Dimarogonas, A. D., "Identification of Cracks in Circular Plates Welded at the Contour," ASME Paper No. 79-DET-106, 1979.
65. Chondros, T. G. and Dimarogonas, A. D., "Identification of Cracks in Welded Joints of Complex Structures," Journal of Sound and Vibration, Vol. 69, No. 4, 1980, pp. 531-538.

66. Anifantis, N. and Dimarogonas, A. D., "Identification of Peripheral Cracks in Cylindrical Shells," ASME Paper No. 83-WA/DE-14, 1983.
67. Dentsoras, A. J. and Dimarogonas, A. D., "Resonance Controlled Fatigue Crack Propagation in Cylindrical Shafts Under Combined Loading," ASME Paper No. 83-WA/DE-26, 1983.
68. Chamis, C., Sinclair, J. H. and Lark, R. F., "Dynamic Response of Damaged Angleplied Fiber Composites," Modern Developments in Composite Materials and Structures, ASME, 1979, pp. 31-51.
69. Tracy, J. J., Dimas, D. J. and Pardeon, G. C., "Advanced Composite Damage Detection Using Modal Analysis Techniques," Proceedings of the Second Modal Analysis Conference, 1984, pp. 665-670.
70. Crema, L. B., Castellani, A. and Peroni, I., "Modal Tests on Composite Material Structures: Application in Damage Detection," Proceedings of the Third Modal Analysis Conference, 1985, pp. 708-713.
71. Tsai, T., Yang, J. C. S. and Chen, R. Z., "Detection of Damages in Structures by the Cross Random Decrement Method," Proceedings of the Third International Modal Analysis Conference, 1985, pp. 691-700.
72. Akgun, M., Ju, F. D. and Paez, T. L., "Transmissibility as a Means to Diagnose Damage in Structures," Proceedings of the Third International Modal Analysis Conference, 1985, pp. 701-707.
73. "Modal Analysis Methods Applied to Structural Integrity Monitoring," Structural Dynamics Research Corporation, June 1985.
74. West, Walter, Fault Detection in Orbiter OV-101 Structure Related Structural Test Specimen, Loads and Structural Dynamics Branch Report, NASA/Johnson Space Center, September 1984.
75. West, Walter, "Single Point Random Modal Test Technology Application to Failure Detection," Shock and Vibration Bulletin, No. 52, Part 4, 1982, pp. 25-31.
76. West, Walter, "Illustration of the Use of Modal Assurance Criterion to Detect Structural Changes in an Orbiter Test Specimen," Proceedings of the Fourth International Modal Analysis Conference, 1986, pp. 1-6.

77. Haisty, B. S., West, W. and Mitchell, C., "Damage Detection in the Space Shuttle Orbiter Body Flap Test Specimen Using the Modal Assurance Criterion," Proceedings of the Advanced Composites Conference, 1985.
78. Yao, J. T. P., Toussi, S. and Sozen, M. A., "Damage Assessment From Dynamic Response Measurements," Proceedings of the Ninth United States National Congress of Applied Mechanics, 1982, pp. 315-322.
79. Yao, J. T. P., "Probabalistic Methods for the Evaluation of Seismic Damage in Existing Structures," Soil Dynamics and Earthquake Engineering, Vol. 1, No. 3, 1982.
80. Stephens, J. E. and Yao, J. T. P., "Survey of Available Structural Response Data for Damage Assessment," University of California Paper No. CE-STR-83-23, March 1984.
81. Adams, R. D. and Cappendale, J., "Measurement of the Elastic Moduli of Structural Adhesives by a Resonant Bar Technique," Journal of Mechanical Engineering Science, Vol. 18, No. 3, 1976, pp. 149-158.
82. Cempel, C., "Diagnostically Oriented Measures of Vibroacoustical Processes," Journal of Sound and Vibration, Vol. 73, No. 4, 1980, pp.547-561.
83. Cheng, J. S., Dunham, M. and Joanides, J., "Acoustic Test Response of the Space Shuttle Orbiter Body Flap," Proceedings of the Second International Modal Analysis Conference, 1984, pp. 635-637.
84. Griesbach, T. J. and Ayers, D. J., "Opening and Extension of Circumferential Cracks in a Pipe Subject to Dynamic Loads," Nuclear Engineering Design, Vol. 57, No. 1, April 1980, pp. 141-152.
85. Koester, D. L., "The Dynamic Behavior of Center Crack Tension Specimens During High Frequency Material Fatigue Tests," Proceedings of the Third International Modal Analysis Conference, 1985, pp. 794-801.
86. Mutch, Gordon F. and Russell, Richard, "Troubleshooting In-Plant Equipment Using Combined Test and Analysis," Proceedings of the First International Modal Analysis Conference, 1982, pp. 252-258.
87. Sproat, W. H. and Rowe, W. J., "Ensuring Aircraft Structural Integrity Through Nondestructive Evaluation," Lockheed-Georgia Company.

88. Verdonck, E. and Snoeys, R., "Life Time Prediction Based on the Combined Use of Finite Element and Modal Analysis Data," Proceedings of the Second International Modal Analysis Conference, 1984, pp.572-579.

530-18
N88-15631 116732
238

1987

NASA/ASEE SUMMER FACULTY RESEARCH FELLOWSHIP PROGRAM

MARSHALL SPACE FLIGHT CENTER
THE UNIVERSITY OF ALABAMA IN HUNTSVILLE

TETHER ELEVATOR CRAWLER SYSTEMS (TECS)

Prepared by:	Frank R. Swenson
Academic Rank:	Professor
University and Department:	Tri-State University Mechanical and Aerospace Engineering
NASA/MSFC:	
Directorate:	Program Development
Office:	Advanced Systems
Group:	Orbital Support Systems
NASA Colleagues:	James K. Harrison Charles C. Rupp
Date:	August 24, 1987
Contract No:	The University of Alabama in Huntsville NGT-01-008-021

ABSTRACT

One of the needs of experimenters on Space Station is the access to steady and controlled-variation microgravity environments. A method of providing these environments is to place the experiment on a tether attached to the Space Station. This provides a high degree of isolation from structural oscillations and vibrations. Crawlers can move these experiments along the tethers to preferred locations, much like an elevator. This report describes the motion control laws that have been developed for these crawlers and the testing of laboratory models of these tether elevator crawlers.

ACKNOWLEDGEMENTS

The author wishes to acknowledge the NASA/ASEE Summer Faculty Fellowship Program, along with Dr. Gerald Karr, the UAH University Program Co-Director, and Ms. Ernestine Cothran, the NASA/MSFC Co-Director.

To NASA counterparts Mr. James K. Harrison and Mr. Charles C. Rupp of the Orbital Support Systems Group, Advanced Systems Office of the Program Development Directorate, a very special thanks is offered for their help with the analytical, assembly, design and organizational activities.

A further thanks is due to Mr. James P. McGee and Mr. James B. Herring of the Dynamics Test Branch, Structural Test Division, of the Test Laboratory for their assistance with the experimental activities.

LIST OF FIGURES

<u>Figure Number</u>	<u>Title</u>	<u>Page:XXXI-</u>
1.	Crawler Motion Control Laws	6
2.	Mirror Image Motion Control Law (MIMCL): Characteristic Curves	7
3.	Three Successive Phases of the Mirror Image Motion Control Law	8
4.	Time to Travel Total Distance: Mirror Image Motion Control Law	9
5.	Comparison of Motion Control Laws: Distance Travelled versus Time	10
6.	Comparison of Motion Control Laws: Velocity versus Time	11
7.	Comparison of Motion Control Laws: Acceleration versus Time	12
8.	Tether Crawler Engagement Mechanism and Drive Train	13
9.	Drive Control System	14
10.	6-Ft Air Table	15
11.	32-ft Air Table	16
12.	TECS Schedule: 1987-1990	17
13.	Tether Elevator Crawler System (TECS): Shuttle Flight Demonstration	18

1. Introduction

Tethers attached to orbiting spacecraft can be used to provide parking locations and paths for microgravity environment experiments if a crawler system moves the experiment along the tether. Two tether configurations are possible - one, a clothesline configuration, in which both ends of the tether are rigidly fixed to the spacecraft structure; and the second, a free end mass or pendant configuration, in which one end is fixed to the spacecraft and the other to an end mass which by gravity-gradient forces pulls the tether taut either outward from the center of the orbit or inward toward the center of the orbit.

These two tether configurations have different environment ranges and provide conditions for different types of microgravity experiments. These differences can be stated as:

Fixed Ends (Clothesline)

- Steady G-Level Experiments
- 10^{-5} to 10^{-2} G

Free-End Mass (Pendant)

- Variable-G Experiments
- Microgravity, 10^{-6} to 10^{-5} G.

Crawler motions in space along a tether are a combination of the responses to the instructions of a motion control law, to the vibrations transmitted from the spacecraft, and to the dynamics of motion of the entire orbiting tether/crawler system. The response to each of these is of interest in this study.

2. Mirror Image Motion Control Law (MIMCL)

A number of control laws (Fig 1) for the motion of a crawler along a tether have been developed starting with Rupp (1) in 1975. A major step to provide more flexibility by independently controlling the maximum velocity and accelerations during the motion was made in the hyperbolic tangent motion control law developed by Lorenzini (2) in 1986. This new control law was one continuous function throughout the motion and had a smooth acceleration from rest to a peak velocity followed immediately by a smooth deceleration which approached zero velocity exponentially so that a cutoff distance had to be introduced to terminate the motion at a small but finite velocity and a selected small proximity to the total distance. In this motion control law the peak deceleration is smaller than the peak acceleration and the time interval for deceleration is much longer than the time interval for acceleration. However, the slow initial accelerations and final decelerations made this very attractive as a motion control law, especially when operating a crawler close to the spacecraft on a pendant (free end mass) configuration tether.

Later in the same year, Swenson (3) added a constant-velocity middle phase to the hyperbolic tangent control law at the maximum velocity point where the acceleration was zero. This retained the advantages of the hyperbolic tangent motion control law but also allowed the same distance to be covered in the same time interval but with a lower value of peak acceleration. However, even this modification did not eliminate either the time-inefficient, long exponential tail of the hyperbolic tangent motion control law or the necessity of stopping the motion when the velocity was small but still finite and at a cutoff distance from the expected end of the motion.

In 1987 Rupp and Swenson (4) changed the tail end of the modified hyperbolic tangent motion control law so that the deceleration tail was the mirror image of the acceleration beginning of the motion. This resulted in symmetrical motion curves (Fig 2) in distance, velocity and acceleration. The motion then occurs in three successive phases (Fig 3) in which the acceleration and deceleration phases are mirror images of each other and the peak acceleration and the peak deceleration have the same value.

The equation of motion during the beginning acceleration phase is:

$$L(t) = \Delta L_c' [\tanh(\alpha t)]^\gamma, 0 \leq t \leq t_A \quad (1)$$

where, the time at the end of the acceleration phase is:

$$t_A = \frac{1}{\alpha} \sinh^{-1} \left[\sqrt{\frac{\gamma-1}{2}} \right] \quad (2)$$

and, the maximum velocity is:

$$L'_{c,m} = \Delta L_c' \alpha \left[\frac{2\gamma}{\gamma+1} \right] \left[\frac{\gamma-1}{\gamma+1} \right]^{\frac{\gamma-1}{2}} \quad (3)$$

The mirror image motion control law provides the system designer and the tether elevator crawler system motion programmer with considerable flexibility, part of which can be shown with these equations for this first phase. The parameters in the equations for the hyperbolic tangent acceleration and deceleration phases of the motion are the distance parameter, $\Delta L_c'$, the time parameter, α ; and the shape parameter, γ . Two advantages that go back to using the power function of the hyperbolic tangent function as a motion control law are that the time to reach maximum velocity (zero acceleration point) is independent of the selected distance interval and that the maximum velocity function can be divided by the distance interval to give another function which depends only on the values of the time parameter and the shape parameter. With three independent parameters in the equations, independent selections may be made of the distance, the maximum velocity and the time to reach maximum velocity.

The addition of the constant-velocity phase increases the flexibility to the motion control law user by adding a section of travel at maximum velocity along the tether which has a distance parameter, $\Delta L_c''$, which is independent of the other parameters. The transition into this phase is also smooth as it is made at the point of zero acceleration. The equation for the total distance travelled through the acceleration phase and to the end of the constant-velocity phase is:

$$L(t) = \Delta L_c' [\tanh(\alpha t_A)] + \dot{L}_{c,m} (t - t_A), \quad t_A \leq t \leq t_B \quad (4)$$

where, the time to the end of the constant-velocity phase is:

$$t_B = t_A + \frac{\Delta L_c''}{\dot{L}_{c,m}} \quad (5)$$

Another aspect of this flexibility is that the time interval for this phase, $t_B - t_A$, is a function only of the distance to be travelled at constant velocity and the value of the maximum velocity.

Being a mirror image, the deceleration phase is already determined by the parameters selection for the acceleration phase. The equation for distance in this phase is:

$$L(t) = \Delta L_T - \Delta L_c' \{ \tanh[\alpha(t_T - t)] \}, \quad t_B \leq t \leq t_T \quad (6)$$

where, the total distance travelled during the three phases of the motion is:

$$\Delta L_T = \Delta L_c' + \Delta L_c'' \quad (7)$$

and the total time to travel this total distance is:

$$t_T = t_A + (t_B - t_A) + t_A = t_A + t_B \quad (8)$$

A summary of the features of the mirror image motion control law is:

- smooth accelerations and decelerations
- smooth transitions
- three independent acceleration and deceleration phases parameters
- one independent constant-velocity phase parameter.

The mirror image motion control law (MIMCL) is very time efficient (Fig 4). When comparison is made to the modified hyperbolic tangent motion control law (MHTMCL), the shortening in travel time can be seen in graphs for distance (Fig 5), velocity (Fig 6), and acceleration (Fig 7). For the same total distance traveled (4km in Figs 5 and 6, 384-in in Fig 7) and the same values of equation time and shape parameters, the motions using two forms of the mirror image motion control law (MIMCL) both end much quicker than with the modified hyperbolic tangent motion control law (MHTMCL).

Additional conclusions can be reached from the curves. For the same control law equation parameters, the change to a mirror image always results in a shorter time for deceleration. It also results in the shorter distance travelled during deceleration becoming the same distance as the acceleration distance. The result is that the sum of the nominal distances for acceleration, deceleration and constant-velocity is larger than the distance actually travelled, and an adjustment must be made in either the nominal distance to calculate the acceleration and deceleration phases or in the distance actually travelled during the constant-velocity phase.

Therefore, there are two possible forms of the mirror image motion control law that correspond to the same modified hyperbolic tangent motion control law. If the fraction, Y , of the total distance that is at constant-velocity is the same in the MIMCL and the MHTMCL, then the time to complete the motion is shortest. However, the peak acceleration and deceleration are increased to higher values. If the fraction, X , of total distance for acceleration and deceleration is kept the same in the MIMCL as in the MHTMCL, then an intermediate value of travel time results. The peak values of acceleration are the same and the peak value of deceleration in the MIMCL is equal to the peak value of acceleration.

The mirror image motion control law has features which make it the best to date in this series of the tether elevator motion control laws and can be used as a standard for comparison of motion control laws.

Lorenzini (5) has recently developed a retarded exponential (RE) motion control law which is especially useful for short-distance maneuvers. It is another step forward in this succession of motion control laws.

3. Crawler System Development and Testing

The tether crawler system that has been developed has the engagement mechanism and drive train similar to those shown in Fig 8. The tether is gripped between a toothed drive wheel and a toothed belt. The drive wheel moves both the tether and the belt and the entire system crawls up or down along the tether. If there is no slip between the drive and the tether, the position change of the crawler along the tether can be found from measurement of the rotation of the drive wheel.

A control system (Fig 9) has been developed to control the drive system to follow inputs from a motion control law that is a real-time model in a microprocessor. The desired location and velocity from the model are compared with the measured location and/or velocity to give an error signal that drives the motor. Two types of motors - stepping motors and DC motors - are being used in three different laboratory crawler systems.

Two flat-surface tables are being used for testing the crawler drive and control systems. The first, a 6-foot long glass

surface (Fig 10) is used for crawler and instrumentation system development. The second, a 32-foot long plastic surface (Fig 11), is being built for the testing of crawler/tether system dynamics. Both tables have the tether suspended horizontally over the length of the flat surface and have strain gages mounted on the end supports for the measurement of tether tension forces in the segments in front and in back of the moving crawler. For two-dimensional testing, the crawler rides on an air film that is generated by an air bearing. This thin film provides very-low frictional resistance to longitudinal (along the tether) and lateral movements of the crawler.

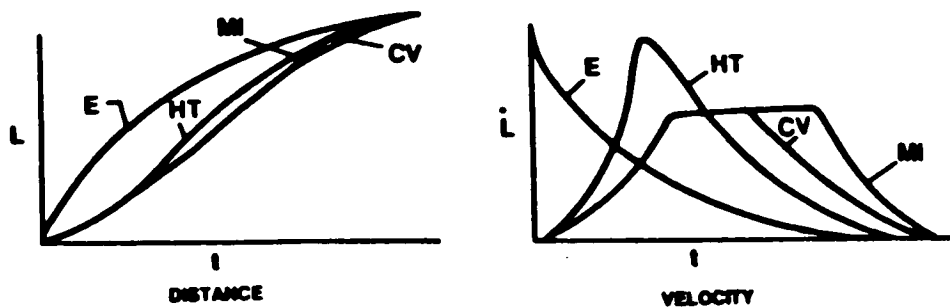
The end conditions of the tether may be changed from being rigidly attached to the end support to give a fixed-end condition to going through a hole in the end support to give a free-end condition. Strain gages attached to the sides of the end support sense the changes in tether tension and accelerometers sense the movements of the crawler. An infra-red communications link is being developed to replace the present electrical umbilical which carries instructions and information to and from the crawler system.

In summary, a list of the components that are part of the crawler system is

- tether engagement mechanism
- drive train
- drive control system
- acceleration measurement
- communications link
- on-board microprocessor.

The testing equipment is represented in the Figs 10 and 11 by the trajectory grids underneath the clear, flat surfaces; the tension sensors on the end supports; the preprocessor which sends motion law parameter values to the microprocessor on-board the crawler; the tether tension recorder and the time-base counter. Not shown are the magnetic tape recorders for data storage, the on-board flasher unit, and the videocamera and still camera for recording the crawler trajectories.

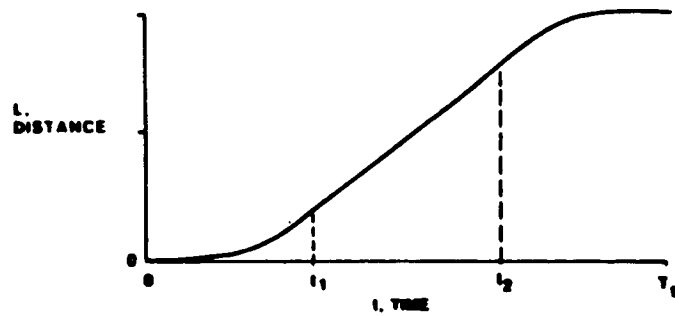
All of these development and testing activities are part of the schedule (Fig 12) for the tether elevator crawler systems. The demonstration flights on balloon, KC-135 and rocket vehicles are all paths to the demonstration of tether elevator crawler system (TECS) capabilities in space on board the Shuttle (Fig 13). This demonstration on a clothesline-configuration tether will culminate the initial development and testing of the TECS. Then it will be ready for application on board the Space Station.



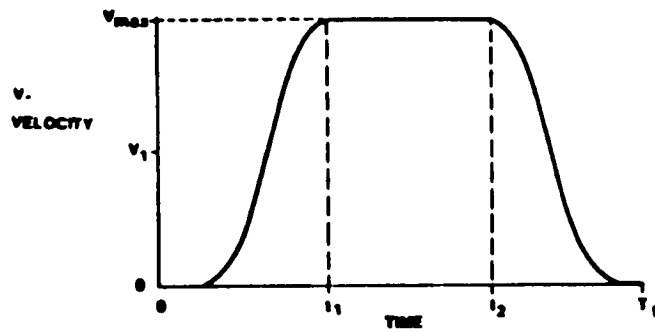
- EXPONENTIAL (RUPP 1975)
- HYPERBOLIC TANGENT (LORENZINI 1986)
- CONSTANT-VELOCITY ADDITION (SWENSON 1986)
- MIRROR IMAGE (RUPP/SWENSON 1987)

TETHER CRAWLER MOTION CONTROL LAWS

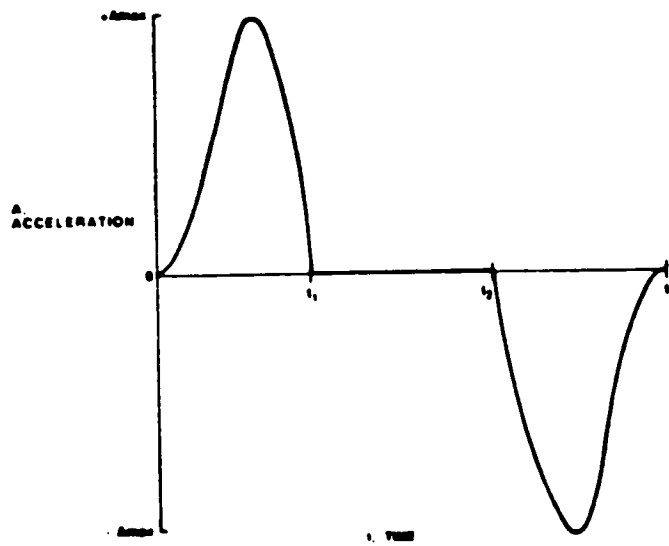
FIG 1



DISTANCE TRAVELED VERSUS TIME -

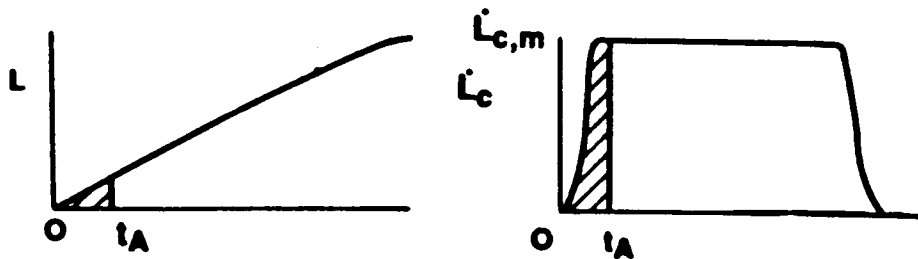


VELOCITY VERSUS TIME

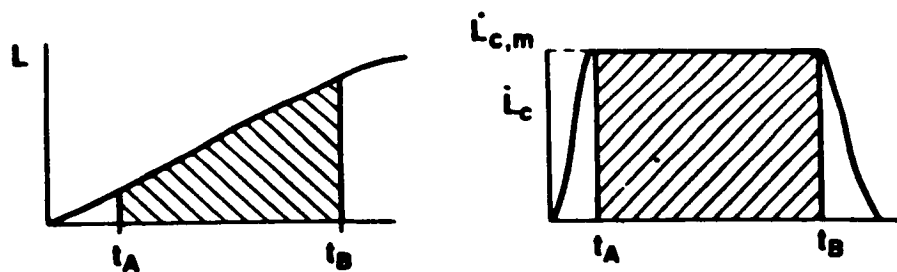


ACCELERATION VERSUS TIME

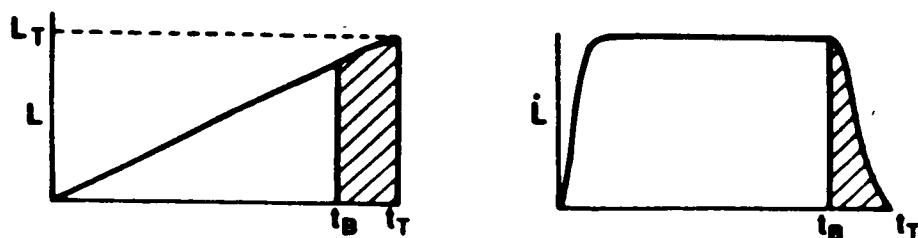
FIG 2 MIRROR IMAGE MOTION CONTROL LAW:
CHARACTERISTIC CURVES



ACCELERATION PHASE



CONSTANT-VELOCITY PHASE

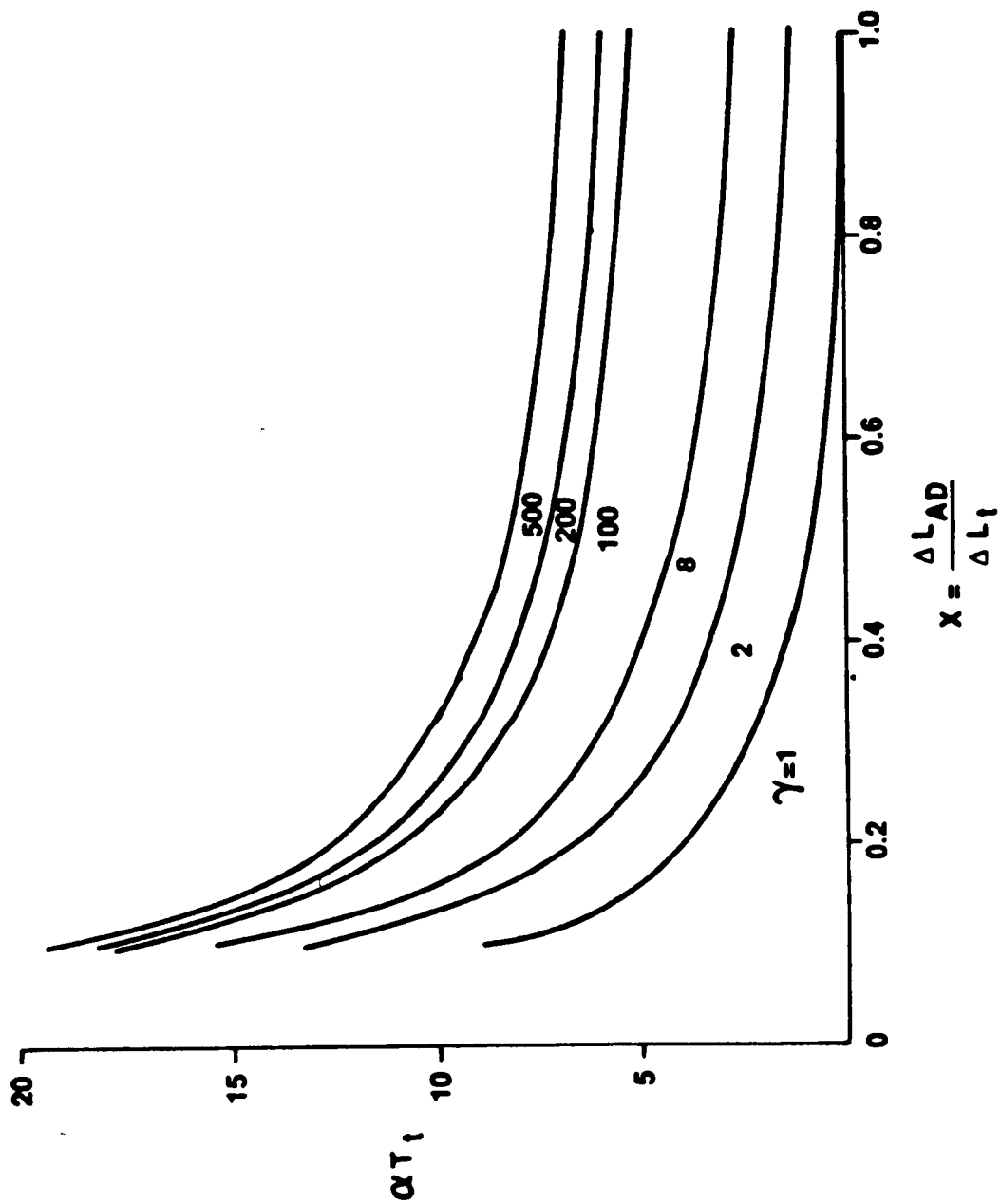


DECELERATION PHASE

DISTANCE

VELOCITY

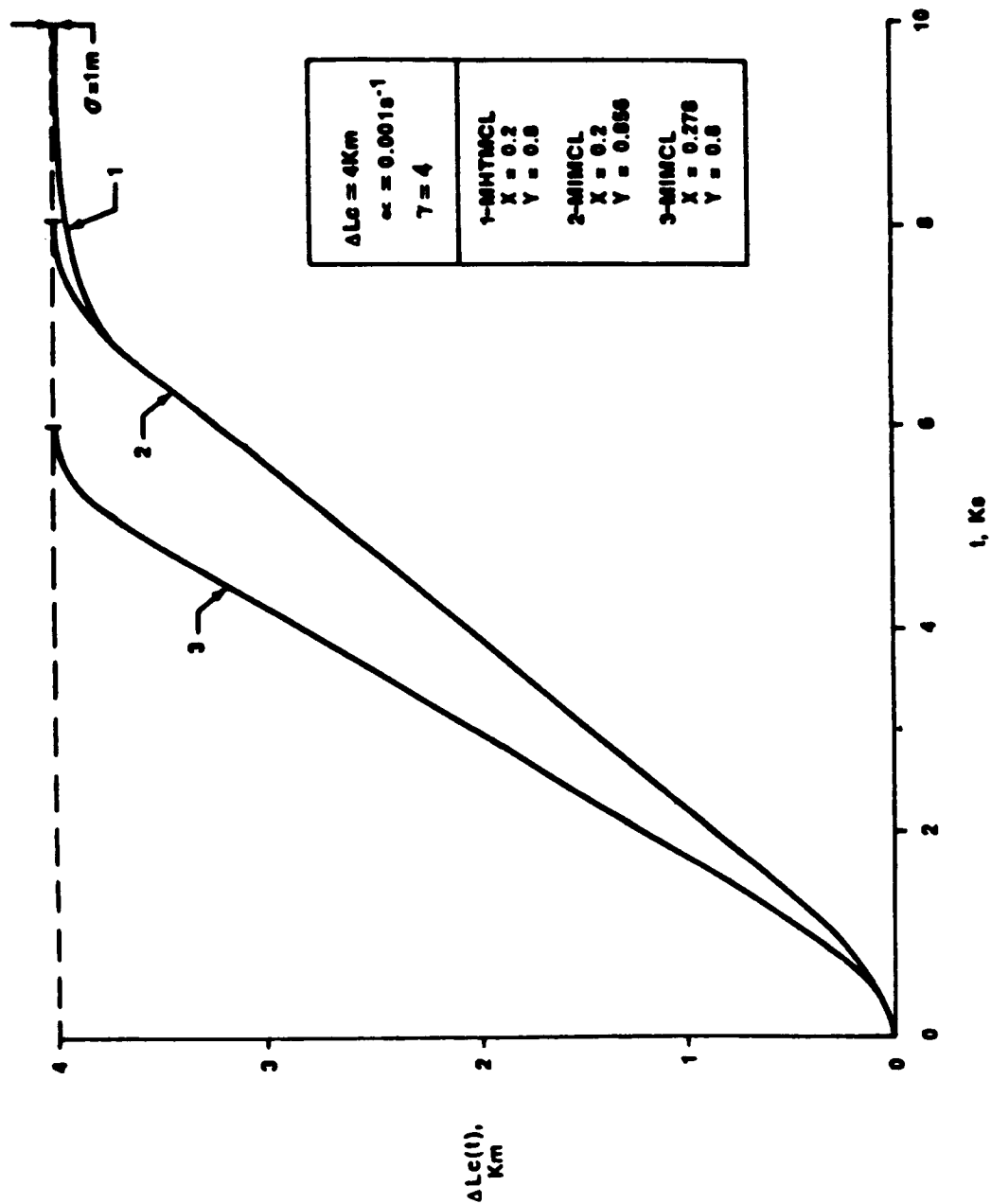
FIG 3 THREE SUCCESSIVE PHASES OF THE MIRROR IMAGE MOTION CONTROL LAW



$$X = \frac{\Delta L_{AD}}{\Delta L_i}$$

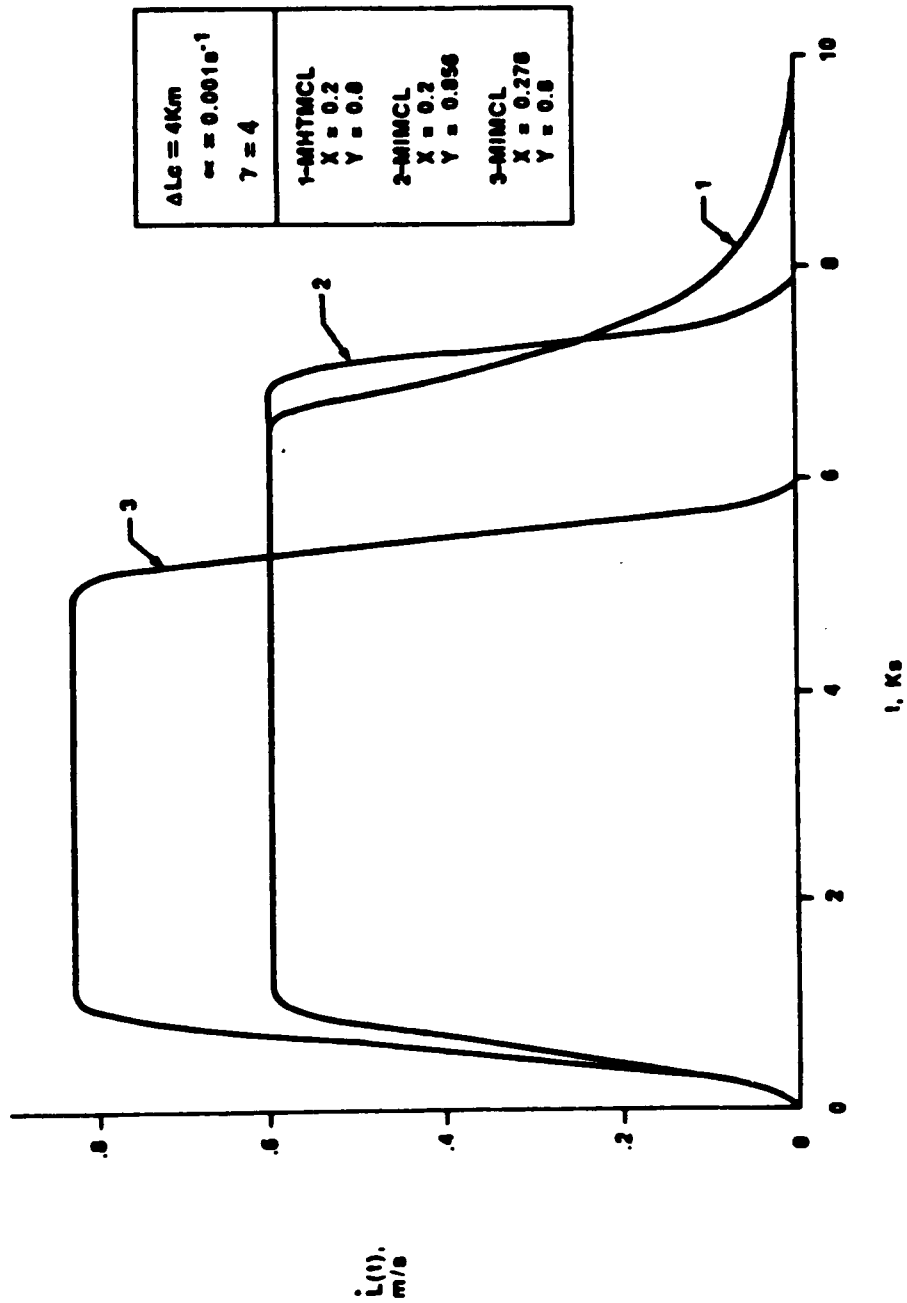
TIME TO TRAVEL TOTAL DISTANCE
MIRROR IMAGE MOTION CONTROL LAW

FIG 4



COMPARISON OF MOTION CONTROL LAWS
DISTANCE TRAVELED VERSUS TIME

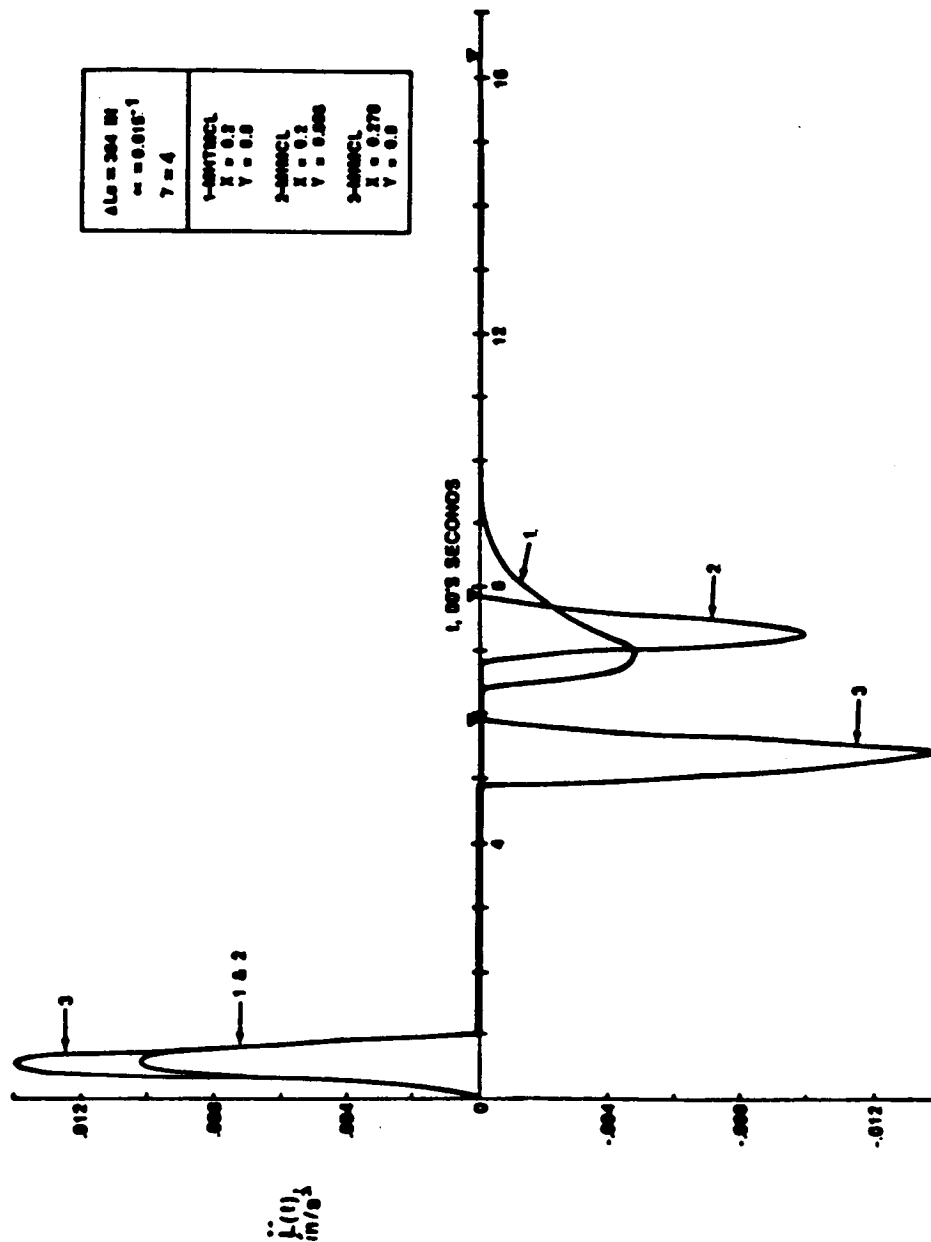
FIG 5



COMPARISON OF MOTION CONTROL LAWS
VELOCITY VERSUS TIME

FIG 6

ORIGINAL PAGE IS
OF POOR QUALITY



ACCELERATION VERSUS TIME
COMPARISON OF MOTION CONTROL LAWS

FIG 7

ORIGINAL PAGE IS
OF POOR QUALITY

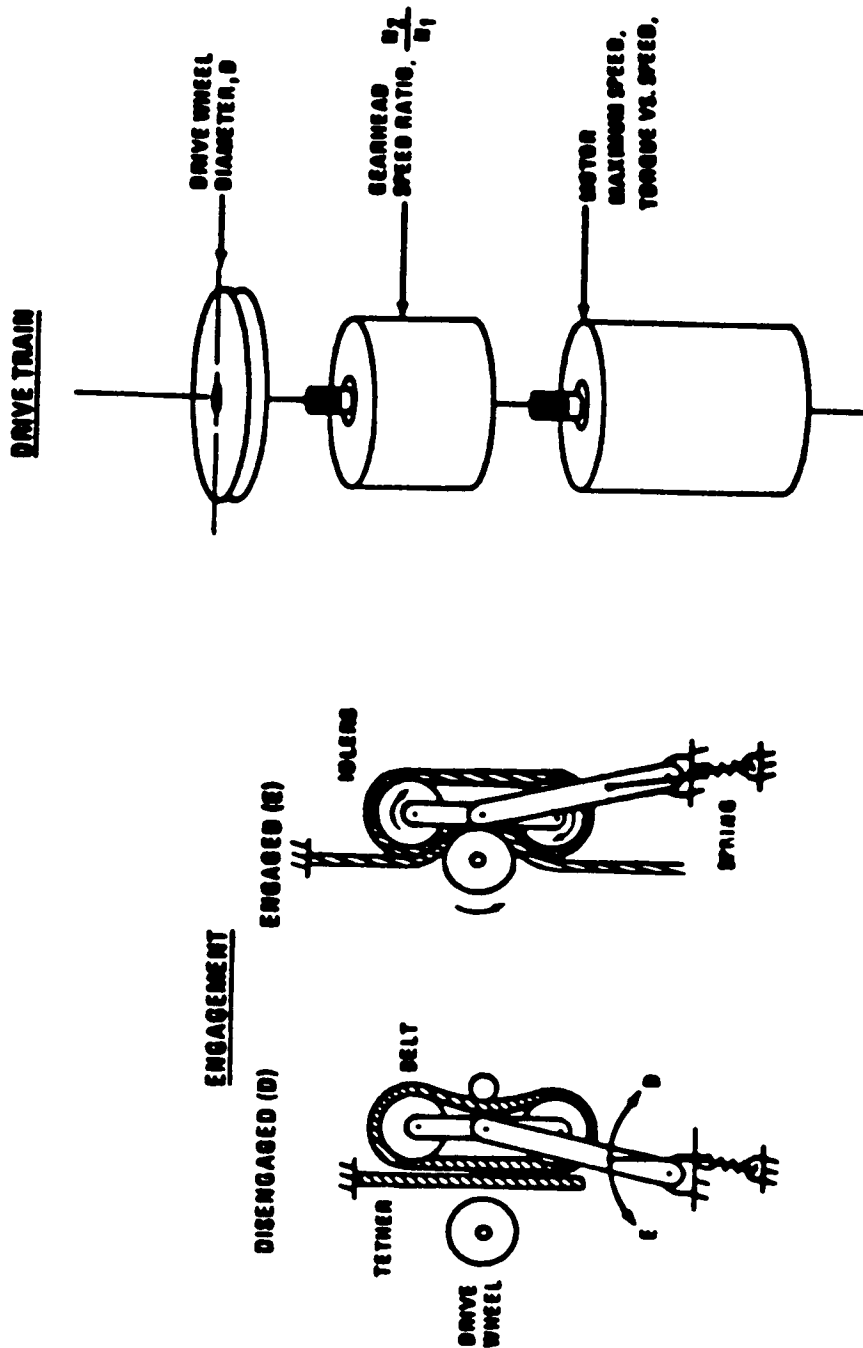


FIG 8 TETHER CRAWLER ENGAGEMENT MECHANISM AND DRIVE TRAIN

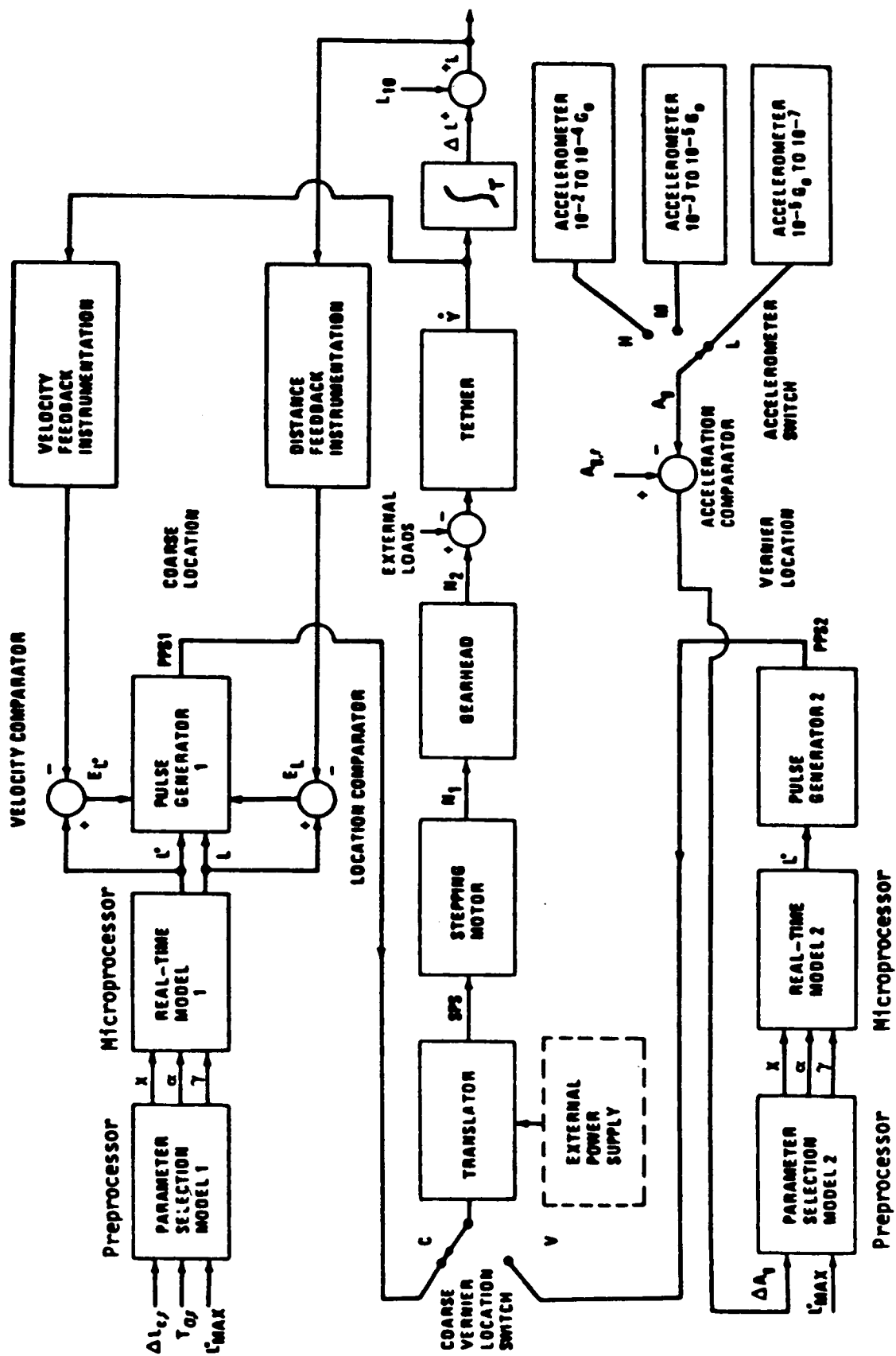
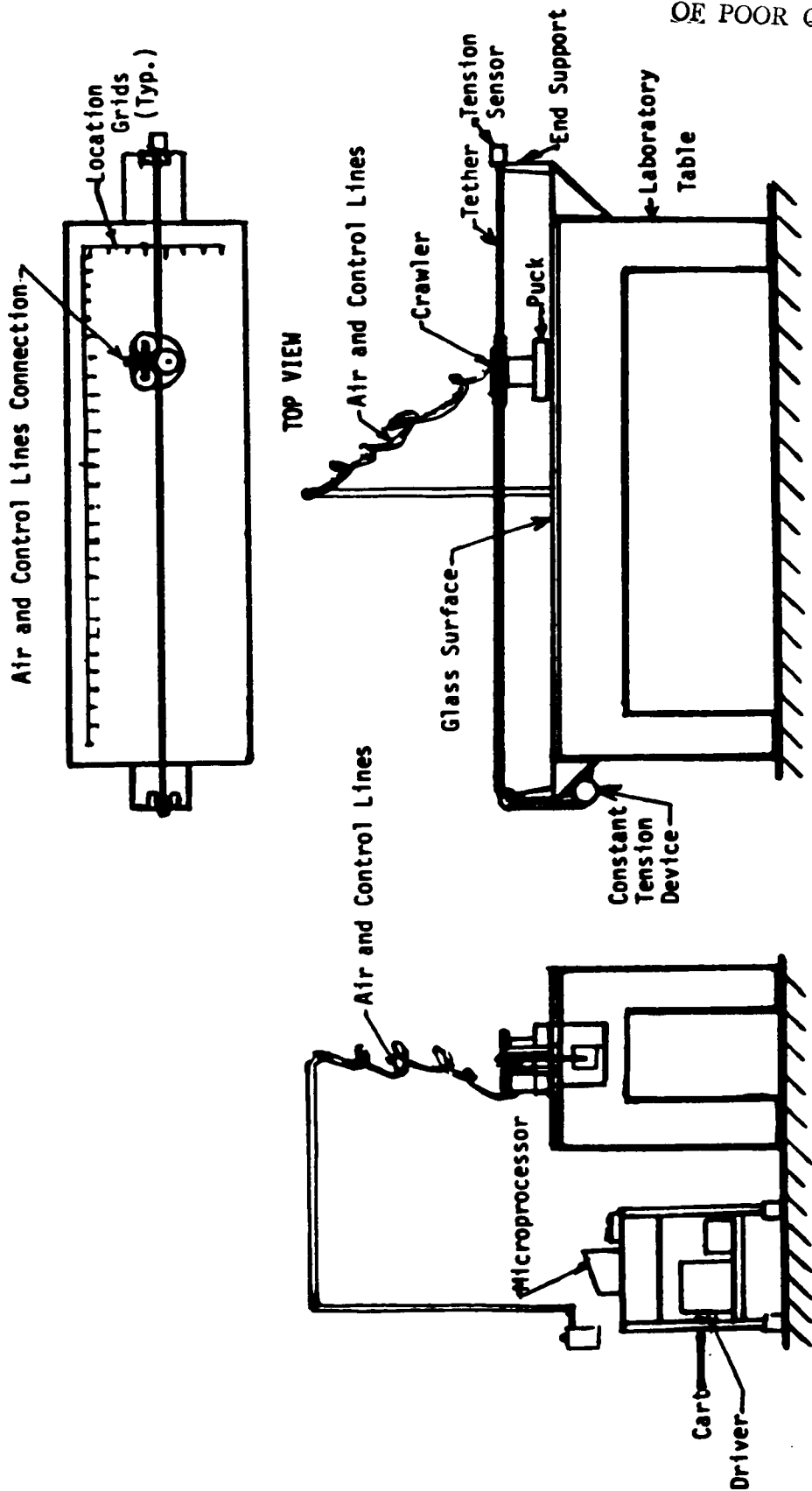


FIGURE 9 DRIVE CONTROL SYSTEM



ORIGINAL PAGE IS
OF POOR QUALITY

SIDE VIEW; Configuration Shown:
Constant Longitudinal Tension and
Free Lateral Position

FIGURE 10 6-FT AIR TABLE

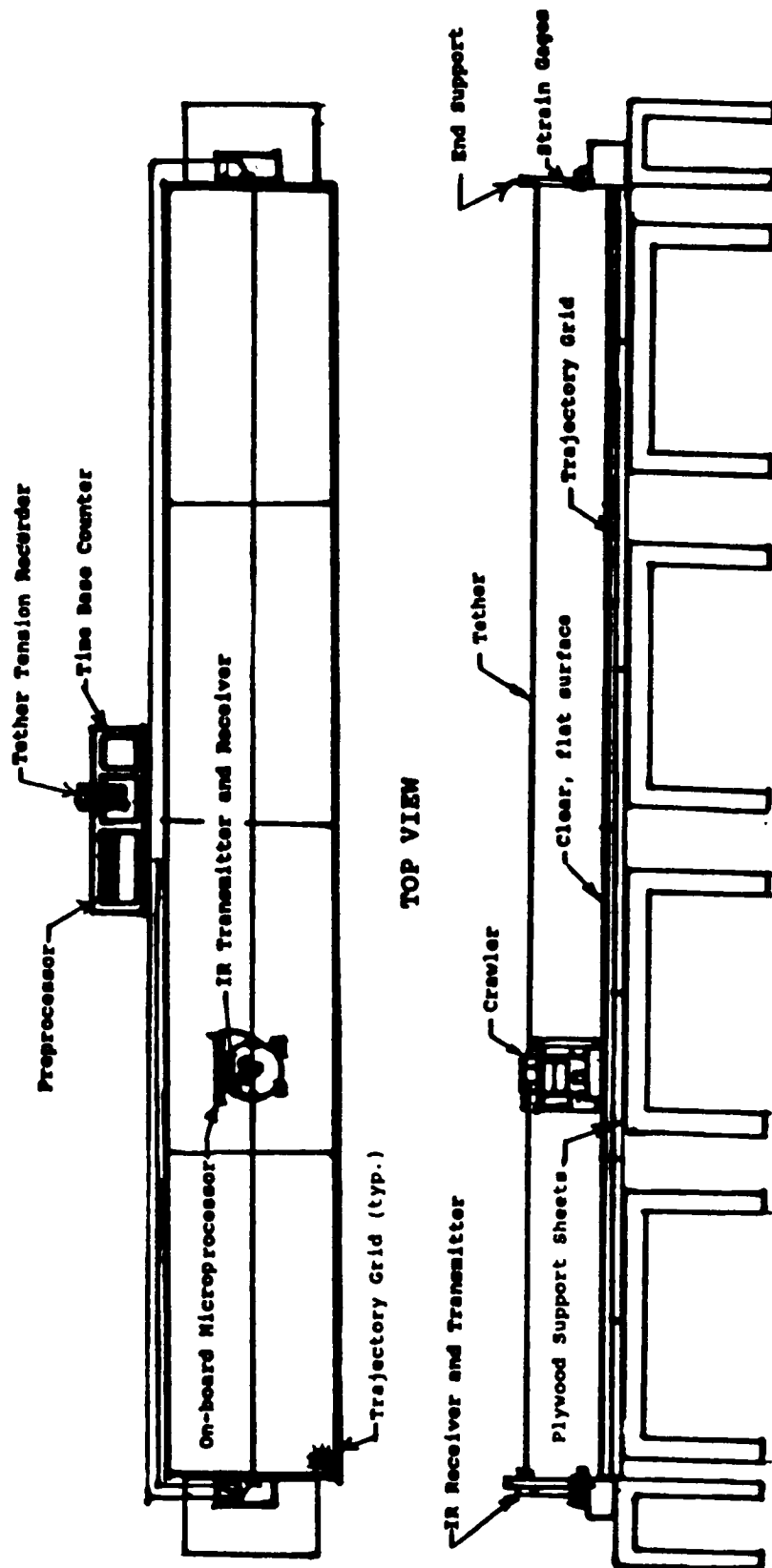


FIGURE 11 32-FOOT AIR TABLE

ORIGINAL PAGE IS
OF POOR QUALITY

ITEMS	SU87	F87	W88	SP88	SU88	F88	W89	SP89	SU89	F89	W90	SP90
DESIGN & OPERATIONS PARAMETERS DEFINITION:												
CRAWLER												
TETHER WEAR VS. GRIP												
LABORATORY TESTS:												
2-D CRAWLER (C) (32-FT)												
(60-FT)												
3-D CRAWLER (C&P)												
DEMONSTRATION FLIGHTS:												
BALLOON (P)												
KC-135 (C)												
ROCKET TO LEO (P)												
SHUTTLE (C & P)												

C - CLOTHESLINE TETHER (FIXED ENDS)
P - PENDANT TETHER (FREE END)

TECS SCHEDULE 1987 - 1990

FIG 12

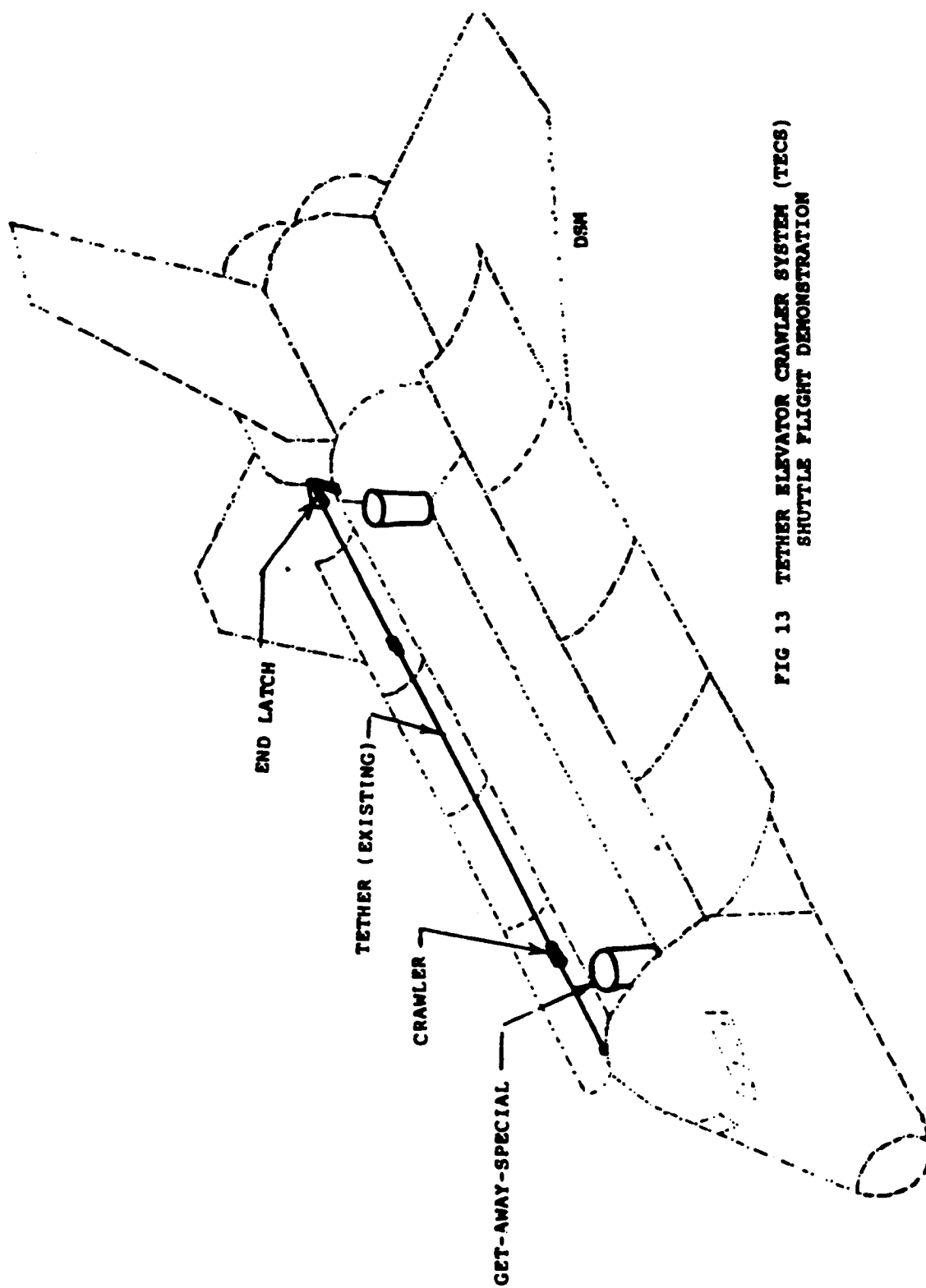


FIG 13 TETHER ELEVATOR CRAWLER SYSTEM (TECS)
SHUTTLE FLIGHT DEMONSTRATION

REFERENCES

1. Rupp, C.L., A Tether Tension Control Law for Tethered Subsatellites Deployed Along the Local Vertical, NASA TMX-94963, Marshall Space Flight Center, September, 1975.
2. Lorenzini, E. C., "A Three-Mass Tethered System for Micro-g/Variable-g Applications", Journal of Guidance, Control and Dynamics, Vol.10, No.3, May-June 1987, pp.242-249.
3. Swenson, Frank R., "Tether Crawler System", Research Projects - 1986, NASA/ASEE Summer Faculty Fellow Program, NASA CR-178966, November, 1986.
4. Swenson, Frank R., First Moves: Tether Elevator Crawler System (TECS), submitted for publication, 1987.
5. Lorenzini, E.C., Analytical Investigation of the Dynamics of Tethered Constellations in Earth Orbit (Phase II), Smithsonian Astrophysical Observatory, Quarterly Report No. 9 for NASA/MSFC under Contract NAS8-36606, July, 1987.

N88-15632

531-28
116733
148

PROPULSION ESTIMATION TECHNIQUES

Prepared by:	Enoch C. Temple, Ph.D.
Academic Rank:	Associate Professor
University and Department:	Alabama A&M University Department of Mathematics
NASA/MSFC Laboratory:	Structures and Propulsion
MSFC Colleagues:	James Crafts Klaus Gross
Date:	August 1987
Contract No.:	NGT-01-008-021 The University of Alabama in Huntsville

ACKNOWLEDGMENTS

I would like to thank NASA, MSFC, and ASEE for providing this excellent research opportunity. Thanks are also extended to the staff of the Propulsion Laboratory for the help willingly given during this ten-week period. Special thanks go to James Crafts and Klaus Gross, my NASA counterparts, for suggesting and discussing the topic addressed in this report. Further appreciation is extended to Judy Maples who typed this report.

PROPULSION ESTIMATION TECHNIQUES

by

Enoch C. Temple

Associate Professor of Mathematics
Alabama A&M University
Normal, Alabama

ABSTRACT

This paper gives a brief overview of statistical tools that are needed to perform post flight/test reconstruction of state variables. Linear regression, recursive linear regression, and the exact connection between the Kalman filter and linear regression are discussed. The regression connection is expected to serve as an aid in the application of a recently developed analytical method of flight reconstruction to single engine test firing data.

1. INTRODUCTION

This paper considers the issue of post flight/test state variable reconstruction through the application of observations made on the output of the Space Shuttle propulsion system. The incentive for the concepts discussed here is rooted in a NASA contract report by Rogers (1987). Rogers used the Kalman filtering procedure to reconstruct the state variables of the Space Shuttle propulsion system.

Since its development by Kalman (1960), the Kalman filtering methodology has been a popular procedure with control engineers. Within recent years, it has seen increased applications in other engineering areas as well as in nonengineering areas. Although the applications have been diverse and research on some of its defects has been quite extensive, applied statisticians have not taken full advantage of the tool. This lack of use by some applications areas may be because many publications on the topic have obscured statistical simplicity. Often times the basic statistics concepts are embedded in a discussion of numerical solutions to differential equations.

An objective of this paper is to give the general setup of the Kalman filter and its connection to linear regression. A second objective is to examine the Rogers (1987) reconstruction methodology for application to the reconstruction of the state vector of a single Space Shuttle Main Engine (SSME) by using static test firing data.

Throughout this paper, underlined capital letters are used to denote vectors, capital letters denote matrices, and the identity matrix is denoted by the letter I . All vectors are of the column type and the transpose of any matrix or vector is denoted by using the letter T at the superscript position. The letter E denotes the expectation operator, $N(\underline{U}, \Sigma)$ denotes the multivariate normal probability distribution with

mean vector \underline{U} and covariance matrix Σ . The caret symbol " \wedge " written directly above a scalar or vector denotes a statistical estimator of that vector or scalar.

2. ESTABLISHMENT OF NOTATION

For any Space Shuttle flight, let \underline{Z}_t denote the observed values of vector \underline{Z} at time t . Each component of \underline{Z}_t represents a relevant output of the Space Shuttle propulsion system that can be measured. For example, the components of \underline{Z}_t may be chamber pressure, oxygen flow rate, hydrogen flow rate, etc., for each of the three SSME's. Rogers (1987) lists 71 components for vector \underline{Z}_t and 35 components for vector \underline{X}_t where \underline{X}_t is defined below.

Vector \underline{X}_t is a state vector of parameters to be estimated at time t . It is assumed that the observation vector \underline{Z}_t is a function of the state vector \underline{X}_t . That is,

$$\underline{Z}_t = \underline{h}(\underline{X}_t) + \underline{V}_t \quad (2.1)$$

where \underline{h} is some function and $\underline{V}_t \sim N(\underline{0}, R_t)$. State vector \underline{X}_t is known to change with respect to time according to the equation

$$\dot{\underline{X}}_t = \underline{f}(\underline{X}_t, t) + \underline{W}_t \quad (2.2)$$

where \underline{f} is some function, $\underline{W}_t \sim N(\underline{0}, Q_t)$ and $E(\underline{W}_t \underline{V}_t^T) = 0$.

If it is assumed that \underline{f} and \underline{h} in equations (2.1) and (2.2) are linear, then numerical procedures allow us to transform these equations to the form

$$\underline{X}_K = F_K \underline{X}_{K-1} + \underline{W}_K \quad (2.3)$$

$$\underline{Z}_K = H_K \underline{X}_K + \underline{V}_K \quad (2.4)$$

where K represents discrete values of t , $\underline{W}_K \sim N(\underline{O}, Q_K)$ and $\underline{V}_K \sim N(\underline{O}, R_K)$.

After a Space Shuttle flight has taken place, the post flight reconstruction procedure seeks to use the observed values of \underline{Z}_K and the equations in (2.3) and (2.4) to reconstruct (estimate) the parameters \underline{X}_K so that the estimation error is minimized. The estimated value of \underline{X}_K is denoted by $\hat{\underline{X}}_K$.

3. A RECURSIVE ESTIMATOR OF \underline{X}

In order to complete the development of the reconstruction process mentioned in section 2, we consider a system of equations

$$\underline{Z} = H \underline{X} + \underline{\epsilon} \quad (3.1)$$

where (3.1) is a system of linear equations that has been generated by making n observations on the single equation

$$\underline{Z}^* = H^* \underline{X} + \underline{\epsilon}^* \quad (3.2)$$

where \underline{Z}^* and $\underline{\epsilon}^*$ are vectors or scalars. H^* is a $j \times p$ matrix where j = number of components in vector \underline{Z}^* and \underline{X} is fixed. Vector \underline{X} being fixed means that \underline{X} does not change with time or does not change as the number of observations on \underline{Z} increase. If $\text{Cov}(\underline{\epsilon}) = \Sigma$ and $\det(\Sigma) \neq 0$, then the weighted least squares estimate of vector \underline{X} is given by

$$\hat{\underline{X}} = (H^T \Sigma^{-1} H)^{-1} H^T \Sigma^{-1} \underline{Z} \quad (3.3)$$

and the covariance of the estimate is given by

$$\text{Cov}(\hat{\underline{X}}) = E [(\hat{\underline{X}} - \underline{X})(\hat{\underline{X}} - \underline{X})^T] = (H^T \Sigma^{-1} H)^{-1} = P. \quad (3.4)$$

The reader should be reminded that with the appropriate assumptions, the maximum likelihood, the minimum variance unbiased linear as well as the minimum mean-squared error estimator of \underline{X} are identical to the estimator given by equation (3.3). We also remark that $\text{Cov}(\hat{\underline{X}})$ is a measure of the quality of the estimates in vector $\hat{\underline{X}}$. A detailed discussion of these estimators may be found in Elbert (1984).

In the sequel that follows, the estimator in equation (3.3) will be rearranged so that \underline{X} can be estimated by using a recursive process. The development of the recursive process is started by assuming that there are K observations on equation (3.2) which form the system

$$\underline{Z}_K = H_K \underline{X} + \underline{\varepsilon}_K \quad (3.5)$$

where $\text{Cov } \underline{\varepsilon}_K = \Sigma_K$ and $\det(\Sigma_K) \neq 0$. By equation (3.3)

$$\hat{\underline{X}}_K = (H_K^T \Sigma_K^{-1} H_K)^{-1} H_K^T \Sigma_K^{-1} \underline{Z}_K \quad (3.6)$$

is the estimate of \underline{X} where observations up to and including observation K are used. The covariance of the estimator is denoted by P_K and

$$P_K = E[(\hat{\underline{X}}_K - \underline{X})(\hat{\underline{X}}_K - \underline{X})^T] = (H_K^T \Sigma_K^{-1} H_K)^{-1}. \quad (3.7)$$

Assume that an additional measurement \underline{Z}_{K+1} has been made. Let

$$\underline{Z}_{K+1} = H_{K+1} \underline{X} + \underline{\varepsilon}_{K+1} \quad (3.8)$$

where $\text{Cov}(\underline{\varepsilon}_{K+1}) = \Sigma_{K+1}$ and $E(\underline{\varepsilon}_K \underline{\varepsilon}_{K+1}^T) = 0$. Note that $E(\underline{\varepsilon}_K \underline{\varepsilon}_{K+1}^T) = 0$ means that the $(K+1)$ th observation is independent of the 1st K observations. Putting the K observations with the $(K+1)$ th observation yields the system

$$\begin{pmatrix} \underline{z}_K \\ \text{---} \\ \underline{z}_{K+1} \end{pmatrix} = \begin{pmatrix} \underline{H}_K \\ \text{---} \\ \underline{H}_{K+1} \end{pmatrix} \underline{x} + \begin{pmatrix} \underline{\varepsilon}_K \\ \text{---} \\ \underline{\varepsilon}_{K+1} \end{pmatrix} \quad (3.9)$$

where

$$\text{Cov} \begin{pmatrix} \underline{\varepsilon}_K \\ \text{---} \\ \underline{\varepsilon}_{K+1} \end{pmatrix} = \begin{pmatrix} \Sigma_K & 0 \\ 0 & \Sigma_{K+1} \end{pmatrix}.$$

By substituting into equation (3.3) we get

$$\hat{\underline{x}}_{K+1} = \left[\begin{pmatrix} \underline{H}_K^T & \underline{H}_{K+1}^T \end{pmatrix} \begin{pmatrix} \Sigma_K^{-1} & 0 \\ 0 & \Sigma_{K+1}^{-1} \end{pmatrix} \begin{pmatrix} \underline{H}_K \\ \text{---} \\ \underline{H}_{K+1} \end{pmatrix} \right]^{-1} \begin{pmatrix} \underline{H}_K^T & \underline{H}_{K+1}^T \end{pmatrix} \begin{pmatrix} \Sigma_K^{-1} & 0 \\ 0 & \Sigma_{K+1}^{-1} \end{pmatrix} \begin{pmatrix} \underline{z}_K \\ \text{---} \\ \underline{z}_{K+1} \end{pmatrix}. \quad (3.10)$$

Note that we can write

$$\hat{\underline{x}}_{K+1} = \hat{\underline{x}}_K + (\hat{\underline{x}}_{K+1} - \hat{\underline{x}}_K). \quad (3.11)$$

Substituting results from (3.6) and (3.10) into (3.11) and using matrix algebra, we get

$$\hat{\underline{x}}_{K+1} = \hat{\underline{x}}_K + (\underline{P}_K^{-1} + \underline{H}_{K+1}^T \Sigma_K^{-1} \underline{H}_{K+1})^{-1} \underline{H}_{K+1}^T \Sigma_{K+1}^{-1} (\underline{z}_{K+1} - \underline{H}_{K+1} \hat{\underline{x}}_K). \quad (3.12)$$

By substituting into equation (3.7) and using matrix algebra, we get

$$\underline{P}_{K+1} = \left[\begin{pmatrix} \underline{H}_K^T & \underline{H}_{K+1}^T \end{pmatrix} \begin{pmatrix} \Sigma_K^{-1} & 0 \\ 0 & \Sigma_{K+1}^{-1} \end{pmatrix} \begin{pmatrix} \underline{H}_K \\ \text{---} \\ \underline{H}_{K+1} \end{pmatrix} \right]^{-1} = (\underline{P}_K^{-1} + \underline{H}_{K+1}^T \Sigma_{K+1}^{-1} \underline{H}_{K+1})^{-1}.$$

Substituting \underline{P}_{K+1} into equation (3.12) yields

$$\hat{\underline{X}}_{K+1} = \hat{\underline{X}}_K + P_{K+1} H_{K+1}^T \Sigma_{K+1}^{-1} (\underline{Z}_{K+1} - H_{K+1} \hat{\underline{X}}_K) \quad (3.13)$$

and

$$P_{K+1} = (P_K^{-1} + H_{K+1}^T \Sigma_{K+1}^{-1} H_{K+1})^{-1}. \quad (3.14)$$

Equations (3.13) and (3.14) provide recursive equations for estimating \underline{X} and its corresponding covariance matrix P .

Recall that the estimator given in equation (3.3) may be identified by using the symbol $\hat{\underline{X}}_n$. Therefore, if \underline{X} is fixed as it is in equation (3.1), the recursive equations of (3.13) and (3.14) have no statistical advantage over the estimator given in equation (3.3). However, if \underline{X} changes with time where there is one observation per time interval, then the recursive equations are quite useful. In fact, equations (3.13) and (3.14) when combined with equations (2.3) and (2.4) form the Kalman filtering process.

4. THE KALMAN FILTER

It is worthwhile to mention that Brown (1983) and Gelb (1974) used matrix theory to express equations (3.13) and (3.14) as

$$P_{K+1} = (I - K_{K+1} H_{K+1}) P_K \quad (4.1)$$

$$\hat{\underline{X}}_{K+1} = \hat{\underline{X}}_K + K_{K+1} (\underline{Z}_{K+1} - H_{K+1} \hat{\underline{X}}_K) \quad (4.2)$$

where

$$K_{K+1} = P_K H_{K+1} (\Sigma_{K+1} + H_{K+1} P_K H_{K+1}^T)^{-1} \quad (4.3)$$

and K_{K+1} is called the gain matrix.

For the convenience of the reader, equations (2.3) and (2.4) are reprinted here. That is,

$$\underline{X}_{K+1} = F_K \underline{X}_K + \underline{W}_K \quad (4.4)$$

and

$$\underline{Z}_{K+1} = H_{K+1} \underline{X}_{K+1} + \underline{V}_{K+1}. \quad (4.5)$$

When equations (4.1) and (4.2) are combined with equations (4.4) and (4.5), two types of estimates of \underline{X}_{K+1} are possible for each K. A notation by Gelb (1974) allows for the two estimators to be distinguished. That notation is

$\hat{\underline{X}}_{K+1}^{(-)}$ = the estimate of \underline{X}_{K+1} using all observations up to and including observation K.

$P_{K+1}^{(-)}$ = the estimate of P using all observations up to and including observation K.

$\hat{\underline{X}}_{K+1}^{(+)}$ = the estimate of \underline{X}_{K+1} using all observations up to and including observation (K+1).

The values of $\hat{\underline{X}}_{K+1}^{(-)}$ and $P_{K+1}^{(-)}$ are obtained by using equations (4.4) and (4.5). The $\hat{\underline{X}}_{K+1}^{(-)}$ vector is often called the extrapolated or predicted value of \underline{X}_{K+1} and $P_{K+1}^{(-)}$ is called the extrapolated variance of $\hat{\underline{X}}_{K+1}^{(-)}$.

The values of $\hat{\underline{X}}_{K+1}^{(+)}$ and $P_{K+1}^{(+)}$ are computed by substituting $\hat{\underline{X}}_{K+1}^{(-)}$ for \underline{X}_K in equation (4.2) and $P_{K+1}^{(-)}$ for P_K in equation (4.1).

The computation summary is

$$\hat{\underline{X}}_{K+1}^{(-)} = F_K \hat{\underline{X}}_K^{(+)} \quad (4.6)$$

$$P_{K+1}^{(-)} = F_K P_K^{(+)} F_K^T + Q_K \quad (4.7)$$

$$\hat{\underline{X}}_{K+1}^{(+)} = \hat{\underline{X}}_{K+1}^{(-)} + K_{K+1} (\underline{Z}_{K+1} - H_{K+1} \hat{\underline{X}}_{K+1}^{(-)}) \quad (4.8)$$

$$P_{K+1}^{(+)} = (I - K_{K+1} H_{K+1}) P_{K+1}^{(-)} \quad (4.9)$$

$$K_{K+1} = P_{K+1}^{(-)} H_{K+1}^T (H_{K+1} P_{K+1}^{(-)} H_{K+1}^T + R_{K+1})^{-1} . \quad (4.10)$$

Equations (4.6) to (4.10) completely describe the Kalman filtering process when the original functions \underline{f} and \underline{h} of equations (2.1) and (2.2) are linear.

However, when functions \underline{f} and \underline{h} are nonlinear, the state vectors \underline{X}_K ($K = t_0, t_1, \dots, t_T$) are estimated through the application of an extended Kalman filtering procedure. This procedure requires a linearization of functions \underline{f} and \underline{h} about some known state value \underline{X}_K^* . The next paragraph provides a brief overview of the extended Kalman filter concept.

Let \underline{X}_K^* be some known value of \underline{X} and assume that $\Delta \underline{X}$ is small. A first degree Taylor series approximation of functions (2.1) and (2.2) may be

$$\dot{\underline{X}}_K^* + \Delta \dot{\underline{X}} \approx f(\underline{X}_K^*, K) + \left[\frac{\partial f}{\partial \underline{X}} \right]_{\underline{X}=\underline{X}_K^*} \cdot \Delta \underline{X} + \underline{W}_t \quad (4.11)$$

and

$$\underline{Z}_t \approx h(\underline{X}_K^*) + \left[\frac{\partial h}{\partial \underline{X}} \right]_{\underline{X}=\underline{X}_K^*} \cdot \Delta \underline{X} + \underline{V}_t . \quad (4.12)$$

If it is assumed that \underline{X}_K^* is selected so that $\dot{\underline{X}}_K^* = f(\underline{X}_K^*, K)$, then equations (4.11) and (4.12) become

$$\Delta \dot{\underline{X}} = \left[\frac{\partial \underline{f}}{\partial \underline{X}} \right]_{\underline{X}=\underline{X}_K^*} \Delta \underline{X} + \underline{W}_K \quad (4.13)$$

and

$$\underline{Z}_K - h(\underline{X}_K^*) = \left[\frac{\partial h}{\partial \underline{X}} \right]_{\underline{X}=\underline{X}_K^*} \Delta \underline{X} + \underline{V}_K \quad (4.14)$$

Equation (4.13) is called the linearized dynamics equation and (4.14) is the linearized measurement equation. Note that equations (4.13) and (4.14) may be transformed to equations that are equivalent to equations (2.3) and (2.4). Hence for each discrete time K , $\Delta \underline{X}_K$ can be estimated and error covariance matrices can be determined. The state vector estimate at time K is then given by

$$\hat{\underline{X}}_K^{(+)} = \underline{X}_K^* + \Delta \hat{\underline{X}}_K^{(+)}$$

where $\Delta \hat{\underline{X}}_K^{(+)}$ is computed by substituting from equations (4.13) and (4.14) into equation (4.8). Vector $\hat{\underline{X}}_{K+1}$ is computed by letting $\underline{X}_{K+1}^* = \hat{\underline{X}}_K$ and repeating the above procedure.

The extended Kalman filter has performed well in a large class of applications. However, there are occasions when divergence occurs in the state vector estimates. Divergence occurs when the computed entries of the error covariance matrix P_K become small as compared to the actual error in the estimate of the state vector. The cause of this divergence is not due to a defect in the filtering procedure, but may be caused by the linear approximation procedure, numerical rounding error, or an inadequate model of the system being studied. Additional possible causes of divergence are mentioned by Gelb (1974).

A publication by Varhaegen and Van Dooren (1986) is representative of the theoretical and experimental analyses that are currently being done on the divergence problem. The Rogers (1987) computer code has implemented the U-D factorized algorithm as a means of controlling numerical roundoff error that may lead to divergence in the state vector. Checks for other sources that may generate divergence are conducted through computer evaluations.

5. CONCLUSION

At this point we have reviewed the general setup for a regression problem where the parameters to be estimated are fixed. This lead to recursive equations (4.1), (4.2), and (4.3) which allowed for the development of an estimation procedure for a time varying parameter. When functions \underline{f} and \underline{h} are linear, it has been clearly stated that equations (2.3) and (2.4) are the essential ingredients for state variable reconstruction. If \underline{f} and \underline{h} are nonlinear, \underline{X}_K can be estimated by linearizing \underline{h} and \underline{f} about some known vector and treating the linearized equations as if they are equations (2.3) and (2.4).

The problem of applying the extended Kalman filtering procedure to the static test firing data remains. The basic approach for the application is identical to the presentation given in Section 4. Therefore, the computer codes that have been prepared by Rogers (1987), which are currently operational on the MSFC computer system, may be modified so that static test data may be analyzed. The static test setup differs from the actual flight data in that many flight associated modules will become inactive. Therefore, after adjustments are made for the analysis of static test data, it will be necessary to evaluate the performance of the computer code for the divergence of parameter estimates.

REFERENCES

- Brown, R. G. (1983), Introduction to Random Signal Analysis and Kalman Filtering, New York: John Wiley and Sons, Inc.
- Elbert, T. F. (1984), Estimation and Control of Systems, New York: Van Nostrand Reinhold Company.
- Gelb, A. (Editor, 1974), Applied Optimal Estimation, Cambridge: MIT Press.
- Kalman, R. E. (1960), "A New Approach to Linear Filtering and Prediction Problems," Journal of Basic Engineering, March 1960, pp. 35-46.
- Rogers, R. M. (1987), Space Shuttle Propulsion Estimation Development Verification, Final report for Contract NAS8-36152.
- VerHaegen, M. and Van Dooren, P. (1986), "Numerical Aspects of Different Kalman Filter Implementations," IEEE Transactions (AC), October 1986, pp. 907-917.

N 88 - 15633

532-27
116734
218

1987

NASA/ASEE SUMMER FACULTY RESEARCH FELLOWSHIP PROGRAM

MARSHALL SPACE FLIGHT CENTER

THE UNIVERSITY OF ALABAMA IN HUNTSVILLE

THE DEVELOPMENT OF TEST METHODOLOGY

FOR TESTING GLASSY MATERIALS

Prepared By:	Dennis S. Tucker
Academic Rank:	Asistant Professor
NASA/MSFC:	
Laboratory:	Materials and Processes
Division:	Non-Metallic Materials
Branch:	Ceramics and Coatings
NASA Colleague:	Ronald L. Nichols
Contract No.:	The University of Alabama in Huntsville 5-30109

ABSTRACT

The inherent brittleness of glass invariably leads to a large variability in strength data and a time dependence in strength (i.e. static fatigue). Loading rate plays a large role in strength values. Glass is found to be weaker when supporting loads over long periods as compared to glass which undergoes rapid loading. In this instance the purpose of rapid loading is to fail the glass before any significant crack growth occurs. However, a decrease in strength occurs with a decrease in loading rate, pursuant to substantial crack extension. These properties complicate the structural design allowable for the utilization of glass components in applications such as mirrors for the Space Telescope and AXAF for Spacelab and the Space Station.

This report describes the test methodology to obtain strength and fracture mechanics parameters which can be used to predict the reliability and lifetimes of such glass components.

List of Figures

<u>Figure No.</u>	<u>Caption</u>
1	4-Point Bend Fixture
2	Double-Ring Bend Fixture
3	Typical Fracture Plot for a Brittle Material
4	Double Cantilever Beam Specimen Configuration
5	Edge Cracked, Three Point Bend Specimen for Determination of K_{Ic}

Nomenclature

a	Moment are in four-point bend test (Eq. 1)
b	Specimen width for four-point bend test (Eq. 1)
c_o	Distance from neutral axis to outer fibers in a beam (Eq. 2)
C	Crack Length
d	Specimen thickness for four-point bend test (Eq. 1)
E	Young's Modulus
ΔF	Increase in test force (Eq. 3)
F_{max}	Maximum force (Eq. 3)
I	Moment of inertia
K_I	Stress intensity factory
K_{Ic}	Critical stress intensity factor
L	Breaking load (Eq. 1)
ℓ	Crack length (Eq. 8)
m	Bending moment
r	Spatial distribution of stresses at a crack tip (Eq. 7)
s	Specimen thickness (Eq. 3 and 4)
S	Bending Stress
Δt	Variation in time (Eq. 3)
Y	Dimensionless parameter (Eq. 8)
γ	Surface energy
$f(\theta)$	Angular distribution of normal stresses at a crack tip
ν	Poisson's ratio
σ	Applied stress (Eq. 6)

Nomenclature

σ_N	Normal stress at a crack tip
σ_2	Applied stress (Eq. 8)
σ^*	Griffith stress
$\Delta\sigma_b$	Change in bending stress (Eq. 3)
σ_{bB}	Bending strength

ACKNOWLEDGEMENT

The author wishes to acknowledge the NASA/ASEE Summer Faculty Fellowship Program along with Gerald Karr, the UAH Director.

To NASA counterpart Ronald L. Nichols of the Ceramics and Coatings Branch, Non-Metallic Materials Division, gratitude is offered.

Thanks to Bill Kennedy, without whose assistance this work would not have progressed as well as it did.

INTRODUCTION

The aim of this program is to provide the necessary data to predict and improve the reliability and lifetime of glass components which will be utilized in the following program applications:

- o AXAF Mirrors
- o Space Telescope Mirrors
- o Spacelab Windows
- o Space Station Windows
- o Future Space Structures
- o Equipment with Optical Lenses
- o Large Deployable Structures

The establishment of this investigation will be accomplished in three phases. Phase I will include the determination of materials properties, surface treatments, and inspection techniques for maximum flaw size detection. Phase II will be the development of a reliable structural model and Phase III will be model verification by sub-assembly testing and evaluation.

Due to time constraints this study will concentrate solely on Phase I, consisting of four tasks. The tasks are as follows:

Task I - Review and compilation of current properties, inspection techniques, surface treatments, and test methodologies of glass.

Task II - The effects of surface treatment on glass strength.

Task III - Utilization of various inspection techniques such as microscopy, polarization, XRD, thermography, ultrasonics to determine maximum flaw size existing in the glass.

Task IV - Materials property generation.

- o Design and fabricate the required test fixtures and equipment.

- o Selection candidate glass materials and prepare test specimens.
- o Test specimens with specific surface/thermal procedure.
- o Inspect the specimens with the most promising flaw detection techniques. Test materials to determine "A" basis properties of stress model parameters from the defined stress model equation.
- o Analyze the "A" basis properties data for required inclusion into the stress model.

Initial strength and delayed fracture techniques are used to generate materials properties in Task IV. Four point bending and double ring bending will be used to characterize initial strength properties. Delayed fracture properties will be developed utilizing fracture mechanics theory by establishing stress intensity factors and critical stress intensity factors for each glass system.

Technical Discussion

Initial Strength

Modulus of Rupture (MOR) will be determined using four point bend flexure testing ¹ as shown in Figure 1. For this test the modulus of rupture is given by:

$$S = \frac{3LA}{bd^2} \quad (1)$$

where:

L = breaking load

a = moment arm

b = specimen width

d = specimen thickness.

This relationship can be readily derived from the formula for maximum bending stress in a rectangular beam. This formula is stated as: ²

$$S = \frac{mc_o}{I} \quad (2)$$

where:

S = maximum bending stress

m = bending moment at any section (equal to the applied load times the moment arm)

c_o = distance from the neutral axis to the outer fibers on which the stress acts

I = moment of inertia.

The double ring bending strength test method will also be used to determine initial strength.³ Figure 2 is a graphical representation of this technique. In this case a disc shaped specimen is loaded between two concentric rings. For limited forces, a tensile stress field will be set up in the central region of the convexly bent specimen surface. Outside the load ring the radial and tangential stresses in the specimen decrease towards the edge, so that the possibility of fracture there is small. By increasing the force the tensile stress in the specimen center is increased at a constant rate until fracture occurs, with the expectation that the fracture is initiated in the region of the surface subjected to the maximum stress, underneath the load ring. Obviously, a major advantage of this technique is the elimination of edge effects.

To calculate the rate of increase of the bending stress in circular specimens the following is applicable:

$$\frac{\Delta \sigma_b}{\Delta t} = \frac{1.08}{s^2} \cdot \frac{\Delta F}{\Delta t} \quad (3)$$

where:

ΔF = Increase of test force, measured in the time interval Δt near the fracture initiation.

s = Specimen thickness.

1.08 = Numerical constant related to the load ring and specimen ring diameters and Poisson's ratio.

The bending strength (σ_{bB}) belonging to the maximum force (F_{max}) from the above equation is:

$$\sigma_{bB} = 1.08 \frac{F_{max}}{s^2} \quad (4)$$

where

σ_{bs} = bending strength

F_{max} = greatest force

s = specimen thickness.

Delayed Fracture

(Fracture Mechanics Parameters)

It is well established that the fracture strength of glass is excellent when loaded in compression. However, in tension, strengths are substantially lower than the theoretical strength calculated on the basis of interatomic bonding.⁴ It is understood that this decrease in strength is due to the presence of flaws which act as stress raisers. In glass these flaws are usually surface cracks. Griffith⁵ developed a failure criterion based on an energy inventory at the crack tip; i.e., a crack will propagate in a material provided

$$\frac{\partial E}{\partial C} = \left[\frac{\pi \sigma^2 C^2}{E} (1 - \nu^2) + 4C\gamma \right] \leq 0 \quad (5)$$

where:

C = crack length

σ = applied stress

E = Young's modulus

ν = Poisson's Ratio

γ = Energy per unit area of surface created by fracture propagation.

When equation (5) is solved for σ , one obtains the Griffith stress:

$$\left(\frac{2\gamma E}{\pi C (1 - \nu^2)} \right)^{1/2} \equiv \sigma^* \quad (6)$$

Thus if the applied stress equals or exceeds the Griffith stress, σ^* the crack will propagate.

Although glass is relatively inert to most corrosive atmospheres, it is susceptible to stress corrosion caused by water in the environment. This phenomenon is known as stress corrosion, static fatigue, or delayed failure. Griffith failed to take this property into consideration in the determination of σ^* in equation 6, above. It is now believed that static fatigue results from the growth of small surface cracks until the crack length C , in equation 6, causes the stress to exceed σ^* . At this point catastrophic failure will occur.

One method for studying stress corrosion is to measure the velocity of macroscopic cracks as a function of selected variables such as load and environment. These experimental determinations are generally called fracture mechanics studies. Fracture mechanics is important in characterizing subcritical crack growth because the crack tip stresses that cause crack growth are directly proportional to the stress intensity factor.

The angular (θ) and spatial (r) distribution of normal stresses at the tip of a crack, σ_N , for plane strain crack displacement can be given by:

$$\sigma_N = \frac{K_I f(\theta)}{(2\pi r)^{1/2}} \quad (7)$$

where K_I is the stress intensity factor. The subscript I stands for Mode I cracking (opening model). A simple dimensional analysis of a body containing a crack of length $2a$ subjected to an applied stress, σ , indicates that the stress enhancement at the crack is related to a and σ by:

$$K_I = \sigma \sqrt{2a} Y \quad (8)$$

Where Y is a dimensionless parameter depending upon the specimen and crack geometry. K is a measure for all stresses and strains. Crack extension will occur when the stresses and strains at the crack tip reach a critical value. This means that fracture is expected to occur when K_I reaches a critical value K_{Ic} . The critical value may be expected to be material parameter. A typical plot of stress intensity factor (K_I) vs. Crack Growth and the definition of critical stress intensity factor (K_{Ic}) is shown in Figure 3. Although the point called K_{Ic} is simply one point on the curve in Figure 3 it is useful for predicting critical flaw sizes or in calculations of impact or erosion behavior.

There are two generally accepted theories of delayed fracture. Charles and Hillig⁶ stated that delayed fracture is due to a stress enhanced chemical reaction, with the parameters being stress intensity factor, environment of the crack tip (moisture content) and the character of the material itself. Wiederhorn's⁷ stress corrosion studies have confirmed much of the Charles-Hillig theory. Hasselman⁸ asserts that the micro-cracks grow by the stress enhanced, thermally activated formation of vacancies at the crack tip. This theory agrees well with data taken on a typical industrial glass.

The stress intensity factor is established for a brittle material utilizing a specimen with an initial crack of known length. The most common method of testing for K_I is the double cantilever beam technique as shown in figure 4. With this method a specimen is ground to force glass fracture in the central portion of the specimen. A crack is then initiated by localized thermal shock. The stress intensity factor is then determined by monitoring the crack growth relative to a controlled load. The advantage of this technique is that a constant moment rather than a constant load is applied⁹. This results in the strain energy release rate being independent of crack length. Also, corrections for shear or beam rotation are unnecessary.

Obviously this technique can be used to identify the critical stress intensity factor. Fracture toughness may also be obtained from three-point bend testing of a specimen with an initial edge crack (Figure 5).

Experimental Procedures

Completion of the materials testing was precluded by the short duration of the summer term.

Four optical grade glasses were selected for testing. These are: Corning's Ultra Low Expansion (ULE) titanium silicate glass, Schott's BK-7 glass and Zero-Dur glass and Corning's 7740 Pyrex glass. Twenty eight disc-shaped ULE glass specimens were coarse ground to a thickness of 6 mm. All were polished to a 400 grit finish. Half of these were then tested for MOR using the double ring bending method. The testing was performed using an Instron 1125 testing machine using a crosshead rate of 0.02 in/min. The remaining specimens will be further polished to a diamond finish and tested in the same manner.

It is planned to use either a one or two-stage replica technique to obtain information on flaw size and flaw size distribution. The technique basically consists of coating the sample surface with carbon or formvar and carbon. When the coating is removed it may then be examined by transmission electron microscopy. The disadvantage of this technique is that it only gathers details from the surface. Therefore, a means to investigate volume or bulk flaws is needed. A literature search is under way to elucidate if such a means exists.

RESULTS

Table I shows the results of the MOR test of the ULE glass samples. All samples were observed to fail centrally (i.e. under the load rings with cracks spreading radially to the specimen edge).

CONCLUSIONS

1. Double ring bend fixture was machined to adapt to the Instron 1125 test machine.
2. A four-point bend fixture was ordered from the Instron Company.
3. Samples of ULE glass were polished to a 400 grit finish for testing by the double ring bend method.
4. Pyrex and BK-7 glasses were contracted to be cut and polished to produce specimens for four-point bend and double-ring bend tests.
5. Samples of Zero-Dur glass will be provided by Schott Glass Inc., for both MOR tests.

Bibliography

1. "Flexure Testing of Glass", ASTM No. C158-72, 1984.
2. E. P. Popov, Introduction to Mechanics of Solids, Prentice-Hall, Inc., 1968.
3. "Testing of Glass and Glass Ceramics; Determination of Bending Strength", German Standard DK 666.151:620.174, April 1984.
4. E. Orowan, Inst. of Engineers and Shipbuilders in Scotland, 89, 165 (1945-6); Proc. of International Conference on Physics, The Physical Society, London, 2, 81, 1934.
5. A. A. Griffith, "The Phenomena of Rupture and Flow in Solids", Phil. Tran. Roy. Soc., (London), A221, 163 (1920-21).
6. R. J. Charles and W. B. Hillig, "The Kinetics of Glass Failure and Stress Corrosion", Symposium of Mechanical Strength and Ways of Improving It, Florence, Italy, 25-29, Sept. 1961, Union Scientifique Continentale du Verre, Charleroi, Belgium (1962), p. 511.
7. S. M. Wiederhorn, "Influence of Water Vapor on Crack Propagation in Soda-Lime Glass", J. Am. Cer. Soc., 50, 407 (1967).
8. D. P. H. Hasselman, "Proposed Theory for the Static Fatigue Behavior of Brittle Ceramics", Ultrafine-Grain Ceramics, Syracuse Univ. Press, Syracuse, N.Y. (1970), Chapt. 14.
9. S. W. Freiman, D. R. Mulville, and P. W. Past, "Crack Propagation Studies in Brittle Materials", J. of Mat. Sci., 8 (1973) pp. 1527-1533.

Figure 1.

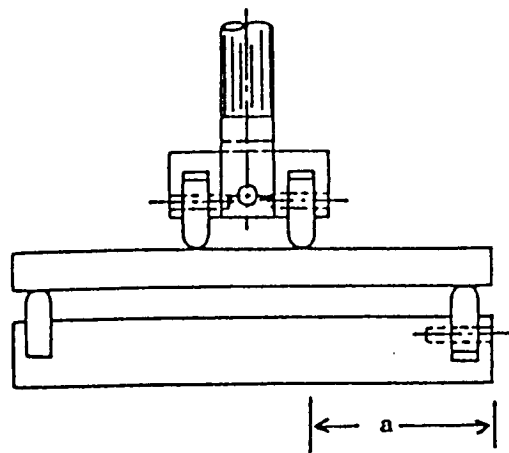


Figure 2.

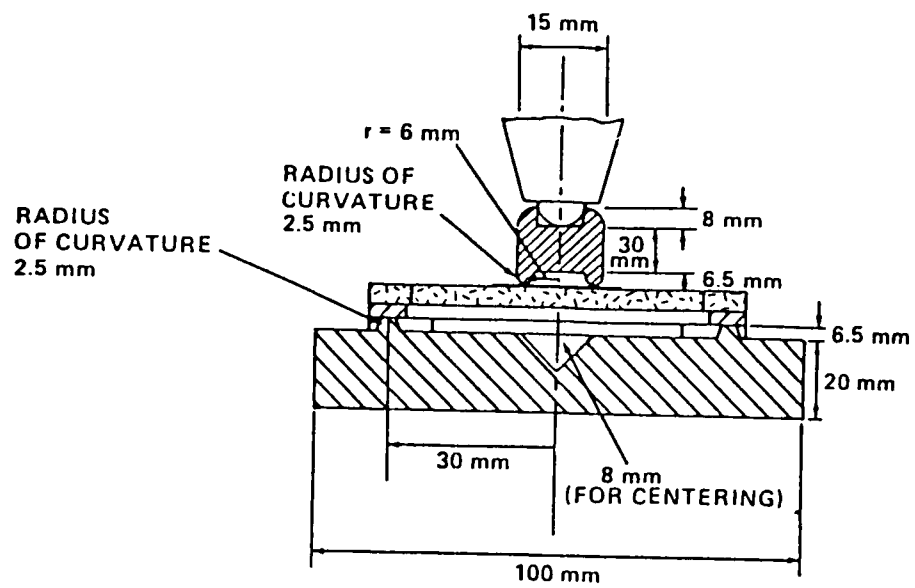


Figure 3.

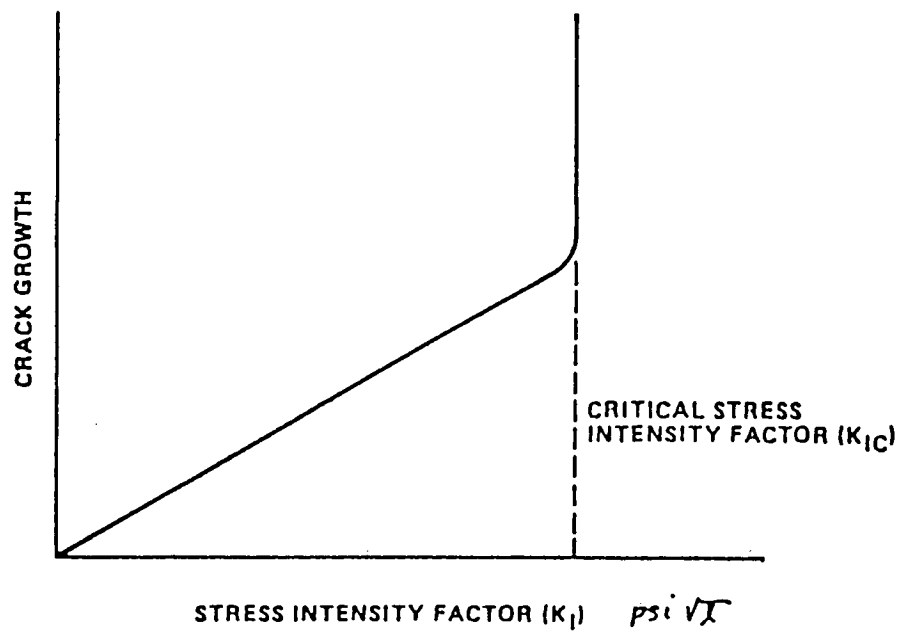


Figure 4.

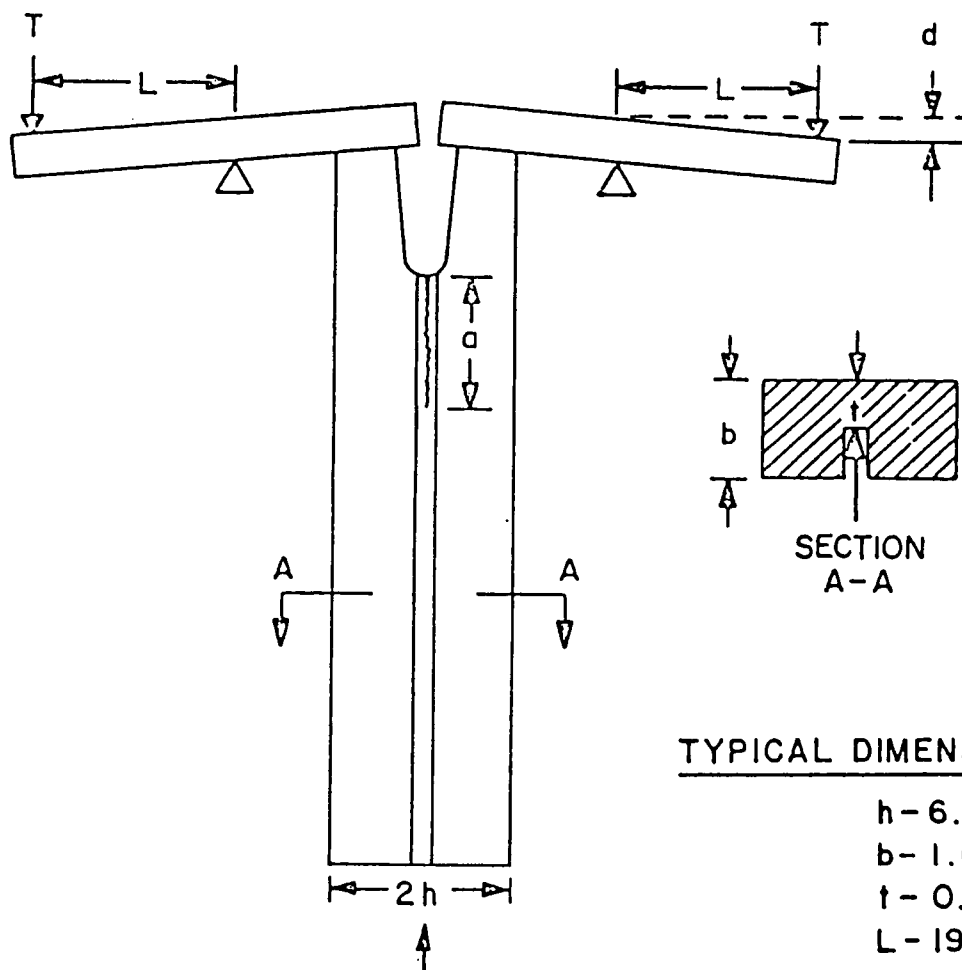


Figure 5.

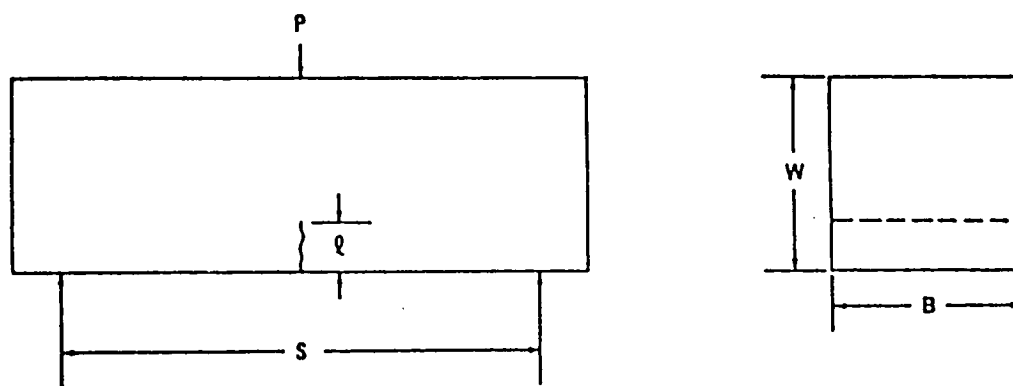


TABLE I - MOR OF ULE GLASS SAMPLES

<u>Sample No.</u>	<u>t (in.)</u>	<u>F max (lb)</u>	<u>MOR (psi)</u>
1	0.232	307	6140
2	0.231	235	4788
3	0.232	283	5660
4	0.231	302	6154
5	0.228	288	5981
6	0.233	400	8000
7	0.233	280	5600
8	0.230	440	8966
9	0.233	335	6700
10	0.234	230	4516

N88-15634

533-37

116735

26P

1987

NASA ASEE SUMMER FACULTY RESEARCH FELLOWSHIP PROGRAM

MARSHALL SPACE FLIGHT CENTER

THE UNIVERSITY OF ALABAMA HUNTSVILLE

Examination of the Physical Processes Associated With the
Keyhole Region of Variable Polarity Plasma Arc Welds in
Aluminum Alloy 2219

Prepared By: Daniel W. Walsh Ph.D.
Academic Rank: Associate Professor
University and Department: California Polytechnic State
University, San Luis Obispo
Metallurgy and Materials Eng
NASA/MSFC
Laboratory: Materials and Processes
Division: Process Engineering
Branch: Metals Processes
NASA Colleague: Arthur C. Nunes Jr., Ph.D.
Date: August 31, 1987

Contract Number:

ABSTRACT

The morphology and properties of the Variable Polarity Plasma Arc (VPPA) weld composite zone are intimately related to the physical processes associated with the keyhole. This study examined the effects of oxide, halide, and sulfate additions to the weld plate on the keyhole and the weld pool. Changes in both the arc plasma character and the bead morphology were correlated to the chemical environment of the weld. Pool behavior was observed by adding flow markers to actual VPPA welds. A low temperature analog to the welding process was developed. The results of the study indicate that oxygen, even at low partial pressures, can disrupt the stable keyhole and weld pool. The results also indicate that Marangoni surface tension driven flows dominate the weld pool over the range of welding currents studied.

Acknowledgement

The author wishes to express his gratitude to all those who made his summer experience both worthwhile and enjoyable. Thanks to Ernestine Cothran, the NASA coordinator and to Jerry Kerr, the UAH coordinator. Thanks also to Billie Swinford and Dina Engler of the respective program offices. The list of NASA and contractor employees who deserve my thanks would read much like the Marshall Directory, the list includes Benji Swaim, Dave Newman, Jeff Ding, Carolyn Kurgan, Frank Zimmerman, Chip Jones, Bill McGee, Wayne Owen, Joe Montano, Wendell Deweese, Ken Swaim, Sam Clark, Tim Vaughn, Tom Morris, Joe Bucher, Bob Ives, Tim Titsworth, Terry Craig, and Bertha Gildon. Thanks to Ernie Bayless for his helpful comments. I would like to thank the a.m. discussion group (Carl Wood and Art Nunes) for conversation at least as stimulating as the concomitant coffee (and less a load on ones kidneys!). I would also like to thank Carl for his help in acquiring both information and hardware. I would like to thank Charles Dickinson for his interest, ideas, and efforts. At many junctures it was his insight that allowed continued progress. Finally, a special thanks to Art Nunes who made me feel so welcome this summer. Neither his willingness to share his knowledge, nor his willingness to discuss the program ever waned. Art was a continual source of quality information, quality insight, and enjoyment. In short, "auctoritas".

Introduction

The physics associated with VPPA process is interesting for three reasons. First, the keyhole and pool are not well understood. In fact the VPPA keyhole process has not been as well characterized as either of the two high energy density beam keyhole processes, laser and electron beam. Second, fluid flow and heat transfer fix the distribution of microstructure and properties in the weld composite region. Finally, fluid flow in the pool and static forces on the pool determine weld bead morphology. The steady state keyhole, is shown in Figure 1. Energy is transferred to the work via a heated plasma directed by the plasma torch. The transfer process has been studied (1-4), and is quite different from other arc processes including the GTA process. Much of the energy transfer is accomplished by convective mechanisms in the hot, directed efflux plasma and by radiation from an arc that is buried in the keyhole region. In VPPA welding the arc polarity switches many times a second, but the work is principally anodic. The oxide film associated with Al 2219 is disrupted by the sputtering action of argon ions during the reverse polarity portion of the cycle, and the arc is stabilized. A majority of the heat transfer occurs at the leading edge of the keyhole, where the anode spot is located and the plasma is directed. In this location the liquid is thin and the thickness uniform regardless of depth in the keyhole (<0.5mm). Around the keyhole, until the longitudinal centerline is passed, the fluid remains thin, but the thickness is not as uniform, becoming slightly larger deeper in the keyhole. At the keyhole rear, a large croissant shaped fluid pool exists.

Several forces determine shape of the trailing pool: surface tension, weight, stagnation pressure of incident gas, and forces arising from flows in the fluid. Several authors have attempted to predict droplet shape, a priori, from a consideration of these forces. Most of these efforts treated fluids in situations less complex than that found in a weld pool(5,6). Heat transfer and pool flow are critical in determining pool and nugget shape. Many investigators have sought to relate penetration to flow in the weld pool. Several (7) postulated that electromagnetic (Lorentz) forces in the weld pool controlled flow. The Lorentz force is given by $\vec{F} = \vec{j} \times \vec{B}$, where j is the current density and B is the magnetic field strength. The force is directly proportional to current density and to magnetic field strength. These authors demonstrated parabolic relations between flow velocities and current in mercury baths, Figure 2. Further, the authors demonstrated an inverse relation

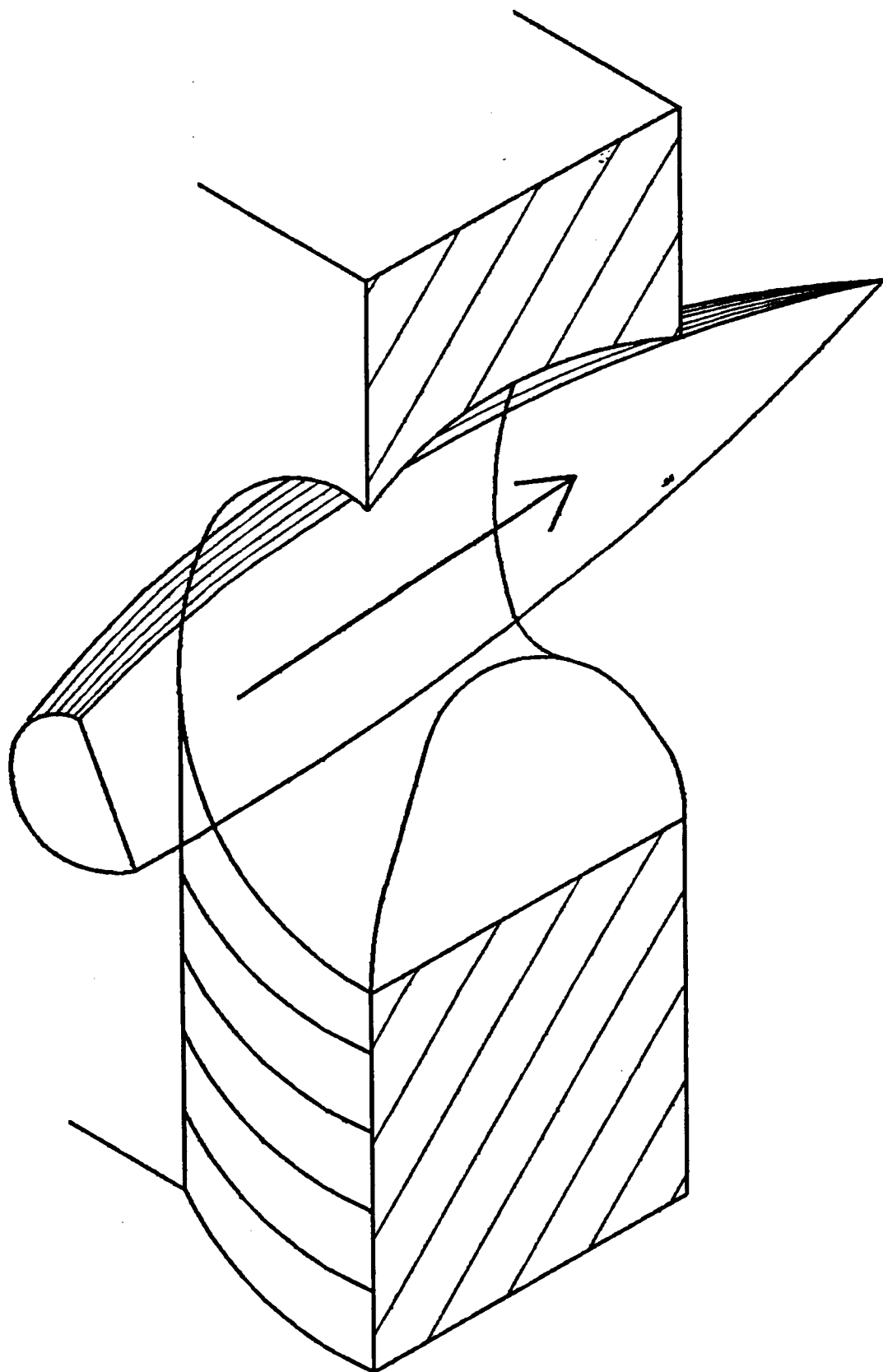


Figure 1 - Plasma Keyhole
XXXIV-2

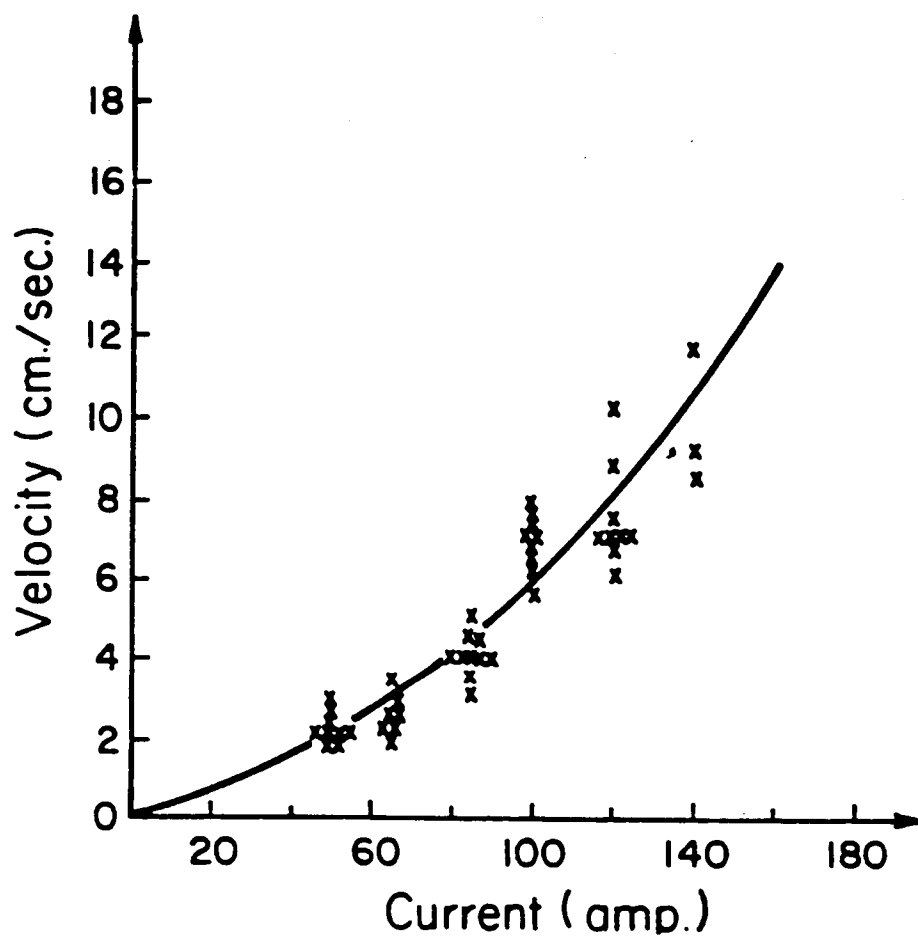


Figure 3 - Flow of Mercury Driven by Lorentz Forces
XXXIV-3

between the velocity of flow and the electrode diameter. Lorentz forces promoted the establishment of downward flows under the arc supported by radially inward flows on the surface.

Surface-tension driven flows arise in welding systems because a surface-tension gradient exists on the pool surface. Material flows from regions of low surface tension to regions of high surface tension. The arc on the surface of the pool provides a radial thermal gradient, with higher temperatures in the regions directly beneath the arc. Many have modeled the pool surface temperature distribution and some have determined it experimentally. The temperature decays to the effective liquidus temperature at the pool boundary. Because surface tension is a strong function of temperature, a surface tension gradient is induced by the presence of an arc. The flow direction will depend strongly on the sign of the temperature coefficient of surface tension. Deep penetration is associated with those systems that have a positive coefficient (promoting inward flow). In this case the hottest fluid directly under the arc will be channeled downward to the base of the pool. Conversely, if the coefficient is negative, outward flow results and the hot metal erodes the edge of the pool increasing pool width, Figure 3. Elements that are not surface active themselves can have a profound effect on the pool flow by interacting with the surfactants.

The question of the hierarchy of flows in the weld pool can be addressed based on the work of several authors. Andrews and Craine, (8) and Atthey (9) discussed Lorentz induced flows in weld pools, generated by a distributed source of current. These authors predict flows that agree well with the empirical data. Mills (10) examined buoyancy, natural convection, as a source of pool flow. The ratio of thermal stirring to Lorentz stirring is less than 0.05 for values typical of welding arcs at less than 250 amperes. Furthermore, the Peclet number a ratio of heat transferred by convection to that transferred by conduction, falls in the range of 10 to 70 for weld pools. This indicates that convective heat transfer totally dominates in the pool, even when only Lorentz forces are considered.

Landau and Lifshitz (11) and Levich (12) have derived expressions for the surface velocity developed by a surface tension gradient: $Vel = (h/4\eta)(\partial\sigma/\partial T)(\partial T/\partial x)$ Where $\partial\sigma/\partial T$ and $\partial T/\partial x$ are the surface tension and thermal gradients respectively, h is L , and η is the kinematic viscosity. The substitution of conservative values for the parameters in this expression leads to the astounding conclusion that

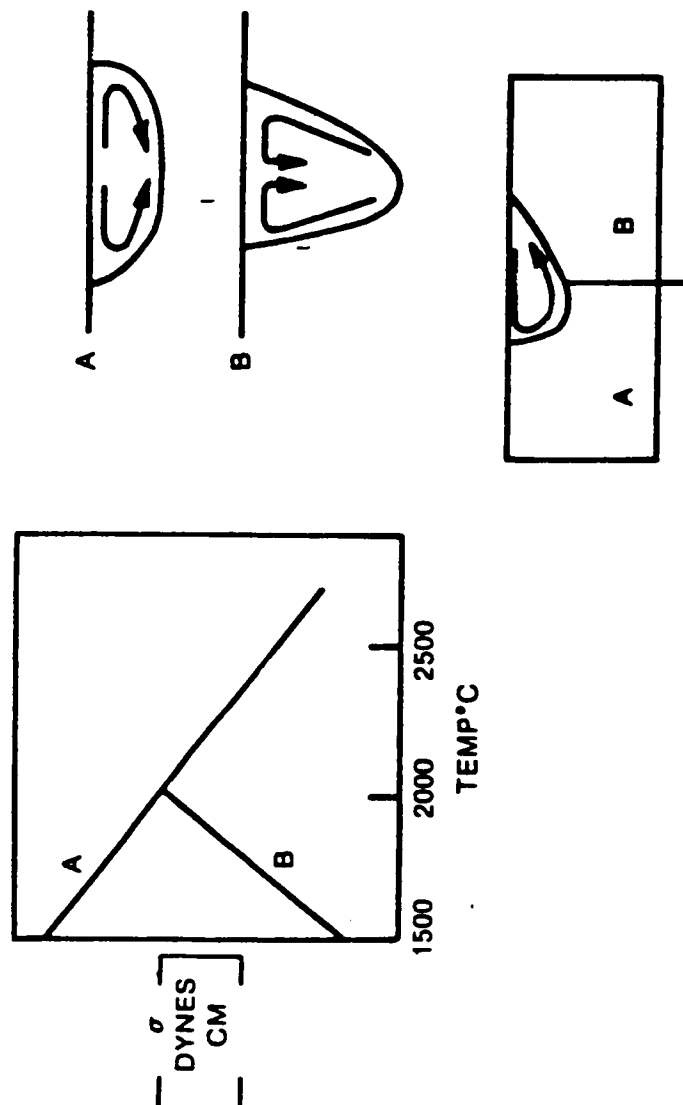


Figure 4 - Marangoni Flow in Weld Pools
XXXIV-5

surface-tension-driven flows develop a velocity of 50 to 150 cm/sec. This flow exists whether or not surface active species are present, only the direction of flow is affected by the fluid constitution. Kou (13) and Oreper (14) have developed computer codes to generate the predicted shape of stationary arc welds; both show that the surface-tension forces and the Lorentz forces dominate.

In conclusion, computations show that surface tension driven flows are dominant in the weld pool. Further, convective transfer in the pool is fifty times more efficient than conduction. The forces on the weld pool, at currents up to 250 amperes, produce velocities up to the following magnitudes; buoyancy, 0.5 cm/sec; Lorentz, 10.0 cm/sec; Marangoni 125 cm/sec. The flow generated by each of these mechanisms is depicted in Figure 4. The Lorentz force is expected to be even less significant in the case of VPPA welds because it acts on a very thin liquid layer at the leading edge of the keyhole. Even though the polarity, and thus the magnetic fields, change rapidly the Lorentz force will act consistently because the current density vector reverses with the magnetic field.

Figure 5 is a photograph of the rear keyhole of a VPPA weld on Al 2219. The backside appearance supports the contention that direct Marangoni flow dominates the pool. The weld bead is set off by two parallel rectangles that extend along its entire length. These are regions where a tightly adherent oxide skin has served to retain a fully fluid region beneath. In the peaked central region of the reinforcement a corrugated, heavily oxidized surface is evident. The appearance is derived from the "ice jam" of oxide residues freed up on the front side by cathodic cleaning and carried to the backside by the convergence of vigorous Marangoni flows.

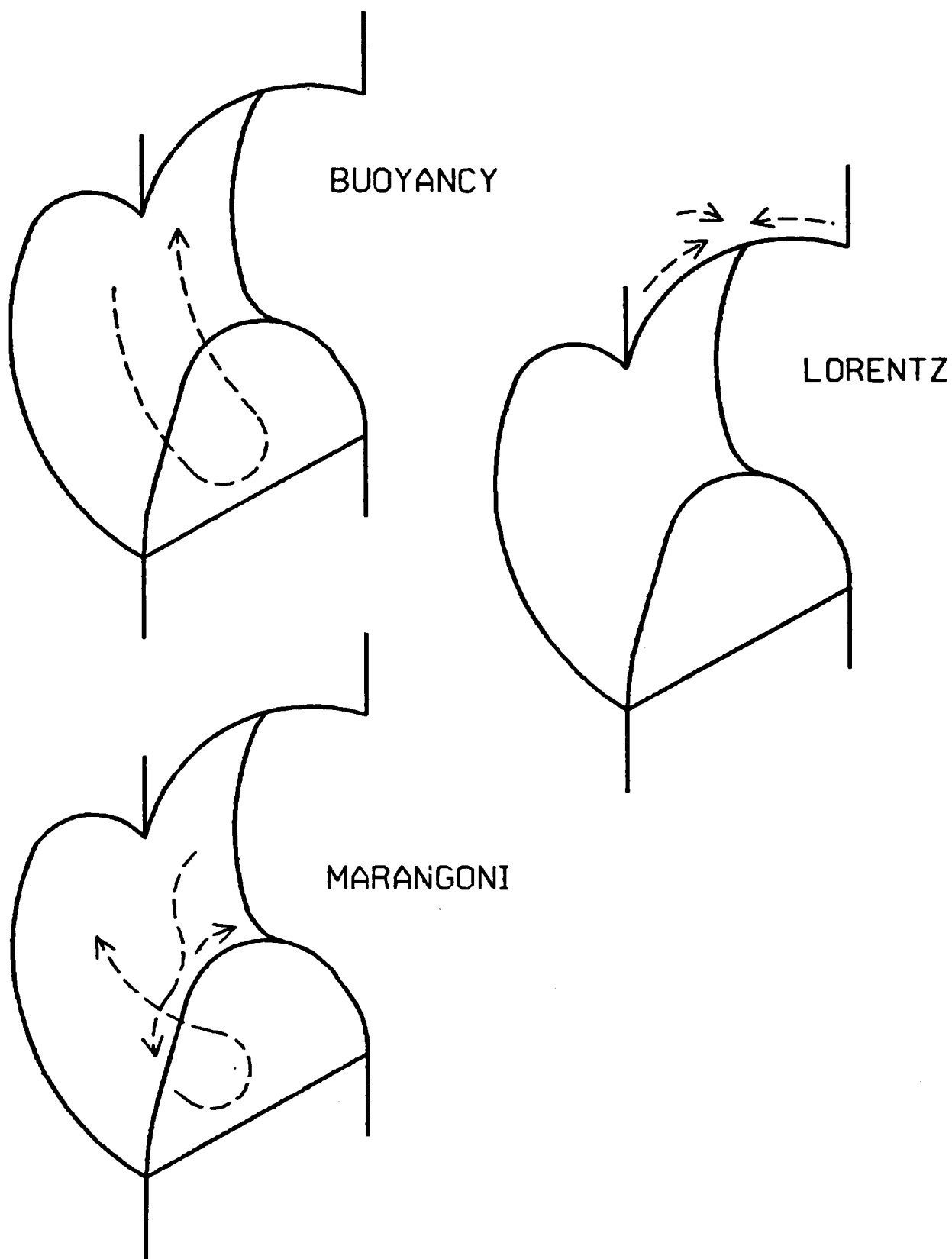


Figure 5 - Flow in Plasma Keyholes
XXXIV-7

ORIGINAL PAGE IS
OF POOR QUALITY



Figure 5. Rear Side, Actual Keyhole.

Materials and Procedures

The experimental portion of this study is comprised of three major programs:

- (1) Determination of the effects of chemical additions on weld bead shape and keyhole morphology.
- (2) Determination of the flow in regions surrounding the keyhole using a marker technique.
- (3) Development of an easily studied analog to fluid flow in the keyhole regions of VPPA welds in Aluminum 2219 T87. (Al 2219)

In the first program a series of 0.375 inch thick Al 2219 plates were treated with chemicals prior to welding. After the entire plate was thoroughly cleaned with solvent, a small region (2" by 4") was coated with the chemical agent of interest. The chemicals were placed on the plate surface as water based slurries or saturated aqueous solutions. The amount of chemical deposited on the surface was estimated as 0.02 to 0.20 grams (200 to 2000 parts per million).

Each plate was welded in the vertical position, employing a welding schedule developed for production welds in plates of this thickness. When stable, steady state welding conditions were attained, the welding head standoff was fixed rigidly. In order to attain the steady state condition, a total weld length of fourteen inches was used, only the final four inches of each weld was altered by chemical addition. All welding parameters were recorded during the test, the readings were taken at two second intervals. The posterior of the keyhole was recorded on videotape. The videosystem was used in an effort to discern pool flows. The welding operation was abruptly terminated to retain a "fossil" record of the keyhole. After the process was complete, the keyhole was characterized by its exit and entry hole diameters. The Oldefit system was used to acquire contour plots of sections of the crater, with the intent of assembling them into a three dimensional plot on the Viacom Image Analysis System. RTV-41 male replicas of the keyhole were made to help visualize the keyhole shape. The weld bead asymmetry, depth of undercut or grooving at the weld toe on the anterior surface, and sag on the posterior surface were characterized.

In the second program, production welding schedules were once again employed to produce keyhole welds on 0.375 inch Al 2219 plate. However, in addition to (and occasionally in place of) Aluminum 2319 filler wire, pure copper and Inconel 718 filler wires were used. Each of these surrogate filler materials has a melting point in excess of the aluminum alloy. (Al 2219, 660 deg. C; IN 718, 1500 deg.

C; Cu 1080 deg. C) The copper is quite soluble in the aluminum alloy and forms a series of ordered compounds in copper as well. The Inconel is not soluble in aluminum to an appreciable extent. Despite the fact that the density of these two materials is much greater than aluminum, it was hoped that solidified globules of these materials would be swept along in the pool currents, and that the distribution of these globules could indicate pool flows. The shape of the pool could be deduced by the addition of these fillers immediately prior to arc termination. Longitudinal and transverse sections of weld beads in the vicinity of the terminal keyhole were made and sequentially polished to determine pool flow patterns and pool shapes.

The third program was undertaken in order to to overcome difficulties associated with the "in situ" examination of the VPPA keyhole and molten weld pool. The observation of the keyhole is limited on the anterior surface by the presence of the bulky torch. The arc light and heat tend to obscure observation of the keyhole from the posterior. Under optimal conditions, only the surface of the pool is visible.

An analog was sought so that "in situ" examination of an analog keyhole and pool could improve understanding of the VPPA process. The following properties were sought:

- (1) Low melting point
- (2) Ease and safety of handling
- (3) Verisimilitude to the hierarchy of forces in an actual weld
- (4) Transparency in the liquid state, so that volume flows could be directly observed, not inferred from surface flows.

Paraffin was found to satisfy the above desiderata fairly well. The experimental apparatus is shown in Figures 6 and 7. A soldering iron served as the source of heat for the analog operation. Gas is heated in a coiled copper tube, wound around the heating element and sealed by compound. A small metal tip removed from a felt tip marker was press fit into the output end of the copper coil in order to provide a directed flow of heated inert gas. The delivery pressure was regulated by supplying argon to the coil through the P2 flow controller of the VPPA apparatus. The entire "torch" assembly was mounted on a side beam that could be moved horizontally to affect precise control of the standoff distance between the assembly and the workpiece.

Plexiglas sheets (3"X5") were machined to various known thicknesses, and slotted (2"X4") to serve as holding fixtures for paraffin plates. After being taped down to Aluminum chill plates these templates were filled with molten wax. The wax

ORIGINAL PAGE IS
OF POOR QUALITY

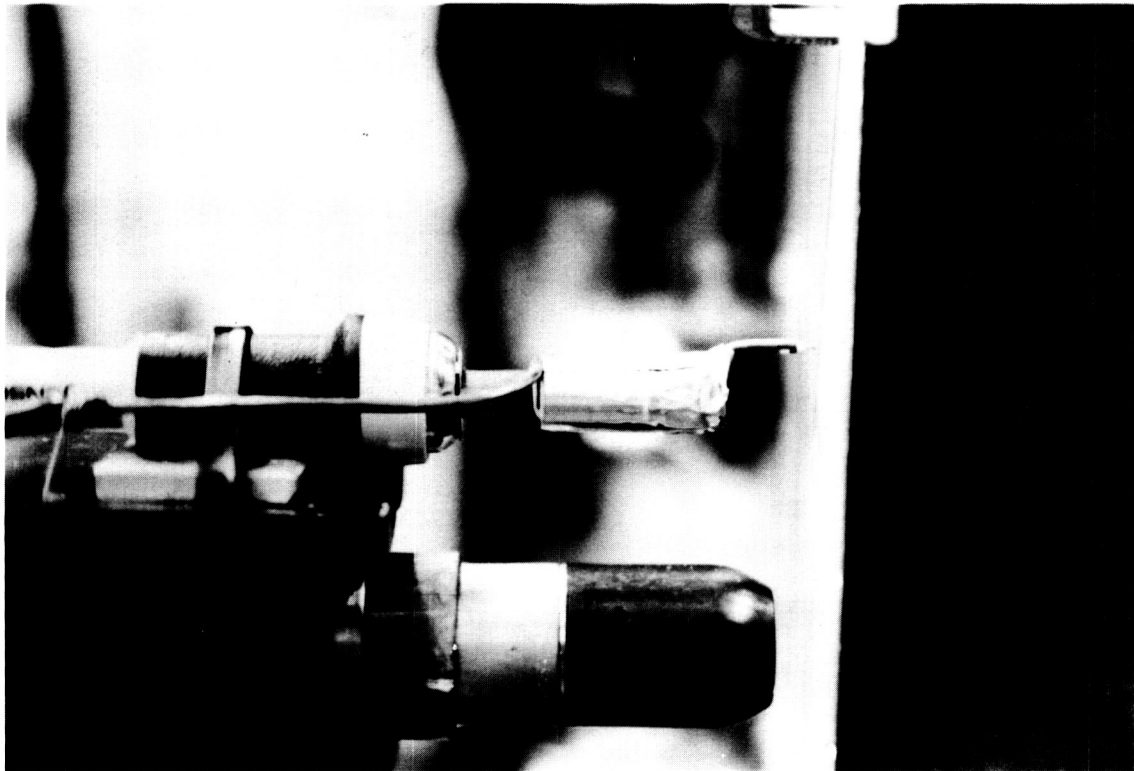


Figure 6. Analog Welding Apparatus

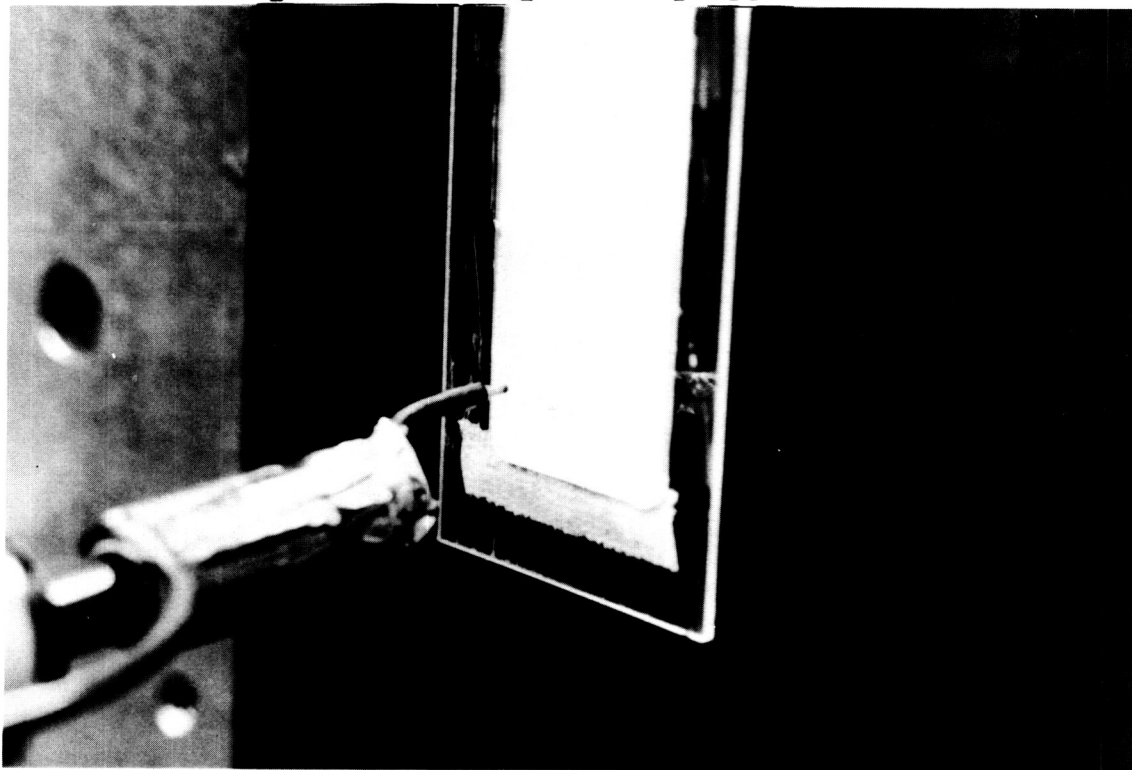


Figure 7. Wax Template and Welding Tip.

was allowed to harden, and was then shaved to uniform thickness. Small starter holes were drilled in the wax, and the template was placed on a vertical fixture capable of travel speeds up to one hundred inches per minute. The paraffin welding operation was recorded on videotape. The effects of changes in travel speed, standoff, gas flow rate, side angle and lag angle (torch lagging puddle) were examined and compared to similar changes in the VPPA process applied to Al 2219.

Results and Discussion

Chemical Additions

Table 1 lists the data collected for a variety of chemical additions to the weldment surface. The chemicals used are listed in the first column. (The letter B indicates that the chemical was placed on the posterior surface.) The second column lists the changes in plasma voltage caused by the presence of the chemical agent. The third indicates whether or not the agent produced a pool asymmetry. The next two columns list the depth of groove found at the deeper side of the bead, and the posterior reinforcement height respectively. The next two columns indicate the size of the entry and exit keyhole both without (WO) and with (WC) the addition. The next columns indicate the partial pressure of oxygen, listed as the base ten logarithm, of the pressure in atmospheres, expected in equilibrium with the oxides listed. Pressures are shown at temperatures of 1000, 1500, and 2000 degrees centigrade.

The partial pressures were estimated from available thermodynamic data. The free energy change associated with a reaction is

$$\Delta G = \Delta G_o + RT \ln K$$

ΔG = free energy of reaction

ΔG_o = free energy of reaction at standard state

K = the equilibrium constant

at equilibrium $\Delta G = 0$
and

$$\Delta G_o = -RT \ln K, \text{ or}$$

$$-\Delta G_o / RT = \ln K$$

for the reaction $M + O_2 \rightleftharpoons MO_2$

K is given by

$$\frac{a_{MO_2}}{a_m a_{O_2}} \quad a_i = \text{the activity of species } i$$

for pure solid elements or compounds, the activity is unity, thus

$$\Delta G_o / RT = -\ln p \quad \text{and}$$

$$\exp (\Delta G_o / RT) = p$$

Many of the chemicals added had no discernible effect. Furthermore, otherwise active chemicals, when added to the posterior surface, produced no effect. Apparently there is little flow between the front and rear of the pool in Al 2219. Many chemicals altered the arc voltage, in each case raising it. The increase in voltage is not associated with increased standoff, but caused by electrical interactions in the plasma. A priori the voltage of the arc would be expected to fall in the presence of easily ionizable species. However the increase in the arc voltage can be explained if it is

Effects of Chemical Additions

Matl	ΔV	Asym	Groove	Sag	Entry WO/WC	Exit WO/WC	Temperature°C		
							1000	1500	2000
							lg 10 p O ₂		
LiCl B	0	N	-	-	-	-			
MgSO B	0	N	-	-	-	-			
KBr B	0	N	-	-	-	-			
S	0	N	-	-	-	-			
Se	0	N	-	-	-	-			
Cu O	2.6	Y	0.12	0.22	.44/.5	.40/.54	-7	-3	-1
CaO	0	N	-	-	-	-	-41	-25	-17
TiO	0	N	-	-	-	-	-26	-15	-11
Al O	0	N	-	-	-	-	-38	-21	-15
Cr O	0	N	-	-	-	-	-20	-13	-8
CuSO	5.4	Y	BLOWTHROUGH		.44/.56	.34/.48			
CaSO	4.5	Y	BLOWTHROUGH		.40/.55	.36/.50			
CaCl	2.4	N	-	-	-	-			
CuCl	4.0	Y	0.09	0.16	.38/.46	.34/.39			
Fe O	4.5	Y	0.10	0.19	.40/.52	.36/.44	-5	-1	>1
MgSO	4.6	Y	BLOWTHROUGH		.44/.56	.38/.46			

Table 1 - Effects of Chemical Additions

associated with a small anode drop region that occupies the space above the anode spot to a height of several thousand angstroms. The presence of negatively charged species would be expected to increase the energy transfer to the pool at the anode spot. The most dramatic effects are caused by those species that contain oxygen. However, many of the oxides do not affect the welding process. This apparently anomalous behavior can be explained if the partial pressures of oxygen in contact with the oxide are reconciled to keyhole/pool behavior. The oxides CaO , TiO_2 , Al_2O_3 , and Cr_2O_3 have no effect on arc voltage or on pool shapewhen added to the keyhole environment. The oxides Cu_2O , and Fe_2O_3 foster an increase in plasma voltage, and lead to a pool asymmetry. Prior research has shown that oxygen at the 100 part per million level can drastically alter the amount of energy delivered to the pool. The maximum pool temperature can be estimated based on the activity (or lack thereof) of certain chemicals. Thus the maximum temperature expected would be between 1000 and 1200 degrees centigrade, and would be limited to that region directly beneath the anode spot. This contention is supported by the lack of incandescence associated with the trailing edge of the pool. Observations of the keyhole indicate that the anode spot is located on the leading edge of the pool, a region where the liquid film thickness is slight. This belief is supported by the observations that the efflux plasma is tilted downwards. The tilt is fostered by

- (1) the shape of the keyhole channel
- (2) an electromagnetic effect described by Maekler and Pfennder. (15,16)

Sulfates also produce dramatic effects. Oxygen present as water of hydration, and in the sulfate ion greatly increase the energy transfer to the pool. This results in an increase in the volume melted, and an imbalance in the forces that restore pool shape. Both molten volume and swept keyhole area increase as ΔV increases.

Pool Flow Markers

Filler additions facilitated identification of the steady state pool shape by distinctive etching characteristic. The flow was not well characterized by the distribution of filler rich regions. The addition of IN 718 as a continuously fed filler caused a disruption in the pool and periodic blow-through. This blowthrough is probably caused by the build up of heavy particles in the molten pool, the rupture of the retaining oxide film by shards of filler, or the weakening of oxide films in the presence of alloying elements.

Pool Analog

A pool analog was sought for the reasons listed previously. Table 2 lists the properties of paraffin and aluminum pertinent to a discussion of the model development, as well as a series of dimensionless numbers characterizing the two molten fluids. (17,18) As a basis for selection, a surface to weight force ratio was developed for an unsupported fluid contained in a cylinder of radius r and height h . The restoring force is simply

$$\gamma 2\pi r$$

where γ is the surface tension.

The force caused by gravitational attraction is

$$\rho g \pi r^2 h$$

the ratio is therefore

$$2\gamma / \rho g r h$$

allowing $r = h$

$$2\gamma / \rho g r^2$$

this ratio becomes

The value of this parameter is similar for aluminum and paraffin. Rearranging the expression

$$r = \sqrt{\frac{2\gamma}{\rho g}}$$

Thus the stable wax puddle will be somewhat smaller than the similar stable puddle in aluminum. (0.2 to 0.4 cm vis a vis 0.8cm)

The Marangoni number

$$\frac{\Delta T L_r (\partial \gamma / \partial T)}{\rho \alpha \nu}$$

is indicative of the influence of surface tension driven flows in a material. It is the ratio of force produced by a thermally generated surface tension gradient, to forces resisting such flow. The large values of the Marangoni number observed for each fluid indicate that surface tension flows will exist in the molten pools.

The dynamic Bond number

$$\left(\frac{\partial \gamma}{\partial T}\right) \frac{1}{\Delta T \rho g L_r^3}$$

is a ratio between the forces produced by surface tension, and those that arise from buoyancy effects. Again, the value listed indicates that surface tension driven flows will dominate the fluid in the keyhole region.

The final listed value is that for the Peclet number

$$\frac{u_r L_r}{\alpha}$$

This number is indicative of the relative importance of convection and conduction in the weld pool. Convection dominates the transfer of heat in the molten metal. The pool morphology will be affected by any physical process that alters pool flow. In this respect VPPA keyhole welds are not unlike weld pools produced by other arc processes.

	ρ g/cm ³	m_p °C	θ_p °C	β °C ⁻¹	$\frac{d\gamma}{dT}$ dyne/cm ²	C_p cal/g ^o C	γ dyne/cm	K cal/cm ² sec	μ cp
Aluminum	2.4	660	2450	114×10^{-6}	0.35	0.26	520	0.27	1.9
Parafin	0.9	55	--	12×10^{-6}	0.15	0.5	32	5×10^{-4}	1.0

ALUMINUM WAX COMMENTS

Surface to Weight
Force Ratio

0.220 0.314

Design Parameter

Marangoni Number

2.4×10^5 1.2×10^7

Surface Tension Flows

Dynamic Bond Number

1.3×10^3 2.7×10^4

Surface Tension Flows/
Buoyancy Flows

Peclet Number

3.0×10^2 4.5×10^2

Relative importance of
convection/conduction

Table 2 - Parameters of Comparison
Al and Paraffin

A procedure was developed to produce successful keyhole welds on paraffin of several different thicknesses. Figures 8 and 9 are photographs of wax keyhole welds made in paraffin 0.10 inches thick. Parameters for the welds depicted were chosen to intentionally produce asymmetric bead shapes (Fig. 8), and unstable beads (Fig. 9). The excessive undercut and asymmetry evident in the former case was generated by tilting the torch at a side angle of five degrees. It is interesting to note that one of the mechanisms known to produce undercut in actual VPPA weldments is arc misdirection. The instability in the latter case was caused by an increased lag angle (torch lags puddle). The effect is similar in VPPA welds when the "angle of attack is increased. The mass of molten fluid builds up until the restorative force of surface tension can no longer support the puddle. Interestingly parameters can also be chosen to produce a cutting action. In wax, or in aluminum this is accomplished by increasing the plasma pressure and by traveling faster. Furthermore, for a particular stable weld condition in paraffin increased standoff leads to a wider entrance hole and a diminished exit hole. This behavior is again analogous to the VPPA welding of aluminum.

A videotape of a keyhole weld in paraffin was made. Flow in the molten regions of the weld pool was readily apparent. Small solid paraffin fragments serve as excellent markers in a transparent pool. Two very strong vortices ($v = 35$ cm/s) were observed near the head of the pool at the plate boundary. A strong general circulation was also noted in the center of the pool. These flows are consistent with those postulated based on Marangoni driven circulations. Figures 10 and 11, photographs of the paraffin keyhole, show very different pool shapes. The difference is caused simply by a change in travel speed. The shape of the weld pool in Figure 11 is similar to that found in VPPA welds studied during this investigation. The increase in pool length and the loss of elliptical shape is expected when the velocity increases, and has been observed in a variety of materials.

ORIGINAL PAGE IS
OF POOR QUALITY



Figure 8. Analog weld in Paraffin, asymmetry.

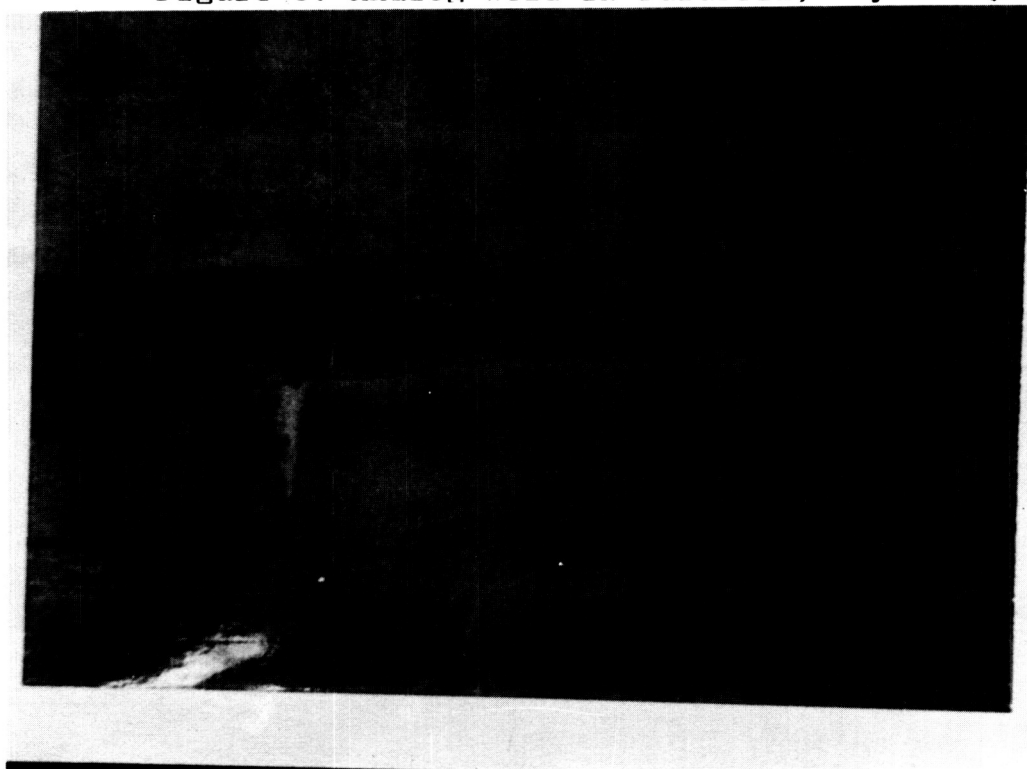


Figure 9. Analog Weld in Paraffin, Unstable Bead.

ORIGINAL PAGE IS
OF POOR QUALITY



Figure 10. Paraffin weld, high travel speed.

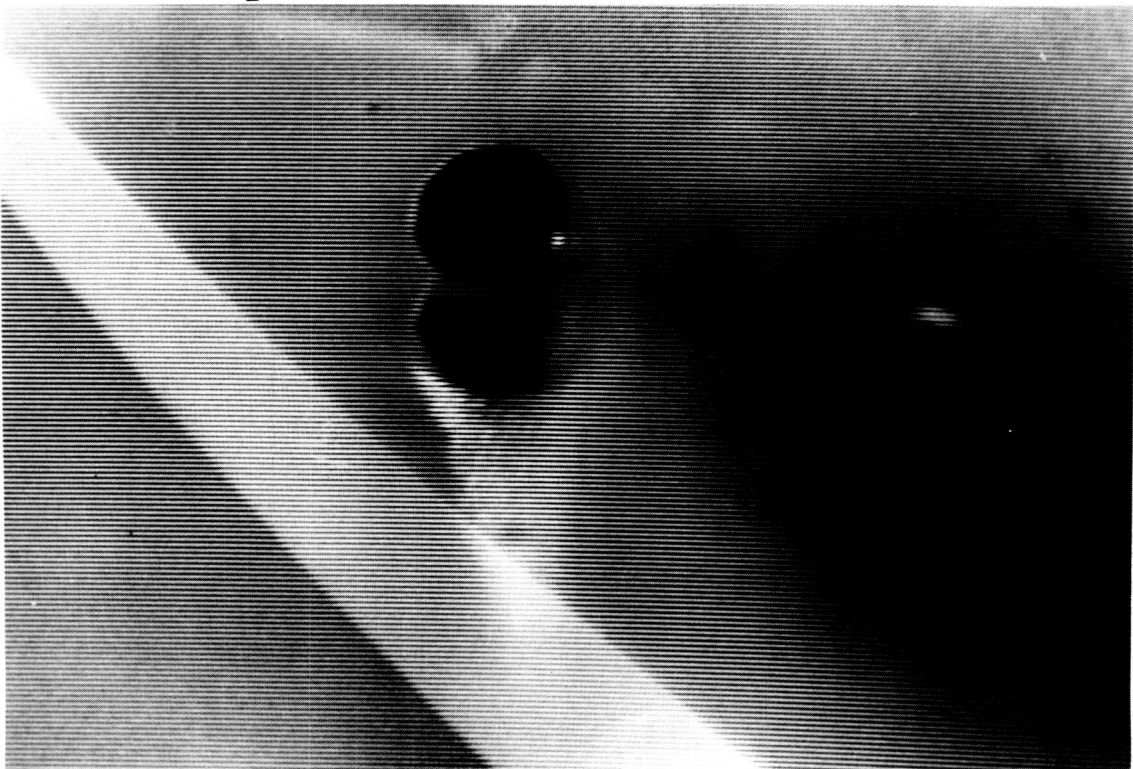


Figure 11. Paraffin weld, low travel speed

Conclusions

The results of this investigation indicate that:

- 1) The presence of oxygen in the keyhole regions of Al 2219 welds is damaging.
- 2) The critical level of oxygen is 10 atmospheres, a level easily developed by slight moisture contamination or by atmospheric permeation through gas hoses.
- 3) Oxygen interferes with the pool by altering processes at the anode. This increases the molten volume, and produces an instability caused by the increased weight of the pool. Volume considerations are primary, shifts in surface tension gradients caused by changing thermal gradients are secondary.
- 4) The presence of oxygen in the plasma increases the plasma voltage at fixed standoff. The voltage change is primarily associated with the anode drop region.
- 5) Marangoni surface tension driven flows dominate flow in the fluid surrounding the VPPA keyhole.
- 6) Pool flow in Al 2219 is direct Marangoni flow, no surface active elements produce flow reversals.
- 7) Flow in IN 718 and lithium added aluminum based alloys may be altered by the presence of surface active elements, and could be subject to flow reversals.
- 8) Chemical additions to the weld pool that increase the oxygen partial pressure in the keyhole region cause
 - a) asymmetries that are similar to those produced by increased standoff and arc misdirection
 - b) blow through in the pool if excessive melting and a weight imbalance occurs.
- 9) Chemical agents can be used to estimate pool surface temperature. The temperature in Al 2219 is 1000 to 1200 deg.C
- 10) The paraffin analog models a variety of VPPA effects.
- 11) The paraffin model allows convenient observation of bulk flows in the molten pool.
- 13) Solidified keyhole regions do not reflect the true shape of the keyhole "in process".

Suggestions for Future Work

- 1) Employ the -wax analog to permit an extension of the understanding of fluid behavior in the keyhole. The analog can model a variety of VPPA parameters inexpensively.
- 2) Initiate a designed experimental program, in both Al 2219 and paraffin, to determine the relationship between the independent process variables and the dependent bead shape variables.
- 3) Examine the effects of shield gas additions on keyhole shape, deposit microstructure, and heat affected zone properties in Al 2219. This would improve understanding of the relationship between process and properties. Possible improvements in joint efficiency could lead to reduced flight weight.
- 4) Study Al 2519, and Al-Li alloys as available per the program outlined in (3). The program should be applied to IN 718 as well. The Al-Li alloys and IN 718 may behave quite differently than Al 2219. These alloys contain surface active elements that can cause surface tension driven flow reversal in the molten pool, and welding behavior unlike Al 2219. (This prediction is supported by the experience that MSFC personnel have had with IN718 and Al-Li) In the case of IN 718, the problem would be insidious, different heats of material could have grossly different flow characteristics.
- 5) Develop an impulse decanting system to allow exact determination of pool shape. This system would instantly remove over 99% of the molten pool and thus aid in the understanding of keyhole processes. The program would help to identify control variables for smart welding systems.
- 6) Develop vision systems to image the keyhole region, both front and rear. Employ the Viacom image analysis system to maximize the quantitative data gained in the effort. This would permit a clearer understanding of the metallurgy and physics of the keyhole region, while providing improved real time process control capability.
- 7) Use the arc/pool model developed by A. Nunes to model surface tension driven flow in VPPA welds, and in the analog. This would allow simplified quantitative modeling of puddle flows through use of quadrupoles. A study of the potential of this model for quantitative representation of puddle behavior could provide a useful tool for analysis of and control of weld phenomena.

References

- 1) Metcalfe, J.C. and Quigley, M.B., "Heat Transfer in Plasma Arc Welding", Welding Journal Research Supplement, 54, (3), 99s-103s, 1975.
- 2) Metcalfe, J.C. and Quigley, M.B., "Keyhole Stability in Plasma Arc Welding", Welding Journal Research Supplement, 54, (11), 401s-404s, 1975.
- 3) Tomsic, M.J. and Jackson, C.E., "Energy Distribution in Keyhole Mode Plasma Arc Welds", Welding Journal Research Supplement, 53, (3), 109s-115s, 1974.
- 4) Shaw, C.B., "Diagnostic Study of the Plasma Arc", Welding Journal Research Supplement, 58, (4), 121s-125s, 1980.
- 5) Andrews, J.G., Atthey, D.R. and Byatt-Smith, J.G., "Weld Pool Sag", J. Fluid Mechanics, 100, (4), 785-800, 1980.
- 6) Okamoto, I., Omori, A., and Kihara, H., "Role of Surface Tension in Fusion Welding, Pt.2", Transactions of the Japanese Welding Research Institute, 12, (1), 1983.
- 7) Woods, R.A. and Milner, P.R., "Motion in the Weld Pool in Arc Welding", Welding Journal Research Supplement, 50, (4), 1971.
- 8) Andrews, J.G. and Craine, R.E., "Fluid Flow in a Hemisphere Induced by a Distributed Source of Current", J. Fluid Mechanics, 84, (2), 1978.
- 9) Atthey, D.R., "A Mathematical Model for Fluid Flow in a Weld at High Currents", J. Fluid Mechanics, 98, (4), 1980.
- 10) Mills, M.S., "Fundamental Mechanisms of Penetration in GTA Welding", Welding Journal Research Supplement, 58, (1), 1979.
- 11) Landau, L. and Lifshitz, E., Fluid Mechanics, Addison Wesley, 1959, p252.
- 12) Levitch, V.G., Physiochemical Hydrodynamics, Prentice Hall, 1962, p388.
- 13) Kou, S., and Konevesky, T., "Welding Thin Plates of Aluminum", Welding Journal Research Supplement, 61, (6), 1972.
- 14) Oreper, G.M. and Eagar, T.W., "Convection in Arc Weld Pools", Welding Journal Research Supplement, 62, (11), 1983.
- 15) Pfender, E. and Eckert, E.R., "Plasma Energy Transfer to Surface With and Without Electric Current", Welding Journal Research Supplement, 46, (10), 471s-480s, 1967.
- 16) Maecker, H., Z. Physik., 141, 198, 1955.
- 17) CRC Handbook of Chemistry and Physics, 1975.
- 18) Physical Properties of Liquid Metals, Oak Ridge National Laboratory, 1959.

534-65
N88-15635 116736
288

1987

NASA/ASEE Summer Faculty Fellowship Program

Marshall Space Flight Center
The University of Alabama in Huntsville

Expert System Development for Commonality Analysis in
Space Programs

Prepared by:	Dorian P. Yeager
Academic Rank:	Associate Professor
University and Department:	The University of Alabama Computer Science
NASA/MSFC:	
Laboratory:	Systems Analysis and Integration
Division:	Space Station Systems
Branch:	Systems Integration
NASA Colleague:	L. Dale Thomas
Date:	August 7, 1987
Contract No.	The University of Alabama in Huntsville NGT-01-008-021

ABSTRACT

The work represented by this report is a combination of foundational mathematics and software design. A mathematical model of the Commonality Analysis problem was developed and some important properties were discovered. The complexity of the problem is described herein and techniques, both deterministic and heuristic, for reducing that complexity are presented. Weaknesses are pointed out in the existing software (System Commonality Analysis Tool) and several improvements are recommended. It is recommended that: (1) an expert system for guiding the design of new databases be developed; (2) a distributed knowledge base be created and maintained for the purpose of encoding the commonality relationships between design items in commonality databases; (3) a software module be produced which automatically generates commonality alternative sets from commonality databases using the knowledge associated with those databases; and (4) a more complete commonality analysis module be written which is capable of generating any type of feasible solution.

ACKNOWLEDGEMENTS

The author wishes to thank NASA and ASEE for their support of a fine program. My experiences here have been extremely rewarding. Thanks also to Gerald Karr and Ernestine Cothran for their capable administration and their personal involvement in the program.

Special thanks go to my NASA colleague, L. Dale Thomas, without whose help the fundamental nature of the problem would not have been evident.

Thanks go also to Charlie Cothran and the crew at EL83, who made me feel welcome and comfortable from the beginning. You have an outstanding team.

INTRODUCTION AND OBJECTIVES

The purpose of this work is to assess the feasibility of an artificially intelligent software tool to aid in the process of identification of commonality alternatives. Commonality is the degree to which two or more end items share common characteristics. A high degree of commonality is to be desired as an engineering design criterion for obvious economic reasons. Commonality analysis attempts to enhance commonality by choosing a set of end items which spans all the needed functionality of a larger set, and choosing that set which represents a minimum cost according to some previously agreed-upon cost measure. The recommendation which is inferred by such a minimum-cost set of items is that only those items be implemented and that the functionality of the remaining items be achieved by a systematic substitution of additional copies of the items in the implementation set.

The commonality analysis process necessarily involves three key activities:

1. The gathering and organization of data.
2. Identification of commonality alternatives.
3. Evaluation of alternatives.

Automation by software is a desirable goal in all three areas. What this report recommends is the development of an integrated set of software packages which interacts with existing software to solve a variety of problems in commonality analysis.

CRITIQUE OF EXISTING SOFTWARE.

The Systems Commonality Analysis Tool (SCAT) is presently the only available tool for automating the above process. SCAT provides limited assistance in all three areas; however, definite improvements can be made, as explained below.

1. For the gathering and organization of data, SCAT provides a front end to a commercial database management system (DBMS). Through SCAT, one may create and modify commonality databases, and for sophisticated database functions one may enter the DBMS proper from within SCAT. SCAT assumes that certain attributes (the so-called "generic" attributes) apply to all databases. There are two sets of such generic attributes - one set for hardware items and one set for software components. The generic attributes are simply those attributes which are directly relevant to SCAT's Life Cycle Cost (LCC) analysis of the item. One advantage of requiring data to be entered via the SCAT front end is that the user is constrained to always include these generic attributes.

There are two crucial ingredients missing from the above data gathering strategy. Firstly, SCAT gives almost no guidance concerning the selection, naming, and use of other attributes besides those specifically needed for its analysis. These other attributes, dubbed "discriminating" attributes, are chosen by the database administrator, based on his expert knowledge of the items in the database. A predictable consequence of this lack of guidance is that similar data will be encoded in dissimilar fashion. For example, one database administrator will create a new database which incorporates an attribute named LIQUID which takes on values "Y" or "N", the first value indicating liquid and the second gas. Another database administrator may create a database which incorporates similar items with similar properties, but will use a different name and different values for his attributes. For example, he may use the name TYPE with values "LIQUID" and "GAS".

The second missing ingredient is the information needed to form groups of commonality alternatives for the analysis process. The database creator possesses essential knowledge about which items may be considered common. The first way that such knowledge is brought to bear on the problem is that a set of sorting criteria is communicated to SCAT, whereupon SCAT sorts the data as specified. The hope is that when SCAT or the DBMS displays or prints the data, groups of common items will coalesce. The second kind of knowledge is that needed for selecting commonality alternatives from a sorted set of records. The SCAT user needs to possess the ability to scan the sorted data and pick out groups of common items. Thus

there is "sorting" knowledge and there is "grouping" knowledge. The SCAT paradigm indicates that a sequence of sorting and grouping operations will identify one or more sets of items which qualify for comparative LCC analysis.

It must be said here that certain kinds of commonality options do not fit neatly into the SCAT paradigm. SCAT does not provide facilities to aid in identifying ways of "extending" the function of an item, nor is it capable of automatically doing a componentwise breakdown analysis of a set of complex alternatives. Such sophisticated techniques are aided by a tool like SCAT, but SCAT does not provide a framework to support them.

Putting aside for now the idea of developing a completely general tool, a more modest goal is to somehow automate the "sorting and grouping" technique. In order to do this, it is necessary to capture the knowledge needed in the sorting and grouping process. This knowledge may be the most important kind of "data" available. It is certainly the most difficult to capture. SCAT provides no help in capturing such knowledge.

2. For the identification of commonality alternatives, as indicated above, SCAT provides only the standard database sorting, marking, and subsetting functions. No guidance is given regarding what is a "good" sort criterion, or what are "good" criteria for displaying, marking, and saving subsets of a database. Indeed, unless expert knowledge is available, no software product can provide such guidance. Thus an improvement in this area requires an improvement in the facilities available for data gathering.

We have a definite advantage with knowledge of this form, however. It can be easily encoded. A sort operation is encoded as a series of (key,direction) pairs. For example, {(TYPE, Ascending), (VOLTAGE, Ascending), (DIAMETER, Descending)}. A subsetting operation is encoded as a relational expression involving the attributes of the database. An example is 8.6 LT VOL AND VOL LT 12.8. Finally, a grouping operation is encoded as a relational expression involving the attributes of two or more records of the database. An example of this is $ABS(VOL(1)-VOL(2)) < 0.5$. The third type of operation is especially interesting, since it is not an operation directly supported by standard DBMS's.

It must be said here that knowledge of this sort cannot be gathered once and for all. The content and meaning of the data determine the content of the knowledge. As data is entered and as new databases are built, the knowledge needed to analyze that data for commonality alternatives will change. It is impractical, also, to require that all such knowledge reside in

a central place such as a single file of data or a single program. This sort of knowledge belongs with the data itself. The knowledge relevant to a piece of data must be physically and logically associated with that data.

Once the knowledge is gathered and made available as an integral component of a given commonality database, the selection of alternatives in that database may be automated with the use of a "shell" program which reads both data and knowledge from the database and produces as its output a series of database subsets representing proposed sets of commonality alternatives. Each such set would be presented to the user for closer scrutiny. An opportunity would then be presented for the user to approve or disapprove of these choices. In case a given choice of commonality alternatives was too restrictive or not restrictive enough, the system would prompt the user for additional knowledge which might help to avoid repeating the error.

3. SCAT provides a sophisticated resource for evaluating commonality alternatives, once such alternatives have been identified. The SCAT user presents a subset database which he or she has identified as a set of potentially common items, and SCAT provides a comparative study of the LCC differences between producing each item as an individually designed and produced component (the "unique" option) and producing a single item from the set of items to serve its own function as well as those of all other items in the set. If there are n items, SCAT computes $n+1$ LCC estimates: one for each item, assuming it is chosen as the common item, plus one for the unique option. It then sorts on the computed life cycle costs, and displays the sorted data.

The problem with the above approach is that it makes two basic assumptions that may not in general be valid. The first is that every item in a set of commonality alternatives can be substituted for every other item. The second is that either (a) there will always be a single, optimal common item, and the most economical alternative is to replace all items by that common item, or (b) it is cheaper to produce all items separately, i.e. to choose the unique option.

Now it is doubtful that the designers of SCAT really believed the above assumptions. Indeed, if the SCAT user is aware that those assumptions are not always valid, he may still make considerable progress by using SCAT repeatedly and/or throwing away unnecessary information. But SCAT leads its user into false assumptions.

In fact, there are often asymmetric constraints that allow, say, a larger device to be substituted for a smaller one, but

will not allow the smaller device to be used in the place of the larger one. The only feature of SCAT that has bearing on this situation is its use of what are called "critical" attributes. A critical attribute is one whose value must never be diminished in a substitution. For example, if diameter is critical then when substituting item A with diameter 5 for item B with diameter 7 we are obliged to use two of item A. In practice, substitution of multiple copies of one item for a single copy of another is not always feasible. The result is that commonality is not always a symmetric relationship. There is no room in the SCAT model for asymmetric commonality relations. In order to handle a case like this, the user typically has to perform a standard SCAT analysis and ignore certain alternatives.

Also, it may often happen that the best commonality solution does not present a single item to be substituted for all other items, but instead requires keeping some items, discontinuing development on other items, and making selected substitutions of items in the first set for items in the second. This type of solution is not only beyond the scope of SCAT, but cannot easily be solved even with repeated applications of SCAT. The extreme complexity of such a solution, even in cases involving relatively few alternatives, would cause a solution by repeated SCAT analyses to require months to complete. It is a moot point that such a solution is possible with repeated applications of SCAT, not only because of the potentially prohibitive amounts of time required, but also because SCAT does not present to the user an interface that suggests such solutions are possible, nor does it offer any features to simplify the extremely complex process of arriving at a general solution.

MATHEMATICAL CONSIDERATIONS

The complexity of a general solution to the commonality problem is immense. Furthermore, there is no significant body of knowledge available in technical and scientific literature which can be drawn upon to guide the solution process. Therefore a large part of the work represented by this report was foundational in nature. Due to the creative, mathematical nature of that work, it was felt that the most appropriate forum for its presentation was in an applied mathematics journal. A complete mathematical formulation of the problem is to be found in a paper (Yeager, 1987) submitted by the author to the journal, Operations Research. In that article some foundations are laid for an orderly assault on the general problem. The details of the paper are omitted from the report, but preprints are available from the author. An illustrative summary of the major results is presented below.

The data in a database is a collection of records describing a set $A = \{a_1, a_2, \dots, a_n\}$ of items. The items may be valves, pumps, circuit boards, or anything for which sufficient data is available for analysis. There is a set of attribute functions defined on A , which represents a set of values associated with the items. Some example attributes are weight, density, volume, composition, and power consumption. A Life-Cycle-Cost (LCC) estimate on a given item requires that certain attributes apply to that item. The SCAT program requires that data on hardware items include 12 generic attributes, 11 of which have direct bearing on the LCC analysis.

Let us begin with an illustration of the magnitude of the mathematical problem and the complexity of a potential solution. There are two sources of complexity - one is the sophistication of the LCC formula itself, and another is the complexity of the algorithm one uses to select which items to retain and which to replace. The SCAT program does a thorough treatment of the first area and pays little attention to the second. In what follows we will attempt a preliminary investigation of that second question.

A solution to the commonality analysis problem has two components: (1) a partition of the set A into smaller subsets, and (2) a set of representatives of the subsets of the partition. For example, for $n = 6$ we may propose the following as a solution:

Partition: $\{\{a_1, a_2, a_3\}, \{a_4\}, \{a_5, a_6\}\}$.
Set of representatives: $\{a_3, a_4, a_5\}$.

The above "proposed solution" stipulates that we produce only items a_3 , a_4 , and a_5 , that a_3 replace a_1 and a_2 , and that a_5 replace a_6 . A proposed solution "works", i.e. is a true solution to the problem, if the substitution strategy it advocates yields a minimum cost according to some agreed-upon scheme for assigning costs to proposed solutions.

To gain an appreciation for the complexity of the commonality analysis problem, consider that the number of possible solutions of the above type is given by the formula

$$\sum_{i=0}^{n-1} C_{n,i} (n-i)^i$$

where $C_{n,i}$ is the number of combinations of n things, taken i at a time.

The size of this number is on the same order as $n!$. The following table investigates its behavior for some small values of n .

n	2^n	$\sum_{i=0}^{n-1} C_{n,i} (n-i)^i$	$n!$
1	2	1	1
2	4	3	2
3	8	10	6
4	16	41	24
5	32	196	120
6	64	1057	720
7	128	6322	5040
8	256	41393	40320
9	512	293608	362880
10	1024	2237921	3628800
11	2048	1.821010E+07	3.991680E+07
12	4096	1.573291E+08	4.790016E+08
13	8192	1.436630E+09	6.227021E+09
14	16384	1.381086E+10	8.717829E+10
15	32768	1.393056E+11	1.307674E+12
16	65536	1.469959E+12	2.092279E+13
17	131072	1.618459E+13	3.556874E+14
18	262144	1.855042E+14	6.402374E+15
19	524288	2.208842E+15	1.216451E+17
20	1048576	2.727262E+16	2.432902E+18

Thus a computer with the capability to generate a million potential solutions per second (a very powerful computer indeed) would require about 865 years to generate all solutions for a set of 20 items.

Thus a "brute force" approach consisting of an algorithm to enumerate all possible solutions and choose one with the smallest associated cost would be impractical for values of n much greater than 10. The interesting thing is that the nature of commonality problems is that very seldom will one have more than ten to twenty candidates available for comparison, so that the "brute force" technique is not to be completely discounted. It must be applied very judiciously, however, with full knowledge of its high degree of complexity.

Fortunately, there are quite effective ways of "paring down" the size of the solution space. The simplest of these is the feasibility relation. There are two processes involved in the generation of a potential commonality solution: (a) choose a partition, and (b) choose a representative from each set of the partition. The feasibility relation constrains us in the number of ways we may choose such a representative.

The feasibility relation tells us when a given item may be realistically substituted for another. It may be quite simple, stating for example that item a_i may be substituted for item a_j only if a_i is "larger" in some sense than a_j . Or it may be quite complex, calling into play such attributes as chemical composition, weight, diameter - literally hundreds of possible factors.

The best situation is that in which the feasibility relation linearly orders the set of candidates. In that case there is only one choice for a representative of a given subset, i.e. the only item in that subset which is substitutable for every other item in that set. In this situation we can reduce the size of the solution space to the number of partitions of a set with n elements. Unfortunately, that too is a very large number even for relatively small n . We proceed, then, to develop a class of techniques for significantly reducing the size of the solution space. These techniques concentrate on reducing the number of partitions which must be examined.

In order to prevent our formulas from becoming too unwieldy and obscuring the essential nature of the problem, we will make some simplifying assumptions about the LCC formula. The primary simplification will be to assume linearity. In particular, we will use the following abstract formulation of the LCC cost of an item. Our LCC formula requires only three attributes. For item a_i , we will call these attributes d_i , q_i , and k_i . d_i is the design, development, test and engineering

cost of producing the item. q_i is the quantity, i.e. the number of copies of a_i which will be needed. Finally, k_i is the per-unit cost of producing, deploying, operating, and maintaining the item. Many factors go into computing the per-unit cost attribute, such as weight, volume, density, energy consumption, mean time between failure, and expected service life of the space system. Actually k_i is the total of all cost factors which are directly proportional to the number q_i of items needed. For our purposes it suffices to assume they are precomputed and stored as a single attribute. We use the following as a simple first approximation to the cost of the item:

$$c_i = d_i + k_i q_i$$

The natural interpretation we now give to the cost of implementing the functionality of all items in a set K of items by substituting item a_i for every other item in K is

$$d_i + k_i \sum_{x \in K} q_x$$

We will refer to the above as the linear cost function. In contrast, the SCAT formula is a more complex sum of terms, most of which are either constant or linear in q_i . An exception is the PROD term, the production costs incurred in producing q_i copies of item a_i . PROD is nonlinear in q_i , but it is constant if $q_i = 1$ and approaches linearity in q_i as the "Learning Curve" parameter approaches 100%. (The Learning Curve is a user-adjustable system default in SCAT, assumed to be the same for all items in a given analysis.) When we say we are assuming linearity in q_i , then, we deviate slightly from the SCAT model. What we say about a solution using the above formula can be carried over into the general SCAT formula analysis only in a heuristic sense. We can be certain that in passing to the more general SCAT formula we will be introducing more, not less, complexity. What we get out of using the above formula, then, is a mathematical model which represents the simplest model that we may hope to obtain. Much can be said about a general solution to the problem without so constricting the form of the cost function. But the more complex the cost function the less can be said about a general solution.

The quantities d_i , k_i , and q_i are constants for a given item a_i , and we assume $q_i > 0$ for all i . The quantity q_i represents the total needed number of items for the period over which our cost projections are valid.

The linear cost function is well-behaved in a very important sense. It can be proven that if the feasibility relation makes no constraints on item substitutions (i.e. if every item may be substituted for every other item), and if the

linear cost function is being used, then the minimum-cost solution will always be a SCAT-type solution. In particular, there will always be a single item which, when substituted for every other item, yields a minimum cost. There are only two reasons, then, to doubt the SCAT recommendations. One is that not always is it feasible to allow every item to substitute for every other item. Another is that the SCAT formula is not linear. The SCAT formula may be close enough to linear, however, to feel reasonably good about a SCAT analysis, provided the feasibility relation does indeed permit us to apply the recommendation SCAT gives.

Another interesting mathematical fact is that if we assume a more liberal substitution policy, that is if we for the purpose of analysis assume that more substitutions can be made than are in practice permissible, and if we then apply a procedure which leads to a minimum cost solution under the more liberal assumptions, and if the solution thus obtained is consistent with the original feasibility constraints, then the solution we obtain is the minimum cost solution. Thus the recommendations made by SCAT may be used with a fair amount of confidence whenever they make sense.

The real problem with the SCAT recommendations is that they will not always make sense. There is no structure within SCAT to handle a feasibility relation which makes real constraints on substitutions. To create a framework in which such constraints may be factored into the solution requires some foundational mathematics.

The first tool which we wish to apply to aid in obtaining a solution to the commonality problem is the concept of a "separator". A separator is a relation used to separate a single set of a partition into two disjoint subsets. For example, if δ is a separator and $a_1 \delta a_2$ (read " a_1 is δ -related to a_2 "), then the partition $\{\{a_1, a_2, a_3, a_4\}\}$, with a_1 being the chosen substitute, is less cost-effective than $\{\{a_1, a_3\}, \{a_2, a_4\}\}$, or $\{\{a_1\}, \{a_2, a_3, a_4\}\}$, or $\{\{a_1, a_3, a_4\}, \{a_2\}\}$, or any partition where a_1 is in one set and a_2 is in the other, if a_2 is chosen as the substitute in the latter.

For the above linear cost function, the relation δ defined as follows is a separator:

$a_i \delta a_j$ is true whenever a_i is a feasible substitute for a_j and

$$k_i \geq k_j + d_j / q_j$$

Note that the above is equivalent to saying that $k_i q_j \geq c_j$. In short, what we say when we say that this relation is a

separator is that if we can always produce item a_j from scratch for no more than the cost of producing " q_j more" of item a_i , then we will never be better off to recommend a strategy which includes substituting item a_i for item a_j .

For examples of other cost functions and separator relations associated with those cost functions, see the paper (Yeager 1987).

What we are aiming for with the introduction of the concept of a separator relation is a way of reducing the number of potential solutions which must be examined. The overall strategy is to introduce an initial "solution" which is close to the actual solution in the sense that we can obtain the latter by a series of refinements of the former.

Suppose we partition the set of items into subsets which have the following property: each set K of the partition which contains item a_i also contains all items a_j which are not δ related to a_i in either direction. That is, if it is false that a_i is related to a_j and it is false that a_j is related to a_i , then a_i and a_j are in the same subset of the partition. This defines a unique partition of the set of items, which we will call the partition induced by the separator δ . Under certain conditions it can be shown that every true solution of the commonality problem is obtained by "refining" this particular partition, i.e. splitting its subsets into smaller subsets.

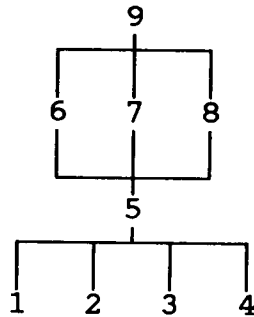
It turns out that one of the situations under which the above partition represents a valid initial estimate of a solution is that in which the elements of the set are linearly ordered by the feasibility relation.

Example 1. The following comes from a set of design data on nine types of storage tank intended for use on the NASA Space Station Project. Cost figures are in thousands of dollars.

Tank #	DDTE d_i	Unit cost k_i	Quantity q_i	Cost c_i	$k_i + d_i / q_i$
1	46.166	36.116	1	82.29	82.29
2	49.374	40.204	1	89.57	89.57
3	67.833	64.598	4	326.23	81.56
4	71.860	70.598	4	354.25	88.57
5	92.819	102.514	2	297.85	148.92
6	355.772	775.184	2	1906.14	953.07
7	366.685	810.760	6	5231.25	871.87
8	378.240	844.656	3	2912.21	970.74
9	464.314	1152.108	4	5072.75	1268.19

"Unique Cost" 16272.54

The feasibility relation is based solely on size. Since the tanks are numbered in increasing order according to size, the relation allows each tank to replace all tanks numbered lower than it, thus establishing a linear order. The separator δ defined above is graphically depicted in the following diagram. Here the nodes are identified by tank number and the tanks which are δ -related to tank t are reachable from node t via a downward-trending path. For example, tank 9 is δ -related to all other tanks, and tank 7 is δ -related to tanks 1, 2, 3, 4, and 5.



The subsets forming chains of non-related items are {9}, {6,7,8}, {5}, and {1,2,3,4}. The mathematical properties we have established for separator relations assure us that any solution of this commonality problem is obtained by refining this partition.

Now let us contrast the performance of a "heuristic" solution with that of a solution using the above knowledge of the structure of the problem. A Prolog program to selectively search for the optimal feasible partition of this set took six minutes on an IBM XT to produce the following solution:

Set	Representative	Cost
{1,2}	{2}	129.78
{3,4}	{4}	636.64
{5}	{5}	297.85
{6,7,8}	{8}	9669.46
{9}	{9}	5072.75

Minimum cost 15806.48

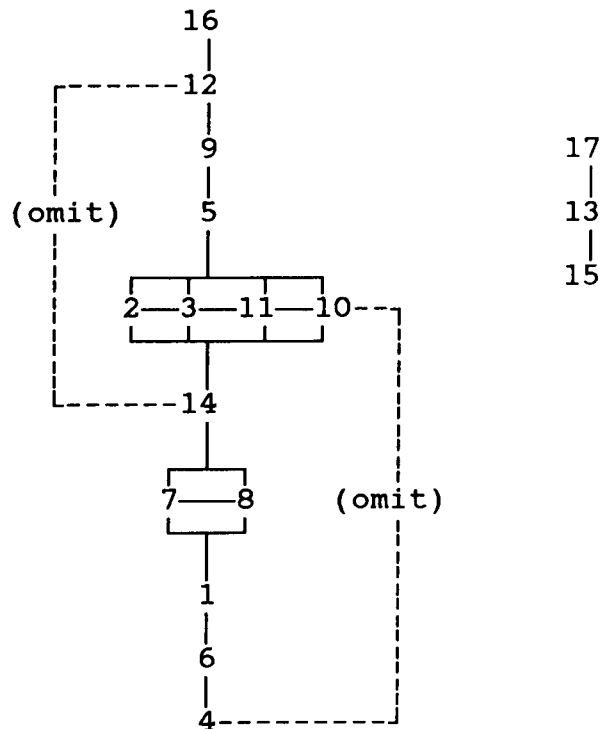
The same program, utilizing partition {{1,2,3,4}, {5}, {6,7,8}, {9}} as a starting point, arrived at the same solution in three seconds. Note that the optimal solution is only one immediate refinement away from that partition.

Example 2. A second set of data from an independent source, also pertaining to tanks proposed for use on the Space Station Project, is given below:

Tank #	DDTE d_i	Unit cost k_i	Quantity q_i	Cost c_i	$k_i + d_i / q_i$
1	153.110	192.750	2	538.61	269.31
2	566.140	1395.895	2	3357.92	1678.97
3	573.640	1388.401	4	6127.24	1531.81
4	91.985	88.815	3	358.43	119.48
5	606.570	1551.440	2	3709.45	1854.73
6	106.660	109.060	4	542.90	135.73
7	178.570	259.000	1	437.57	437.57
8	178.570	259.000	1	437.57	437.57
9	663.290	1883.300	1	2546.59	2546.59
10	566.140	1395.895	2	3357.92	1678.97
11	549.650	1412.390	1	1962.04	1962.04
12	604.520	3877.855	4	16115.92	4028.99
13	200.900	701.580	4	3007.22	751.81
14	306.376	1295.465	12	15851.90	1321.00
15	101.800	236.377	12	2938.32	244.86
16	1382.490	13966.940	5	71216.99	14243.44
17	459.315	2517.827	5	13048.42	2609.69

"Unique Cost" 145555.01

The feasibility relation α for this set is more complex, and is illustrated by the following diagram:



This feasibility relation has two components: tanks 13, 15, and 17, which are linearly ordered with 17 being "most substitutable", and the others, which are related in a more complex way. This in fact represents two separate problems. No tank in one group may be substituted for any tank in the other group. So we split the problem up and attack it in two pieces. Looking at the larger, more complex group, we see that it is "almost" linearly ordered. Tank 16 may be substituted for any other tank in the group, for example. But tanks 7 and 8 are mutually interchangeable, and the tanks in the group 2, 3, 10, and 11 are mutually interchangeable. The most glaring exceptions are the two "omitted" relationships. If the relation were "transitive", then tank 10 would be an acceptable substitution for tank 4, and tank 12 would be an acceptable substitute for tank 14. But the source supplying the data specifically forbids those two substitutions. So we have a non-transitive feasibility relation.

Extending the feasibility relation to include the two omitted pairs gives us a transitive feasibility relation. If we obtain a valid solution based on that expanded relation, we have solved the problem. If not, we will have to approach the solution in another manner.

Let us assume for now that our relation is transitive. Even so, we cannot treat this problem the same as Example 1

because the feasibility relation is not linear. To handle this case, we introduce the notion of a selector. A selector is a relation β on the set A which has the property that if $a \beta b$ then not only can a be substituted for b but whenever a and b are in the same set K and each of a and b can be substituted for any element of K , then a is always a more economical choice. The selector relations on a set, like the separator relations, are dependent on the cost function being used. A very simple selector σ for the linear cost function is defined as follows:

- $a_i \sigma a_j$ if and only if
- (1) a_i is substitutable for a_j ,
 - (2) $k_i \leq k_j$, and
 - (3) $d_i \leq d_j$.

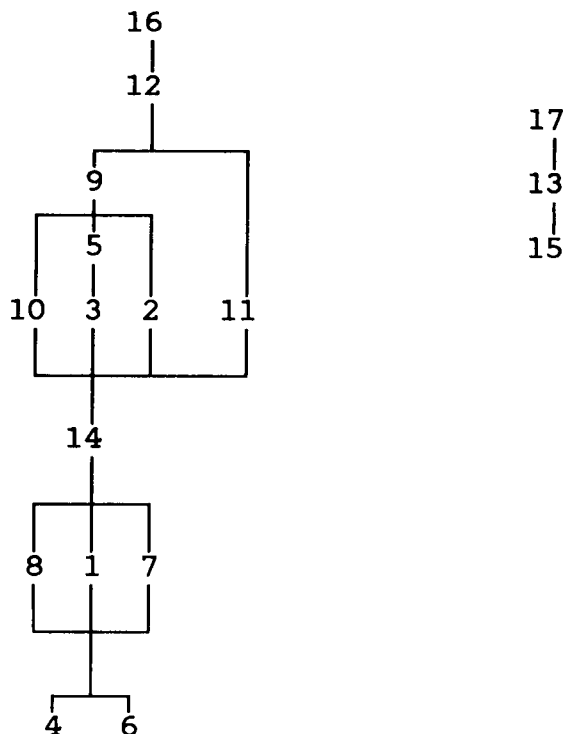
This is a very intuitive selector. It should be obvious that if both the initial costs and the per-unit costs associated with item a_i are less than those respective costs for item a_j , then a_i is always a better choice than a_j . We should point out here that there is another more finely discriminating selector for the linear cost function (Yeager, 1987), but this one will do for the current example.

Another selector, which works for any cost function, is the selector α' defined as $a \alpha' b$ if and only if a can be substituted for b but b cannot be substituted for a . Since there does not exist a set K containing both a and b in which both of a and b can be substituted for all elements of K , α' vacuously satisfies the requirements for a selector.

Finally, we observe that "the union of two selectors is a selector". In particular, if we combine the selectors α' and σ above into one relation, we still have a selector σ' .

It can be shown that if a separator δ is contained in a selector σ' , and if the partition induced by δ has the property that for each set K of the partition there is an element t which is σ' -related to every element of K , then there is a minimum-cost solution which is a refinement of the partition induced by δ whose set of representatives includes all such elements t .

Now let us look at the relation δ :



The reader is invited to inspect this graph and confirm that whenever two elements are δ -related they are also σ' -related - i.e. δ is contained in σ' .

Here we see the importance of treating the example as two separate problems. If we consider tanks 13, 15, and 17 as part of the same set, then δ will give us essentially no information. If we throw them out, then the chains of non- δ -related elements are {16}, {14}, {12}, {2,3,5,9,10,11}, {4,6}, and {1,7,8}. The substitution choices are forced by the relation σ' , except that we are free to choose either tank 7 or tank 8 in the final set, since the costs of the two tanks are identical and each is σ' -related to the other.

Using the above as an "initial approximation" to a solution, the following results were obtained by an exhaustive search which occupied less than a minute on an IBM AT:

Set	Representative	Cost
{1,7,8}	{7}	1082.07
{2,3,10,11}	{3}	13069.25
{4,6}	{6}	809.35
{5}	{5}	3709.45
{9}	{9}	2546.59
{12}	{12}	16115.92
{13}	{13}	3007.22
{14}	{14}	15851.90
{15}	{15}	2938.32
{16}	{16}	71216.99
{17}	{17}	13048.42

Minimum cost 143395.48

Notice that the above solution is a valid solution to the original problem, since it separates the pairs (4,10) and (12,14).

To further document the results of the above search, we present the following analysis of the partitioning of the largest set, i.e. the set {2,3,5,9,10,11}. The representative of each set in a given partition is underlined.

Number k of sets in the partition	Best partition into k subsets	Cost of partition
1	{{2,3,5, <u>9</u> ,10,11}}	23262.89
2	{{2, <u>3</u> ,10,11},{5, <u>9</u> }}	19382.44
3	{{2, <u>3</u> ,10,11},{ <u>5</u> },{ <u>9</u> }}	19325.29
4	{{2, <u>3</u> ,10},{ <u>5</u> },{ <u>9</u> },{ <u>11</u> }}	19898.93
5	{{ <u>2</u> },{ <u>3</u> ,10},{ <u>5</u> },{ <u>9</u> },{ <u>11</u> }}	20480.06
6	{{ <u>2</u> },{ <u>3</u> },{ <u>5</u> },{ <u>9</u> },{ <u>10</u> },{ <u>11</u> }}	21061.18

In each of the above examples we had mathematical proof that the solutions we obtained were correct. In the first example it was practical to find the solution by an exhaustive search strategy. In the second example we have reason to doubt that such a search strategy is practical. In that example, even after the initial partition (in which tanks 13, 15, and 17 were identified as forming a separate component), the solution obtained by an exhaustive search would have taken almost four hours even on our hypothetical million-potential-solutions-a-second computer. In an environment in which several sets of items need to be presented to a computer at a setting, this is unacceptable. What's more, it is likely that even larger sets of different items would need to be subjected to analysis. So

the existence of mathematical properties that guarantee a minimal-cost solution to lie in a highly restricted area of the solution space is significant.

But even in situations where such mathematical laws are not operating we need some help. We need to guide our search for solutions more precisely, even if we may be steering toward a near-optimal rather than an optimal solution. Consider the following observation: the operation of finding and examining all immediate refinements of a given partition (i.e. all partitions obtained by splitting a single set of the original partition into two smaller subsets) is equivalent to the operation of finding all subsets of the set and thus has a complexity no worse than 2^n , where n is the number of elements of the set. Suppose we begin with a one-set partition, choose the immediate refinement of minimum cost, and restrict our search for solutions to refinements of this partition. Repeat the procedure until all immediate refinements result in an increase in cost. This is a natural, intuitive approach which may have some mathematical basis.

Another approach which may have even more merit because of its reduced complexity is to start with a partition consisting of n singleton subsets and successively join pairs of subsets until we can no longer reduce the cost with such a joining. The complexity of the search for the 'best' joining is no worse than $C_{n,2}$. For this type of strategy, a relation called a joiner may be of some help. A joiner is a relation β which has the property that when $a \beta b$ and a and b are the chosen representatives of respective sets K_1 and K_2 of a partition, then it is always more economical to join the two sets into one and use the item a as the chosen representative. For some examples of joiners for different cost functions, see (Yeager, 1987).

Notice in the last example that in breaking down the set $\{2,3,5,9,10,11\}$ into finer and finer partitions and exhaustively searching for the most economical partition the six "best" partitions of orders 1, 2, 3, 4, 5, and 6 satisfied a very interesting property. The best partition of order k was always a refinement of the best partition of order $k-1$ and a 'joining' of the partition of order $k+1$. To test whether this might always be the case, when no mathematical basis was discovered for the property, a large number of trials were performed using random data. In a large majority of cases this behavior was indeed present. However, several exceptions were noted.

CONCLUSIONS AND RECOMMENDATIONS

Figures 1-6 detail the recommended architecture for a collection of software tools to aid the commonality analysis process. Integration of these tools using a single, consistent user interface is also recommended. A menu structure is the simplest approach, but a natural language interface may be the best long-term solution.

We are assuming here a "loosely coupled" configuration, in which the actual creation and maintenance of the database is performed by the DBMS itself. Commands and data are passed to the DBMS from "front end" software modules and data is passed from the DBMS back to those modules for the performance of operations outside the capabilities of the DBMS.

The database creation module is illustrated in Figure 1. During database creation the database administrator makes a number of decisions which will seriously affect the usefulness of the database for the purpose of commonality analysis. Attributes, names of attributes, representation (character string or integer, for example), default values, and many other database configuration factors must be carefully chosen. Knowledge is an important component of the skills needed to create such a database. Some of that knowledge will be of such an ad hoc nature that it must reside with the database administrator himself. The knowledge needed to enforce consistency and uniformity across all commonality databases is of a less changeable nature, however, and could conceivably be encoded as rules which the database creation module would draw upon in its interaction with the human creator.

An essential ingredient of the database creation module is its synonym bank. The purpose of the synonym bank is to insure that different names are not being used in different commonality databases to refer to logically equivalent attributes. Each group of synonymous attribute names has a default representative to be used as the actual attribute name. The database administrator is informed of the substitution and is given the chance to over-ride for good cause.

Figure 2 details the software component used for entering of new data and new knowledge. As discussed above, knowledge concerning commonality relationships among the data is inherently associated with the data and should not be separated from it. When new data is entered, the database administrator should be prompted to review and perhaps modify the knowledge about commonality relationships in the data.

In Figure 3 we see the first stage of the commonality alternative selection module. Here the user requests a given

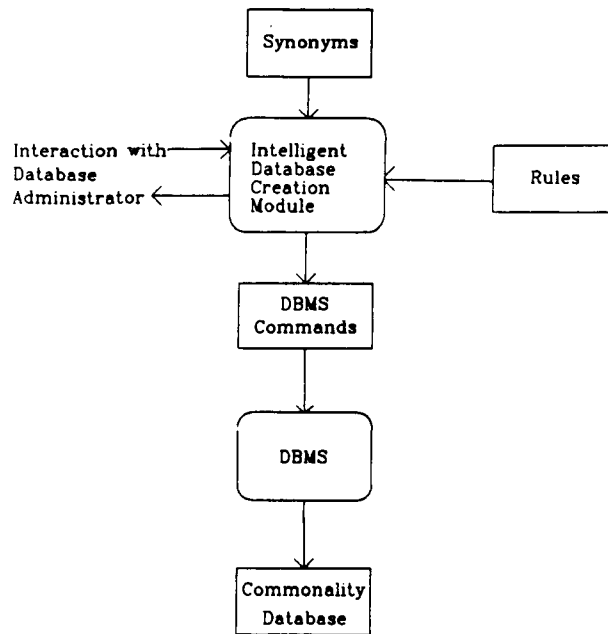


Figure 1. Intelligent database creation module.

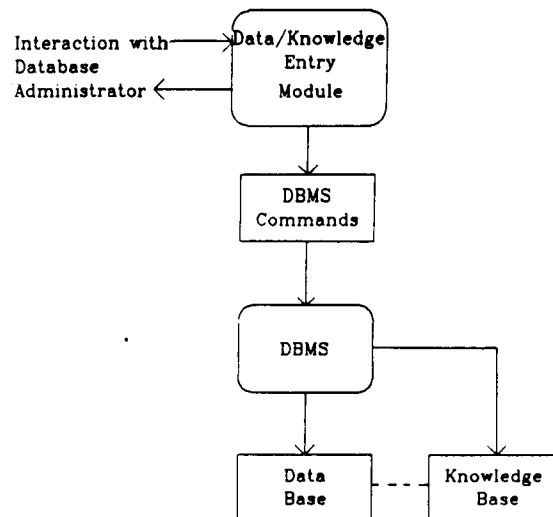


Figure 2. Data and Knowledge Entry Module.

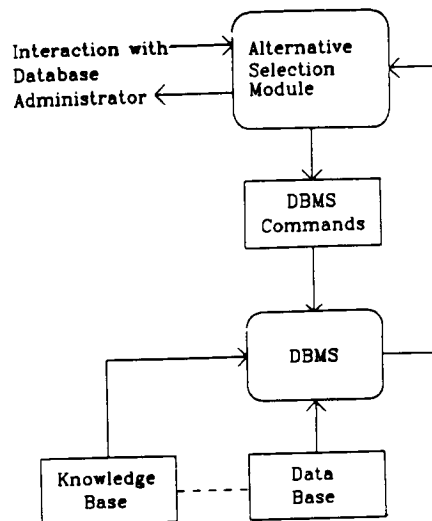


Figure 3. Commonality Alternative Selection.
Stage 1: Input.

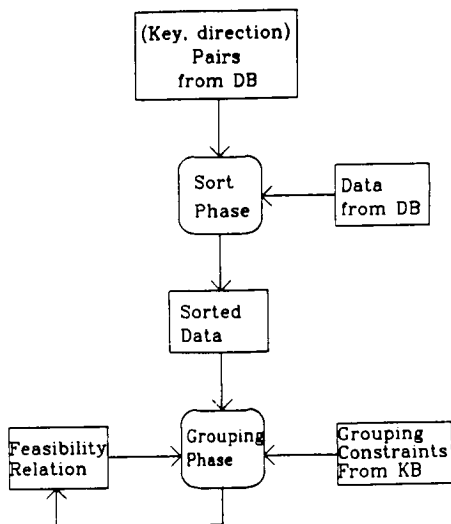


Figure 4. Commonality Alternative Selection
Stage 2: Construction of the
Feasibility Relation.

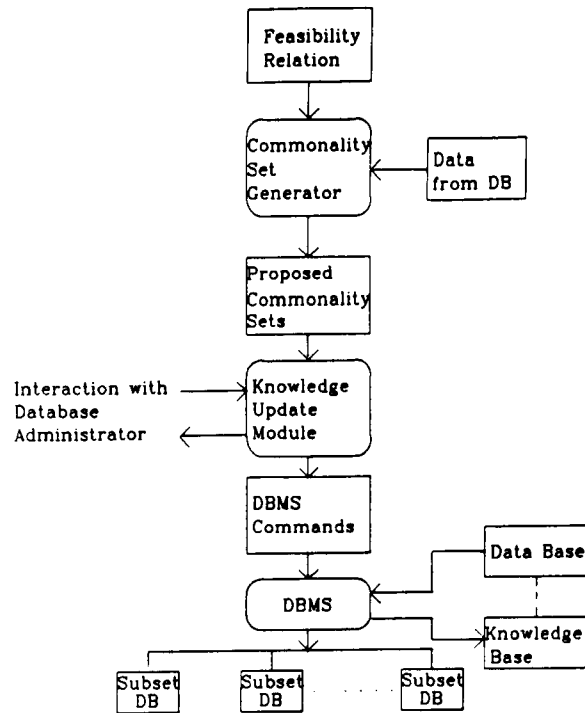


Figure 5. Commonality Alternative Selection. Stage 3. Generation, Approval, and Output of Subset data bases.

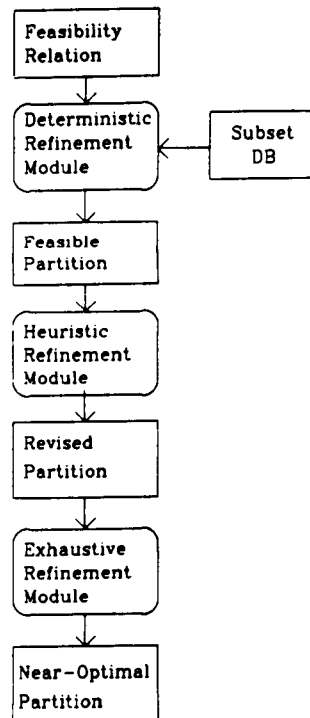


Figure 6. Commonality Analysis.

set of data from a commonality database, and that data is transferred to the front-end module along with the knowledge needed for constructing a feasibility relation on the data. Figure 4 depicts the data being alternately sorted and grouped using the information from the knowledge base. This sorting and grouping phase is applied iteratively, and the feasibility relation is extended in size with each such application. Finally, we see in Figure 5 the process in which commonality alternative sets are created using the feasibility relation and in which a subset database is generated for each set of alternatives. If α denotes the feasibility relation, then each set of alternatives is an α -connected component. What this means is that records a and b are in the same set if there exists a series of records x_1, x_2, \dots, x_k for which $a = x_1$, $b = x_k$, and for each $i = 1, 2, \dots, k-1$, either $x_i \alpha x_{i+1}$ or $x_{i+1} \alpha x_i$. Each subset is presented to the database administrator or other user as it is generated. The user has the opportunity then to (a) accept the set of alternatives as a valid set, (b) discard the set of alternatives, or (c) accept a subset of the set presented. In the latter two cases, the system has reason to doubt the encoded knowledge which led to the generation of that particular set of alternatives. It is important at that point for the system to engage in a dialog with the user and attempt to update its knowledge base so that the same mistake does not recur.

The final module to discuss is the enhanced commonality analysis module, shown in Figure 6. Here a given subset of commonality alternatives is analyzed to find an optimal or near-optimal substitution strategy. An essential ingredient here is the feasibility relation generated in stage 2 of the commonality alternative selection process. The commonality analysis process breaks down into three sub-modules. The first utilizes deterministic mathematical rules which narrow the solution space as much as possible. The output from this sub-module is a feasible partition which may be the true minimum-cost solution or may be many refinements removed from the minimum-cost solution, depending on the properties of this particular feasibility relation and this particular set of data. If the feasible partition is not known to be optimal, then it is passed on to a submodule which attempts to produce a lower-cost partition using heuristic strategies. Finally, if it can be ascertained during the heuristic refinement process that the number of possibilities remaining to be checked is small enough that a complete pass through the entire set of remaining partitions can be reasonably undertaken, the sub-module for exhaustive search continues the refinement process to produce the final solution.

REFERENCES

- COLLIER, D. A. 1978. A Product Structure Measure: the Degree of Commonality. Proc. Tenth National AIDS Meeting, St. Louis, Missouri.
- COLLIER, D. A. 1980. Justifying Component Part Standardization. Proc. Twelfth National AIDS Conference, Las Vegas, Nevada.
- COLLIER, D. A. 1981. The Measurement and Operating Benefits of Component Part Commonality. Decision Science 12, No. 1.
- COLLIER, D. A. 1982. Aggregate Safety Stock Levels and Component Part Commonality. Management Science Vol. 28, No. 11.
- MSFC. 1986. Commonality Analysis Program Review, October 9, 1986. Contract NAS8-36413, NASA George C. Marshall Space Flight Center, Alabama.
- MSFC. 1987. Commonality Analysis Study, User Manual for the System Commonality Analysis Tool (SCAT), D483-10064, March 1987. Contract NAS8-36413, NASA George C. Marshall Space Flight Center, Alabama.
- YEAGER, D. P. 1987. A Formulation of the Commonality Analysis Problem and Some Partial Solutions, submitted to Operations Research.

535-64
N 88 - 15636 / 16737
378

1987

NASA/ASEE SUMMER FACULTY RESEARCH FELLOWSHIP PROGRAM

MARSHALL SPACE FLIGHT CENTER
THE UNIVERSITY OF ALABAMA IN HUNTSVILLE

THE JEFFCOTT EQUATIONS IN NONLINEAR ROTORDYNAMICS

Prepared By:	R. A. Zalik
Academic Rank:	Professor
University and Department:	Auburn University Algebra, Combinatorics, and Analysis
NASA/MSFC:	
Laboratory:	Structures and Dynamics
Division:	Control Systems
Branch:	Mechanical Systems
NASA Colleague:	Tom Fox

The Jeffcott Equations in Nonlinear Rotordynamics

R. A. Zalik

Auburn University

Division of Mathematics

120 Mathematics Annex Building

Auburn, AL 36849-3509

Acknowledgement

This work was written at Marshall Space Flight Center with the support of a NASA/ASEE Faculty Fellowship. The author would like to thank NASA for the use of their facilities, and acknowledge with gratitude the assistance of several MSFC personnel, in particular P. Broussard, T. H. Fox, and S. Ryan.

Abstract. The Jeffcott equations are a system of coupled differential equations that represent the behavior of a rotating shaft. This is a simple model that allows investigation of the basic dynamic behavior of rotating machinery. Nonlinearities can be introduced by taking into consideration deadband, side force, and rubbing, among others.

In this paper we study the properties of the solutions of the Jeffcott equations with deadband. In particular, we show how bounds for the solutions of these equations can be obtained from bounds for the solutions of the linearized equations. By studying the behavior of the Fourier transforms of the solutions, we are also able to predict the onset of destructive vibrations. These conclusions are verified by means of numerical solutions of the equations, and of power spectrum density (PSD) plots.

This study offers insight into a possible detection method to determine pump stability margins during flight and hot fire tests, and was motivated by

the need to explain a phenomenon observed in the development phase of the cryogenic pumps of the Space Shuttle, during hot fire ground testing: namely, the appearance of vibrations at frequencies that could not be accounted for by means of linear models.

1. Introduction

H. H. Jeffcott [10] was one of the first to study the vibration characteristics of an unbalanced, uniform, flexible shaft supported by bearings. He did so by considering a linear system of differential equations of the form

$$\begin{aligned}y'' + Cy' + Ay &= F \cos wt \\z'' + Cz' + Az &= F \sin wt\end{aligned}\tag{1}$$

where the differentiation is with respect to the parameter t , and the shaft is assumed to rotate along the x -axis with angular velocity w , y and z describe the displacement of the center of the shaft, and the coefficients have the following physical interpretation: $C = C_s/m$, $A = K_s/m$, $K = K_b/m$, and $F = uw^2$, where m is the mass of the shaft, C_s is the seal damping, K_s and K_b are the seal and bearing stiffnesses, and u is the displacement of the shaft's center of mass from the geometric center.

In [12] Yamamoto studied the effect of deadband (i.e. the clearing between housing and bearing), but his treatment was not rigorous. Other works dealing with nonlinearities include [3], [4], [8] and [11]. In [7], Day used the method of multiple scales to gain new insight into the properties of the solutions. He discovered a frequency, which he termed "nonlinear natural frequency" that appears in the PSD plots of solutions of the nonlinear model and is absent from the PSD plots of solutions of the linear model. The nonlinear natural frequency seems to have been observed during early ground testing of both LOX and fuel pumps of the second stage Main Engine of the Space Shuttle but, until now, there has been no explanation of its origin. If $r = (y^2 + z^2)^{1/2}$, δ is the deadband, $K = K_b/m$, where K_b is the bearing stiffness, $B = Q_s/m$, with Q_s denoting the cross-coupling stiffness of the seal, and

$$h(t) = \begin{cases} 1 & \text{if } r < \delta \\ \delta/r & \text{if } r > \delta, \end{cases} \quad (2)$$

then the model studied by Day can be described by the system

$$\begin{aligned} y'' + Cy' + [A + K(1-h)]y + Bz &= f_1(t), \\ z'' + Cz' - By + [A + K(1-h)]z &= f_2(t), \end{aligned} \quad (3)$$

where $f_1(t) = F \cos \omega t$, $f_2(t) = F \sin \omega t$, and $K(1-h)$ is the nonlinearity associated with the deadband (see Fig. 1). Note that (1) is a particular case of (3).

In this paper we shall explain the nature of the nonlinear natural frequency and apply our conclusions to the signature analysis of the nonlinear Jeffcott model described by (3), where $f_1(t)$ and $f_2(t)$ are arbitrary bounded and continuous functions, B , C , K , and δ are positive, and A and t are nonnegative.

2. Properties of the solutions of Jeffcott's equations.

2.1 Existence, uniqueness, and a representation formula.

If $x_1 = y$, $x_2 = y'$, $x_3 = z$, $x_4 = z'$, $r = (x_1^2 + x_3^2)^{1/2}$ and $h(t)$ is given by (2), then (3) is equivalent to

$$\dot{x}_1 = x_2$$

$$\dot{x}_2 = - [A + K(1-h)]x_1 - Cx_2 - Bx_3 + f_1(t) \quad (4)$$

$$\dot{x}_3 = x_4$$

$$\dot{x}_4 = - Bx_1 - [A + K(1-n)]x_3 - Cx_4 + f_2(t)$$

or, more concisely,

$$\underline{x}' = \underline{g}(\underline{x}, t).$$

Since $\underline{g}(\underline{x}, t)$ is continuous, and satisfies a Lipschitz condition on \underline{x} , from

standard existence and uniqueness theorems (cf., eg. [5]), we know that

every initial value problem for (4) has a unique solution. Thus, we also

infer that every initial value problem for (3) has a unique solution. Let

$v = y + iz$, $f(t) = f_1(t) + if_2(t)$, and $M = A + K - iB$; then (3) is also

equivalent to

$$v'' + Cv' + Mv - Khv = f(t). \quad (5)$$

Before studying (5), let us first consider a linear system of the form

$$v'' + Cv' + Mv = g(t). \quad (6)$$

Then

$v = C_1 \exp(\lambda_1 t) + C_2 \exp(\lambda_2 t) + v_p$, where $C_1 \exp(\lambda_1 t) + C_2 \exp(\lambda_2 t)$ is a solution of

$$v'' + Cv' + Mv = 0, \quad (7)$$

and therefore $\lambda_{1,2} = (1/2) [-C \pm (C^2 - 4M)^{1/2}]$. If $Q = C^2 - 4(A + K)$, a straightforward computation shows that $\lambda_1 = \alpha + i\beta$, $\lambda_2 = \alpha' - i\beta$, where

$$\beta = 8^{-1/2} [-Q + (Q^2 + 16 B^2)^{1/2}]^{1/2}, \quad (8)$$

$$\alpha = [\beta^{-1} B - C]/2, \quad \alpha' = -[\beta^{-1} B + C]/2, \quad (9)$$

and therefore

$$\alpha' = -\beta^{-1} B + \alpha \quad (10)$$

Applying, e.g. [5, Theorem 6.4] we readily deduce that the Green's function of the differential operator $(d^2/dt^2) + C(d/dt) + M$ is $G(t - s)$, where

$$G(t) = (\lambda_2 - \lambda_1)^{-1} [\exp(\lambda_1 t) + \exp(\lambda_2 t)], \text{ i.e. } \int_0^t G(t-s)q(s)ds \text{ is a}$$

particular solution of (6), and therefore

$$v = c_1 \exp(\lambda_1 t) + c_2 \exp(\lambda_2 t) + \int_0^t G(t-s)q(s)ds.$$

If in particular $g(s) = K h(s) v(s) + f(s)$, then (6) reduces to (5), and we have:

$$v = c_1 \exp(\lambda_1 t) + c_2 \exp(\lambda_2 t) + \int_0^t G(t-s)f(s)ds + K \int_0^t G(t-s)h(s)v(s)ds.$$

In other words,

$$v(t) = u(t) + P(t), \tag{11}$$

where

$$u(t) = c_1 \exp(\lambda_1 t) + c_2 \exp(\lambda_2 t) + \int_0^t G(t-s)f(s)ds \tag{12}$$

is a solution of the linear differential equation $v'' + Cv' + Mv = f(t)$,

(henceforth called the linear part of (5)), and

$$P(t) = K \int_0^t G(t-s) h(s)v(s)ds. \tag{13}$$

Note that we have a closed form formula for u , whereas $P(t)$ is expressed in terms of the unknown function $v(t)$. Our analyses will be based on a study of the properties of the perturbation term $P(t)$.

2.2 Bounds.

The definition (2) of $h(s)$ implies that $|h(t)v(t)| \leq \delta$; thus,

$$|P(t)| \leq K\delta \int_0^t |G(t-s)| ds \leq$$

$$K\delta (\beta^{-2} B^2 + 4\beta^2)^{-1/2} \int_0^t [\exp(\alpha(t-s)) + \exp(\alpha'(t-s))] ds.$$

Since (9) and (10) imply that if $\alpha = 0$, then $\beta = B/C$, and when $\alpha = \beta^{-1}B$

then $\alpha' = 0$, we have

$$|P(t)| \leq \begin{cases} K\delta (\beta^{-2} B^2 + 4\beta^2)^{-1/2} [(1/\alpha)(\exp(\alpha t) - 1) + (1/\alpha')(\exp(\alpha' t) - 1)] & \text{if } \alpha \neq 0, \beta^{-1}B \\ K\delta (C^2 + 4B^2/C^2)^{1/2} [t + (2/C)(1 - \exp[(-C/2)t])] & \text{if } \alpha = 0, \\ K\delta (\beta^{-2} B^2 + 4\beta^2)^{-1/2} [(\beta/B)(\exp[(B/\beta)t] - 1) + t] & \text{if } \alpha = \beta^{-1}B \end{cases} \quad (14)$$

From (11), (12), (13), and (14) we derive the following conclusions:

1. If $\alpha < 0$ and $|\int_0^t G(t-s) f(s) ds| \leq M$, then the steady state

solution v_∞ of (5) satisfies the following inequality:

$$|v_\infty| \leq M + K\delta (\beta^{-2} B^2 + 4\beta^2)^{-1/2} |1/\alpha + 1/\alpha'|$$

2. If $\alpha = 0$, the perturbation term $P(t)$ can grow at most linearly.

3. If $\alpha > 0$, the order of growth of $P(t)$ cannot exceed $\exp(\alpha t)$; note

that the order of magnitude of all nonzero solutions of (7) cannot exceed $\exp(\alpha t)$.

Thus, since we have assumed that $f(t)$ is bounded, the study of the boundedness of the solutions of (5) reduces to the study of the boundedness of the solutions of its homogeneous part. If $\alpha < 0$ we shall say that (5) is stable, if $\alpha > 0$ that (5) is unstable, and if $\alpha = 0$ that (5) has reached the stability boundary. This nomenclature is consistent with that used for linear systems (cf. [9, pp. 83, 84]).

2.3 Estimates for β .

In this section we will prove that β is between B/C and $(A+K)^{1/2}$.

The importance of this observation will become clear in the sequel. In what follows, let $\gamma = A + K$ and $\xi = (B/C)^2$; thus $Q = C^2 - 4\gamma$.

Assume that $\alpha < 0$; then from (9) we see that $B/C < \beta$. Squaring and applying (8), we have

$$\xi < (1/8) [-Q + (Q^2 + 16 B^2)^{1/2}].$$

Thus, ξ satisfies the inequality $4\xi^2 + Q\xi - B^2 < 0$, which can be written as

$$4\xi^2 + [C^2 - 4\gamma] \xi - B^2 < 0, \text{ or}$$

$$C^2 - 4\gamma < (B^2 - 4\xi^2) \xi^{-1} = B^2 \xi^{-1} - 4\xi. \text{ Since } \xi = (B/C)^2, \text{ we have that}$$

$$C^2 - 4\gamma < C^2 - 4\xi, \text{ and therefore } \gamma > \xi, \text{ i.e.}$$

$$B^2 < C^2 \gamma$$

Thus,

$$16\gamma^2 + C^4 - 8C^2\gamma + 16B^2 < 16\gamma^2 + C^4 + 8C^2\gamma,$$

i.e.

$$Q^2 + 16B^2 < (4\gamma + C^2)^2,$$

and therefore

$$[Q^2 + 16 B^2]^{1/2} < 4\gamma + C^2.$$

Subtracting Q from both sides of this inequality we see that

$$8\beta^2 = -Q + [Q^2 + 16B^2]^{1/2} < 8\gamma,$$

and we conclude that $\beta < (A + K)^{1/2}$.

The cases $\alpha = 0$ and $\alpha > 0$ are treated similarly, and we shall omit the details. The conclusions are the following:

1. If $\alpha < 0$, then $B/C < \beta < (A + K)^{1/2}$, and $\alpha' < 0$.
2. If $\alpha = 0$, then $B/C = \beta = (A + K)^{1/2}$, and $\alpha' < 0$.
3. If $\alpha > 0$, then $(A + K)^{1/2} < \beta < B/C$.

From these conclusions we also infer that if $f(t)$ is bounded, then (5) is stable if and only if $B/C < (A + K)^{1/2}$.

2.4 Resonance.

From the results of 2.3 it is clear that (5) is in resonance if and only if its linear part is in resonance. If for example $f(t) = F_0 \exp(i\omega t)$, then we

readily see that the linear part of (5) has a particular solution of the form

$A_0 \exp(i\omega t)$, where

$$A_0 = F_0 / [(A + K - \omega^2) + i(\omega - \beta)].$$

Since the denominator in the preceding formula vanishes if and only if

$\beta = \omega$ and $\omega = (A + K)^{1/2}$, we deduce that $\beta = (A + K)^{1/2}$, and therefore that $\alpha = 0$. Thus (5) can be in resonance only on the stability boundary.

3. Harmonic Analysis of the solutions.

3.1 Introduction

In practice, the coefficients of (5) and, in general, the equations that describe the movement of rotating machinery, are imperfectly known. The approach taken is to sample the system response over a time interval (in our case, that would mean measuring $y(t_i)$ and $z(t_i)$, $i = 0, \dots, N$, where the t_i are equally spaced points), and to approximate the Fourier transforms of

$y(t)$ and $z(t)$ by means of the Discrete Fourier Transforms of the sequences $\{y(t_i)\}$ and $\{z(t_i)\}$. (See, e.g. [1]). The absolute values of the coefficients in the Discrete Fourier expansions are then plotted on graphs called Power Spectrum Density (PSD) plots, which represent the response of the mechanical system at different frequencies. One then tries to determine the condition of the mechanical system by an examination of these plots. This is known as "signature analysis". (See, e.g. Collacott [6].) In this section we examine the properties of the Fourier transforms of the solutions of (5), whereas in section 4 we show, by means of examples, how to apply these conclusions to the signature analysis of the system.

From now on, we shall assume that $\alpha < 0$.

3.2 Properties of the continuous Fourier transform.

Let $G(t)$, $v(t)$, $u(t)$, and $P(t)$ be defined to equal 0 for $t < 0$. Then

(11) is valid on $(-\infty, \infty)$. If

$$q(t) = h(t) v(t),$$

it is clear that $q(t)$ vanishes for $t < 0$. Thus, from (13) we readily see that

$$P(t) = K \int_{-\infty}^{\infty} G(t-x) q(x) dx = K(G * q)(t), \quad (15)$$

where "*" denotes the convolution product. If $p_1(t) = \exp(\lambda_1 t)$, $p_2(t) = \exp(\lambda_2 t)$ for $t \geq 0$, and equal zero for $t < 0$, and $u_p(t)$ denotes a particular solution of the linear part of (5), then (11) can be written in the form

$$v(t) = c_1 p_1(t) + c_2 p_2(t) + u_p(t) + P(t). \quad (16)$$

Note, moreover, that

$$G(t) = (\lambda_2 - \lambda_1)^{-1} [p_1(t) + p_2(t)] \text{ and therefore}$$

$$P(t) = (\lambda_2 - \lambda_1)^{-1} [(p_1 + p_2) * q](t). \quad (17)$$

Let F denote the Fourier transform operator; thus, if $g(t)$ is

integrable on $(-\infty, \infty)$, then $F[g](s) = \int_{-\infty}^{\infty} g(t) \exp(-ist) dt$.

In particular, when $\alpha < 0$ we have

$$F[p_1](s) = 1/[i(s - \beta) - \alpha] \quad (18)$$

and

$$F[p_2](s) = 1/[i(s + \beta) - \alpha + \beta^{-1}B]. \quad (19)$$

If $u_p(t)$ and $q(t)$ are integrable on $(-\infty, \infty)$, from (16) and (17) we see that

$$F[v] = c_1 F[p_1] + c_2 F[p_2] + F[u_p] + (\lambda_2 - \lambda_1)^{-1} (F[p_1] + F[p_2]) F(q).$$

Since $F[p_1](\beta)$ diverges as $\alpha \rightarrow 0^-$, we therefore conclude that if α approaches 0 from the left, then the graphs of the real and imaginary parts of $F[v]$ will exhibit increasingly large spikes at β , where α and β are linked by (9). At first glance, this does not appear to be very useful, since in most applications u_p will not be integrable on $(-\infty, \infty)$ (as for example when $f(t) = F \exp(i\omega t)$). We shall now show that the range of

validity of our conclusions can be greatly extended if we consider windows.

3.3 Windowing and the nonlinear natural frequency

3.3.1 Analysis of the transient terms

In practice, Fourier transforms are computed for samples taken over a time interval of the form (a, b) , (called a "window"), where a is in general larger than zero. Let $g^{(a,b)}(t) = g(t)$ if $a \leq t \leq b$, let $g^{(a,b)}(t)$ equal zero otherwise, and let $g^{(b)} = g^{(0,b)}$. Clearly

$$F[p_1^{(a,b)}](s) = [\exp(\lambda_1 - si)b - \exp(\lambda_1 - si)a]/(\lambda_1 - si),$$

and

$$F[p_2^{(a,b)}](s) = [\exp(\lambda_2 - si)b - \exp(\lambda_2 - si)a]/(\lambda_2 - si).$$

Since $\lambda_1 - \beta i = \alpha$, we see that $F[p_1^{(a,b)}](\beta)$ diverges as $\alpha \rightarrow 0^-$; thus,

also the graphs of the real and imaginary parts of $F[v^{(a,b)}]$ should have

spikes at β . However, since $\lim_{a \rightarrow \infty} F[p_1^{(a,b)}](s) = \lim_{a \rightarrow \infty} F[p_2^{(a,b)}](s) = 0$, we

conclude that for fixed α and sufficiently large a , these spikes may be detected only if α is extremely close to 0. (Whether they will be detected at all depends on the numerical stability of the computations). Thus, in order to obtain useful data we have to analyze the Fourier transform of the perturbation term $P(t)$.

3.3.2 Analysis of the perturbation term

Let $P_b(t) = K \int_{-\infty}^{\infty} G(t-x) q^{(b)}(x) dx = \int_0^t G(t-x) q^{(b)}(x) dx$. From (15) we

see that if $t \leq b$, then $P_b(t) = P(t)$, whereas for $t \geq b$,

$P_b(t) = \int_0^b G(t-x) q(x) dx$. Thus,

$$F[P^{(b)}](s) = F[P_b](s) - K I_b(s), \quad (20)$$

where

$$I_b(s) = \int_b^{\infty} \exp(-st) \int_0^b G(t-x) q(x) dx dt.$$

We can write I_b in the form

$$I_b = (\lambda_2 - \lambda_1)^{-1} [I(\lambda_1) - I(\lambda_2)],$$

with

$$I(\lambda) = \int_0^\infty \exp(-st) \int_0^b \exp[\lambda(t-x)] q(x) dx dt.$$

If $\operatorname{Re}(\lambda) < 0$, reversing the order of integration we have:

$$\begin{aligned} I(\lambda) &= \int_0^b \exp(-\lambda x) q(x) dx \int_0^\infty \exp[(\lambda - s)t] dt \\ &= M(b, \lambda) \exp[(\lambda - s)b]/(\lambda - s), \end{aligned}$$

$$\text{where } M(b, \lambda) = \int_0^b \exp(-\lambda x) q(x) dx.$$

Thus,

$$\begin{aligned} I_b &= (\lambda_2 - \lambda_1)^{-1} M(b, \lambda_1) \exp[(\lambda_1 - s)b]/(\lambda_1 - s) \\ &\quad + (\lambda_2 - \lambda_1)^{-1} M(b, \lambda_2) \exp[(\lambda_2 - s)b]/(\lambda_2 - s). \end{aligned} \tag{21}$$

Moreover, since $q^{(b)}(x)$ is of bounded support it is integrable. Thus,

since $P_b(t) = K (G * q_b)(t)$, we know that

$$F[P_b](s) = K F[G](s) F[q^{(b)}](s) \tag{22}$$

Since $G(t) = (\lambda_2 - \lambda_1)^{-1} [p_1(t) + p_2(t)]$, from (18) and (19) we have:

$$F[G](s) = (\lambda_2 - \lambda_1)^{-1} [(\lambda_1 - s)^{-1} + (\lambda_2 - s)^{-1}].$$

Combining (20), (21), and (22), we thus obtain:

$$F[P^{(b)}](s) =$$

$$K(\lambda_2 - \lambda_1)^{-1} \{F[q^{(b)}](s) - M(b, \lambda_1) \exp[(\lambda_1 - s)b]\} / (\lambda_1 - s) +$$

$$K(\lambda_2 - \lambda_1)^{-1} \{F[q^{(b)}](s) - M(b, \lambda_2) \exp[(\lambda_2 - s)b]\} / (\lambda_2 - s).$$

$$\text{Thus, since } F[P^{(a,b)}](s) = F[P^{(b)}](s) - F[P^{(a)}](s),$$

setting

$$Q(a, b, \lambda, s) = \tag{23}$$

$$F[q^{(a,b)}](s) - M(b, \lambda) \exp[(\lambda - s)b] + M(a, \lambda) \exp[(\lambda - s)a],$$

we conclude that

$$F[P^{(a,b)}](s) = Q(a, b, \lambda_1, s) / (\lambda_1 - s) + Q(a, b, \lambda_2, s) / (\lambda_2 - s). \tag{24}$$

If $Q(a, b, \lambda_1, \beta) \neq 0$, we conclude that $F[P^{(a,b)}](\beta)$ will diverge as

$$\alpha \rightarrow 0^-.$$

We shall now show that, for any $\epsilon > 0$, the functions $Q(a, b, \lambda_1, s)$

and $Q(a, b, \lambda_2, s)$ are bounded, uniformly on s , provided that

$-\epsilon < \alpha < 0$. From (23) it is clear that

$|Q(a, b, \lambda, s)| \leq |F[q^{(a,b)}](s)| + |M(b, \lambda)| + |M(a, \lambda)|$. Now, the definition of $G(t)$ implies that $|G(t)| \leq 2|\lambda_2 - \lambda_1|^{-1}$. Since

$|h(t)v(t)| \leq \delta$, it is clear from (13) that $|P(t)| \leq 2K|\lambda_2 - \lambda_1|^{-1}\delta t$.

Assuming that $|f(t)| \leq M_1$, it is readily seen from (11) and (12), that

$$|v(t)| \leq |C_1| + |C_2| + 2|\lambda_2 - \lambda_1|^{-1} (k\delta + M_1)t.$$

The constants C_1 and C_2 depend on the initial conditions. We shall now show that, for the same set of initial conditions and any $\epsilon > 0$, C_1 and C_2 are bounded, uniformly on α .

Assume that $v(0) = v_0$, and $v'(0) = v_1$. From (11), (12), and (13), it is clear that

$$C_1 + C_2 = v_0. \tag{25}$$

On the other hand, since

$$(d/dt) \int_0^t G(t-x)g(x)dx = G(0)g(t) + \int_0^t (\partial/\partial t)G(t-x)g(x)dx,$$

(cf., e.g. Bartle [2]), differentiating (11) we have

$\lambda_1 C_1 + \lambda_2 C_2 + G(0)g(0) = v_1$, where $g(t) = f(t) + Kh(t)v(t)$, and from (25)

we obtain

$$\lambda_1 C_1 + \lambda_2(v_0 - C_1) + G(0)g(0) = v_1.$$

If $|f(t)| \leq M_1$, and $M = M_1 + K\delta v_0$, it is easy to see that $|g(0)| \leq M$.

Thus, since $G(0) = (\lambda_2 - \lambda_1)^{-1}$, we deduce that

$$|c_1| \leq |\lambda_2 - \lambda_1|^{-1} |\lambda_2 v_0| + |\lambda_2 - \lambda_1|^{-2} |M| + |\lambda_2 - \lambda_1|^{-1} |v_1|.$$

Since we are assuming that B and C stay positive, from (9) and (10) we

see that, as $\alpha \rightarrow 0$, λ_1 , λ_2 and $(\lambda_2 - \lambda_1)^{-1}$ remain bounded. Thus, also

c_1 and c_2 remain bounded, and from (24) we see that if K remains bounded,

then for every $\varepsilon > 0$ there are constants A_0, B_0 , that do not depend on α ,

such that $|v(t)| \leq A_0 + B_0 t$ for α in $(-\varepsilon, 0)$. Applying this inequality

it is now easy to see that for any $\varepsilon > 0$, $Q(a, b, \lambda_1, s)$ and

$Q(a, b, \lambda_2, s)$ are bounded, uniformly on α , provided that $-\varepsilon < \alpha < 0$.

Thus, we conclude that there are constants $K_1 = K_1(\varepsilon)$, and $K_2(\varepsilon)$, such that

$$|F[P^{(a,b)}](s)| \leq K_1/|\lambda_1 - s| + K_2/|\lambda_2 - s|.$$

This means that the only value for which $F[P^{(a,b)}](s)$ diverges as $\alpha \rightarrow 0^-$

is $s = \beta$. Also, there is no obvious reason why $F[P^{(a,b)}](\beta)$ should vanish as $a \rightarrow \infty$ (provided that we keep the difference $b - a$ constant).

3.3.3 Conclusions

In summary, we have shown that $F[v^{(a,b)}](\beta)$ diverges as $\alpha \rightarrow 0^-$, that β is the only value for which this may happen, that for α negative and constant, but sufficiently close to zero, the graphs of the absolute values of the real and imaginary parts of $F[v^{(a,b)}](s)$ will have spikes at $s = \beta$, and that the magnitude of these spikes need not decrease with time (i.e., as $a \rightarrow \infty$).

In [7, p. 784], Day equates the nonlinear natural frequency with the ratio Q_g/C_g (which, in our notation, equals B/C). Later on, (on p. 786), he notes that the nonlinear natural frequency is actually not B/C , but a number close to it. In this paper we have gone one step further and shown that β (i.e. the transient frequency of the linear part of (5)), and the nonlinear natural frequency are one and the same. This is a very surprising result.

On the practical side, our conclusions suggest that, all other things being equal, the introduction of nonlinearities (as induced, e.g. by deadbands) in a mechanical system, may give an earlier warning of the approach to the instability boundary.

4. Examples

We now study the behavior of the solutions of (5) for $C = 240$, $A = 0$, $\delta = 0.0000285$, $K = 1,305,000$, $f(t) = uw^2 \exp(i\omega t)$, $u = 0.00006915$, and $\omega = 1,000\pi s$, where s will vary. We also make the realistic assumption -based on empirical data- that the bearing stiffness changes with the forcing frequency ω , by setting $B = 60\omega$. Let f_c (the "critical frequency") be defined to equal $(A+K)^{1/2}/(2\pi) = K^{1/2}/(2\pi)$. We readily see that $f_c \approx 181.8$ Hz., and that the value of s that corresponds to f_c is $s_c \approx 1.4545$. For $s = 10/3$ our example reduces to Example 1 of [7].

Let $f_1 = w/2\pi$ denote the forcing frequency; clearly $f_1 = 500$ s. We know that (5) will be stable for $s < s_c$, and unstable for $s > s_c$. In Figs. 2 through 5 we show, for various values of s , plots of the numerical solutions of (5), (obtained by a fourth order Runge-Kutta algorithm), and of PSD's for the real part y and imaginary part z of v . The solution plots are for $0.1 < t < 0.256$, and the PSD plots for the window $[0, 0.256]$. Note that all the PSD plots have two distinct spikes: one corresponding to the forcing frequency, and one corresponding to the nonlinear natural frequency. For $s = 0.5$ (i.e. far from the stability boundary), the forcing function $f(t)$ dominates the perturbation term $P(t)$. Thus, the solution is nearly circular (we see a thick circular curve; the thickness is caused by $P(t)$), and the PSD plots exhibit larger spikes for the forcing frequency than for the nonlinear natural frequency. As s increases, the solution becomes annular, and the nonlinear natural frequency begins to dominate. Finally, for $s > s_c$

the solutions begin to diverge. Since the PSD plots are obtained by approximating Fourier transforms by discrete Fourier transforms, (which are intrinsically bounded) they show no obvious qualitative difference when compared with plots for values of s close to, but smaller than, s_c .

Figures 6 and 7 show PSD plots for $s = 1.2$ and $s = 1.3$ and various windows. Note that if we compare the PSD plots for $0 < t < 0.256$ (Figs. 3 and 4) and $0.256 < t < 0.512$ (Figs. 6 and 7), we see a large decrease in the height of the spike that corresponds to the nonlinear natural frequency, and a very small decrease when we compare the plots for $0.256 < t < 0.512$ and $1.024 < t < 1.28$, but there is no change in magnitude on subsequent windows. This is due to the disappearance of the transient terms $F[p_1]$ and $F[p_2]$.

References

1. E. Oran Brigham, The Fast Fourier Transform, Prentice Hall, Englewood Cliffs, 1974.
2. R. G. Bartle, The Elements of Real Analysis, John Wiley & Sons, New York, 1964.
3. D. W. Childs, The Space Shuttle main engine high-pressure fuel turbopump rotordynamics instability problem, Trans. ASME, J. Engineering for Power, 48-57 (January 1978).
4. D. W. Childs, Rotordynamic characteristics of the HPOTP (high pressure oxygen turbopump) of the SSME (Space Shuttle main engine), NASA MSFC Contract NAS8-34505, Turbomachinery Laboratories Report FD-1-84 (30 January 1984).
5. E. A. Coddington and N. Levinson, Theory of Ordinary Differential Equations, McGraw Hill, 1955. Reprint, Robert E. Krieger Publishing Co., Malabar, Florida, 1984.
6. R. A. Collacott, Vibration Monitoring and Diagnosis, John Wiley & Sons, New York, 1979.
7. W. B. Day, Asymptotic Expansions in Nonlinear Rotordynamics, Quart. Appl. Math. 44 (1987), 779-792.
8. P. K. Gupta, L. W. Winn, and D. B. Wilcock, Vibrational characteristics of ball bearings, Trans. ASME, J. of Lubrication Technology, 99F No. 2 (1977), 284-189.
9. J. K. Hale, Ordinary Differential Equations, 2nd Ed. Robert E. Krieger Publishing Co., Malabar, Florida, 1980.
10. H. H. Jeffcott, The lateral vibration of loaded shafts in the neighborhood of a whirling speed - The effect of want of balance, Philos. Mag., Series 6, 37 (1919), 304-314,
11. B. F. Rowan, Rotordynamics Technical Manual, Rockwell International, Rocketdyne Division, Canoga Park, California, November 1981.
12. T. T. Yamamoto, On critical speeds of a shaft, Mem. Fac. Engineering, Nagoya Univ. 6 (1954), 106-174.

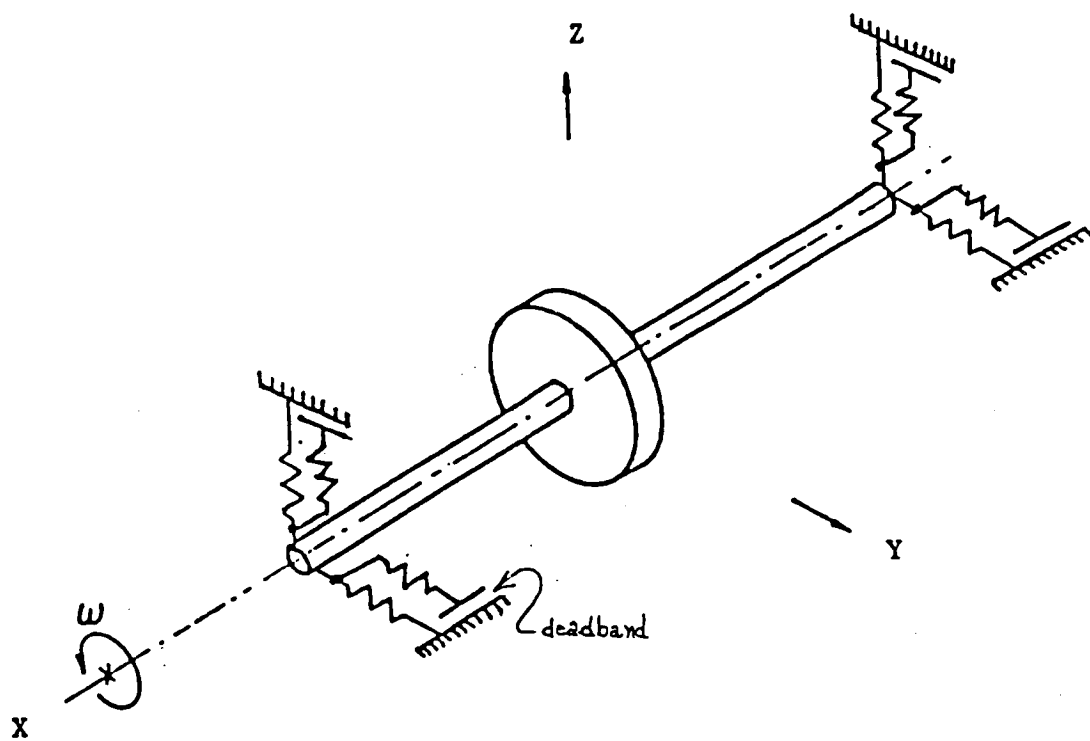


FIG. 1

ORIGINAL PAGE IS
OF POOR QUALITY

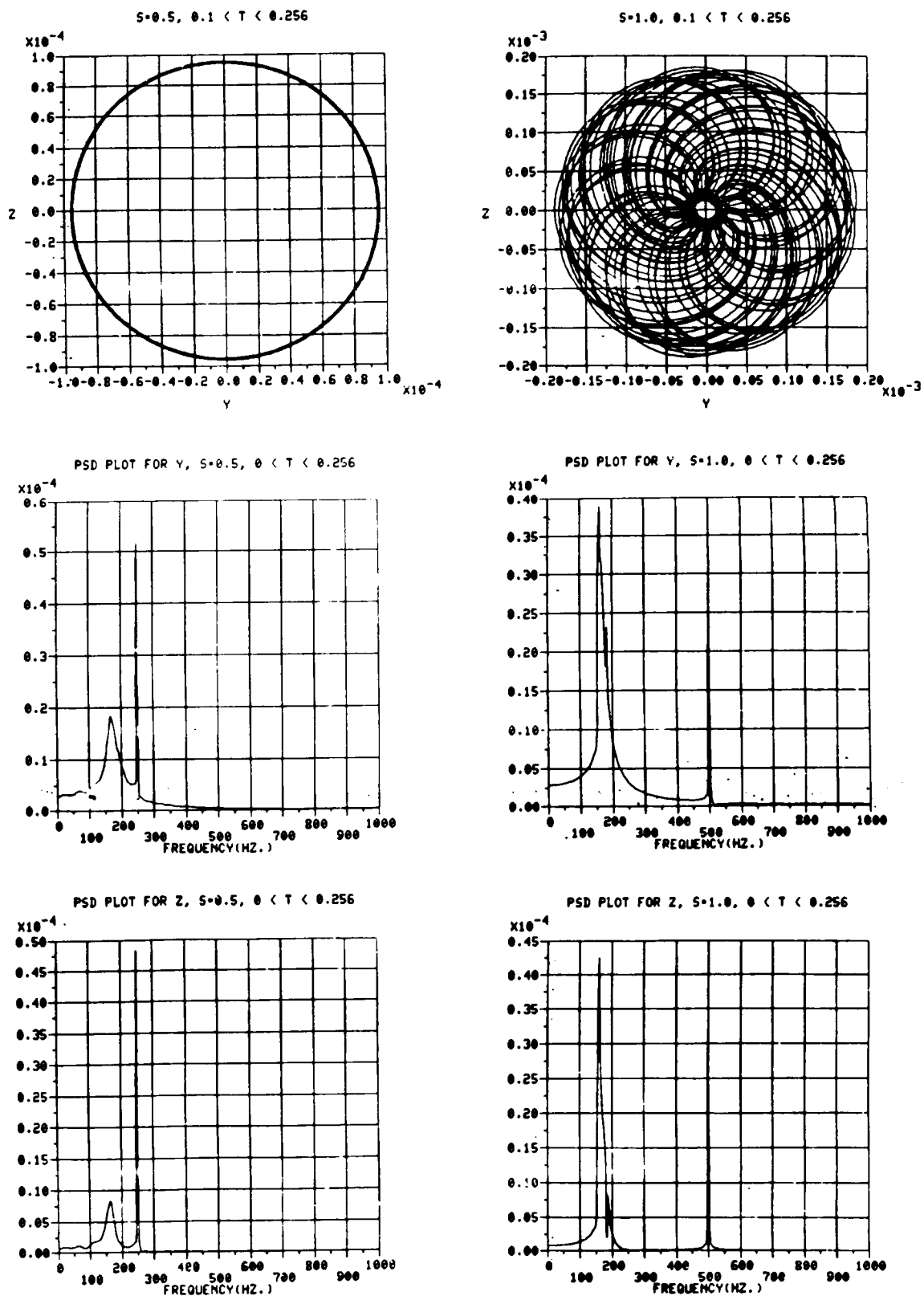


FIG. 2

ORIGINAL PAGE IS
OF POOR QUALITY

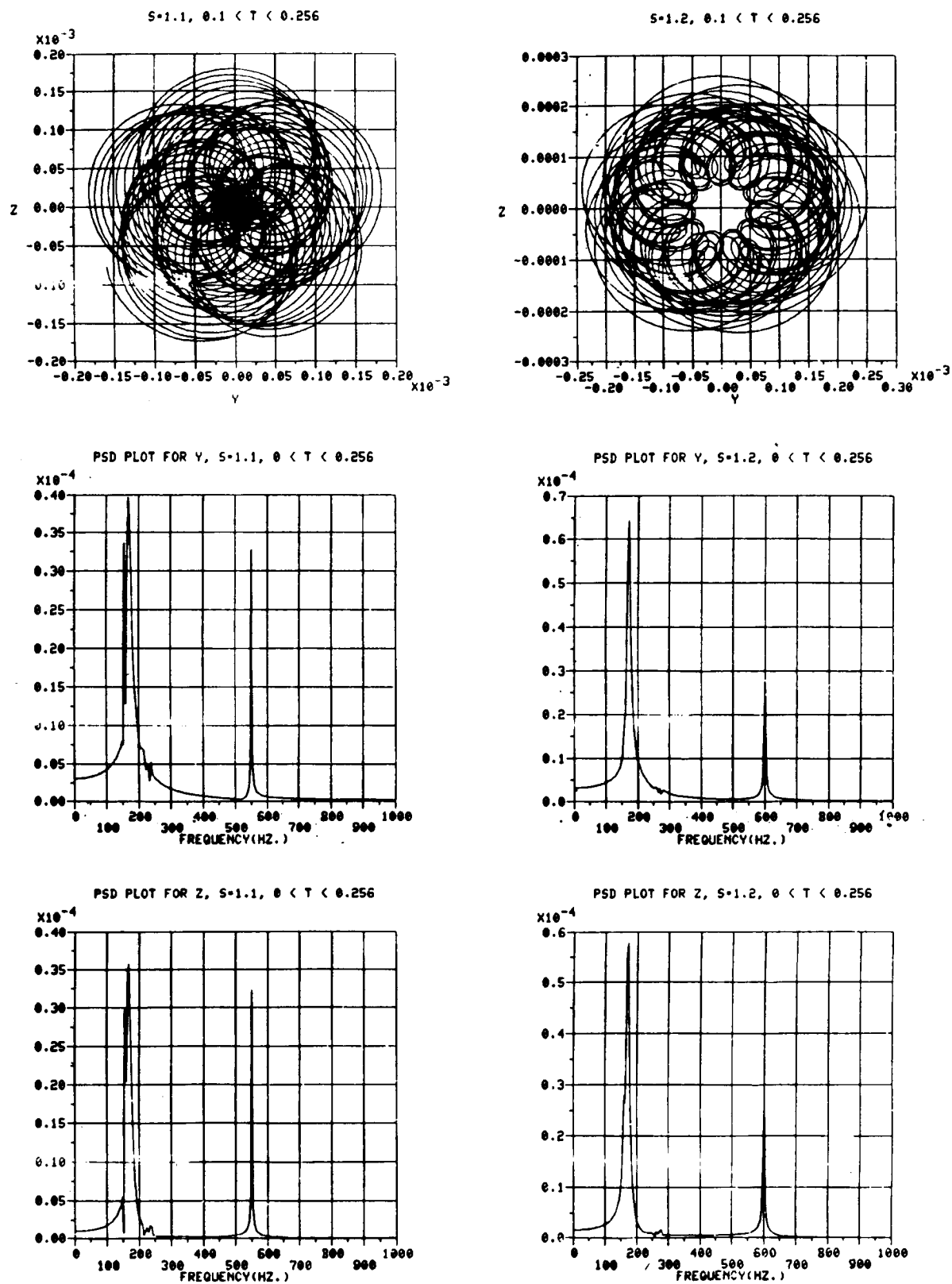


FIG. 3

ORIGINAL PAGE IS
OF POOR QUALITY

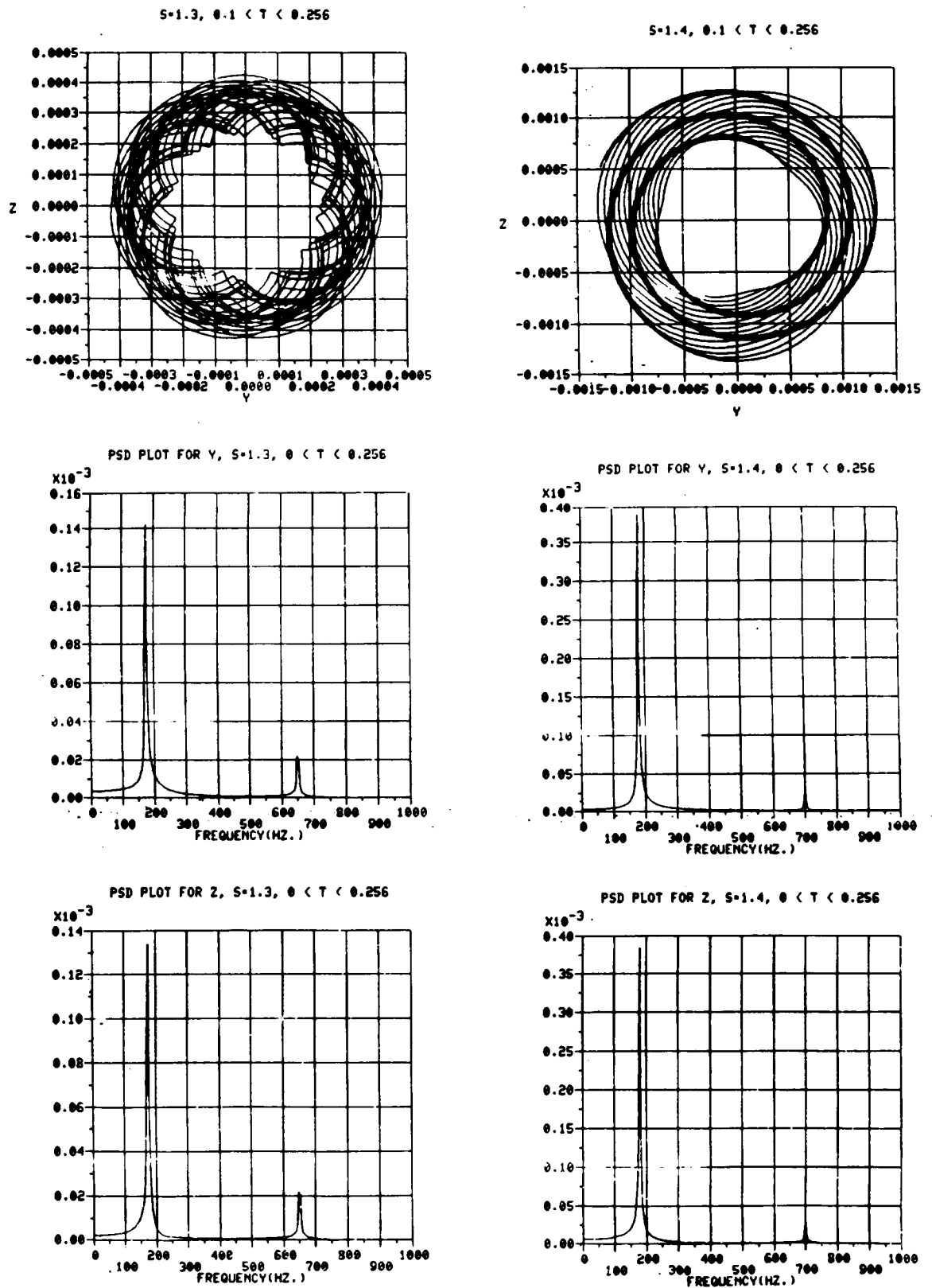
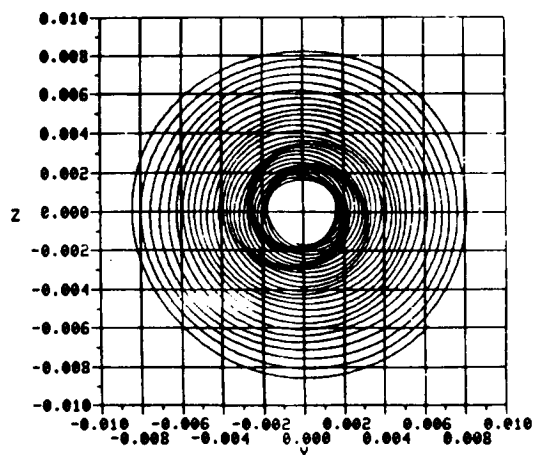


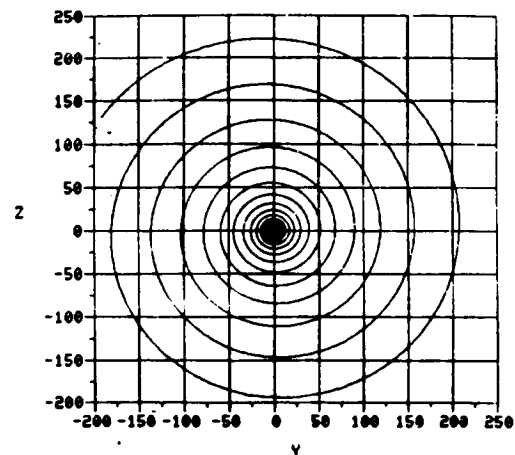
FIG. 4

ORIGINAL PAGE IS
OF POOR QUALITY

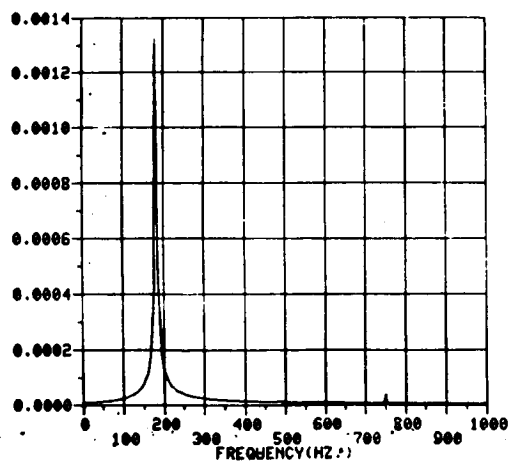
$S=1.5, 0.1 < T < 0.256$



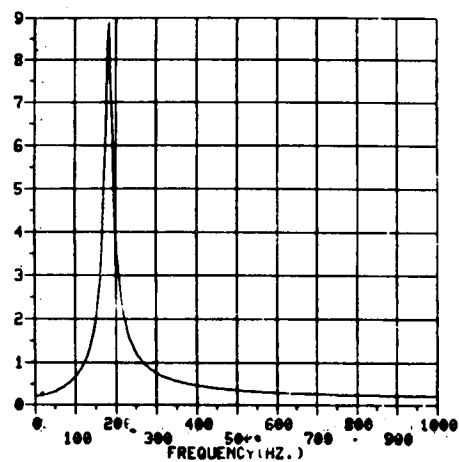
$S=2.0, 0.1 < T < 0.256$



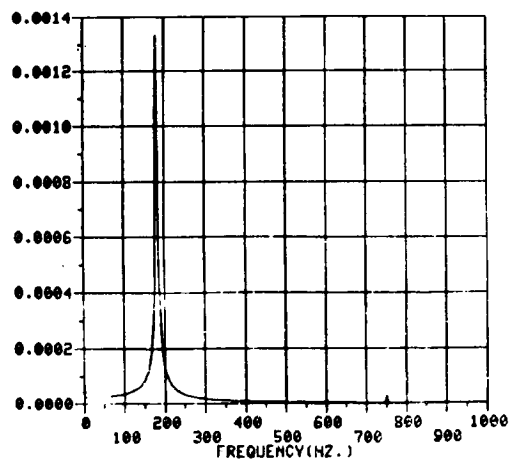
PSD PLOT FOR Y, $S=1.5, 0 < T < 0.256$



PSD PLOT FOR Y, $S=2.0, 0 < T < 0.256$



PSD PLOT FOR Z, $S=1.5, 0 < T < 0.256$



PSD PLOT FOR Z, $S=2.0, 0 < T < 0.256$

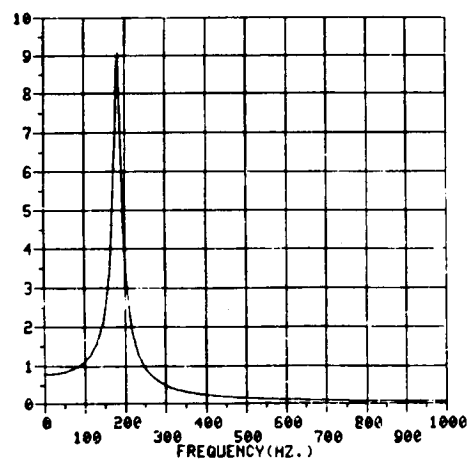


FIG. 5

COPYRIGHT PAGE IS
OF POOR QUALITY

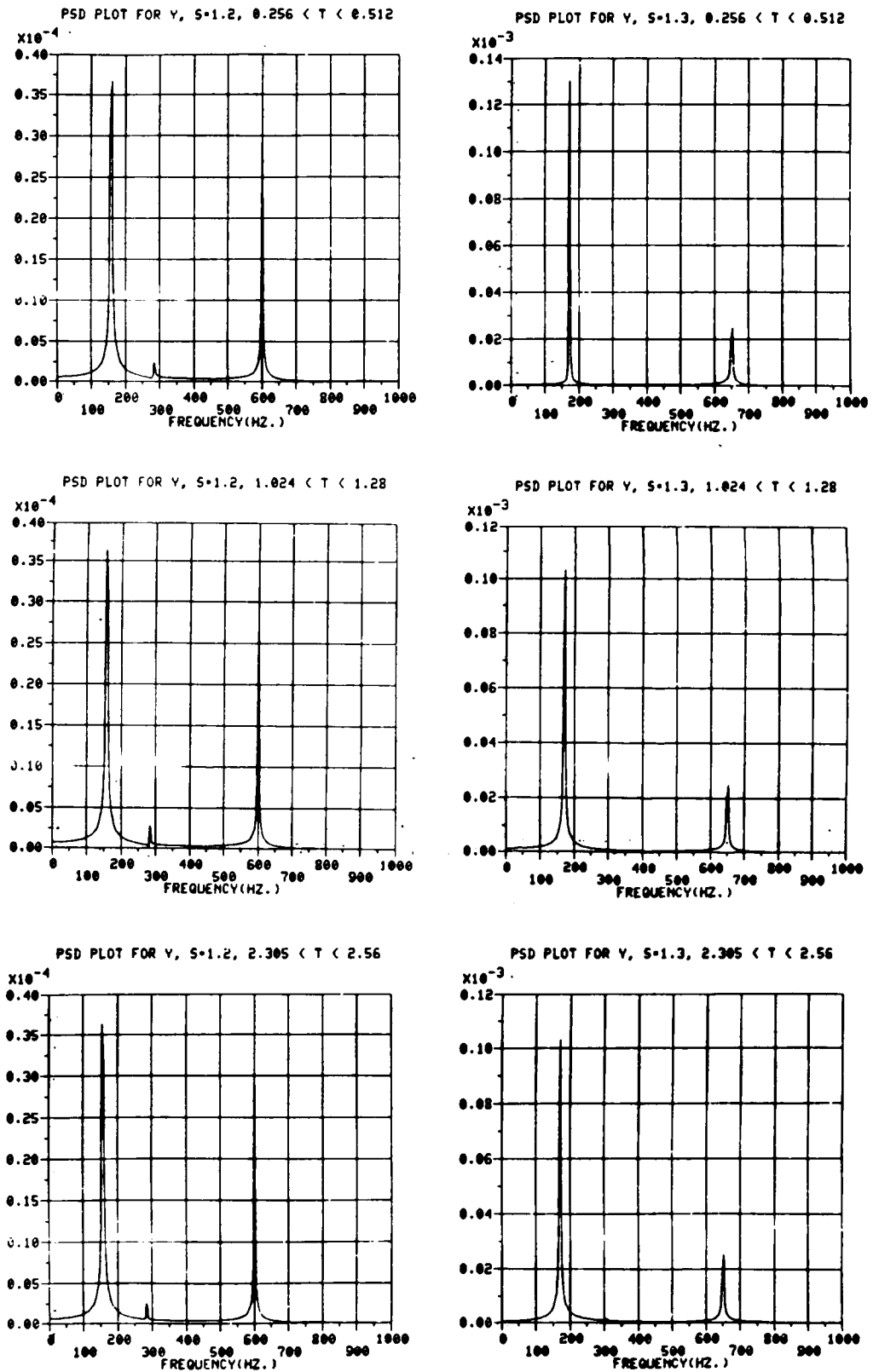


FIG. 6

ORIGINAL PAGE IS
OF POOR QUALITY

